

Books/Book Chapters/Conference Papers 2015-16

SI No.	Name of the Teacher	Title of the Paper/Books/Book Chapter	Title of the proceedings of the conference	Name of the conference	Natio nal/ Intern ationa l	Year of publicat ion	ISBN/ISS N number of the proceedin g	Affiliating Institute at the time of publication	Name of the Publisher
1	Y Madhu Maheswara Reddy, M Prasad, V S Ramesh Reddy	Thermal Analysis On Disc Brakes	Proceedings of the Int.Conf. on Paradigms in Engg and Tech. (ICPET-2016)	Int.Conf. on Paradigms in Engg and Tech. (ICPET-2016)	Intern ational	March 2- 3, 2016,	ISBN: 978-93- 5258-110- 9	Methodist College of Engg and Tech., Hyd	Methodist College of Engg and Tech., Hyd
2	Y Madhu Maheswara Reddy, M Prasad, V S Ramesh Reddy	Load Bearing Simulation Studies Of Various Honeycomb Structures For Use As Impact Barriers In Automobiles	Proceedings of the Int.Conf. on Paradigms in Engg and Tech. (ICPET-2016)	Int.Conf. on Paradigms in Engg and Tech. (ICPET-2016)	Intern ational	March 2- 3, 2016,	ISBN: 978-93- 5258-110- 10	Methodist College of Engg and Tech., Hyd	Methodist College of Engg and Tech., Hyd
3	A Rajasekhar	Testing and Estimation of mechanical properties of E- Glass (v-9) composite material	Proceedings of the Int.Conf. on Paradigms in Engg and Tech. (ICPET-2016)	Int.Conf. on Paradigms in Engg and Tech. (ICPET-2016)	Intern ational	March 2- 3, 2016,	ISBN: 978-93- 5258-110- 8	Methodist College of Engg and Tech., Hyd	Methodist College of Engg and Tech., Hyd
4	Dr. A Rajasekhar	Influence of Heat treatment on mechanical properties of Garter spring made by Zirconium alloy”	Proceedings of the Int.Conf. on Paradigms in Engg and Tech. (ICPET-2016)	Int.Conf. on Paradigms in Engg and Tech. (ICPET-2016)	Intern ational	March 2- 3, 2016,	ISBN: 978-93- 5258-110- 8	Methodist College of Engg and Tech., Hyd	Methodist College of Engg and Tech., Hyd
5	Dr. A Rajasekhar	Optimization of process parameters of Ultrasonic machining of Titanium”	Proceedings of the Int.Conf. on Paradigms in Engg and Tech. (ICPET-2016)	Int.Conf. on Paradigms in Engg and Tech. (ICPET-2016)	Intern ational	March 2- 3, 2016,	ISBN: 978-93- 5258-110- 8	Methodist College of Engg and Tech., Hyd	Methodist College of Engg and Tech., Hyd
6	R.Swetha,Dr.L. Siva Rama Krishna	Multi-objective optimization of EDM process parameters on Ti Alloy(BT20L) using Taguchi method and Grey Relational Analysis	Proceedings of the Int. Conf. on Paradigms in Engg and Tech. (ICPET-2016)	Int.Conf. on Paradigms in Engg and Tech. (ICPET-2016)	Intern ational	March 2- 3, 2016,	ISBN: 978-93- 5258-110- 8	MCET	NA
7	Y Madhu Maheswara Reddy, Dr P Usha Sri, M Prasad	Structural Analysis Of Automotive Disc Brakes	Proceedings of the Int.Conf. on Paradigms in Engg and Tech. (ICPET-2016)	Int.Conf. on Paradigms in Engg and Tech. (ICPET-2016)	Intern ational	March 2- 3, 2016,	ISBN: 978-93- 5258-110- 8	Methodist College of Engg and Tech., Hyd	Methodist College of Engg and Tech., Hyd
8	K Srinivasa Raghavan	Experimentation and characterization of CI engine Performance with Design Modifications in piston: by inducing turbulence	Proceedings of the Int.Conf. on Paradigms in Engg and Tech. (ICPET-2016)	International Conference on Paradigms in Engineering and technology (ICPET 2016).	Intern ational	March 2- 3, 2016,	ISBN: 978-93- 5258-110- 10	Methodist College of Engg and Tech., Hyd	Methodist College of Engg and Tech., Hyd

PRINCIPAL
METHODIST COLLEGE OF ENGG. & TECH.
 King Koti Road, Abids, Hyderabad

Books/Book Chapters/Conference Papers 2015-16

SI No.	Name of the Teacher	Title of the Paper/Books/Book Chapter	Title of the proceedings of the conference	Name of the conference	Natio nal/ Intern ationa l	Year of publicat ion	ISBN/ISS N number of the proceedin g	Affiliating Institute at the time of publication	Name of the Publisher
9	Lavanya Pamulaparty	Revealing of Near-Duplicate Web Documents in Software systems	International Conference On Paradigms In Engineering And Technology(ICPET – 2016)	International Conference On Paradigms In Engineering And Technology(ICPET – 2016)	Intern ational	March 2-3, 2016,	ISBN No. 978-93-5258-110-8	Methodist College of Engineering & Technology	Methodist College of Engineering & Technology
10	Lavanya Pamulaparty	Comparitive Analysis of Novel Text Steganographic Techniques with Character and Space Wrapping	International Conference On Paradigms In Engineering And Technology(ICPET – 2016)	International Conference On Paradigms In Engineering And Technology(ICPET – 2016)	Intern ational	March 2-3, 2016,	ISBN No. 978-93-5258-110-8	Methodist College of Engineering & Technology	Methodist College of Engineering & Technology
11	Vedala Rama Sastry and Garimella Raghu Chandra	Assessment of Seismic Energy obtained from Blast induced Ground Vibrations using Signal Processing Computation Techniques	2016 IEEE International Conference on Recent Trends in Electronics, Information & Communication Technology (RTEICT)	IEEE – International Conference on Recent Trends in Electronics Information and Communication Technology (RTEICT-2016)	Intern ational	21/May/16	ISBN: 978-1-5090-0774-5	National Institute of Technology, Karnataka, Surathkal	IEEE
12	V. Rama Sastry, G. Raghu Chandra, and C. Karthik	Ground vibrations & Water Borne Shock Waves caused due to Underwater Blasting in Ports – A Case Study	Proceedings of International Conference on Civil, Agricultural & Environmental Engineering (CAGEE-16)	International Conference on Civil, Agricultural & Environmental Engineering (CAGEE-16)	Intern ational	16th to 17th May 2016	ISBN: 978-93-84468-88-0	National Institute of Technology, Karnataka, Surathkal	IIE and URUAE Organizing Committee
13	V.R. Sastry, B. Rajasekhar, and G. Raghu Chandra	Assessing the Explosive Energy Utilization in Mine Blasting – Role of High Speed Videography	Proceedings Volume of National Conference on “Advanced Trends in Civil Engineering and Sustainable Development” [ATCESD-16]	National Conference on Advanced Trends in Civil Engineering and Sustainable Development	Nation al	26-27 Feb 2016	ISBN: 978--93--5258--252--5	National Institute of Technology, Karnataka, Surathkal	Mangalore Institute of Technology & Engineering, Moodabidri
14	Rajini Kanth P.	Mitigation of balanced and unbalanced voltage sag and improving the power quality using DVR	Proceedings of the International conference on Paradigms in Engineering and Technology	ICPET-2016	Intern ational	March 2-3, 2016,	ISBN: 978-93-5258-110-8	Methodist college of Engineering and Technology	Methodist College of Engineering and Technology
15	V. Saketha Reddy and M. Thirupathaiah	Power Quality Improvement in distribution systems using super capacitor based DVR	Proceedings of the International conference on Paradigms in Engineering and Technology	ICPET-2016	Intern ational	March 2-3, 2016,	ISBN: 978-93-5258-110-8	Methodist College of Engineering and Technology	Methodist College of Engineering and Technology
16	Ramesh Jatoth and Ramesh Babu Jarapala	Micro Genetic Algorithm Based Optimal Power Flow	Proceedings of the International conference on Paradigms in Engineering and Technology	ICPET-2016	Intern ational	March 2-3, 2016,	ISBN: 978-93-5258-110-8	Methodist College of Engineering and Technology	Methodist College of Engineering and Technology

PRINCIPAL
METHODIST COLLEGE OF ENGG. & TECH.
 King Kotl Road, Abids, Hyderabad

Books/Book Chapters/Conference Papers 2015-16

SI No.	Name of the Teacher	Title of the Paper/Books/Book Chapter	Title of the proceedings of the conference	Name of the conference	National/ International	Year of publication	ISBN/ISSN number of the proceeding	Affiliating Institute at the time of publication	Name of the Publisher
17	K. Pulla Reddy	A new proposal for mitigation of power quality problems using DSTATCOM	Proceedings of the International conference on Paradigms in Engineering and Technology	ICPET-2016	International	March 2-3, 2016,	ISBN: 978-93-5258-110-8	Methodist College of Engineering and Technology	Methodist College of Engineering and Technology
18	Dr.G.Aravind	Structure and Morphology of Co _{1-x} Cd _x Fe ₂ O ₄ nano ferrites by citrate gel auto combustion method”	International Conference on Science and Engineering of Materials for Future Needs (ICSEMF-2015)	International Conference on Science and Engineering of Materials for Future Needs (ICSEMF-2015)	International	21-22 December 2015	ISBN No: 978-1-329-77555-8		
19	Dr.G.Aravind	Editor of the Proceedings of the Two Day National Conference On Recent Advances in Applied Nano Materials	Two Day National Conference On Recent Advances in Applied Nano Materials	Two Day National Conference On Recent Advances in Applied Nano Materials	National	4-5 March 2016	978-93-5258-222-8	Methodist college of Engineering and Technology	
20	John William Carey M	“Study of Normal and Abnormal EEG Using Wavelets (Scopus Cited)	proceedings of the 2016 IEEE International Conference on Advanced Computing and Communication Systems	IEEE ICACCS-2016	INTERNATIONAL	22-23 JANUARY 2016			
21	Md. Fakhruddin H. N.	Phenomenon of Gravitational Waves Reaching the Earth Surface due to Black holes in Space		International conference on Paradigms in Engineering & Technology (ICPET)	International	March 2-3, 2016,		Methodist College of Engg and Tech., Hyd	
22	Md. Fakhruddin H. N.	Solar Powered Compressed Air Engine		International conference on Paradigms in Engineering & Technology (ICPET)	International	March 2-3, 2016,		Methodist College of Engg and Tech., Hyd	
23	Md. Fakhruddin H. N.	Experiment on Single Cylinder CI Engine with Various Proportion of WCOBD in Diesel		International conference on Paradigms in Engineering & Technology (ICPET)	International	March 2-3, 2016,		Methodist College of Engg and Tech., Hyd	
24	Md. Fakhruddin H. N.	Performance Test of Diesel Engine for Waste Cooking Oil Biodiesel Blended with Diesel		National Conference in Emerging Trends in Engineering & Technology, NCETET	National	2016		Methodist College of Engg and Tech., Hyd	
25	Dr P Shailesh	Preparation and characterization of GFRPC material		5rd International Conference of Material Processing and Characterization (ICMPC 2016).	International	2016		Methodist College of Engg and Tech., Hyd	

PRINCIPAL
METHODIST COLLEGE OF ENGG. & TECH.
 King Koti Road, Abids, Hyderabad

Books/Book Chapters/Conference Papers 2015-16

SI No.	Name of the Teacher	Title of the Paper/Books/Book Chapter	Title of the proceedings of the conference	Name of the conference	National/ International	Year of publication	ISBN/ISSN number of the proceeding	Affiliating Institute at the time of publication	Name of the Publisher
26	U S Varaprasad, K.Madhu Murty, G. AmbaPrasadRao, M.Vinod Babu	Influence of FUEL INJECTION PARAMETERS on the performance & emissions of CI engine with neat biodiesel		Int.Conf. on Paradigms in Engg and Tech. (ICPET-2016)	International	March 2-3, 2016,		MCET	
27	B.Naik,P. Singh, K.K.Khatua	Different techniques for boundary shear stress predictions for open channel flow	National	National Conference on Water Recourses and Hydro Power	National	17-18 JUNE 2016		Civil Engg. Deptt. UPES, Dehradun	
28	E SHAILAJA	A STUDY ON NATURE INSPIRED METAHEURISTIC ALGORITHMS	INTERNATIONAL CONFERENCE ON PARADIGMS IN ENGINEERING AND TECHNOLOGY	ICPET 2016	INTERNATIONAL	March 2-3, 2016,	978-93-5258-110-8	MCET	
29	T. Sravan Kumar	Optimization Technique of Digital FIR Filter Coefficients using Genetic Algorithm	INTERNATIONAL CONFERENCE ON PARADIGMS IN ENGINEERING AND TECHNOLOGY	International Conference on Paradigms in Engineering and technology (ICPET 2016).	INTERNATIONAL	March 2-3, 2016,		MCET	
30	Dr.K.Anuradha Reddy	Electrical Studies in Silver Doped Gallium Oxide Glasses	National Conference On Recent Advances in Applied Nano Materials NCRAANM-2016	National Conference On Recent Advances in Applied Nano Materials NCRAANM-2016	National	4-5 March 2016	978-93-5258-222-8		
31	Md. Fakhruddin H. N.	4 Stroke Engine with 2 Power Strokes		2nd International Conference on Innovative Research in "Mechanical	International	22nd to 23rd August 2015		Methodist College of Engg and Tech., Hyd	
32	Bandita Naik , K. K. Khatua, S. S. Satapathy	A multi variable regression model for prediction Water surface profile in a converging compound channels	Hydro-2015 International	20th International Conference on Hydraulics, Water Resources and River Engineering	International	17-19 DECEMBER 2015		IIT Roorkee	
33	Shiba Shankar Satapathy, B. Naik, Rahul Sahoo, K.K. Khatua	Flow Modelling of Boundary Shear Stress Distribution for a Converging Compound Channel using ANSYS	Hydro-2015 International	21st International Conference on Hydraulics, Water Resources and River Engineering	International	17-19 DECEMBER 2015		IIT Roorkee	

PRINCIPAL
METHODIST COLLEGE OF ENGG. & TECH.
 King Koti Road, Abids, Hyderabad

Books/Book Chapters/Conference Papers 2015-16

Sl. No.	Name of the Author	Title of the Paper/Book/Book Chapter	Title of the Journal/Conference	National/International	Year	ISBN/ISS	Page No.

is, Hyderabad

King Koti Road, Ab

Thermal Analysis on Disc Brakes

M Prasad
Assistant Professor, Mechanical
Engineering Department,
Methodist Coll. of Engg. &Tech.
Hyderabad, India.
prasadamatam@gmail.com.

Y Madhu Maheswara Reddy
Asst Professor, Mechanical
Engineering Department
Methodist Coll. of Engg. &Tech.
Hyderabad, India.
mmr315@gmail.com.

VS Ramesh Reddy
Asst. Professor, Mechanical
Engineering Department,
Methodist Coll. of Engg. &Tech.
Hyderabad, India.
vsreddy@gmail.com.

Abstract—Braking system is one of the most essential functions of an automobile. Therefore, it is a must for all vehicles to have proper brake system. Due to critical system in the vehicle, many of researchers have conducted a study on brake system and its entire component. In this project, we has conducted a study on normal & drilled disc brake rotor of normal passenger vehicle with full load of capacity. The study is more likely concern of heat and temperature distribution on disc brake rotor .The motive of undertaking this project of "Thermal Analysis of Disc Brake" is to study and evaluate the performance under severe braking conditions and there by assist proper design of disc rotor out of thermal analysis. Transient state response has been conducted through the heat transfer analysis where to predict the worse case scenario and temperature behaviors of disc brake rotor. In this study, finite element analysis approached has been conducted in order to identify the temperature distributions and behaviors of disc brake rotor in transient responses. Ansys has been used as finite elements software to perform the thermal analysis on responses. Thus, results provide better understanding on the thermal characteristic of disc brake rotor and assist the automotive industry in developing optimum and effective disc brake rotor.

Keywords: *Disc Brake, Ansys, Temperature, Solid works*

I. INTRODUCTION

Brakes are most important safety parts in the vehicles. Generally all of the vehicles have their own safety devices. Brakes function to slow and stop the rotation of the wheel. To stop the wheel, braking pads are forced mechanically against the rotor on both surfaces. They are compulsory for all of the modern vehicles and the safe operation of vehicles. In short, brakes transform the kinetic energy of the vehicle into heat energy, thus slowing its speed.

The braking system must be decelerate a vehicle in a controlled and repeatable fashion and when appropriate cause the vehicle to stop. The braking should permit the vehicle to maintain a constant speed when traveling downhill. The braking system must hold the vehicle stationary when on the flat or on a gradient.

Nowadays, there are lot of software has been developed in order to cater the modeling and the finite element analysis on the vehicle component such as (Automatic Dynamic of Mechanical Systems), SOLIDWORKS, ANSYS. There is an advantage of using that powerful computational analysis

software where by using those would make it easier, less cost better accuracy and less computing time. Most of the software is used in the wide range of industries such as automotive, oil and gas, aerospace, marine, heavy duty engineering, construction, electro-mechanical and general mechanical industries. In this project, design package SOLIDWORKS and finite element package will be used to generate model and run analysis on the chosen component.

II. STATEMENT OF PROBLEM

Beside overall automotive parts, like engines, there are more crucial parts that engineers need to look into consideration. Suspension, brake, electrical, hydraulic and gear are all the crucial systems in the automotive areas. Each of the parts has their own functionality which brings life to the automation industries. Brakes are the crucial system in stopping the vehicle on all moving stages including braking during high speed, sharp cornering, traffic jam and downhill. All of those braking moments give a different value of temperature distribution and thermal stress. Good performance of disc brake rotor comes from good material with better mechanical and thermal properties. Good designs of disc brake rotor are varying across the range of the vehicles. There are different design and performance of disc brake rotor if compared between passenger, commercial and heavy duty vehicle. There are also other constraints such as cost, weight, manufacturing capability, robustness and reliability, packaging, maintenance and servicing.

This paper concerns of the temperature distribution and constraint of the disc brake rotor. Most of the vehicles today have disc brake rotors that are made of grey cast iron Grey cast iron is chosen for its relatively high thermal conductivity, high thermal diffusivity and low cost . In this paper, we will investigate on the thermal issues of normal two wheeler motor vehicle disc brake rotor, where the investigation is to determine the temperature behavior of the disc brake rotor due to severe braking of the disc brake rotor by using Finite Element Analysis (FEA).

Braking performance of a vehicle can be significantly affected by the temperature rise in the brake components. High temperature during braking will caused to Brake fade, premature wear, Brake fluid vaporization, Bearing failure, Thermal cracks, Thermally-excited vibration. Therefore, it is important to study and predict the temperature rise of a given

brake component and assess its thermal performance in the early design stage. Finite element analysis (FEA) has been preferred and chosen method to investigate some of the above concerns such as disc brake rotor temperature rise and thermal cracks.

III. RESEARCH METHODOLOGY

Begin with a literature review, a lot of paper and journal has been read up and a part of it has been considered in this paper. Meanwhile, vernier calipers and steel rule used to measure the major coordinate of real disc brake rotor. Later, the precise dimensions have been used to translate in 2D and 3D drawing by using SOLIDWORKS.

In the second stage, load analysis has been done where the heat flux and convectional heat transfer coefficients has been calculated. Load analysis calculated based on full load of passenger in the two wheeler vehicle. Later, value of load analysis has been applied on finite element analysis. Next fractional 3D model of disc brake rotor has been transfer to hyper mesh where the inputs are given. Assigning material properties, load and meshing of the model has been done in this stages. Then, completed meshing model has been submitted for analysis. Now the 3D model of disc brake rotor has been transfer to finite element software which is ANSYS. Thermal analysis has been done on transient responses. Finally an expected result from the transient responses of thermal analysis has been obtained.

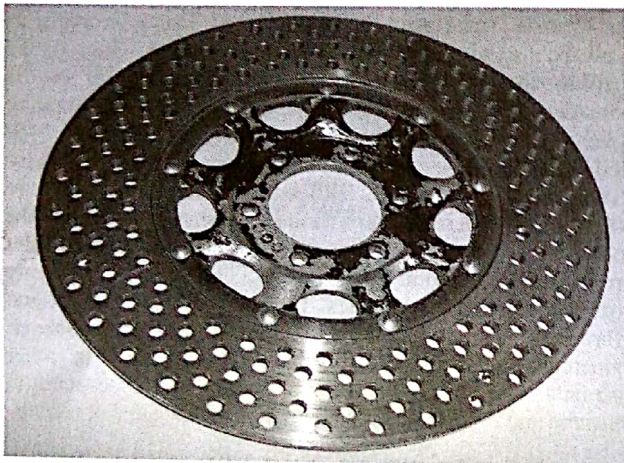


Fig1: Drilled Disc

A. Modeling Softwares

Some of the different software's available for 3D modeling are

- Solid works
- Pro E
- Inventor
- Mechanical desktop
- Unigraphics
- Catia

The Solid Works CAD software is a mechanical design automation application that lets designers quickly sketch out ideas, experiment with features and dimensions, and produce models and detailed drawings.

General Modeling Process for Each Part

- Plan the part
- Create the base feature
- Create the remaining features
- Analyze the part
- Modify the features as necessary

B. Types of modes

3 modes in solid works;

- part modeling
- assembly
- part drawing

C. Part Modeling

A 2D engineering drawing, typically a part or assembly. Parts are the building blocks of every Solid Works model. Each assembly and drawing you create is made from parts.

D. Assembly

A 3D arrangement of parts and other assemblies. In this section, you use the vanity cabinet parts described and built in Parts to build subassemblies, such as the spigot and the faucet handles. Then you bring the subassemblies together to create an assembly, the vanity.

E. Part Drawing

A 3D representation of a single design component. Drawings are 2D documents that convey a design to manufacturing.

IV. THERMAL ANALYSIS

A thermal analysis calculates the temperature distribution and related thermal quantities in brake disk. Typical thermal quantities are

- The temperature distribution
- The amount of heat lost or gained
- Thermal fluxes

A. Types of thermal analysis

- A steady state thermal analysis determines the temperature distribution and other thermal quantities under steady state loading conditions. A steady state loading condition is a situation where heat storage effects varying over a period of time can be ignored.
- A transient thermal analysis determines the temperature distribution and other thermal quantities under conditions that varying over a period of time.

B. Planning the analysis

In this step a compromise between the computer time and accuracy of the analysis is made. The various parameters set in analysis are given below

C. Thermal modeling:

- Analysis type .thermal h-method.
- Steady state or Transient? Transient
- Thermal or Structural? Thermal
- Properties of the material? Isotropic
- Objective of analysis- to find out the temperature distribution in the brake disc
- when the process of braking is done
- Units- SI

D. Modeling and analysis

It is very difficult to exactly model the brake disk, in which there are still researches are going on to find out transient thermo elastic behavior of disk brake during braking applications. There is always a need of some assumptions to model any complex geometry. These assumptions are made, keeping in mind the difficulties involved in the theoretical calculation and the importance of the parameters that are taken and those which are ignored. In modeling we always ignore the things that are of less importance and have little impact on the analysis. The assumptions are always made depending upon the details and accuracy required in modeling. The assumptions which are made while modeling the process are given below

- The disk material is considered as homogeneous and isotropic.
- The domain is considered as axis-symmetric.
- Brakes are applied on the entire both sides.
- The specific heat of the material used is constant throughout and does not change with temperature.
- The kinetic energy of the vehicle is lost through the brake disks i.e. no heat loss between
- The tyre and the road surface and deceleration is uniform.
- The disk brake model used is of solid type.
- The thermal conductivity of the material used for the analysis is uniform throughout.
- Only ambient air-cooling is taken into account and no forced Convection is taken

E. Specifications Of Vehicle And Vehicle Disc

- Manufacturer's Name: KTM-Sport motorcycle AG.
- Model Identification Name : KTM 200 DUKE
- Minimum weight :129.5 kg
- Vehicle weight considered with fuel + person weight : 200kg
- Type of Engine : Four Stroke
- Cubic capacity : 199.50 cc

Brakes

- Type of brake : Disc brakes
- Number of pads per wheel : 2
- Number of calipers per wheel : 1
 - Caliper Material : Aluminum Alloy
 - Thickness of new disc : 4 ± 0.1 4 ± 0.1 mm
 - External diameter of disc : 280 ± 0.3 230 ± 0.3 mm
- External diameter of pads rubbing surface : 280 ± 0.2 229 ± 0.2 mm
 - Internal diameter of pads rubbing surface : 224 ± 0.2 169 ± 0.2 mm
- Overall friction length of pads : 68.4 ± 0.3 55 ± 0.3 mm
- Number of pistons per caliper : front wheel: 4
- Rear wheel: 1
- Outer Diameter of piston in caliper front wheel: 28 mm rear wheel : 32 mm

Finite Element Formulation for Heat Conduction

$$\text{Kinetic energy} = 0.5m(v_1^2 - v_2^2) \text{ J}$$

Heat Generated (Qg) = Kinetic Energy generated / unit breaking time W

$$\text{Rubbing Surface area of the Rotor \& Pad } (A_r) = \pi(r_1^2 - r_2^2) \text{ m}^2$$

$$\text{Heat Flux } (q) = \text{Heat Generated} / \text{Rubbing Surface area of Rotor \& Pad } (W/m^2)$$

F. Modeling Drilled rotor

The 3D modeling of drilled rotor of KTM Duke 200 is done in CAD software - Solid works 2012. It is done in Part modeling mode by considering the dimensions mentioned in the above specification of the vehicle.

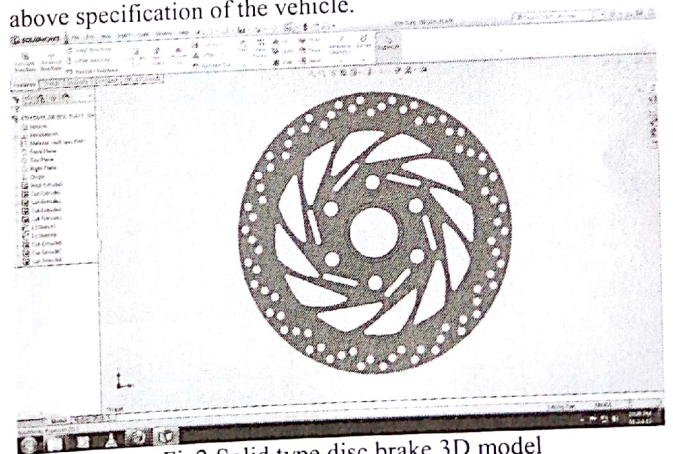


Fig2:Solid type disc brake 3D model

G. Calculations(Drilled Disc)

Weight of the vehicle including body weight = 200 Kg
 Velocity of the vehicle (v_1) = 70 KMPH
 Velocity of the vehicle is decelerated to (v_2) = 20 KMPH
 Braking time = 4 sec
 Kinetic energy = $0.5 \times 200 \times (19.44^2 - 5.55^2)$
 = 34705.5575 joule
 Heat generated (Qg) = kinetic energy generated/ braking time
 = $34705.5575/4$
 = 8676.38 watt

Rubbing surface area of pad and rotor (A_r) = area of rotor contact with brake pad - area of drilled holes

$$[\pi (d_1^2 - d_2^2)/4] - [(\pi d_{drills}^2/4) \times \text{no. of drills}]$$

$$[\pi \times (280^2 - 223.8^2)/4] - [(\pi \times 8^2/4) \times 75 \text{ drills}]$$

$$22237.41 - 3769.9 = 18467.50 \text{ mm}^2 = 0.018467 \text{ m}^2$$

Heat flux (q) = heat generated / rubbing area
 = $8676.38/0.018467$
 = 469810 w/m²

H. Meshing in Hypermesh

The 3d model of drilled rotor which was done in solid works is imported to hyper mesh to proceed for meshing.

Inputs

Material Properties

Material of disc rotor = cast iron (< 4% C)
 Density of cast iron (ρ) = 7272 kg/m³
 Young's modulus (E) = 125×10^9 N/m²
 Specific heat (Cp) = 420 J/kg k
 Thermal conductivity (k) = 520. W/m k
 Heat flux (q) = 469810 w/m²

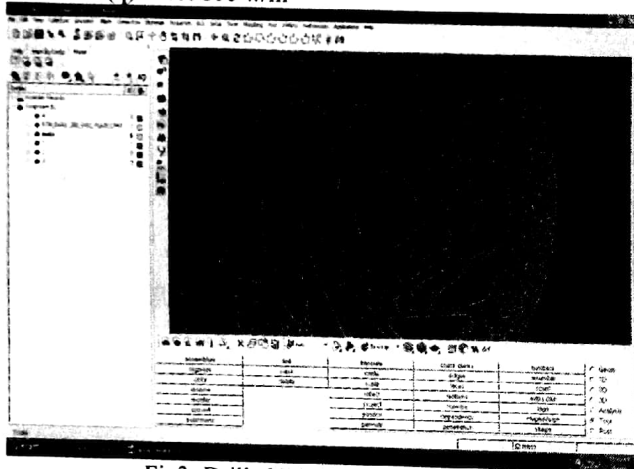


Fig3: Drilled Disc Brake Mesh Model

Number of nodes: 9512

Heat generated per unit element: 471.77

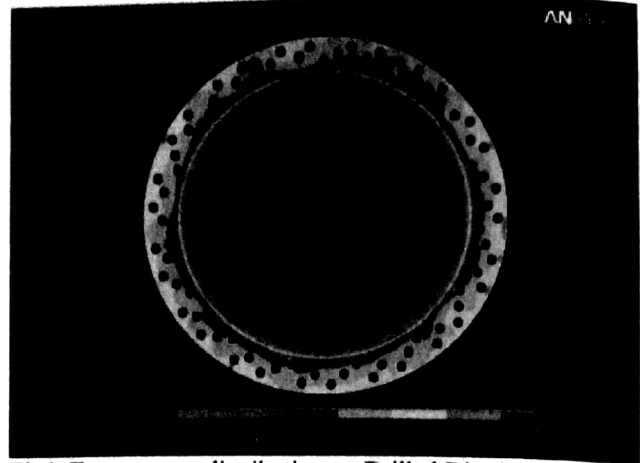


Fig4: Temperature distribution on Drilled Disc brake on the front side

The 3D modeling of drilled rotor of KTM Duke 200 is done in CAD software - Solid works 2012. It is done in Part modeling mode by considering the dimensions mentioned in the above specification of the vehicle.

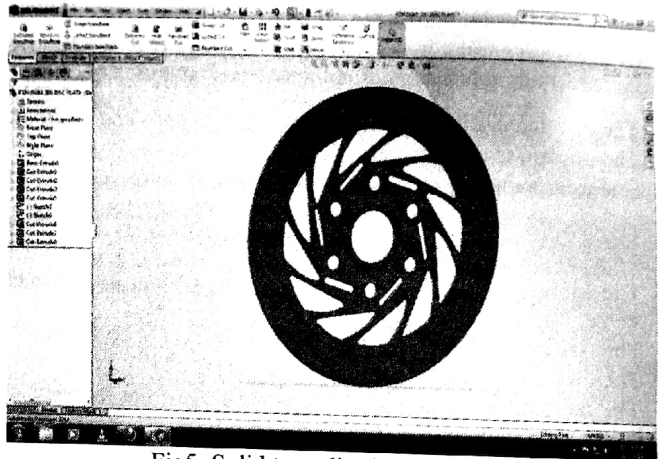


Fig5: Solid type disc brake 3D model

Calculations (Solid Disc)

Weight of the vehicle including body weight = 200 Kg
 Velocity of the vehicle (v_1) = 70 KMPH
 Velocity of the vehicle is decelerated to (v_2) = 20 KMPH
 Braking time (t) = 4 sec
 Kinetic energy = $0.5 \times 200 \times (19.44^2 - 5.55^2)$
 = 34705.5575 joule
 Heat generated (Qg) = kinetic energy generated/ braking time
 = $34705.5575/4$
 = 8676.38 watt
 Rubbing surface area of pad and rotor (A_r) = $[\pi (d_1^2 - d_2^2)/4]$
 $\pi \times (280^2 - 223.8^2)/4$
 = 22237.41802mm²
 = 0.0222374102 m²

Heat flux (q)

= Heat Generated / Rubbing Area
 = $8676.38/0.0222374102$
 = 390100 w/m^2

paper we had studied about the process of thermal analysis in disc brake. Here by we studied that the temperature in the drilled disc is more compared to the normal disc.

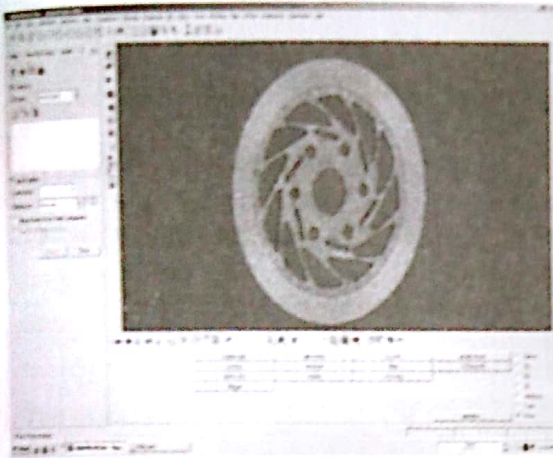


Fig6: Solid type disc brake mesh model
 Number of nodes: 11972
 Heat generated per unit element: 471.77

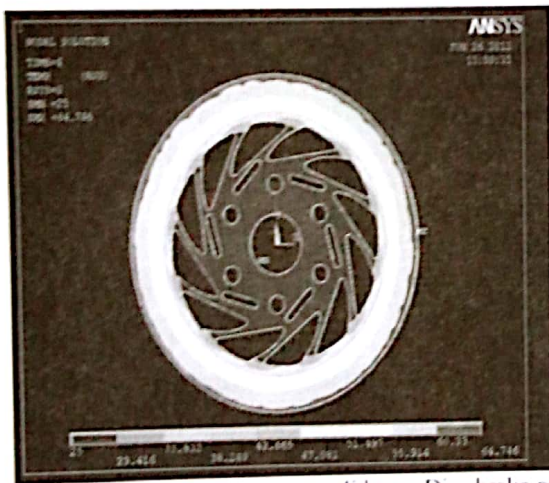


Fig7: Temperature distribution on solid type Disc brake on the front side

V. CONCLUSION

In general discussions, the associates of mechanical engineering opine that more heat is generated in a normal disc is more than in a drilled disc during the braking process. This study provides a clear analysis on the heat generated in both the cases. Nevertheless, More convection can be observed in drilled disk which lead to the above notion.

The present study can provide a useful design tool and improve the brake performance of disc brake system. In this

REFERENCES

- [1] ISHWAR GUPTA, GAURAV SAXENA (2013), (ISSN(Print): 2277-4785) Structural Analysis Of Rotor Disc Of Disc Brake Of BAJA SAE 2013 Car Through Finite Element Analysis, International Journal of Automobile Engineering Research and Development.
- [2] V.CHENGAL REDDY, M.GUNASEKHAR REDDY, DR. G. HARINATH GOWD (2012), Modelling & Analysis of FSAE Car Disc Brake Using FEM. International Journal of Emerging Technology & Advanced Engineering Volume 3, Issue 9, ISSN 2250-2459
- [3] MATT LOMBARD.(Solid Works 2012) for basic model design. Published By wiley
- [4] What'sNew - 3D CAD Design Software SolidWorks. BY Solid works tutorial
- [5] METALS HANDBOOK VOLUME 1, Properties & Selection. Iron, Steel & High Performance Alloys, American Society of Metals Inc.
- [6] SAE HANDBOOK VOLUME 1, Materials by Society of Automotive Engineers Inc.
- [7] ROTOR DISC MANUALS (2013), Qingdao Allsuper International Trade Co., Ltd. China.
- [8] ANSYS HELP FILE (2014), made By ANSYS Inc. USA
- [9] SAEED MOAVENI (1999), (ISBN-0-13-785098-0) Finite Element Analysis Theory & Application with ANSYS, Prentice Hall Publications.
- [10] BAJA SAE INDIA RULE BOOK (2013), Published by Society of Automotive Engineers Inc.
- [11] C.P. KOTHANDARAMAN, S.SUBRAMANYAN. (Heat And Mass Transfer Data Book). Published By New Age International Publishers. Seventh Edition.(2010).
- [12] R.K.RAJPUT. (Heat And Mass Transfer) for problems. Published By S.Chand & Company Ltd. Third Revised Edition.(2006).

Load Bearing Simulation Studies of Various Honeycomb Structures for Use as Impact Barriers in Automobiles

VS Ramesh Reddy
Assistant Professor, Mechanical
Engineering Department
Methodist College of Engg. & Tech.
Hyderabad, India
Vsrreddy.mtech@gmail.com

M. Prasad
Asst Professor, Mechanical
Engineering Department
Methodist College of Engg. & Tech.
Hyderabad, India
prasadmatam@gmail.com

Y Madhu Maheswara Reddy
Asst. Professor, Mechanical
Engineering
Methodist College Of Engg. & Tech.
Hyderabad, India
mnr315@gmail.com

Abstract: The present work studied the efficiency of the square shaped honey comb structures under different minute variation of the cells aspect ratios, rib thickness for these different materials Aluminium 1060 alloy, E-GLASS & S2-GLASS in with standing the loads that could arise in impact in impact of automobiles collisions. The width of the cells was studied in 3 different variations namely

- Equal width in 'x' and 'z' direction
- Width in 'x' direction > 'z' direction
- Width in 'z' direction > 'x' direction

The thickness of the ribs was studied under 2 different conditions

- Thickness of ribs in 'z' direction > that of in 'x' direction
- Thickness of ribs in 'x' direction > that of in 'z' direction

All the various conditions in the geometry of square cell honey comb structure are carried out under the condition of contact volume & weights of the structure, thus making that impact resistance comparison relevant. The rib thickness varies are adjusted subjected to this important constraints of constant weight of the material in all the impact barriers thus making the comparison of different designs meaningful as it is independent of weight or mass density for a given material.

1. INTRODUCTION

This project gives better shape for textile composite impact barriers by analyzing results using FEM based software COMSOL for impact analysis on

honey comb box type and triangular and hexagonal models, Solid Works software to model 3D models of honeycomb structures. This is going to help in finding out a alternative geometric shape which can be used as a replacement to the traditional hexagonal honeycomb structure and which can help in reducing the delimitation problem of honeycomb structure.

- Selection of different geometric structures for better inner cores
- Selection of different materials (composite fibers).

- Use of solid Works to prepare 3D models.
- Use of COSMOS to perform analysis.
- Comparison of results of different geometric structures with traditional-hexagonal honeycomb structure.
- To provide a best suitable alternative for traditional hexagonal honeycomb structure.

2. MATERIALS

Composite Material For the specific carbon and glass fiber based composite materials often referred to loosely as 'composites' Composites are formed by combining materials together to form an overall structure that is better than the individual components.

Composite materials (also called composition materials or shortened to composites) are materials made from two or more constituent materials with significantly different physical or chemical properties that when combined, produce a material with characteristics different from the individual components. The individual components remain separate and distinct within the finished structure. The new material may be preferred for many reasons: common examples include materials which are stronger, lighter or less expensive when compared to traditional materials. Typical engineered composite materials include:

3. HONEYCOMB STRUCTURES

Honeycomb structures are natural or man-made structures that have the geometry of a honeycomb to allow the minimization of the amount of used material to reach minimal weight and minimal material cost. The geometry of honeycomb structures can vary widely but the common feature of all such structures is an array of hollow cells formed between thin vertical walls. The cells are often columnar and hexagonal in shape. A honeycomb shaped structure provides a material with

minimal density and relative high out-of-plane compression properties and out-of-plane shear properties.

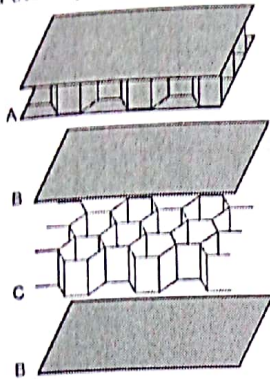


Figure 3.1 A composite sandwich panel (A) With honeycomb core (C) and face sheets (B)

Man-made honeycomb structural materials are commonly made by layering a honeycomb material between two thin layers that provide strength in tension. This forms a plate-like assembly. Honeycomb materials are widely used where flat or slightly curved surfaces are needed and their high strength-to-weight ratio is valuable. They are widely used in the aerospace industry for this reason, and honeycomb materials in aluminum, fiberglass and advanced composite materials have been featured in aircraft and rockets since the 1950s. They can also be found in many other fields, from packaging materials in the form of paper-based honeycomb cardboard, to sporting goods like skis and snowboards.

3.1 Applications

1. They are widely used in the aerospace industry.
2. They are widely used in the aerospace industry.
3. From packaging materials in the form of paper-based honeycomb cardboard, to sporting goods like skis and snowboards.
4. Used as front barriers in heavy vehicles.
5. Used in Automobile industries.

3.2 Advantages

1. Very low weight
2. High stiffness
3. Durability
4. Production cost savings

4. RESEARCH METHODOLOGY

Selection of different geometric structures for better inner cores: It is important to understand the stiffness and strength performances of honeycombs when they are used in load-bearing

structure. Gibson and Ash-by (1997) specified that generally, if a honeycomb is compressed in-plane that is the plane along X1 and X2 direction in Figure 3, the cell wall at first bend, giving linear elastic deformation. Beyond a critical strain, the cells collapse by elastic buckling, plastic yielding, creep or brittle fracture, depending on the nature of the cell wall material. Cell collapse ends once the opposing cell walls begin to touch each other and as the cells closed up, the stiffness of the structure increases rapidly. When the loading is along out-of-plane direction, which is along X3 direction in Figure 3, the stiffness and strength are much higher because they require extra axial extension or compression of the cell walls.

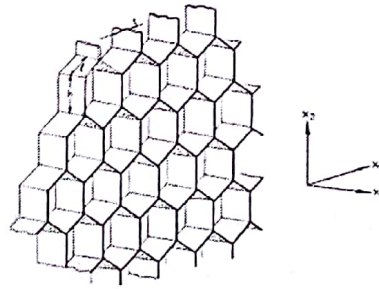
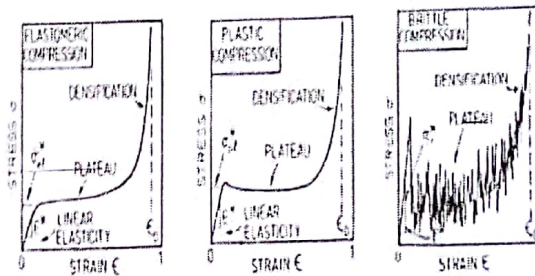


Figure 4.1: Honeycomb structure with hexagonal cells



Graph 4.2 Stress-Strain Curves for Cellular Solid

5. RESULTS

5.1. Various geometric configurations analyzed by using solid works

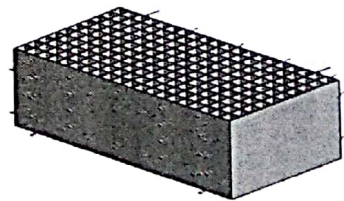


Fig.5. Basic Geometry of square type honeycomb structure Case-I ($t_x=t_y$) [Al 1060 alloy, E-glass&S2-glass]

5.1.1 Various geometric configurations analyzed by using solid works Case-I ($t_x=t_y$) [Al 1060 alloy, E-glass&S2-glass)

Case-I	L_x	$L_y=L_y$	L_z	l_x	l_z	t_x	t_z	T_x	T_z	nc_x	nc_z
$t_x=t_z$	442	222	222	20	20	2	2	42	22	20	10

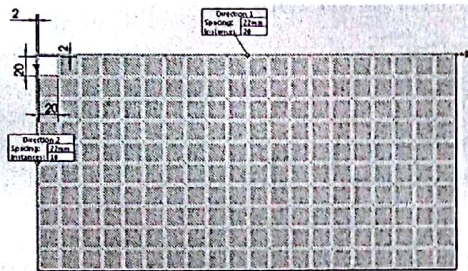


Fig. 5.1.1 Geometric configuration of case-I

5.1.2 Various geometric configurations analyzed by using solid works Case-II ($t_x>t_y$) [Al 1060 alloy, E-glass&S2-glass)

Case-II	L_x	$L_y=l_y$	L_z	l_x	l_z	t_x	t_z	T_x	T_z	nc_x	nc_z
$t_x>t_z$	442	222	222	20	20	3	1	63	11	20	10

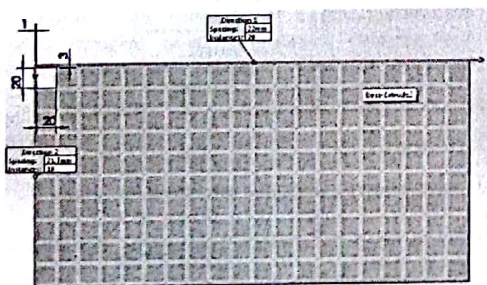


Fig. 5.1.2 Geometric configuration of case-II

5.1.3 Various geometric configurations analyzed by using solid works: CASE-III ($t_z > t_x$) [Al 1060 alloy, E-glass&S2-glass)

Case-III	L_x	$L_y=l_y$	L_z	l_x	l_z	t_x	t_z	T_x	T_z	nc_x	nc_z
$t_z>t_x$	442	222	222	21.164	18.9	0.89141	3	18.79	33	20	10

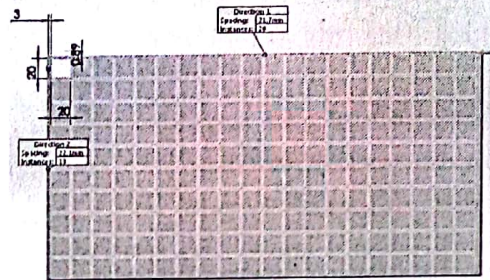


fig. 5.1.3 Geometric configuration of case-III

5.1.4 Various geometric configurations analyzed by using solid works: CASE-IV ($T_z>T_x$) [Al 1060 alloy, E-Glass&S2-Glass)

Case-IV	L_x	$L_y=l_y$	L_z	l_x	l_z	t_x	t_z	T_x	T_z	nc_x	nc_z
$T_z>T_x$	442	222	222	40	20	3.818	2	18.79	33	20	10

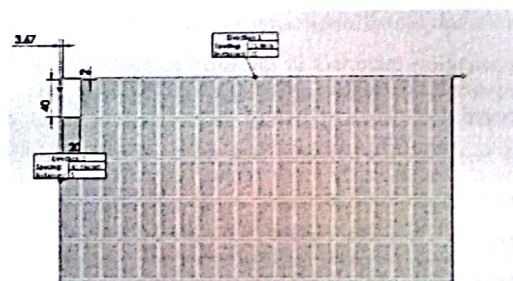


Fig. 5.1.4 Geometric configuration of case-IV

5.1.5 Various geometric configurations analyzed by using solid works: CASE-V ($T_x > T_z$) [Al 1060 alloy, E-Glass & S2-Glass]

Case-V	Lx	L _y =ly	Lz	lx	lz	tx	tz	Tx	Tz	ncx	ncz
Tz>Tx	442	222	222	21.164	18.9	0.89141	3	18.79	33	20	10

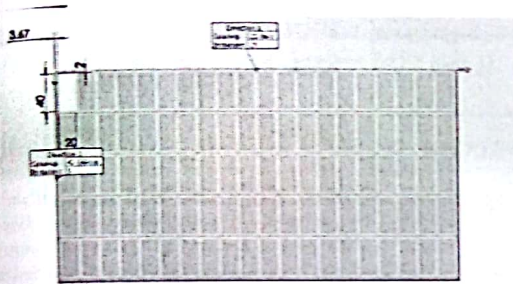


Fig. 5.1.5 Geometric configuration of case-V

5.2 Simulation analysis of CASE-I ($t_x = t_z$): ALLUMINIUM-1060 ALLOY

5.2.1: VON-MISES STRESS

Figure 5.2.1 shows von-mises stress value of square type Al 1060 alloy fiber honeycomb impact barrier. Analysis was done at constant volume as well as const force 15000Kgf using cosmos software which are a part of solid works. Von-mises stresses obtained in simulation of Max = 1.86E+07 N/mm² (Mpa).

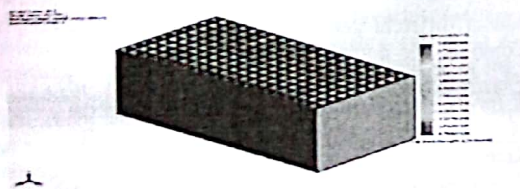


Fig. 5.2.1 VON-MISES STRESS FOR Al 1060 ALLOY IN CASE-I

5.2.2 DISPLACEMENT

Figure 5.2.2 shows displacement value of square type Al 1060 alloy fiber honeycomb impact barrier. Analysis was done at constant volume as well as const force 15000Kgf using cosmos software which are a part of solid works. Displacement obtained in simulation of Max = 0.047413 mm.

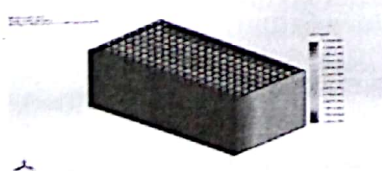


Fig 5.2.2 DISPLACEMENT FOR Al 1060 ALLOY IN CASE-I

5.2.3. E-STRAIN

Al 1060 alloy fiber honeycomb impact barrier. Analysis was done at constant volume as well as const force 15000Kgf using cosmos software which are a part of solid works. Estrain Obtained in simulation of Max = 0.000229

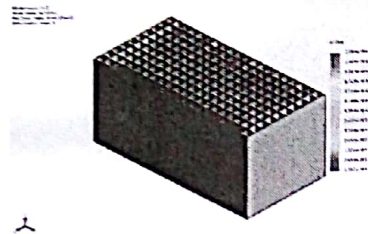


Fig5.2.3 ESTRAIN FOR Al 1060 ALLOY IN CASE-I

5.3 DISCUSSIONS

The results obtained by using analysis done on square honeycomb structure are as fallows table shows the strain, stress and displacement values of different materials used for different cases of honeycomb barrier.

Name	Material	Von - mises Stress In (N/mm ²)	Displacement in (mm)	Strain
SQUARE (CASE-I)	E-Glass	18765800	4.72984E-08	2.02834E-10
	S ₂ -Glass	18234700	0.3921	0.0017
	Aluminium	18603900	0.0474	0.0002
SQUARE (CASE-II)	E-Glass	26795600	4.76602E-08	3.00884E-10
	S ₂ -Glass	26628800	0.3938	0.0026
	Aluminium	26404300	0.048	0.0003
SQUARE (CASE-III)	E-Glass	25606800	5.47116E-08	2.77741E-10
	S ₂ -Glass	25412900	0.4527	0.0024
	Aluminium	24736600	0.0552	0.0003
SQUARE (CASE-IV)	E-Glass	21229500	5.17769E-08	2.39538E-10
	S ₂ -Glass	21263100	0.4286	0.002
	Aluminium	21263100	0.0524	0.0003
SQUARE (CASE-V)	E-Glass	21229500	5.17769E-08	2.39538E-10
	S ₂ -Glass	21229500	5E-08	2E-10
	Aluminium	23359600	0.0555	0.0002

Table: Comparison of Results for different cases.

6. CONCLUSION:

By the analysis of above results find out these values and materials should be optimized for CASE-I type.

5.4 GRAPHS

5.4.1. Von-misses stress vs geometric configuration

Fig 5.4.1 shows the graphical representation of Von-mises stress values for different materials like E-Glass, S2-Glass and Aluminium types of materials assigned to different geometries. This graph helps to compare the material stress values.

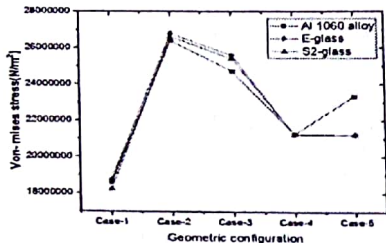


Fig.5.4.1 VON-MISES STRENGTH GRAPH

5.4.2. Displacement vs geometric configuration

Fig 5.4.2 shows the graphical representation of Displacement values for different materials like E-Glass, S2-Glass and Aluminium types of materials assigned to different geometries. This graph helps to compare the material stress values.

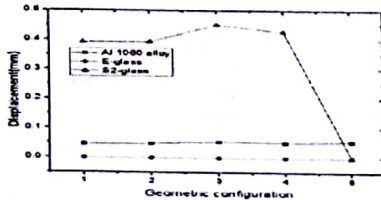


Fig 5.4.2 DISPLACEMENT GRAPH

5.4.3. E-Strain vs geometric configuration

Fig 5.4.3 shows the graphical representation of Von-mises stress values for different materials like E-Glass, S2-Glass and Aluminium types of materials assigned to different geometries. This graph helps to compare the material stress values.

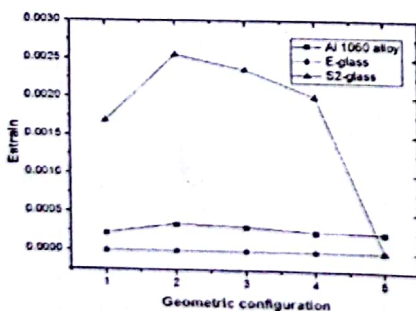


Fig.5.4.3 STRAIN GRAPH

MATERIAL	VON-MISES STRESS (N/m²)	YIELD STRENGTH (N/m²)
S2-LASS	1.82e+07	4.89e+009
AL 1060	2.56e+07	2.75742e+07
E-GLASS	2.47e+07	1.725e+009

Table 6. RESULTS ANALYSIS

- FUTURE SCOPE OF WORK:**
1. Number of different works are possible to be investigated to extend the current findings in higher level of discovery.
 2. Analysis has conducted in 2D, and more 3D models can analyzed to validate experiment results or for more deep investigation
 3. Manufacturing procedure has to be established to get more accurate angles, to produce from thickness of walls of impact Barrier.

REFERENCES

- [1] Investigation of different geometric structure parameter for honeycomb textile composites on their mechanical performance. A thesis submitted to the university of Manchester for the degree of Doctor of Philosophy in the Faculty of Engineering and Physical Sciences By Xiaozhou Gong.
- [2] A New Method of Model Aluminum Honeycomb Based Crash barriers in Lateral and Front Load Cases by Thomas Jost, Thomas Heubrandtner, Christian Ruff, Bernhard Fellner, Kompetenzzentrum-Das Virtuelle Fahrzeug Forschungsgesellschaft mbH, Graz, Austria.
- [3] Development of the Advanced Finite Element Model for Impact Barrier by Mehrdad Asadi (m.asadi@cellbond.com) Cellbond Composites Ltd. (UK), Brian Walker ARUP (UK), Hassan Shirvani, Anglia Ruskin University (UK).
- [4] Experiences in reverse-engineering of a "finite element automobile crash model Z.Q. Chenga, J.G. Thackera, W.D. Pilkeya, W.T. Hollowellb, S.W. Reagana, E.M. Sievekaa.

TESTING AND ESTIMATION OF MECHANICAL PROPERTIES OF E-GLASS (V-9) COMPOSITE MATERIAL

Syed Habeeb Rehan, Dareddy Ramana Reddy, A. Rajasekhar

¹ Assistant Professor, Department of Mechanical Engineering, GFEC, Hyderabad
email:rehaan.habeeb@gmail.com, mobile: 91-9700913780

² Professor, Department of Mechanical Engineering, MCET, Hyderabad- 500001,
India. ramana4u.iti@gmail.com

³ Professor, Department of Mechanical Engineering, MCET, Hyderabad-500001,
India

Abstract

Heat resistant composites are widely used for high temperature thermal protection systems and as flame deflectors for aerospace applications. Advanced composites made of fiber reinforced polymer matrix composites because of their strength, stiffness, low weight and their excellent thermal properties made them to replace metallic components. In this project work E-glass (v-9) phenolic and Rayon phenolic laminates were made by wet hand lay-up auto clave vacuum bagging process and their properties were evaluated by destructive and non-destructive testing methods. Laminate with known defect was examined by Ultrasonic method. Effect of modification of matrix system was studied on laminate properties. Composite made with modified phenolic resin was compared with conventional phenolic composite. Defect in the composite was analysed by Ultrasonic Test and Radiography methods. Oxy-acetylene erosion tests were carried out on laminate specimens and data was generated for ablative materials characterization.

1. Introduction:

Today's Heat resistant composites are essential for the successful launch and operation of all space vehicles. The selection of a composite material depends upon the mission of the space craft. While often the temperature capability is a major concern, the goal remains to protect the internal components at a minimal weight. This means extra insulation if the exterior material has a high heat capacity. In order to meet the mission objectives and the criteria the heat resistant material essential properties are it should have high heat of ablation, specific heat and low thermal conductivity, expansion coefficient, erosion rate.

Fiber reinforced polymer matrix composite materials has constituted a major breakthrough in the construction of lightweight structures. In particular significant benefits have been realized in the aerospace sector to meet the severe performance requirements with stringent demands of reliability. Almost all aerospace structural components – airframes of fighter aircraft, helicopters, control surface and fins of civil aircraft, various planes in satellites, antennas, rocket motor casings and some complete airframes of small aircraft are witnessing an increasing use of the advanced composites. An important technological development that has contributed significantly to this growth of composites is the development of strong and stiff fibers such as Glass, Carbon and Aramid along with concurrent developments in the

polymer chemistry resulting in a various polymeric materials to serve as matrix materials. In particular the versatility of the technology of the carbon fibers having various properties has played a key role in this growth. With complimentary developments in computer hardware and software technology, and in computational methods of analysis rendering help to the analyze and understand the material behavior and to provide predictive as well as design tools, the complexity of the polymer – matrix composites has been overcome to facilitate the extensive applications. Composites have the applications in many fields some of them are given in the following, since we are interested in aerospace applications it illustrated briefly. The creation of reliable heat resistant laminate composites for space applications requires precision design and proper tests. Because composite materials are necessary to meet heat resistant requirements for the aerospace applications such as nose cones, flame deflectors, airframes etc., some of aerospace applications where different types of materials are being used.

2. Experimental procedure

2.1 Work piece material

In this project the matrix is conventional phenolic resin and it is modified with Di-amine and ether. By this modification it is observed that when phenolic resin is modified with Di- amine the gel time is increased. And point of trouble is decreased considerably. Similar changes are observed in the properties of the resin by modifying with ether.

- E-Glass (V-9)/Phenolic composite
- E-Glass (V-9)/Di-amine modified phenolic composite
- E-Glass (V-9)/ether modified phenolic composite
- Rayon carbon/ether modified Phenolic composite
- Rayon carbon/Di-amine modified Phenolic composite

2.2 Preparation of Laminate by Hand Lay-Up Process:

Even though the method has been replaced with automated techniques, the lay-up of pre impregnated material by hand is the oldest and most common fabrication method for advanced composite structures. Furthermore, the basic features of the method remain unchanged.

Autoclave Curing: Autoclaves have been used extensively for processing high-performance composite materials in the civilian and military aerospace industries. An autoclave consists of a large cylindrical metal pressure vessel with end enclosures that is thermally insulated and heated. Most autoclaves have a forced-hot-gas circulation system as well. An autoclave is pressurized using air or an inert gas such as nitrogen

Laminate Machining & Cutting:

laminates made by fiber reinforcement's polymer matrixes normal cutter will not be useful. Hence it should be cut by the machine, since it is having the diamond edge to cut so that it can appear like smooth surface since it is having the diamond edge

2.3 Testing of composite material

2.3.1 Non Destructive Tests

NDT is used to detect defects and as a check either in new items or in items already in service, as maintenance checks. In both cases the items is not damaged in any way by the test procedure. The main aim is to detect poor compaction leading to resin-rich areas or low fibre loading, bad surface appearance or internal defect such as:

Lack of reinforcement, Porosity, Poor fibre- matrix bonding (delamination), Cracks of all sizes, Failure of the adhesive bond between components, Inclusions

2.3.2 Destructive Tests

The destructive tests are to determine the physical properties of the material. For the laminates that we made with fibre reinforcement's and matrix the destructive tests are done according to the ASTM standards. The test procedures are as follows.

(a) Density Test (ASTM-D-792):

(Density of object/density of fluid)= (weight/weight-apparent immersed weight).

(b) Resin Content Test:

This test is done by burn off method because the fabric in laminate is E-Glass V-9. For Rayon fibre we use nitric acid digestion method

©Nitric Acid Digestion Method (ASTM D-3171):

This test is done using nitric acid. Measure the temperature of the Rayon carbon using pykinometer. Keep the rayon carbon in the nitric acid until they are digested. Then separate the acid and fibre. Now the fibre is free of resin, hence measure the weight of that fibre. Calculate the difference between the total test specimen and the fibre is resin content value.

Table:1 Density & Resin content test results

S.NO.	Material	Density (gm/cc)	Resin (% of wt)	Fiber (% of wt)	Vf (% of Vol.)
1	E-GlassV-9/Ph(DA)	1.92	19.16	80.84	61.1
2	E-GlassV-	1.767	19.1	80.9	56.27

	9/Ph(E)				
3	Rayon/Ph(DA)	1.3	28.49	71.51	53.12
4	Rayon/Ph(E)	1.29	29.13	70.87	52.24

(d) ILS (ASTM D 2344):

Keep the specimen in the UTM with the span length of four times of the thickness of specimen. Now gradually apply the load on mid span of the specimen. Note down at which load the shear is occurred. Using that load calculate the ILS of the specimen. Repeat this for ten specimens and consider the average value of which

(e) Flexural Strength (ASTM D-790):

The FLEXURAL STRENGTH (FS) is done using a 3-point test of flexure. The specimen is as per the standard dimensions. The material direction under investigation must be oriented along the length of the specimen.

3. Results and discussion

The following are the test results of composite laminates made for this project work. These test results are obtained by destructive testing process, the test results are given in below tables for comparison. Flexural load and inter laminar shear strength graphs are given in below figures.

Table 2 Test results comparison

S.NO.	Material	Density (gm/cc)	Resin content (% of wt)	Fiber content (% of wt)	Vf (% of Vol.)
1	E-GlassV-9/Ph(DA)	1.92	19.16	80.84	61.1
2	E-GlassV-9/Ph(E)	1.767	19.1	80.9	56.27
3	Rayon/Ph(DA)	1.3	28.49	71.51	53.12
4	Rayon/Ph(E)	1.29	29.13	70.87	52.24

Table 3 Test results comparison

S.NO.	Material	ILSS (Mpa)	F.S (Mpa)	Young's Modulus (Gpa)	E (44.01)	Impact Energy I (KJ/m)	Erosion rate (mm)
1	E-GlassV-	29.53	462.79			265.34	6.000374

	9/Ph(DA)					
2	E-GlassV-9/Ph(E)	14.45	220.92	26.74	121.83	0.000436
3	Rayon/Ph(DA)	16.32	205.69	23.43	48.74	0.000126
4	Rayon/Ph(E)	13.13	106.64	19.9	61.54	0.000133
5	E-GlassV-9/Ph	32.79	365.72	30.54	223.51	0.000294

Discussion

It is observed from the tested data E-glass V-9/phenolic conventional composite compared with modified phenolic E-glass V-9 composite, the Flexural strength and Impact strength of the Di-amine modified phenolic composite gave higher values. Whereas ether modified phenolic composite with E-glass V-9 gave poor values indicates the compatibility problem of the matrix to reinforcements. Where ever Impact application is more one can go for Di-amine modified phenolic composite. The density variation in the composite is because of the compatibility of the matrix to reinforcements. Consolidation of composite during fabrication plays a major role on properties of the material. It is obvious from the test data better compaction has high density and will have low porosity. Composite density is calculated theoretically may not always be same with the experimentally determined value. This is due to poor compaction and voids present in the composite. A good composite for better properties should have higher density. Composite with modified Di-amine is having is having good compatibility so is its density. Even though E-glass V-9 is having high density its composites are used as insulating applications particularly where large amounts of heat to be absorbed or deflected.

Rayon carbon/phenolic composite erosion rate is low due to amorphous nature of the material. Aerospace applications such as heat shields, nose cones and nozzles where ablative property is important these rayon/phenolic are used because they absorb large quantity of heat with the sacrificial loss of minimum material. A Known defect which was identified with NDT tests such as Ultrasonic test and Radiography test. Ultra sonic through transmission loss observed at particular zone gave the resemblance of introduced defect. This is studied by Radiography which shown the defect by the difference of the material densities. Both these NDT tests are complimentary to each other. Defect in the composite leads to bad performance so composite products for aerospace applications should meet all quality control checks before being inducted into the machine.

4. Conclusions

The Applications of fibre reinforced polymer matrix composites for aerospace structures have been studied. Different fibre reinforced polymer matrix composite laminates were fabricated by Autoclave vacuum bagging process. Specimens were cut by diamond edge cutter as per ASTM standards and their physical, mechanical and thermal properties were evaluated by destructive and non-destructive techniques. Conventional phenolic resin and modified phenolic resin were studied with E-glass V-9 and Rayon carbon fabrics. Phenolic resin is used as a matrix material because of its excellent thermal properties. Phenolic resin modified by Di-amine exhibited high

flexural and impact strength. Composites made of E-glass V-9 and Rayon carbon replaced many metallic components because of their low density and high heat capacity. For high temperature applications in aerospace carbon phenolic are used as ablative materials because of their low erosion. E-glass composites because of their insulating character utilized for heat resistant composite. Quality control checks play crucial role in the fabrication of aerospace components. Defect free components ensure better performance of the mission.

In this project work we dealt with fabrication and testing of aerospace composite materials. Composite laminate properties were evaluated both by destructive and non-destructive techniques. Fibre volume fraction, density, non-destructive evaluations are essential for the acceptance of any composite product for its intended end use.

Acknowledgement

I want to say thanks to ASL/DRDO for given me an opportunity to carry out my project work.

References

1. Khaled R. Mohamed, Zenab M. El-Rashidy, Aida A. Salama, "Preparation and characterization of nano hydroxyapatite/ polymeric composites materials", Materials Chemistry and Physics Volume 130, Issues 1-2, 17 October 2011, Pp:561-568.
2. Zhang Peng li Fuguo, "Microstructure- based simulation of plastic deformation behavior of SiC particle reinforced Al matrix composites", Chinese journal of aeronautics 22(2009), Pp: 663-669.
3. Yongxiang Yang Rob Boom, Brijaniron, Derk-Jan van Heerden, Pieter Kupier, Hans de Wit, "Recycling of composites materials", Chemical Engineering and Processing ; Process Intensification, Volume51 . January , Pp: 53-68.
4. Skopp, M. Woydt, "Ceramic- ceramic composite materials with improved friction and wear properties," Tribology International, Volume 25, issue1, 1992, Pp: 61-70.
5. Loujaine Mehrez, David Moens, Dirk Vandepitte, "Stochastic identification of composite material properties from limited experimental databases, part I: Experimental Database Construction", Mechanical System and Signal Processing Volume 27 February 2012, Pp:471-483.

Influence of Heat Treatment on Mechanical Properties of Garter Spring Made By Zirconium Alloy

K. Anusha, B. Pravalika and A.Rajasekhar

Dept. of Mechanical Engineering
Methodist College of Engineering
Hyderabad, India

anushakrissy795@gmail.com; pravalika1991@gmail.com; arsekhar06@gmail.com

Abstract -Garter springs are used as spacer between the coolant tube and Calandria tube in pressurised heavy water reactors (PHWR). These are made from Zirconium alloy containing 2.5% Nb and 0.5% Cu. The springs are basically manufactured by coiling a wire of cross section 1.7mm*1.0mm, which is produced by series of drawing and swaging operations using hot extruded rods of 19mm diameter. Pure Zr has lower strength, hence alloying elements are added. Nb addition gives higher strength with moderate ductility. Resilience is achieved by addition of 0.5% Cu in garter springs. It will give a very small deflection under large applied load. Apart from resilience, deflection and stiffness properties, the strength and hardness of the material are crucial in deciding the applicability of the material for this application. Heat treatment (Solutionizing and ageing) influence the properties of non ferrous alloys. Hence this project describes the influence of heat treatment on mechanical properties of garter spring made of Zirconium alloy.

Key words- zirconium alloy; tensile strength; hardness; heat treatment.

I. INTRODUCTION

A garter spring is a coiled steel spring that is connected at each end to create a circular shape, and is used in oil seals, shaft seals, belt-driven motors, and electrical connectors.[1] The garter spring is also used as spacer between the coolant tube and Calandria tube in pressurized heavy water reactors (PHWR). This is one of the most important and critical component that goes into the reactor. The purpose of garter spring is to maintain the annular gap between Calandria and pressure tubes. The materials that are normally employed in the manufacture of garter springs are carbon steel, stainless steel etc. In pressurized heavy water reactors (PHWR), Zirconium alloy is commonly used to manufacture the garter spring.[2] Zirconium does not absorb neutrons, making it an ideal material for use in nuclear power stations whereas stainless steel and carbon steel does not. Pure Zr has lower strength, hence alloying elements are added. Nb addition gives higher strength with moderate ductility. Resilience is achieved by addition of 0.5% Cu in garter springs. It will give a very small deflection under large applied load.

Zirconium can be heat treated using standard equipment and processes used for other materials with some

additional considerations. Because zirconium is reactive with carbon-containing substances at elevated temperatures, it is important to remove all dirt, oils, greases, and other residues before heat treatment. A level of cleanness comparable to that used before welding is ideal.[3]

Either furnace heat treatment or localized heat treatment can be used for zirconium. Typically, electric, gas-fired, or oil-fired air furnaces are used to heat treat zirconium, but vacuum- or argon-purged electric furnaces are preferred when surface oxidation is not desirable. When using gas-fired heating, a slightly oxidizing or neutral atmosphere is mandatory. Direct flame impingement must be avoided.

Zirconium alloy 702 typically does not require stress relieving, but a stress relief heat treatment at 565 °C (1,050 °F) for 30 to 60 minutes at temperature can relieve residual stresses for machining stability, improve fatigue performance, and improve corrosion performance. [6]

Zirconium alloy 705 requires a stress relief heat treatment within 14 days after welding to prevent delayed hydride cracking. ASME Boiler and Pressure Vessel code gives guidance for heat treatment requirements of zirconium grade 705.[4]

Heat treatment is also used to enhance the surface oxide on zirconium to improve wear resistance. A typical treatment at 565 °C (1,050 °F) for four to six hours at temperature will provide an increase in near-surface hardness to about 480 on the Vickers scale, comparable to 47 Rockwell [1].

Common methods of heat treatment of zirconium alloys include, solutionizing and ageing to improve mechanical properties. [5]

II. EXPERIMENTATION

A. Material

The material used for garter spring is zirconium alloy, whose composition is Zr-97%, Nb-2.5%, and Cu-0.5%. The material is taken in the form of cast ingot with about 290mm diameter. It is subjected to a series of drawing and swaging operations and extruded with the rectangular cross section of 1.7mm*1.0mm.

B. Heat Treatment

The material is subjected to intermediate annealing to produce the final shape. All the intermediate annealing between the stages has been carried out at full annealing temperature of 732C making the material suitable for further working and the finished rectangular wire is coiled in the form of springs to the required lengths. These springs are loaded into a fixture where it is compressed fully over a mandrel. About 150 No's of springs are loaded into a fixture and the fixture is loaded into the heating chamber.

The heat treatment cycles with pre determined heating time and temperature soaking time etc are programmed in the temperature controller. After attaining the desired vacuum the heating of the material is carried out. After completing the heating cycle, the material is transferred to the cold chamber in auto mode in the shortest possible time (10 seconds) and quenching completed in oil, simultaneously purging argon into the quench chamber. The solutionised springs after checking the hardness and determining the corresponding ageing temperature are aged in the same furnace by heating for six hours under vacuum.

The garter spring in the form of wire coil of 1.7*1.0mm³ size as been subjected to solutionizing, solutionizing and ageing at different temperatures. The heat treatment procedures are described below in table 1.

TABLE.1 Types of heat treatment processes applied to Zirconium alloy

S.No	Heat Treatment	Period Of Ageing (Hours)
1	Solutionised at 732°C	6
2	Solutionised at 732°C ageing at 440°C	6
3	Solutionised at 732°C ageing at 460°C	6
4	Solutionised at 732°C ageing at 500°C	6
5	Solutionised at 732°C ageing at 520°C	6

C. Mechanical Testing

The specimens for conduct of tensile test are made as per ASTM standards with the following sizes: Thickness- 0.07 inches, Breadth- 0.0445 inches, Original length- 2inches. To conduct hardness test the material is cut into 2cm length & it is subject to Vickers hardness test.

III. RESULTS

A. Tensile Properties

The specimens after different heat treatments are subjected to tensile test to determine yield strength, ultimate tensile

strength and %elongation of the spring material. The results are given in the table 2.

TABLE.2. Tensile properties of zirconium alloy after various heat treatments.

S.No.	Sample	UTS (MPa)	YS (MPa)	%Elongation
1	Solutionised	122.44	96.47	8.0
2	Solutionised & aged at 440°C(A1)	145.16	106.63	6.6
3	Solutionised & aged at 460°C(A1)	120.27	100.2	6.3
4	Solutionised & aged at 500°C(A1)	115.92	93.75	4.5
5	Solutionised & aged at 520°C(A1)	116.0	96.8	4.7

After solutionizing it is observed that the ultimate tensile strength is 122.44 MPa. From the results it is observed that the ultimate tensile strength and yield strength are increased after ageing. After ageing at 440°C. The ultimate tensile strength has gone up to 145.16 MPa. Further increase in ageing temperature led to decrease in ultimate tensile strength i.e to a value of 116 MPa at 520°C. Similar trends are observed in yield strength value also. The % elongation is decreased after ageing. The increase in ultimate tensile strength and yield strength after 440°C ageing may be the result due to precipitation of second phase particles of Niobium (Nb), as Nb increases the strength of the alloy. When the ageing temperature is increased beyond 440°C the strength is decreased which may be due to grain coarsening of the matrix that may takes place at high temperature [7]

B. Hardness

The hardness data of various heat treated samples after conduct of Vickers Hardness Test are given in the table 3.

TABLE.3 The hardness data of zirconium alloy after various heat treatments

S.No.	Sample	VHN
1	Solutionised	175
2	Solutionised & aged at 440°C	262
3	Solutionised & aged at 460°C	263
4	Solutionised & aged at 500°C	260
5	Solutionised & aged at 520°C	254

From the data it is observed that hardness is increased after ageing at 440°C as mentioned earlier. This may be due to precipitation hardening which takes place due to precipitation of Niobium. Ageing at higher temperature i.e beyond 500°C reduces the hardness of the material due to coarsening of grains at high temperature.

IV. CONCLUSION

- The Heat Treatment process i.e solutionizing & ageing can successfully adapted to Zr alloy.
- Increase in tensile strength, yield strength & hardness resulted after ageing at 440°C.
- Further increase in ageing temperature may reduce the mechanical properties.

Acknowledgment

The authors would like to thank the authorities of Nuclear Fuel Complex, for providing support in carrying out the project experimentation.

References

- [1] Springs - www.wikipedia.com
- [2] Garter springs - N.P.C. library
- [3] Machine design - Dr. Sadhu Singh
- [4] Design data hand book - K. Mahadevan and K. Balasubramanyam
- [5] Deven, G.E., Mechanical metallurgy, 1989, 3rd edition, McGraw-Hill.
- [6] Walkers P.M.H., Materials science and technology dictionary, 1989, Chambers Harring Publisher.
- [7] Richard, Subbarao, welding aluminium and zirconium alloys part 06, joining dissimilar metals, pp - the rules & page journal@ January/February 2005.

OPTIMIZATION OF PROCESS PARAMETERS OF ULTRASONIC MACHINING OF TITANIUM

B. James Prasada Rao,

Dept. of Mechanical Engg, JBR Engineering College,
Moinabad, Telangana, India

D.V. Srikanth,

Dept of Mech Engg, ST MARTIN'S Engineering College,
Secunderabad, Telangana, India

A. Rajasekhar,

Dept of Mech. Engg, Methodist College of Engg. & Tech.
Hyderabad, Telangana, India

M. Sreenivasa Rao,

Dept. of Mech Engg, JNTUH, Kukatpally, Hyderabad,
Telangana, India.

Abstract: Ultrasonic Machining (USM), as a non-traditional machining system, has been giving essential help with the machining of hard and fragile materials, whether electrically leading or non-directing. In spite of the fact that the material removal rate of the process is less, USM is better than most of other non-traditional machining strategies. This is on account of the procedure is free of warm or electrical properties of workpiece and does not thermally harm or present lingering stresses in the workpiece. The goal of the present work was to improve the process parameters like grain size, slurry fixation, power rating for acquiring most extreme Material Removal Rate utilizing Genetic Algorithms. The Taguchi Method was utilized to arrange the trials and consequent examination. Tests for process parameters on the nature of the gap bored in earthenware tiles as workpiece by Ultrasonic Drilling. The parameters taken for this examination and optimization are: Size of Abrasive Grains, Concentration of Abrasive Slurry, Power Rating of Machine and thickness of work Material. A three-level orthogonal cluster table is utilized to decide the sign to-clamor (SN) proportions taking into account Taguchi's configuration of trials. Besides, examination of difference (ANOVA) has been performed to think about the relative criticalness of the diverse variables on cutting power and MRR of zirconia artistic. At long last, check tests were done to look at the anticipated estimations of the yields with their test values keeping in mind the end goal to affirm the adequacy of the Taguchi Optimization.

Keywords – Ultrasonic machining, process parameters, Taguchi Technique, ANOVA

I. INTRODUCTION

Titanium is a synthetic component with image Ti and nuclear number 22. It is a glistening metal with a silver shading, low thickness and high quality. It is exceptionally impervious to erosion in ocean water, water regna and chlorine. The component happens inside of various mineral stores, mainly rutile and ilmenite, which are generally circulated in the Earth's hull and lithosphere, and it is found in every single living thing, rocks, water bodies, and soils[3]. The metal is removed from its important mineral metals by means of the Kroll process[4] or the Hunter process. Its most basic compound, titanium dioxide, is a famous photocatalyst and is utilized as a part of the assembling of white pigments[5].

Other mixes incorporate titanium tetrachloride ($TiCl_4$), a segment of smoke screens and impetuses; and titanium trichloride ($TiCl_3$), which is utilized as an impetus as a part of the creation of polypropylene.

Ultrasonic machining [1] is a machining operation in which a vibrating device swaying at ultrasonic frequencies is utilized to expel material from the workpiece, supported by a rough slurry that streams openly between the workpiece and the tool[2]. It contrasts from most other machining operations in light of the fact that almost no warmth is produced [2]. The apparatus never contacts the workpiece and therefore the crushing weight is once in a while more than 2 pounds [1] which makes this operation ideal for machining amazingly hard and weak materials, for example, glass, quartz, sapphire, ferrite, aluminum oxide, silicon, silicon carbide, silicon nitride, ruby, precious stone, fiber optics—and earthenware production.

The device that does the cutting is made of a harder material than the workpiece. Normally utilized device materials are nickel and delicate steels [3]. As the device vibrates, it pushes down the grating slurry, a fluid containing rough grains, until the grains sway the work piece. On account of the fragility of the workpiece, under the effect of the grating particles its surface rubs, while the gentler device material just misshapes marginally.

II. METHODOLOGY

Taguchi's technique for test plan gives a basic, effective and deliberate way to deal with and decide ideal machining parameters. Taguchi has suggested orthogonal clusters (OA) for the outlining of examinations. In taguchi technique, the consequences of trials are dissected to accomplish one or a greater amount of the goals as to set up the best or the ideal condition for an item or procedure. Investigation of fluctuation (ANOVA) is the measurable treatment connected to the aftereffects of the examinations in deciding the percent commitment of every parameter against an expressed level of certainty. The investigation of ANOVA table for a given examination figures out which of the parameters need control

and which don't. Taguchi recommended two unique courses to do the complete examination. In the first place, the standard methodology, where the aftereffects of a solitary run or the normal of dull runs are prepared through fundamental impact and investigations of change. The second approach, which Taguchi emphatically suggests for numerous runs, is to utilize sign-to-clamor (S/N) proportion for the same strides in the examination. The S/N proportion is a simultaneous quality metric connected to the misfortune capacity. Outline of test (DOE) techniques results in a proficient trial calendar and create a factual investigation to decide effortlessly as to which parameters have the most huge consequences for the last results. The utilization of sign-to-clamor (S/N) proportion in framework examination gives a quantitative worth to reaction variety correlation. The prerequisite to test numerous variables implies that a full factorial trial plan that depicts every conceivable condition would bring about countless. There are a few S/N proportions accessible relying upon the sorts of qualities; lower is better (LB), ostensible is best (NB), and higher is better (HB).

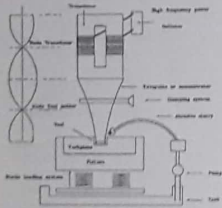


Fig 1: The setup of Ultrasonic Machining

Lower-the-better type problem

$$\eta = -10 \log_{10} \left(\frac{1}{n} \sum_{i=1}^n y_i^2 \right) \quad (1)$$

where (S/N) is the inspection index, defined as the signal-to-noise ratio (unit db), n is the number of repetitions for each trial, independent of the values assigned to noise factors, and y_i is the value of the response obtained in the ith repetition of the trial.

Higher-the-better type problem

In this type of problem, the quality characteristic is again continuous and non-negative and it is to be made as large as possible. There is no adjustment factor to be used in

this case as well and one is interested in maximizing the objective function expressed as:

$$\eta = -10 \log_{10} \left(\frac{1}{n} \sum_{i=1}^n \frac{1}{y_i^2} \right) \quad (2)$$

Nominal-the-best type problem

In the nominal-the-best type problem, the quality characteristic is continuous and non-negative, but its target value is non zero and assumes some finite value. For these types of problems, if the mean becomes zero the variance also tends to become zero. A scaling factor can be used as an adjustment factor to shift the mean closer to the target for such type of problems. The objective function that is to be maximized can be expressed as:

$$\eta = 10 \log_{10} \left(\frac{\mu^2}{\sigma^2} \right) \quad (3)$$

$$\mu = \frac{1}{n} \sum_{i=1}^n y_i^2 \quad (4)$$

$$\sigma = \frac{1}{(n-1) \sum_{i=1}^n (y_i - \mu)^2} \quad (5)$$

The values of SS, DOF, MS, F and P as shown in ANOVA tables are calculated using MINITAB14.0 Software.

III. RESULTS & DISCUSSIONS

The parameters selected for this process are feed rate of abrasive particles and frequency of vibration. Table 1 indicates parameters at three levels and table 2 indicates surface roughness, Psura1 and Pmean1.

Table 1 Selected process parameters

Parameters	Level1	Level2	Level3
Feed rate (mm/min)	0.5	1	1.5
Frequency of vibration (KHz)	0	30	40

Response Table for Signal to Noise Ratios

Nominal is best (10 * Log10(Ybar^2/S^2))

FEED RATE Level (MM/MIN)	FREQUENCY VIBRATION(KHZ)
1 23.08	32.11
2 24.16	20.33

3	18.96	20.79
Delta	5.21	11.78
Rank	2	1

TABLE 2 Influence of process parameters

Feed Rate (mm/Min)	Frequency of Vibration (KHz)	Surface Roughness 1	Surface Roughness 2	Psur1	Pmean1
0.5	0	0.28	0.29	32.051	0.201
0.5	30	0.32	0.28	18.2248	0.20133
0.5	40	0.37	0.3	18.2032	0.20166
1	0	0.35	0.33	37.7088	0.201
1	30	0.45	0.38	21.9386	0.40111
1	40	0.43	0.45	24.0713	0.41166
1.5	0	0.42	0.42	32.9036	0.401
1.5	30	0.47	0.42	24.718	0.40111
1.5	40	0.59	0.47	19.0049	0.51166

Response Table for Means

FEED RATE Level (MM/MIN)	FREQUENCY VIBRATION(KHZ)
1 0.3067	0.3517
2 0.4017	0.3867
3 0.4650	0.4350
Delta 0.1583	0.0833
Rank 1	2

A. ANOVA (Analysis of Variance)

Examination of fluctuation (ANOVA) tests the specimens that the methods for two or more populations are equivalent. ANOVAs survey the significance of one or more components by looking at the reaction variable means at the distinctive element levels. The invalid speculation expresses that all populace implies (component level means) are equivalent while the option theory expresses that no less than one is distinctive.

To perform an ANOVA, one should have a consistent reaction variable and no less than one investigated component with two or more levels. ANOVAs require information from roughly regularly appropriated population with equivalent fluctuations between element levels. Be that as it may, ANOVA strategies work entirely well regardless of the possibility that the typicality presumption has been abused, unless one or a greater amount of the distributions are profoundly skewed or if the fluctuations are very distinctive. Changes of the first dataset might rectify these infringements. For instance, we plan a trial to survey the solidness of four test rug items, we put a specimen of every

Fig 2: Main effect plot for S/N ratio of parameters

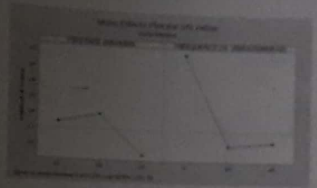


Fig 2: Main effect plot for S/N ratio of parameters

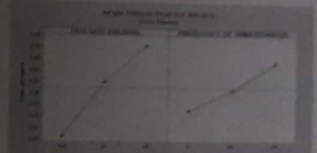


Fig 3: Main effect plot for mean of parameters

In the event that the p-value is not exactly alpha, this infer that no less than one strength mean is distinctive. For more integrity data about the contrast between particular means, utilize a numerous correlation strategy, for example, Tukey's. The main "investigation of change" depends on the methodology in which the technique utilizes fluctuations to figure out if the methods are distinctive. The strategy works by looking at the difference between gathering implies versus the change inside gathering as a method for figuring out if the gatherings are all piece of one bigger populace or separate population with various attributes. Minitab has diverse sorts of ANOVAs to take into account extra elements, sorts of elements, and distinction plans to suit your particular needs.

General Linear Model: SURFACE ROUGHNESS 2 versus FEED RATE (MM/MIN), FREQUENCY OF VIBRATION Method

Factor coding (-1, 0, +1)

Factor Information

Factor Type	Levels	Values
FEED RATE (MM/MIN)	Fixed	3 0.5, 1.0, 1.5
FREEQUENCY OF VIBRATION(KHZ)	Fixed	3 0, 30, 40

Analysis of Variance

Source	DF	Adj SS	Adj MS	F-Value	P-Value
FEED RATE	2	0.034067	0.017033	32.97	0.003
F OV(KHZ)	2	0.005067	0.002533	4.90	0.084
Error	4	0.002067	0.000517		
Total	8	0.041200			

Model Summary

S	R-sq	R-sq(adj)	R-sq(pred)
0.0227303	94.98%	89.97%	74.61%

Coefficients

Term	Coef	SE Coef	T-Value	P-Value	VIF
Constant	0.37333	0.00758	49.27	0.000	

FEED RATE (MM/MIN)

0.5	-0.0833	0.0107	-7.78	0.001	1.33
1.0	0.0200	0.0107	1.87	0.135	1.33

FREEQUENCY OF VIBRATION(KHZ)

0	-0.0200	0.0107	-1.87	0.135	1.33
30	-0.0133	0.0107	-1.24	0.281	1.33

Regression Equation

$$\begin{aligned} \text{SURFACE ROUGHNESS} &= 0.37333 - \\ & 0.0833 \text{ FEED RATE (MM/MIN)}_{0.5} \\ & + 0.0200 \text{ FEED RATE (MM/MIN)}_{1.0} \\ & + 0.0633 \text{ FEED RATE (MM/MIN)}_{1.5} - \\ & 0.0200 \text{ FREEQUENCY OF VIBRATION(KHZ)}_0 \\ & - 0.0133 \text{ FREEQUENCY OF VIBRATION(KHZ)}_{30} \\ & + 0.0333 \text{ FREEQUENCY OF VIBRATION(KHZ)}_{40} \end{aligned}$$

It is proved that the value of R-Square is more than 90 percent, which proves that the Taguchi approach we performed is validated by using Analysis of Variance.

I. CONCLUSION

The exploration has completely exhibited Taguchi's information investigation technique which makes the determination as below: a) The orthogonal exhibit strategy presented by Taguchi is suitable in selecting the right outline with lesser number of runs.

(b) Taguchi technique gives a straight forward, methodical productive system with an orderly approach in examining the trial information.

(c) The deliberate surface unpleasantness is diminishing with the augmentation of feed rate and recurrence settings.

(d) Feed rate, which measures how quick the device goes through the work piece is the fundamental factor which affected the machining execution.

The R-Square value achieved is 94.08 which proves that the Taguchi approach is suitable for the parameters towards objective.

Fig 4 : Main effect plot of surface roughness

REFERENCES:

- [1] Z. C. Lim, Y. Jiao, T. W. Deines, Z. J. Pei and C. Treadwell, Rotary Ultrasonic Machining of Ceramic Matrix Composites: Feasibility Study and Designed Experiments. International Journal of Machine Tools and Manufacture, 45, 2005, pp. 1402-1411.
- [2] G.S. Peace, Taguchi Methods: A Hands-On Approach. Reading, Massachusetts: Addison-Wesley Publishing Company, 1993.
- [3] T. P. Bagchi, Taguchi Methods Explained Practical Steps to Robust Design. New Delhi, Prentice Hall of India Private Limited, 1993.
- [4] G. Z. Yin and D. W. Jillie, Orthogonal Design for Process Optimization and Its Application in Plasma Etching. Solid State Technology, May, 1987, pp. 127-132.
- [5] Yang, K. and El-Haik, B. Design for Six Sigma: A Roadmap for Product Development. USA: Mc-Graw Hill Companies, 2003.
- [6] R. K. Roy, Design of Experiments Using the Taguchi Approach: 16 Steps to Product and Process Improvement. USA: John Wiley & Sons, Inc. 2001.
- [7] Z. J. Pei and P. M. Ferreira, An Experimental Investigation of Rotary Ultrasonic Face Milling. International Journal of Machine Tools and Manufacture, 39, 1999, pp. 1327-1344.
- [8] M. Nalbant, H. Gokkaya and G. Sur, Application of Taguchi Method in the Optimization of Cut-tng Parameters for Surface Roughness in Turn-ing Operation. Materials and Design, 28, 2006, pp. 1379-1385.

Multi-Objective Optimization of EDM Process Parameters on Ti Alloy (BT20L) Using Taguchi Method and Grey Relational analysis

R. Swetha^{1, a} and L. Siva Rama Krishna^{2, b}

¹ Dept. of Mechanical Engineering, Methodist College of Engineering & Technology
Hyderabad, India - 500001

² Dept. of Mechanical Engineering, University College of Engineering, Osmania University,
Hyderabad, India - 500007

^ashwetagandra@gmail.com, ^blsrkou@gmail.com

Abstract. EDM is an energy-based non-traditional technique extensively used in machining hard, high-strength and temperature-resistant materials in a contactless manner. The aim of this paper is to present multi-objective optimization of the EDM process parameters on Ti Alloy (BT20L) using Taguchi method and Grey relational analysis. The Performance characteristics considered are electrode wear rate, material removal rate and surface roughness. These are chosen to evaluate the machining effects on Ti alloy (BT20L). The process parameters selected are discharge current, pulse-on time, pulse-off time and flushing pressure. Experiments based on the appropriate orthogonal array according to Taguchi method are conducted first. The normalized experimental results of the performance characteristics are then introduced to calculate the coefficient and grades according to grey relational analysis. The optimized process parameters simultaneously lead to a lower electrode wear rate, higher material removal rate and better surface roughness. They are validated by conducting confirmation experiment.

Keywords: EDM, Orthogonal Array, Taguchi Method, Grey relational analysis.

Introduction

Electrical Discharge Machining (EDM) is the most extensively used non-traditional machining processes used for die-making, precision machining and manufacturing of prototypes. EDM is particularly used in aerospace industries when compared with the conventional machining process due to the intricacy involved. Titanium alloys are widely used due to their excellent corrosion resistance, light weight and mechanical properties. The aim of this paper is to find out the optimum values of the process parameters of the EDM process on Ti Alloy (BT20L) in order to increase the metal removal rate, decrease the electrode wear rate and reduce the surface roughness. The process parameters chosen in this work are discharge current, pulse-on time, pulse-off time, flushing pressure. Initially, by using orthogonal array (OA) technique of Taguchi method an appropriate OA is chosen. Three different levels are chosen for each process parameter and hence L9 orthogonal array (L9 OA) is chosen. Experimentation is carried out with the proposed L9 OA to find out the optimum values of process parameters and the grey relational analysis is used to find out the optimum values of process parameters.

The rest of this paper is organized as follows: Section 2 presents literature review concerned to the work. Problem definition is presented in Section 3. Section 4 describes the research methodology adopted to solve the problem. Results and Discussions are presented in section 5. Finally, Section 6 presents the Conclusions & Future scope of this work.

Literature Review

Ahmet Hascalk, Ulas caydas [1] presents a comparative study of surface integrity of Ti–6Al–4V alloy machined by EDM and AECG. This paper discusses the importance and very wide application areas

of titanium alloys due to excellent corrosion resistance, light weight and mechanical properties. It also clearly explains Electrical discharge machining (EDM) as one of the most effective manufacturing processes available for creating complex or simple shapes and geometries within parts and assemblies. Sundaravel vijayan[2] et.al presented a paper on Multiobjective Optimization of Friction Stir Welding Process Parameters on Aluminum Alloy AA 5083 Using Taguchi-Based Grey Relation Analysis. N. Tosun, L. Ozler [3] presented a paper on ‘Optimisation for hot turning operations with multiple performance characteristics’. This paper presents an investigation on the optimisation and the effect of cutting parameters on multiple performance characteristics (the tool life and the workpiece surface roughness) obtained by hot turning operations. P.J.Ross [4] in his book ‘Taguchi techniques for quality engineering’ discusses Taguchi methods and how ANOVA can be applied to multi objective problems.

Problem Definition

In this paper, the multi-objective optimization of EDM process parameters is done on Ti Alloy (BT20L) using Taguchi method and Grey relational analysis. The performance characteristics considered are electrode wear rate, metal removal rate and surface roughness. The process parameters chosen for the study are discharge current, pulse-on time, pulse-off time and flushing pressure. Following are objectives of this paper:

- To maximize material removal rate (MRR), minimize electrode wear rate (EWR) and surface roughness (R_a) by applying optimization techniques such as Taguchi method and to find the optimal values of EDM process parameters.
- To find the optimal process parameter set from Taguchi method.
- To find the optimal process parameter set using grey theory prediction design.
- To compare the values of MRR, EWR, R_a obtained from Taguchi method and Grey theory.

Research Methodology

The various steps involved for solving the problem described earlier are selection of the process parameters and performance characteristics, selection of the appropriate orthogonal array, conducting the experiment, calculation of MRR, EWR, R_a and S/N ratios by Taguchi method using the experimental values, applying ANOVA to calculate sum of squares and percentage contribution of each process parameter, determination of Grey relational grades, Applying ANOVA for the obtained Grey relational grade, Conducting a confirmation experiment to compare the results of the experimental run which has the highest value of Grey relational grade and the optimal grey theory prediction design.

Selection of process parameters. The process parameters chosen are discharge current, pulse-on time, pulse-off time and flushing pressure. Three levels are chosen for each process parameter.

Table 1 Process parameters

symbol	Process parameter	Level 1	Level 2	Level 3
A	Current (I) [Amp]	5	15	25
B	Pulse-on time (T_{on}) [μ sec]	100	200	300
C	Pulse-off time (T_{off}) [μ sec]	230	200	130
D	Flushing pressure[kgf/cm ²]	0.25	0.5	0.75

Selection of orthogonal array and conducting the experiments. Four process parameters are chosen and hence L_9 orthogonal array is chosen. The experimental runs are conducted with the EDM machine on TI alloy for time duration of 20 min. Two trials of experiments (T_1 & T_2) are conducted in order to account for the unknown or unaccounted errors.

Calculation of MRR, EWR, R_a and s/n ratios by Taguchi method. The weights of the electrode (material-copper) and the work piece (material-Ti alloy) are weighed before and after the

experiments. After obtaining the MRR, EWR and R_a for both trials (T_1 & T_2), the S/N ratio for MRR is calculated by the following formula. Table 2 shows the S/N ratios for MRR, EWR, SR.

$$\eta_{ij} = -10 \log(1/n \sum_{j=1}^n 1/y_{ij}^2). \quad (1)$$

The S/N for EWR and R_a is calculated with the following formula

$$\eta_{ij} = -10 \log(1/n \sum_{j=1}^n y_{ij}^2). \quad (2)$$

Table 2 Experimental results and s/n ratios for MRR, EWR, R_a

Exp. No.	A	B	C	D	Material Removal Rate (MRR) [mg/min]		S/N Ratio for MRR	Electrode Wear Rate (EWR) [mg/min]		S/N Ratio for EWR	Surface Roughness (R_a) [μ m]		S/N Ratio for R_a
					T_1	T_2		T_1	T_2		T_1	T_2	
1.	1	1	1	1	1.045	0.91	-0.1977	-0.08	-0.015	29.7623	3.16	2.88	-9.60014
2.	1	2	2	2	1.18	1.145	1.3079	-0.1	0.02	27.9588	4.66	4.01	-12.74
3.	1	3	3	3	1.49	1.185	2.526	-0.115	0.095	40	4.33	3.91	-12.3
4.	2	1	2	3	6.99	7.07	16.94	2.25	1.92	-6.3821	5.53	6.11	-15.3
5.	2	2	3	1	9.325	8.95	19.2166	1.33	-0.13	4.4369	5.88	6.06	-15.52
6.	2	3	1	2	9.885	6.93	17.40	0.38	3.195	-5.0449	5.88	5.57	-15.155
7.	3	1	3	2	21.655	22.34	26.85	12.7	7.885	-20.2504	5.63	6.12	-15.38
8.	3	2	1	3	15.835	14.31	23.563	6.1	11.81	-19.0413	5.64	6.91	-15.9522
9.	3	3	2	1	15.865	14.7	23.684	3.435	1.02	-6.9563	7.68	6.42	-16.9637

ANOVA results. Table 3 shows performance of ANOVA to calculate sum of squares(S.S) and percentage contribution and to find the significance of each parameter on the performance characteristics.

Table 3 ANOVA results for MRR, EWR, R_a

Process parameter	ANOVA results for MRR		ANOVA results for EWR		ANOVA results for R_a	
	S.S	% Contribution	S.S	% Contribution	S.S	% Contribution
A	875.424	98.47	3692.5289	93.3	35.7055	84.6
B	0.06228	0.007	104.164	2.63	3.737	8.85
C	11.8967	1.34	57.1267	1.44	3.2877	7.79
D	1.6366	0.184	100.7219	2.54	0.526	1.246

Determination of Grey relational coefficient and Grades.

Table 4 values of Grey relational coefficient for MRR, SR, EWR

Exp.	S/N Ratio			Normalisation			Deviation sequence			Grey relational coefficient		
	MRR	SR	EWR	MRR	SR	EWR	MRR	SR	EWR	MRR	SR	EWR
1	-1.977	-9.600	29.7623	0	1	0.83	1	0	0.17	0.333	1	0.7462
2	1.3079	-12.74	27.9588	0.0556	0.5736	0.8001	0.9444	0.4264	0.1999	0.3461	0.5397	0.7144
3	2.526	-12.3	40	0.1007	0.633	1	0.8933	0.3667	0	0.3573	0.577	1
4	16.94	-15.3	-6.3821	0.6336	0.226	0.23	0.3664	0.774	0.77	0.5771	0.3924	0.3937
5	19.216	-15.52	4.4369	0.7178	0.196	0.4097	0.2822	0.804	0.5903	0.6392	0.3834	0.4585
6	17.4	-15.15	-5.0449	0.6506	0.2456	0.2523	0.3494	0.7544	0.7477	0.886	0.3986	0.4007
7	26.85	-15.38	-20.25	1	0.2151	0	0	0.7849	1	1	0.3891	0.333
8	23.563	-15.95	-19.041	0.8785	0.1373	0.0201	0.1215	0.8627	0.9799	0.8045	0.367	0.3378
9	23.684	-16.96	-6.9563	0.8829	0	0.2206	0.1171	1	0.7794	0.8102	0.333	0.3908

The S/N ratio's of MRR, EWR, SR are normalised and the deviation sequence is calculated from these normalized values. Finally, the Grey Relational coefficient is calculated and the values are given in the Table 4 above. For normalisation, the following formula is used

$$x_i^*(k) = \frac{x_i^{(o)}(k) - \min x_i^{(o)}(k)}{\max x_i^{(o)}(k) - \min x_i^{(o)}(k)} \quad (3)$$

The Grey Relational Coefficient is given by

$$\gamma (x_o^*(k), x_i^*(k)) = \frac{\Delta_{\min} + \zeta \cdot \Delta_{\max}}{\Delta_{oi}(k) + \zeta \cdot \Delta_{\max}} \quad (4)$$

The Grey relational grades and their order is calculated and the values are shown in the Table 5 below.

Table 5 Grey relational grades and their order

Exp. No.	A	B	C	D	Grey Relational Grade	Order
1.	1	1	1	1	0.6925	1
2.	1	2	2	2	0.53286	4
3.	1	3	3	3	0.6441	2
4.	2	1	2	3	0.45	9
5.	2	2	3	1	0.4932	7
6.	2	3	1	2	0.46217	8
7.	3	1	3	2	0.5734	3
8.	3	2	1	3	0.5026	6
9.	3	3	2	1	0.5108	5

ANOVA is performed for the obtained values of Grey relational grades and the results are shown in Table 6 below.

Table 6 ANOVA Results for Grey relational grades

Process Parameter	S/N Ratio			S.S	Variance	% Contribution
	Level 1	Level 2	Level3			
A	0.62315	0.4684	0.529	0.0366	0.0183	67
B	0.572	0.51	0.539	0.007415	0.003707	13.58
C	0.5524	0.4978	0.5702	0.008236	0.004118	15.08
D	0.5655	0.5228	0.532	0.0024	0.0012	4.4

Confirmation tests

After the optimal EDM process parameter set is obtained, the confirmation tests are processed to verify the performance characteristics improvement. The results of confirmation experiment are compared with the outcome of the orthogonal array and grey theory prediction of the design operating parameters. Table 7 shows the comparison of the experimental results using the initial (orthogonal array, A₁B₁C₁D₁) and optimal (grey theory prediction design, A₁B₁C₃D₁) EDM parameters on BT20L Alloy. The corresponding improvement in EWR is 16%, MRR 17% and surface roughness 12%, respectively.

Table 7 EDM performance results using initial and optimal process parameters

Level	Optimal Process Parameters	
	Orthogonal array	Grey theory prediction design
	A ₁ B ₁ C ₁ D ₁	A ₁ B ₁ C ₃ D ₁
EWR [mg/min]	-0.0325	-0.038
MRR [mg/min]	0.9775	1.125
SR [μm]	3.02	2.65

Results and discussions

Fig. below shows that discharge current significantly affect material removal rate, Electrode wear rate and surface roughness. A₃B₂C₃D₂ parameter set is optimal for the performance characteristic of the MRR. A₁B₃C₃D₁ parameter set is optimal for the performance characteristic of the EWR. The optimal parameter set for the performance characteristic of Surface roughness is A₁B₁C₁D₁.

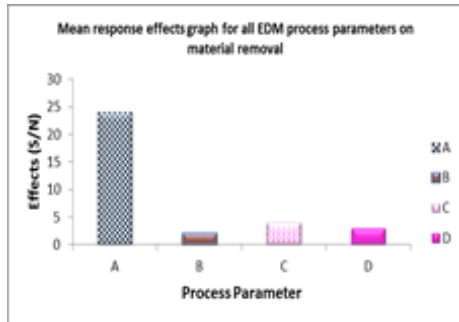
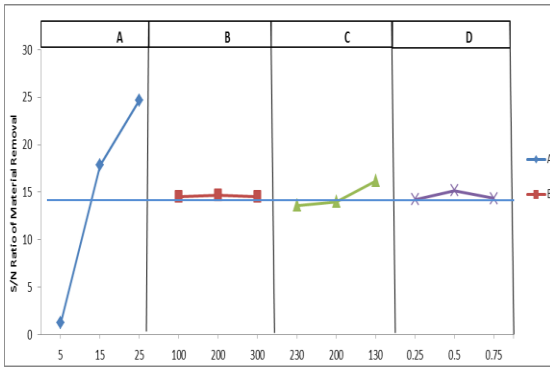


Fig. 3 S/N and mean response effects graph for all parameters on MRR

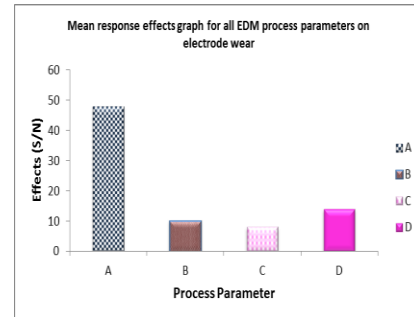
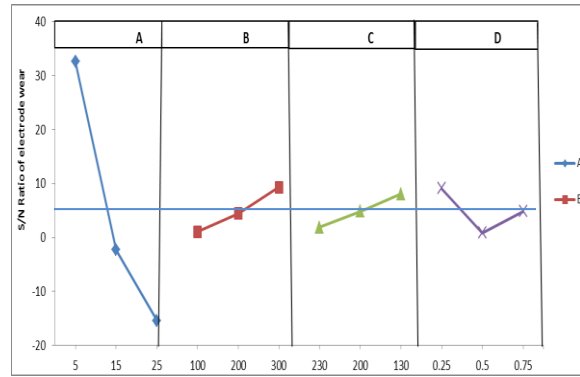


Fig. 4 S/N and mean response effects graph for all parameters on EWR

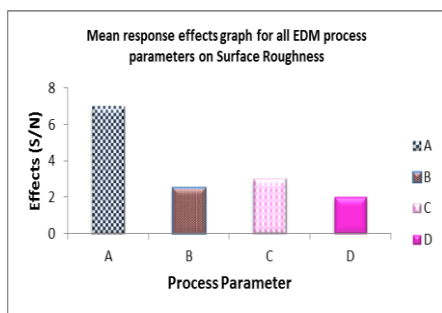
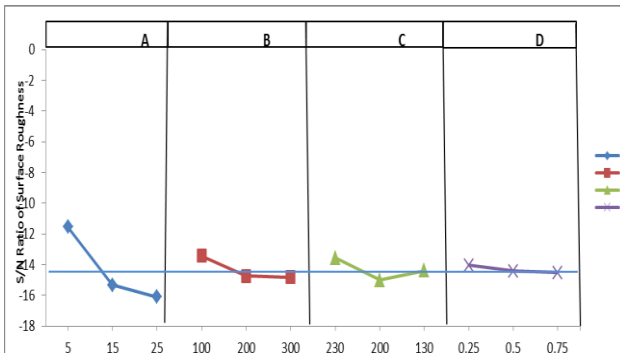


Fig. 5 S/N and mean response effects graph for all parameters on SR

Fig. 6 below shows the S/N response effects graph for Grey relational grade.

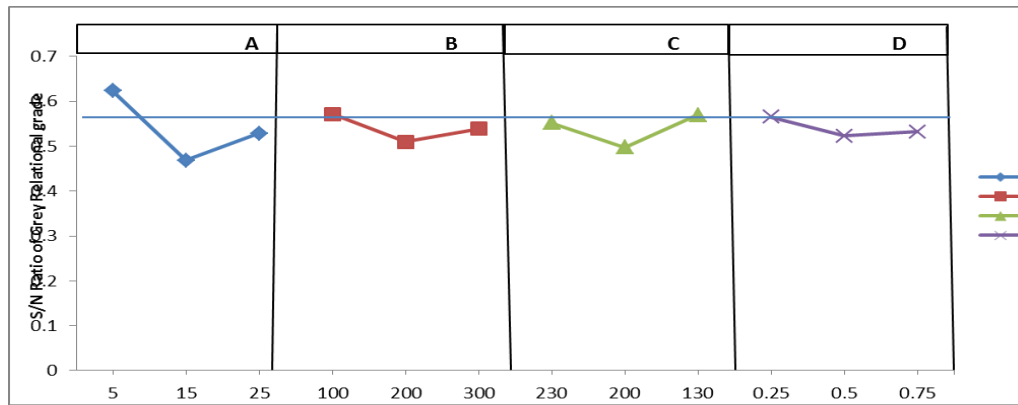


Fig. 6 S/N response graph for Grey relational grade

Conclusions and future scope of work

Taguchi method is effectively used to improve the multiple performance characteristics of the electrode wear rate, material removal rate and surface roughness in the Electrical Discharge Machining of Ti alloy (BT20L). The future scope of this work is to do the SEM Analysis and to acquire the relationship of the EDM parameters to the EWR, MRR, SR and to generate linear regression expression by using software 'SPSS'

References

- [1] Ahmet Hascalk, Ulas caydas, "A comparative study of surface integrity of Ti-6Al-4V alloy machined by EDM and AECG", *Journal of Materials Processing Technology*, 190, 173-180, 2007.
- [2] Sundaravel Vijayan, R. Raju, S. R. K Rao, "Multiobjective Optimization of Friction Stir Welding Process Parameters on Aluminum Alloy AA 5083 Using Taguchi-Based Grey Relation Analysis", *Journal of Materials and Manufacturing Processes*, vol 25, page no. 1206-1212, 2010.
- [3] N.Tosun, L.Ozler, "Optimisation for hot turning operations with multiple performance characteristics", *International journal of Advance Manufacturing Technology*, vol 23, page no. 777-782, 2004.
- [4] P.J.Ross in his book 'Taguchi techniques for quality engineering' discusses taguchi methods and how ANOVA can be applied to multi objective problems. The author explains how taguchi's s/n ratio can be combined with ANOVA in order to solve multi objective problems and also to find out the contribution of each process parameter to the performance characteristics under consideration.
- [5] J.L. Deng, "Introduction to Grey system", *Journal of Grey system*, vol 1, page no. 1-24, 1989.
- [6] TR Lin, "Optimization technique for face milling stainless steel with multiple performance characteristics", *International journal of manufacturing technology*, vol 19, page no. 330-335, 2002.
- [7] H.S. Lu, C.K. Chang, N.C. Hwang, C.T. Chung, "Grey relational analysis coupled with principal component analysis for optimization design of the cutting parameters in high-speed end milling", *journal of materials processing technology*, 209, 3808-3817, 2009.

Structural Analysis of Automotive Disc Brakes

Y Madhu Maheswara Reddy
Assistant Professor, Mechanical
Engineering Department
Methodist College of Engg. & Tech.
Hyderabad, India
mmr315@gmail.com

DR. P Usha Sri
Professor, Mechanical
Engineering Department
Osmania University
Hyderabad, India

M Prasad
Assistant Professor, Mechanical
Engineering
Methodist College of Engg. & Tech.
Hyderabad, India
prasadamatam@gmail.com

Abstract - The braking system plays the crucial role in the safety of a vehicle and its design poses a critical challenge. The heat dissipation and thermal performance of ventilated brake discs strongly depends on the aerodynamic characteristics of the air flow through the rotor passages.

In this thesis, the 3D CAD models for Solid disc and discs with different fin configurations namely, Straight Elliptical fins, Backward curved fins and Forward curved fins are designed. Each finned model disc with 12, 24 and 36 number of fins were developed using Catia V5R20. The 3D FE models have been developed for the above disc configurations using Hypermesh V11 and to know the structural strength of the disc brake, due to the introduction of fins commercial structural analysis ANSYS13.0 was used. It was observed that the introduction of fins is having a very little effect on the structural strength of the discs. Hence Forward curved disc with 36 numbers of fins is suggested for higher structural strength.

Key Words - Brake, Structural Analysis, Disc, Fins, Ansys.

I. INTRODUCTION

The disc brake or disk brake is a wheel brake which slows rotation of the wheel by the friction caused by pushing brake pads against a brake disc with a set of calipers. The brake disc (or rotor in American English) is usually made of cast iron, but may in some cases be made of composites such as reinforced carbon-carbon or ceramic matrix composites. This is connected to the wheel and/or the axle. To stop the wheel, friction material in the form of brake pads, mounted on a device called a brake caliper, is forced mechanically, hydraulically, pneumatically or electro magnetically against both sides of the disc. Friction causes the disc and attached wheel to slow or stop. Brakes convert motion to heat, and if the brakes get too hot, they become less effective, a phenomenon known as brake fade.

Disc-style brakes development and use began in England in the 1890s. The first caliper-type automobile disc brake was patented by Frederick William Lanchester in his Birmingham, UK factory in 1902 and used successfully on Lanchester cars. Compared to drum brakes, disc brakes offer better stopping performance, because the disc is more readily cooled. As a consequence discs are less prone to the "brake fade"; and disc brakes recover more quickly from immersion (wet brakes are less effective). Most drum brake designs have at least one leading shoe, which gives a servo-effect. By contrast, a disc

brake has no self-servo effect and its braking force is always proportional to the pressure placed on the brake pad by the braking system via any brake servo, braking pedal or lever, this tends to give the driver better "feel" to avoid impending lockup. Drums are also prone to "bell mouthing", and trap worn lining material within the assembly, both causes of various braking problems. The aerodynamic characteristics of the mass flow were found to be reasonably independent of rotational speed, but highly dependent upon rotor geometry. Johnson et al. [2] used PIV (Particle Image Velocimetry) to measure air velocities through a high solidity radial flow fan utilized as a vented brake rotor. Choi and Lee [3] performed a transient thermo-elastic analysis of disc brakes in repeated braking applications, using a finite element method with frictional heat generation. Grieve et al.[4] performed parametric sensitivity studies to define suitable design-material combinations for a disc brake prototype.

For solid rotors, the highest temperature occurs on the surfaces of the rotors. To decrease the maximum temperature, the most effective way is to increase the thickness of the rotors. However, the increase is limited by the pistons. Materials also have effects on the rotor's temperature. From this research, steel is a better alloy to dissipate heat from the rotors. But in practical design problems, the thermal performance is not the only requirement. From the perspective of stiffness, friction resistance and cost, the cast iron material is common used in industry.

The powerful simulation packages HYPERMESH and FLUENT give more accurate solutions to fin and pillar post rotors. From the sensitivity studies, the fin rotors have better cooling performance.

The objective of current study is to estimate Von Mises Stress generated in solid discs. The combinations of various fin configurations namely Straight Elliptical, Backward Curved, Forward curved and the various numbers of fins (12, 24 and 36) are studied to predict the effect of these variables on the performance of disc brakes. The drawings for the Solid disc are modelled. The 3D CAD models were developed for various disc configurations, namely Solid disc, discs with Straight elliptical fins, Backward curved fins and Forward curved fins with 12, 24 and 36 fins were created using CATIA V5R20. The 3D FE models were created for the above mentioned disc configurations using HYPERMESH V11. The static structural analysis was carried out to assess the effect of fins on the structural integrity of various disc models considered. The result plots were taken

The brake disc specifications considered for the analysis will be tabulated

Vehicle Specifications	Disc Brake Specifications
Manufacturer = OEM	Brake Disc Thickness (mm): 21.9
Model = OEM XYZ	Brake Disc Type: Vented Disc
Year of Manufacture = 1998	Centering Diameter (mm): 67.0
Curb weight = 1600 Kg	Fitting Position: Front Axle
	Height (mm): 48.2
	Minimum Thickness (mm): 20.0
	Number of Holes: 5
	Outer Diameter (mm): 262.4

Table.1 Vehicle specifications

III. ANALYSIS AND RESULTS

With introduction of fins the strength of the disc may reduce as material is removed for fins. So static structural analysis is carried out for the models obtained from the analysis.

The results of Von-Mises Stress distribution at pressure of 10 bar for 1 solid model and 3 models of finned discs such as Straight, Backward and Forward curved are presented in this section

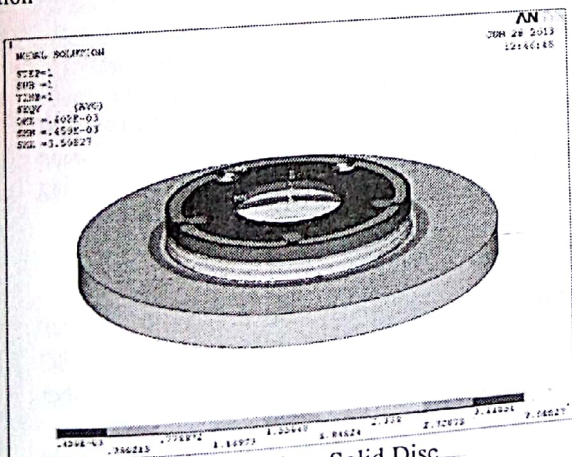


Fig.10 Von-Mises Stress Plot - Solid Disc

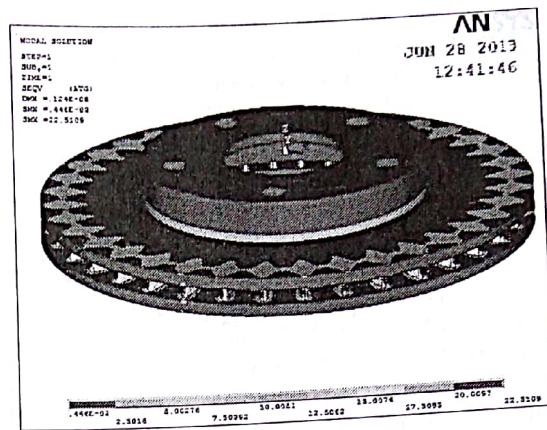


Fig.11 Von-Mises Stress Plot -Straight Elliptical Disc

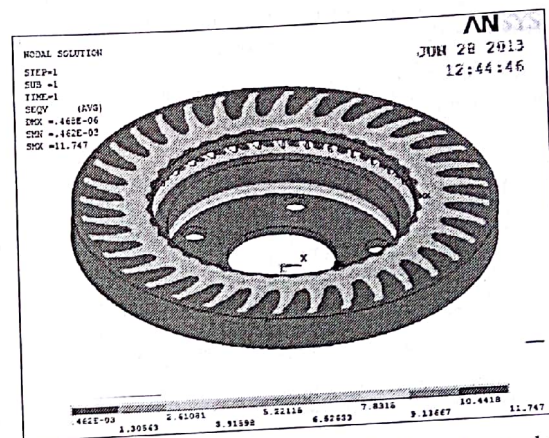


Fig.12 Von-Mises Stress Plot - Backward curved disc

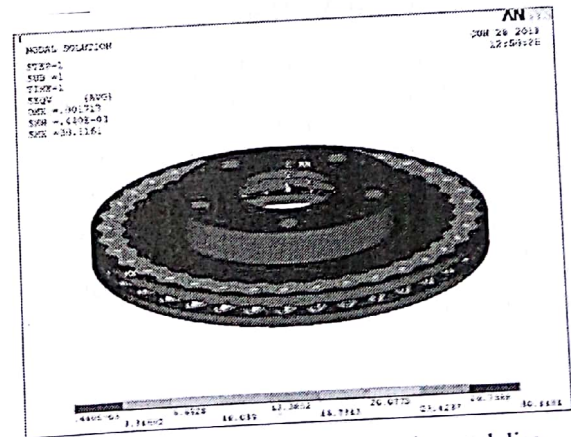


Fig.13 Von-Mises Stress Plot - Forward curved disc

The Von-Mises Stress distribution in the solid disc at a velocity of 40 mph is shown in Fig.10, for Straight elliptical rotor at a velocity of 40 mph with 36 fins is shown in Fig.11, for Backward curved rotor at a velocity of 40 mph with 36 fins is shown in Fig.12 and for Forward curved rotor at a velocity of 40 mph with 36 fins is shown in Fig.13 respectively.

The values of Von-Mises Stress from the above figures 10,11,12 and 13 are listed below.

- > Solid Disc (with no Fins) - 3.50827 N/mm²
- > Straight Elliptical Fins - 22.51 N/mm²
- > Backward Curved Fins - 30.12 N/mm²
- > Forward Curved Fins - 11.747 N/mm²

Even though the Solid disc is having less Von-Mises stress value when compared to the other disc models with fins, the maximum stress value is with in the allowable range even after the introduction of fins, by considering the enhancement in the heat transfer characteristics, we can go for the fin additions.

The variation of VonMises Stress with respect to number of fins, for various fin shapes is shown in Fig.14.

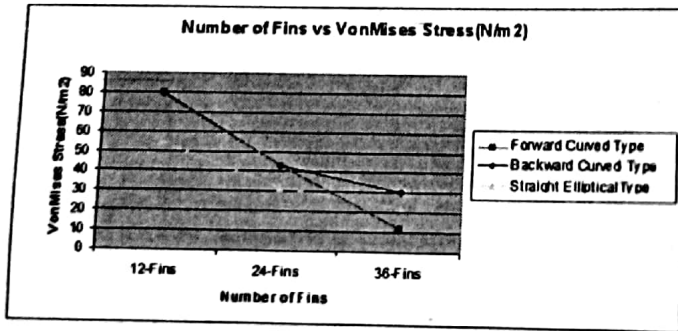


Fig.14 Number of Fins vs. VonMises Stress

From Fig.14 it is observed that the VonMises Stress is decreasing as the numbers of fins are increasing from 12 to 24 and 24 to 36. From Fig.14 it is clear that the Forward curved fins with 36 numbers of fins are having lowest VonMises Stress compared to the other.

The values of VonMises Stress for Solid disc and discs with different fin shapes namely Straight elliptical fins, Backward curved fins and Forward curved fins for 12 fins, 24 fins and 36 fins are shown in the Table 2

Fin Shape	Number of Fins	Von Mises Stress (N/mm ²)
Solid	--	3.51
Straight Elliptical Fins	12-Fins	54.88
	24-Fins	31.90
	36-Fins	22.51
Backward Curved Fins	12-Fins	79.19
	24-Fins	42.80
	36-Fins	30.12
Forward Curved Fins	12-Fins	79.98
	24-Fins	43.11
	36-Fins	11.75

Table.2 Values of VonMises Stress

From Table 2 it is observed the addition fins are adding strength in the axial direction and due to that the stresses are reduced as the numbers of fins are increased from 12 to 36.

But it may be possible that if we increase the number of fins further it may lead to decrease in the structural strength of the discs and gives rise to higher stresses. But in the current thesis, it is limited to 36 fins only.

The structural integrity of the rotor configurations were checked at a brake pressure of 10 bar.

It is observed the addition fins are adding strength in the axial direction and due to that the stresses are reduced as the number of fins are increased from 12 to 36.

But it may be possible that if we increase the number of fins further it may lead to decrease in the structural strength of the discs and gives rise to higher stresses. But in the current thesis, it is limited to 36 fins only.

IV.FUTURE WORK

More detailed geometrical optimization of finned rotors is desired. The structural strength of the disc may also depend upon thickness of the fin, inner and outer radius of the fin. By varying these parameters optimum design of disc can be obtained.

REFERENCES

- [1] Y Madhu Maheswara Reddy, Dr. P Usha Sri HEAT TRANSFER ANALYSIS OF AUTOMOTIVE DISC BRAKES IJARSE, Vol. No.3, Issue No.9, September 2014 ISSN-2319-8354(E)
- [2] D. A. Johnson, B. A. Sperandei, R. Gilbert, Analysis of the Flow Through Vented Automotive Brake Rotor, Journal of Fluids Engineering, ASME, Nov. 2003, Vol. 125/979.

- [3] J. H. Choi, I. Lee, Finite Element Analysis of Transient Thermo elastic Behaviors in Disk Brakes, *Science Direct, Wear* 257 (2004) 47-58.
- [4] D. G. Grievc, D. C. Barton, D. A. Crolla, J. T. Buckingham, Design of a lightweight Automotive Brake Disc Using Finite Element and Taguchi Techniques, Institution of Mechanical Engineers; 1998; 212, 4; ProQuest Science Journal.
- [5] Chi, Y. He and G. F. Naterer, Geometrical Optimization of Vented Brake Discs of Automotive Vehicles, submitted to CATS 2008, Toronto, Canada, 2008.
- [6] Z. Chi, G. F. Naterer and Y. He, Thermal Performance Analysis of Vented Automotive Brake Discs, CSME Forum 2008, University of Ottawa, Ottawa, Canada, 2008.
- [7] D. G. Grievc, D. C. Barton, D. A. Crolla, J. T. Buckingham, Design of a lightweight Automotive Brake Disc Using Finite Element and Taguchi Techniques, Institution of Mechanical Engineers; 1998; 212, 4; ProQuest Science Journal.
- [8] S. Aus Der Wiesche, Heat Transfer from a Rotating Disk in a Parallel Air Cross flow, *International Journal of Thermal Sciences* 46(2007) 745-754.
- [9] Z. Chi, G. F. Naterer and Y. He (2008) Effects of Brake Disc Geometrical Parameters and Configurations on Automotive Braking Thermal Performance, CSME Transactions 2008, University of Ottawa, Ottawa, Canada, 2008
- [10] A. D. Mcphec and D. A. Johnson, Experimental Heat Transfer and Flow Analysis of a Vented Braked Brake Rotor, *International Journal of Thermal Sciences*, Vol. 3, No. 6, 2007.
- [11] M. Najji, M. Al-Ninr, S.Masoud, Transient thermal behavior of a cylindrical brake system, *Heat and Mass Transfer* 36 (2000) 45-49, Springer-Verlag 2000.
- [12] Bejan, Adrian, *Convection heat transfer*, 3rd edition. Hoboken, N.J.: Wiley, c2004.
- [13] Latif M. Jiji, *Heat Convection*, Berlin ; New York : Springer, c2006
- [14] *Brake Design and Safety*, 2E, Rudolf Limpert

Experimentation and Characterization of CI Engine Performance with Design Modifications in Piston: By Inducing Turbulence

K. Srinivasa Raghavan¹, K Vijaya Kumar²

¹Mechanical Engineering Department
MCET, Affiliated to Osmania University
HYDERABAD, INDIA
srinivasaraghavan343@gmail.com

J A Ranga Babu², P Shailesh¹
²Mechanical Engineering Department
NIT Warangal, Deemed University
Warangal, INDIA
vijay701414@gmail.com

Abstract— Transportation sector plays a critical role in the world energy consumption. As the petroleum reserves are running at depleting rate, so that it defining the country economy and also these fuels are cause for many environmental issues. It is high time to improve the performance of engine and minimize the emission rates to the Environmental Protection Agency standards and also search for an alternative fuel to reduce the dependency on fossil reserves. The present work focusing on improves the performance of Compression Ignition Engine by doing modifications in combustion chamber and also analyses the performance and emission characteristics by conducting the experiments with diesel. A stirrer is introduced on the top of the piston so as to induce turbulence in incoming charge for enhancing the vaporization rate. Whirling motion is created in combustible mixture by providing rotating blades in the cavity/bowl on the reciprocating piston head. The oscillatory motion of the connecting rod will cause to rotate the blade by an angle of 60°. This arrangement induces the turbulence in combustible mixture during engine operation, there by facilitating a better combustion performance. The effects of various operating parameters like induced turbulence, injection pressure, compression ratio, injection timing and diesel mixture proportion in combustion are investigated.

Keywords— CI Engine, Piston, Stirrer, Turbulence, Diesel.

I. INTRODUCTION

DI Diesel engines, having the evident benefit of a higher thermal efficiency than all other engines, have served for both light-duty and heavy-duty vehicles. The in-cylinder fluid motion is one of the most important factor that controlling the combustion process in IC engines. It governs the fuel-air mixing and burning rates in diesel engines. The charge would flow prior to combustion and turbulence will generated during the induction process and it would develop during the compression stroke. Therefore, a better understanding of fluid motion during the induction process is critical for developing engine designs with the most desirable for effective functioning and emission characteristics of the combustion process.

To obtain a better combustion with lesser emissions in direct-injection diesel engines, it is necessary to achieve a good spatial distribution of the injected fuel throughout the

combustion chamber. Therefore, matching the combustion chamber geometry, fuel injection and gas flows are the most crucial factors for attaining a better combustion. In DI diesel engines, swirl can increase the rate of fuel-air mixing, reducing the combustion duration and retarded injection timings. Swirl interaction and squish flow increases turbulence levels in the combustion bowl causes for promoting charge mixing. Since the flow in the combustion chamber develops from interaction of the intake flow with the in-cylinder geometry, the goal of this work is to characterize the role of combustion chamber geometry on in-cylinder flow. Somender Singh et al. [1] studied the effect of design change by forming grooves or channels or passages through the squish areas which further enhance in-cylinder turbulence followed by multi flame front combustion. This provides a faster and efficient burn, with less loss of heat, through his design to improve turbulence in combustion chambers. Yang-Liang Jeng et al. [2] experimentally investigated the quality of the tumbling motion, especially for the engine with a bowl in piston. It is observed that, a small-scale vortex will be reserved inside the bowl in piston. In their further investigation the quality of the vertical flow in the axial plane with the generation of turbulence during the compression stroke is strongly recommended. Kern Y. Kang et al. [3] evaluated the turbulence characteristics of the tumble flow in a four valve engine by Laser Doppler velocimetry (LDV) and analyzed by means of turbulence intensity, integral time and length scales, and energy spectrum. The results showed that tumble causes to increase turbulence intensity during the compression stroke and its distribution to be homogeneous. Henrik W. R. Dembinski et al. [4] studied by applying different inlet port designs and valve seat making, swirl and tumble. To measure the in-cylinder flow around TDC, particle image velocimetry software was used to evaluate combustion pictures thereby mean swirl number was calculated. This offset survives during the compression and combustion. Jeong-Eue Yun et al. [5] A Studied the combined effect of swirl and tumble flow of intake port system in cylinder head. Since both swirl and tumble flows are together induced to the cylinder, in-cylinder flow pattern becomes very complicated so that it is difficult to decide this flow as one major pattern like swirl or tumble. Their study results are to find new evaluation index for in-cylinder flow characteristics instead of

current swirl or tumble coefficient using a steady flow test rig on intake port systems. Yoshihiro Suzuki [6] proposed base line modifications in piston and cylinder liners to enhance mechanical and thermal loading on vital engine parts. Hard anodizing the piston head, reinforcing the piston head with SiC-whisker. He proposed a new process for improving the surface lubrication by introducing numerous finely distributed micro-pits. S.L.V. Prasad et al. [7,8,9] studied the influence of the air swirl in cylinder on the performance and emission of a diesel engine. In order to achieve the different swirl intensities in the cylinder, three design modifications were done on cylinder head, piston crown, and inlet duct. All the modifications are aimed to improve the turbulence in the charge. This intensification of the swirl is done by cutting grooves on the crown of the piston. B.V.V.S.U. Prasad et al. [10] In-cylinder air motion was studied in a number of combustion chamber geometries which produced the highest in-cylinder swirl and Turbulence Kinetic Energy (TKE) around the top dead centre was identified.

It is evident from the literature, that the bowl geometry has a negligible effect on the airflow during the intake stroke and early part of the compression stroke. But when the piston moves towards Top Dead Centre (TDC), the bowl geometry has a significant effect on air flow for creating proper turbulence thereby resulting better mixing and better combustion.

TURBULENCE

Turbulence plays a vital role in combustion phenomenon. In combustion the flame speed is very low in non-turbulent mixtures. A turbulent motion of the mixture intensifies the processes of heat transfer and mixing of the burned and unburned portions in the flame front, which practically increase in proportion to the turbulence velocity. This turbulence can be increased at the end of the compression by suitable design of combustion chamber, which involves the geometry of cylinder head and piston crown. The degree of turbulence increases directly with the piston speed. However, excessive turbulence is also undesirable. The effects of turbulence can be summarized as, turbulence accelerates chemical action so that the combustion time is reduced and hence minimizes the tendency to detonate. Turbulence increases the heat flow to the cylinder wall and in the limit excessive turbulence may extinguish the flame.

II. EXPERIMENTAL SETUP

Table 1: Engine Specifications

Sl. No.	ENGINE PARAMETERS	SPECIFICATION S
1	Engine type	Kirloskar, 4- stroke
2	No. of Cylinders	Single cylinder
3	Rated Power	5.2 kW (7 HP)
4	Bore	87.5mm
5	Stroke	110mm
6	Swept Volume	661cc
7	Compression Ratio	17.5:1
8	Rated Speed	1500 RPM
9	Dynamometer	Eddy Current Dynamometer
10	Type of Cooling	Water cooling
11	Fuel Injection Pressure	190 bar
12	Fuel	Diesel

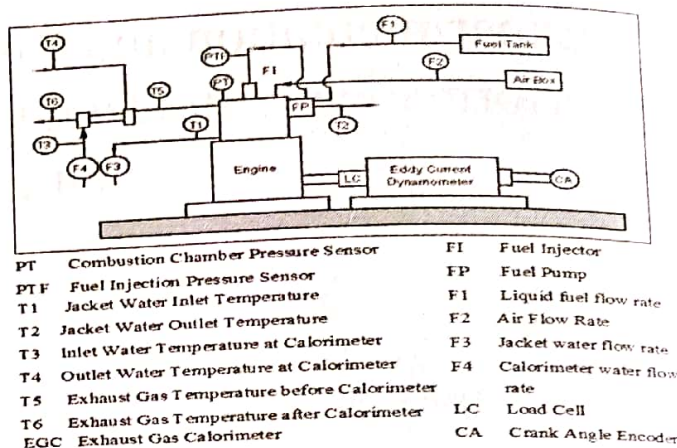


Fig. 1: Schematic Diagram of the Experimental Set-up

Table 1 and Fig. 1 shows the engine specifications and schematic diagram of experimental setup for determining the effects of squish and tumble on the performance of CI engine. It is a computerized single cylinder four stroke water cooled CI engine with an eddy current dynamometer. Engine is provided with Chromium-Aluminum thermocouples to measure the jacket water inlet and out let (T1 & T2), calorimeter water inlet and outlet (T3 & T4), exhaust gas inlet and outlet (T5 & T6) temperature. This engine also provided with pressure sensors, the dynamic pressure with water cooled piezo sensor, combustion gas pressure with differential pressure transducers and fuel injection pressure with differential pressure unit. Cooling water flow with calibrated Rota meter with stainless steel float. An encoder is fixed for crank angle record. The signals from all these sensors are interfaced with a computer to display P- θ , P-V and FIP- θ plots. The provision is also made for the measurement of volumetric fuel flow. A built-in program in the system calculates indicated power, brake power, thermal efficiency, volumetric efficiency and heat balance. The experiments are conducted at constant speed and at four different loads levels viz., 20%, 40%, 60% and 80% of full load.

A. Engine Modification

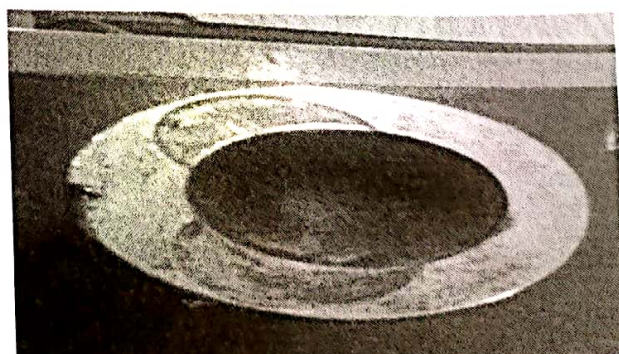


Fig. 2 Normal Piston

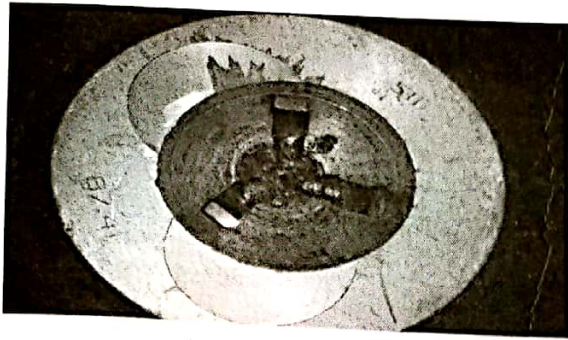


Fig. 3 Modified Piston

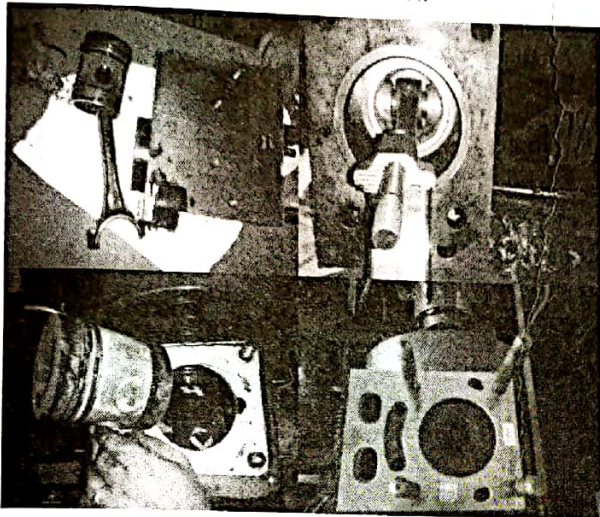


Fig. 4 Modified piston arrangement in cylinder

Fig. 2 and Fig. 3 shows the normal piston and modified piston respectively. Normal piston is having simple bowl shaped structure on the crown of it. But the modified piston (Fig. 4) is made with three blades at 120° to each other. Same aluminum alloy material is used in fabrication of chamber. A 2mm thick small strips are used to make the chambers.

B. METHODOLOGY

The engine was operated with compression ratios of 17.5 at constant speed of 1500 rpm. An injection pressure of 200bar, 250bar and 300bar were used. The engine is first run at steady state with pure diesel at 20%, 40%, 60% and 80% loading. At each load, performance parameters namely speed, exhaust gas temperature, brake power, peak pressure are measured. The experiments are repeated for two compression ratios, injection pressures and injection timings. With the above experimental results, the parameters such as total fuel consumption, brake specific fuel consumption, brake specific energy consumption, brake thermal efficiency are calculated and performance characteristics of the engine are determined. Emission analysis are carried out by INDUS model PEA205 as shown in Fig. 5, it is a 5-gas analyzer for monitoring CO, CO₂, HC, O₂ and NO in automotive exhaust. It meets OIML Class-I specifications. CO, CO₂ and HC (Hydrocarbon residue) are measured by NDIR technology and O₂ and NO are measured by electrochemical sensors.

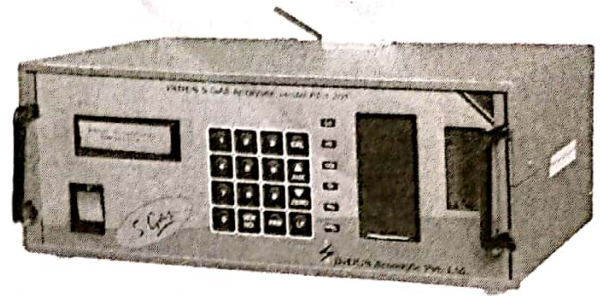


Fig. 5 Five Gas Analyzer

III. RESULTS AND DISCUSSION

The experiments were conducted on a DI diesel engine for various loads with diesel.

A. Performance of Engine

The variation of brake thermal efficiency at different loads is presented and compared the performance of modified piston with normal piston. The Fig. 6 clears that the brake thermal efficiency of modified piston is more compared to normal piston at any given load. A similar trend is observed in brake thermal efficiency at all the loads considered in present work. The fuel is injected at three different rates as advanced, standard and retarded. From the above graphs it is observed that brake thermal efficiency is minimum 13.70% at CR of 17.5, injection pressure of 300bar at retard injection timing for normal piston at 20% load. And this brake thermal efficiency is maximum 35.39% at CR of 17.5, 200bar injection pressure with advanced injection rate for swirl piston at 60% load. The variation of mechanical efficiencies with respect to load for modified piston and normal piston shown in Fig. 7. It can be observed that the indicated thermal efficiency of modified piston is more compared to normal piston at given load. A similar trend in brake thermal efficiency can be observed at all the loads considered in present work. From figs. the mechanical efficiency is minimum at 17.5 CR, 300 Pressure and retard timing for normal piston at 20% load 46.61% and it is maximum at 17.5 CR, 200bar Pressure, advanced timing for swirl piston at 80% load 89.83%.so here brake thermal efficiency varies between 46.61% and 89.83%.

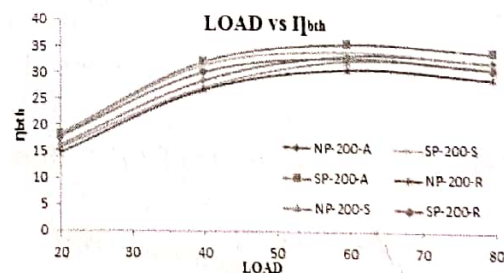


Fig. 6 (a) Load Vs Break Thermal Efficiency for 17.5 CR at 200bar

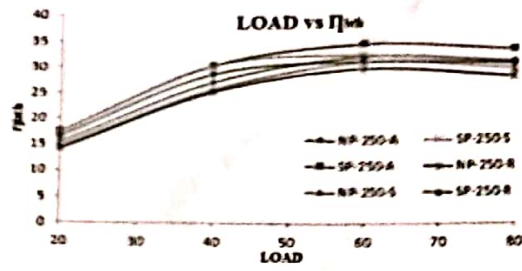


Fig. 6 (b) Load Vs Break Thermal Efficiency for 17.5 CR at 250bar

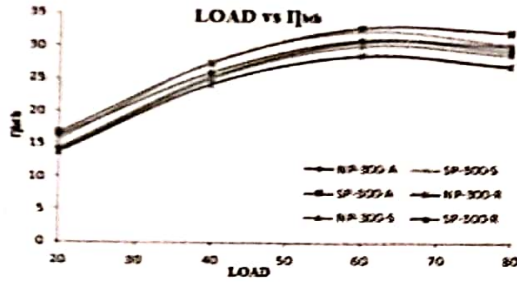


Fig. 6 (c) Load Vs Break Thermal Efficiency for 17.5 CR at 300bar

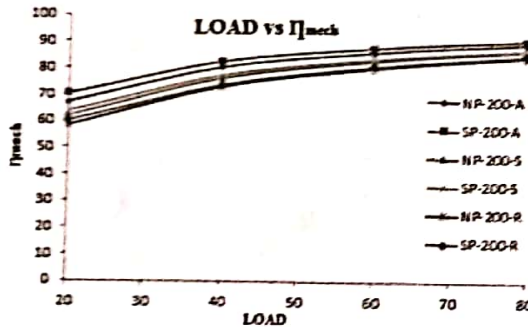


Fig. 7 (a) Load Vs Mechanical Efficiency for 17.5 CR at 200bar

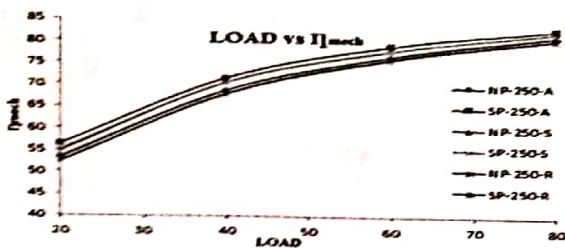


Fig. 7 (b) Load Vs Mechanical Efficiency for 17.5 CR at 250bar

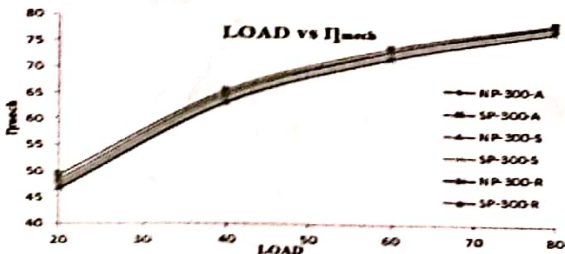


Fig. 7 (c) Load Vs Mechanical Efficiency for 17.5 CR at 300bar

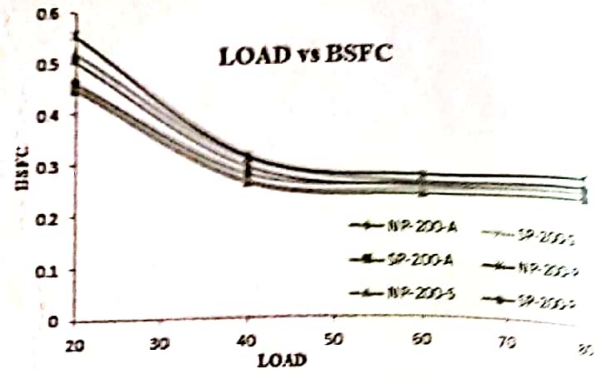


Fig. 8 (a) Load Vs Brake Specific Fuel Consumption for 17.5 CR at 200bar

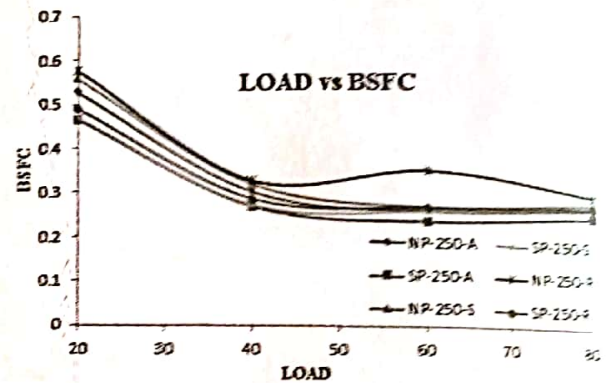


Fig. 8 (b) Load Vs Brake Specific Fuel Consumption for 17.5 CR at 250bar

The variation of brake specific fuel consumption with respect to load for modified piston and normal piston shown in Fig. 8. It can be observed that the brake specific fuel consumption of modified piston is more compared to normal piston at given load. A similar trend in brake specific fuel consumption can be observed at all the loads considered in present work. From figs. the brake specific fuel consumption is minimum at 17.5 CR, 200bar Pressure and advanced timing for normal piston at 60% load 0.231 kg/kw-hr and it is maximum at 17.5 CR, 300bar Pressure, retard timing for swirl piston at 20% load 0.597 kg/kw-hr. So here brake specific fuel consumption varies between 0.231 kg/kw-hr and 0.597 kg/kw-hr.

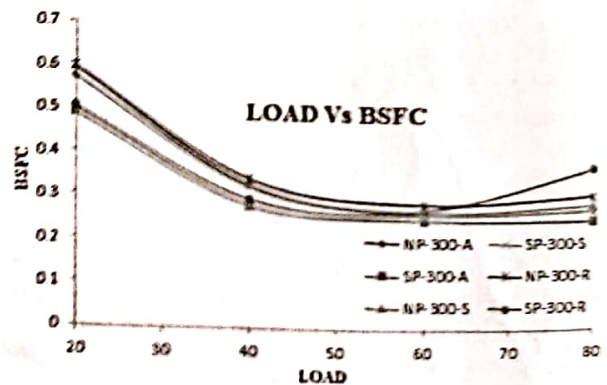


Fig. 8 (c) Load Vs Brake Specific Fuel Consumption for 17.5 CR at 300bar

B. Emissions of Engine

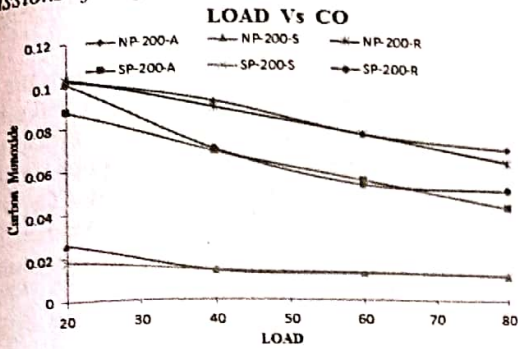


Fig. 9 (a) Load Vs Carbon Monoxide for 17.5 CR at 200bar

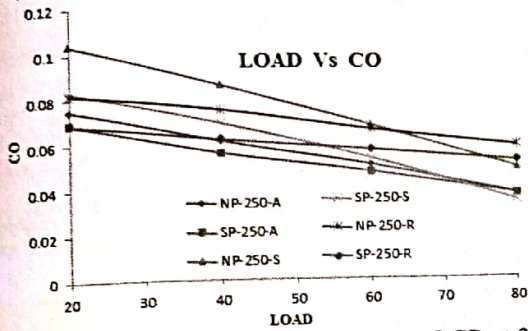


Fig. 9 (b) Load Vs Carbon Monoxide for 17.5 CR at 250bar
The variation of carbon monoxide with respect to load can be observed for normal piston and modified piston as shown in Fig. 9. The results show that Carbon monoxide is minimum at 17.5 CR, 200bar pressure, standard injection timing at 20% load 0.018%vol. and it is maximum at 17.5 CR, 250bar pressure, standard injection timing at 80% load 0.102 %vol.

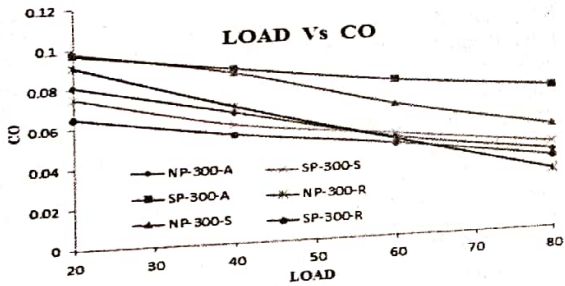


Fig. 9 (c) Load Vs Carbon Monoxide for 17.5 CR at 300bar

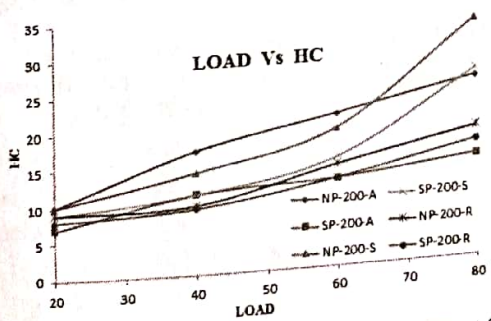


Fig. 10 (a) Load Vs Hydro Carbons for 17.5 CR at 200bar

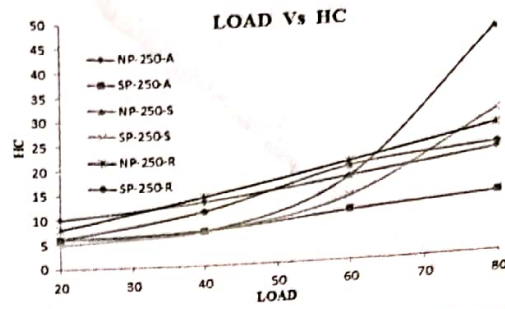


Fig. 10 (b) Load Vs Hydro Carbons for 17.5 CR at 250bar

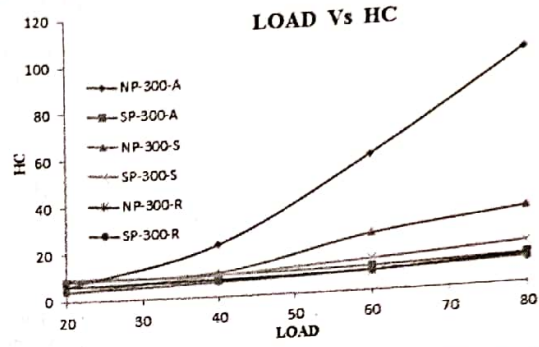


Fig. 10 (c) Load Vs Hydro Carbons for 17.5 CR at 300bar

The variation of hydrocarbons with respect to load for normal piston with modification is depicted in Fig. 10. From the results, it can be noticed that the un burnt hydrocarbon is minimum at 17.5 CR, 300bar Pressure, retard timing for swirl piston at 20% load 4ppm and it is maximum at 17.5 CR, 300bar Pressure, advanced timing for normal piston at 80% load 100ppm.

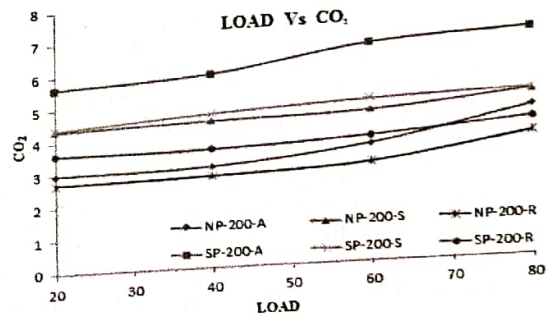


Fig. 11 (a) Load Vs Carbon Dioxide for 17.5 CR at 200bar

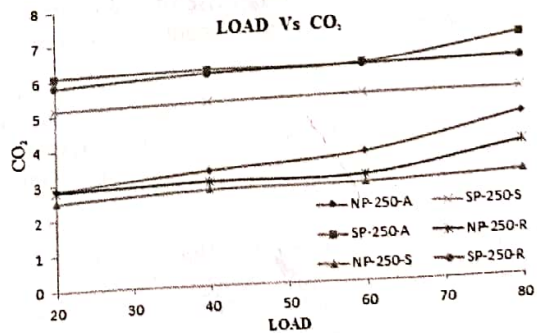


Fig. 11 (b) Load Vs Carbon Dioxide for 17.5 CR at 250bar

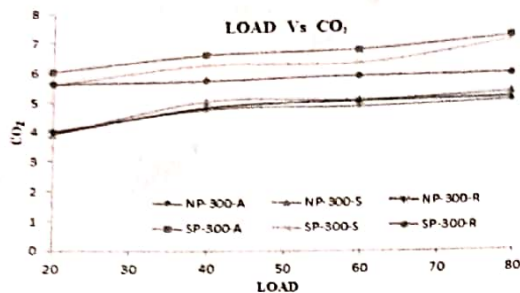


Fig. 11 (c) Load Vs Carbon Dioxide for 17.5 CR at 300bar

The variation of carbon dioxide with respect to load can be observed for normal piston and modified piston is depicted in Fig. 11. The results show that Carbon dioxide is minimum at 17.5 CR, 250bar pressure, standard injection timing for normal piston at 20% load 2.53%vol. and it is maximum at 17.5 CR, 200bar pressure, standard injection timing for swirl piston at 80% load 6.92 %vol.

CONCLUSIONS

Fuel saving will protect the environment and related concern issues. It is necessary to do necessary modification in engine so as to minimize the exhaust emissions. In this context, the geometry of the piston is modified by accommodating rotating blades on the piston crown so as to induce turbulence by means of swirl motion of charge. From the experimental results for a diesel engine with swirl piston:

- The brake thermal efficiency at 17.5 compression ratio, 200 bar pressure and advanced injection timing at 60 % load is found to be maximum value of 35.39 % for swirl piston and it is 33.08 % for normal piston which is an approximate rise of 2-3 % at every load and injection pressures.
- The mechanical efficiency at 17.5 compression ratio, 200 bar pressure and advanced injection timing at 80 % load is found to be maximum value of 89.83% for swirl piston and it is 88.49% for normal piston. Hence there has been a rise of approximately 1-4 % at every condition of the engine for swirl piston. The volumetric efficiency at 17.5 compression ratio, 200 bar pressure and advanced injection timing at 80 % load is found to be maximum value of 82.34% for swirl piston and it is 81.49% for normal piston. Hence there has been a rise of approximately 1-2 % at every condition of the engine for swirl piston
- The brake specific fuel consumption is found to be 0.629 kg/kw-hr for normal piston and 0.543 kg/kw-hr for swirl piston. There has been a decrease of 0.086 kg/kw-hr, the brake specific fuel consumption obtained for swirl piston is less.
- The CO emissions for normal piston is 0.091 % vol and 0.065 % vol. Hence with the use of swirl piston there has been a remarkable decrease of 4% to 20% in CO emissions.
- The HC emission for normal piston is 6 ppm and 4 ppm for swirl piston. Hence with the use of swirl

piston there has been a considerable decrease of 2 ppm in HC emissions.

From the above it can be concluded that with the use of swirl piston there has been an improvement in brake thermal efficiency, mechanical efficiency, volumetric efficiency and decrease of brake specific fuel consumption and have remarkable decrease in exhaust emissions of CO, HC, and increase in CO₂ emissions. Also the results obtained for 200 bar injection pressure are better 250bar injection pressure, 300 bar injection pressure.

References

- [1] Somender Singh, "Design to Improve Turbulence in Combustion Chambers by Creating a Vortex" pure energy systems, 2005-10-13-9600187, 2005.
- [2] Yang-Liang Jeng, Rong-Che Chen and Chao-He Chang, "Studies of Tumbling Motion Generated During Intake in a Bowl-In-Piston Engine", journal of marine science and technology, Vol. 7, No. 1, pp. 52-64, 1999.
- [3] Kern Y. Kang, Je H. Baek, "Turbulence characteristics of tumble flow in a four-valve engine", experimental thermal and fluid science 18 (1998) 231-243.
- [4] Henrik W. R. Dembinski Hans-Erik Angstrom, "Optical Study of Swirl during Combustion in a CI Engine with Different Injection Pressures and Swirl Ratios Compared with Calculations," SAE Technical Paper 2012-01-0682, 2012.
- [5] Jeong-Eue yun, Jae-Joon Lee, "A Study on Combine Effects Between Swirl and Tumble Flow of Intake Port System in Cylinder Head", Seoul 2000 FISITA World Automotive Congress, F2000A094, June 12-15, Korea, 2000.
- [6] Yoshihiro Suzuki, "Surface modifications of pistons and cylinder liners", journal of materials engineering, Vol. 10, Issue 1, PP 61-67, December 1988.
- [7] S.L.V. Prasad, Prof. V. Pandurangadu, V.V. Pratibha Bharathi, V. V. Naga Deepthi, "Experimental Study of the Effect of in Cylinder Air Swirl on Diesel Engine Performance", International Journal of Engineering Science and Technology (IJEST), ISSN: 0975-5462, Vol. 3, No. 2, pp. 1571-1575, Feb 2011.
- [8] Dr. S.L.V. Prasad, Prof. V. Pandurangadu, Dr. P. Manoj Kumar, Dr G. Naga Malleshwara Rao, "Reduction of Emissions by Enhancing Air Swirl in a Diesel Engine with Grooved Cylinder Head" International Journal of Innovative Research in Science, Engineering and Technology, ISSN: 2319-8753, Vol. 2, Issue 12, December 2013.
- [9] Dr. S.L.V. Prasad, Prof. V. Pandurangadu, Dr. P. Manoj Kumar, Dr G. Naga Malleshwara Rao, "Enhancement of Air Swirl in a Diesel Engine with Grooved Cylinder Head" International Journal of Innovative Research in Science, Engineering and Technology, ISSN: 2319-8753, Vol. 2, Issue 8, August 2013.
- [10] B.V.V.S.U. Prasad, C.S. Sharma, T.N.C. Anand, R.V. Ravikrishna, "High swirl-inducing piston bowls in small diesel engines for emission reduction", Applied Energy 88, 2355-2367, 2011.



This is to certify that

Dr./Mr./Ms. Lavanya Pamuloparty


has Presented / Participated in **International Conference** on

Paradigms in Engineering & Technology (ICPET 2016)

Organized by Methodist College of Engineering & Technology, Hyderabad, India,

on 2nd & 3rd March, 2016.

Manuscript Title Revealing of Near Duplicate web Documents
in Software Systems.


Conference Chair

Scanned with
CamScanner



This is to certify that

Dr./Mr./Ms. Lavanya Pamulaparty

has Presented / Participated in **International Conference** on

Paradigms in Engineering & Technology (ICPET 2016)

Organized by Methodist College of Engineering & Technology, Hyderabad, India,

on 2nd & 3rd March, 2016.

Manuscript Title Comparative Analysis of Novel text Steganographic techniques with character and space Wrappings


Conference Chair

Scanned with
CamScanner

Assessment of Seismic Energy obtained from Blast induced Ground Vibrations using Signal Processing Computation Techniques

Vedala Rama Sastry, Garimella Raghu Chandra

Abstract—Enhanced demand for coal and minerals in the country has developed an interest on the environmental problems, which may have potential harm and cause disturbance. Ground vibrations generated due to blasting operations in mines and quarries are very important environmental aspect to be looked into by the researchers. It is clear that a small amount of total explosive energy is being utilized in blasting for breakage of rock mass while the rest is being wasted. The amount of energy which is wasted causes various environmental issues such as ground vibrations, air over pressure and fly rock. Ground vibrations caused by blasting cannot be totally eliminated, yet they can be minimized as far as possible through a suitable blasting methodology. Considerable amount of work has been done to identify ground vibrations and assess the blast performance in terms of the intensity of ground vibrations. However, not much research has gone into the seismic energy and utilizing this energy in understanding performance of blast rounds. In this paper, an attempt was made for the estimation of seismic energy dissipated at different distances from the blast site using Signal Processing Techniques with the help of DADiSP and Advanced Blastware software in three different formations, viz. Limestone, Sandstone and Underground Coal Mine. In total, 116 blast vibration events from Limestone Mines, 96 blast vibration events from Underground Coal Mine and 43 blast vibration events from Sandstone Mines were collected using ground vibration monitors for Signal Processing Analysis of Seismic Energy. Blast induced ground vibrations were recorded in three orthogonal directions collecting 2100-2500 particle motion samples for each.

Keywords—Ground Vibrations, Seismic Energy, Signal Processing Technique, DADiSP Signal Processing Software, Advanced Blastware, Discrete Fourier Transformation (DFT), Power Spectrum Density, Rotational Kinetic Energy

I. INTRODUCTION

When the explosive charge detonates in a blast hole under confinement, the chemical form of explosive energy is converted into gases and work to the surroundings with an enormous pressure according to the first principle of thermodynamics. Explosion of a spherical charge in an infinite rock medium result in three major zones

(Fig. 1): (1) Explosion cavity - where explosion energy is liberated and the process is hydrodynamic; (2) Transition zone - where plastic flow, crushing and cracking occur; and (3)

Vedala Rama Sastry, Professor, Department of Mining Engineering, National Institute of Technology Karnataka, Surathkal, India (vedala_sastry@nitk.edu.in)

Garimella Raghu Chandra, Research Scholar, Department of Mining Engineering, National Institute of Technology Karnataka, Surathkal, India (raghuchandra_mn14f02@nitk.edu.in)

Seismic zone - where strain waves travel as seismic waves [3][6][8].

The partition of the explosive energy in a blast depends on the end effects involved. For instance, part of the fracture work is in its first stage intimately connected to the shock wave flow in the locality of the hole and, in the later stages, also to the rock movement, which begins as the fractures burst open. All other energy transfer takes place obviously, as follows: (a) expansion work of the fractures, that is absorbed as elastic and plastic deformation of the rock in the surface of the fractures as they are penetrated by the gases; (b) heat transferred to the rock from the hot detonation products; and (c) heat and work conveyed as enthalpy of the gases venting to the atmosphere through open fractures and stemming [7].

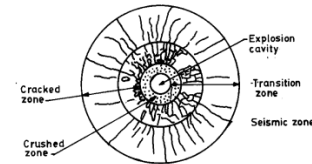


Fig. 1 Zones of rock deformation around a blast hole [3]

Therefore, the energy balance of the blast can thus be expressed by:

$$EE = EF + ES + EK + ENM$$

where,

- EE = Explosive energy
- EF = Fragmentation energy
- ES = Seismic energy
- EK = Kinetic energy
- ENM = Energy forms not measured

Research studies carried out have indicated that in opencast mines there is a potential of seismic energy generation from 2-13J from a given blast. Also studies have indicated possible correlation between maximum charge per delay and the seismic energy. Therefore, a study leading to the possible estimation of energy dissipated at different distances from the blast site may be of industrial utility [10].

Seismic waves are classified as body waves and surface waves. Body waves travel through the interior of earth. Ground vibration waves are of two types, Primary (P-wave) and Secondary (S-wave). Surface waves generate when the

radiating body waves impinge on a stress free plane, like surface or any discontinuity. These waves travel along the surface and discontinuities. Rayleigh waves are the best known surface waves and include both dilation and distortion

of the medium. Surface waves carry maximum percentage of the radiated energy and are predominant at longer distances from the blast source, since their attenuation rate is slower than body waves. In addition, the frequency of surface waves is lower than body waves and frequently found to be in the range most favorable for structural response [4]. All these waves are characterized by exponential decrease in particle oscillation amplitude as distance from energy source increases [11]. Fig. 2 shows the effect of ground vibration waves on the structures.

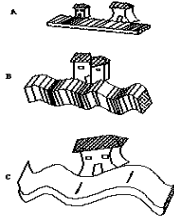


Fig. 2 Effect of Body Waves and Surface Waves

- a. Longitudinal wave
- b. Rayleigh wave
- c. Transverse wave

Vibration monitoring and recording instruments (Seismographs)

Many types of seismographs are available today. Each performs the basic function of measuring ground motion but supplies much additional information. Most seismographs are equipped with meters that register and hold the maximum value of the vibration components and the sound level. Other seismographs are equipped to produce a printout which gives a variety of information such as maximum value for each component, frequency of vibration for the maximum value, maximum displacement, maximum acceleration, vector sum, and sound level. Blast information such as date, blast number, time, location, job designation, and other pertinent information can also be added to the printout [5].

Normally, a seismograph record shows the following information (Fig. 3):

- Three lines or traces, one for each vibration component. A fourth line or trace for the acoustic or sound level.
- A calibration signal for each trace.
- Timing lines which appear as vertical lines running across all or part of the record.

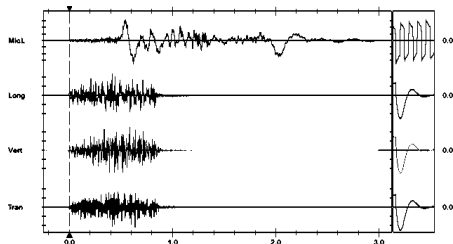


Fig. 3 A Seismograph record

From the studies conducted by previous research [9], it is found that the actual utilization of explosive energy for the productive work is about 15-20%, and remaining energy is wasted in the form of unwanted side effects like ground vibrations. If the energy utilization could be improved even by 1%, there would be huge benefits to the industry, with much reduced environmental effects. In this paper, an attempt

for the estimation of shock wave energy through the analysis of ground vibration waves generated from the blasts conducted in mines was made using signal processing techniques, in order to determine the energy carried / dissipated, later to be used in optimizing the blast design process.

II. FIELD INVESTIGATIONS

Initially for the assessment and estimation of seismic energy, blasts were conducted in three different mine formations in Southern part of India viz. Limestone, Underground Coal and Sandstone. For Signal Processing Analyses purpose, in total 116 blast vibration event samples were collected in three different Limestone Mines by conducting 32 opencast mine blast studies. Similarly, 96 blast vibration event samples were collected from Underground Coal Mine by conducting 34 blast studies. Further, 43 blast vibration event samples were collected in two different Sandstone Mines by conducting 16 opencast mine blast studies.

In Limestone formation, the distance between the monitoring point of vibration monitor (or seismograph) and blast site was varied from 30m to 485m. In Underground Coal formation, the vibration monitor (or seismograph) was placed both on surface (with about 65m parting) and in underground for finding the exact propagation of blast wave. The distance between vibrations monitor and blast location was varied from 15m to 111m in underground and from 54m to 122m on surface. Similarly, in Sandstone formation, the distances of monitoring instrument were varied as 100m to 2033m from the blast location.

III. RESEARCH METHODOLOGY

Vibrations induced from blasting operations were monitored using Ground Vibration Monitors. Ground vibrations generated from all the blasts were monitored at different distances and at specific structures using Microprocessor based Blast Vibration Monitors of InstanTel, Canada. The geophone of the monitor was glued to the structure / ground with Plaster of Paris for effective tapping of ground vibration wave by geophone. Typical monitoring of ground vibrations is shown in Fig. 4. A typical wave form obtained is shown in Fig. 5. The typical vibration event samples were analyzed using Advanced Blastware Software.



Fig. 4 Ground vibrations monitoring at different locations during blast studies

The obtained vibration event samples data from Vibration Monitors were analyzed with the help of Advanced Blastware and DADiSP software using signal processing techniques. Initially, the vibration samples of ground vibration events were converted into ASCII file using Advanced Blastware. The vibrations were analyzed using signal processing techniques available in the Advanced Blastware and found the intensity of blast waves (Fig. 6). The obtained

ASCII values were imported into DADiSP for further signal processing analyses.

DADiSP for reconstruction of Vibration wave which gives rise to quantized discrete signal (Fig. 7). At about 2100-2500 vibration samples were recorded for a vibration in one direction and similarly vibrations in other two orthogonal directions were recorded with about 2100-2500 particle motion samples.

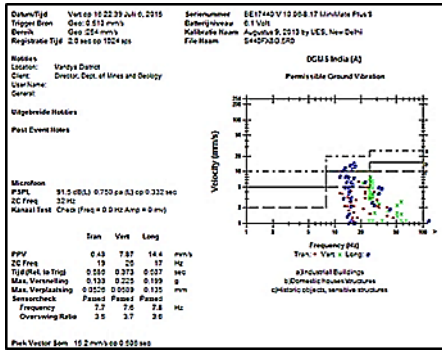


Fig. 5: Typical ground vibration event

Seismic energy can be obtained by considering area under the combination of three orthogonal vibration waves in frequency response.

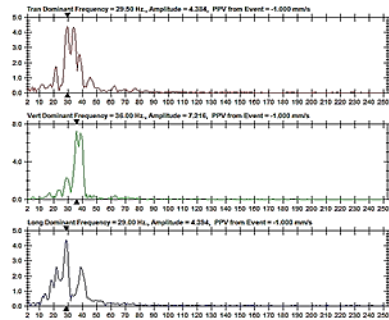


Fig. 6 Signal Processing Analysis of a blast vibration using Advanced Blastware

Initially, the discrete ASCII samples of Vibration wave obtained from Advanced Blastware are imported in

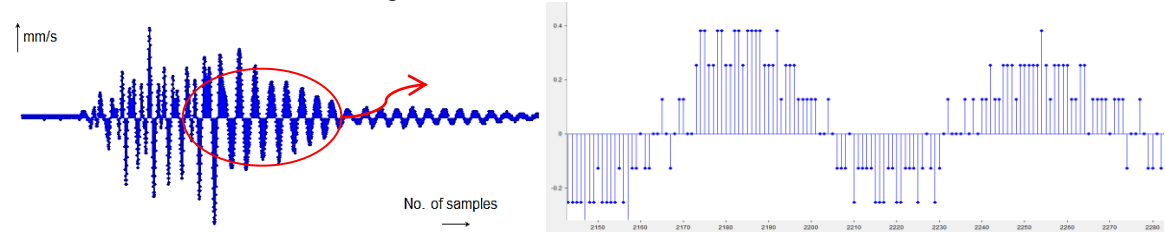


Fig. 8A Signal with discrete sample magnitudes

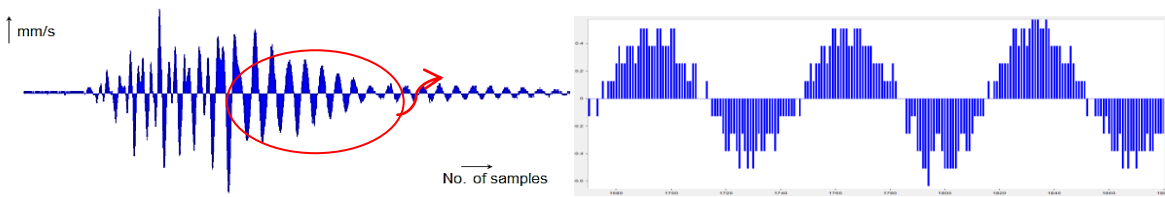


Fig. 8B Reconstruction of a signal with discrete samples

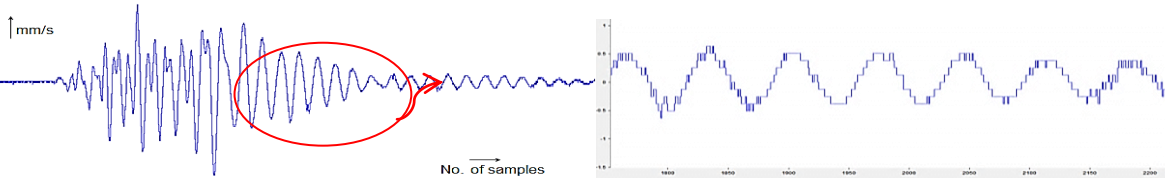


Fig. 8C: Reconstructed quantized signal

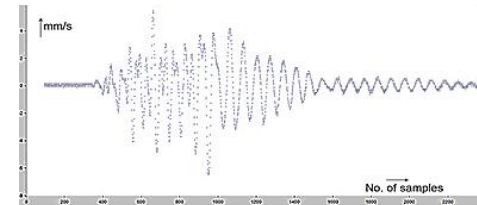


Fig. 7 Quantized discrete signal

The vibration samples were further processed to obtain a reconstructed vibration wave using reconstruction signal analysis available in DADiSP software in steps (Fig. 8). After the reconstruction process, the reconstructed sampled blast induced vibration analog waves were taken considering all three orthogonal directions for further signal processing computation (Fig. 9).

The waveforms which were in time domain were converted to frequency domain by applying Discrete Fourier Transformation (DFT). Since, Blast wave is a non-periodic discrete wave, application of direct Fourier Transformations for finding the frequency is not possible. Application of Discrete Fourier Transformation remains the system magnitude with same units but in frequency domain (Fig. 10).

This indicates no change in the state of the signal. After DFT using DADiSP package, the signals were further processed to find Power Spectrum Density. Power Spectral Density (PSD) is a measure of a signal's power intensity in the frequency domain. In practice, the PSD is computed from the DFT spectrum of a signal. The PSD provides a useful way to characterize the amplitude versus frequency content of a random signal [2].

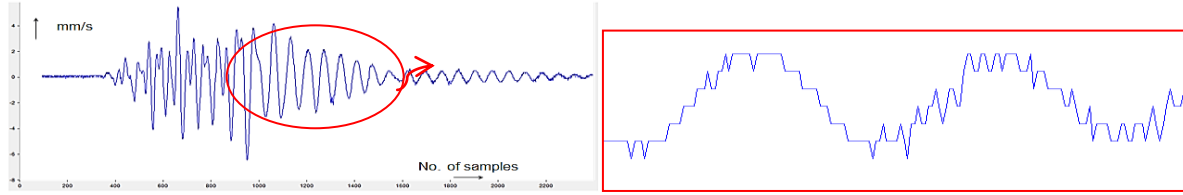


Fig. 8D Reconstructed discrete signal
 Fig. 8: Reconstruction of Discrete Samples using DADiSP Package

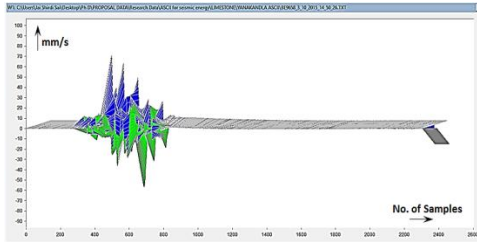


Fig. 9: Typical reconstructed vibration wave in three orthogonal directions

- Input (before DFT) – Vibration Velocity in time domain (mm/s)
- Output (after DFT) – Vibration Velocity in frequency domain (mm/s)

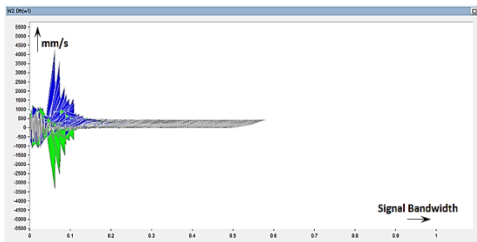


Fig. 10: Computation of DFT to random vibration signal aligned in three directions

When the input random vibration signal in frequency domain having units as ‘G’, the amplitude values of a PSD are normally expressed in ‘G²/Hz’, where the term ‘G’ indicates units of the random vibration signal, mm/s, in frequency domain (Fig. 11). Therefore, application of PSD to the vibration signal gives rise to,

- Input (before PSD) – Vibration Velocity in frequency domain (mm/s)
- Output (after PSD) – (mm/s)²/Hz → (μm²/s²)/Hz → μm²/s

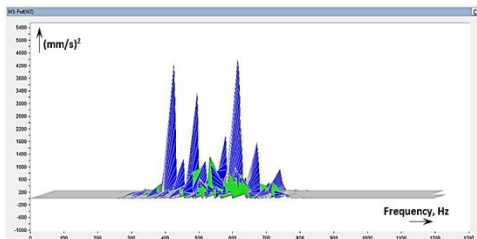


Fig. 11: Computation of Power Spectrum Density to the random vibration signal aligned in three directions after DFT operation

It was assumed that the vibration wave had a unit mass, M in kg. Therefore, the output after PSD operation was changed as μ (kg.m²/s). Output is in the form of angular

momentum (L). The angular momentum, L of a rigid body with moment of inertia I rotating with angular velocity ω, is given by:

$$L = I \cdot \omega$$

where,

$$L = \text{Angular momentum, kg-m}^2/\text{s}$$

$$I = \text{Moment of inertia, kg-m}^2$$

$$\omega = \text{Angular Velocity, rad/s}$$

The Rotational Kinetic Energy for a mechanical system considering the total mechanical energy of a rigid body is defined as,

$$KE_r = \int_0^\omega L d\omega = \int_0^\omega (I \cdot \omega) d\omega = \frac{1}{2} I \cdot \omega^2$$

where,

$$KE_r = \text{Rotational Kinetic Energy, } \mu \cdot \text{Joules}$$

Hence, from the above analysis, it is needed to apply integration to the output of vibration data after PSD operation. Since, Integration is applied only for continuous signals and for discrete signals application of integration is not possible. Hence, “Partial Sum” operation is computed for finding the Rotational Kinetic Energy available in the waveform [1]. Then the area under the vibration waves after “Partial Sum” were calculated which gives rise to the **Seismic Energy** of the blast induced vibration wave by using the command `area(abs(w4))`, which returns the area under the signal,

Seismic energy, at the left side bottom of the window (Fig. 12).

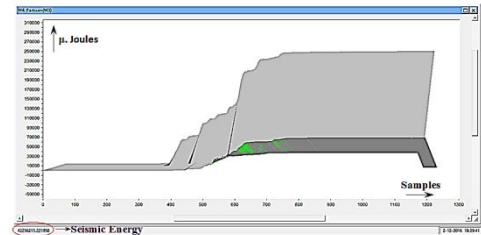


Fig. 12: Seismic Energy of the blast induced vibration wave

IV. CONCLUSIONS

From the studies conducted and analysis computed, the following conclusions are drawn:

- It is understood that Advanced Blastware and DADiSP package are the best tools for signal processing analyses and

are very helpful in finding Seismic Energy of a blast induced vibration wave passing in three orthogonal directions.

- The analysis done on three different rock formations stated that the coefficient of correlation between Seismic Energy and Peak Particle Velocity is higher in case of Sandstone Mine at about 95.19% compared to other two formations Limestone Mine at about 90% and Underground Mine inside coal seam gallery at about 91.94%, whereas from the vibration studies it is concluded that there is no proper correlation between Seismic Energy and Peak Particle Velocity in the case of Underground Mine blasts monitoring on Surface.
- From the regression analysis made, it is observed that there is a proper correlation between Seismic Energy and Scaled Distance in all three different rock formations, Limestone Mine at about 82.92%, Underground Mine at about 81.76% and Sandstone Mine at about 85.68%, respectively.
- From the vibration data obtained, it is understood that the intensity of Vibration Velocity is higher in the case of
- Limestone Formation thereby causing higher loss in Explosive Energy leading to generation of more seismic energy. Also in the case of Underground Mine Formation, the resulted seismic energy is very less, this might be due to more parting between the surface and underground blasting location.

REFERENCES

- [1] Anon, (1997). "Rotational Kinetic Energy", website <http://theory.uwinnipeg.ca/physics/rot/node6.html> (accessed on October 19, 2015).
- [2] Anon, (2015). "PSD (Power spectral density) - description by Brüel & Kjær", (accessed on June 6, 2015).
- [3] Atchison, T.C., Duvail, W.I., and Pugliese, J.M., (1964). "Effect of decoupling on explosion generated strain pulses in rock", USBM RI: 6333.
- [4] Holloway, R., Lundborg, N., and Runquist, G., (1983). "Ground vibrations and damage criteria", SWEDEFO Report R85:1981.
- [5] Konya, C.J., and Walter, E.J., (1990). Surface blast design, Prentice Hall Publishers, USA.
- [6] Nicholls, H.R., (1962). "Coupling explosive energy to rock", Geophysics, 27(3), 305–316.
- [7] Sanchidrian, J.A., Segarra, P., and Lina, M.L., (2007). "Energy components in rock blasting", International Journal of Rock Mechanics & Mining Sciences, 44, 130–147.
- [8] Sastry, V.R., (1989). "A study into the effect of some parameters on rock fragmentation by blasting", Unpublished Ph.D. Thesis, BHU, India.
- [9] Sastry, V.R., (2001). "Study of the effect of ground vibrations and fly rock caused due to blasting operations in Kallakudi limestone mine", An Unpublished Technical Report submitted to Dalmia Cement (Bharat) Limited, Tamilnadu
- [10] Sastry, V.R., and Ramchandar, K., (2014). "Assessment of performance of explosives / blast results based on explosive energy utilization", Unpublished R&D Project Report, Central Mine Planning and Design Institute Ltd., Ranchi, India.
- [11] Taquieddin, S.A., 1982. "The role of borehole containment on surface ground vibration levels at closed scaled distances"

Ground Vibrations & Water Borne Shock Waves Caused due to Underwater Blasting in Ports – A Case Study

V. Rama Sastry, G. Raghu Chandra, and C. Karthik

Abstract— Underwater drilling and blasting is adopted in ports as a part of capital dredging. Underwater blasts affect the ambient environment in terms of ground vibrations and water borne shock waves. Knowledge regarding the pressure due to each underwater blast can help us monitor the safety of structures and workers or other aquatic life. Deepening of draught was carried out in the entrance channel / and turning circle of outer harbour in Vishakhapatnam Port, Southern India, involving underwater blasting in about 2,50,000m² area, for a depth of 8m. Blasts were designed to ensure safety of various structures in the port and its efficacy was established by monitoring of blast vibrations at different structures. The paper describes the methodology adopted, equipment used and various steps taken in the safe execution of the rock dredging project. The paper also discusses the calculation of safe distance from environmental and worker's safety aspect for the safe execution of the rock dredging projects.

Keywords— Ground Vibrations, Rock Dredging, Safety, Underwater Blasting, Water Borne Shock Waves.

I. INTRODUCTION

Fragmentation of hard sea bed rock by underwater blasting is a vital operation in rock dredging projects. While desirable results are good fragmentation and throw of fragmented material, the undesirable effects include damage to surrounding structures, accident to workers in vicinity and harmful effect on surrounding marine flora and fauna. The safety aspects of underwater blasts should ensure that these undesirable effects are minimized. To check or ensure that the structures /and vessels surrounding are safe during the blast, the PPVs of generated ground vibrations are monitored. The protection of various marine species both flora and fauna, divers operating in the location is also of utmost importance from the environmental and safety point of view. The pressure of the water waves generated due to shock waves of blast is monitored and the safe distance is established prior to conduct of blast. Based on these data, sufficient precautionary actions and warning can be given to protect the divers and marine life in the vicinity of blast.

Manuscript received Mar. 25, 2016.

Prof. V. Rama Sastry is with the Department of Mining Engineering, National Institute of Technology Karnataka, Surathkal, Mangalore-575025, INDIA (e-mail: vedala_sastry@yahoo.co.in).

G. Raghu Chandra is with the National Institute of Technology Karnataka, Surathkal, Mangalore-575025, INDIA (e-mail: raghuchandraindia.com)

C. Karthik is with the National Institute of Technology Karnataka, Surathkal, Mangalore-575025, INDIA (e-mail: karthikcsaseendran@gmail.com)

II. LITERATURE REVIEW

A. Ground Vibrations

When the intensity of strain waves generated due to detonation in a blasthole, diminishes to the level where no permanent deformation occurs in the rock mass, i.e. beyond the fragmentation zone, strain waves propagate through the strata in the form of elastic waves. These waves in the elastic zone are known as ground vibrations [1]. Ground vibrations may cause structural damage and annoyance to public, while damage to nearby structures/ vessels and marine life may be caused by excessive underwater shock waves. Whenever blast vibration occurs, it vibrates the ground/soil particle with certain velocity and imparts to it certain amount of acceleration. Ground vibrations are, therefore, quantified as displacements that vary with time (in terms of 'mm'), accelerations (in terms of 'g') and/or particle velocities (in terms of mm/s) at particular ground locations [2]. The damage potential also depends upon the predominant frequency besides the PPV. Reference [3] made extensive studies to evaluate the influence of 14 blast variables considered to be having an influence on the amplitude of ground vibrations. They found that charge weight per delay and length of delay to be having the most significant influence on the intensity of ground vibrations. It is very difficult to define the precise level of vibration at which damage begins to occur in a structure. Safe levels for assessing the damage have been defined in terms of Peak Particle Velocity (PPV - mm/s) in different countries. In India, the Directorate General of Mines Safety has given threshold PPVs for different structures based on dominant frequency of the wave form. Standards of DGMS and USBM were used for assigning threshold values of PPV for different structures.

B. Water Borne Shock Waves

In an underwater blast the water is pressurized and displaced due to burning and detonation. A huge amount of energy is released from the blast and this energy moves away from the blast center and spreads in all directions. Reference [4] states that during a blast, in the region beyond the direct effect of thermal and detonation effect, two major impacts are shock waves and the expanding gaseous reaction products. The initial high – intensity shock wave is the most dangerous but it loses its intensity as it moves outward from the source of the explosion. The waves that follow after initial shock waves are less severe. In an underwater explosion initial shock wave is followed by a succession of oscillating bubble pulses. A shock wave is a compression wave that expands radially out from the detonation point of an explosion. At a distance from a

detonation, the propagation of the shock wave may be affected by several components including the direct shock wave, the surface-reflected wave, the bottom-reflected wave, and the bottom-transmitted wave. The direct shock wave results in the peak shock pressure (compression) and the reflected wave at the air-water surface produces negative pressure (expansion). For an explosion with the same energy and at the same distance, an underwater blast is much more dangerous to animals than an air blast. Shock wave in air dissipates more rapidly and tends to be reflected at the body surface; in water the blast wave travels through the body and may cause internal injury to gas-filled organs due to impedance differences at the gas-liquid interface. The pressure generated due to underwater blasting depends on many factors like – type of explosive, size of the charge, characteristics of the seabed, location of the explosive charge, water depth, distance from the explosion and degree of submersion of the diver. If divers are present underwater while a UW blast is being conducted, it can cause severe damage to the divers depending upon the distance between diver and blast location. The human body can survive relatively high blast overpressure without experiencing barotrauma. Reference [5] in their study found that a blast overpressure of 5psi (3.45MPa) will rupture eardrums in about 1% of people exposed to it, and a 45psi (31.26MPa) overpressure will cause eardrum rupture in about 99% of all subjects. Also the threshold for lung damage was suggested to be about 15psi (10.34MPa) blast overpressure and 35-45 psi (24.13MPa to 31.0MPa) overpressure was found to cause 1% fatalities, and 55(37.92MPa) to 65 psi (44.8 MPa) overpressure to cause 99% fatalities.

Underwater blasts cause severe effect on the marine life as well. Damage to swim bladder and other gas containing organs have been found to be the main cause for the death of fish and other marine mammals [6]. Reference [7] suggested that negative phase of the pressure wave causing the swim bladder to burst outward was the main reason for the death of fishes due to underwater blasts. Studies have found that the damage to gas contained organ was the main reason for the death of marine mammals as well [8]. The lungs and intestinal tract was the organ most affected in these species. Studies by US Army Corps, New York Division found that phenomenon of “cavitation hat,” observed in blasting of aquatic environment is the major reason for increased mortality in aquatic biota. The negative reflected wave generated by the deflection of the water surface toward the air results in a shallow disc of negative pressure centered over the explosive and there is high potential for overextension of air filled organs in aquatic biota due to the negative pressure associated with the cavitation hat.

III. INVESTIGATIONS

The sea bed of Visakhapatnam Port consists of hard Khondalite rock mass. Method of drilling and blasting for fragmenting and displacing the hard rock mass was proposed to enable the dredging activity. A total area of about 2,50,000m² was dredged, from the existing draught of about -8m to -16m, uniformly. As the sea bed consists of hard rock mass, explosive energy was used for breaking the hard sea bed, in order to deploy appropriate dredgers. Fig. 1 shows the plan of the

dredging area with structures around.

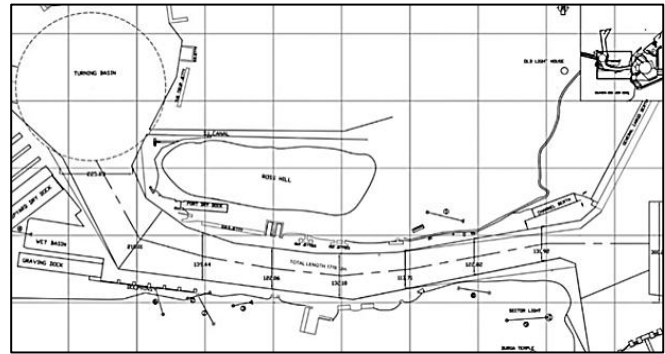


Fig. 1 Entrance channel and turning circle of outer harbor of VPT

A. Methodology for Under Water Blasting

The methodology of underwater blasting for rock dredging consisted of the following stages [9]:

a. Pre-Blast survey

- Study bed rock characteristics
- Study structures around to be protected

b. In-Blast monitoring

- Continuous monitoring of ground vibration
- Reengineering blast design
- Creation of data-bank
- Periodic submission of records

c. Post-Blast survey and analysis

- Study of vibration records
- Study of structures around as a part of Post-blast survey

B. Underwater Blasting

Method of confined charges was used as the depth to be dredged varied from about -2m to -8m at different places. Based on the rock mass characteristics, it was fixed to use blastholes of 110mm diameter. All the operations of drilling of required number of blastholes, charging of blastholes with required quantity of explosive, establishing the connections in the blast round and final firing of the blast round were carried out from the floating drill barge. The drill barge had facility for mounting required number of DTH drills, compressors, separate storage for explosives and detonators etc. Three drill barges fitted with 15, 12 and 7 drills were deployed. Each barge was mounted with two units of DGPS systems, for ensuring precise positioning of barge. The cycle of underwater blasting operations consisted of the following activities:

- Positioning of drill barge
- Drilling required number of holes
- Simultaneous charging of blastholes, immediately after completion of drilling
- Repeating the above operations for required number of rows
- Establishing the blast layout
- Marching the drill barge to safe distance
- Taking all the precautions
- Firing the blast round

Nitrate based slurry explosive available in couplable plastic tubes was used. Each cartridge was of 1kg and 2kg weights.

Required quantity of explosive to be charged, like 2kg, 3kg, 4kg or 6kg was prepared by coupling the plastic tubes containing explosive. The explosive charge in general varied from 3kg to 8kg per hole as per depth of the blast holes. The maximum permissible charge per delay (determined based on trial blast study initially, for protecting various structures simultaneously) was also considered while determining the charging pattern. Initially, electric short delay detonators, and subsequently shock tube system of initiation was used.

IV. RESULTS AND DISCUSSION

A. Ground Vibrations

During the entire period of rock blasting more than 1,345 blasts were conducted and PPVs were monitored at 65 structures, using Blast Vibrations Monitors, Minimate Plus of InstanTel, Canada. Some of the structures of importance are shown in Fig. 2. PPVs recorded using Minimate of InstanTel, Canada, at Hindustan Shipyard Ferry Jetty and ORS VPT Dry Dock are shown in Fig. 3.



A. HSL Ferry Jetty



B. VPT Dry Dock

Fig. 2 Some important structures

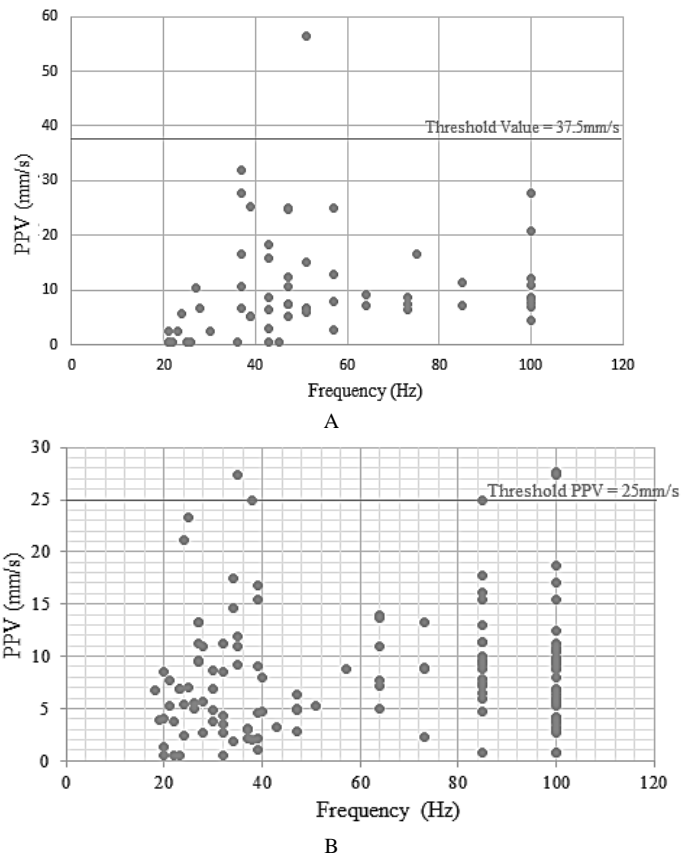


Fig. 3 PPVs recorded at different structures

The PPV values for HSL Ferry Jetty varied from <0.51 mm/s to 56.5 mm/s. Recorded PPV value exceeded the threshold value of 37.5 mm/s only in 1.67% cases and it shows the accuracy and efficiency of blast design. For VPT Dry Dock only in 1.43% cases, the threshold PPV value was exceeded. Similarly, for all other 63 structures in the surroundings, the resulting PPV values were well within limits, indicating very safe underwater blasting operations carried out.

B. Water Borne Pressure Wave and Safe Distances

As per US Navy guidelines the equation given by [10] is used for calculating the overpressure as:

$$P = \frac{13000 \sqrt[3]{W}}{r} \quad (1)$$

where,

P = Pressure on the diver, psi

W = Weight of the explosive (TNT), lb

r = Range of the diver from the explosive, ft

Using the recommended safe exposure values suggested by various standards, reverse calculation was carried out to determine the safe distances using the equation:

$$d_{min} = \frac{13000 \sqrt[3]{w}}{p} \quad (2)$$

where,

P = Pressure on the diver, psi

w = Weight of the explosive (TNT), lb

R = Range of the diver from the blast site, ft

According to US Navy guidelines a safe exposure pressure for underwater blasts is considered to be 50psi (34.5MPa) [11]. Using Greenbaum and Hoff equation, calculations were carried out for the frequently used maximum charge per delays (kg) used for the underwater blasting project at the Vishakhapatnam port [1]. Results obtained are depicted in Fig. 4, as it can be used to interpret safe distance for explosive range up to 60kg.

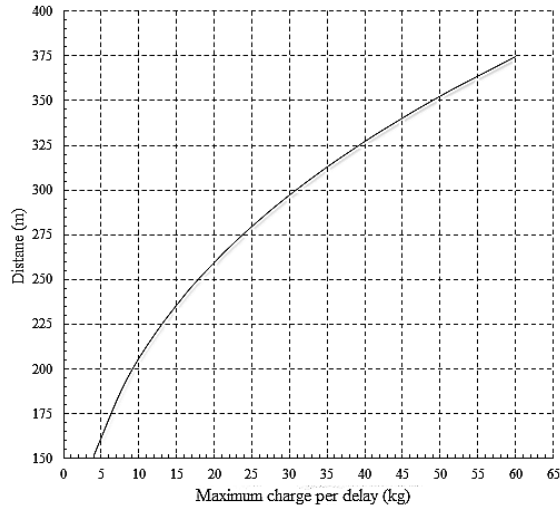


Fig. 4 Safe distance for divers

Reference [12] of the Alaskan Department of Fish and Game's guidelines to protect fish and incubating embryos from the impacts of blasting in and near the water bodies, it is stipulated that blast induced pressures should not exceed 2.7psi (1.9MPa). The Indian Ocean is also home to numerous marine mammals such as dolphins, sharks and porpoise. Studies have shown that blast induced pressures greater than 8psi (5.5MPa) can cause injury to mammals [8]. Accordingly, the safe distances for protecting mammals were determined. The safe distances recommended for fishes, mammals and humans are shown in Fig. 5.

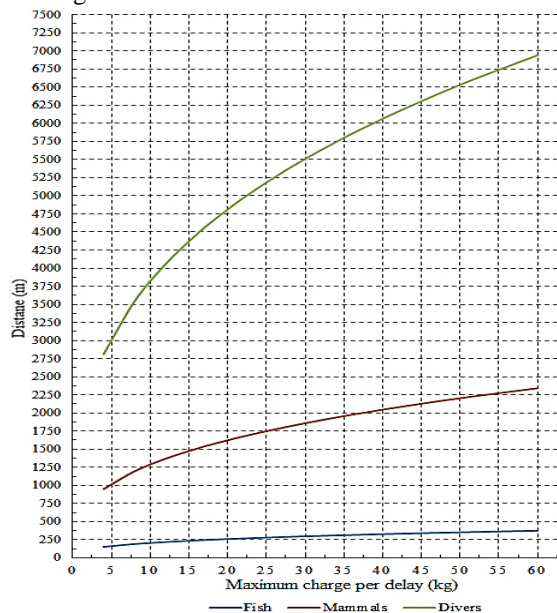


Fig. 5 Combined safety chart for divers, fish and mammals

V. CONCLUSIONS

Underwater blasting is a vital component of rock dredging projects in ports. The major environmental impacts associated with underwater blasting are the water borne shock waves and ground vibration. Use of explosives charge confined in blastholes substantially reduces the effects of ground vibrations on submerged structures and objects in water. Safety criteria recommended in terms of PPV for residential, marine and other structures can be used to monitor and protect them from ground vibrations. Underwater blasting operations were carried out in a safe and efficient manner using down-the-hole delay system, for the first time in the country, by dividing the total explosive column in blastholes into 2 or 3 decks, initiating at different timings, in order to maintain the safe maximum charges per delay for protecting close by structures.

Water borne shock waves are detrimental to the safety of not only the divers, but also to aquatic life like fish and marine mammals.

It is not only important to protect structures, but also the aquatic life from the impact of water borne shock waves from underwater blasts. Various safe distances that can be adopted at site for ensuring safety of divers during underwater blasting were arrived at. For a blast having maximum charge per delay of 20kg in the underwater blast, safe distances were found to be 250m for humans, 1650m for mammals and 4875m for fishes, by considering a threshold pressure value of 1.9MPa for fishes as suggested by Alaskan Department of Fish and Games organization United States. The safe distance values calculated for fishes and marine mammals can be made use in field in other projects also, to ensure that project locations having endangered or rarely existing species can be protected at the time of underwater blasting operations as a part of rock dredging projects.

REFERENCES

- [1] V. R. Sastry, "A report on underwater blasting operations for rock dredging in the entrance channel & turning circle of inner harbour of Vishakhapatnam Port", An unpublished internal report submitted to Vishakhapatnam Port Trust, India, 2013.
- [2] W. I. Duvall, and D. E. Fogelson, *Review of criteria for estimating damage to residences from blasting vibrations*, United States Department of the Interior, pp. 5, 1962.
- [3] J. F. Wiss, and P. W. Linehan, *Control of vibration and blast noise from surface coal mining*, USBM OFR, pp. 79–103, 1978.
- [4] G. L. Hempen, and T. M. Keevin, *The environmental effects of underwater explosions with methods to mitigate impacts*. US Army Corps of Engineers, St. Louis District, LEGACY Report, pp. 22-25, 1997.
- [5] S. Glasstone, and P. J. Dolan, "The effects of nuclear weapons", 3rd ed. *U.S. Department of Defense and the Energy Research and Development Administration*, pp. 552–553, 1997.
- [6] D. R. Richmond, J. T. Yelverton, and E. R. Fletcher, *Far-Field Underwater Blast Injuries Produced by Small Charges*, Defence Nuclear Agency, Department of Defence, Washington, D.C. Technical Progress Report, pp. 17–18, 1973.
- [7] C. L. Hubbs, and A. B. Rechnitzer, *Report On Experiments Designed to Determine Effects of Underwater Explosions on Fish Life*, California Fish & Game Division. pp. 333–352, 1952.
- [8] D. R. Ketten, *Estimates of Blast Injury and Acoustic Trauma Zones for Marine Mammals from Underwater Explosions*, pp. 391 – 407, 1995.
- [9] V. R. Sastry, "Underwater blasting for rock dredging for entrance channel and outer harbour circle of VPT", An unpublished report submitted to Vishakhapatnam Port Trust, India, 2014.

- [10] L. J. Greenbaum, and E. C. Hoff, *A Bibliographic sourcebook of Compressed Air, Diving and Submarine Medicine*, Vol. No.-III, Bureau of Medicine and Surgery, Navy Department, 1966.
- [11] Anon, *U.S Navy Diving Manual*, Revision 6, Change A, Published by Direction of Commander, Naval Systems Command, United States Navy, pp. 2.9-2.10, 2011.
- [12] K. D. Kristen, and A. M. Catherine, *Blasting Effects on Salmonids*, Alaskan Department of Fish and Game, Division of Habitat, pp. 23, 2013.



Prof. V. Rama Sastry, born on Feb. 16, 1959, obtained his BE degree in Mining Engineering from Osmania University in 1980, and subsequently M.Tech degree in 1983 and Ph.D degree in 1990 in the field of Mining Engineering from Banaras Hindu University, India. His fields of research interests are Rock Mechanics, Rock Fragmentation and Rock Dredging.

Rama Sastry is having teaching and research experience of over 31 years. He is presently working as Professor of Mining Engineering at National Institute of Technology Karnataka, Surathkal, Mangalore (Government of India). He produced 7 Ph.Ds and guiding 6 more scholars in the areas of Rock Mechanics, Tunneling, Underground Large Spaces, Seismic Energy. He guided over 32 PG students projects and over 100 UG projects. He handled 17 R&D Projects and over 165 industry sponsored consultancy projects. He has over 160 research publications to his credit in various conferences and journals.

Prof. Rama Sastry bagged two Gold Medals from The Institution of Engineers (India) and One from Mining, Geological Metallurgical Institute (India) for best paper publication. He served as Director on the Boards of Central Mine Planning & Design Institute Limited (A Govt. of India Public Sector Unit) and KIOCL Limited (A Govt. of India Public Sector Unit).



Assessing the Explosive Energy Utilization in Mine Blasting – Role of High Speed Videography

V.R. SASTRY¹, B. RAJASEKHAR², G. RAGHU CHANDRA³

¹Professor - Mining Engineering, National Institute of Technology Karnataka, Surathkal, Mangalore - 575025, INDIA

²PG Student - Civil Engineering, National Institute of Technology Karnataka, Surathkal, Mangalore - 575025, INDIA

³Research Scholar - Mining Engineering, National Institute of Technology Karnataka, Surathkal, Mangalore - 575025, INDIA

Email: vedala_sastry@yahoo.co.in, rajasekhar.ballari@gmail.com

Abstract:

Blasting activity involving the utilization of explosive energy is an important operation in mining and civil engineering projects for obtaining fragmentation and displacement of the hard strata. A study was taken up in three different limestone mines to assess the blast performance. Analysis of the blasts was done using High Speed Video Camera for assessing burden rock movement and wastage of gaseous energy. High Speed Videography revealed the release of gaseous energy prematurely through structural discontinuities in the face. Analysis indicated the maximum burden rock movement of about 15.25m/s in Mine - A, 8.265m/s in Mine - B and 8.667m/s in Mine - C. Analysis of funneling effect of gaseous energy (through stemming ejection) revealed higher gas energy release with shorter stemming columns. Blasts in Mine - C having a bench height of about 7m, resulted in 2.36m gas ejection through stemming zone which is 20% higher funneling compared to blasts in Mine - B whose bench height is about 8m with stemming ejection of about 1.96m. When the stemming height in blastholes increased from 2m to 2.75m, there is 2 - 3 times decrease in the escape of gas energy through stemming zone as observed by High Speed Video Camera.

Keywords: High Speed Videography, Blast Performance, Burden Rock Mass Movement, Funneling, Fragmentation.

1. Introduction:

Rock blasting is the major task in opencast mines to fragment the strata for achieving required production with desirable fragmentation and with minimum side effects. Many technological developments happened in the recent past for safe and efficient usage of explosives. ANFO based explosives are safer and in the study which was taken up in three limestone mines, ANFO is used as explosive column (Anon, 1987),^[1] (Jha, 2013).^[2] The effectiveness of ANFO is assessed in the given limestone formations, along with its ability to produce optimum fragmentation, the side effects like ground vibrations, noise, fly rock etc. Trivedi et al. (2014).^[3]

The proposed paper aims at assessment of the performance of blasts using High Speed Video Camera in three opencast limestone mines located in Southern India. Studies were conducted in a scientific manner in terms of fragmentation, muck pile disposal, and wastage of explosive energy through ground vibrations and escape of gas energy through stemming zone (Mishra, 2012),^[4] Nabiullah et al. (2002).^[5] Investigations were carried out in two limestone

Mines - A and B belonging to Telangana, while one limestone Mine - C belonging to Andhra Pradesh (Figure 1).



Mine - A



Mine - B

Specifications	Blast Number				
	1	2	3	4	5
Bench height (m)	8	9	9	9	9
Burden (m)	3	3	3	3	3
Spacing (m)	6	6	6.3	6	6.3
No of Blastholes	84	53	59	61	68
Explosive/ Hole (kg)	47	54	45	47	49
Total Exp. Charge (kg)	3975	2850	2975	2875	3320
Stemming (m)	2	2.5	2.75	2.5	2.5



Mine - C

Figure 1: View of limestone mines

2. Methodology:

In total, 35 blasts were conducted in all three mines to assess the blast performance. All blasts were recorded by high speed video camera (Figure 2). Various blast parameters used in studies are listed in Table 1. Blastholes were of 115mm diameter. Depth of the blastholes was varying from 8m to 9m in Mine - A, 6m to 8m in Mine - B and 6m to 7m in Mine - C. The fragmentation in blasted muckpiles was analyzed by digital image processing based Wipfrag software.

Specifications	Blast Number						
	1	2	3	4	5	6	7
Bench height (m)	8	7	6	7.5	8	6	7.5
Burden (m)	3	3	3	3	3	3	3
Spacing (m)	6	5.5	5.5	6	6	5.5	5.25
No. of Blastholes	34	30	34	26	34	26	63
Explosive/ Hole (kg)	46	37	31	46	49	34	41
Total Exp. Charge (kg)	155	110	105	120	165	87	257
Stemming (m)	2.5	2.25	2.25	2.5	2.5	2	2



Figure 2: High speed video camera of 1000fps capacity

Table 1: Summary of blasts studied
Limestone Mine - A
Limestone Mine - B
Limestone Mine - C

Specifications	Blast Number						
	1	2	3	4	5	6	7
Bench height (m)	7	7	7	7	7	6	7
Burden (m)	3.5	3.5	3.5	3.5	3.5	3.5	3.5
Spacing (m)	6	6	6	6	6	6	6
No. of Blastholes	16	30	24	18	30	20	10
Explosive/ Hole (kg)	39	37.5	35	37	38	25	28
Total Exp. Charge (kg)	625	1125	841	658	1150	492	283
Stemming (m)	2.5	2.5	3	3	2.5	3.5	3.5

The millisecond delay configuration in all blasts was also monitored. High speed video camera used to record the blasts is of S-MOTION model camera. S-MOTION is a compact, portable high speed camera used in industrial research and biochemical analysis. Camera provides results on the spot and recorded video is played using imaging studio software. It is having the features of downloading/conversion of data to PC non - volatile memory. Use of point and click measurements in software is a practical tool for measurements for recording videos Chiappetta et al. (1988),^[6] Chiappetta et al. (1990),^[7] Sastry et al. (2013).^[8]



Following are the features of the camera adopted:

- It is capable to capture up to 1000 fps
- It has 2 lens
 - One can capture up to 70mm
 - The other external lens can capture from 70mm to 300mm
- The camera has MMC card of 8Gb (can capture a video up to 5 - 6s).

Data obtained from High speed photography is used to determine Chiappetta et al. (1987),^[9]

- Causes of misfires
- Poor loading practices
- Poor firing practices
- Effects of gas venting
- Delay intervals between holes
- Optimum initiating system
- Massive ground movement
- Source of oversize
- Explosive efficiency
- Optimum explosive rock burden combination
- Muck profiles

Studies carried out by Sastry and Chandar (2015)^[10] further established the role high speed videography in assessing the performance of gas energy wastage through stemming zone and the major joints in bench face.

Full scale studies carried out by Sastry et al. (2015)^[11] established a clear correlation between fragmentation and bench height, as per the analogy developed by Ash(1975).^[12] This study also revealed clearly the escape of gaseous energy through major jointing in the benches.

Sequence of some typical blasts with the respective timing intervals from the point of initiation in three limestone mines are shown in Figures 3, 4 and 5. From the analysis made by these videos, it is observed that there was a similarity in the average velocity of burden rock mass in Limestone Mines - B and C.

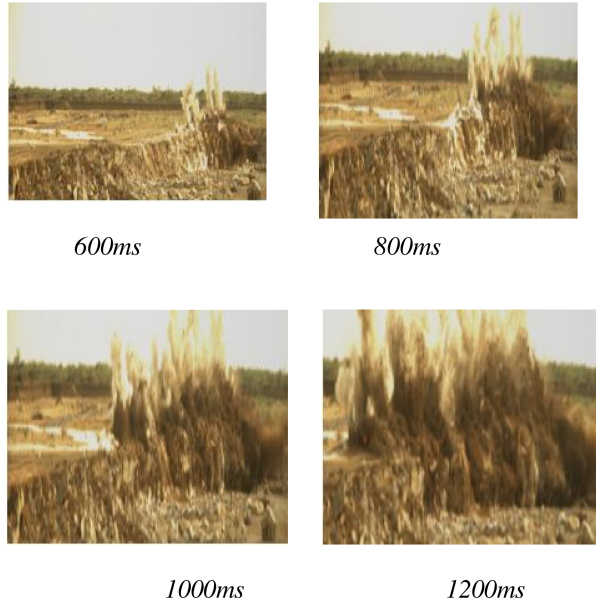


Figure 3: Sequence of a blast with specified delay intervals: limestone mine - A

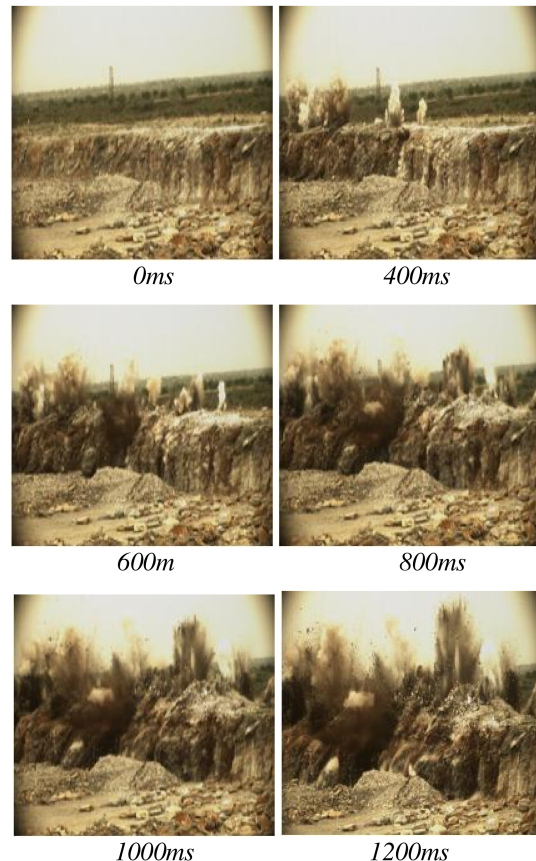
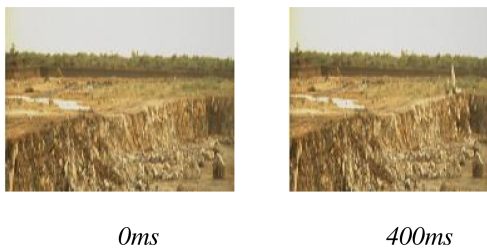
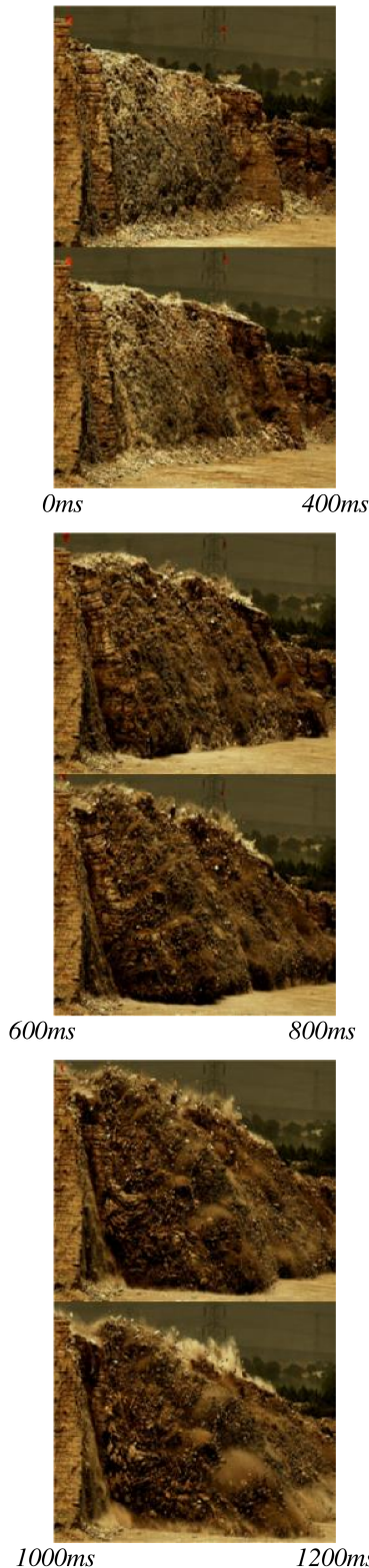


Figure 4: Sequence of a blast with specified delay intervals: limestone mine - B





3. Results and Discussion:

ProAnalyst software was used to track down the rock movement of bench face, find the escape of gaseous energy through stemming zone, and measure the displacement of rock from the bench face and angle of rock trajectory. Also the height of the benches or throw of material was found digitally (Figures 6, 7 and 8).



Height of the bench obtained as 8.538m



Tracking of burden rock mass during blast

Figure 5: Sequence of a blast with specified delay intervals: limestone mine – C



Displacement of rock movement

Figure 6: Analysis made for a blast in limestone mine - A



Tracking of burden rock mass during blast



Height of the bench obtained as 8.075m



Displacement of rock movement obtained as 6.637m

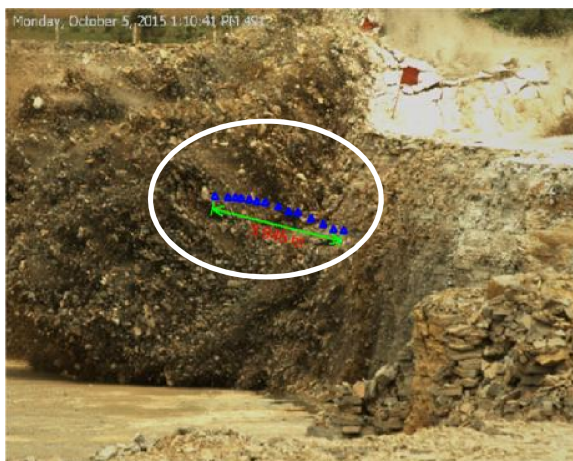
Figure 7: Analysis made for a blast in limestone mine - B



Height of the bench obtained as 7.038m



Tracking of burden rock mass during blast



Displacement of rock movement obtained as 3.945m

Figure 8: Analysis made for a blast in limestone mine - C

Also the escape of gas energy from the bench face, due to geological discontinuities was also analyzed (Figure 9).



Mine - A



Mine - B



Mine - C

Figure 9: Escape of gaseous energy from the bench face

The escape of gas energy through stemming zone was observed in all three limestone mines (Figure. 10).



Mine - A



Mine - B



Mine - C

Figure 10: Analysis of stemming ejection (smallest and largest funnels observed)

The velocity of burden rock mass movement during the blast was observed for some of the blasts conducted (Table 2). The average velocity of bench movement from all the blasts conducted in respective mines was determined to be 15.25m/s in Mine - A, 8.265m/s in Mine - B and 8.876m/s in Mine - C. From the results obtained it is observed that Mine - A with average bench height of 9m is predominantly giving faster moment to burden rock mass compared to that of Mine - B and Mine - C with average bench heights of 8m and 7m respectively. Therefore, from the results it is concluded that with a maximum value of 9m average bench height, the velocity of bench movement will be maximum in Mine - A compared to Mines - B & C whose bench heights are 8m and 7m respectively.

With increase in bench height to burden ratio, velocity of burden rock is observed to increase. Greater BH/B ratio indicates the more flexure the bench in the beam analogy as proposed by Ash (1973).^[13] In Mine - A, it is observed from the High Speed Videography analysis that Blast - 4 with 68 blastholes and a maximum Bench Height to Burden (BH/B) ratio of 3 has maximum velocity of rock movement, of about 27.8 m/s compared to Blasts - 2 and 3 with similar BH/B ratio with blastholes 53 and 59 respectively. Similarly in Mine - B, Blast - 5 with 63 blastholes and a maximum BH/B ratio of 2.67 resulted in a maximum velocity of rock movement about 10.3m/s compared to Blast - 1 with similar BH/B ratio with 34 blastholes. In Mine - C, Blast - 5 with 39 blastholes and a maximum BH/B ratio of 2 resulted in maximum velocity of rock movement 12.6m/s compared to Blasts - 1, 2, 3 and 4 whose blasthole depth is lesser than Blast - 5. From the analysis made, it is concluded



that as BH/B ratio increases, the velocity of rock movement increases due to reduced stiffness of bench (Table 2).

*Table 2: Comparison of velocity of rock movement with Bench Height to Burden ratio
Limestone Mine - A
Limestone Mine - B
Limestone Mine - C*

In Mine - A, Vertical drilling was adopted for blastholes in one blast (Blast - 2) out of five blasts conducted. From the analysis made by ProAnalyst software, it is observed that the Blast - 2 with vertical drilled holes has lesser velocity of rock movement about 9.67m/s compared to Blast - 4 with inclined holes which is having a velocity of 27.8m/s, in which both the blasts have similar volume of about 162m³. Similarly in Mine - B, one blast (Blast - 5) drilled with vertical blastholes resulted in a lesser velocity of rock movement about 7.12m/s compared to Blast - 4 with inclined holes resulted a velocity of 10.13m/s, in which both the blasts have similar volume of about 99m³. In Mine - C, one blast (Blast - 6) with vertical blastholes resulted in a lesser velocity of rock movement of about 6.15m/s compared to other blasts with inclined holes whose velocity of rock movement is about 8m/s (Table 3). Typical method of drilling adopted in three Limestone Mines is depicted in Figure 11.

Parameters	Blast Number			
	1	2	3	4
Displacement (m)	15.1	7.74	8.44	18.07
Time (s)	1	0.8	1	0.65
Velocity (m/s)	15.1	9.67	8.44	27.8
BH/B ratio	2.67	3	3	3

Parameters	Blast Number				
	1	2	3	4	5
Displacement (m)	7.09	6.64	7.45	9.27	5.01
Time (s)	1	0.81	0.9	0.9	0.7
Velocity (m/s)	7.09	8.25	8.28	10.3	7.12
BH/B ratio	2.67	2.34	2.5	2.67	2

Parameters	Blast Number					
	1	2	3	4	5	6
Displacement (m)	3.94	3.71	2.69	2.67	2.47	1.41
Time (s)	0.46	0.42	0.33	0.3	0.19	0.23
Velocity (m/s)	8.58	8.88	8.16	8.89	12.6	6.15
BH/B ratio	2	2	2	2	2	1.71



Inclined drilling



Vertical drilling

Figure 11: Method of drilling adopted

From the analysis made, it is observed that in mine - A, Blast - 3 with lesser charge factor of 0.29kg/m^3 is having a lesser velocity of 8.44m/s compared to Blast - 1 with higher charge factor of 0.34kg/m^3 , which resulted in velocity of rock mass of about 15.1m/s . Similarly in Mine - B, Blast - 1 with lesser charge factor of 0.31kg/m^3 resulted in lesser velocity of 7.09m/s compared to Blast - 5 with higher charge factor of about 0.34kg/m^3 having a velocity of rock mass about 10.3m/s . Also in Mine - C, Blast - 3 with minimum charge factor of 0.2kg/m^3 resulted in lesser velocity of 8.16m/s compared to Blast - 5, whose charge factor is 0.26kg/m^3 , which is the highest amongst all other blasts, resulted in a maximum velocity of rock mass about 12.6m/s . It could be concluded that with the increase in charge factor, there will be an increase in burden rock movement (Table 3).

Study revealed that 8m bench height resulted in 6.157m gas ejection whereas bench height with 7m resulted in 7.24m gas ejection which could be interpreted as lesser gas energy wastage with taller benches. This phenomenon could be correlated with the finer fragmentation resulting from taller benches from the model scale studies carried out by Sastry (1989),^[13] indicating better utilization of explosive energy in taller benches.

Table 3: Comparison of velocity of rock movement with charge factor

Mine - A					
Parameters	Blast Number				
	1	2	3	4	
Type of hole	Inclined	Vertical	Inclined	Inclined	
Volume (m^3)	144	162	170.1	162	
Charge Factor (kg/m^3)	0.34	0.34	0.29	0.29	
Velocity (m/s)	15.1	9.67	8.44	27.8	

Mine - B					
Parameters	Blast Number				
	1	2	3	4	5
Type of hole	Inclined	Inclined	Inclined	Inclined	Vertical
Volume (m^3)	144	115.5	135	144	99
Charge Factor (kg/m^3)	0.31	0.32	0.34	0.34	0.34
Velocity (m/s)	7.09	8.25	8.28	10.3	7.12

Mine - C						
Parameters	Blast Number					
	1	2	3	4	5	6
Type of hole	Inclined	Inclined	Inclined	Inclined	Inclined	Vertical

hole	1	2	3	4	5	6
Volume (m^3)	147	147	126	147	147	147
Charge Factor (kg/m^3)	0.26	0.25	0.24	0.25	0.26	0.2
Velocity (m/s)	8.58	8.88	8.16	8.89	12.6	6.15

4. Conclusions:

- High speed video camera is useful to track down the trajectories of fragmented material from the bench. It is a useful tool to find out the movement of the bench faces. The wastage of gaseous energy through ejection of stemming material could be tracked down for assessing performance of blasts.
- From the results, it is observed that with the increase in Bench Height to Burden Ratio there is an increase in velocity of rock mass.
- Incline blastholes resulted in higher rock mass velocity compared to vertically drilled blastholes.
- High Speed Videography analysis indicated that, increase in the charge factor results in higher burden rock movement.
- Study revealed that 8m bench height resulted in 6.157m gas ejection whereas bench height with 7m resulted in 7.24m gas ejection which could be interpreted as lesser gas energy wastage with taller benches.

5. References:

- [1] A. K. Jha, "Evaluation of Mine Productivity and Economics by Effective Blast Instrumentation - A Techno Economic Proposition", *Journal of Geological Resource and Engineering*, Issue No.1 PP. 31 -38, 2013.
- [2] A. K. Mishra, "Blast Design Using High Speed Video Camera in Coal Measure Rocks", *LAP Lambert Academic Publishing*, ISBN: 384658696X., 2012.
- [3] Nabiullah, M. Jagdish, B. M. P. Pingua, and T. N. Singh, "Application of High Speed Video technique in Blasting." *Journal of Mines, Metals & Fuels*, 50 (3), PP. 54-57., ISSN 0022-2755., 2002.
- [4] Rama Sastry Vedala, K. Raghu Chandra, N. Adithya and Saiprasad, "Application of High - Speed Videography in Assessing the Performance of Blasts." *International Journal of Geological and Geotechnical Engineering*, 1(2), PP. 19-33., 12/2015.
- [5] R. F. Chiappetta and M. E. Mammele, "Analytical High-Speed Photography to Evaluate Air Decks, Stemming Retention and Gas Confinement in Presplitting, Reclamation and Gross Motion Application", *Proceedings, Second International Symposium on Rock Fragmentation by Blasting*, PP. 23-28., Keystone, CO, USA, August., 1987.
- [6] R. F. Chiappetta and M. E. Mammele, "Blasting Analysis and Design Using High-Speed Photography", (Part III) *Proceedings, Society of Mining Engineers Conference*, PP. 25-29., Phoenix, AZ, USA, January 1988.
- [7] R. F. Chiappetta and B. Vandenberg, "Workshop on Using High-Speed Motion Picture Photography for Blast Analysis, Evaluation and Design", *Seminar Proceedings, Second High-Tech Seminar on State-of-the-Art Blasting*



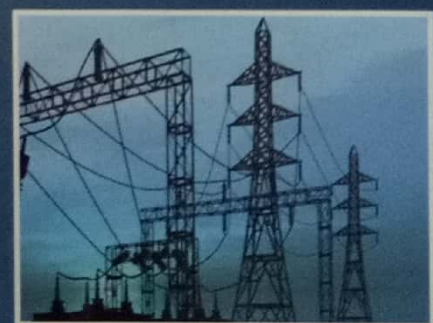
- Technology, Instrumentation and Explosives Applications*, Orlando, Florida, USA, PP. 154., 1990.
- [8] R. Trivedi , T. N. Singh, and A. K. Raina, “Prediction of Blast - induced Fly rock in Indian limestone mines using Neural Networks”, *Journal of Rock Mechanics and Geotechnical Engineering*, Elsevier B.V., 1674-7755.,2014.
- [9] V. R. Sastry and K. Ram Chandar, “Analysis of Delay Timing in Blasting Operations using High Speed Video Recordings”, *National Seminar on Explosives & Infrastructure Industry*, National Institute of Technology Karnataka, Surathkal, 2013.
- [10] Anon,“Explosives and Rock Blasting Bulletin of Atlas Power Co.,” Dallas, TX, 1987.
- [11] Ash, “*The Influence of Geological Discontinuities on Rock Blasting*”, Ph.D Thesis, University Missouri, Rolla, 1973.
- [12] V. R. Sastry, K. Ram Chandar, “Report on the assessment of Blasts/Explosives based on the Explosive Energy Utilization”, sponsored by coal India ltd, an unpublished report submitted to CIL, 2015.
- [13] V. R. Sastry, “*A Study of the Effect of some Parameters on Rock Fragmentation due to Blasting*”, an unpublished Ph.D Thesis, Banaras Hindu University, Varanasi, 1989.

ISBN: 978-93-5258-110-8

Proceedings of The International Conference *on* Paradigms in Engineering & Technology

ICPET 2016

March 2-3, 2016, King Koti Road, Abids
Hyderabad- 500001, Telangana, India



METHODIST COLLEGE OF ENGINEERING & TECHNOLOGY

(Affiliated to Osmania University)

HYDERABAD, TELANGANA

www.methodist.edu.in

Mitigation of Balanced and Unbalanced Voltage sag and Improving the Power Quality Using DVR

Rajini Kanth P

Assistant Professor
Methodist College of Engineering and Technology
Hyderabad, India
raznikanth.nite@gmail.com

Abstract: Voltage disturbances are the most common power quality problem due to increased use of complicated electronic equipment in industrial distribution system. There are many different solutions to compensate voltage sag but the use of a Dynamic Voltage Restorer (DVR) is considered to be the most effective method. This paper gives the investigation on DVR which compensates the balanced and unbalanced voltage sag at the load side. In this paper a new control scheme based on Synchronous reference frame theory is proposed to mitigate Voltage sag. The control scheme is verified using MATLAB/SIMULINK under different fault conditions.

Keywords: DVR, power quality, Voltage Sag voltage swell.

I. INTRODUCTION

Now a day, modern industrial equipments are based on electronic devices such as electrical drives and programmable logic controller. The electronic devices are very sensitive for the disturbances and are less tolerant to power quality problems such as voltage sags. Voltage sags are the most severe disturbances to the industrial equipments.

Voltage support at a load is achieved by reactive power injection at the load point of common coupling. The common method for this is to install mechanically operated shunt capacitors in the primary terminal of the distribution transformer. The mechanical switching may be via signals from a supervisory control and data acquisition (SCADA) system, with some timing schedule. The disadvantage is that, high speed transients cannot be compensated. Some sag is not corrected within the limited time with mechanical switching devices. Transformer taps may be used, but tap changing under load is not economical.

Another power electronic solution to the voltage regulation is by using custom power devices such as Unified power quality conditioner (UPQC), and Dynamic voltage restorer (DVR). DVR is one of the most custom power devices which inject voltage in series with the line to regulate the voltage at the load end..

II. OPERATION OF DVR

The general schematic diagram of DVR consists of an injection transformer, a harmonic filter, a voltage source converter (VSC), an energy storage unit and a control system. The single line diagram of DVR is shown in Fig. 1.

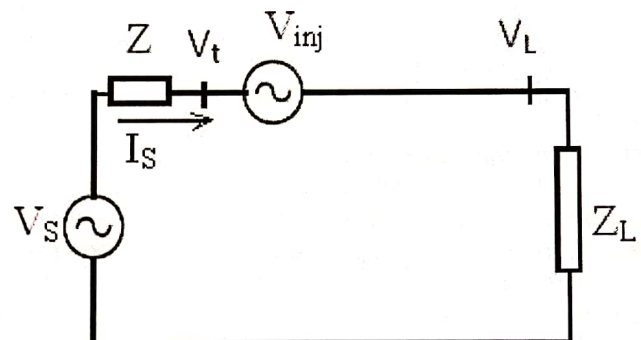


Fig 1: Single line diagram of DVR

The DVR injects a voltage (V_{inj}) in series with the terminal voltage (V_t) so that load voltage (V_L) is maintained a constant magnitude. The equivalent circuit of DVR is shown in Fig. 2. The system impedance Z_{TH} depends on the fault level of load bus. When the voltage (V_{TH}) drops, the DVR injects a series voltage (V_{inj}) through the injection transformer so that the required load voltage magnitude V_L can be maintained.

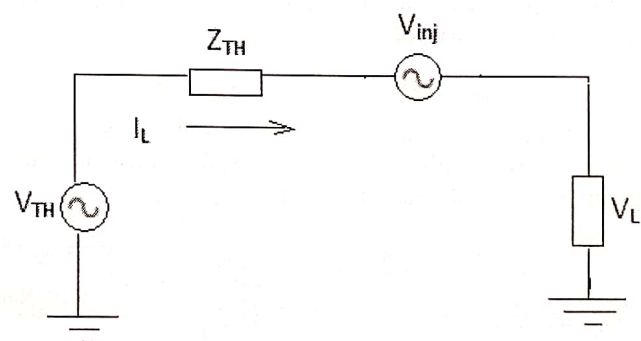


Fig 2: Equivalent circuit of DVR

The series injected voltage of the DVR can be written as

$$V_{DVR} = V_L + Z_{TH} I_L - V_{TH} \quad (1)$$

Where Z_{TH} : The load impedance condition

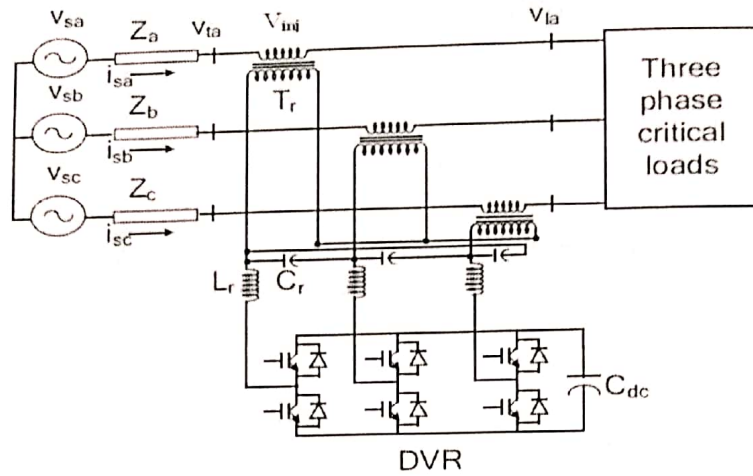


Fig 3: Three phase DVR scheme.

The source impedances (Z_a, Z_b, Z_c) are between source and the terminal. The DVR utilize three single phase transformers (T_r) To inject voltages in series with the terminal voltage. A voltage source converter (VSC) along with a DC capacitor (C_{dc}) is used to realize a DVR. The inductor in series (L_r) and the parallel capacitor (C_r) with the VSC are used to minimize the ripple in the injected voltage. The injected voltage has two components. The voltage injected in quadrature with the current is to maintain the load voltage at constant magnitude and in the in-phase voltage is to maintain the dc bus voltage of VSC and also to meet the power loss in the DVR. The control scheme is to achieve these two components of the injection voltage and this is possible by controlling the supply currents. The currents are sensed and these two components of currents, one is the component to maintain the DC bus voltage of DVR and the second one is to maintain the load terminal voltages, are added with the sensed load current to estimate the reference supply currents.

The series compensator known as DVR is used to inject a voltage in series with the terminal voltage. The sag in terminal voltages are compensated by controlling the DVR and the proposed algorithm inherently provides a self-supporting dc bus for the DVR. The desired source currents (in d-q components) are obtained as

$$i_{sd} = i_d + i_{cd} \tag{2}$$

$$i_{sq} = i_q + i_{cq} \tag{3}$$

Where i_d and i_q are the average values of the d and q axis components of the current. i_{cd} is the output of the DC voltage controller and i_{cq} is the output voltage of the AC voltage controller. Three phase reference supply currents are derived using the sensed load voltages (V_{la}, V_{lb}, V_{lc}), terminal voltages (V_{ta}, V_{tb}, V_{tc}) and dc bus voltage (V_{dc}) of the DVR as feedback signals.

III. CONTROL SCHEME OF DVR

The proposed control scheme is based on estimation of reference supply currents. The proposed control scheme for the control of DVR is shown in Fig. 4.

The synchronous reference frame theory based method is used to obtain the direct and quadrature axis components of the load currents.

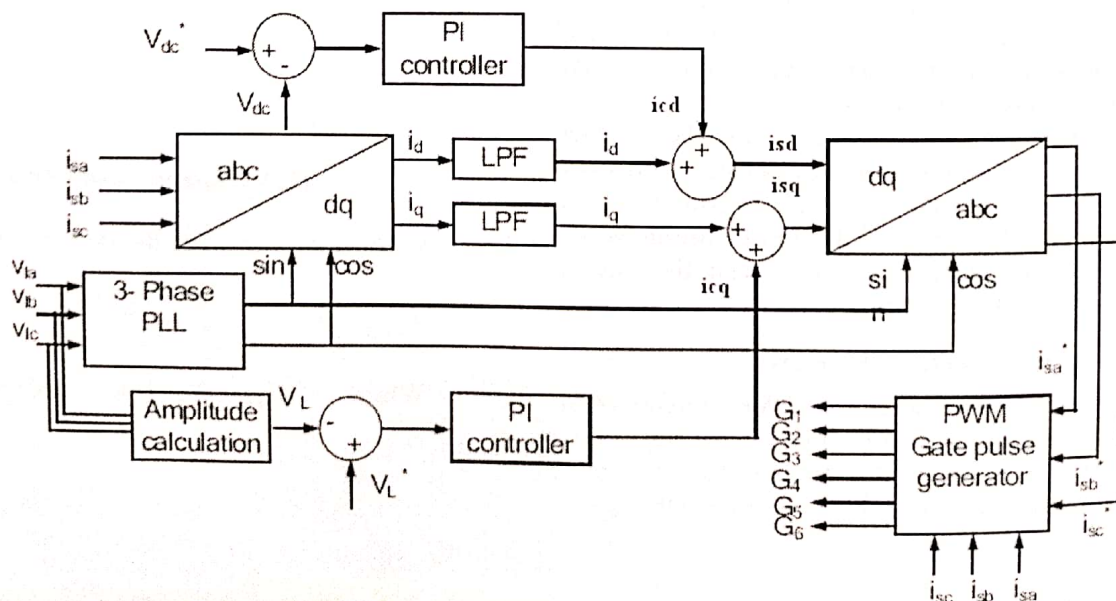


Fig 4: Control scheme of DVR

V. RESULTS AND DISCUSSION

5.1 Under normal condition

The source voltage (V) under normal conditions is shown in Fig 6.1(a). In Fig 6.1(b) the Load voltage has sag at 0.1 sec and occurs up to 0.2 sec. the DVR injects a voltage in series

with the terminal voltage. The load voltage which is maintaining at rated value from 0.1 sec to 0.2 sec after DVR compensation is shown in Fig 6.1(e). The load voltage is observed to be satisfactory for DVR compensation.

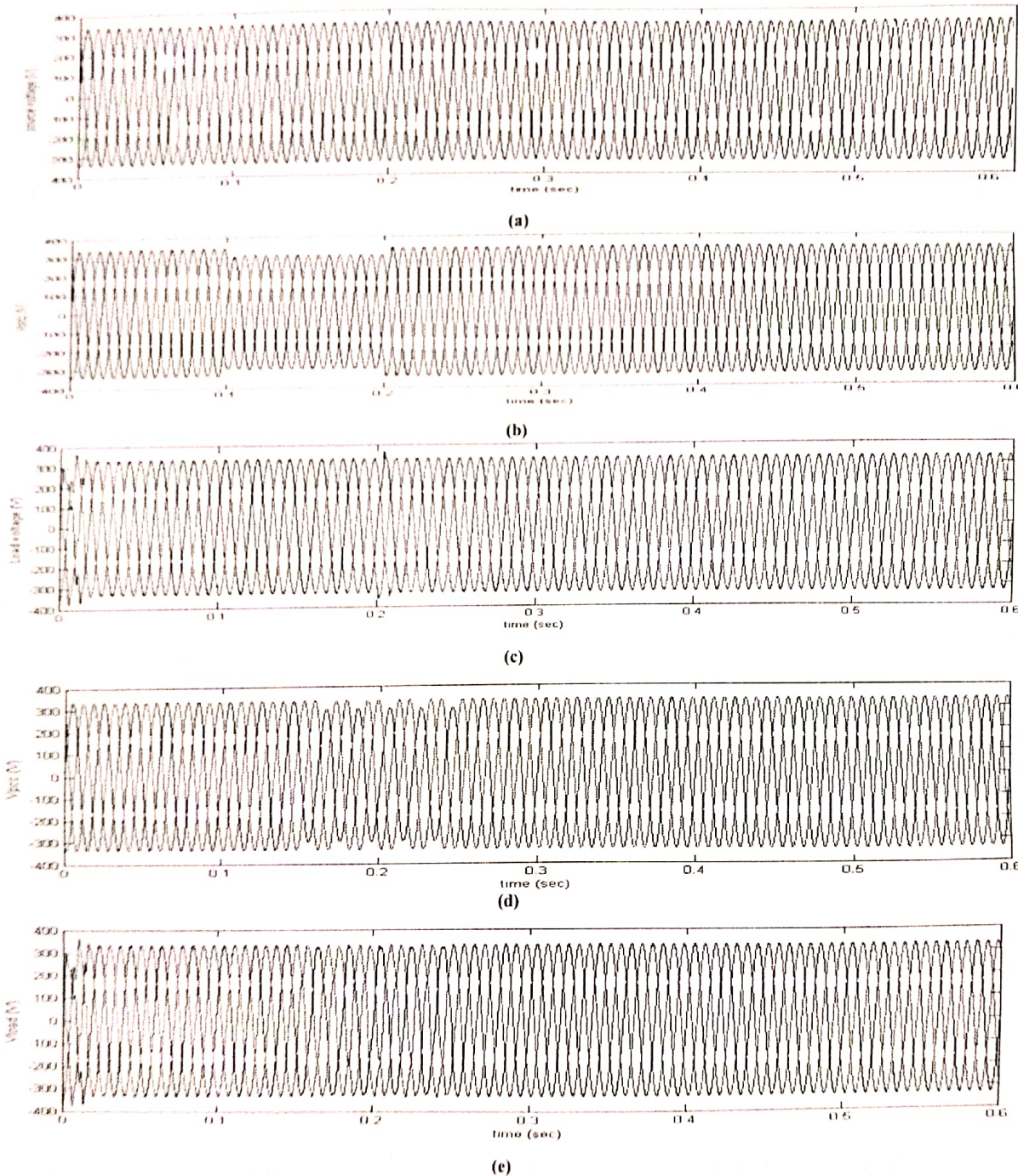


Fig 6.1: Dynamic behavior of DVR for Voltage sag compensation

5.2 During Unbalanced supply

In Fig. 6.1 (d) the load voltage has an unbalanced supply at 0.15 sec and occurs up to 0.25 sec with an L-G fault. The DVR injects a voltage in series with the terminal voltage.

The load Voltage which is maintaining at rated value from 0.15 sec to 0.25 sec after DVR compensation is shown in Fig. 6.1 (e). The load voltage is observed to be satisfactory after DVR compensation

V. CONCLUSION

In this project a new control scheme based on synchronous reference frame (SRF) theory has been used for the DVR for three phase three wire distribution system to improve the performance during balanced voltage sag, and unbalanced voltage sag condition. The performance of the DVR has been observed to be satisfactory through simulation using MATLAB SIMULINK (Sim Power Systems tools) software for compensation of voltage sag, and unbalanced voltage sag.

REFERENCES

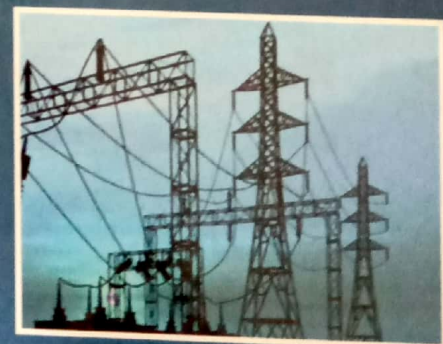
- [1] A. Ghosh, A.K Jindal and A Joshi, "Design of a capacitor supported dynamic voltage restorer (DVR) for unbalanced and distorted loads", IEEE Trans. on Power Delivery, vol.19, no.1, pp. 405-413, Jan,2004.
- [2] K.R. Padiyar, FACTS Controllers in Transmission and Distribution, New Age International, New Delhi, 2007.
- [3] B. N. Singh, A. Chandra, Al-Hadded and B. Singh, "Performance of sliding-mode and fuzzy controllers for a static synchronous series capacitor", IEEE Proc. On Generation, Transmission and Distribution, vol. 146, no. 2, pp. 200-206, March, 2009.
- [4] Amit Kumar Jindal, Arindam Ghosh and Avinash Joshi, "Critical load bus voltage control using DVR under system frequency variation", Electric Power Systems Research, 2007.

ISBN: 978-93-5258-110-8

Proceedings of The International Conference *on* Paradigms in Engineering & Technology

ICPET 2016

March 2-3, 2016, King Koti Road, Abids
Hyderabad- 500001, Telangana, India



METHODIST COLLEGE OF ENGINEERING & TECHNOLOGY
(Affiliated to Osmania University)
HYDERABAD, TELANGANA
www.methodist.edu.in

Power Quality improvement in Distribution Systems using Super capacitor based Dynamic Voltage Restorer (DVR)

V. Saketha Reddy* and M. Thirupathaiah **

*Assistant Professor, EEE Department, Methodist College of Engineering & Technology, Abids, Hyderabad-000001

Phone: +919703836191, Email: sakethareddy02@gmail.com

** Assistant Professor, EEE Department, Chaitanya Bharathi Institute of Technology, Gandipet, Hyderabad-500075

Phone: +91 9963181845, Email: m.thirupathy@gmail.com

Abstract – This paper presents the power quality improvement in distribution system using Dynamic Voltage Restorer (DVR) with super capacitor as energy storage for a three phase four wire system. The proposed system comprises of a super capacitor as energy storage, DC-DC converter and the power circuit of the DVR. The design of proposed DVR consists of filtering scheme, isolation transformer, injection transformer and voltage source inverter (VSI). The main aim of this project is the analysis and design of a Dynamic Voltage Restorer for a three phase four wire system. The energy storage is to supply real power to inverter during disturbances. In control circuit of DVR d-q-o transformation technique and proportional integral (PI) was applied. The design and implementation of a three phase four wire Dynamic Voltage Restorer (DVR) mainly deals with voltage sag and harmonics to mitigate voltage disturbances by injecting an appropriate voltage in series with the grid voltage in order to avoid the loss of power. All the simulations have been performed on the MATLAB/ SIMULINK software.

Keywords: Dynamic voltage restorer, Harmonic filter, Voltage Source Inverter (VSI), Injection transformer

I. INTRODUCTION

Power quality (PQ) is certainly a major concern in the present era; it becomes an important aspect at both transmission and distribution levels. Lack of power quality causes huge economical losses all over the world which makes it more important. Voltage quality [3] is the most important part of power quality from the viewpoint of sensitive load. Voltage disturbances mainly include voltage sags, voltage swells and voltage harmonics [1].

Power quality [4] can be defined as “the concept of powering and grounding sensitive equipment in a manner that is suitable to the operation of that equipment.” Making sure that power and equipment are suitable for each other also means that there must be compatibility between the electrical system and the equipment it powers. There should also be compatibility between devices that share the electrical distribution space. This concept is called Electromagnetic Compatibility (“EMC”) and is defined as: “the ability of an equipment or system to function satisfactorily in its electromagnetic environment without introducing intolerable electromagnetic disturbances to anything in that environment” [2].

II. DYNAMIC VOLTAGE RESTORER

A Dynamic Voltage Restorer (DVR) is a power-electronic converter- based device that has been designed to protect critical loads from all supply-side disturbances other than outages. It is connected in series with a distribution feeder and is capable of generating or absorbing real and reactive power at its ac terminals [5].

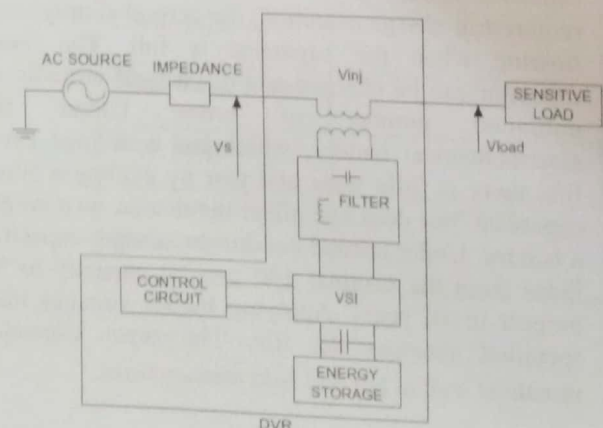


Fig.1. Schematic diagram of DVR

Micro Genetic Algorithm Based Optimal Power Flow

Ramesh Babu Jarapala

Abhinav Hi-tech college of Engineering Hyderabad, Telangana-India
babu.ramesh444@gmail.com

Ramesh Jatoth

Methodist College Of Engineering & Tech Hyderabad, Telangana-India
ramesh.jatoth@gmail.com

ABSTRACT In this work, Micro Genetic Algorithms and Genetic algorithm for the solution of the optimal power flow (OPF) is studied. Traditionally, classical optimization methods were used to effectively solve OPF. But more recently due to incorporation of Flexible A.C. Transmission System (FACTS) devices and deregulation of a power sector, the traditional concepts and practices of power systems are superimposed by an economic market management. So OPF have become complex. In recent years, Artificial Intelligence methods (MGA etc) have emerged which can solve highly complex OPF problems. IEEE 26-bus system has been studied to show the effectiveness of the algorithm.

Keywords: Micro Genetic Algorithms (MGA), Genetic Algorithm (GA), Flexible A.C. Transmission System (FACTS), Optimal Power Flow (OPF)

INTRODUCTION

In OPF[2,3] the main objective is to minimize the cost of meeting the load demand for the power system while satisfying all the security constraints. Since OPF is a non-linear problem, decouple of the control parameter of the FACTS device[1] is a highly nonlinear problem so that Micro Genetic algorithm and Genetic algorithm is used as a methodology to solve. In this context, more control facilities may complicate the system operation. As control facilities influence each other, a good coordination is required in order to bring all devices to work together, without interfering with each other. It has also been noted that the OPF problem with series compensation may be a non-convex and non-linear problem, which will lead the conventional optimization method stuck into local minimum

Micro Genetic algorithms and Genetic algorithm [9] offer a new and powerful approach to these optimization problems made possible by the increasing availability of high performance computers. These algorithms have recently found extensive applications in solving global optimization searching problems when the closed-form optimization technique cannot be applied. Genetic algorithms are parallel and global search techniques that emulate natural genetic operators.

The GA is more likely to converge toward the global solution because it, simultaneously, evaluates many points in the parameter space.

Ramesh babu Jarapala is with Faculty of Abhinav Hi-tech college of Engineering -hyderabad, JNTUH Telangana.

(babu.ramesh444@gmail.com)

Ramesh Jatoth is with Faculty of Methdisce college of Engineering -hyderabad, OU Telangana.

(ramesh.jatoth@gmail.com)

The method is not sensitive to the starting points and capable to determining the global optimum solution to the OPF for range of constraints and objective functions. In this paper a simple Micro genetic algorithm is applied to the problem of optimal power flow. To accelerate the processes of MGAOPF, the controllable variables are decomposed to active constraints that effect directly the cost function are included in the Micro Genetic algorithms process and passive constraints which are updating using a conventional load flow program.

II. PROBLEM FORMULATION

The economic dispatch problem [12] is to simultaneously minimize the overall cost rate and meet the load demand of a power system. The power system model consists of n generating units already connected to the system. The economic dispatch problem can be expressed as the most commonly used objective in the OPF problem[14,15] formulation is the minimization of the total cost of real power generation. The individual costs of each generating unit are assumed to be function, only of active power generation and are represented by quadratic curves of second order. The objective function for the entire power system can then be written as the sum of the quadratic cost model at each generator.

$$\text{Min} \sum_{i=1}^{N_g} (F_i(P_i))$$

$$F_i(P_i) = (a_i + b_i P_{gi} + c_i P_{gi}^2) \quad (1)$$

Where a_i , b_i and c_i are the cost coefficients of i -th generator and n is the number of generators committed to the operating system. P_i is the power output of the i -th generator. The economic dispatch problem subjects to the following constraints

$$P_i^{\min} \leq P_i \leq P_i^{\max} \quad \text{for } i=1, \dots, n \quad (2)$$

$$\sum_{i=1}^{N_g} (P_i) - (P_D) - (P_L) = 0 \quad (3)$$

$$\text{Where } P_L = [P_1 \ P_2 \ \dots \ P_n] \begin{pmatrix} \vdots \\ \vdots \\ \vdots \end{pmatrix} \begin{bmatrix} P_1 \\ \vdots \\ P_{n1} \end{bmatrix}$$

$$[P_1 \ P_2 \ \dots \ P_n] + \begin{bmatrix} B_{01} / 2 \\ \vdots \\ B_{0n} / 2 \end{bmatrix} B_{00} \quad (4)$$

Where P_i^{\min} and P_i^{\max} are the minimum and maximum generating limits respectively for the plant i . P_d is the load demand and P_L represents the transmission losses. B_{ii} and B_{oi} are the loss coefficients.

III. Micro genetic algorithm

Genetic algorithms are simple, robust, flexible, and able to find the global optimal solution. They are especially useful in finding solution to problems for which other optimization techniques encounter difficulties [8]. A basic genetic algorithm is constituted by a random creation of an initial population and a cycle of three stages, namely:

- evaluation of each chromosome;
- chromosomes selection for reproduction;
- genetic manipulation to create a new population, which includes crossover and mutation. Each time, this cycle is completed, it is said that a generation has occurred.

A. Standard Micro genetic algorithm

The disadvantage of GAs is the high processing time associated. That is due to their evolutionary concept, based on random processes that make the algorithm quite slow. However, different methods for reducing processing time have already been proposed, such as more appropriate choice of solution coding and reduction of search space using the specialist knowledge. One alternative method known as micro genetic algorithms, whose processing time is considerably smaller, is shown in [11].

Most GAs produce poor results when populations are small, because insufficient information is processed about the problem and, as a consequence, premature convergence to a local optimum occurs. Population size generally varies from 30 to 300 individuals. In contrast, MGAs explore the possibility to work with small populations (from five to 20 individuals usually) in order to reduce the processing time. From a genetic point of view, it is known that frequent reproductions inside a small population may disseminate hereditary diseases rarely found in large populations. On the other hand, small populations can act as natural laboratories where desirable genetic characteristics quickly can emerge. In MGAs, mutations are unnecessary because after a certain number of generations, the best chromosome is maintained and the rest are substituted by randomly generated ones. On the other hand, it requires adoption of some preventive strategy against loss of diversity in population.

The MGA implemented in the present work is reported in the following algorithm:

- 1) Select a population of n randomly generated individuals. Alternatively, $n-1$ individuals may be generated randomly together with one good individual obtained from previous search
- 2) Evaluate fitness and determine the best individual which is always transferred to the next generation. This "elitist" strategy guarantees against the loss of good information embedded in the best individual produced thus far
- 3) Select individuals for reproduction with the tournament selection strategy (for example with $k=2$)
- 4) Apply crossover with probability equal to 1 to favor exchange of genetic information among the population
- 5) Check for convergence by measuring the amount of diversity left in the population (by counting the total number of bits which are unlike those possessed by the best

individual). If population diversity has fallen under a preselected threshold, go to Step 1; otherwise, go to Step 2.

OPF problem is a nonlinear optimization problem which goal is minimizing objective function subject to equality and inequality constraints. There are many methods to optimize non linear problems. In this study Micro genetic algorithm(MGA) is applied in solving the OPF problem.

IV. GENETIC ALGORITHM

Genetic algorithms[10] are search algorithms based on the process of biological evolution. In genetic algorithms, the mechanics of natural selection and genetics are emulated artificially. The search for a global optimum to an optimization problem is conducted by moving from an old population of individuals to a new population using genetics-like operators. Each individual represents a candidate to the optimization solution. An individual is modeled as a fixed length string of symbols, usually taken from the binary alphabet. An evaluation function, called fitness function, assigns a fitness value to each individual within the population. This fitness value is measure for the quality of an individual. The basic optimization procedure involves nothing more than processing highly fit individuals in order to produce better individuals as the search progresses. A typical genetic algorithm cycle involves four major processes of fitness evaluation, selection, recombination and creation of a new population.

Although the binary representation is usually applied to power optimization problems, in this paper, we use the real valued representation scheme for solution. The use of real valued representation in the GA is claimed by Wright to offer a number of advantages in numerical function optimization over binary encoding. Efficiency of the GA is increased as there is no need to convert chromosomes to the binary type; less memory is required as efficient floating-point internal computer representations can be used directly; there is no loss in precision by discretisation to binary or other values; and there is greater freedom to use different genetic operators. For the real valued representation, the k -th chromosome C_k can be defined as follows:

$$C_k = [P_{k1}, P_{k2}, \dots, P_{k3}] \quad k=1, 2, \dots, \text{pop size}$$

Where $popsize$ means population size and P_{ki} is the generation power of the i -th unit at k -th chromosome. Reproduction involves creation of new offspring from the mating of two selected parents or mating pairs. It is though that the crossover operator is mainly responsible for the global search property of the GA. We used an arithmetic crossover operator that defines a linear combination of two chromosomes. Two chromosomes, selected randomly for crossover, C_{igen} and C_{jgen} may produce two offspring, C_{igen+1} and C_{jgen+1} may produce two offspring, C_{igen+1} and C_{jgen+1} , which is a linear combination of their parents i.e.,

$$C_i^{gen+1} = a \cdot C_i^{gen} + (1-a) \cdot C_j^{gen}$$

$$C_j^{gen+1} = (1-a) \cdot C_i^{gen} + a \cdot C_j^{gen}$$

Where a is a random number in range of $[0, 1]$.

The mutation operator is used to inject new genetic material into the population and it is applied to each new structure individually. A given mutation involves randomly altering each gene with a small probability. We generate a random real value which makes a random change in the m -th element selected randomly of the chromosome. The objective function[11] is used to provide a measure of how individuals have performed in the problem domain. In the case of a minimization problem, the fit individuals will have the lowest value of the associated objective function. The fitness function is normally used to transform the objective function value into a measure of relative fitness. The fitness function is defined as $Fit(x) = g(f(x))$ where $f(x)$ is the objective function, g transforms the value of the objective function to non-negative number. An elitist which GA search is used guarantees that the best solution so far obtained in the search is retained and used in the following generation, n and thereby ensuring no good solution already found can be lost in search process.

V.APPLICATION STUDY

This paper proposes an application of genetic algorithm and Particle Swarm Optimization to solve the Economic Dispatch problems. In this paper transmission losses are included by calculating the B coefficients of transmission losses. The results are taken on 26 bus system (fig-2) to test the effectiveness of the proposed method. The system consists of 46 lines and 6 generators, bus one is taken as reference bus, others are taken as load buses. The initial angle at respective buses is assumed as zero degree

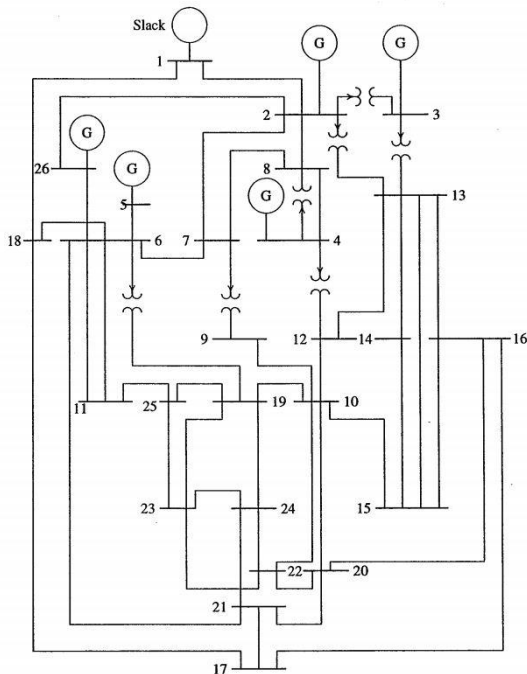


Fig-2: 26-bus power system network

Generator Operating Costs in \$/h, with P_i MW are as follows

$$C_1 = 240 + 7.0 P_1 + 0.0070 P_1^2$$

$$C_2 = 200 + 10.0 P_2 + 0.0095 P_2^2$$

$$C_3 = 220 + 8.5 P_3 + 0.0090 P_3^2$$

$$C_4 = 200 + 11.0 P_4 + 0.0970 P_4^2$$

$$C_5 = 220 + 10.5 P_5 + 0.0080 P_5^2$$

$$C_{26} = 190 + 12.0 P_{26} + 0.0075 P_{26}^2$$

Generator	Minimum (MW)	Maximum (MW)
1	100	500
2	50	200
3	80	300
4	50	150
5	50	200
26	20	120

Economic Dispatch Using Micro Genetic Algorithm and Genetic Algorithm including Transmission Losses

To Find The Loss Coefficients

A. First a power solution is obtained for the initial operating state. This provides the voltage magnitude and phase angles at all buses.

From these results load currents are obtained.

B. Bus matrix is found.

C. Transformation matrices are found.

D. Finally B coefficients are evaluated.

The B coefficients are the functions of the system operating state. If a new scheduling of generation is not drastically different from the initial operating condition, the loss coefficients may be assumed constant. $B =$

$$\begin{matrix}
 0.0014 & 0.0015 & 0.0009 & -0.0001 & -0.0004 & -0.0002 \\
 0.0015 & 0.0043 & 0.0050 & 0.0001 & -0.0008 & -0.0003 \\
 0.0009 & 0.0050 & 0.0315 & -0.0000 & -0.0020 & -0.0016 \\
 -0.0001 & 0.0001 & -0.0000 & 0.0029 & -0.0006 & -0.0009 \\
 -0.0004 & -0.0008 & -0.0020 & -0.0006 & 0.0085 & -0.0001 \\
 -0.0002 & -0.0003 & -0.0016 & -0.0009 & -0.0001 & 0.0176 \\
 B_0 = -0.0002 & -0.0008 & 0.0067 & 0.0001 & 0.0000 & 0.0012 \\
 B_{00} = 0.0056
 \end{matrix}$$

Total system Loss=15.53MW

Total generation cost = 16760.73 \$/h

Optimal Dispatch using Genetic algorithm Genetic algorithm is used to calculate optimum value of generation taking the condition $P = P_D + P_L$

$$P_1 = 472.10$$

$$P_2 = 171.96$$

$$P_3 = 193.77$$

$$P_4 = 150.00$$

$$P_5 = 196.38$$

$$P_6 = 103.73$$

Total generating cost = 15599\$/h

Thus it can also be seen that the total generation cost per hour comes down by $16760.73 - 15599 = 1161.73$ \$/h as a result of optimal dispatch using genetic algorithm.

Optimal Dispatch using Micro genetic algorithm

Micro genetic algorithm is used to calculate optimum value of generation taking the condition $P = P_D + P_L$

$$P_1=444.8835$$

$$P_2=172.5925$$

$$P_3=268.7010$$

$$P_4=123.8442$$

$$P_5=173.4232$$

$$P_6=95.0846$$

Total generating cost = 15483 \$/h

Thus it can also be seen that the total generation cost per hour comes down by $16760.73 - 15483 = 277.73$ \$/h as a result of optimal dispatch using Micro genetic algorithm.

VI. CONCLUSION

In this paper a new method with Micro Genetic Algorithm and Genetic Algorithm is presented to solve the optimal power flow problem of power system. Application of these techniques to Optimal Power Flow has been explored and tested. The simulation results show that this simple algorithm can give a good result using only simple modifications. A case study on IEEE-26 Bus 6 Generator Model test system shows the potential for application of MGA& GA to determine optimal dispatch of generation with FACTS devices.

References

- [1] G. Breuer, "Flexible AC Transmission Systems: Technology for Future", Proceeding of 20th Annual Electrical/Electronic Insulation conference. Boston MA. October 7-10 1991.
- [2] A.J. Wood and B.F. Wollenberg, Power Generation Operation and Control, John Wiley & Sons, New York, 1984.
- [3] Bouktir T., Belkacemi M., Zehar K., Optimal power flow using modified gradient method, Proceedings ICEL'2000, U.S.T. Oran, Algeria, 2000, p. 436-442.
- [4] Galiana G.D. et al, "Assesment and control of impact of FACTS devices on Power system Performance", IEEE trans on Power Sysem vol.11 No.4 Nov 1996 pp 1931-1936.
- [5] J. Kennedy, R. Eberhart, "Particle swarm optimization in," Proceedings of the IEEE International Conference on Neural Networks, pp. 1942-1948 1995.
- [6] Y. Shi, R. C. Eberhart, "Empirical study of particle swarm optimization in," Proceedings of the International Congress on Evolutionary Computation, vol.3, pp. 101-106, 1999.
- [7] Ratnaweera, S.K.Halgamuge, H.C.Watson "Self-organizing hierarchical particle swarm optimizer with time varying acceleration coefficients," IEEE Trans.onEvol. Comput, vol 8, pp. 240-255, June 2003.
- [8] H. Yoshida, K.Kawata, Y.Fukuyama, S.Takayama and Y.Nakanishi, "A particle swarm optimization for reactive power and voltage control considering voltage security assessment," IEEE Trans.on Power Systems, vol.15, pp. 1232-1239, 2000.
- [9] M. Saravanan, S.Mary Raja Slochanal, P.Venkatesh, J.PrinceStephenAbraham," Application of particle swarms optimization technique for optimal location of FACTS devices considering cost of installation and system loadability," Electr. Power Systems Research, vol.77, pp276-283, 2007.
- [10] D. Walters and G.B. Sheble, "Genetic algorithm solution of economic dispatch with valve point loading," IEEE Trans. on Power Systems, vol 8, no. 3, pp. 1325-1331, 1993.
- [11] A. Bakirtzis, V. Petrides and S. Kazarlis, "Genetic algorithm solution to the economic dispatch problem," IEE Proc. Gener. Transm. Distrib., vol.141, no. 4, pp. 377-382, July 1994.
- [12] P.H. Chen and H.C. Chang, "Large-scale economic dispatch approach by genetic algorithm," IEEE Trans. on Power Systems, vol. 10, no. 4, pp. 1919-1926, November 1995.
- [13] N. G. Hingorani, "Flexible AC Transmission," IEEE Spectrum, Vol. 30, No. 4, pp. 40-45, Apr. 1993.
- [14] Lie. TT. And Deng W., "Optimal Flexible AC Transmission Systems (FACTS) Devices Allocation", International Journal of Electrical Power and Energy Systems. Vol 19 No2 1999 pp 125-134.
- [15] Dommel H.W., Tinney W.F., Optimal Power Flow Solutions, IEEE Transactions on power apparatus and systems, vol. PAS.87, No. 10, 1968, p. 1866-1876.
- [16] J. Ramesh Babu1, Bhumaiah Jula2 and J.Ramesh3 "Micro Genetic Algorithm Based on Pricing of Reactive Power Service in Deregulated Electricity Markets," International Journal of Ethics in Engineering & Management Education .ISSN (ISSN: 2348-4748, Volume 1 Issue 7, July 2014), pp. 55-59.
- [17] V. Kranthi Kumar1, J. Ramesh Babu2 and M. Ramesh3 "Micro Genetic Algorithm Based Electrical Power Dispatch for Deregulated Electricity Market," Advance in Electronic and Electric Engineering. ISSN 2231-1297, Volume 3, Number 6 (2013), pp. 739-746.

About the Authors:



Ramesh babu Jarapala received his B.Tech degree in Electrical and Electronics Engineering and M.E in Power system Engineering from University College of Engineering, Osmania University, Hyderabad, Telangana, India, In 2007 To 2009 respectively. 2009 to 2012, he is Assistant Professor in KSIT Engineering college, 2012 to 2014 he is Assistant Professor in PBIT engineering college and 2014 to Till date AHTC engineering college in Hyderabad Telangana.



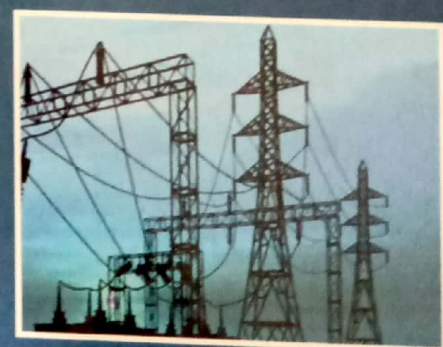
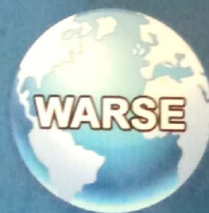
Ramesh Jatoth received his B.Tech degree in Electrical and Electronics Engineering and M.Tech in Power System from NIT calicut, Kerala, India, in 2008 to 2010 respectively. since 2014 he is Assistant Professor Methodist College Of Engineering & Tech Hyderabad, Telangana-India

ISBN: 978-93-5258-110-8

Proceedings of The International Conference *on* Paradigms in Engineering & Technology

ICPET 2016

March 2-3, 2016, King Koti Road, Abids
Hyderabad- 500001, Telangana, India



METHODIST COLLEGE OF ENGINEERING & TECHNOLOGY
(Affiliated to Osmania University)
HYDERABAD, TELANGANA
www.methodist.edu.in

A New Proposal for Mitigation of Power Quality Problems Using D-STATCOM

k.Pulla Reddy, Assistant Professor
Department of Electrical & Electronics Engineering
Methodist College of Engineering & Technology
Email:pullareddy.kasireddy@gmail.com

Abstract: *DSTATCOM (Distribution Static Compensator) is Used for Mitigation of Power Quality Problems under unbalance caused by various loads in distribution system. This paper addresses the modeling and analysis of custom power controllers, power electronic-based equipment aimed at enhancing the reliability and quality of power flows in low voltage distribution networks using DSTATCOM. A new PWM- based control scheme has been proposed that only requires voltage measurements the operation of the proposed control method is presented for D-STATCOM. Simulations and analysis are carried out in MATLAB/SIMULINK with this control method for two proposed systems.*

Keyword: *D-STATCOM, VSC, FACTS Controller, PCC.*

I. INTRODUCTION

In recent years, the custom power technology, the low-voltage counterpart of the more widely known flexible ac transmission system (FACTS) technology, aimed at high-voltage power transmission applications, has emerged as a credible solution to solve many of the problems relating to continuity of supply at the end-user level. Both the FACTS and custom power concepts are directly credited to EPRI [1], [2]. At present, a wide range of very flexible controllers, which capitalize on newly available power electronics components, are emerging for custom power applications. Among these, the distribution static compensator (D-STATCOM) based on the VSC principle [3]-[5] has been used to perform the Modeling and analysis of such controllers for a wide range of operating conditions based PWM control reported in this seminar for the D-STATCOM. It relies only on voltage measurements for its operation, i.e., it does not require reactive power measurements [6]. A sensitivity analysis is carried out to determine the impact of the dc capacitor size on D-STATCOM performance.

When used in low-voltage distribution systems the STATCOM is normally identified as Distribution STATCOM (D-STATCOM). It operates in a similar manner as the STATCOM (FACTS controller), with the active power flow controlled by the angle between the AC system and VSC voltages and the reactive power flow controlled by the

difference between the magnitudes of these voltages. As with the STATCOM, the capacitor acts as the energy storage device and its size is chosen based on power ratings, control and harmonics considerations. The D-STATCOM controller continuously monitors the load voltages and currents and determines the amount of compensation required by the AC system for a variety of disturbances.

A D-STATCOM (Distribution Static Compensator), which is schematically depicted in Fig.4.1 consists of a two-level Voltage Source Converter (VSC), a dc energy storage device, a coupling transformer connected in shunt to the distribution network through a coupling transformer. The VSC converts the dc voltage across the storage device into a set of three-phase ac output voltages. These voltages are in phase and coupled with the ac system through the reactance of the coupling transformer. Suitable adjustment of the phase and magnitude of the DSTATCOM output voltages allows effective control of active and reactive power exchanges between the DSTATCOM and the ac system. Such configuration allows the device to absorb or generate controllable active and reactive power. The VSC connected in shunt with the ac system provides a multifunctional topology which can be used for up to three quite distinct purposes [7]:

1. Voltage regulation and compensation of reactive power
2. Correction of power factor
3. Elimination of current harmonics

Here, such device is employed to provide continuous voltage regulation using an indirectly controlled converter.

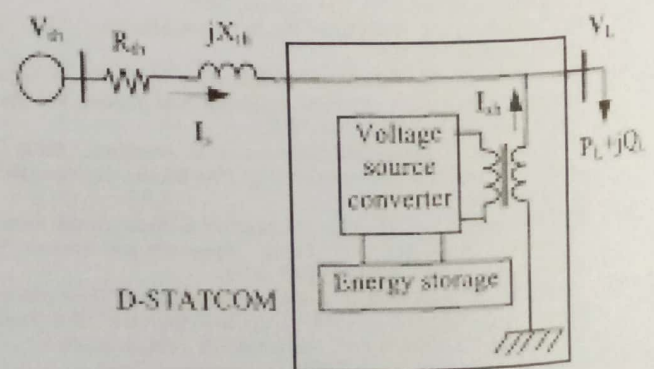


Fig. 1. Single line diagram of D-STATCOM connected distribution system.



International Conference on Science and Engineering of Materials for Future Needs

[Supported by: UGC - SERO & MNRE]

S.R. & B.G.N.R. GOVT. ARTS & SCIENCE COLLEGE

KHAMMAM - 507 002. Telangana, India.

(Re-accredited at B by NAAC)

Certificate

Certified that G. Aravind, O.U. Hyd., has participated in

International Conference on Science and Engineering of Materials for Future Needs

(ICSEMF - 2015) on 21st & 22nd December 2015 held at SR&BGNR Govt. Arts & Science College,

Khammam and presented a Scientific Paper entitled

structure and Morphology of Co-cd Ferrites by Combustion method.

We wish the participant all success.

Dr. M.V. Ramana
Convenor, ICSEMF-2015

Dr. U. Veerabhadraiah
Principal

**PROCEEDINGS OF THE
NATIONAL CONFERENCE
ON
“RECENT ADVANCES IN APPLIED
NANO MATERIALS”
(NCRAANM-2016)**

March 4-5, 2016

Editors

Dr. V. Nathaniel

Dr. Guntha Aravind

Dr. B. Ramaiah

Dr. Ch. Venkateshwarlu

Organised by

DEPARTMENT OF PHYSICS

UNIVERSITY COLLEGE OF SCIENCE, SAIFABAD

Masab Tank, Osmania University, Hyderabad – 500 004. TS

**PROCEEDINGS OF THE NATIONAL CONFERENCE ON
“RECENT ADVANCES IN APPLIED NANO MATERIALS”**

© University College of Science, Saifabad,
Osmania University, Hyderabad

No part of this publication may be reproduced or transmitted in any form by any means electronic or mechanical including photocopy, recording or any information storage and retrieval system without permissions in writing from the copy right owners.

DISCLAIMER

The authors are solely responsible for the contents of the papers compiled in this volume. The publishers or editors do not take any responsibility for the same in any manner. Errors, if any, are purely unintentional and readers are requested to communicate such errors to the editors or publishers to avoid discrepancies in future.

ISBN : 978-93-5258-222-8

PREFACE

In the globalization era material science has become more advanced in many aspects. I tried my level best to organize a two day national conference at our University College of Science, Sifabad, Masab Tank, Osmania University, Hyderabad. In this occasion, I invited the eminent Resource persons like Prof. Ashok Kumar Ganguli, Director, INST, New Delhi, Prof.K.V.Ramanuja Chary, Rowan University, USA, Prof. M. Lakshmi Kantam, IICT, Mumbai, Dr.Tata Narsing Rao, ARCI, Hyderabad, Prof.Subhash Kondawar, RTM University Nagpur, Prof .D.Suresh Babu, Head, Dept Of Physics, Osmania University, Hyderabad, Prof. D.Ravinder, Dept of Physics Osmania University Hyderabad, Prof. K.V.R.Murthy, University of Baroda, Gujarat,etc.

All these Resource persons spoke on various topics, new ideas and suggestions. On behalf of this conference, I extend my regards to them. I thank to our College Principal Prof. B. Laxmaiah and Faculty Members for their support and encouragement in conducting this academic activity in the college to make this event a grand success. In this first attempt, I tried my level best to bring out proceedings of full papers of the conference in the form of a book with ISBN No 978-93- 5258-222-8.

This two day national conference acted as a major forum for the presentation of innovative ideas, approaches, developments and research projects in the area of material science by incorporating different preparation methods in order to fulfill the dreams of sustainable development into reality for the society.

The NCRAANM 2016 committee invited original submissions from the students, researchers, faculties and scientists that illustrate the analytical research results, review works and industrial experiences describing significant advances in the areas related to the relevant themes and tracks of the conference. All the submissions underwent a strenuous peer-review process which comprised expert reviewers. The papers were reviewed based on their technical matter, clarity and originality. The entire process which includes the submission, review & acceptance processes was done electronically.

We extend our thanks to UGC, SERO, Hyderabad, CANARA BANK, Masab Tank Branch and VISHAKA TRUST, Hyderabad for their financial assistance for conducting two day national conference. Finally I thank all the authors who contributed to the success of conference. I also sincerely wish that all attendees will get benefitted academically from the conference and wish them every success in their research endeavor.

Dr. V. Nathaniel

Convener and Organising Secretary

NCRAANM - 2016

INDEX

S.NO.	DESCRIPTION	PAGE NO
1	Synthesis of TiO₂ Nanoparticles and Their Application in Waste Water Treatment Annapoorna Avula ¹ , Kaleem Ahmed Jaleeli ² , Adeel Ahmad ²	1 - 6
2	Fabrication of Hybrid Gel Nanofibrous PVdF/PMMA Polymer Electrolyte for Lithium-Ion Battery Rozi D. Thalal [#] , Monali V. Bhute, Subhash B. Kondawar*	7 - 14
3	Ethnobotanical studies of Peddagattu and Sherepally area, a proposed site for uranium Mining project, Nalgonda District, Telangana State, India A. Baleeshwar Reddy ¹ , V. Vasudeva Rao ² and A. Vijaya Bhasker Reddy ^{1*}	15 – 30
4	Structural Characterization of Nano Crystalline Ni Sm_xFe_{2-x}O₄ferrites Gopal boda ¹ , Nehru boda ² , G. Aravind ² , A. Panasa Reddy ^{1*} , D.Ravinder ^{2*}	31 – 38
5	Validation of Kinetic Modelling in Removal of Sulphonated Dye in Waste Water using Polyaniline/ZnO nanocomposites [#] Neha V. Dambhare, Neha V. Nerkar, Subhash B. Kondawar*	39 – 46
6	Synthesis and Photoluminescence of Tb³⁺ doped Sr₃Y₂ (BO₃)₄ Phosphor - M.Srinivas	47 – 51
7	Highly Sensitive Hydrogen Gas Sensor Based on Polyaniline Coated SnO₂ Nanofibers [#] Megha A. Salorkar, Hemlata J. Sharma, Subhash B. Kondawar*	52 - 58
8	Preparation and Characterization of Cadmium substituted Cobalt Nano ferrites by citrate-gel auto combustion method Nehru boda ¹ , Gopal boda ² , Abdul Gaffoor, D. Ravinder ^{1*} , A. Panasa Reddy ^{2*} .	59 – 68
9	Electrochemical Performance of Polyaniline/Nickel Ferrite/Carbon Nanotubes Ternary Nanocomposites [#] Pooja A. Zingare, Zeenat Parveen, Subhash B. Kondawar*	69 – 76
10	Thermoluminescence studies of Eu³⁺ doped Calcium Lanthanum borate phosphor - M.Srinivas	77 – 82
11	Synthesis and Magnetic properties of CoFe₂O₄ and Mg Fe₂O₄ spinel nano ferrites M. Raghasudha ^{1*} , D. Ravinder ² , P. Veerasomaiah ¹ , Shyamsunder goud ¹ , G. Satyanarayana Goud ³ , B. Rambabu ¹ , N. Venkatesh ¹	83 – 88
12	Impedance spectroscopic studies on PMN-PT UshaPraveena V.J, N. V. Prasad*, G. Prasad and G. S. Kumar	89 – 95
13	Resistive Switching Property of Nickel-Zinc Thin Film Synthesized By Sol Gel Route K. Rama Krishna ¹ K. Vijaya Kumar ² D. Ravinder ³	96 – 101
14	Excluded Energy and Relative Encircled Energy an important role in the Optical Imaging Systems with amplitude and apodised Parameters B. Sambaiah* and D. Karuna Sagar [¶]	102 – 112

15	Structural and Magnetic properties of Mg Ferrite D.Ravi Kumar ^a , B.Kiran Kumar ^a , Ch.Abraham Lincoln ^{a*} , D.Ravinder ^b	113 – 119
16	A study on Infrared Spectroscopy of Human Blood U. Vijaya Ushasree, Kaleem Ahmed Jaleeli & Adeel Ahmad	120 – 123
17	Electrical Studies In Silver Doped Gallium Oxide Glasses K. Veerabadra Rao, C. Anuradha, G.Aravind	124 – 136
18	Biosynthesis and Characterization of Silver Nanoparticles using young leaves extract of Gymnosporia emarginata and their antimicrobial activity P. Shivakumar Singh ¹ , D.S.R. Rajender Singh ² , G.M. Vidyasagar ^{*3}	137 – 147
19	Optical Properties of Pure and TICI Doped Poly (Vinyl Alcohol) Polymer Electrolyte Films C. Anuradha, K.Veerabadra Rao, G.Aravind	148 - 154
20	Structural Properties of Mg_{1-x}Zn_xFe₂O₄ Nano-Ferrites Synthesized by citrate Gel Autocombustion method Shyamsunder Goud ¹ , Nakiraboina Venkatesh ¹ , Nama Hari Kumar ² , B. Rambabu ¹ , B.Shankar ¹ ,P.Naresh ² M.Raghasudha ¹ , P. Veera Somaiah ^{1*}	155 – 166
21	Synthesis, Characterization of (1-x) NaNO₃-xAl₂O₃ Composite Solid Electrolytes A.Vennela ¹ , A. Raju ¹ , A.Mallaiah ³ , S.Narender Reddy ² , A. Sadananda Chary ¹ .	167 – 171
22	Doping effect on crystal structure and phase Properties of Chromium Doped Lithium Nano-Ferrites D. Ravinder Nayak, G.Aravind, B.Neheru, D. Ravinder	172 – 182
23	Thermo Electric Power studies of Li-Co nano ferro spinels G.Aravind ¹ , V.Nathanial ² , A. Ranjith ² , Ch.Sumalatha ² , V.Ludhiya ³ D.Ravinder ³	183 - 189

Synthesis of TiO₂ Nanoparticles and Their Application in Waste Water Treatment

Annapoorna Avula¹, Kaleem Ahmed Jaleeli², Adeel Ahmad²

¹Asst Prof, Dept of Physics, Al-Habeeb College of Engg and Tech, Chevella, India

²Biophysics Research Laboratory, Department of Physics, Nizam College (Autonomous), Osmania University, Hyderabad – 500 001, India

ABSTRACT:

The main objective of this paper is to determine the photo catalytic degradation efficiency for refinery effluent from wastewater by using new generation photo catalytic TiO₂ Nanoparticles synthesized using Green synthesis. The obtained TiO₂ nanoparticles have been characterized by X-ray diffractometer (XRD). In the present work, photo catalysis has been used as tertiary treatment for petroleum refinery wastewaters in order to reduce the amount of pollutants to the level of the regulatory discharge limits and to oxidize persistent compounds that had not been oxidized in the biological treatment. The potential use of nanotechnology improves access to clean water and basic sanitation.

Keywords: Green Synthesis, Photo catalytic, TiO₂ Nanoparticle and Wastewater.

INTRODUCTION:

Water pollution is a major environmental issue in India. Rivers, lakes and surface water in India are polluted. Drinking water pollution is most important; as such pollution is directly connected with human health. The main source of freshwater pollution can be attributed to the discharge of untreated waste, dumping of industrial effluent, and run-off from agricultural fields. By always increasing pollution it becomes more difficult to guarantee the fundamental right to water. Water has a self-cleaning capacity that ensures the natural break of a number of substances. Water is however too much polluted, and then the self-cleaning capacity is damaged (1). In terms of wastewater treatment, nanotechnology is applicable in detection and removal of various pollutants. Heavy metal pollution poses as a serious threat to environment. Various methods such as Photolysis, Nano filtration, Adsorption and Electrochemical oxidation involve the use of TiO₂, ZnO, ceramic membranes,

nanowire membranes, polymer membranes, carbon nanotubes, submicron Nanopower, metaloxides, magneti nanoparticles, nanostructured boran doped diamond are used to resolve or greatly diminish problems involving water quality in natural environment(2). Photo catalysis is being applied for the elimination of several pollutants (e.g., alkenes, alkenes, phenols, aromatics, pesticides) with great success. In many cases, total mineralization of the organic compounds has been observed. The wastewaters of an oil refinery are the waters resulting from washing the equipments. These effluents have high oil and grease contents, besides other organic compounds in solution. These pollutants form a residual COD that may pose serious toxic hazards to the environment. Composition for these effluents is troublesome. In the present work, photo catalysis has been used as tertiary treatment for petroleum refinery wastewaters in order to reduce the amount of pollutants to the level of the regulatory discharge limits (3). Photo catalyst TiO₂ is synthesized using Orange fruit peel extract using Green synthesis. Titanium dioxide is a white colour metal oxide, which have advanced properties like hydrophobic, non-wet ability, high surface to volume ratio and large band gap. Hence, it can be used in the different types of applications self-cleaning devices, dye sensitized solar cell, photo catalysis, electrochemistry, anti bacterial products and textiles. The green synthesis process is environmental friendly technique, due to it uses the extracts of plant parts such as peels, leaves, flowers, roots, stem and seed. It is a one of the best method among physical and chemical methods as it does not require any high end equipments, hazardous chemicals and high temperatures. Orange peel acts as reducing agent for synthesis of TiO₂ because it contains Citric acid as main source. Orange peel can be used in bath oil, room freshen air, face creams, mosquito repellent and weight loss

MATERIALS AND METHODS:

Make Orange peel into small pieces. A 50 g of orange peel was directly taken into the beaker and extracted with 150 ml of water for 2 hrs at 90 C. The extract was filtered using what man filter paper. The filtrate was stored for the further synthesis of nanoparticle (4). Dissolve 1.5 N of titanium tetra iso prop oxide in 100 ml of distilled water for synthesis the TiO₂ nanoparticles. Added extract drop wise under constant stirring up to achieve pH of solution became 7. The mixture was subjected

to constant stirring for 3 hours continuously at room temperature. In this process formation of nanoparticles were occurred, these nanoparticles were separated using what man filter paper and washed the materials with distilled water repeatedly to remove the by-products. The obtained wet nanoparticles were dried at 80 C for overnight. Finally particles were calcined at 600 C for 3 hours for obtaining Rutile phase (5).

CHARACTERIZATION TECHNIQUE:

The crystal structure and average crystalline size was measured by Bruker D8 X-ray diffractometer.

PHOTO CATALYTIC EXPERIMENTS:

The wastewater was collected at the exit pipe of a series of aerated lagoons and stored at 4°C with a pH<2. The wastewater characterization, along with the pollutant limits, are presented in Table 1

Parameters	Average Concentration of Wastewater(mg/L)	Concentration
pH	6.7	6
COD(filtrated)	250	200
DOC	28	
Oil and grease	27	15
Ammonia	26	5
Phenol	3.7	0,2

Table 1 The wastewater characterization

The experiment was carried out with, a Pyrex[®] annular reactor containing 550 mL of wastewater. The reaction mixtures inside the reactors were maintained in suspension by magnetic stirring. In the experiment, air was continuously bubbled through the suspensions. A 250 W Phillips HPL–N medium pressure mercury vapor lamp was used as the UV-light source. The lamp was inserted into the well; The experiment was performed at 25± 1°C. The catalyst concentration ranged from 0.5

to 5.5 g/L and the initial pH from 3.5 to 9. In order to remove photo catalyst particles before analyses, samples were filtered through 0.45 μm pore size cellulose acetate filters.

RESULTS AND DISCUSSION:

X-RAY DIFFRACTOMETER:

The XRD pattern of TiO_2 nanoparticles obtained from green synthesis were as shown in Figure 1. The result showed that the structure was in tetragonal structure and these results were good agreement with JCPDS card number 87-0920. Peaks were absorbed at 27° , 36° , 39° , 41° , 44° , 54° , 56° , 62° , 64° and 69° along with miller indices values (1 1 0), (1 0 1), (2 0 0), (1 1 1), (2 1 0), (2 1 1), (2 2 0), (0 0 2), (3 1 0) and (1 1 2) respectively. As the width of the peak increases size of particle size decreases, which resembles that present material in nano range.

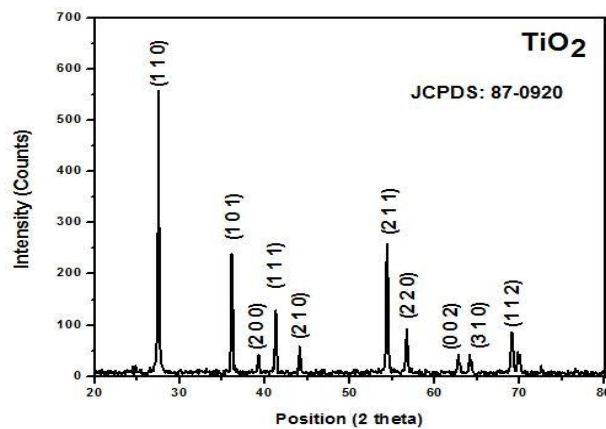


Fig: 1XRD Pattern of TiO_2 Nanoparticles

The lattice parameters were obtained $a=b=0.4594$ nm and $c=0.2958$ nm. The average crystallite size was measured by Debye-Scherrer's equation

$$D = \frac{K\lambda}{L \cos \theta}$$

Where D is the average crystallite size of the particles, K - is Debye Scherer's constant ($=0.94$), λ - is the wavelength of the $\text{CuK}\alpha$ -radiation ($=0.154$ nm), L is the full width half maximum (FWHM) of the peak, θ is the Bragg's angle. The average crystallite size was measured as 19 nm using the above formula.

FINAL WASTEWATER CHARACTERIZATION:

After photo catalytically treatment of the wastewater in the Pyrex® annular reactor, under the optimized conditions, its general quality was significantly improved. The results are summarized in Table 2. It is noteworthy that phenol and oil and grease contents, which had been above the legislated limits, were reduced to discharge levels. Also, more than half of the DOC was removed from the wastewater. Finally, an insignificant amount of ammonia was removed (not more than 10%).

TiO ₂	Degradation% UV Area	Phenols,mgr/L
pH	6.7	7
DOC	20	10
Oil and grease	23	<10
Ammonia	70	50
Phenols	3.7	0.5

Table 2-Wastewater Photo catalytic treatment

CONCLUSION:

The TiO₂ nanoparticles can be synthesized successfully in green synthesis method using Orange peel and XRD analysis of the sample was obtained 19 nm with the Tetragonal structure. . Undoubtedly, the TiO₂ was the most active photo catalyst. . Moreover, it offers two other advantages: less photo catalyst can be used and the pH is already near the effluent discharged, requiring no adjustment of pH. The use of TiO₂ /UV (photo catalysis) resulted in a significant increase in phenol removal (93%). 56% of the DOC was removed. This is probably due to the fact that photo catalysis is a much more oxidative process than H₂ O₂ /UV, so the reactions that take place are much faster. Therefore, the use of helio-photocatalysis with this wastewater would be feasible.

REFERENCES:

1. Ijoer vol.3. S3, 2015, issn: 2321-7758 ncerfm-2015
2. Nanotechnological methodology for treatment of waste water I. Nageswara
rao
3. & Table 2 Brazilian journal of chemical engineering-vol. 23, no. 04, pp. 451
- 460, October - December, 2006
4. P. Balashanmugam, R. Nandhini, V. Vijayapriyadharshini, P.T Kalaichelvan;
(2013) Biosynthesis of Silver Nanoparticles from Orange Peel Extract and its
Antibacterial Activity against Fruit and Vegetable Pathogens, International
Journal of Innovative Research in Science & Engineering, 1(2): 6 page
5. Synthesis of tio₂ nanoparticles from orange fruit waste international journal
of multidisciplinary advanced research trends issn : 2349-7408 volume ii,
issue I, February 2015
6. Table 1 limits imposed by the Iran Department of Environment (DOE).

Fabrication of Hybrid Gel Nanofibrous PVdF/PMMA Polymer Electrolyte for Lithium-Ion Battery

Rozi D. Thalal[#], Monali V. Bhute, Subhash B. Kondawar*
Dept. of Physics, Rashtrasant Tukadoji Maharaj Nagpur University,
Nagpur - 440033, India

*Corresponding Author Email: sbkondawar@yahoo.co.in

[#]Presenting Author Email: thalalrosy@gmail.com

ABSTRACT

In this paper, hybrid gel polymer electrolyte (HGPE) based on PVdF/PMMA nanofibrous membranes were prepared by electrospinning technology. The microstructure of the nanofibrous membranes, the physical and electrochemical performances of the activated HGPEs were studied systematically by scanning electron microscopy (SEM), Fourier transform infrared spectroscopy (FTIR), X-ray diffraction (XRD), Linear sweep voltammetry (LSV) and electrolyte uptake. The properties of the nanofibrous membranes and the corresponding HGPEs were found to be varied with the relative weight ratio of the blending polymers. The thickness of the nanofibrous membrane was found to be around 100 μ m via the controlled procedure parameters. The polymer electrolytes from electrospun nanofibrous membranes were prepared by soaking the membranes in 1 M LiPF₆ (lithium hexafluorophosphate) in ethylene carbonate : diethylene carbonate (EC:DEC) in 1:1 (v/v) ratio. For HGPE, the most important character is its electrochemical performance. When the weight percentage of PVdF/PMMA was 15%, the maximum ionic conductivity of the prepared HGPE was found to be 3.51×10^{-3} S/cm with electrochemical stability up to 3.8 V versus Li⁺/Li at room temperature indicate the good suitability of the polymer electrolyte membranes for polymer lithium-ion battery.

Keywords: Electrospinning; Polymer electrolyte; Electrochemical performance; Lithium-ion battery.

1. Introduction

Polymer electrolytes have attracted great interest compared to traditional liquid electrolytes, which provide the advantages to develop lighter and safer batteries with long shelf life, leak proof construction and easy fabrication into desired shape and size [1]. Electrospinning technique is a very unique and useful way to prepare Polymer electrolyte with superior performance. Electrospinning is an efficient fabrication process that gives fibrous and porous membranes with an average diameter ranging from 100 nm to 5 μm [2, 3]. Poly(vinylidene fluoride) (PVdF) is a well-known semi-crystalline thermoplastic polymer with excellent film-forming ability and thermal stability. Due to the high dielectric constant and strong chemical and electrochemical resistance, it has become a favorable polymer matrix for porous polymer electrolytes in lithium-ion batteries [4, 5]. The crystalline domains of PVdF hinder the penetration of liquid electrolytes and the migration of lithium ions, and hence the high-crystalline PVdF becomes one of the major factors to give the low ionic conductivity of polymer electrolytes [6]. For the purpose of tackling the aforementioned problems, several attempts have been carried out, one of the best ways to introduce other blending polymers like polyacrylonitrile (PAN), poly(methyl methacrylate) (PMMA), and thermoplastic polyurethane (TPU) into electrospun PVdF membranes. PMMA is a common thermoplastic polymer with well known chemistry. Its amorphous structure is beneficial to ionic conduction. PMMA based polymer electrolytes exhibit high electrolyte uptake, ionic conductivity and good electrochemical stability. Also, PMMA has the ability to increase the mechanical strength and the electrolyte solution retention ability of the polymer electrolytes [7]. The characterizations and measurement of porosity, electrolyte uptake and ionic conductivity of the electrospun PVdF-PMMA membrane were investigated. These results showed that PVdF-PMMA composite nanofibrous membrane prepared by electrospinning had a good prospect as PE for lithium-ion batteries.

2. Experimental

Materials

Poly(vinylidene fluoride) (PVdF), poly (methylmethacrylate) PMMA, hexafluorophosphate (LiPF₆, battery grade, dry 99.99%) and plasticizers ethylene carbonate: diethylene carbonate (EC:DEC) were purchased from Sigma-Aldrich.

Synthesis of PVdF/PMMA composite nanofibrous membrane

Poly(vinylidene fluoride) PVdF and PMMA were used as the starting materials for the preparation of fibrous nanocomposite polymer membranes by electrospinning technique. A 15% solution of PVDF/PMMA (8/2,w/w) in DMF/acetone (2/6, v/v) was prepared by magnetic stirring for 12 hr. The resultant optimized viscous solution was taken into a 10 ml syringe and loaded in a syringe pump to form nanocomposite fibers by setting the electrospinning parameters. The following electrospinning parameters are used for all the compositions: solution feed rate 0.6 ml/hr, applied voltage between spinneret and collector is 18 kV. Nanofibers were collected on aluminum foil wrapped on rotating collector which was grounded. The electrospun fibrous membranes were collected and dried in vacuum oven at 60°C for 24 h to remove the solvent for further use.

3. Results and discussion

Fig.1 shows the surface morphology of electrospun pure PVdF (Fig. 1a) and nanocomposite fibrous polymer membrane with PMMA (Fig.1b). It can be seen that the membranes exhibit a three dimensional web structure with fully interconnected pores of ultrafine multi-fibers with bead free morphology. The interlaying of multi-fiber layers generates a porous structure between the fibers in the electrospun membrane, which can good absorb and retain the liquid electrolyte effectively.

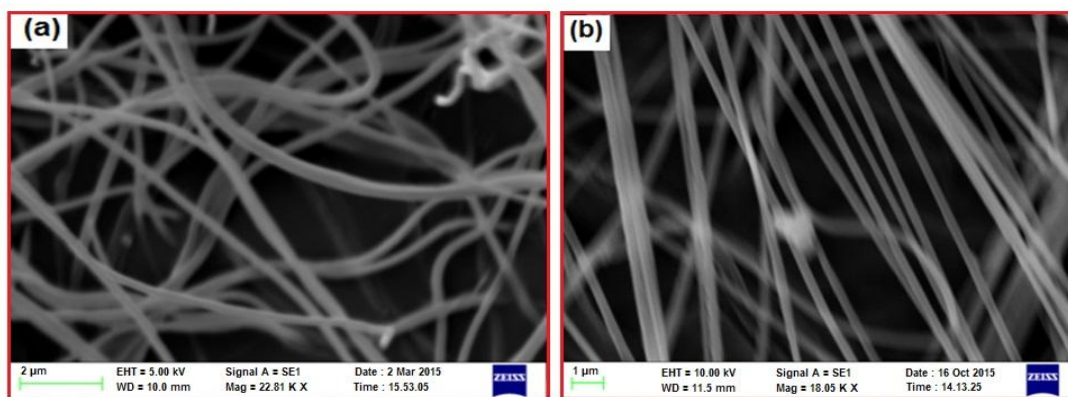


Fig.1: SEM images of electrospun (a) PVdF and (b) PVdF-PMMA nanofibrous membrane

Fig. 2 shows the FT-IR spectra of electrospun pure PVdF and PVdF-PMMA nanofibrous membranes. The bands appearing at 1397, 1275, 840 cm^{-1} are assigned to CF stretching, CF_2 stretching, and characteristic frequency of vinylidene compound respectively in PVdF. The characteristic absorption peaks of PMMA (692, 879, 1729 cm^{-1}) are found in the composite nanofibrous membrane. An absorption peak appears at 1729 cm^{-1} , which is related to C=O stretching vibration of PMMA. The appearance of new peaks along with changes in the existing peaks in the FTIR spectra confirms the miscibility of PMMA with PVdF in the composite PVdF-PMMA fibrous membrane. The XRD pattern of PVdF and PVdF-PMMA nanofibrous membranes are shown in **Fig. 3**. The presence of crystalline peaks and amorphous humps indicates the semi crystalline nature. There are two broad diffraction peaks at $2\theta = 18.5^\circ$ and 27.2° corresponding to the crystal diffraction peaks of PVdF. The intensity of the crystalline peaks is decreased due to incorporation of PMMA in composite.

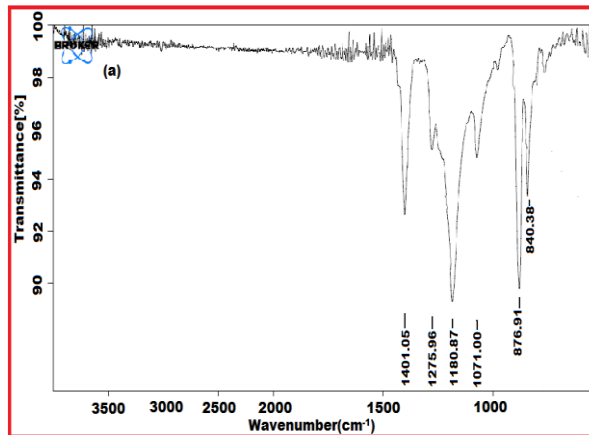


Fig. 2(a): FTIR spectrum of PVdF nanofibrous membrane

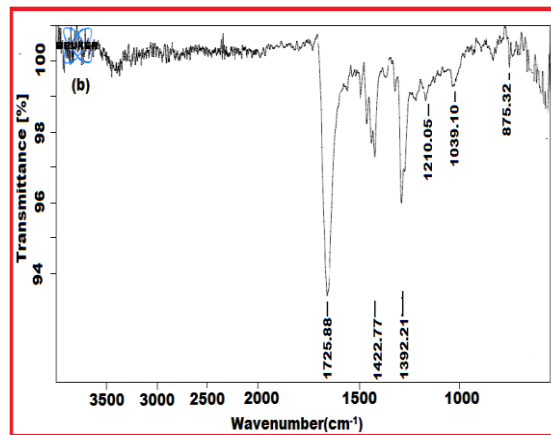


Fig. 2(b): FTIR spectrum of PVdF-PMMA nanofibrous membrane

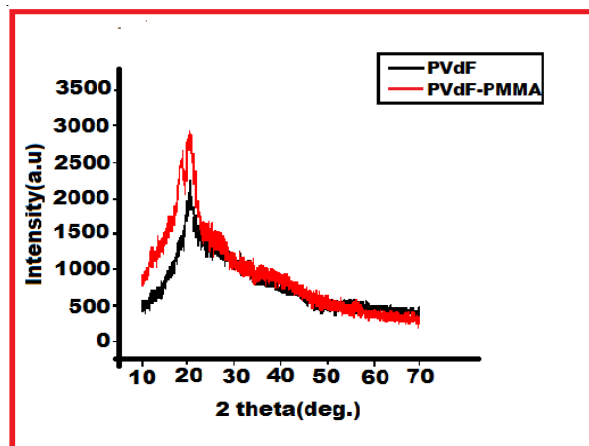


Fig 3: XRD patterns of membranes

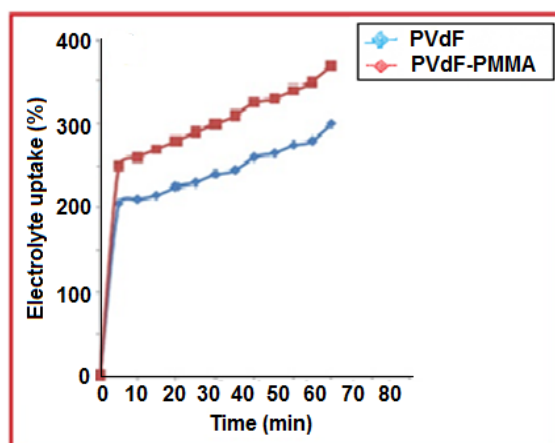


Fig. 4: Electrolyte uptake of membranes

The electrochemical measurements of the PEs were obtained by immersing the electrospun nanofibrous membrane in 1 M LiPF_6 - EC:DEC (volume 1:1) solution for 60 minute at 25 °C in a dry glove box [8]. The ionic conductivity was calculated by AC impedance measurement using Zahner Zennium electrochemical analyzer. The frequency of testing ranged from 100 mHz to 100 kHz at AC amplitude of 5mV. **Fig.4** represents the electrolyte uptake behavior of the electrospun PVdF and PVdF-PMMA membranes. It has been calculated by soaking the membrane in the liquid electrolyte 1M LiPF_6 - EC:DEC (volume 1:1) solution for 60 min [9]. The unique fibrous structure of this membrane induces fast liquid penetration into the membranes to form the polymer electrolyte with interpenetrating polymer network within 30 minute. The higher electrolyte uptake can make an improvement of ionic conductivity. The ionic conductivities of the polymer electrolyte were determined at room temperatures by ac impedance spectroscopy (**Fig. 5**). The ionic conductivity of pure PVDF-based GPE was found to be 3.07×10^{-3} S/cm and increased with the addition of PMMA for PVdF-PMMA nanofibrous membrane of about 3.51×10^{-3} S/cm. Good ionic conductivity of PVdF-PMMA nanofibrous membrane shows the most stable performance with the temperature.

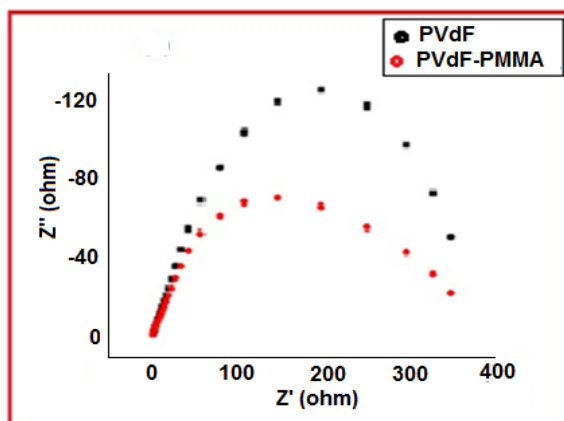


Fig. 5: Impedance spectra of polymer electrolytes

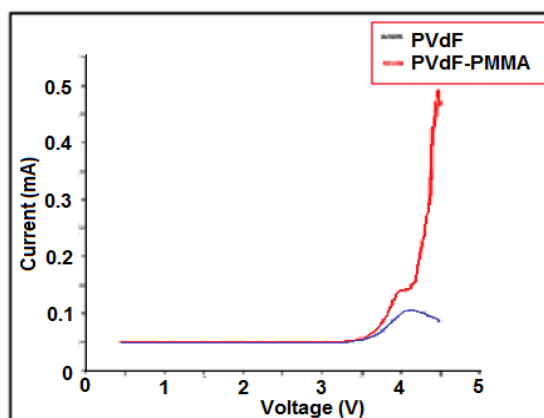


Fig 6: Linear sweep voltammetry of polymer electrolytes

The results of electrochemical stability tests of the polymer electrolytes by linear sweep voltammetry are shown in **Fig. 6**. The linear sweep voltammetry was applied for Li/polymer electrolyte/ SS cell at room temperature. The electrochemical stability was found to be 3.5 V for the PVdF polymer electrolyte and with the addition of the addition of PMMA, the stability was further enhanced to 3.8 V.

4. Conclusion

Electrospun PVdF and PVdF-PMMA composite nanofibrous polymer electrolyte membranes were successfully prepared by electrospinning method. The ionic conductivity, impedance and electrolyte uptake were found to be improved after the addition of PMMA in PVdF. Thus, PVdF-PMMA composite nanofibrous membranes prepared via electrospinning is a good candidate compared to that of pure PVdF as the polymer electrolyte for polymer lithium-ion batteries.

References

1. Xi.Y. J., Qiu.P. X., Tang. Z. X., Zhu.T.W and Chen. Q. L, *Journal of Power Sources*, (2006), 157(1), 501-506.
2. Hwang. J.Y., Nahm. S. K, Kumar. P.T and Stephan.M. A, *Journal of Membrane Science*, (2008), 310, 349–355.
3. Muniyandi. N., Kalaiselvi.N., Periyasamy.P.,Thirunakaran R., Babu.R.B., Gopukumar .S, Renganathan. G.N, Raghavan .M., *Journal of Power Sources*, (2001), 96, 14–19.
4. Liu, F., Hashim, N.A., Liu, Y.T., Abed, M.R.M., Li, K., *Journal of Membrane Science*, (2011), 375, 1-27.
5. Stephan, M.A . *Europium Polymer Journal*, (2006), 42, 21–42.
6. Li, X.Y, Cao, Q, Wang, X.Y, Jiang, S.H, Deng, H.Y, Wu, N., *Journal of Applied Polymer Science*, (2011), 122, 2616-2620.
7. Tatsuma, T., Taguchi, M., Oyama, N., *Electrochimica Acta*, (2001), 46, 1201-1207.
8. Chung, S.H., Wang, Y., Persi , L. Croce , F.S, Greenbaum, G., Scrosati, B. and Plichta, E., *Journal of Power Sources*, (2001), 97, 644-648.
9. Wu, N., Qi, C., Wang, X., Li, S., Li, X., Deng, H., *Journal of Power Sources*, (2011), 196, 9751–9756.

Ethnobotanical studies of Peddagattu and Sherepally area, a proposed site for uranium Mining project, Nalgonda District, Telangana State, India

A. Baleeshwar Reddy¹, V. Vasudeva Rao² and A. Vijaya Bhasker Reddy^{1*}

¹ Department of Botany, University College of Science, Osmania University,
Saifabad, Hyderabad-500 004, Telangana State, India.

² AINP on Vertebrate Pest Management, Prof. Jayashankar Telangana State
Agricultural University, Rajendranagar, Hyderabad- 500030, Telangana State, India.

*Corresponding author e-mail: avijayabhaskerreddy@gmail.com

ABSTRACT

The present study aimed to record the information of medicinal plants used by tribal groups in the study area. 83 medicinal plants used as a cure for 47 ailments were recorded. They are distributed across 78 genera and 41 families. Of these 83 species, the maximum contribution was recorded for herbs (32.5%) and trees (32.5%) followed by shrubs (23%) and climbers (12%). Among these species, parts used wise contribution was maximum recorded for leaf (42 %) followed by root (13 %), bark (12%), fruits (10%), whole plant (9%), and seed (7%). The large numbers of remedies were used to treat external injuries, skin diseases, and snake bite.

Key words: Ethnobotany, external injuries, Peddagattu, Sherepally, uranium project.

INTRODUCTION

The first human beings were food gatherers and hunters of food, but subsequently concentrated on plants that are useful for other purposes, such as shelter and health care etc. They understood the use of various plant parts for different purposes such as food, resins, beverages and medicines since immemorial time. This knowledge was passed through orally from generation to the next generation. The indigenous people of various regions have developed their own way of using plants for their health care and following their own culture, customs and food habits (Ramakrishna et al., 2014).

Indians herbal knowledge base is very diverse and it consists of many streams like Ayurveda, Unani, Siddha and other systems. In India ethnobotany was initially well cited in different folklore practiced for curing various ailments similarly in other parts of the world like China, Africa and South America were

highlighted the importance of herbal uses. People of the world are still dependent on traditional plant based healing practices as it is cheap and easily available. The World Health Organization has estimated that over 80% of the world populations rely chiefly on traditional medicine (Akerle., 1992). It was officially recognized that 2500 plant species have medicinal value over 6000 plant species are estimated to be explored in traditional, folk and herbal medicine (Huxley., 1984).

Different workers have documented the uses of medicinal plants from different parts of Telangana and Andhra Pradesh states (Kapoor., 1980, Singh et al., 1981, Hemdri et al., 1987 a & b, Raja Reddy et al., 1989, Venkanna., 1990., Basi Reddy et al., 1991, Ravishanker &Herny.,1992, Chandra et al., 2010, Murthy.,2012 and Ramakrishna et al., 2014, Saynasi Rao and Varma., 2014). The literature revealed that there are only few attempts on ethnobotanical studies of this region (Reddy., 2013). The main focus of the present study is to ascertain the detailed information on the use of the ethnomedicinal plants mostly used by tribals such as Sugalis, Yerukali and Chenchus of the study area.

MATERIALS AND METHODS

The present study area (Peddagattu and Sherepally area) is a part of the Nalgonda District covering of 4781.35km² (Fig 1). Peddagattu and Sherepally area was explored during the 2010- 2013. The tribals, Sugali (Lambadi) is the highest population followed by Chenchu and Yerukala are living in the study area. Local informants with the knowledge of medicinal plants were selected based on the experience in the preparation of medicines, the way they acquired knowledge on the medicinal plants and their ability to treat a specific disease. The data was collected through questionnaires, discussions among the tribal people. The information on useful plants species, parts used, local names and mode of utilization was collected. Plants used in their traditional medicine were identified with the help of regional floras (Gamble & Fischer 1915-1935., Jain S.K., 1991, Pullaiah et al. 1997 a, b and c., Rao et al. 2001 & Pullaiah et al. 2000). The plants specimens were pressed and deposited in the Deccan Regional Center, Botanical Survey of India (BSI), Hyderabad.

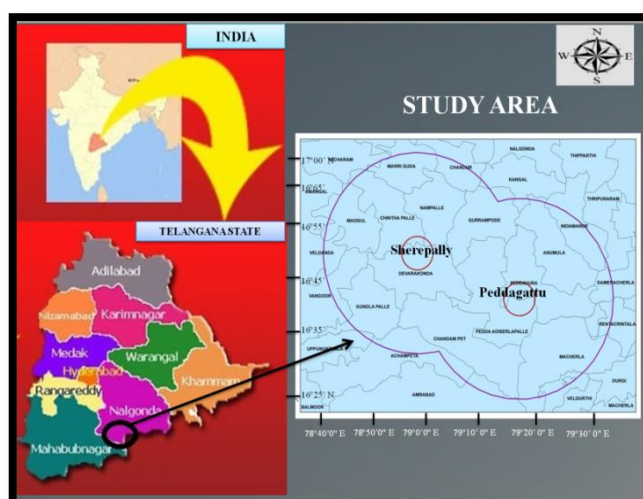


Figure 1. Location map of the study area

RESULTS AND DISCUSSION

A total of 83 medicinal plants belonging to 78 genera and 41 families were recorded. Asteraceae has the highest number of species (7 species) followed by Asclepiadeaceae (6 species), Euphorbiaceae (6 species), Caesalpiniaceae (5 species), Lamiaceae (4 species), Fabaceae, Liliaceae, Mimosaceae (3 species each), Acanthaceae, Amaranthaceae, Cappariaceae, Lythraceae, Menispermaceae, Moraceae, Rubiaceae, Rutaceae, Sapindaceae, Simarubaceae, Solanaceae, Sterculiaceae, and Verbenaceae (2 species each) and rest of the families (21 families) contain one species each (Table 1). Out of these 83 species, the maximum contribution was recorded for herbs 27 (32.5%) and trees 27 (32.5%) followed by shrubs 19 (23%) and climbers 10 (12%) (Fig 2). Among these species, parts used wise contribution was maximum recorded for leaf (42 %) followed by root (13 %), bark (12%), fruits (10%), whole plant (9%), seed (7%), stem (2%) and Flowers, Gum, Latex and Wood (1% each) (Fig 3).

A total of 47 diseases are known to cure by using 83 medicinal plant species. A maximum of 14 plant species are used for cure wounds healing. Seven species are recorded to cure skin diseases, cut injuries and snake bite. Five species have diabetes control properties and four species are recorded for cure cold and cough. Burns, Eczema and Mosquitoes control are known to cure individually by using of 3 species. Two species are used to cure aphrodisiac, bone fracture, relieve from headache, jaundice, rheumatism, anti helminthes and diuretic. Astringent, abdominal

pain, bladder stones melt, blood purification, boils, broken limbs, bronchitis, whooping cough, cleaning teeth, constipation, dyspepsia, fever, hair health, hernia, indigestion, joint pains, kidney stones melts, pustules, rejuvenate, respiratory diseases, ring worm, scabies, rheumatic swellings, rubefacient, toothache and ulcers are known to cure individually by usage of single species (Table 1).

Whole plant powder of *Aerva lantana* is mixed with milk and small amount of sugar is used for kidney stones melts. Branches of *Dodonaea viscosa* used for dentifrice and relief from dental diseases. Root paste of *Echinops echinatus* is applied to externally on wounds. Seed powder of *Abrus precatorius*, root bark power of *Alangium salviifolium*, dry root paste of *Dregea volubilis*, seed paste of *Strychnos nux-vomica* and root paste of *Aristolochia indica*, *Calotropis gigantea* and *Pergularia daemia* applied on snake bite used as antidote against snake bite. Leaf juice of *Datura metal* is applied over the affected areas of ring worm. Leaves of *Andrographis paniculata* is chewed with betel leaf for control diabetes and fever. Stem of *Senna auriculata* used as tooth brush and leaf paste with egg albumen used for bone fracture. Leaf paste of *Lawsonia inermis* used for hair dye, wound healing and other beautification purpose. Root paste of *Hemidesmus indicus* used as cooling agent and root powder with milk is used for blood purification. The stem bark of *Holoptelea grandis* make into paste form used for healing wounds. Leaf juice of *Leucas aspera* is mixed with milk then taken orally for cure skin diseases and rheumatic swellings. The juice of *Oxystelma esculentum* leaves externally applied on cut and wounds. Juice of *Parkinsonia aculeata* stem bark and fruit juice of *Solanum pubescens* are used to treat indigestion. Leaf smoke of *Vitex negundo*, *Azadirachta indica*, *Hyptis suaveolens* and *Chloroxylon swietenia* are used for control of mosquitoes and mites in houses. Fresh stem bark of *Morinda pubescense* and Leaf juice of *Phyllanthus amarus* used for cure jaundice. Wood paste of *Vitex leucoxylon* is applied on externally to cuts, burns and wound healing. Leaf juice of *Xanthium strumarium*, *Albizia amara*, *Cocculus hirsutus* and *Ageratum conyzoides* are applied to cure cut and wounds healing. Juice of *Croton bonplandianus* whole plant is applied to treat cut and wound healing. Latex of *Euphorbia hirta* is applied on cut and injuries twice a day until healed. Leaf paste of *Ziziphus oenopolia* is used to cure wound healing. Leaf smoke of *Azadirachta indica* is used for control of

mosquitoes and leaf paste is used for anti helminthes and skin diseases. Leaf juice of *Caesalpinia bonduc* used as anti helminthes and raw leaves used for hernia. The leaf paste of *Cassia fistula* mixed with turmeric used for cure skin diseases. Leaf juice of *Ficus mollis* is used on externally to cure eczema and skin diseases. Fresh bark paste of *Acacia nilotica* is used for skin diseases and burns. Succulent leaf paste of *Aloe vera* is applied in skin diseases and cure diabetes. Fresh leaves of *Ammannia baccifera* used in skin diseases. Fruit decoction of *Syzygium cumini* and leaf juice of *Ficus hispida* used for control diabetes. *Terminalia arjuna* bark extraction is used relief from urinal problems and decoction of leaves cures diabetes. Raw leaves of *Tinospora cordifolia*, succulent leaf of *Aloe vera* and leaves of *Andrographis paniculata* are used for control diabetes. Fresh leaves *Anisochilus carnosus* squeezed and inhaled for relieve cold and cough. Fruit powder of *Balanites aegyptiana* is given with milk once in a day for cough and cold cure. Seeds of *Pongamia pinnata* used for cure bronchitis and whooping cough. The stem bark of *Acacia leucophloea* is crashed and inhaled to relieve cough and cold. Leaf paste of *Leonotis nepetifolia*, Wood paste of *Vitex leucoxydon*, Fresh bark paste of *Acacia nilotica* are applied on the burns. Fruits of *Sapindus trifoliatus* and Leaf juice of *Ficus mollis* and *Senna occidentalis* are used for eczema. Whole plant extraction of *Cleome gynandra* used to cure peptic ulcers. Leave juice of *Persicaria glabra* and leaf paste of *Senna auriculata* are applied for setting of fractured bones. Root extraction of *Coccinia grandis* and flower paste of *Pandanus odorifer* used to relief and cure headache. Fruits of *Cordia dichotoma* and *Diospyros chloroxylon* are taken internally for diuretic. Juice of whole plant of *Flueggea leucopyrus* is used for cure joint pains and rheumatism. Tubers of *Gloriosa superba* make to paste and applied over boils. Root juice of *Asparagus racemosus* and seeds of *Spermacoce neohispida* are used for aphrodisiac. Leaf extraction of *Tinospora cordifolia* is given orally once in a day for the removal of bladder stones. Dried root of *Tephrosia purpurea* is burned and the smoke inhaled to cure respiratory diseases. Leaf extraction of *Eclipta prostrata* mixed with coconut oil and applied on head for hair health. Leaf paste of *Annona squamosa* applied to hair and on the pustule. It is noted that the tribals use most of the medicinal plants to cure their day to day health problems like fever, snake bite,

skin diseases, wound healing, jaundice, ring worm, joint pains and mosquitoes control (Table 1).

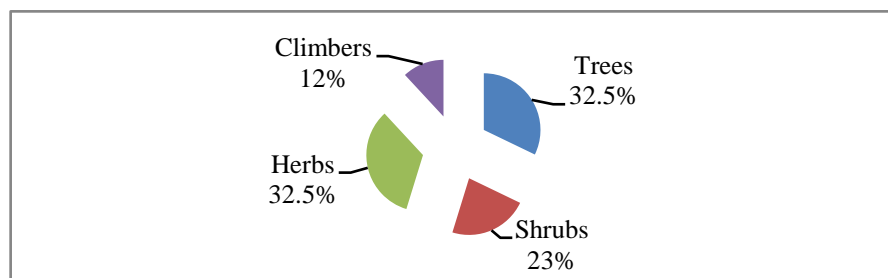


Figure 2. Growth form pattern of plant species

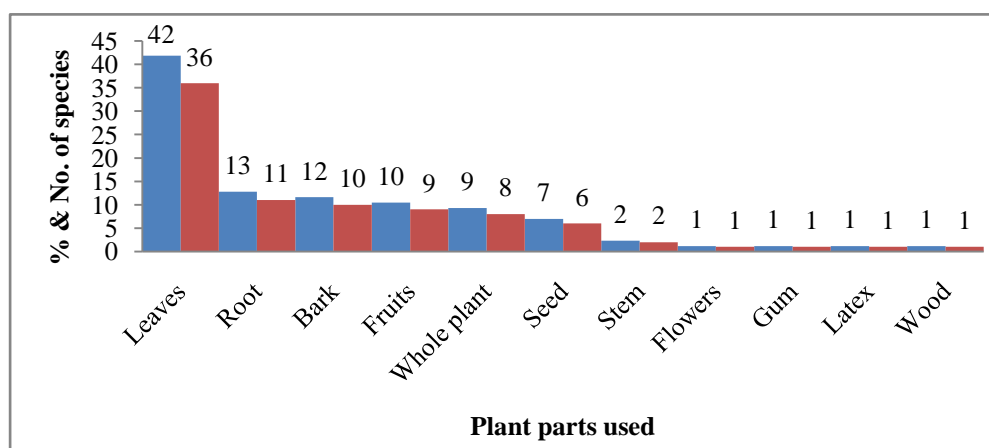


Figure 3. Showing percentage of organoleptic part used in medicines

Table 1. Showing Ethnomedicinal plants and their medicinal importance.

S. No	Family / Species name	Growth form	Vernacular name	Parts used	Medicinal importance
1	Acanthaceae				
1	<i>Andrographis paniculata</i> (Burm.f.) Nees	H	Nelavemu	Leaves	Leaves are chewed with Betel leaf for control diabetes.
2	<i>Elytraria acaulis</i> (L.f.) Lindau	H	Eddu adugu	Leaves	Leaf paste is applied on wounds twice in a day until cured.
2	Alangiaceae				
3	<i>Alangium salviifolium</i> (L.f.) Wangerin	T	Uduga chettu	Root bark	Root bark is used as an antidote for snake bites.

3	Amaranthaceae				
4	<i>Achyranthes aspera</i> L.	H	Uttareni	Roots	Fresh root is used for tooth cleaning and toothache.
5	<i>Aerva lantana</i> (L.). Juss.	H	Telanga pindi	Whole plant	Whole plant powder mixed with milk is used for kidney stones.
4	Annonaceae				
6	<i>Annona squamosa</i> L.	T	Sitaphalamu	Leaves	Leaf paste applied joint pains.
5	Apocynaceae				
7	<i>Wrightia tinctoria</i> R.Br.	T	Palakudise	Leaves	Extraction of leaves and roots relieve tooth pain and wounds.
6	Aristolochiaceae				
8	<i>Aristolochia indica</i> L.	C	Thella usiri	Roots	Root paste is applied to cure snake bite.
7	Asclepiadaceae				
9	<i>Calotropis gigantea</i> (L.) Dryand.	S	Tella jilledu	Root	Root paste is used externally and given orally as an antidote for snake bite.
10	<i>Decalepis hamiltonii</i> Wight & Arn.	C	Nannari	Root	Root extract is taken orally to rejuvenate the body and it is the popular health tonic for rural people.
11	<i>Dregea volubilis</i> (L.f.) Benth. ex Hook.f.	SS	Pala teega	Root, leaves	Dry root paste is used as an antidote for snake bite. Leaf extraction used for wounds.
12	<i>Hemidesmus indicus</i> (L.) R.Br.ex Schuult.	H	Sughandhi pala	Roots	Root paste used as cooling agent and root powder with milk is used for blood purification.
13	<i>Oxystelma esculentum</i> (L. f.) Sm.	C	Dudipala teega	Leaves	Leaf juice applied on cut and wounds.
14	<i>Pergularia daemia</i> (Forssk.) Chiov.	C	Dushtapu teega	Root	Root paste is used for snake bite.
8	Asteraceae				

15	<i>Ageratum conyzoides</i> (L.) L.	H	Pumpulla	Leaves	The leaf paste is externally used for cuts.
16	<i>Cyanthillium cinereum</i> (L.) H.Rob.	H	Kalupumokk a	Whole plant	Whole plant extraction used to cure urinary infection and abdominal pain.
17	<i>Echinops echinatus</i> Roxb.	H	Bramha danthi	Roots	Root paste is applied on wounds.
18	<i>Eclipta prostrata</i> (L.) L.	H	Guntaguru ra	Leaves	Leaf extraction mixed with coconut oil used as hair tannic.
19	<i>Lagascea mollis</i> Cav.	H	Nallagada	Leaves	The juice of fresh leaves used for bleeding control.
20	<i>Tridax procumbens</i> (L.) L.	H	Allammokka	Leaves	Leaf paste used for wound healing.
21	<i>Xanthium strumarium</i> L.	US	Pallaru	Leaves	Leaf juice is applied to cut and wounds.
9	Boraginaceae				
22	<i>Cordia dichotoma</i> G.Fo rst	T	Banka iriki	Fruits	Fruits are taken internally as an astringent and diuretic.
10	Caesalpiniaceae				
23	<i>Caesalpinia bonduc</i> (L.) Roxb.	S	Gachhakaya	Leaves	Leaf juice used as anthelmintic and raw leaves used for hernia.
24	<i>Cassia fistula</i> L.	T	Rela	Leaves	Leaf paste and turmeric is used for skin diseases.
25	<i>Parkinsonia aculeata</i> L.	T	Seemathu ma	Stem bark	Stem bark is used to treat indigestion.
26	<i>Senna auriculata</i> (L.) Roxb.	S	Thangedu	Stem, Leaf	Stem used as tooth brush and leaf paste with egg albumen used for bone fracture.
27	<i>Senna occidentalis</i> (L.) Link	US	Kasivinda	Leaves	Leaf juice is applied externally to treat eczema.
11	Capparidaceae				

28	<i>Cadaba fruticosa</i> (L.) Druce.	S	Vuttarasi chettu	Leaves	Leaf paste used to cure skin diseases (leucoderma).
29	<i>Cleome gynandra</i> L.	H	Talake	Whole plant	Whole plant extraction used to cure peptic ulcers.
12	Combretaceae				
30	<i>Terminalia arjuna</i> (Roxb. ex DC.) Wight & Arn.	T	Tellamaddi	Bark	Bark extraction gives relief from urinal problems and decoction of leaves cures diabetes.
13	Convolvulaceae				
31	<i>Rivea hypocrateriformis</i> Choisy.	TH	Boddikura	Whole plant	Plant juice used for cure of fever.
14	Cucurbitaceae				
32	<i>Coccinia grandis</i> (L.) Voigt.	TH	Donda	Root, Fruit	Root extract is applied to relief and cure headache.
15	Ebenaceae				
33	<i>Diospyros chloroxylon</i> Roxb.	T	Ullinda	Stem bark, Fruits	Bark powder is applied on wounds and fruits used for diuretic and constipation.
16	Euphorbiaceae				
34	<i>Jatropha curcas</i> L.	S	Adavi amudam	Twigs	The tender twigs are used for cleaning teeth.
35	<i>Croton bonplandianus</i> Baill.	H	Verrimirapa	Whole plant	Juice of whole plant is applied to treat cuts and wound healing.
36	<i>Euphorbia hirta</i> L.	H	Alumu	Latex	Latex is applied for cut and injuries twice a day until healed.
37	<i>Flueggea leucopyrus</i> Wild.	S	Tellapulichettu	Leaves	Juice of whole plant is used for joint pains and rheumatism.
38	<i>Phyllanthus amarus</i> Schumach. & Thonn.	H	Nela usiri	Leaves	Leaf juice is administered for

					Jaundice.
39	<i>Phyllanthus reticulatus</i> Poir.	S	Pulichari	Root	Root or stem with coconut oil is applied on joint pains.
17	Fabaceae				
40	<i>Abrus precatorius</i> L.	C	Guruvinda	Seed	Seed powder is used as antidote for snake bite
41	<i>Pongamia pinnata</i> (L.) Pierre	T	Kanuga	Seeds	Seeds are used for bronchitis and whooping cough.
42	<i>Tephrosia purpurea</i> (L.) Pers.	H	Vempali	Root	Dried root is burned and the smoke inhaled to cure respiratory diseases.
18	Lamiaceae				
43	<i>Anisochilus carnosus</i> (L.f.) Wall.	H	Karpuravalli	Leaves	Fresh leaves squeezed and inhaled for cold and cough.
44	<i>Hyptis suaveolens</i> (L.) Poit.	US	Danthitulasi	Whole plant	Plant smoke is used for mosquitoes control.
45	<i>Leonotis nepetifolia</i> (L.) R.Br.	H	Ranabheri, Seeranta	Leaves	Leaf paste is applied on the burns.
46	<i>Leucas aspera</i> (Willd.) Link	H	Thummi	Leaves	Leaf juice mixed with milk is taken orally for skin diseases and rheumatic swellings.
19	Lauraceae				
47	<i>Cassytha filiformis</i> L.	C	Pachiteega	Stem	The stem with sugar, make in to powder used for heat.
20	Liliaceae				
48	<i>Aloe vera</i> (L.) Burm.f.	H	Chinna kalbandha	Leaves	Succulent leaf paste is applied in skin diseases, cool agent and cure diabetes.
49	<i>Asparagus racemosus</i> Willd.	SS	Pillipeechari gaddalu	Tubers	Root juice is mixed with honey used for dyspepsia. Root powder is taken with

					milk as aphrodisiac.
50	<i>Gloriosa superba</i> L.	C	Konda Nabhi	Tubers	Tubers paste applied over boils.
21	Loganiaceae				
51	<i>Strychnos nux-vomica</i> L.	T	Vishamushti	Seed	Seed paste used for snake bite.
22	Loranthaceae				
52	<i>Dendrophthoe falcata</i> (L.f) Ett.	C	Bhajanaka	Stem	Stem paste is used as an external application to cure wounds.
23	Lythraceae				
53	<i>Ammannia baccifera</i> L.	H	Agnivendra paku	Leaves	Fresh leaves are used in skin diseases.
54	<i>Lawsonia inermis</i> L.	T	Gorinta	Leaves	Leaf paste used for hair dye, wound healing.
24	Meliaceae				
55	<i>Azadirachta indica</i> A.Juss.	T	Vepa	Leaves	Leaf smoke is used for control of mosquitoes and leaf paste is used for anti helminthes and Skin diseases.
25	Menispermaceae				
56	<i>Cocculus hirsutus</i> (L.) W.Theob.	C	Dusari teega	Leaves	Leaves crushed and applied to cut and wounds.
57	<i>Tinospora cordifolia</i> (Willd.) Miers	SC	Tippatheega	Leaves	2or 3 raw leaves eaten for Diabetes.
26	Mimosaceae				
58	<i>Acacia leucophloea</i> (Roxb.) Willd.	T	Tellathumma	Stem bark	The stem bark is squeezed and inhaled to relieve from cold and cough.
59	<i>Acacia nilotica</i> (L.) Delile	T	Nallathumma	Bark	Fresh bark paste is used for Skin diseases and Burns.
60	<i>Albizia amara</i> (Roxb.) B.Boivin	T	Narlinga	Leaves	Leaf juice is applied externally on cut and

					wounds.
27	Moraceae				
61	<i>Ficus hispida</i> L.f.	T	Bramha mamedu	Leaves, Fruits	Leave juice is applied to treat boils and fruit and root is used for diabetes.
62	<i>Ficus mollis</i> Vahl	T	Juvvi	Leaves	Leaf juice is used externally to cure eczema and skin diseases.
28	Myrtaceae				
63	<i>Syzygium cumini</i> (L.) Skeels	T	Allaneredu	Seeds	Fruit decoction used for diabetes.
29	Pandanaceae				
64	<i>Pandanus odorifer</i> (Forssk.) Kuntze	S	Mogali	Flowers	Flower paste is applied for headache.
30	Polygonaceae				
65	<i>Persicaria glabra</i> (Willd.) M.Gómez	H	Neetiganner u	Leaves	Leaf juice is applied for setting of fractured bones.
31	Rhamnaceae				
66	<i>Ziziphus oenopolia</i> (L.) Mill.	S	Pariki	Leaves	Leaf paste is used wound healing.
32	Rubiaceae				
67	<i>Morinda pubescense</i> Sm.	T	Maddi	Stem bark	Fresh stem bark is crushed and the infusion given orally for jaundice.
68	<i>Spermacoce neohispida</i> Govaerts	H	Madana chettu	Seed	Seeds are intensifying sexual desires (aphrodisiac).
33	Rutaceae				
69	<i>Atalantia monophylla</i> DC.	S	Adavi nimma	Fruits	Berries yield oil used externally on joints pains.
70	<i>Chloroxylon swietenia</i> DC.	T	Billudu	Leaves	Leaf smoke is used for mosquitoes control.

34	Sapindaceae				
71	<i>Sapindus trifoliatus</i> L.	T	Kunkudu	Fruit	Fruits are used for eczema.
72	<i>Dodonaea viscosa</i> (L) Jacq.	S	Bandaru	Branch stem	Branches are good dentifrices.
35	Simarubaceae				
73	<i>Ailanthus excelsa</i> Roxb	T	Peddamanu	Stem bark	The stem bark paste is used to cure skin diseases.
74	<i>Balanites aegyptiana</i> (L.)	T	Garachettu	Fruit	Fruit powder is given with milk once in a day for cough and cold.
36	Solanaceae				
75	<i>Datura metal</i> L.	H	Ummetha	Leaves	Leaf juice is applied over the affected areas of ring worm.
74	<i>Solanum pubescens</i> .Willd.	S	Usintha	Fruit, seed	Fruit juice about 10 ml, 2 times for day for two days for indigestion.
37	Sterculiaceae				
77	<i>Firmiana simplex</i> (L.) W.Wight	T	Tapsi	Gum	Gum used for constipation.
78	<i>Helicteres isora</i> L.	T	Gubatada	Fruits	Fresh fruits made into paste and prepared a pills, given ones a day for 10days to cure scabies.
38	Ulmaceae				
79	<i>Holoptelea grandis</i> (Hutch.) Mildbr.	T	Tharisa	Stem bark	Stem bark paste used for healing wounds.
39	Verbenaceae				
80	<i>Vitex leucoxydon</i> L. f.	T	Konda vavili	Leaves	Leaf paste is applied to cuts, burns.
81	<i>Vitex negundo</i> L.	S	Vavili	Leaves	Leaf smoke used for removal of mosquitoes and mites.
40	Vitaceae				

82	<i>Cissus quadrangularis</i> L.	C	Anduatukula teega	Whole plant	Plant paste is for broken limbs.
41	Zygophyllaceae				
83	<i>Tribulus terrestris</i> L.	H	Palleru kaya	Leaves	Leaf extract is given orally once in a day for the removal of bladder stones.

C= Climber; H= Herb; S= Shrub; T= Tree; US= under shrub; TH= Twining herb;

SC= Shrubby climber; SS= straggling shrub.

CONCLUSION

The present study clearly indicates the presence of rich diversity of medicinal plants. The use of herbal remedies among the tribal people in study area reflects the revival of interest in traditional medicine. This data provides basic source for future studies aimed at conservation, cultivation, improvement of ethnic traditional medicines and economic welfare of rural and tribal population of region. The ethnic knowledge has been rapidly eroded due to various factors such as lack of proper documentation, lack in transmission of knowledge to next generation, modernization and loss of floral diversity. Hence, conservation of floral diversity will be important tool to sustain and carry such important knowledge to the future generation.

ACKNOWLEDGMENTS

The Authors thank to the tribal people who shared their traditional knowledge and extend our grateful to Board of Research on Nuclear science (BRNS), BARC, Government of India, for funding the project.

REFERENCES

- Akerele. O (1992). WHO guidelines for assessment of herbal medicines. *Fitoterapia* 63: 99-118.
- Basi Reddy M. Raja Reddy K. & Reddy M.N. (1991). Ethnobotany of Cuddappah District, Andra Pradesh, India. *Int. Journal of Pharmacognosy*, 29: 1-8.

- Chandra Babu N.M. Tarakeswar Naidu & Venkaiah (2010). Ethnobotanical plants of Kotia hills of Vijayanagaram District, Andrapradesh, India. *Journal of Phytology*. 2(6): 76-82.
- Gamble J.S. & Fischer C. E. C. (1915-1935). Flora of the Presidency of Madras (repr. ed. 1957. Calcutta).
- Harshberger J.W. (1895). The purpose of ethnobotany-1. *Botanical Gazette*, 21: 146-154.
- Hemdri K. Shara C.R.R & Rao S.S. (1987 a). Medicinal plants of Andra Pradesh, Part –I. *Ancient Science of life*. 6: 167 – 186.
- Hemdri K. Shara C.R.R & Rao S.S. (1987 b). Medicinal plants of Andra Pradesh, Part –II. *Ancient Science of life*. 7 (5): 5- 64.
- Huxley. (1984). *Green inheritance: The World wildlife Fund Book of India*. (Collins/ Harvel, London).
- Jain S.K. (1991). *Dictionary of Indian folk medicine and Ethnobotany*. Deep publications, New Delhi.
- Murthy, E.N (2012): Ethno medicinal plants used by gond of Adilabad District, Andhra Pradesh, India. *International journal of Pharmacy & life sciences*. Vol 3 (10): 2034-2043.
- Kapoor S.L. and Kapoor L.D. (1980). Medicinal plantwealth of Karimnagar District of Andhra Pradesh. *Bull. Med. Ethnobot. Res.* 7: 120-144.
- Pullaiah T. (1997a.) *Flora of Andhra Pradesh. Vol.III, Monocotyledons*, Scientific Publishers, Jodhpur.
- Pullaiah T. & Ali Moulali D. (1997b). *Flora of Andhra Pradesh, Vol .II. Rubiaciae-Urticaceae*. Scientific Publishers, Jodhpur.
- Pullaiah, T. & Chennaiah E.(1997c). *Flora of Andhra Pradesh, Vol. I. Ranunculacea-Alangiaceae*. Scientific Publishers, Jodhpur.
- Pullaiah T. Ramakrishnaiah V. Sadhya Rani S. & Rao P. N. (2000). *Flora of Guntur district, Andhra Pradesh, India*. Regency Publications.

Raja Reddy K.G. Sudarsanam & Gopala Rao. (1989). Plant drugs of Chittoor District, Andhra Pradesh, India. *Journal of Crude drugs Research*. 27: 41-54.

Rama Krishna N. Varma Y.N.R. and Saidulu Ch. (2014). Ethnobotanical studies of Adilabad District, Andhra Pradesh, India. *Journal of pharmacognosy and Photochemistry*. 3 (1). 18-36.

Rao P.N. Raghava Swamy. & Pullaiah T. 2001. Flora of Nalgonda district, Andhra Pradesh. Shipra publication, Delhi.

Ravisanker T and Herry A.N. (1992). Ethnobotany of Adilabad District, Andhra Pradesh, India. *Ethnobotany* 4: 45-52.

Reddy N.M. (2013). Ethno botanical Study of Medicinal Plants in and around NAR Agriculture Farms area of Appannapeta village at Nalgonda district, Telangana, India. *Journal of Medicinal Plants Studies*. Vol. 1: 27-29.

Sanyasi Rao M. L. and Varma Y.N.R (2014): Folklore traditional knowledge on digestive disorders of domestic animals (cattle, sheep and goats) in the Medak District, Telangana, India. *Biolife*, Vol 2(3): 858-865.

Singh K.K. Palvi S.K and Singh H.B. (1981). Survey and biological activity of some medicinal plants of Mannanur forest, Andhra Pradesh. *Indian Journal of forestry* 4: 115-118.

Venkanna P. (1990). Medicinal plant wealth of Krisna District, Andhra Pradesh. A preliminary survey. *Ancient Science of life*. 102: 137-140.

Structural Characterization of Nano Crystalline

Ni Sm_xFe_{2-x}O₄ferrites

Gopal boda¹, Nehru boda², G. Aravind², A. Panasa Reddy^{1}, D.Ravinder^{2*}*

¹Department of chemistry, college of Engineering, Osmania University, Hyderabad,

²Department of physics, Osmania University, Hyderabad, 500007, Telangana, India

*Correspondence author email: ravindergupta28@rediffmail.com.

ABSTRACT: Nano crystalline Samarium doped Nickel ferrites having compositional formula NiSm_xFe_{2-x}O₄ where (x=0.00 to 0.10 with a step of 0.01) were synthesized by the citrate-gel auto combustion method. Synthesized powders were sintered at 500⁰C for four hours in air and characterized by XRD, SEM, and EDS. X-ray diffraction analysis of the investigated samples showed cubic spinel structure of the ferrites without any impurity peak and the values of lattice parameter (a) and X-ray density (d_x) increases with the increase of Sm content. Scanning Electron Microscope (SEM) studies revealed morphology of the Nano crystalline samples. An elemental composition of the sample was studied by Energy Dispersive spectroscopy (EDS). The observed results can be explained on the basis of composition.

1. Key Words:-Ni-Sm Nano ferrites, citrate-gel auto combustion method, XRD, SEM and EDS.

1. Introduction:-Ferrites have diverged practical applications as high density magnetic data storage, Microwave absorbing materials. Magnetic resonance imaging contrast agents and targeted release of drugs preparation conditions influence the cation distribution. Which in term reflects In the chemical and physical of ferrites to a great extend [1]

Properties of ferrites are highly sensitive to the substitution of different metal ions in its tetrahedral and octahedral sites

Substitution of large rare earth ions In place of small ions will result in strain which induce structural distribution and there by modify the properties of samples in Nano-region

The properties of ferrites are dependent on several factors, chemical composition, method of preparation, grain size, sintering temperature and atmosphere [2]

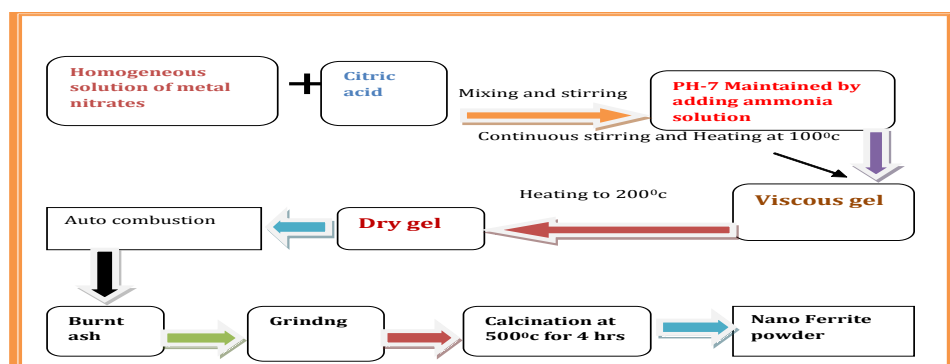
2. Experimental Details: The Nickel-Samarium nano ferrites having the chemical formula $\text{NiSm}_x\text{Fe}_{2-x}\text{O}_4$ were synthesized by citrate gel auto combustion method using the below raw materials

2.1 Raw Materials:

- Nickel nitrate 99% pure(AR Grade)[$\text{Ni}(\text{NO}_3)_2$]
- Samarium nitrate 99.9% sigma Aldrich [$\text{Sm}(\text{NO}_3)_3 \cdot 6\text{H}_2\text{O}$]
- Ferric nitrate –99.9% pure(AR Grade) ($\text{Fe}(\text{NO}_3)_3 \cdot 9\text{H}_2\text{O}$)
- Citric acid –99% pure(AR Grad) ($\text{C}_6\text{H}_8\text{O}_7 \cdot \text{H}_2\text{O}$)
- Ammonia Solution -99% pure(AR Grade)(NH_3)

2.2. The flow chart of synthesis of Ni-Sm Nano ferrites:

The calculated quantities of metal nitrates were dissolved in minimum amount of distilled water to get clear homogeneous solution an aqueous solution of citric acid was added to the metal nitrate solution. The molar ratio of citric acid to the total moles of citric acid to the total moles of nitrate ions was adjusted to 1:3 the flow chart shown in fig ;(1)



Fig(1): The flow chart for synthesis

2.3 Structural characterization by XRD:

The structural characterization was done by X-Ray Diffract meter were recorded using Regakumaniplex powder X-ray diffractometer ($\text{Cu-K}\alpha$ $\lambda=1.5406\text{\AA}$) with

diffracted mono chromatic beam with radiation of wave length (1.5405\AA) the diffraction pattern of Ni-Sm between bragg Angles 10° to 80° in the steps of $0.04^\circ/\text{sec}$. nano ferrites particles Were shown in fig.

The crystalline size was calculated for the sample using the high intensity 311 peak and using Debay Scherrer formula [3] while taking into account the intensity broadening [4].

$$\text{Crystalline size of the sample } D = \frac{0.91\lambda}{\beta \cos \theta}$$

Where λ the wavelength of X-ray is used [5]. β is the width of diffraction peak i.e. full width Half Maximum (FWHM), θ is the peak position.

Lattice parameter (a) of the sample was calculated by the formula. $a = d * \sqrt{h^2 + k^2 + l^2}$ [6] Where a=Lattice constant, (hkl) are the Miller indices, d is the inter planner space The X-ray density of the prepared sample was calculated using the relation $\rho_x = \frac{8M}{a^3 N}$ (g/cm^3) [7] where M= molecular weight of the sample, a is the lattice parameter and N is the Avogadro number.

3. Result and Discussion;-

3.1. XRD Analysis:

A phase analysis using X-ray diffraction technique was performed to confirm the formation of single-phase cubic spinel structure as shown in **fig-(2)**. With no extra lines corresponding to any other crystallographic phase. The results obtained from XRD pattern for all the samples of $\text{NiSm}_x\text{Fe}_{2-x}\text{O}_4$ with the (hkl) values corresponding to the diffraction peaks of different planes (220), (311), (400), (422), (511), and (440) are spinel cubic phase

The calculated values of crystalline size for the different compositions are given in the table (1). It can be seen from the table that the values of the crystal size varies from 28.53nm to 39.45nm of the various Sm concentrations

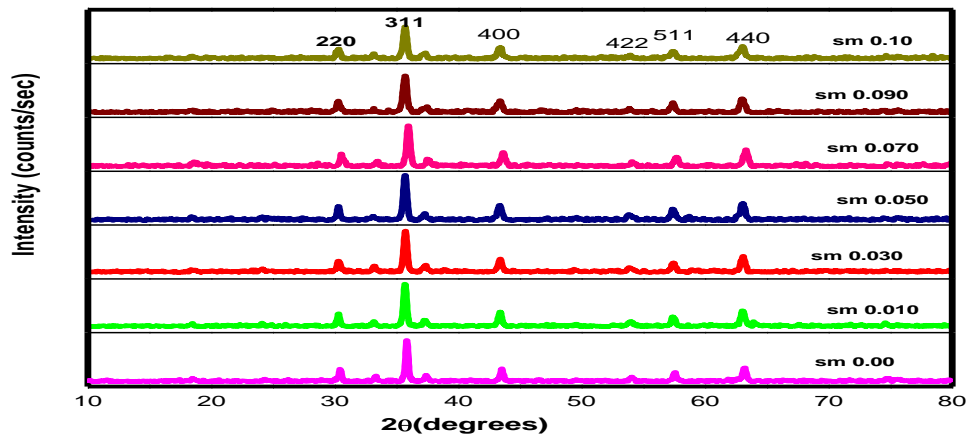
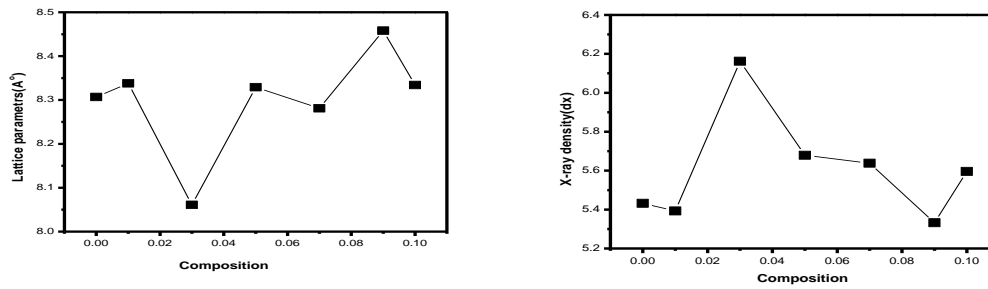


Fig (2): XRD pattern of Ni-Sm Nano ferrites

The lattice parameter values of all the composition of Samarium doped Iron ferrites have been calculated from the d- spacing and are given in the table.(1)

A plot is drawn between the lattice parameter vs Samarium composition is shown in Figure (3) variation of lattice constant with Sm^{+3} content in $\text{NiSm}_x\text{Fe}_{2-x}\text{O}_4$ is ($x=0.00$ to 0.10 with a step of 0.01) is observed that the Lattice parameter increases with increase in Sm content. This is attributed to replacement of smaller ionic radii Ni (0.78\AA) by larger ionic radii Sm^{+3} (\AA) ions. This linear variation indicates that the Ni-Sm ferrite system obeys Vegard's law [8] and table 1 shown below

Ferrite composition	Crystalline size(D)nm	Lattice parameter(a) \AA	X-ray density(d_x)[gm/cc]
NiFe_2O_4	39.45	8.307	5.432
$\text{NiSm}_{0.010}\text{Fe}_{1.99}\text{O}_4$	33.37	8.338	5.393
$\text{NiSm}_{0.030}\text{Fe}_{1.97}\text{O}_4$	30.72	8.061	6.162
$\text{NiSm}_{0.050}\text{Fe}_{1.95}\text{O}_4$	30.74	8.329	5.679
$\text{NiSm}_{0.070}\text{Fe}_{1.93}\text{O}_4$	31.65	8.281	5.638
$\text{NiSm}_{0.090}\text{Fe}_{1.91}\text{O}_4$	28.53	8.458	5.332
$\text{NiSm}_{0.10}\text{Fe}_{1.9}\text{O}_4$	29.53	8.334	5.596



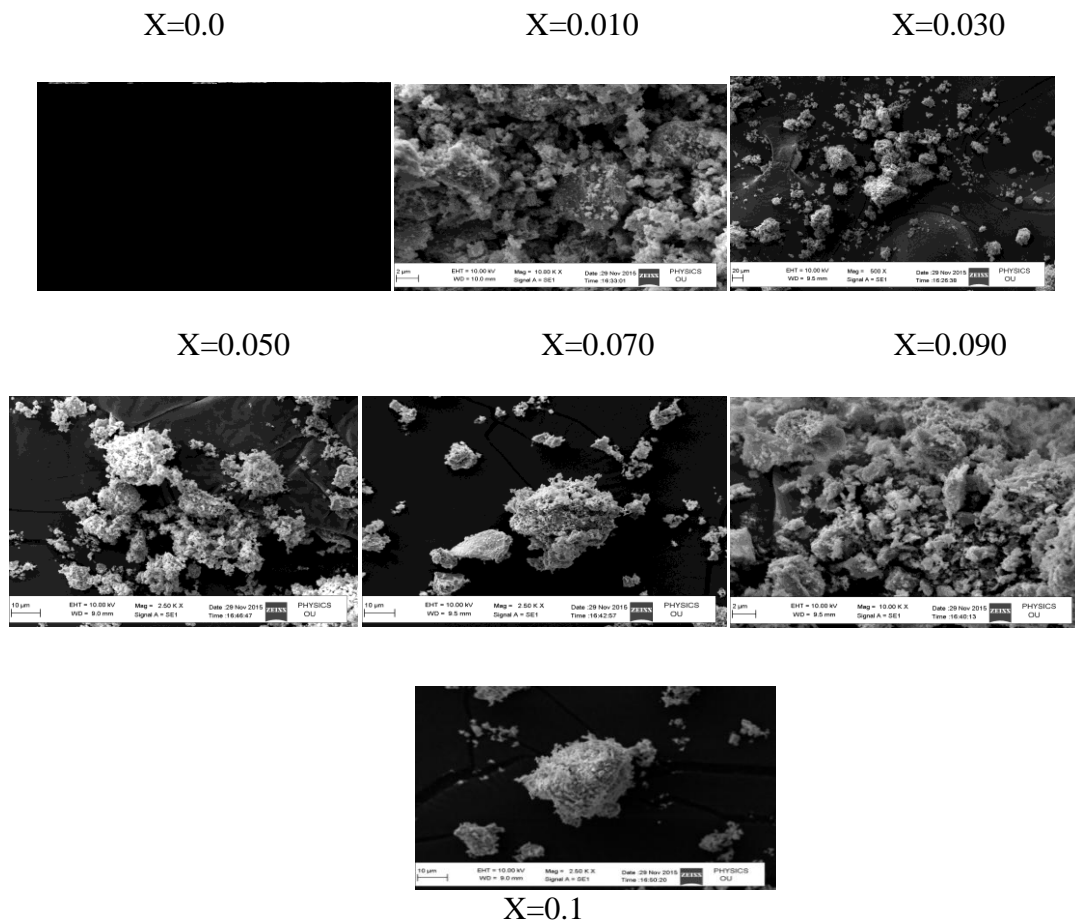
Fig; (3)) variation of lattice constant with Sm^{+3} content and figure (4) shows the X-ray density (d_x) vs Sm^+ concentration

The **figure (4)** shows the X-ray density (d_x) vs concentration, The X-ray density (d_x) is depend on the lattice parameter and molecular weight of the sample. From the table one can observe that molecular weight of the sample is increases with Samarium concentration and lattice parameter is also increases with the increase of Sm compositions. This may due to the grater atomic weight of sm 150.36gm/mol and lesser atomic weight of Fe-55.845gm/mol(8) shown in figure[4, 5].

Samarium was very small .the calculated values of the lattice constant tabulated in table:1 show that there has been no structural distortion for the various ratios. The fact that samarium goes as substitution into the cubic spinel lattice evident from the absence of any extra peaks in the XRD spectrum

3.2. Morphology by SEM: studied microscope (prepared samples by Citrate- Gel Auto combustion method was using scanning electron SEM) where the secondary electron images were taken at different magnifications to study the synthesized samples were shown in **figure (5)**.

The sem images of Ni-Sm ferrite are shown in the Fig the images show that the particles have an almost homogeneous distribution ,and some of the samples are agglomerated form .it evidenced by SEM images that the agglomeration of particles lies in nano region.the particles were observed as uniform grain (in different SEM images) sizes[9]

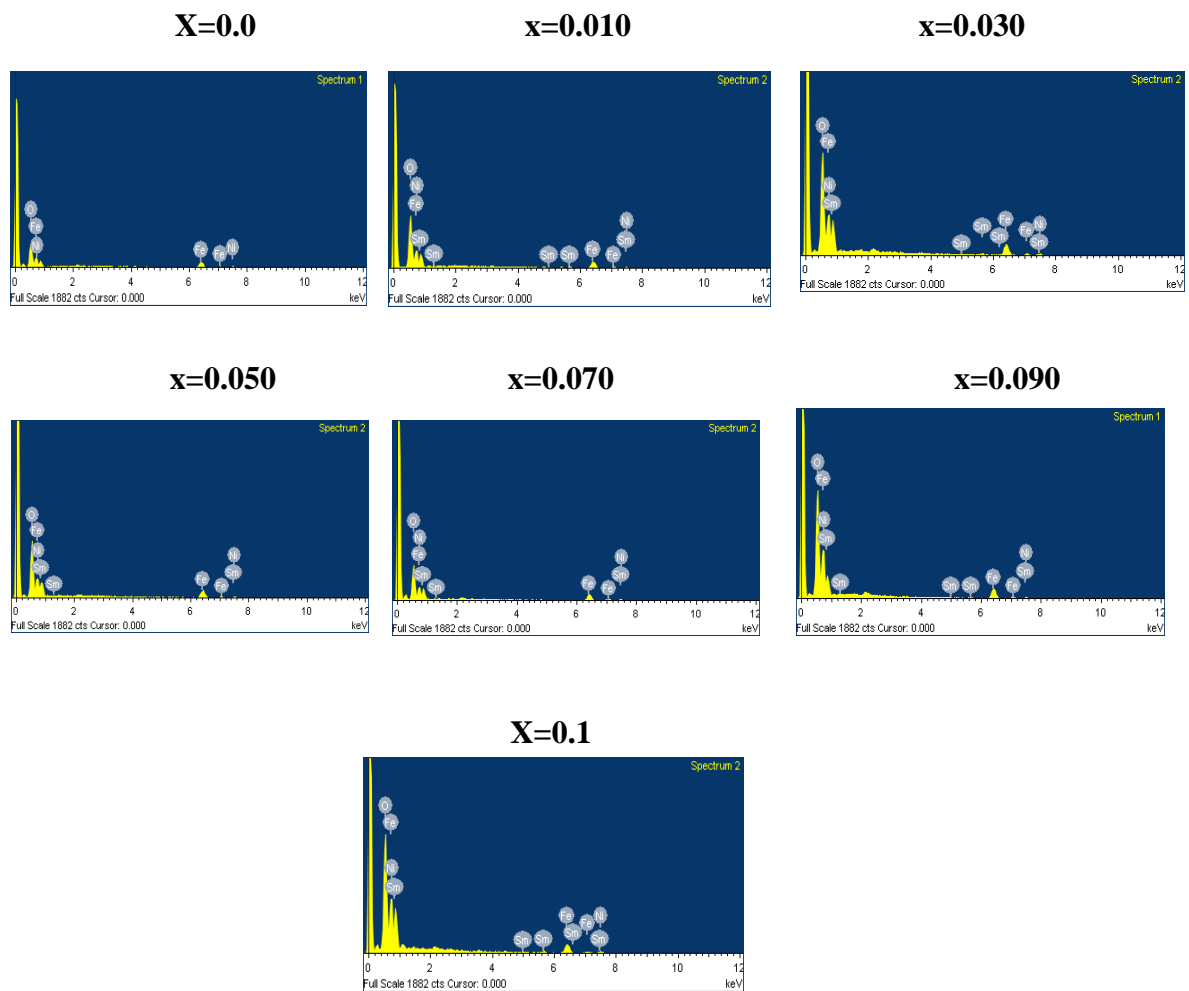


Fig(5) : SEM micrographs of compositions of Ni-Sm nano ferrites

3.3. Elemental Analysis by EDS:

The EDS spectra give information about the chemical composition of the elements present from the surface to the interior of the solids, and they are used to confirm the homogeneity of the investigated samples.

The spectra indicated the presence of O, Fe, Ni, and Sm as the major elements in the synthesized material with no impurities are observed along with elemental mapping. The EDX spectra of the samples are shown in figure (6)



Fig(6) : EDS micrographs of compositions of Ni-Sm nano ferrites

4. Conclusion:

- Citrate Gel Auto Combustion technique is a convenient way for obtaining a homogeneous nano sized mixed ferrites, it is very simple and economical method where no specific heating or cooling rate is required .
- X-ray diffraction pattern confirms the formation of single phase cubic spinel structure. From standard data JCPDS.
- The crystalline size of the various NiSm ferrites was in the range of 28 to 39 nm.
- The Lattice parameter has increased with the increase of Sm concentration in Ni-Sm ferrites which indicate that the mixed Ni-Sm ferrite system obey the vegard's law

- SEM micrographs of various compositions indicate the morphology of particles is similar .they reveal that largely agglomerated.
- EDS data give the elemental % and atomic % in the mixed Ni-Sm ferrites and it shows the presence of Ni, Sm, Fe and O without precipitating cations.

5. Acknowledgements:

The authors are very grateful Prof.G.Venkateshwarlu Head Department of Chemistry University college of science Osmania University Hyderabad, And thankful to Prof .M.Vithal Chairman board of studies .Department of Chemistry, University college of science O.U.Hyderabad for his support in characterization (XRD)one of the author Gopal Bodais thankful to **UGCNON- NET fellowship** for their financial assistance,

References:

- [1] Smitha Thankachan,Binu P. Jacob, Sheena Xavier, E.M Mohammed 348 (2013) 140-145
- [2] K.Kondo, T. Chiba, S. Yamada, Journal of Mag Mater **541**, 254(2003)
- [3] Cullity B D, Elements of X-ray diffraction (addition Wesley, Reading, Mass), 1959. P132.
- [4] Mahmud ST, Akther Hossain AKM, Abdul Hakim AKM, Seki M, Kawai T. Tabata H (2006) j Magn Mater 305;269 doi; 10.1016/j.jmmm.2006.01.012.
- [5] B.D. Cullity, Elements of X-ray diffraction, Wesely Pub,Co.,Massachusetts,1987,101-356
- [6] B.P.Ladgaonkar, P.P.Bakare,S.R. Sainkar and A.S.Vaingankar, "Influence of Nd³⁺ substitution on permeability spectrum of Zn-Mg ferrite". Materials Chemistry and Physics, Volume 69,Issues 1- 3,March 1, 2001, pages 19-24.
- [7] R.C.Kumbale. P.A.Shaikh, S.S. Kamble, Y.D.Kolekar J.Alloys Comp., 478(2009), p.599 doi:10.1016/j.jmmm.2005.03.007
- [8] K.B.Modi, J.D.Gajera, M.P.Pandya,H.G.Vora, H.H.Joshi, Pramana Journal of Physics, Vol 62, No 5,May, 2004, pages 1173-1180
- [9] M. Maria lumina Sonia, S. Pauline, Mary N. L ISSN-2319-8354(E).

Validation of Kinetic Modelling in Removal of Sulphonated Dye in Waste Water using Polyaniline/ZnO nanocomposites

[#]Neha V. Dambhare, Neha V. Nerkar, Subhash B. Kondawar*

Department of Physics, Rashtrasant Tukadoji Maharaj Nagpur University,
Nagpur – 440033, India

*Corresponding Author E-mail: sbkondawar@yahoo.co.in

[#]Presenting Author E-mail: nehadambhare1994@gmail.com

ABSTRACT

Sulphonated dyes are some of the biggest contributors to water pollution and very harmful to environment for human health concerned. In this study, a method for the removal of cationic sulphonated methyl orange (MO) dye from aqueous solution using chemical interaction of dye molecule with PANI/ZnO nanocomposites are reported. PANI/ZnO nanocomposites have been prepared by in-situ polymerization. Morphological study using SEM revealed that PANI/ZnO was found to be best promising candidate for adsorption of dyes due to more porosity compared to that of pure PANI. UV-Vis spectroscopy was done to study adsorption of MO dye. Percentage of removal of dye was then studied comparatively for PANI and PANI/ZnO nanocomposites. The percentage adsorption was found to be 79% for PANI/ZnO compared to that of 53% for pure PANI. In order to evaluate kinetic mechanism the pseudo first order model, pseudo second order model and intra particle diffusion model were tested the validity of the models were verified by the linear equation analysis. The second-order kinetic model was found to be the best linearity compared to other models which indicate that it is physical adsorption. The adsorption process was shown to be an efficient for dye removal from water solutions. The results clearly demonstrated that ZnO contributed to the adsorption mechanism through electrostatic interactions between sulphonic groups of the adsorbent (which are known as strong cation exchangers) and the cationic sites of methyl orange dye and it gives very novel and green method of removal of hazardous dye.

Keywords: Adsorption, conducting polymer, PANI/ZnO nanocomposites, UV-Vis spectroscopy, sulphonated dyes.

1. Introduction

Coloured wastewater is particularly associated with reactive dyes; these dyes make up approximately 30 % of total dye market. Reactive dyes are the most common dyes used due to their advantages, such as bright colours, excellent colour fastness and ease of application. Reactive dyes are highly soluble in water and the resultant change in the water colour is unattractive to the public. The characteristic structures of dyes, particularly reactive dyes, are very complex, chemically stable and difficult to degrade or eliminate. Moreover, the contamination of public streams with these dyes may present a risk to human beings since aquatic living creatures such as fish that can accumulate dyes in their tissues. And the toxicity of reactive dyes has been reported at concentration as low as 5.2 mg/l. Water pollution by high levels of pollutant dyes from textile industry is a serious problem owing to the toxicity effect of these compounds. Complete removal or at least decolourization of these compounds from the environment is therefore an important issue. The dyes from textile industries are major sources of environmental pollution because they are non-biodegradable. Many methods such as flocculation, reverse osmosis and activated carbon adsorption have been used in wastewater treatment. However, photocatalysis is often used as a technique to degrade dyes because it is simple and cost effective. Conventionally inorganic semiconductors are used as photocatalysts and TiO_2 , doped TiO_2 , and ZnO are extensively used for the degradation of dyes in waste water. Conducting polymers are becoming the most promising new materials for next-generation electronic devices [1]. Polyaniline (PANI) is one of the conducting polymers that generated a great interest over the past two decades because of its potential applications in many fields. Its high electrical and electronic properties, ease of preparation, and low costs render the polymer promising material for several technological applications. These applications include rechargeable batteries, sensors, separation membranes and corrosion inhibitor. Conducting polymers have band gaps in the same range as inorganic semiconductors. Further, the band gaps of these polymers can be tuned by chemical manipulation of the backbone. Therefore conducting polymers composites with suitable band gaps, could, in principle, act as photocatalysts for dye. Polyaniline (PANI) is a poly aromatic amine that can be

easily synthesised. It is one of the most potentially useful conducting polymers and has received considerable attention in recent years. Chemical polymerization of aniline in aqueous acidic media can be easily performed. The oxidation process is accompanied by the insertion of anions of acid electrolyte in order to maintain the charge neutrality of the final polymer product. Ammonium persulfate is a popular and frequently used chemical oxidant for polymerization of aniline in acidic aqueous solutions [2]. In this study, we report that polyaniline/zinc oxide composites can remove anionic (sulfonated) dyes with the application of UV and visible light through a chemical interaction with the sulfonated dyes. Thus, the objective of the article is to examine the use of polyaniline/ZnO composites for the removal of various sulfonated dyes from aqueous solutions and propose a mechanism of chemical interaction between the sulfonated dyes and PANI/ZnO. Methyl orange is intensely coloured compound used in dyeing and printing textiles. It is also known as C.I. acid orange 52. Chemist used methyl orange as an indicator of weak bases with strong acids. It is water soluble azo dye. It is carcinogenic and mutagenic in nature and hence it has bad impact on nature as well as human habitat [3, 4].

2. Experimental

Synthesis of Polyaniline/ZnO nanocomposites

ZnO nanoparticles were prepared by colloidal route method and 5 wt% of it sonicated with 0.2M aniline and 0.2M HCl solution in 100 ml water for half an hour. The mixture was stirred continuously and 0.2M ammonium persulphate was added drop wise. The colour was changed from colourless to blue and finally dark green. The mixture was kept overnight, filtered and washed with ethanol and distilled water. The precipitate was dried in vacuum oven at 80°C [5]. Similarly, pure polyaniline was prepared with out the use of ZnO for comparison.

3. Result and Discussions

The SEM micrographs of PANI powder and PANI/ZnO are shown in **Fig. 1(a)** and **(b)**, respectively. It can be seen that the surface morphology of PANI powder was composed of irregular agglomeration of particles. On the other hand, PANI/ZnO aggregates have regular diameter which merge tightly with each other to exhibit a

net like macro porous state. This macro porous structure of the immobilized PANI is expected to contribute to the efficient adsorption of adsorbents since it provides a path for the insertion and extraction of molecules or ions within the inner layer of the immobilized adsorbent. The thickness of the immobilized PANI would depend on the amount of PANI deposited on ZnO.

For adsorption experiments, the synthesized PANI and PANI/ZnO were added to methyl orange dye solution with concentration of 50 ppm. The chemical interaction of dye molecule with the PANI and PANI/ZnO provided the energy for chemical reaction between sulphonated dyes and charged backbone of PANI, leading to significant adsorption of the dyes. The solution was stirred for 1 hr. During this process, samples were collected from the reaction beaker at different time intervals, and the concentration of the dye was determined by UV-Vis absorption spectroscopy. The dye concentration was calibrated with the Beer-Lambert law at λ_{\max} . It was found that the polymer adsorbs the respective dye from the solution. After adsorption of the dye, the PANI and PANI/ZnO samples were washed with distilled water, dried and used for absorption spectroscopy [6]. **Fig. 2(a)** and **2(b)** shows the variation of the dye concentration with time in the presence pure PANI and PANI/ZnO. All experiments were carried out for 1 hr., but after 40 min there was no significant adsorption after this time. The experiments were conducted with different initial concentrations of methyl orange in the presence of PANI and PANI/ZnO for 1 hr. When the initial concentration of the dye was less, the dye was completely adsorbed in solution. At higher concentrations of the dye, it was not completely adsorbed, indicating that there is a saturation limit for the polymer above which it does not remove the dye [7].

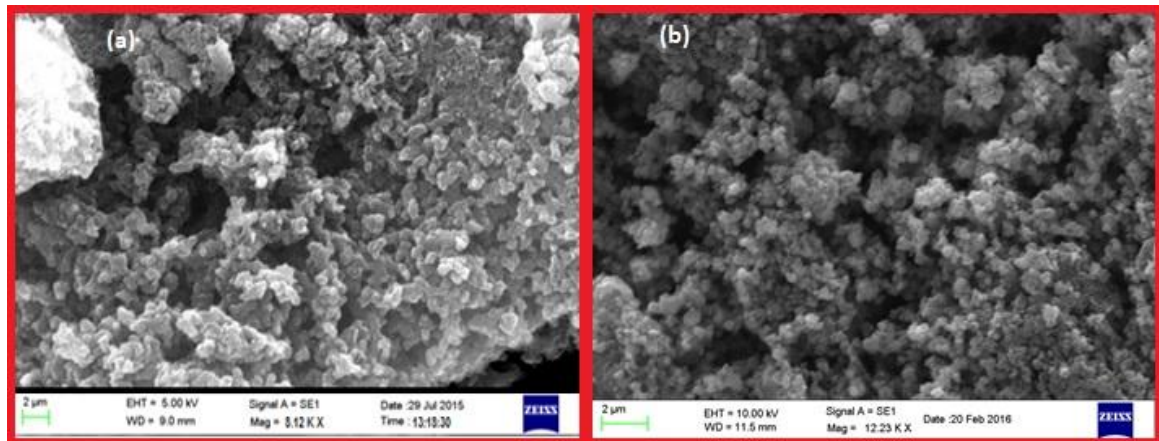


Fig. 1: SEM images of pure PANI and PANI-ZnO

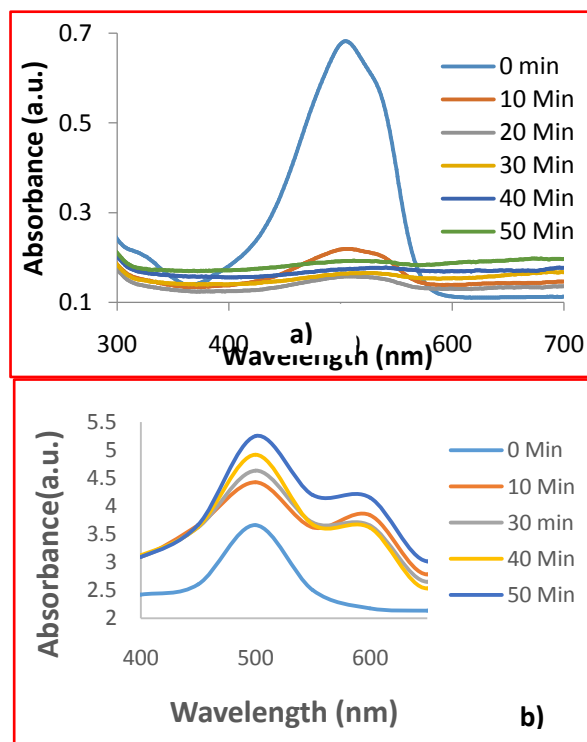


Fig. 2: Absorption spectra of PANI and PANI/ZnO in methyl orange dye of 50ppm

It is observed that adsorption amount increased in PANI/ZnO compared to that of pure PANI. The extent of MO dye adsorption onto PANI/ZnO composite is highly accessible as compared to pure PANI due to higher surface area and electronic interaction in PANI/ZnO composite. The binding sites of interactions available in PANI/ZnO composite would be larger hence more interactions with anionic dye MO occurred. Molecules containing π -electrons or non-bonding electrons (n-electrons) can absorb the energy in the form of ultraviolet or visible light to excite these

electrons to higher anti-bonding molecular orbital. The more easily excited the electrons (i.e. lower energy gap between the HOMO and the LUMO), the longer the wavelength of light it can absorb [8]. The characteristic peak of 507 nm assigned to the $n-\pi^*$ transition from the nonbonding nitrogen lone pair to the conduction band π^* . This peak shows high absorbance with the presence of methyl orange in the solution. With respect to time, the absorbance was found to be decreased. PANI-ZnO absorbed more methyl orange compared to that of pure PANI [9]. It is well known that the degree of ionization of a dye molecule depends on the pH of the aqueous medium. Methyl orange contains one sulfonated group ($-\text{SO}_3\text{Na}$). In acidic aqueous solutions, the functional group of methyl orange ($-\text{SO}_3\text{Na}$) gets ionized, and the dye exists in anionic form. **Fig 3** shows the percentage removal of the methyl orange with dye concentrations. It is obvious that it is higher for lower concentration and lower for higher concentrations. In order to find kinetic mechanism pseudo first order model, pseudo second order model were tested and the validity of the models verified. The pseudo-first-order rate equation is given by equation (1)

$$\text{Log}(Q_e - Q_t) = \text{log}Q_e - \frac{k}{2.303}t \quad (1)$$

Where Q_e and Q_t (mg g^{-1}) refer to the amount of dye adsorbed at equilibrium and time t (min), respectively, and k is the rate constant. **Fig. 4** shows the plot of the pseudo-first-order.

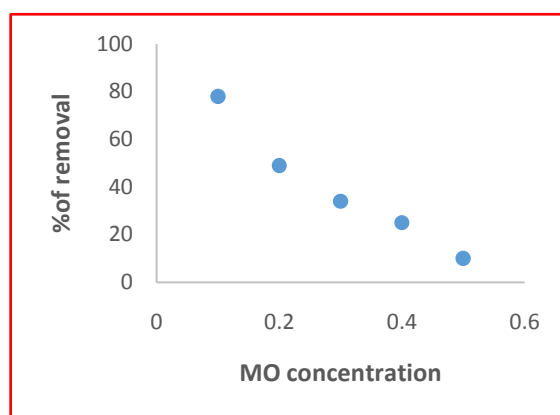


Fig. 3: % removal of dye

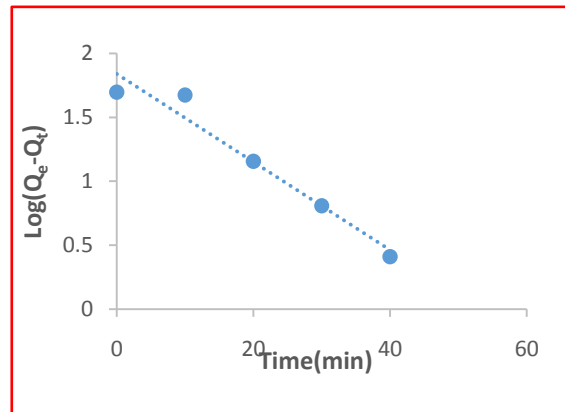


Fig. 4: Kinetic plot of MO adsorption onto PANI-ZnO composites (Pseudo first order reaction for 50mgL⁻¹)

The pseudo-second-order model can be represented by equation (2);

$$\frac{t}{Q_t} = \frac{1}{k_2} Q_e^2 + \frac{t}{Q_e} \quad (2)$$

Where, k_2 is the rate constant of the pseudo-second-order model. **Fig. 5** shows the curve-fitting plot of (t/Q_t) vs. time. The third model is an Intraparticle diffusion model. Weber and Morris stated that if Intraparticle diffusion is the rate-controlling factor, uptake of the adsorbate varies with the square root of time. The root time dependence is expressed by (3);

$$Q_t = k_i t^{1/2} + C \quad (3)$$

Where, k_i is an Intraparticle diffusion rate parameter. Figure 8 shows a plot of Q_t vs. $t^{1/2}$.

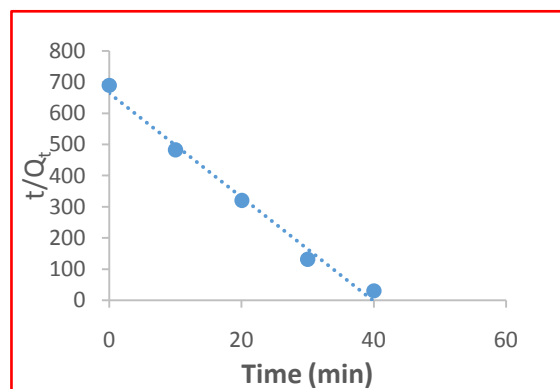


Fig. 5: Kinetic plot of MO adsorption onto PANI-ZnO (pseudo second order kinetic plot for dye concentration 50mgL⁻¹)

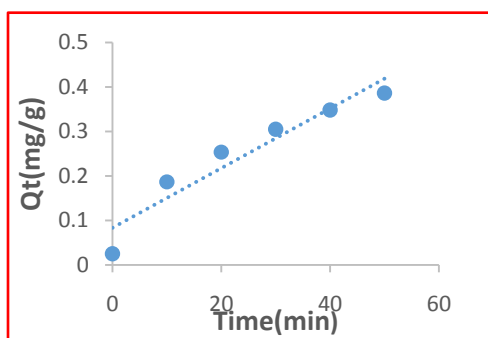


Fig. 6: Kinetic plot of MO adsorption onto PANI-ZnO (Intraparticle diffusion model for dye concentration 50mgL^{-1})

4. Conclusion

PANI/ZnO nanocomposites have been successfully prepared by in-situ polymerization. The adsorption of anionic sulfonated dye MO from aqueous solutions onto PANI/ZnO nanocomposite was studied. Percentage of removal of dye was studied comparatively for PANI and PANI/ZnO nanocomposites. It is concluded that the adsorption amount increased in the PANI/ZnO composites nearly about 79% which is much more than that of pure PANI, hence PANI/ZnO composite provides a more efficient adsorbent. The second-order kinetic model was found to be the best linearity compared to other models which indicate that it is physical adsorption.

References

1. Ozcan, A. S., Ozcan, A., *Journal of Colloid Interface and Science*, (2004), 276, 39–46.
2. Forgacs, E., Tibor, C., Gyula, O., *Environmental Monitoring*, (2004), 30, 953–971.
3. Annadurai, G., Chellapandian, M., Krishnan, M. R.V., *Environmental Monitoring* (1999), 59, 111–119.
4. Debajyoti, M., Giridhar, M., Radhakrishnan, S., Satish, P., *Journal of Physical Chemistry B*, (2009), 113, 2293–2299.
5. Mahanta, D., Giridhar, S., Madras, R., Patil, S., *Journal of Physical Chemistry B*, (2008), 112, 10153–10157.
6. Nerkar, N. V., Kargirwar, S. R., Kondawar, S. B., Burghate, D. V., Burghate, P. D., *International Symposium Ultrasonic*, (2015), 22(24), 195-198
7. Ayad, M., El-Nasr, A., *Journal Nanostructure Chemistry*, (2012), 3, 1-9.
8. Sharma, Y. C., Uma, S. N., Upadhyay, G. F., *Journal Applied Science and Environmental Sanitation*, (2009), 4, 21–24.
9. Kulkarni, M, Thakur, P, *Nepal Journal of Science and Technology*, (2014), 15(2), 105-110.

Synthesis and Photoluminescence of Tb³⁺ doped Sr₃Y₂ (BO₃)₄ Phosphor

M.Srinivas

Department of Physics, Osmania University, Hyderabad, 500007, India

*Corresponding author. E-mail: msrinivas.ou@gmail.com

ABSTRACT : Polycrystalline Sr₃Y₂(BO₃)₄ phosphor doped with Terbium ions (Tb³⁺) were synthesized by conventional solid state reaction method. These samples are characterized by X-ray techniques (XRD), energy dispersive spectroscopy (EDS) and photoluminescence (PL) respectively. Strong photoluminescence spectrum was obtained at 543 nm. Emission spectra can be assigned to the emission lines of Terbium activators corresponding to 490, 543, 588 and 622 nm attributed to the ⁵D₄→⁷F_J (J = 3, 4, 5, 6) transitions of Tb³⁺ ions observed under UV excitation spectrum. PL peak intensity was found to increase with increase in the dopant concentration. These phosphors may provide a new kind of luminescent material for light emitting diodes under uv excitation.

Keywords: Phosphor, XRD, EDS, Sr₃Y₂(BO₃)₄:Tb³⁺ and photoluminescence

1. Introduction

The study on luminescence properties of the rare earth elements hosted in numerous crystalline matrices such as oxides, silicates, aluminates, aluminoborates, aluminosilicates, nitrides, borates and inorganic materials are strongly interesting because of their potential application in solid-state lighting devices. [1]. Luminescence of several inorganic borate phosphors doped with rare earth ions, such as Eu⁺³, Ce⁺³, Tb⁺³ etc. have been studied. Owing to their simple and low-cost fabrication along with high thermal and chemical stability as well as transparency over a wide spectral range (beginning from UV and extending in to visible) borate hosts are considered as potential candidates for many optoelectronic applications [2]. The presence of sensitizer ions or activators, and the photoluminescence (PL) properties of the phosphor materials depend on the nature of host lattice, especially on the local geometry of the rare earth ion sites. Examples of these known borate phosphors are M₃Al₆B₈O₂₄:Ce³⁺ (M=Ca, Sr, Ba), YCa₃(AlO)₃(BO₃)₄:Eu³⁺, Sr₃Y₂(BO₃)₄:Eu³⁺, Na₂Y₂B₂O₇:Eu³⁺, Sr₂Mg(BO₃)₂:Ce³⁺ [3-6] have been reported in the

literature. The main aim of this work is to report the synthesis and photoluminescence (PL) of $\text{Sr}_3\text{Y}_2(\text{BO}_3)_4:\text{Tb}^{3+}$ phosphor.

2 Experimental

The phosphors $\text{Sr}_3(\text{Y}_{1-x}\text{Tb}_x)_2(\text{BO}_3)_4$ ($x = 0, 0.01, 0.03$ and 0.05) were synthesized by traditional solid-state reaction technique. The Stoichiometric amounts of starting materials are AR grade as SrCO_3 (99.99%), Y_2O_3 (99.99%), H_3BO_3 (99.9%) and Tb_2O_3 (99.99%), were mixed and then ground thoroughly in an agate mortar for 8 hours to give homogenous mixture. The resultant powders were initially dried at 80°C and then kept in an alumina boat inside a tubular furnace made up of alumina tube and slowly heated to 1300°C in air. These samples were kept at this temperature for 3 h and then annealed at 850°C for 1 hour in air. These samples were rapidly cooled down to room temperature and were grinded to get fine powder for further studies.

In order to characterize the phase purity and structure of the as-prepared $\text{Sr}_3\text{Y}_2(\text{BO}_3)_4:\text{Tb}^{3+}$ samples have been studied by X-ray powder diffraction (XRD). The Powder X-ray diffractograms were recorded on Philips X'pert Analytical X-ray diffractometer using Nickel filtered Cu-K α ($\lambda = 1.5406 \text{ \AA}$) radiation. The operation voltage and current of the instrument were maintained at 40 kV and 30 mA respectively. All the compositions of as prepared samples were confirmed by energy dispersive spectroscopy (EDS) using a HITACHI S-3700N equipment. The photoluminescence spectra were measured using Spectrofluorophotometer (Shimadzu, RF 5301 PC) with a 150 w a xenon arc lamp. All measurements were recorded at room temperature. All measurements were carried out at room temperature.

3 Results and discussion

3.1. Powder XRD

The X-ray diffractograms of $\text{Sr}_3(\text{Y}_{1-x}\text{Tb}_x)_2(\text{BO}_3)_4$, ($x = 0.01, 0.03$ and 0.05) are shown in Fig.1 it is conformed that all the samples are shown in single phase diffraction peaks match very well with the reported values [7,8,9], which can be assigned to orthorhombic structures.

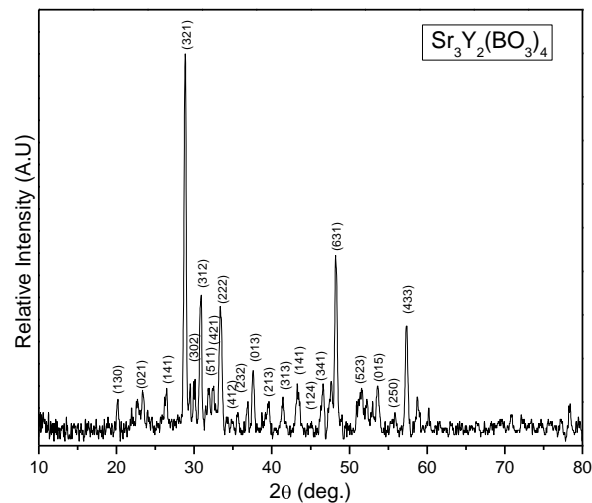


Fig 1 XRD of $\text{Sr}_3\text{Y}_{1.9}\text{Tb}_{0.1}(\text{BO}_3)_4$ phosphor

3. 2. EDS

The EDS spectrum of 0.1 mol % Tb^{3+} doped $\text{Sr}_3\text{Y}_2(\text{BO}_3)_4$ is shown in Fig.2. The results of the $\text{Sr}_3\text{Y}_2(\text{BO}_3)_4:\text{Tb}^{3+}$ samples show peaks corresponding to Sr, Y, Tb and O. The EDS pattern confirms the presence of terbium in the $\text{Sr}_3\text{Y}_2(\text{BO}_3)_4$ powders and its wt% is nearly equal to the doped value of Tb in $\text{Sr}_3\text{Y}_2(\text{BO}_3)_4$.

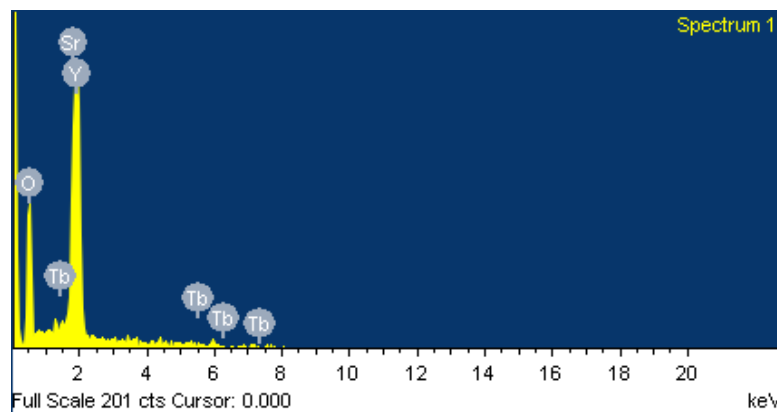


Fig.2 EDAX spectra of $\text{Sr}_3\text{Y}_2(\text{BO}_3)_4$ phosphor

3.3. Luminescence properties

The luminescence studies of Tb^{3+} activated $\text{Sr}_3\text{Y}_2(\text{BO}_3)_4$ phosphor which can efficiently emit under UV light excitation. The excitation and emission spectrum shown in figure 3(a) and (b)

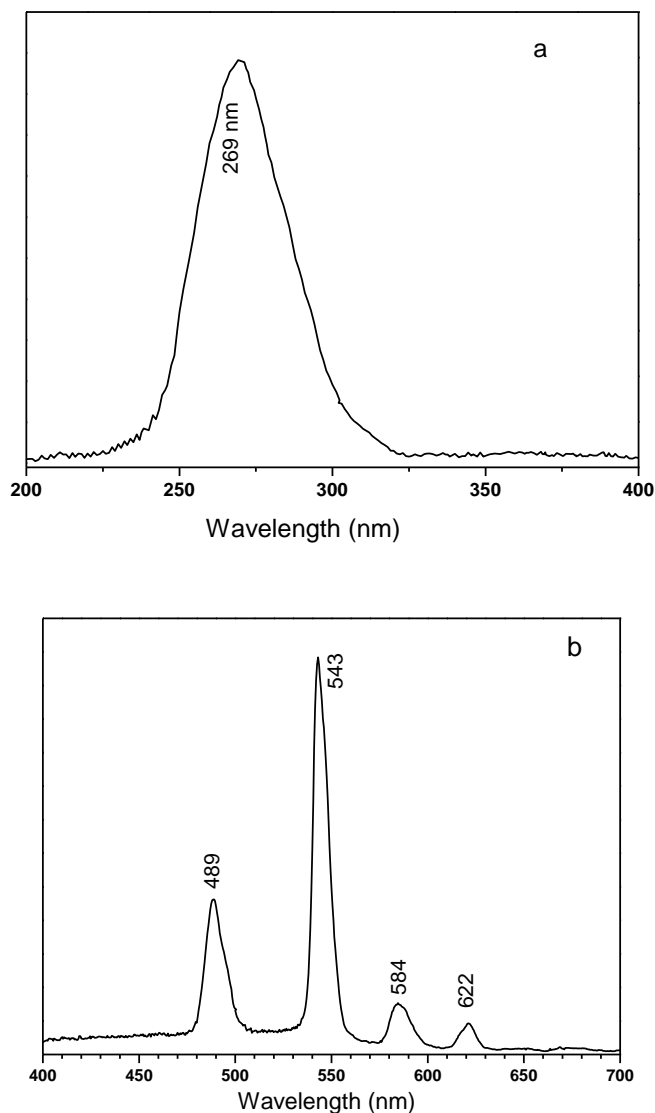


Fig.3 (a) Excitation and (b) Emission spectrum of $\text{Sr}_3\text{Y}_2(\text{BO}_3)_4:\text{Tb}^{3+}$ phosphor for 0.1 concentration

The emission spectrum of $\text{Sr}_3\text{Y}_2(\text{BO}_3)_4:\text{Tb}^{3+}$ phosphor recorded under the 269 nm excitation shown in fig.3. The emissions from Tb^{3+} ions confirm the presence of the RE ion into the cordierite matrices in the crystals. The sharp lines of Tb^{3+} ions were observed, which were attributed to the $^5\text{D}_4 \rightarrow ^7\text{F}_j$ ($J = 3, 4, 5$ and 6) transitions of Tb^{3+} ions and were situated at 490, 543, 588 and 622 nm, when the samples were excited with wavelengths 269 nm. Among the emission lines from the $^5\text{D}_4$ state the dominant emission is observed at 543 nm, corresponding to the $^5\text{D}_4 \rightarrow ^7\text{F}_j$ transition

of Tb^{3+} ions [8,9]. It is seen that the PL emission intensity are increased with the increase of dopant concentration.

4. Conclusions

$Sr_3Y_2(BO_3)_4$ were synthesized by conventional high temperature solid state reaction method and confirmed phase purity by XRD. The photoluminescence spectra indicate that the main emission peak at 543 nm under UV excitation due to $^5D_4 \rightarrow ^7F_5$ transition of Tb^{3+} ions. PL peak intensity was found to increase with increase in the dopant concentration. These phosphors may provide a new kind of luminescent material as green light emitting diodes under ultraviolet excitation.

Acknowledgements:

The author acknowledge to the UGC, New Delhi for awarding MRP scheme to carried out this work.

References

- [1] Bing Yan, Kun Zhou ,*J. Alloys. Compd.*,398 (2005) 165-169.
- [2] Allu AmarnathReddy, Subrata Das, Ashtosh Geol, Rupam Sen, Renee Siegel, *AIP Advance* 3,022126(2013).
- [3] T.R.N.Kutty, *Mater.Res.Bull.*, 1990, 25, 343.
- [4] L.Wang and Y.Wang, *Mater. Sci. Eng., B*, 2007, 139, 232.
- [5] Y.Zhang and Y.Li, *J.Alloys Compd.*, 2004, 384, 88.
- [6] H.Liang, H.Lin, G.Zhang, P.Dorenbos and Q.Su., *J.Lumin.*,2010
- [7] A.Boultif, D.Louer, *J App.Crystallogr.*24 (1991) 987.
- [8] Ling He, Yuhua Wang *J, Alloys. Compd.*, 431 (2007) 226-229.
- [9] Li Pan-Lai, Yang Zhi-ping,, WANG Zhi-jun, GUO Qing-lin,*Chinese Physics B*, 17(5) 2008.
- [10] R. G. DeLosh, T. Y. Tien, F. F. Gibbon, P. J. Zacmanidis and H. L. Stadler, *J. Chem. Phys.* 53, 681 (1970).
- [11] Lianhua Tian and Sun-il Mho, Byung-Yong Yu, Hong Lee Park, *J of the Korean Physical Society*, Vol. 47, No. 6, December 2005, pp. 1070

Highly Sensitive Hydrogen Gas Sensor Based on Polyaniline Coated SnO₂ Nanofibers

[#]Megha A. Salorkar, Hemlata J. Sharma, Subhash B. Kondawar*
Department of Physics, Rashtrasant Tukadoji Maharaj Nagpur University,
Nagpur – 440033, India

*Corresponding Author Email: sbkondawar@yahoo.co.in

[#]Presenting Author Email: megisalorkar@gmail.com

ABSTRACT

Tin oxide (SnO₂) nanofibers were synthesized by using polyvinylpyrrolidone (PVP) as template through electrospinning technique and subsequent calcination at 300 °C for 4 hr to decomposition organic PVP and formation of SnO₂ from its hydroxide form. SnO₂-Polyaniline (SnO₂/PANI) heterostructure sensors have been developed for sensing hydrogen gas at room temperature with high specificity. SnO₂/PANI heterostructure has been prepared and the heterostructures have been optimized by chemical deposition of PANI on nanofibers of SnO₂ (size ~200 nm). The as-grown films were studied for some of the useful physicochemical properties by X-ray diffraction (XRD), scanning electron microscopy (SEM), UV/visible absorption spectroscopy (UV–vis) and Energy Dispersive X-ray spectroscopy (EDX). SEM micrograph revealed that pure SnO₂ nanofibers were ~200 nm and when PANI was coated then diameter increased to ~500 nm due to the micellar templates of PANI around them. XRD studies showed peak broadening and the peak positions shift from standard values, indicating the interaction of tin oxide nanoparticles with polyaniline. Optical absorbance spectra showed shifting of the characteristics peaks for PANI, which may be due to presence of tin oxide in PANI matrix. SnO₂/PANI composite sensor exhibited good sensitivity and much higher response magnitude towards H₂ gas. Space charge modulation occurring at various interfaces such as SnO₂/PANI interface and boundaries between the SnO₂ nanograins explains the high toxic gas sensitivity observed for the SnO₂/PANI heterostructured nanofibres sensor.

Keywords: Nanofibers; Polyaniline-SnO₂; Nanocomposites; Electrospinning; Gas Sensing.

1. Introduction

In recent years, gas sensors have seen fast development worldwide due to their wide applications in a large variety of fields such as environmental monitoring and protection, modern industrial and agricultural production, national defence, anti-terrorism and even disease diagnosis. Among the huge number of gas sensing materials investigated, SnO₂, which is a typical metal-oxide semiconductor, has received much attention owing to its fascinating gas sensing properties including highly sensitive and fast detection of a broad spectrum of species, such as H₂S, H₂, C₂H₅OH, CO, NH₃, volatile organic compounds, etc. However, hydrogen is colourless, odourless, and extremely flammable gas due to which there have been significant efforts to enhance the sensitivity of hydrogen sensors to be operated at low temperature [1]. By now, a great deal of work on H₂ sensors has been reported. Despite the great success of SnO₂ based gas sensors in both scientific research and practical applications, they generally have to work at high temperatures, which bring about the problems such as high power consumption and reduced working life. Additionally, their sensitivity and selectivity need further improvement. Moreover, greater efforts have been devoted to the nanocomposites of SnO₂ with conducting polymers, including polyaniline (PANI), since the nanocomposites are easy to prepare and could show much improved gas sensing characteristics than the constituent components at room temperature [2]. Electrospinning (ES) is a versatile method for the preparation of one-dimensional (1D) nanomaterials such as polymers, inorganic materials, or the composites. The preparation of nanostructured SnO₂ by ES generally involves high temperature calcination of electrospun nanofibers containing the precursor of tin salt for the removal of the polymer template and the conversion of the precursor to SnO₂. Moreover, the sensors based on nanocomposites of SnO₂ with conducting polymers are generally prepared by depositing nanostructured SnO₂ or the nanocomposite dispersions onto the substrates by dropping, dip coating or screen printing. In this work, a high-efficiency hydrogen sensor based on polyaniline-SnO₂ composite nanofibers has been demonstrated via electrospinning technique and calcination procedure [3].

2. Experimental

Materials

$\text{SnCl}_2 \cdot 2\text{H}_2\text{O}$, Aniline monomer (distilled under reduced pressure), ammonium peroxydisulphate (APS) and Polyvinyl pyrrolidone (PVP, $M_w=1,300,000$) were purchased from Aldrich. All supplement chemicals were of AR grade and used as received.

Preparation of SnO_2 nanofibers and SnO_2/PANI composite nanofibers

In a typical procedure, 0.4 g of $\text{SnCl}_2 \cdot 2\text{H}_2\text{O}$ was dissolved in 4.4 g of DMF and 4.4 g of ethanol under vigorous stirring for 10 min. Subsequently, 1.0 g PVP was added into the above solution under vigorous stirring for 30 min. The mixture was loaded into a glass syringe with a needle of 0.5 mm in diameter at the tip and was electrified using a high-voltage DC supply. Calcination (300°C in air for 4 h) was performed to remove the organic constituents of PVP and crystallize the SnO_2 . Electrospinning apparatus consists of a syringe pump, DC high voltage source and rotating or stationary collector. The spinning solution was kept in a vertical syringe with a stainless steel needle having an orifice of 0.5mm. The needle was electrically connected to a positive high voltage. 17 kV was provided between the tip of the spinning nozzle and the collector at a distance of 20 cm and the solution flow rate was kept at 0.4ml/h was maintained using computer control programmer. Thus, the nanofibers were prepared successfully. The SnO_2/PANI composite nanofibers were prepared by dipping SnO_2 nanofibers as substrate during chemical oxidative polymerization of 0.5 M aniline using 0.2 M camphor sulphonic acid (CSA) as a dopant and 0.2 M ammonium peroxodisulphate (APS) as an oxidizing agent.

3. Results and discussion

Fig. 1 shows the XRD pattern of composite nanofibers. All the strong diffraction peaks of SnO_2 present in composite can be perfectly indexed as the tetragonal rutile structure for SnO_2 (ICDD DATA CARD (41-1445) [4, 5]. The main dominant peaks of polyaniline- SnO_2 were identified at $2\theta = 26.66^\circ$ and 52.3° , which corresponding to the indices (1 1 0) and (2 1 1). The average diameter of composite nanofibers was found to be around 300 nm as conformed from SEM image (**Fig. 2**).

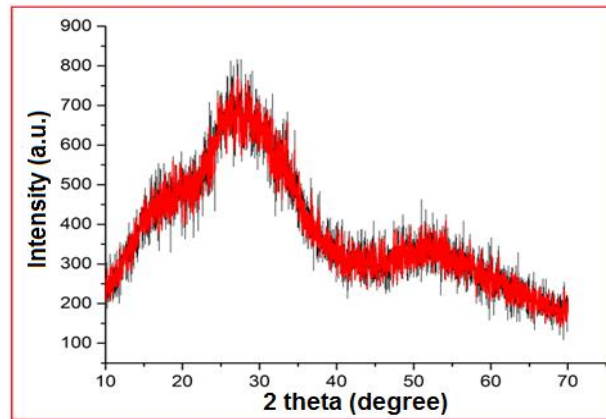


Fig. 1: XRD pattern of polyaniline-SnO₂ composite nanofibers

From SEM micrograph, it is revealed that diameter of as-synthesized SnO₂/PANI composite nanofibers increased due to encapsulation of PANI over SnO₂ nanofibers. Morphologically, composite nanofibers showed highly porous structure which favors SnO₂/PANI composite nanofibers for better sensing properties. EDX has been used to investigate the elemental compositions of composite nanofibers showing the presence of Sn, O, C, and N as illustrated in **Fig. 3**.

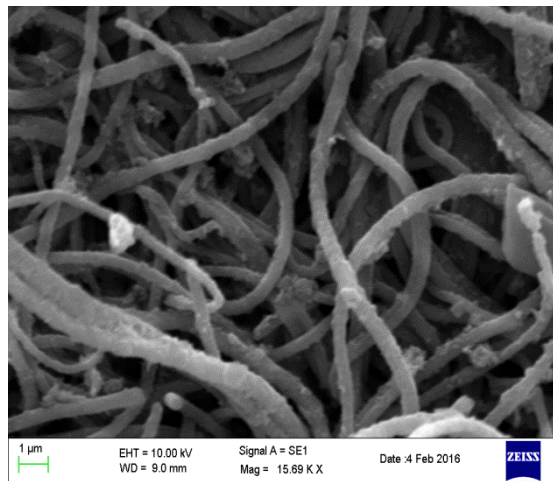


Fig. 2: SEM image of PANI-SnO₂ nanofibers

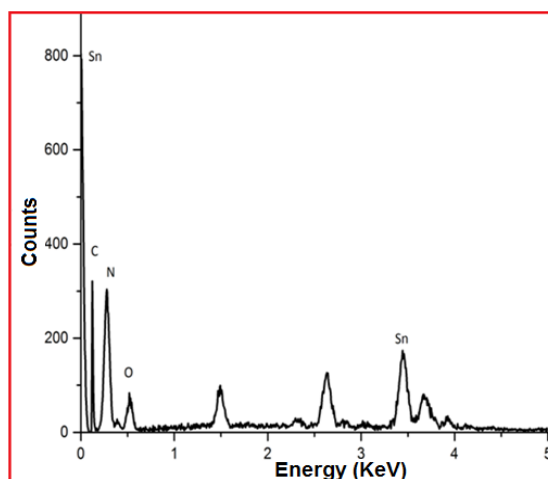


Fig.3: EDX spectrum of PANI-SnO₂ nanofibers

Hydrogen sensing mechanism

On exposure to H₂ gas, the composite film resistance changes from its original value, indicating that the electrical resistance of Polyaniline-SnO₂ composite film is a sensitive parameter in the presence of gas analyte. In presence of SnO₂ crystallites, the PANI matrix gets a modified structure electronically. On exposing the composite film with hydrogen (which can be permeated into the PANI matrix freely), some of the gas analyte molecules might reach into the depletion region, which is surrounding the SnO₂ crystallite and act as a dielectric between the PANI and SnO₂ border. The depletion region field might polarize the hydrogen molecules, and in turn provide a positive charge to PANI molecules, which can become mobile on its transfer to the central N atom of PANI molecule. This process creates some free holes on PANI molecules, which increase the hopping conductivity of the film, and therefore make the composite film relatively more conducting electrically.

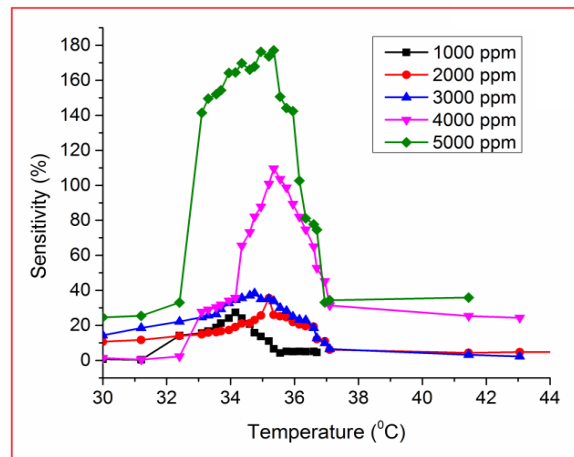


Fig.4: Sensitivity of PANI-SnO₂ nanofibers

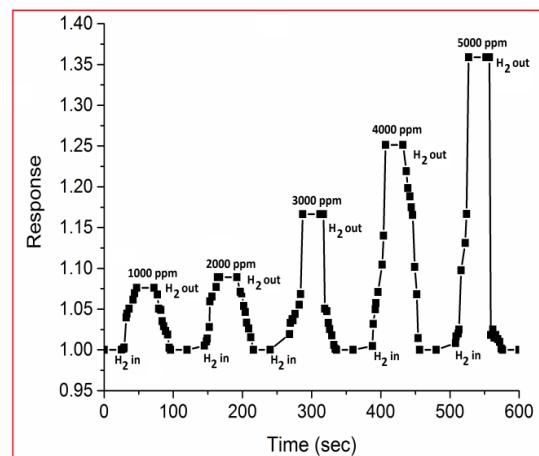


Fig.5: Response-Recovery of PANI-SnO₂ nanofibers

The Polyaniline-SnO₂ composite nanofibers showed a very high sensitivity to H₂ gas at room temperature and as the concentration of gas increases then sensitivity increases rapidly, as shown in **Fig. 4**. Sensitivity factor was monitored in terms of the % sensitivity calculated by $\% \text{ sensitivity} = \Delta R/R_0$. Where ΔR is the variation in resistance of composite films from baseline after exposure to gas analyte, R_g is the resistance of the sensor in presence of H₂ gas and R_0 is the initial baseline resistance of the sensor. **Fig. 5** shows the Response-Recovery Time graph for 1000-5000 ppm of H₂ gas at 35°C [6-9]. From literature survey available in this regard, there is no appreciable change noticed in the nanofibers film resistance for the case of pure SnO₂, on exposure to different concentrations of H₂ gas and films remained insensitive to this gas near to room temperature. However, SnO₂/Polyaniline

composite nanofibers film showed appreciable sensitivity for 1000 ppm of H₂ gas. The sensitivity of composite nanofibers was found to be increased and reached its maximum around 35 °C for H₂ gas.

4. Conclusion

The nanofibers of polyaniline-SnO₂ composite were successfully fabricated using electrospinning technique. Presence of SnO₂ crystallites in the polyaniline-SnO₂ composite nanofibers drastically influenced the electronic property of PANI matrix. XRD study shows the interaction of SnO₂ nanoparticles with PANI. SEM image revealed the formation of fibers of average diameter in nanoscale regime (≤ 300 nm). The Polyaniline-SnO₂ composite nanofibers showed good sensitivity and response to H₂ gas at room temperature.

References

1. Rad, A. S., Nasimi, N., Jafari, M., Shabestari, D. S. and Gerami, E. *Sensors and Actuators B: Chemical*, (2015), 220 (1), 641–651.
2. Deshpande, N.G., Gudage, Y.G., Sharma, R., Vyas, J.C., Kim, J.B. and Lee, Y.P. *Sensors and Actuators B*, (2009), 138 (1), 76–84.
3. Sharma, H.J., Jamkar, D.V. and Kondawar, S.B. *Procedia Materials Science*, (2015), 10, 186 – 194.
4. Sharma, H.J., Sonwane, N.D. and Kondawar, S.B. *Fibers and Polymers*, (2015), 16(7), 1527-1532.
5. Kim, B.J., Oh, S.G., Han, M.G. and Im, S.S. *Synthetic Metals*, (2001), 122 (2), 297–304.
6. MacDiarmid, A.G. and A.J. Epstein. *Synthetic Metals*, (1994), 65(2-3), 103–116.
7. Monredon, S., Cellot, A., Ribot, F., Sanchez, C., Armelao, L., Gueneau, L. and Delattre, L., *Journal Materials Chemistry*, (2002), 12(8), 2396–2400.
8. Chang, S.J., Hsueh, T.J., Chen, I.C., Hsieh, S.F., Chang, S.P., Hsu, C.L., Lin, Y.R. and Huang, B.R. *IEEE Transactions on Nanotechnology*, (2008), 7(6), 754-759.
9. Zhang, H.N., Li, Z.Y., Liu, L., Wang, C., Wei, Y. and MacDiarmid, A., *Talanta*, (2009), 79 (3), 953-958.

Preparation and Characterization of Cadmium substituted Cobalt Nano ferrites by citrate-gel auto combustion method

Nehru boda¹, Gopal boda², Abdul Gaffoor, D. Ravinder^{1*}, A. Panasa Reddy^{2*}.

1. Department of physics, Osmania university, Hyderabad, , 500007, Telangana, India.

2. Department of chemistry, college of Engineering, Osmania university, Hyderabad, 500007, Telangana, India.

*Correspondence Author; D. Ravinder; email: ravindergupta28@rediffmail.com

ABSTRACT: Co-Cd Nano Ferrites with chemical formula $\text{Co}_{1-x}\text{Cd}_x\text{Fe}_2\text{O}_4$ ($x=0.1, 0.2, 0.3, 0.4, 0.5, 0.6$) were synthesized by the citrate-gel auto combustion method. Synthesized powders were sintered at 500°C for four hours in air and characterized by XRD, FTIR. XRD analysis showed cubic spinel structure of the ferrites and the values of lattice parameter (a) and X-ray density (dx) increased with the increase of Cd content. The FTIR spectra shows the two significant absorption bands in the wave numbers range of $400\text{-}600\text{cm}^{-1}$ arising due to the inter-atomic vibrations in the tetrahedral and octahedral coordination compounds. The observed results can be explained on the basis of composition.

KEY WORDS:- Co-Cd Nano ferrites, citrate-gel auto combustion Technique, XRD, FTIR.

Introduction:

The study of nano ferrites has interested to attention of the scientific and technological advances. The ability to prepare nano structures with defined morphologies and sizes in large scale is an essential requirement for applications in nano materials.

Spinel ferrites have been studied extensively because they play a vital role in the technological application. Ferrites have good electric and magnetic properties and a large number of applications

The interest in ferrites nanoparticles is due to their important physical chemical properties and potential for various technological applications such as high capability data storage, electric and microwave devices, sensors, magnetically guided drug delivery etc.

These are of tremendous academic interest as these are considered as potential tools for developing our understanding about the fundamentals of nano magnetism [1]. Among these, spinel ferrites having the general formula MFe_2O_4 , Properties of ferrites are highly sensitive to the substitution of different metal ions in its tetrahedral and octahedral sites [2].

The properties of ferrites are dependent on several factors, chemical composition, method of preparation, grain size, sintering temperature and atmosphere [3]. Various chemical technique have been used the synthesis of spinel ferrites [4] several researchers have reported the synthesis of Co-Cd ferrites using different techniques like co-precipitation method [5], ceramic method [6], combustion method [7]. so in the present work we reported the results of synthesis and structural and morphology of Co-Cd ferrites by Citrate Gel Auto Combustion method

2. Experimental Details:

The Cobalt- Cadmium nano ferrites having the chemical formula $Cd_x Co_{1-x}Fe_2O_4$ were synthesized by citrate gel auto combustion method using the below raw materials.

2.1 Raw Materials:

Cadmium Nitrate- 99% pure (AR Grade) ($CdNO_3$), Cobalt Nitrate- 99% Pure(AR Grade) ($CoNO_3$)

Ferric Nitrate-99%pure(AR Grade) ($Fe(NO_3)_3 \cdot 9H_2O$), Citric acid-99.5% Pure (AR Grade) ($C_6H_8O_7 \cdot H_2O$).

Ammonia solution-99% Pure (AR Grade) (NH_3).

2.2 The flow chart of the synthesis of Co- Cd nano ferrites:

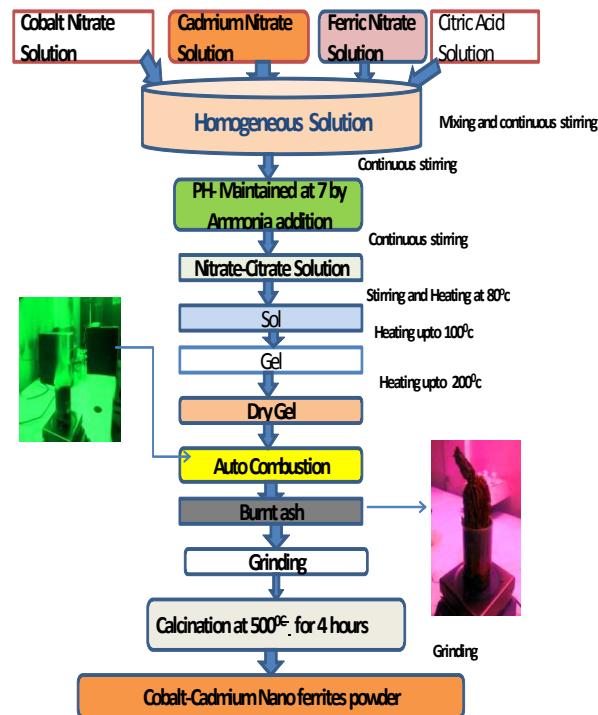


Fig (1): The flow chart of synthesis

The calculated quantities of metal nitrates were dissolved in minimum amount of distilled water to get clear homogeneous solution. An aqueous solution of citric acid was added to the metal nitrate solution. The molar ratio of citric acid to the total moles of nitrate ions was adjusted to 1:1. The flow chart shown in fig; (1)

2.3 Structural Characterization by XRD:

The structural characterization was done by X-Ray Diffractometer Philips x-pert pro system with diffracted monochromatic beam with Cu-K α radiation of wavelength (1.5405Å⁰). The diffraction pattern of Co-Cd between the Bragg Angles 10° to 80° in the steps of 0.04°/sec. nano ferrites particles Were shown in fig.

The crystalline size was calculated for the sample using the high intensity 311 peak and using Debay Scherrer formula [8] while taking into account the intensity broadening [9].

$$\text{Crystalline size of the sample } D = \frac{0.91\lambda}{\beta \cos \theta}$$

Where λ the wavelength of X-ray is used [10]. β is the width of diffraction peak i.e. full width Half Maximum(FWHM) , θ is the peak position .

Lattice parameter (a) of the sample was calculated by the formula. $a = d * \sqrt{h^2 + k^2 + l^2}$ [11] Where a=Lattice constant, (h k l) are the Miller indices, d is the inter planner space

The X-ray density of the prepared sample was calculated using

the relation $\rho_x = \frac{8M}{a^3N}$ (g/cm³) [12] where **M**= molecular weight of the sample, **a**

is the lattice parameter and **N** is the Avogadro number.

The Volume of the Unit cell $V=a^3$

The distance between the magnetic ions (hopping length) on A-site(Tetrahedral) and B site (Octahedral) is calculated according to the following relations

$$d_A = 0.25a\sqrt{3} \quad \text{and} \quad d_B = 0.25a\sqrt{2} \quad [13]$$

3. Result and Discussion;-

3.1. XRD Analysis:

A phase analysis using X-ray diffraction technique was performed to confirm the formation of single-phase cubic spinel structure as shown in **fig-(2)** . With no extra lines corresponding to any other crystallographic phase. The results obtained from XRD pattern for all the samples of $Cd_xCo_{1-x}Fe_2O_4$ with the (hkl) values corresponding to the diffraction peaks of different planes (220), (311), (400), (422), (511), and (440) are spinel cubic phase

The calculated values of crystalline size for the different compositions are given in the table (1).

It can be seen from the table that the values of the crystal size varies from 11nm to 17nm of the various Cd concentrations

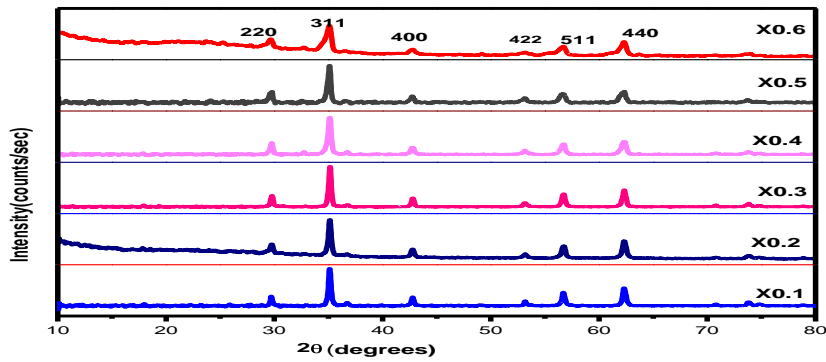


Fig (2): XRD pattern of Co-Cd Nano ferrites

The lattice parameter values of all the composition of Cadmium doped Cobalt ferrites have been calculated from the d- spacing and are given in the above table. A plot is drawn between the lattice parameter vs Cadmium composition is shown in **fig (3)**.

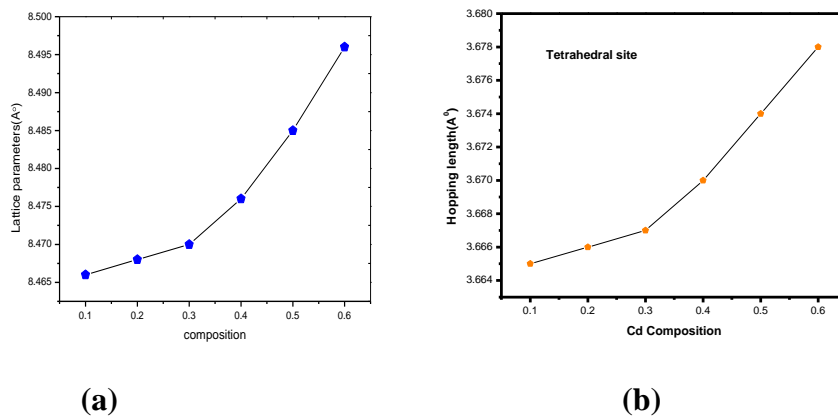
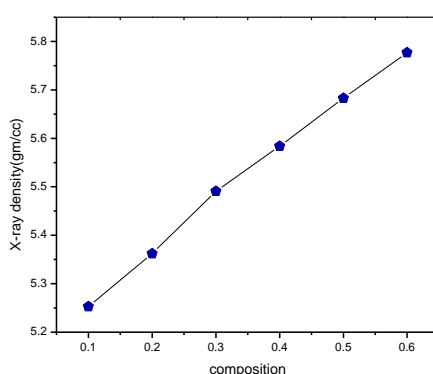


Fig (3): a. Variation of lattice constant vs Cd composition 3.b. Variation of hopping length vs Cd composition

Ferrite composition	Lattice Constant (Å)	Crystalline Size(nm)	Volume (Å ³)	Hoping length A-site(d _A)	Hoping length B-site(d _B)
$Cd_{0.1}Co_{0.9}Fe_2O_4$	8.466	11.12	606.784	3.665	2.992
$Cd_{0.2}Co_{0.8}Fe_2O_4$	8.468	14	607.215	3.666	2.993
$Cd_{0.3}Co_{0.7}Fe_2O_4$	8.470	14.62	607.645	3.667	2.994
$Cd_{0.4}Co_{0.6}Fe_2O_4$	8.476	14.62	608.937	3.670	2.996
$Cd_{0.5}Co_{0.5}Fe_2O_4$	8.485	14.62	610.879	3.674	2.999
$Cd_{0.6}Co_{0.4}Fe_2O_4$	8.496	17.82	613.258	3.678	3.003

Figure (3) variation of lattice constant with Cd^{2+} content in $\text{Co}_{1-x}\text{Cd}_x\text{Fe}_2\text{O}_4$ ($x=0.1, 0.2, 0.3, 0.4, 0.5, 0.6$), is observed that the Lattice parameter increases with increase in Cd content. This is attributed to replacement of smaller ionic radii $\text{Co}(0.78\text{\AA})$ by larger ionic radii $\text{Cd}^{2+}(0.99\text{\AA})$ ions. This linear variation indicates that the Co-Cd ferrite system obeys Vegard's law [14]



Fig(4): X-ray density vs Cd concentration

The **figure (4)** shows the X-ray density (ρ_x) vs Cd concentration, The X-ray density (ρ_x) is depend on the lattice parameter and molecular weight of the sample. From the table one can observe that molecular weight of the sample is increases with Cadmium concentration and lattice parameter is also increases with the increase of Cd compositions. This may due to the grater atomic weight of Cd-112.411gm/mol and lesser atomic weight of Co-55.845gm/mol(15) shown in below figure

SNO	Ferrite composition	X-ray Density(gm/cc)	$\vartheta_1(\text{cm}^{-1})$	$\vartheta_2(\text{cm}^{-1})$
01	$\text{Cd}_{0.1}\text{Co}_{0.9}\text{Fe}_2\text{O}_4$	5.253	576.73	410.85
02	$\text{Cd}_{0.2}\text{Co}_{0.8}\text{Fe}_2\text{O}_4$	5.362	580.59	412.78
03	$\text{Cd}_{0.3}\text{Co}_{0.7}\text{Fe}_2\text{O}_4$	5.491	582.52	418.56
04	$\text{Cd}_{0.4}\text{Co}_{0.6}\text{Fe}_2\text{O}_4$	5.584	576.73	418.57
05	$\text{Cd}_{0.5}\text{Co}_{0.5}\text{Fe}_2\text{O}_4$	5.683	570.94	418.56
06	$\text{Cd}_{0.6}\text{Co}_{0.4}\text{Fe}_2\text{O}_4$	5.777	574.80	418.57

FTIR Spectral analysis

Fig.(5) shows FTIR spectra of the ferrite samples in the range of wave numbers from 350 to 650 cm^{-1} . The two absorption bands Observed at 582 cm^{-1} (ϑ_1) and 410 cm^{-1} (ϑ_2) corresponds to vibrations of tetrahedral and octahedral complexes

respectively, and According to Waldron which confirms the formation of single phase cubic spinel structure of ferrites [16, 17]. From the figures it is to be noted that the shifting of band position (600 cm^{-1}) ϑ_1 towards lower wavelength region is due to the increase of Cd^{2+} ion in ferrite And preferably occupies the tetrahedral (A-site) [18, 19]. However, Co^{2+} ions occupy the octahedral(B-site) [20],

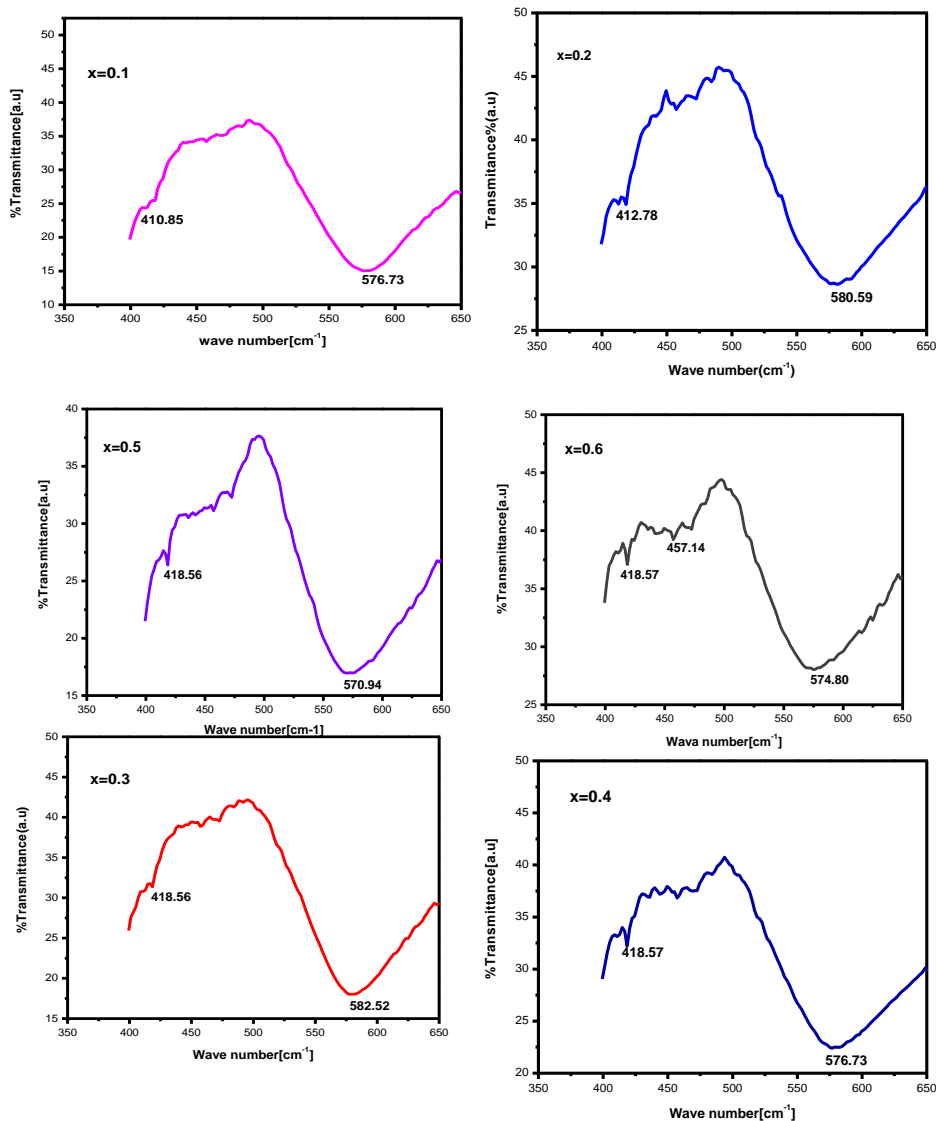


Fig.5.FTIR absorption spectra of the $\text{Cd}_x \text{Co}_{1-x} \text{Fe}_2 \text{O}_4$ ferrite samples

But Fe^{3+} ions occupy both tetrahedral and octahedral sites. Substitution of Cd^{2+} ion in the system decreases the amount of Co^{+2} and increases the amount of Cd^{+2} ions in the octahedral B-site and shifts band position at (410 cm^{-1}) ϑ_2 towards lower wavelength.

4. Conclusion:

- Citrate Gel Auto Combustion technique is a convenient way for obtaining a homogeneous nano sized mixed ferrites, it is very simple and economical method where no specific heating or cooling rate is required.
- X-ray diffraction pattern confirms the formation of single phase cubic spinel structure. From standard data JCPDS.
- The crystalline size of the various Co-Cd ferrites was in the range of 11 to 17 nm.
- The Lattice parameter has increased with the increase of Cd concentration in Co-Cd ferrites which indicate that the mixed Co-Cd ferrite system obey the Vegard's law
- The FTIR spectra of the ferrite samples in the range of wave numbers from 350 to 650 cm^{-1} .
- The two absorption bands observed at 582 cm^{-1} (ν_1) and 410 cm^{-1} (ν_2) corresponds to vibrations of tetrahedral and octahedral complexes respectively

5. Acknowledgements:

The authors are very grateful to **Prof. D. Suresh Babu**, Head, Department of physics, and **Prof. J. Shiva Kumar**, Chairmen Board of studies in physics, University college of science Osmania University Hyderabad, One of the author Nehru Boda is very thankful to **UGC, BSR-section** New Delhi, for their financial assistance.

References:

- [1] y. Qi, Y. Yang, X. Liu, P. Wu, Particuology 8(2010) 207-211.
- [2] Y. Koseoglu, F. Gozuak, A. Baykal, H. Kavas, Structural and magnetic properties of $\text{Co}_x\text{Zn}_{1-x}\text{Fe}_2\text{O}_4$ nanoparticles synthesized by microwave method, Polyhedron 28(2009)2887–2892.
- [3] K.Kondo, T. Chiba, S. Yamada, Journal of Magnetism and Magnetic Materials **541**, 254(2003)

- [4] P.K.Roy and J.Bera, *J Magn Magn mater* 298,38,(2006)
- [5] ch. Venkata Reddy, chan Byon, B. Narender, D. Basker, G.Srinivas,Jaesool shim, S. V. Prabhakar *Vattikuti* 82(2015) 165-173.
- [6] S.E. Jacobo, s,Duhalde and H.R.Bertorello “ Rare earth influence on the structural and magnetic proper ties of Ni-Zn Ferrites” *J of Mag and Mag Matrels* Vol 272-276 N0 3, 2004pp 2254Doi:10.1016/j.jmmm.2003.12.564
- [7] S.A.Morrison, C.L.Cahill, E.E.Carpenter,S.Calvin, R.Swaminnathon, M.E.McHenryand V G Harris *Magnetic And Structrural Properties of Ni-Zn Ferrite nano particles synthesised by At room temperature*J of Applied physics, Vol95,no 11 2004, pp.6392-6395doi 10.1063/1.171513
- [8] Cullity B D, *Elements of X-ray diffraction* (addition Wesley, Reading, Mass), 1959. P132.
- [9] Mahmud ST, Akther Hossain AKM, Abdul Hakim AKM, Seki M, Kawai T. Tabata H (2006) *j Magn Mater* 305;269 doi; 1016/j.jmmm.2006.01.012.
- [10] B.D. Cullity, *Elements of X-ray diffraction*, Wesely Pub, Co., Massachusetts, 1987,101- 356
- [11] B.P.Ladgaonkar, P.P.Bakare,S.R. Sainkar and A.S.Vaingankar, “Influence of Nd⁺³ substitution on permeability spectrum of Zn-Mg ferrite”. *Materials Chemistry and Physics*, Volume 69,Issues 1-3,March 1, 2001, pages 19-24.
- [12] B. Vishvanathan, V. R.K. Murthy, *Ferrite Materials Science and Technology*, narosa Public House, New Delhi(1990).
- [13] R.C.Kumbale. P.A.Shaikh, S.S. Kamble,Y.D.Kolekar *J.Alloys Comp.*, 478(2009), p.599 doi:10.1016/j.jmmm.2005.03.007
- [14] L. Vegard, “The Constitution of Mixed Crystals and the Space Occupied by Atoms,” *Zeitsch rift fir Physics*, Vol. 5, No. 17, 1921, pp.17-23
- [15] K.B.Modi, J.D.Gajera, M.P.Pandya,H.G.Vora, H.H.Joshi, *Pramana Journal of Physics*, Vol 62, No 5,May, 2004, pages 1173-1180

- [16] B.P. Ladgaonkar, C.B. Kolekar, A.S. Vaingankar, Bull. Mater. Sci. 25 (4) (2002)351.
- [17] R.D. Waldron, Phys. Rev. 99 (1955) 1727
- [18] S.A. Patil, V.C. Mahajan, A.K. Gatge, S.D. Lotake, Mater. Chem. Phys. 57 (1998)86.
- [19] O.M. Hemeda, M.M. Barakat, J. Magn. Magn. Mater. 223 (2001) 127.
- [20] G.K. Joshi, A.Y. Khot, S.R. Savant, Solid State Commun. 65 (1988) 1593.

Electrochemical Performance of Polyaniline/Nickel Ferrite/Carbon Nanotubes Ternary Nanocomposites

[#]Pooja A. Zingare, Zeenat Parveen, Subhash B. Kondawar*

Department of Physics, Rashtrasant Tukadoji Maharaj Nagpur University, Nagpur – 440033, India

*Corresponding Author Email: sbkondawar@yahoo.co.in

[#]Presenting Author Email: pooz11071994@gmail.com

ABSTRACT

The synthesis process of polyaniline/nickel ferrite/carbon nanotubes (PANI/NiFe₂O₄/CNT) nanocomposite electrodes via simplest in-situ oxidative chemical polymerization is reported. Nanocrystalline NiFe₂O₄ was prepared by simple approach of co-precipitation method. The morphology and chemical structure of PANI/NiFe₂O₄/CNT was characterized by means of scanning electron microscopy (SEM), energy dispersive X-ray spectroscopy (EDX), Fourier transform infrared (FTIR) and X-ray diffraction (XRD) analysis. The electrochemical performance of as-synthesized PANI/NiFe₂O₄/CNT electrode was studied by cyclic voltammetry (CV) in an aqueous solution at different scan rate using three electrodes electrochemical cell. The CV curve of PANI/NiFe₂O₄/CNT electrode compared with that of the PANI/NiFe₂O₄ and PANI/CNT binary nanocomposites. The improved electrochemical performance of PANI/NiFe₂O₄/CNT film is due to interaction between carbon nanotubes, NiFe₂O₄ nanoparticles and conducting polymers because the nitrogen atoms of polymers can bond to the metal ions of NiFe₂O₄ through their lone pairs and encapsulates the carbon nanotubes. Due to the synergistic effect of pseudo capacitance generated by polyaniline, nickel ferrite and electric double layer capacitance generated by carbon nanotubes at the interface between electrode and electrolyte, the specific capacitance of the ternary nanocomposite was found to be increased compared to that of binary nanocomposites. This improvement in electrochemical performance suggests that PANI/NiFe₂O₄/CNT electrodes are promising for the next generation high performance electrochemical capacitors.

Keywords: Nanocomposites, Nickel ferrite, Polyaniline, Carbon nanotubes, Cyclic voltammetry.

1. Introduction

The flexible and environmentally friendly energy storage devices have attracted much attention for sustainable energy and portable electronics. As intermediate systems between batteries and traditional dielectric capacitors, supercapacitors exhibit the desirable properties, e.g. high power density, high specific capacitance, long cycle life (>100,000 cycles), and rapid charging/discharging rates, thus they are probably one of the most important next-generation energy storage devices [1, 2]. According to the energy storage mechanism, supercapacitors are generally classified into electrochemical double layer capacitors (EDLC), using carbon-active materials (CNT, graphene) based on the surface area of the electrode materials, and pseudocapacitors, using redox-active materials based on the fast and reversible Faradic reactions. The specific capacitance just from the electrical charges at the electrode-electrolyte interface of EDLC is lower than pseudocapacitance based on conducting polymers and transition metal oxides. While poor cycle ability due to structural degradation through the redox process limits the applications of pseudocapacitors [3]. Combining the advantages of EDLC and pseudocapacitors has attracted vast interests due to the synergistic effect. On the basis of this point, it is apparent that the electrochemical performances can be enhanced by incorporating carbon materials with pseudocapacitive materials. However, the electrochemical properties of electrodes play a crucial role in determining the performance of supercapacitors. To overcome this obstacle, most of recent studies are urgent to develop excellent electrode materials for supercapacitors. It is well known that transition metal oxides possess multiple oxidation states/structures that enable rich redox reactions for pseudocapacitance generation [4]. But, simple metal oxides exhibit low specific capacitance, particularly at higher charge/ discharge rates. Therefore, it is of great interest to design complex metal oxide-based systems having high specific capacitance and low cost. Recently, spinel transition metal oxides (AB_2O_4) with two metal elements provide the feasibility to tune the energy density and working voltage by varying the metal content. Spinel ferrites (MFe_2O_4 , $M = Fe, Co, Ni, Cu, Mn$) have been conceived as a promising cost-effective and scalable alternative for supercapacitors due to their greater electronic conductivity and

electrochemical activity than single component metal oxides [5, 6]. Pure ferrites only exhibited very less capacitance and hence a prospective way to enhance the electrochemical performance is designing novel ferrite-based hybrids. Over the past decades, conducting polymer, carbon nanotubes and graphene sheets have emerged as important materials in the development of new generations of energy storage and conversion devices [7]. Ternary hierarchical systems composed of carbon nanomaterials, conducting polymers and transition metal oxides have been explored. These novel ternary hybrids exhibited much higher specific capacitance than the individual components or the binary carbon nanomaterials (or conducting polymers)/transition metal oxides composites [8]. Therefore, it is interesting to design novel ternary nanocomposites, which may exhibit enhanced electrochemical capacitance performance compared with its individual components. Among numerous kinds of conducting polymer, polyaniline (PANI) has been considered as one of the most promising materials for electrode materials in pseudocapacitors because of its low cost, ease of synthesis, simple acid-doping/base-dedoping chemistry, and relatively high pseudocapitance. Nickel ferrite (NiFe_2O_4), an inverse spinel in which Ni^{2+} occupies the octahedral site and half of the Fe^{3+} ions occupy the tetrahedral sites, has been reported as a pseudocapacitive candidate combined with carbon based materials. Herein, we present the fabrication of ternary polyaniline/nickel ferrite/carbon nanotubes (PNC) nanocomposites as electrode materials for supercapacitor.

2. Experimental

NiFe_2O_4 particles were synthesized by solution combustion technique. In a typical process, 0.372 g of $\text{Ni}(\text{NO}_3)_2 \cdot 6\text{H}_2\text{O}$ and 1.035 g of $\text{Fe}(\text{NO}_3)_3 \cdot 9\text{H}_2\text{O}$ were added to 10 ml of absolute ethanol with constant stirring for 30 min. 10 g of urea was dissolved in above solution and stirred for 30 min. The resulting mixture was transferred into Teflon-lined stainless steel autoclave and heated to 180 °C for 18 hr. It was then allowed to cool to room temperature. NiFe_2O_4 particles were obtained by filtered, washed and then dried in vacuum oven.

PANI particles were synthesized by chemical oxidative polymerization in acidic aqueous medium using ammonium persulphate (APS) as oxidant. For the typical

synthesis, aniline monomer 0.2 M was dissolved in 40 ml of 1 M H₂SO₄. 0.2 M of APS was dissolved in 50 ml of double distilled water. After that, APS solution was added drop wise into the monomer-solution which is maintained under constant stirring for 2 h. The polymerization process was identified by the change of colorless solution into green color. The collected sample was washed with double distilled water and methanol for several times. Finally, the sample was dried in vacuum oven at 80°C.

Ternary PNC nanocomposite was synthesized via in situ polymerization of aniline monomer in the presence of as-synthesized nickel ferrite and functionalized carbon nanotubes (f-CNT). 10 wt% NF and f-CNT were ultrasonicated and then mixed with aniline solution under constant stirring and drop wise addition of APS turned to PNC nanocomposites after washing and drying in vacuum oven. Similarly, binary PN nanocomposite was prepared with out using CNTs.

To prepare working electrode, 80 wt.% of the prepared material (40 mg), 15 wt.% of carbon black (7.5 mg) and 5 wt.% of PVDF (2.5 mg) were dissolved in 0.2 ml of N-methyl 2-pyrrolidinone and made into slurry form. Then, slurry was placed on the carbon electrode. The electrochemical studies were performed with three electrode cell configurations. An active material coated electrode as working electrode, Pt wire as counter electrode and Ag/AgCl as reference electrode were used. 1M KCl aqueous solution was used as electrolyte.

3. Results and discussion

The morphology and microstructure of nickel ferrite (NF), polyaniline/nickel ferrite (PN) and polyaniline/nickel ferrite/carbon nanotubes (PNC) nanocomposites were confirmed by SEM images as shown in **Fig. 1(a)**, (b) and (c). As can be seen from Fig. 1(a), NF particles show the roughly uniformity spherical-like morphology quite separated from each other. Fig. 1(b) and (c) shows the SEM images of PN and PNC nanocomposites. It can be clearly seen that highly agglomerated granular-like morphology was observed for PN composite, indicates that ferrite particles are surrounded by polymer chains of PANI. In other words, the polymer is coated on the surface of NF particles due to in situ polymerization. For PNC nanocomposite, it is seen that the CNTs are uniformly coated by NF and PANI due to which the average

diameter of the coated CNTs increased as shown in Fig. 1(c). The morphology of PN composite represents embedment of NF particles into the PANI matrix. In contrast to Fig. 1(c), a thin PANI film covering on the surface of NF-CNT is also recognized clearly, revealing the PNC composites were fabricated successfully. However, the NF nanoparticles and PANI also can hold back the aggregation of CNTs, and thereby improve the electrochemical properties, which can be approved by XRD and electrochemical tests. Moreover, the elemental mapping of PNC for carbon, nitrogen, iron, nickel and oxygen (**Fig. 2**), reveals that the various elements are homogeneously distributed in the PNC nanocomposite, confirming the existence of NF and PANI on the surface of CNTs.

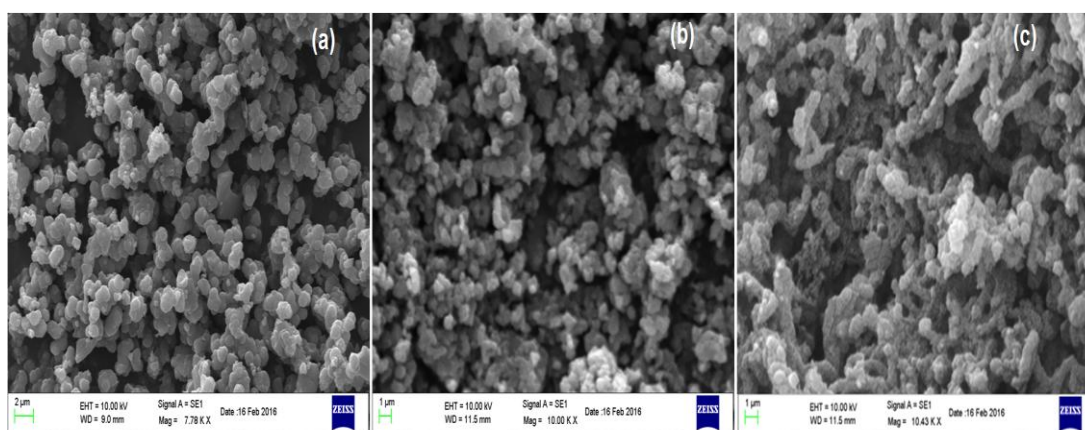


Fig. 1: SEM images of (a) NF, (b) PN and (c) PNC.

XRD diffraction patterns of the as-prepared NF, PANI and PNC are demonstrated in **Fig. 3**. In the pattern of PANI, a broad peak was observed at 26° which is due to the periodicity perpendicular to the PANI chains and there are no sharp peaks observed which indicates the amorphous nature and emeraldine salt form of the prepared PANI. NF represents sharp diffraction peaks at 30.3 , 35.7 , 43.4 , 57.4 , 63.0 and 75.2° which correspond to (hkl) plane of (220), (311), (400), (511), (440) and (622), respectively. The observed peaks elucidate the single phase formation and spinel group of NF and are in good agreement with the JCPDS (44-1485) file [9]. The XRD pattern of PNC showed the characteristic peaks related to the peaks of NF and that of CNTs peaks at $2\theta = 43.6$, 50.1° corresponding to the planes (111) and (200) respectively [10], indicating the interaction of NF, PANI and CNT in ternary nanocomposites.

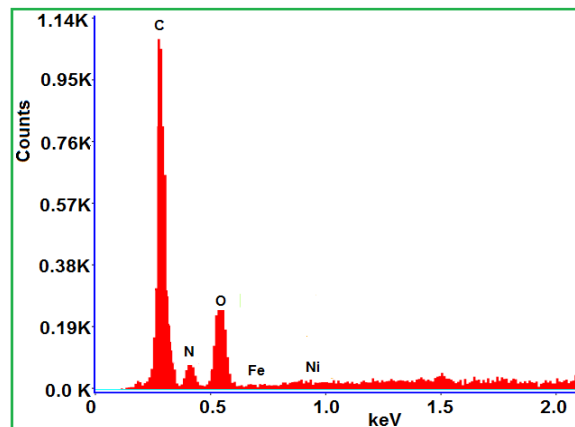


Fig. 2: EDX spectrum of PNC nanocomposite

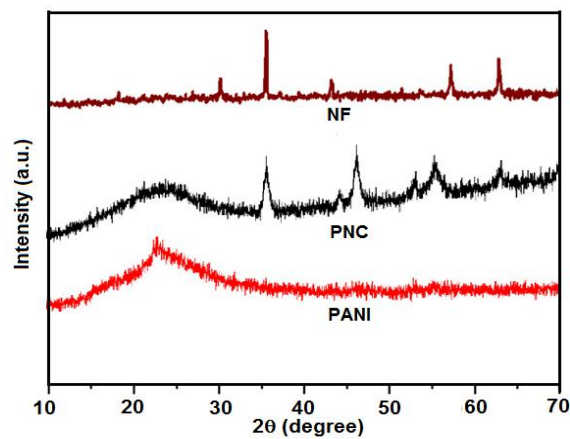


Fig. 3: XRD patterns of NF, PANI and PNC

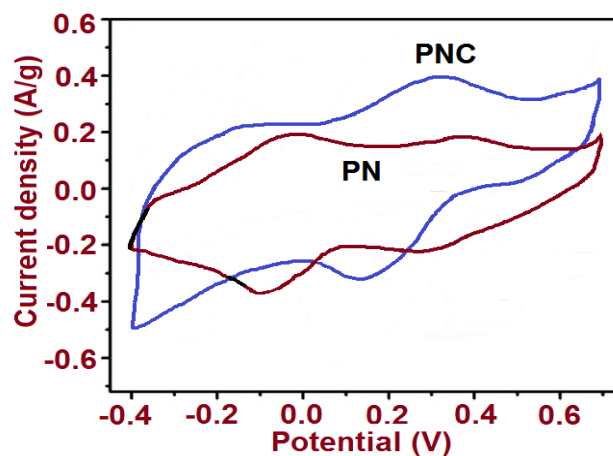


Fig. 4: CV curves of PN and PNC recorded at 1 mV/s

Electrochemical measurements were performed with a three electrode system from -0.4 to 0.7 V in 1 M KCl solution to evaluate the electrochemical performance as

supercapacitor electrode materials. **Fig. 4** shows the CV curves of PN and PNC recorded at 1 mV/s, revealing that the ternary PNC electrodes have the best electrochemical properties because of the largest current density responses. The electrochemical behaviour of PNC is distinctly improved owing to the combined effects between EDLC and pseudocapacitors. CV for PN evidently shows the redox peaks, indicating that PN has main pseudocapacitive performance coming from PANI. Therefore, the roles of NF and PANI are to enhance the specific capacitance, especially pseudocapacitance. The result further implies that the synergetic effect among three components leads to the additional capacitance produced. PNC nanocomposites achieved maximum specific capacitance value of 409.09 F/g, on the other hand PN showed specific capacitance value of 272.72 F/g at 1 mV/s scan rate. The achievement of such highest specific capacitance of the PNC nanocomposite may be due to the presence of highly accessible surface area of the CNTs in nanocomposites enhances the specific capacitance and the strong interaction among the π -bonded CNTs surface with the conjugated structure of polymer improves the specific capacitance of PNC [11].

4. Conclusion

We have successfully synthesized the ternary nanocomposites by in-situ chemical oxidative polymerization technique. Morphological analysis confirmed the uniform coating of NF and PANI over CNTs surface. The PNC nanocomposite showed highest specific capacitance than that of binary PN nanocomposite makes it superior for high electrochemical performance for supercapacitor application.

References

1. Wang, G., Zhang, L., Zhang, J., Chem. Soc. Rev. (2012), 41, 797–828.
2. Devadas, A., Baranton, S., Napporn, T. W., Coutanceau, C., J. Power Sources, (2011), 196, 4044–4053.
3. Chabi, S., Peng, C., Hu, D., Zhu, Y., Advance Mater. (2014), 26(15) 2440-2445.

4. Wei, T.Y., Chen, C.H., Chien, H.C., Lu, S.Y., Hu, C.C., *Advance Mater.* (2010), 22 (3), 347-351.
5. Zhu, M., Meng, D., Wang, C., Diao, G., *ACS Appl. Mater. Interfaces* (2013), 5(13), 6030-6037.
6. Wang, L., Ji, H., Wang, S., Kong, L., Jiang, X., Yang, G., *Nanoscale* (2013), 5, 3793-3799.
7. Yan, J., Wei, T., Fan, Z., Qian, W., Zhang, M., Shen, X., Wei, F., *Journal of Power Sources*(2010), 195, 3041–3045.
8. Jiang, H., Dai, Y., Hu, Y., Chen, W., Li, C., *ACS Sustainable Chem. Eng.* (2014), 2(1), 70-74.
9. Du, X., Wang, C., Chen, M., Jiao, Y., Wang, J., *J. Phys. Chem. C* (2009), 113, 2643–2646.
10. Chauhan, N., Narang, J., Rawal, R., Pundir, C.S., *Synth. Met.* (2011), 161, 2427– 2433.
11. Patil, D. S., Shaikh, J.S., Dalavi, D.D., Karanjkar, M.M., Devan, R.S., Ma, Y.R., Patil, P.S., *J. Electrochem. Soc.*(2011) 158 A653–A657.

Thermoluminescence studies of Eu^{3+} doped Calcium Lanthanum borate phosphor

M.Srinivas

Department of Physics, Osmania University, Hyderabad, 500007, India

*Corresponding author. E-mail: msrinivas.ou@gmail.com

ABSTRACT: $\text{Ca}_3\text{La}_2(\text{BO}_3)_4$ phosphor doped with Eu^{3+} have been synthesized by high temperature solid-state reaction method. The crystalline structure and elemental analysis of these phosphors are carried out by using X-ray powder diffraction (XRD) and Energy dispersive X-ray spectroscopy (EDS) techniques. The thermoluminescence (TL) properties have been investigated. For TL studies, samples were γ -irradiated with 1320 Gy dose rates using ^{60}Co source. TL of these phosphors showed a sharp glow peak with maxima at 394 K. Incorporation of europium activator in $\text{Ca}_3\text{La}_2(\text{BO}_3)_4$ phosphor resulted in the increase of peak intensity. The trap parameters viz., order of kinetics (b), activation energy (E) and frequency factor (S) associated with the most intensive glow peak of $\text{Ca}_3\text{La}_2(\text{BO}_3)_4:\text{Eu}^{3+}$ phosphor were determined using glow curve shape (Chen's) method.

Keywords: Phosphor, XRD, EDS, $\text{Ca}_3\text{La}_2(\text{BO}_3)_4:\text{Eu}^{3+}$, Thermoluminescence

1 Introduction

The study of new thermoluminescent (TL) materials to be used as TL dosimeters has made necessary to have a deeper knowledge of the trapping energy as well as of the average time the electron stays in its trap. This information can be obtained from the glow curve analysis which is obtained after exposing the material to ionizing radiation in order to excite the electrons from the valence band to the conduction band and back to metastable states in the forbidden band over the Fermi level. Then, by heating, those electrons can be released from their traps and recombine with trapped holes emitting light. Hence, TL is considered as a thermally stimulated process [1]. The glow curve can exhibit various peaks (maximum intensity) originated from different trapping states. There are many different methods for determining the trapping parameters [2] (i.e., the activation energy or trap depth, the kinetic order and the frequency factor). Most of the existing methods of obtaining the frequency factors make use of the determination of the trap depth (activation energy) relying on

some assumptions about the order of the kinetics. This causes inconsistencies in the reported values of the trapping parameters due to appreciable differences in the activation energy obtained by different methods. Then, it is necessary to use a method independent of the determination of the trap depth.

The TL characteristics of borate compounds have been reported such as un-doped and Ce-doped BaB_4O_7 [3], Tb^{3+} -doped $\text{Ba}_2\text{Ca}(\text{BO}_3)_2$ [4], un-doped and Cu- and Mn-doped $\text{K}_2\text{B}_4\text{O}_7$ [5], $\text{MgB}_4\text{O}_7:\text{Dy,Na}$ [6], $\text{SrB}_4\text{O}_7:\text{Dy}$ [7], rare-earth-doped $\text{Sr}_2\text{Mg}(\text{BO}_3)_2$ [8], $\text{Li}_2\text{B}_4\text{O}_7:\text{Cu,In}$ [9,10] and $\text{BaB}_4\text{O}_7:\text{Dy}$ [11] these results provide useful information concerning the defects and trap structure that are helpful in the search for new borate TLD materials. In this paper, we report the method making use of isothermal decay of the TL was studied to determine the trapping parameters of $\text{Ca}_3\text{La}_2(\text{BO}_3)_4:\text{Eu}^{3+}$ phosphor by using the glow curve shape method.

2 Experimental

The Phosphor materials of composition $\text{Ca}_3\text{La}_2(\text{BO}_3)_4$ [CLB] doped with europium were synthesized by the solid state reaction method. Stoichiometric amounts of AR grade CaCO_3 , La_2O_3 , Eu_2O_3 and H_3BO_3 were thoroughly mixed and ground together with ethanol in an agate mortar for 5 hours to give homogenous mixture. The resultant powders were initially dried at 100°C for 1 h, kept in an alumina boat and heated at 1200°C in air for 3 hrs. Later, the temperature is brought down to 950°C and the samples were held at that temperature for 1 hour in air. These samples were rapidly cooled down to room temperature and were grinded to get fine powder for further studies.

The phase purity of the as synthesized phosphor were characterized using X-ray diffraction (XRD) patterns with $\text{Cu-K}\alpha$ radiation of wave length 1.5406 \AA in the 2θ range of $10 \sim 80^\circ$ with a step size of $0.04^\circ/\text{sec}$. The operation voltage and current of the instrument were maintained at 40 kV and 30 mA respectively. The compositions of the phosphor samples were obtained from energy dispersive spectrum (EDS). The EDS was attached to the HITACHI S-3700N model instrument. All measurements were recorded at room temperature. Thermoluminescence Analyzer system (type 1007) supplied by Nucleonix Systems Private Ltd., Hyderabad, India. offering an irradiation volume approximately 1000

cc had 2370 curies ^{60}Co source, used for γ -irradiation. The glow curves were recorded by heating the sample at a uniform rate of 2 K Sec $^{-1}$ with the help of a temperature controller.

3. Result and Discussions

3.1. Powder XRD

The powder X-ray diffractograms of CLB are shown in fig.1 and the observed d-lines are indexed for higher concentration of Eu^{3+} shown in fig.2. The CLB belongs to the orthorhombic system with space group $Pnam$, and unit cell parameters are show as following: $a = 7.279 \text{ \AA}$, $b = 16.417 \text{ \AA}$, $c = 8.654 \text{ \AA}$. All the compounds are very close to that of reported values for CLB [12]. It is indicated that the doping Eu^{3+} ions do not form new phases in the synthesis process.

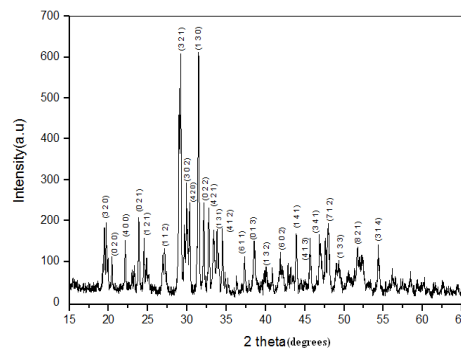


Fig 1 XRD of $\text{Ca}_3\text{La}_{1.9}\text{Eu}_{0.1}(\text{BO}_3)_4$ phosphor

3.2. Energy Dispersive Spectrum

The energy dispersive spectrum analysis of 0.1 mol % Eu^{3+} doped CLB sample peaks shown in Fig.2 corresponding to Ca, La, Eu, B and O. The EDS pattern confirms the presence of europium in the CLB powders and its wt% is nearly equal to the doped value of Eu in CLB.

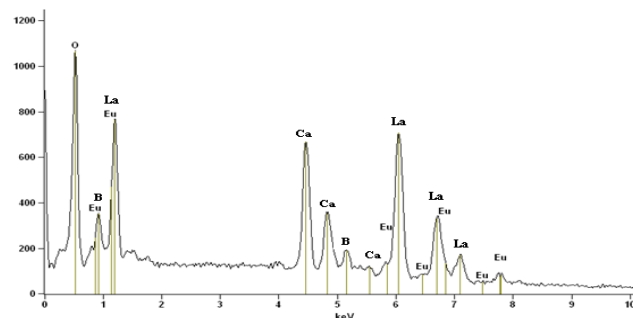


Fig 2 EDS of $\text{Ca}_3\text{La}_{1.9}\text{Eu}_{0.1}(\text{BO}_3)_4$ phosphor

3.3.1 Thermoluminescence of $\text{Ca}_3\text{La}_2(\text{BO}_3)_4: \text{Eu}^{3+}$

The observation of Eu^{3+} afterglow in the $\text{Ca}_3\text{La}(\text{BO}_3)_4$ host, it is necessary to take the TL spectrum into consideration. Fig. 3 represents the TL glow curve of $\text{Ca}_3\text{La}_{1.9}\text{Eu}_{0.1}(\text{BO}_3)_4$ phosphor. During this study, glow curves of Eu^{3+} doped $\text{Ca}_3\text{La}(\text{BO}_3)_4$ samples were recorded at dose rate of γ -irradiation (1320 Gy) at room temperature. A strong TSL glow peak is observed at 394 K. It is observed that the intensity of this glow peak is found to increase with the increase of Eu concentration.

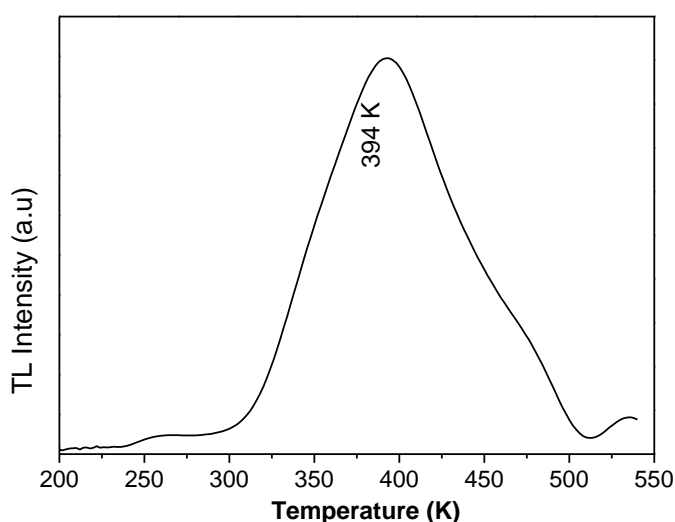


Fig 3 TL glow curve of $\text{Ca}_3\text{La}_{1.9}\text{Eu}_{0.1}(\text{BO}_3)_4$ phosphor

3.3.2. Glow curve shape method

The method based on the shape of glow curve proposed by Chen was used to verify the trapping parameters. To determine these parameters the following shape parameters were determined: the total half intensity width ($\omega = T_2 - T_1$), the high temperature half width ($\delta = T_2 - T_m$), the low temperature half width ($\tau = T_m - T_1$), where T_m is the peak temperature and T_1 and T_2 are temperature on either side of T_m corresponding to half peak intensity. In order to calculate the trapping parameters associated with the 394°C glow peak by glow curve shape method using chen's method [13,14] and given in Table 1.

Sample	Dose (Gy)	T _m ±2K	τ (K)	δ (K)	Ω (K)	μ _g	Activation Energy (eV)				S (Sec ⁻¹)
							E _τ	E _δ	E _ω	E _{av}	
Ca ₃ La ₂ (BO ₃) ₄	1320	394	32	44	76	0.579	0.677	0.648	0.659	0.661	2.704 x 10 ⁷
Ca ₃ La _{1.9} Eu _{0.10} (BO ₃) ₄		394	35	46	81	0.568	0.596	0.596	0.596	0.596	3.523 x 10 ⁶
Ca ₃ La _{1.9} Eu _{0.10} BO ₃) ₄		394	31	42	73	0.575	0.700	0.671	0.683	0.684	5.522 x 10 ⁷
Ca ₃ La _{1.9} Eu _{0.10} (BO ₃) ₄		394	35	49	84	0.583	0.609	0.591	0.598	0.599	3.860 x 10 ⁶

4.0 Conclusions

In this work, we report the chemical synthesis of a new Ca₃La₂(BO₃)₄ thermoluminescent phosphor. The experimental evidence presented shows that these novel materials exhibit very good thermoluminescence properties, as to be considered for the development of new dosimeter phosphor materials.

5 Acknowledgements

The author gratefully acknowledge to the UGC, New Delhi for finance assistance under MRP scheme to carried out this work.

Reference

- [1] J. Azorin, Luminescence Dosimetry: Theory and Applications, Ediciones Te ´cnico-Cienti ´ficas, Me ´xico D.F., 1990.
- [2] J. Azorin, Int. J. Radiat. Appl. Instrum. Part D: Nucl. Tracks 11 (1986) 159.
- [3] A.N. Yazici, M. Dogan, V.E. Kafadar, H. Toktamis, Nucl. Instrum. Methods B 246 (2006) 402.
- [4] L.Y. Liu, Y.L. Zhang, J.Q. Hao, C.Y. Li, Q. Tang, C.X. Zhang, Q. Su, Phys. Stat. Sol. (a) 202 (2005) 2800.
- [5] J. Manam, S.K. Sharma, Nucl. Instrum. Methods B 217 (2004) 314.
- [6] C. Furetta, G. Kitis, P.S. Weng, T.C. Chu, Nucl. Instrum. Methods A 420 (1999) 441.
- [7] J. Li, J.Q. Hao, C.Y. Li, C.X. Zhang, Q. Tang, Y.L. Zhang, Q. Su, S.B. Wang, Radiat. Meas. 39 (2005) 229.

-
- [8] L.Y. Liu, Y.L. Zhang, J.Q. Hao, C.Y. Li, Q. Tang, C.X. Zhang, Q. Su, *Mater. Lett.* 60 (2006) 639.
- [9] C. Furetta, M. Prokic, R. Salamon, V. Prokic, G. Kitis, *Nucl. Instrum. Methods A* 456 (2001) 411.
- [10] M. Prokic, *Radiat. Meas.* 33 (2001) 393.
- [11] J. Li, J.Q. Hao, C.X. Zhang, Q. Tang, Y.L. Zhang, Q. Su, S. Wang, *Nucl. Instrum. Methods B* 222 (2004) 577.
- [12] J. Azorin, *Luminescence Dosimetry: Theory and Applications*, Ediciones Técnico-Científicas, México D.F., 1990.
- [13] R. Chen, S.W.S. McKeever, *Theory of Thermoluminescence and Related Phenomena*, World Scientific, Singapore, 1997.
- [14] H.Nagabhushana, N.Lakshminarasappa, and Fouran Singh, *J. Radiat.Meas.* Vol.43, (2008), pp. S651.

Synthesis and Magnetic properties of CoFe_2O_4 and MgFe_2O_4 spinel nano ferrites

M. Raghasudha^{1*}, D. Ravinder², P. Veerasomaiah¹, Shyamsunder goud¹,
G. Satyanarayana Goud³, B. Rambabu¹, N. Venkatesh¹

1. Department of Chemistry, Osmania University, Hyderabad-500007

2. Department of Physics, Osmania University, Hyderabad-500007

3. Department of Chemistry, M.V.S. Govt Degree College, Mahabubnagar-509001

ABSTRACT

Crystalline, magnetic CoFe_2O_4 and MgFe_2O_4 nano particles were prepared by citrate-gel auto combustion method . The synthesized samples were subjected to calcinations at 500°C for 4our hours. XRD analysis of the prepared ferrites confirmed the formation of single phased cubic spinel structure with a low particle size of 7nm for CoFe_2O_4 and 23nm for MgFe_2O_4 . Room temperature magnetic measurements were carried out using Vibrating Sample Magnetometer. The hysteresis loops obtained for the synthesized ferrites revealed that MgFe_2O_4 nano particles are soft magnetic materials with very small area inside the loop. CoFe_2O_4 nano particles are hard magnetic materials with large area inside the loop when compared to the MgFe_2O_4 . Due to soft magnetic properties of MgFe_2O_4 they are desirable for their utility in transformers, inductor cores, recording heads, microwave devices, and magnetic shielding. Due to excellent magnetic properties of nanocrystalline CoFe_2O_4 they can be used in high frequency devices, memory cores, recording media, and in biomedical field.

Keywords: Nano ferrites, Citrate-gel method, XRD, VSM

1.Introduction

Among the materials, Ferrites have attracted immense attention of the scientific community because of their novel properties and technological applications especially when the size of the particles approaches to nanometer scale [1]. As magnetic materials, nano-sized ferrites cannot be replaced by any other magnetic material because they are relatively inexpensive,

stable, and have a wide range of technological applications [2]. Among ferrites, the spinel ferrites have remarkable magnetic and electrical properties. The magnetic

properties of the nanosized ferrites are entirely different from those of their bulk counterparts. Nanosized ferrites with uniform particle size and narrow size distribution are desirable for a variety of applications like targeted drug delivery, medical imaging, magnetic data storage and other biomedical applications, etc. [3].

Magnesium nano ferrites are the potential materials for various applications due to their high electrical resistivity, low magnetic and dielectric losses [4]. On the other hand, CoFe_2O_4 is also interesting because of its perfect chemical properties, thermal stability, high electrical resistivity, and excellent magnetic properties [5]. Nanocrystalline CoFe_2O_4 with such properties has potential applications in high frequency devices, memory cores, recording media, and in biomedical field [6]. The author is interested in comparing the magnetic properties of Magnesium and Cobalt ferrites for their potential applications.

Among Various methods used to prepare nano-sized ferrites such as co-precipitation method, micro-emulsion procedures, microwave plasma, mechanical milling and sol-gel auto-combustion method, the sol-gel auto combustion method is most suitable for the synthesis of nano-sized ferrite materials. This is because of its advantages such as good stoichiometric control and the production of ultrafine particles with a narrow size distribution in a relatively short processing time at a very low temperature. The present work reports the synthesis of nanocrystalline MgFe_2O_4 and CoFe_2O_4 and the study of their magnetic properties.

2. Materials and methods

The nanocrystalline MgFe_2O_4 and CoFe_2O_4 were prepared using Citrate-Gel auto combustion method. The following chemicals are used as starting materials for the synthesis.

Magnesium Nitrate - $\text{Mg}(\text{NO}_3)_2 \cdot 6\text{H}_2\text{O}$

Cobalt Nitrate-Co $(\text{NO}_3)_2 \cdot 6\text{H}_2\text{O}$

Ferric Nitrate - $\text{Fe}(\text{NO}_3)_3 \cdot 9\text{H}_2\text{O}$,

Citric acid ($\text{C}_6\text{H}_8\text{O}_7 \cdot \text{H}_2\text{O}$)

Ammonia (NH_3) (all 99% pure).

Calculated quantities of metal nitrates were dissolved together in a minimum amount of distilled water to get clear solution. An aqueous solution of Citric Acid was then added to the metal nitrate solution. The mixture was stirred to obtain a homogeneous solution and then was slowly heated to 80°C. pH of the solution was adjusted to 7 by adding Ammonia (NH₃) solution. The resulting solution was evaporated to dryness by heating at about 150°C on a hot plate with continuous stirring which has started to form a viscous gel. When finally all water molecules were removed from the mixture by increasing the temperature to 200°C, the viscous gel began frothing. The gel has undergone a flameless auto combustion reaction with the evolution of large amounts of gases. The reaction was completed in a minute giving rise to dark grey voluminous product with a structure similar to Branched tree. Finally the burnt powder was ground and was calcined in air at temperature 500°C for four hours to obtain a spinel phase.

The resultant powder was subjected X-ray Diffraction analysis with CuK_α ($\lambda = 1.54 \text{ \AA}$) to study the single phase nature and nano-phase formation of the ferrites under investigation at room temperature by continuous scanning in the range of 2°C to 85°C. The magnetic measurements of prepared ferrites were measured by using Vibrating Sample Magnetometer at room temperature in the range of 15 kOe.

3. Results and discussion

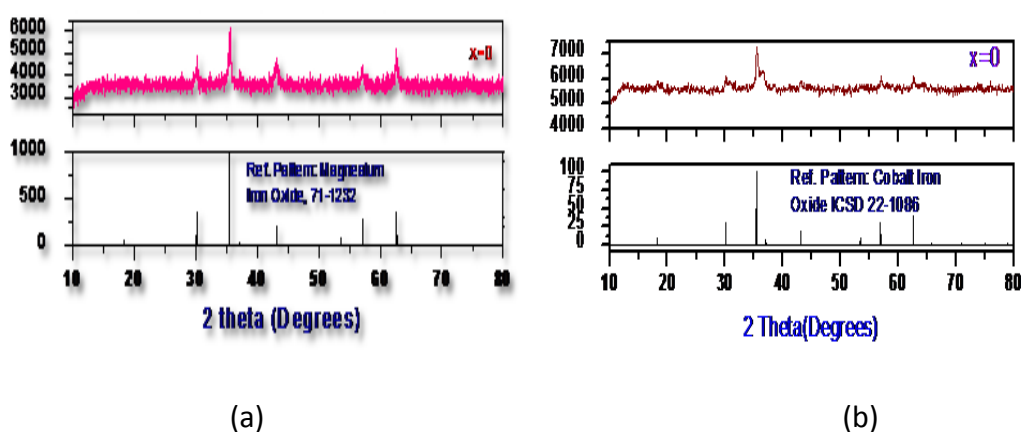


Fig.1. XRD patterns of (a) MgFe₂O₄ and (b) CoFe₂O₄

Figure 1 (a) and (b) shows the x-ray diffraction patterns of Magnesium and Cobalt ferrites and reference data of magnesium iron oxide and cobalt iron oxide respectively. The figure showed a homogeneous single phased cubic spinel belonging to the space group $Fd\bar{3}m$. All the Bragg's re-flections have been indexed as (111), (220), (311), (400), (511) and (440) which confirmed the formation of a well defined single phase cubic spinel structure without any impurity peaks. All the peaks are allowed peaks. The strongest reflection is from (311) plane that indicates spinel phase. Crystallite size (D) of prepared ferrites was calculated from Scherrers Formula [7] mentioned below by using high intensity peak (311).

$$D = \frac{0.91\lambda}{\beta \cos \theta}$$

where λ = Wavelength of X-ray,

β = Full width and Half Maxima in radians,

θ = Bragg's angle at the peak position.

The crystallite size was found to be 23nm for magnesium ferrite and 7 nm for Cobalt ferrite. Figure 2 show the magnetic hysteresis loops for the Magnesium and cobalt ferrite samples obtained from Vibrating Sample Magnetometer measurements at room temperature in the range of 15Koe.

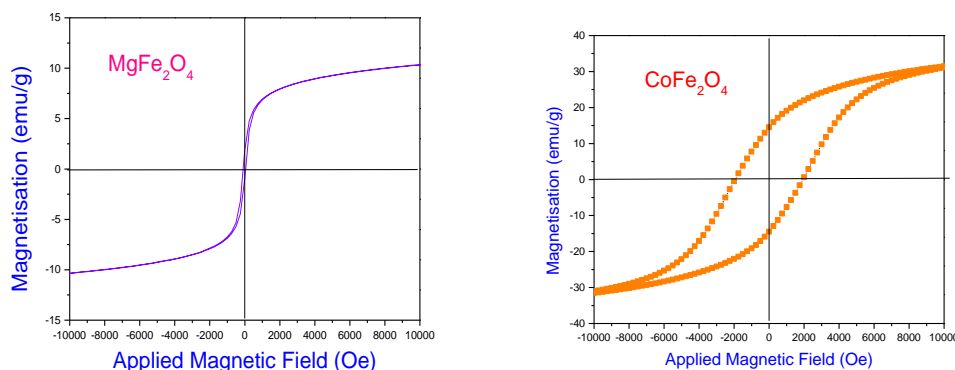


Figure 2. Magnetic Hysteresis loops of $MgFe_2O_4$ and $CoFe_2O_4$

The relation between the Magnetization (M) and the applied field (H) is given by Hysteresis loops. Various magnetic parameters extracted from the hysteresis loops

are Saturation Magnetization- M_s (maximum value of magnetization), Remanence Magnetization- M_r (magnetization at zero field), Coercivity- H_c (magnetic field required to reduce the magnetization of that material to zero after the magnetization of the sample has been driven to saturation), Remanence ratio or Squareness ratio (M_r/M_s). The magnetic parameters calculated for both the samples were tabulated in table 1.

Table 1. Magnetic parameters of Magnesium and Cobalt nano ferrites

Composition	Saturation magnetization M_s (emu/g)	Coercivity H_c (Oe)	Remanent Magnetization M_r (emu/g)	Remanence ratio $=M_r/M_s$
MgFe ₂ O ₄	11.08	1.794	97.06	0.16
CoFe ₂ O ₄	33.8448	14.540	1,954.66	0.4296

From the data it is clear that area inside the hysteresis loop for MgFe₂O₄ is very less where as it is more for CoFe₂O₄ which is a measure of magnetic property of a material. Due to the smaller area of the loop, MgFe₂O₄ is a magnetically soft material whereas CoFe₂O₄ is a hard magnetic material due to its larger loop area. Hence Magnesium ferrites are desirable for their utility in transformers, inductor cores, recording heads, microwave devices, and magnetic shielding.

Cobalt ferrites are desirable in high frequency devices, memory cores, magnetic storage systems such as magnetic tape for recorders and for recording heads. Magnetic storage is also widely used in some specific applications, such as bank cheques and credit/debit cards.

4. Conclusions

MgFe₂O₄ and CoFe₂O₄ nano ferrites were successfully synthesized through citrate-gel method with a particle size 23nm and 7 nm respectively. X-ray diffraction analysis confirmed the formation of single phased cubic spinel structure of the prepared ferrites. Magnetic measurements using VSM revealed that Magnesium nano ferrites are magnetically soft materials and Cobalt nanoferrites are magnetically hard materials. Hence, MgFe₂O₄ find applications in transformers, inductor cores, recording heads, microwave devices, and magnetic shielding and

CoFe₂O₄ are used in high frequency devices, memory cores and magnetic storage systems.

References

1. Subhash, C, Srivastava, BK, Anjali, K: Indian J. Pur. Appl. Phy 42, 366–367, (2004)
2. Costa, MM, GFM, PJ, Sombra, ASB: Int. J. Mater. Chem. Phy. 123, 35–39, (2010).
3. Kaur, Balwinder.; Arora, Manju.; Shankar, Ajay.; Srivastava, Avanish Kumar.; Pant, Rajendra Prasad. Adv. Matt. Lett., 3(5), 399, (2012)
4. C. Chen, Magnetism and Metallurgy of Soft Magnetic Materials, Dover, New York, NY, USA, 1986.
5. Muzquiz-Ramos, EM, Cortes-Hernandez, DA, Herrera-Romero, OA, Escobedo-Bocardo, J.C.: Mater Sci Forum 644, 39–42, (2010)
6. Pervaiz, E, Gul, IH: J. Magn. Magn. Mater. 324, 3696–3703, (2012)
7. B. D. Cullity, “Elements of XR-Diffraction,” Addison Wesley Publishing, Reading, 1959, p. 132.

Impedance spectroscopic studies on PMN-PT

UshaPraveena V.J, N. V. Prasad*, G. Prasad and G. S. Kumar

Department of Physics, Materials research Laboratory
Osmania University, Hyderabad 500007.

ABSTRACT

Impedance spectroscopic studies are done on PMN-PT (lead magnesium niobate-lead titanate) ceramic. The maxima of the impedance as well as modulus are found to shift towards higher frequencies with increasing temperature, indicating a deviation from Debye behaviour. Cole-Cole plots show two-depressed semicircles, confirming grain and grain-boundary contributions. Double logarithmic spectroscopic plots, as a function of frequency, in the range of 1 kHz to 1 MHz, were used as a tool to study the electrical behavior of the sample. The results are corroborated to the new Euryod's conduction model.

Key words: PMN-PT, Impedance, conductivity, hopping mechanism

*Corresponding author's Email: nvp_phy@osmania.ac.in

1. Introduction

Lead magnesium niobate (abbreviated as PMN) with general formula $\text{Pb}(\text{Mg}_{1/3}\text{Nb}_{2/3})\text{O}_3$ is known for its specific properties like high dielectric permittivity, near-zero hysteresis, a diffuse phase transition, and high electrostrictive coefficients [1-5]. Smolenskii [1] was first to explain the relaxor characteristics of PMN, based on the compositional fluctuations on a microscopic scale globally. In addition, Cross et al [2] reported that ferroelectric (polar) and paraelectric (non-polar) micro-regions exist simultaneously in the PMN material over a broader temperature interval. Lead titanate (abbreviated as PT) is a normal ferroelectric (different from PMN), where the dielectric maximum is sharp and it is independent of frequency.

It is a known fact that PMN forms a solid solution with PT, near morphotropic phase boundary (MPB) [3]. Keeping this in view, the chemical composition of PMN-PT (70/30) was prepared in the present investigation.

Impedance analysis helps us in studying the dielectric behavior of crystalline, polycrystalline, and amorphous materials [6]. This technique is often used to separate the contributions of grains and grain boundaries to the dielectric properties. The main objective of the study is to investigate the electrical properties of PMN-PT solid solutions near the MPB.

2. Experimental

The specimens under the investigation were prepared according to the chemical composition PMN-PT (70/30). The starting raw materials were AR grade (99.9%) pure. The specimens were prepared by the columbite precursor method [2,5,8]. A detailed preparation of PMN-PT is summarized in the following flow chart. The procedure and XRD results would be presented elsewhere [9].

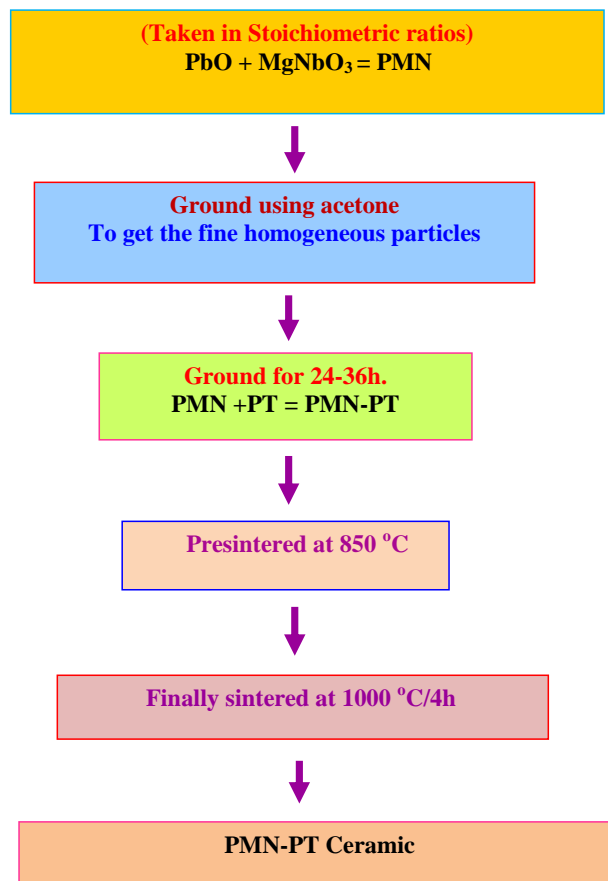


Fig 1. Flow chart for PMN-PT preparation

Prior to the impedance measurements, the sintered circular pellets were coated with silver paste. Impedance measurements were done at different temperatures, using HP 4192A impedance analyzer over a wide frequency range (100 Hz to 1 MHz). The dielectric data was extracted from the impedance data.

3. Results and Discussion

In our earlier results, the variation of imaginary part of impedance (Z'') and modulus (M'') for the PMN-PT with frequency showed non-Debye behavior. This behavior generally observed in the lead based perovskite materials. This is prompted us in relooking into the data.

Fig 2a show the complex impedance plot, drawn between Z'' and Z' for a particular temperatures. The depressed two-semicircles indicate a deviation from Debye behavior. Each semi-circle is the representation of a relaxation mechanism, and the semicircle drawn at lower as well as higher frequency region represents grain-boundary and grain relaxation process.

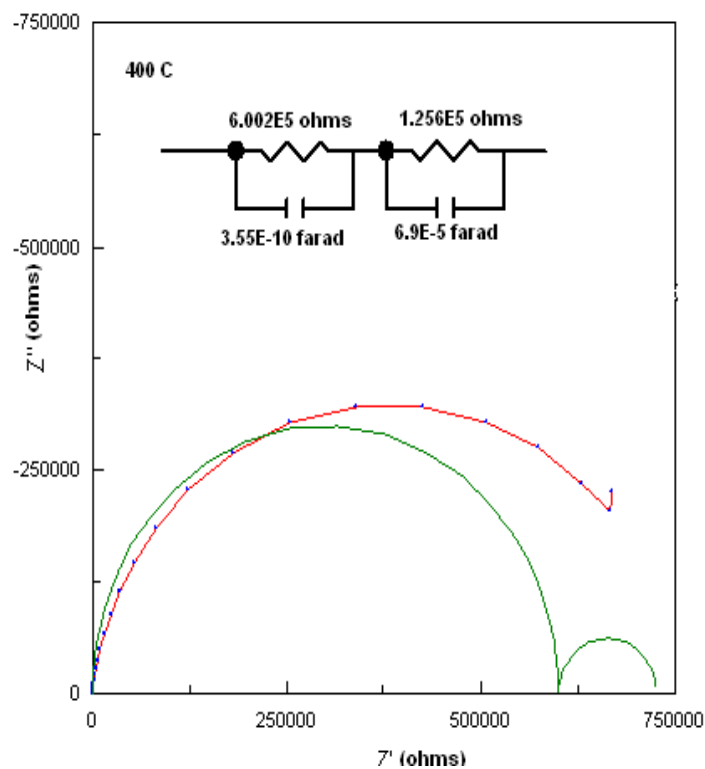


Fig 2 a Cole-Cole plot (Z'' vs, Z')

conduction by electron. The linear nature observed in real respond plots can be described by the exponential relation ($\epsilon \propto \omega^{n-1}$) with the frequency. The dispersion observed in the lower frequency of conductance plot (fig 3b) is ascribed to the continuous jumps or hopping type mechanism of non-Debye materials [10]. The overall behavior could be described by the multiple ionic migrations or transportation.

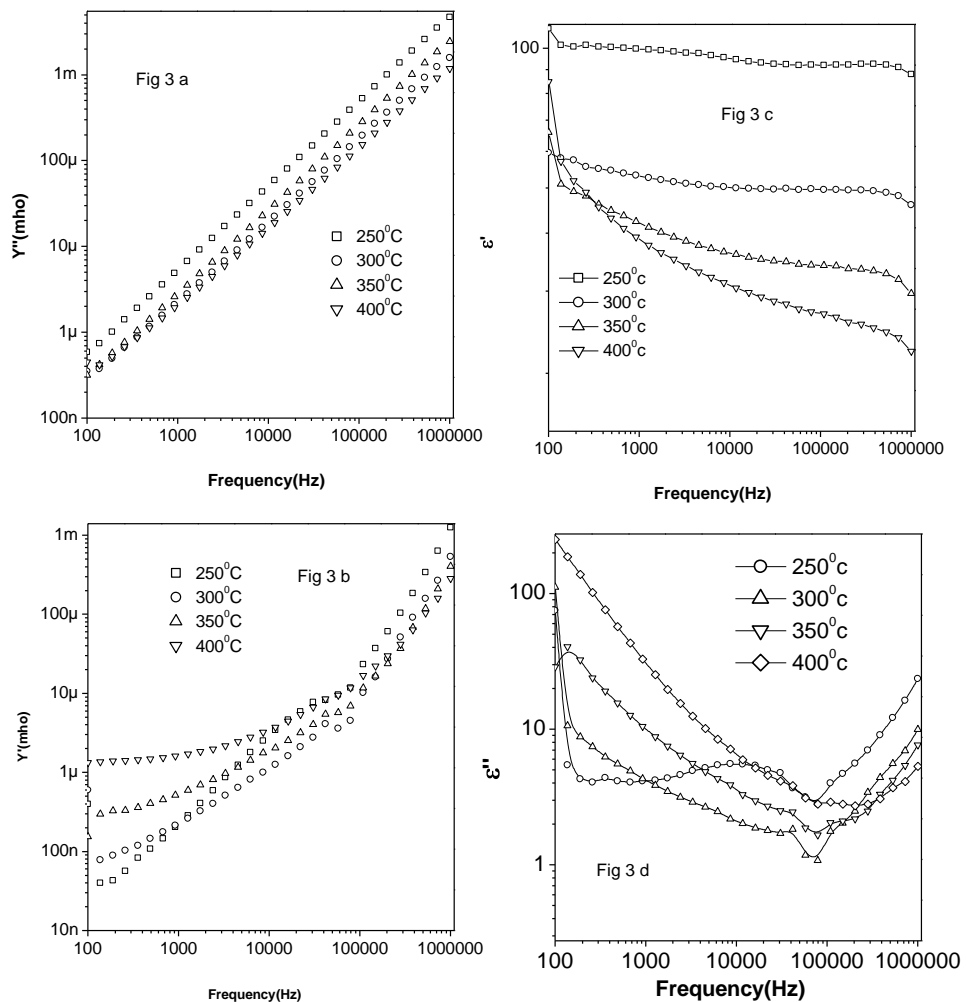
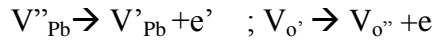
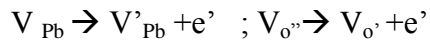


Fig 3 (a) Y' vs. frequency (b) Y'' vs. frequency (c) Z' vs. frequency (d) Z'' vs. frequency

The results are consistent with Eyraud’s [11] model, where Pb-based ceramics have fully ionizes cation and anion vacancies. The following exchange reaction, proposed by Eyraud [11] is seems to be more adequate. The terms V_{Pb}^{\cdot} ,

V_o' and V_o'' indicates lead vacancy, single ionized vacancy and double ionized vacancies respectively.



4. Conclusions

- (i) Spectroscopic plots as well as depressed semicircular Cole-Cole plots reveals the non-Debye behavior.
- (ii) Double logarithmic plots of conductivity and permittivity indicate hopping between neighboring donor sites. Imaginary part of conductance and permittivity shows temperature dependent.
- (iii) Real part of conductivity vs. frequency showed that the conduction is through hopping of electrons at extrinsic region and migration of oxygen vacancies at intrinsic region. An increasing of e'' at higher frequency indicates the migration of both V_o' (single ionized) and V_o'' (double ionized vacancies). However, the migration of V_o'' predominates over V_o' . The results are consistent with our earlier results [9] as well as Euryod's conduction model.
- (iv) Based on the double logarithmic plots and our earlier results [9], it is concluded that electron hopping is easier between double ionized and single ionized vacancies of both lead as well as oxygen vacancies. Finally, both single and double ionized oxygen and lead vacancies contribute in the conduction mechanism.

Acknowledgements: One of the authors UshaPraveena V.J. thanks the management of St. Francis College for women, Hyderabad for constant encouragement and support.

References

1. G.A.Smolenskii and A.I.Agronovskaya, Dielectric polarization of a number of complex compounds, sov. Phys.Tech. Phys. A3 (1958) 1380
2. L.E.Cross, Relaxor ferro electrics, Ferroelectrics 76, (1987) 241
3. V.K.Wadhawan, Introduction to ferric materials, Gordon & Breach, UK (2000)
4. K.Uchino , Ferroelectric Devices, Marcel Dekker Inc, NY (2000)
5. B.Jaffe , W.R.Cook and H.Jaffe, Piezoelectric Ceramic, Academic Press, London (1971)
6. J.R.Mac Donald, Impedance spectroscopy, Wiley, NY(1987)
7. M.E Lines and AM Glass , principles and application of ferroelectric and related materials, Clarendon press, Oxford (1977).
8. S.W. Choice , T.R.Shrout, S.J.Jang and A.S.Bhalla, Dielectric and pyro electric properties in the $\text{Pb}(\text{Mg}_{1/3} \text{Nb}_{2/3})\text{O}_3\text{-PbTiO}_3$ system, Ferroelectrics 100 (1989) 29
9. N.V.Prasad, M.ChandraSekar and G.S.Kumar, Ferroelectrics, 366 (2008) 55
10. A.K.Jonscher, Dielectric relaxation in solids, Chelsea Dielectrics, London (1983); Universal Relaxation law ,Chelsea Dielectrics, London (1996)
11. L.Eyraud, B. Guiffard, L.Lebruen and D.Guyomar, Ferroelectrics 330 (2006) 51.

Resistive Switching Property of Nickel-Zinc Thin Film Synthesized By Sol Gel Route

K. Rama Krishna¹ K. Vijaya Kumar² D. Ravinder³

1. Department of Physics, Malla Reddy College of Engineering & Technology,
Secunderabad – 500 014. A.P. India.

2. Department of Physics, Jawaharlal Nehru Technological University Hyderabad,
College of Engineering, Nachupally (Kondagattu), Karimnagar-Dist., 505 501,
A.P., India

3. Department of Physics, Osmania University, Hyderabad – 500 007. A.P. India
*Corresponding author email id: ramu521@gmail.com

ABSTRACT : Ni_{0.8}Zn_{0.2}Fe₂O₄ nano thin films were synthesized using spin coating chemical process, by depositing a solution of iron (III) nitrate, nickel acetate, zinc chloride and ethylene glycol solutions on a glass Substrate. This substrate is subjected to pre and post annealing at 350⁰ C & 550⁰C for 30 & 60 min which results the formation of nano thin film. The conformation of single phase formation and structural analysis were carried by employing X-ray diffraction technique and Atomic force micro scope (AFM). The I-V measurements of the sample is were done using Keithley 4200 Semiconductor Characterization System (SCS)

Key words: Ni-Zn nano ferrite thin film, Spin coating method, topography. I-V measurements

1. INTRODUCTION

Ferrites, which are magnetic oxides, are best examples for very good electrical materials because of their high resistivity and low loss behavior hence they have vast technological applications over a wide range of frequencies [1 2]. Ni-Zn ferrite is a significant magnetic material for practical applications because of its better properties at high frequency and high resistivity.

2. EXPERIMENTAL

A precursor solution of Ni_{0.8}Zn_{0.2}Fe₂O₄ was prepared from iron (III) nitrate, nickel acetate, zinc chloride and dissolved in anhydrous 2-mithoxyethanol. The mixture obtained in such a manner was stirred in a magnetic stirrer for about 4 hrs. at room temperature. It was observed that the solubility of nickel acetate, zinc chloride

wasn't as good in ethanol. Due to this, the associated acetate forms colloids and a solution is obtained. The technique stabilizers were added to the respective solutions to eliminate/minimize the turbidity and precipitates. In some cases the solution was kept in the ultrasonic bath to promote the reaction. Among various stabilizers, mono-ethanolamine (MEA) is widely used as effective capping agent, to not only control the crystallite size but also to obtain oriented films. The solution was hydrolyzed with water per mole of metal by adding water dissolved in 2-methoxyethanol at 20 wt. % drop-wise, along with roughly 2 wt. % MEA in order to remove turbidity and precipitates completely. Clear, transparent, and homogenous solution with no precipitations used for deposition.

Double size polished soda lime glass, SiO_2 (quartz) of size 15 x 10 x 1 mm squares were used as substrates, after being thoroughly cleaned in an ultrasonic cleaner (PCI corporation, Mumbai, frequency of 33 kHz) in following sequence : double distilled water \rightarrow acetone \rightarrow distilled water for a total duration of 40 minutes. The substrates were rinsed with deionized water for 5 min and then dried in air atmosphere. The cleaned substrates were spin coated at rpm of 4000 to 4500 for 20 seconds at room temperature. Films were very slowly dried at 250 °C for 30min. This cycle was repeated 5-6 times until the desired thickness was obtained. The thickness of the films was in the range of some nm. The deposited films were annealed in air at temperature of 550°C for 60 min. The Schematic flow chart of CSD route of $\text{Ni}_{1-x}\text{Zn}_x\text{Fe}_2\text{O}_4$ thin films is as shown in the fig 1.

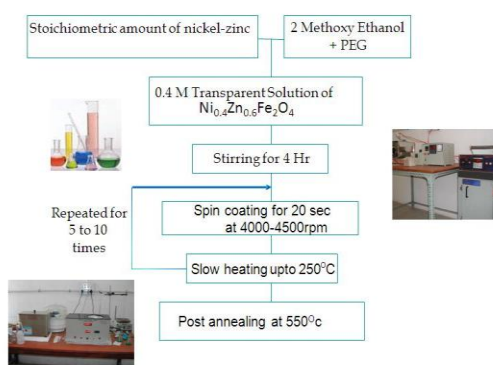
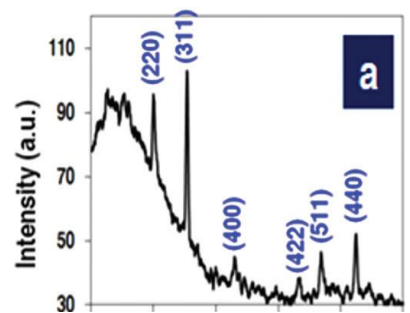


Fig 1.1 Flow chart

3. RESULTS AND DISCUSSION

$\text{Ni}_{0.8}\text{Zn}_{0.2}\text{Fe}_2\text{O}_4$ thin film is characterized by X-ray diffraction confirms the single phase formation of ferrite to cubic structure and corresponding X-rd is as shown in the fig 2.



3.1 Lattice parameter

The Fig. 2 X-rd of $\text{Ni}_{0.8}\text{Zn}_{0.2}\text{Fe}_2\text{O}_4$ thin film is calculated by using the following equation [3] and it was found to be 8.42 \AA , different researchers found that the lattice parameter is in the same order [4].

$$a = d (h^2 + k^2 + l^2)^{1/2}$$

Where, a = lattice constant

d = inter planar distance &

(h, k, l) are the Miller indices

3.2 Particle Size:

The particle size of the samples are calculated by using Sherrer's formula [5] by using the following equation and the particle size is found to be 20 nm

$$d_{hkl} = \frac{0.91\lambda}{\beta \cos\theta}$$

Where

d_{hkl} is the crystalline size perpendicular to $(h k l)$ pane,

λ --- The wave length of X-ray used,

β --- Width of diffraction peak i.e., Full Width Half Maxima (FWHM)

θ --- The peak position.

3.3 X-ray density:

X- ray density (d_x) was determined using the following equation and it was found to be 5.20 gm/cm^3

$$d_x = ZM/Na^3$$

Where ‘Z’ is the number of molecules per unit cell ($Z=8$), ‘M’ is the molecular weight and ‘N’ is Avogadro number.

3.4 AFM MEASUREMENTS

The AFM measurements (NANO SURF 2.0, VERSION 1.6) of the film annealed at 550 C as shown in the figure 3 below displays a particle size of the film to be around 20 nm , and an rms roughness of around 5.2 nm

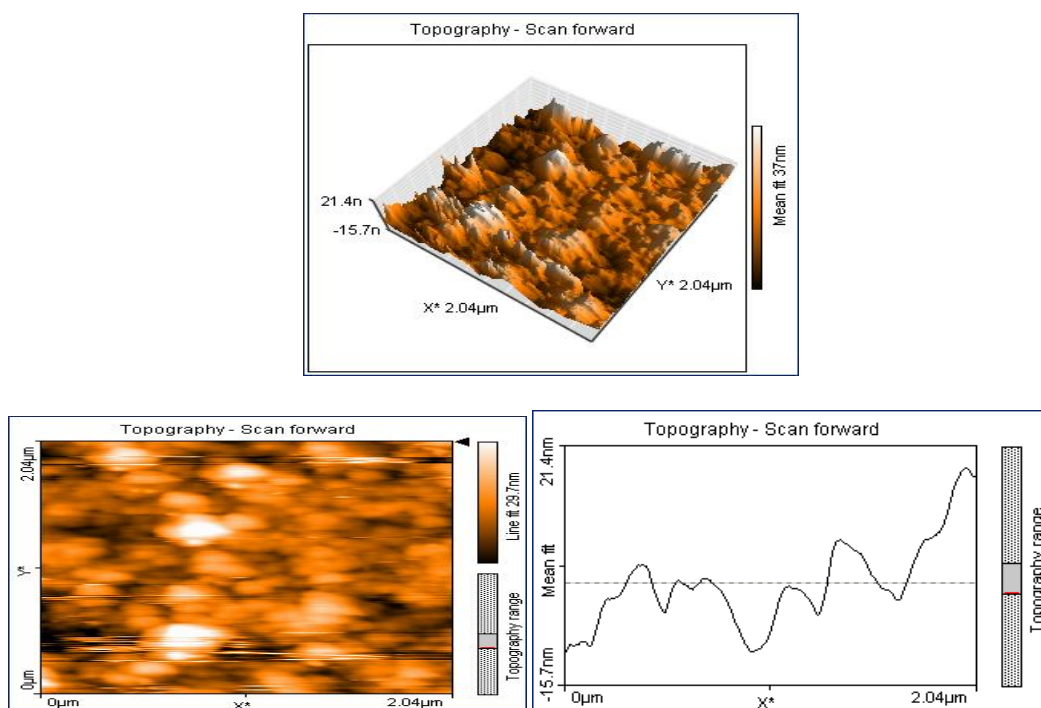


Fig 3 AFM images of samples

Film annealed at $550 \text{ }^{\circ}\text{C}$

AFM Particle Size – 20 nm

Film roughness – 5.2 nm

3.5 ELECTRICAL PROPERTIES

For electrical measurements, stripe shaped, 3 mm long electrodes of Ag were prepared by using silver paste to form planar Ag/Ni_{1-x}Zn_xFe₂O₄/Ag structures and copper probes were pressed directly on the films to use as electrodes. Typical current voltage (log I vs. V) characteristics of Ag/ Ni_{0.8}Zn_{0.2}Fe₂O₄ /Ag planar structure are shown in fig 4.

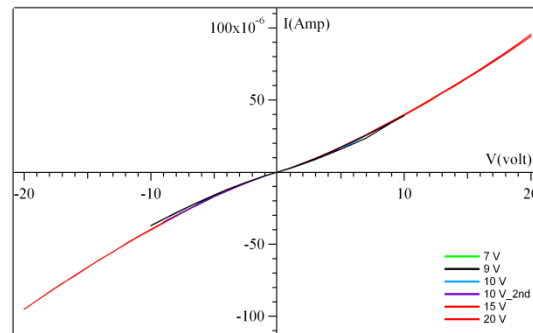


Fig 4 I-V characteristics of Ni_{0.8}Zn_{0.2}Fe₂O₄

The inset shows the I-V properties at low voltages. A continuous voltage sweep with a sequence -20V→0V→+20V→0V was applied through outer terminals and current was measured at the inner points. Current values for several voltage sweep cycles were recorded over a span of three to four hours to reproducibility of the results and even by reversing the polarity. The I-V of the film displays diode like dynamic characteristics [6]. It shows a nonlinear behavior that indicates different resistance at different bias. This behavior needs further investigation.

CONCLUSIONS

Ni_{0.8}Zn_{0.2}Fe₂O₄ nano thin film is successful prepared by spin coating method with particle size 20 nm. This ferrite is subjected I-V characteristics, from this characteristics we can concluded that this ferrite is not suggestible for switching property

References

1. M. G. Patil , V. C. Mahajan, A. K. Ghatage , and S. A. Patil, Indian J. Pure Appl.Phys.34, 166(1996).
2. M.Ul-Islam, M.Ashraf Chaccdhry, T. Abbas, and M. Umar, Mater. Chem..phys. 48, 227 (1997).
3. Iqbal MJ, Siddiquah MRJ Magn Magn Mater 320(2008) p 487
4. SS Bellad BK Chougule - Materials research bulletin, 33 1998, p.1165–1173
5. Cullity B D, Elements of X-ray diffraction Addition Wesley, Reading, Mass),1959, p132
6. Yamashiro T Jpn. J. Appl. Phys. 1973 12, 148

Excluded Energy and Relative Encircled Energy an important role in the Optical Imaging Systems with amplitude and apodised Parameters

B. Sambaiah* and D. KarunaSagar[†]

Optics Research Group, Department of Physics, University College of Science, O.
U., Hyderabad – 500 007, India*

Professor, Department of Physics, University College of Science, (O.U.), Hyderabad
– 500 007, India[†]

Email: sam.bokkala@gmail.com

ABSTRACT

Encircled Energy Factor (EE), Excluded Energy and Relative Encircled Energy are important corollaries of the Point Spread Function (PSF) of an optical system. In this paper, we have studied the Excluded Energy, Relative Encircled energy to understand their role as Point Image quality assessment parameters of Optical systems with amplitude apodised rotational symmetric filter functions.

Key-words: Mathematical Optics, Apodisation, Encircled Excluded Energy Factor, Relative Encircled Energy, Pupil Function etc..

1. Introduction

Encircled energy is an important parameter which can be studied as a measure of image quality. According to Wetherill¹, “Excluded energy” is the energy difference between total energy and the energy concentrated within a specified circle of radius δ . It is denoted with $E_x[\delta]$ and is also useful to study the structure of a specified ring in detail. It is also known as the “Dispersion Factor”, as designated by Dossier², higher value of this factor indicates better functioning of the pupil function. The most desirable pupil function is that which can minimize the excluded energy and maximize the encircled energy. Surender³ has remarked on the importance of the excluded energy as follows. “The contrast at the centre of the image of a black disc, seen against a uniform incoherent background is what can be interpreted as the physical significance of $E_x(\delta)$ ”. If the energy in the outer rings of the diffraction pattern is to be examined in details, it is convenient to focus more on the excluded energy rather the encircled energy. This aspect has made the study on $E_x(\delta)$ more

useful, in various techniques of apodisation, to change the ring structures in a pre-determined way. The study of $E_x(\delta)$ is also useful in several photometric analysis. Relative encircled energy the most important corollary of the Point Spread Function (PSF) is the "Relative Encircled Energy". It measures the fraction of the total energy in the PSF, which lies within a specified radius ' δ ' in the plane of observation or detection. We will designate this important parameter by the symbol $REE(\delta)$. Lord Rayleigh⁴ was the first to point out the importance of the encircled energy factor to find the illuminations in the various rings of the diffraction pattern and presented a formula for calculating the

same. When a converging spherical wave is diffracted by a circular aperture the classical theory of focusing predicts that light energy is highly concentrated in the geometrical focal plane. It means that there is a maximum amount of energy within a receiving circle of a given radius centered at the aperture axis and placed in the geometrical focal plane which contains more energy per unit area than any other plane parallel to it. Thus, it comes out that the $EE()$ is the primary corollary of the and is the factor, which describes the integrated behavior of the point source diffraction image. It is a sensible image quality evaluation parameter of an optical system, with this phenomena Excluded energy Factor, Relative Encircled energy are very close to Encircled energy we have studied in this paper these two parameters. Murthy⁵ was investigated the PSF Based corollaries viz Encircled energy Excluded energy and energy increment in the presence of defocusing by employing co-sinusoidal amplitude filters. Karunasagar⁶ has studied the Encircled energy Relative encircled energy and Excluded energy, Displaced energy and zonal increment for rotationally symmetric Ratnam⁷ similar studies have been carried out for multiple coded apertures and complimentary multiple annuli coded apertures Steal⁸ and Mehatha⁹ have studied the encircled energy in the Fraunhofer diffraction pattern with circular apertures with triangular apodisation filters Surender, Seshagiri Rao and Mondal¹⁰ have studied the encircled energy and its complimentary quantity, Excluded energy using Lanczos apodisation filters. Keshavulu¹¹ was investigated the encircled energy in the presence of individual and the combined effects of defocusing and primary spherical aberration in the case of optical systems apodised

by shaded aperture systems. V.N Mahajan¹² have obtained a closed form solution for the excluded power, using the well known recurrence relations of Bessel functions of the first kind. In our investigation we are using filter function $f(r) = \cos \pi\beta r$ and get results for Excluded energy Factor, Relative encircled energy, we have discussed the results with figures and tabular. This paper organized as follows.

2. mathematical formulations:

Excluded Energy can be represented mathematically as Excluded Energy and Relative-Encircled Energy apodisation Parameters. According to WETHERELL (1980) excluded energy is the energy difference between total energy and energy concentrated within a specified circle of radius δ . It can be represented a

$$XE(\delta) = 1 - EE(\delta) \quad (2.1)$$

It is an important quality factor to examine the performance of the pupil function and also to study the structure of a specified ring in detail. Minimum value of this factor indicates well functioning of the pupil function. The best pupil is that which can minimize the excluded energy and maximize the encircled energy. The above equation (3.11) can be expressed in terms of intensity as,

$$XE(\delta) = \frac{\int_{\delta}^{\infty} |G_F(\theta, Z)|^2 Z dz}{\int_0^{\infty} |G_F(\theta, Z)|^2 Z dz} \quad (2.2)$$

Where $G(0, z)$ is the amplitude in the image plane at a point z , it is defined¹⁴ as

$$G_F(\theta, Z) = 2 \int_0^1 f(r) J_0(\theta r) J_0(Zr) r dr \quad (2.3)$$

Where $f(r)$ is the pupil function which defines the nature of transmission over the pupil of the aperture of the optical system the pupil-function $f(r)$ can be mathematically represented as

$$f(r) = \cos(\pi\beta r) \quad (2.4)$$

Where β is the apodisation parameter which controls the amplitude transmission of the pupil and r is the normalized distance of a point on the pupil from its centre and $J_0(Zr)$ is the Bessel function of the first kind with zero order for the argument (Zr) finally from equation (2.1) and (2.2) we get the mathematical expression for $EE[\delta]$. Relative Encircled energy is defined as the ratio of the light energy within a specified circle of radius δ centered on the diffraction head due to the non-airy pupil to the total light energy in the diffraction pattern due to the Airy-pupil. Mathematically, it can be represented as:

$$EE_{rel}(\delta) = \frac{\int_0^\delta |G_F(\rho, Z)|^2 \rho d\rho}{\int_0^\infty |G_A(\rho, Z)|^2 \rho d\rho} \quad (2.5)$$

where the subscripts A and F stand for Airy filtered and non-airy pupils respectively. It has been observed that for rotationally symmetric pupil functions, For Airy pupil function the apodisation parameter β values are difference from zero, Non-airy pupil function the apodisation parameter β values are equal to zero in this case the numerator function $G_F(\rho, z)$ is defined as below,

$$G_F(\rho, Z) = 2 \int_0^1 J_0(\rho r) r dr \quad (2.6)$$

Substituting amplitude functions in both cases airy pupil and non-airy pupil in equation (2.5) then we get corresponding results for Relative Encircled energy.

3. Results and Discussions

The results from the amplitude studies made on the effects of apodisation and defect-of-focus, when the optical imaging system is under the influence of primary spherical aberration and primary coma are presented in the following sections. WOLFRAM MATHEMATICA-7.0 has been used to evaluate the relevant expressions for the corollaries of point spread function. The apodisation parameter β is varied from 0 to 1 in steps of 0.25.

i. Excluded Energy [xe (δ):

Expression (2.2) has been employed in evaluating the excluded energy values for various values of δ ranging from 0.2 to 12 in steps of 0.2 when the apodisation parameter (β) is varied from 0 to 1.0 in increment of 0.25. Excluded energy (XE (δ)) represents the fraction of the total energy in the diffraction pattern present in the outer specified ring. The desirable energy distribution is one, which corresponds to the greatest concentration of energy in the near vicinity of the center of the diffraction pattern. Hence, the minimization of this factor and consequent maximization of the encircled energy have a greater influence in mitigating the degrading effects and resulting in enhanced quality of the imaging system. The variations of excluded energy with δ for various amounts of apodisation are presented in Table 1. Figs.1 and 2 gives the distribution of excluded energy for defect-of-focus $\phi_d = \pi$ and primary spherical aberration $\phi_s = \pi$. It is clear that the excluded energy decreases rapidly for values of δ up to 3.8 for $\beta = 0.50$ which in terms of results in the enhancement of the encircled energy for $\beta = 0.50$.

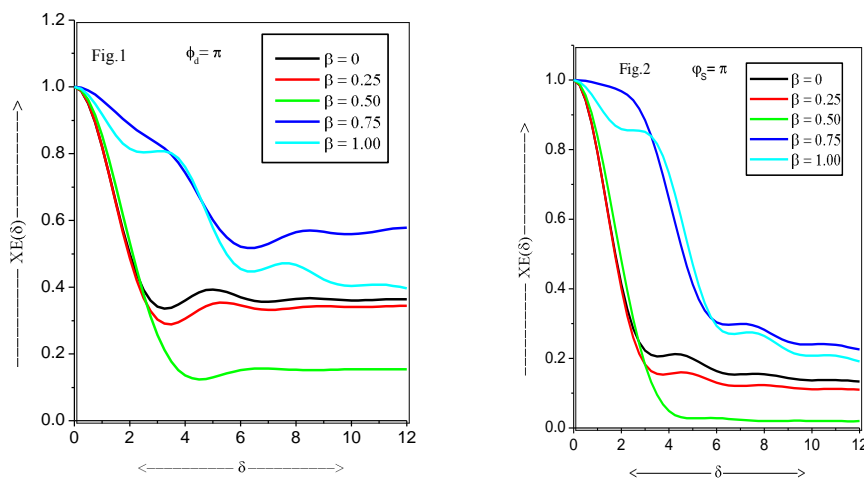
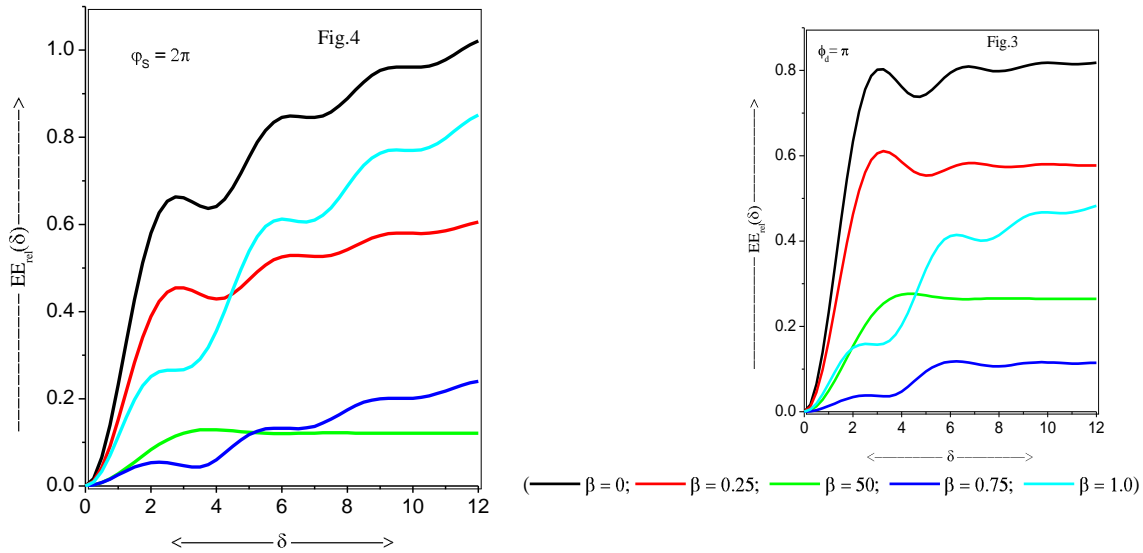


Fig.1 & 2 Excluded Energy with δ various values of β

TABLE 1 Excluded Energy

δ = 0.25	$\phi_a = \pi$					$\phi_s = 2\pi$			
	$\beta = 0$	$\beta = 0.25$	$\beta = 0.5$	$\beta = 0.75$	$\beta = 1.0$	δ	$\beta = 0$	β	
0.25	0.0166	0.0182	0.0077	0.0081	0.0101	0.25	0.0137	0.0205	0.0099
	0.0131	0.0118							
0.50	0.0645	0.0708	0.0301	0.0310	0.0387	0.50	0.0531	0.0794	0.0389
	0.0507	0.0456							
0.75	0.1378	0.1516	0.0657	0.0650	0.0818	0.75	0.1128	0.1692	0.0850
	0.1080	0.0968							
1.00	0.2282	0.2520	0.1119	0.1050	0.1330	1.00	0.1851	0.2789	0.1453
	0.1779	0.1584							
1.25	0.3256	0.3611	0.1657	0.1450	0.1855	1.25	0.2612	0.3957	0.2159
	0.2520	0.2226							
1.50	0.4201	0.4685	0.2235	0.1800	0.2327	1.50	0.3324	0.5071	0.2928
	0.3226	0.2820							
1.75	0.5034	0.5649	0.2818	0.2060	0.2700	1.75	0.3917	0.6025	0.3717
	0.3832	0.3309							
2.00	0.5695	0.6436	0.3376	0.2214	0.2949	2.00	0.4343	0.6742	0.4485
	0.4296	0.3660							
2.25	0.6155	0.7008	0.3882	0.2261	0.3079	2.25	0.4581	0.7178	0.5198
	0.4606	0.3870							
2.50	0.6419	0.7362	0.4318	0.2214	0.3120	2.50	0.4629	0.7315	0.5827
	0.4773	0.3963							
2.75	0.6515	0.7519	0.4670	0.2096	0.3121	2.75	0.4504	0.7158	0.6350
	0.4828	0.3983							
3.00	0.6489	0.7522	0.4937	0.1943	0.3139	3.00	0.4234	0.6725	0.6753
	0.4811	0.3986							
3.25	0.6399	0.7424	0.5120	0.1817	0.3226	3.25	0.3870	0.6056	0.7028
	0.4764	0.4024							
3.50	0.6303	0.7284	0.5227	0.1824	0.3421	3.50	0.3503	0.5236	0.7171
	0.4723	0.4137							
3.75	0.6255	0.7161	0.5270	0.2061	0.3742	3.75	0.3280	0.4439	0.7187
	0.4712	0.4346							
4.00	0.6299	0.7103	0.5263	0.2531	0.4183	4.00	0.3372	0.3981	0.7083
	0.4742	0.4645							
4.25	0.6456	0.7146	0.5221	0.3144	0.4714	4.25	0.3838	0.4200	0.6875
	0.4808	0.5010							
4.50	0.6718	0.7298	0.5157	0.3799	0.5288	4.50	0.4570	0.5070	0.6580
	0.4893	0.5400							
4.75	0.7052	0.7540	0.5087	0.4406	0.5849	4.75	0.5406	0.6261	0.6220
	0.4972	0.5770							

5.00	0.7410 0.7834 0.5020 0.4905 0.6345 0.5024 0.6079	5.00	0.6206 0.7480 0.5824
5.25	0.7742 0.8131 0.4964 0.5261 0.6738 0.5039 0.6296	5.25	0.6880 0.8547 0.5419
5.50	0.8011 0.8390 0.4926 0.5468 0.7007 0.5021 0.6410	5.50	0.7375 0.9364 0.5036
5.75	0.8198 0.8583 0.4904 0.5548 0.7154 0.4992 0.6427	5.75	0.7675 0.9895 0.4703
6.00	0.8300 0.8703 0.4899 0.5543 0.7199 0.4984 0.6375	6.00	0.7791 1.0145 0.4442
6.25	0.8334 0.8754 0.4905 0.5507 0.7181 0.5032 0.6293	6.25	0.7761 1.0157 0.4268
6.50	0.8326 0.8756 0.4919 0.5496 0.7143 0.5166 0.6230	6.50	0.7635 0.9995 0.4182
6.75	0.8305 0.8734 0.4934 0.5560 0.7130 0.5401 0.6234	6.75	0.7474 0.9740 0.4170
7.00	0.8301 0.8715 0.4948 0.5731 0.7176 0.5733 0.6342	7.00	0.7345 0.9484 0.4212
7.25	0.8336 0.8720 0.4958 0.6018 0.7302 0.6144 0.6572	7.25	0.7304 0.9318 0.4285
7.50	0.8423 0.8765 0.4963 0.6401 0.7510 0.6598 0.6912	7.50	0.7389 0.9311 0.4364
7.75	0.8560 0.8854 0.4962 0.6842 0.7781 0.7052 0.7329	7.75	0.7606 0.9495 0.4433
8.00	0.8733 0.8981 0.4957 0.7290 0.8086 0.7463 0.7773	8.00	0.7924 0.9847 0.4479
8.25	0.8921 0.9129 0.4949 0.7695 0.8387 0.7796 0.8191	8.25	0.8290 1.0301 0.4498
8.50	0.9100 0.9279 0.4940 0.8019 0.8651 0.8027 0.8541	8.50	0.8646 1.0774 0.4489
8.75	0.9250 0.9412 0.4932 0.8243 0.8854 0.8153 0.8795	8.75	0.8943 1.1193 0.4457
9.00	0.9357 0.9513 0.4926 0.8366 0.8987 0.8187 0.8943	9.00	0.9152 1.1506 0.4408
9.25	0.9419 0.9577 0.4923 0.8410 0.9053 0.8161 0.8995	9.25	0.9264 1.1692 0.4351
9.50	0.9442 0.9605 0.4923 0.8408 0.9069 0.8114 0.8975	9.50	0.9289 1.1755 0.4295
9.75	0.9440 0.9608 0.4925 0.8398 0.9061 0.8091 0.8918	9.75	0.9252 1.1721 0.4247
10.00	0.9431 0.9599 0.4928 0.8419 0.9055 0.8130 0.8860	10.00	0.9188 1.1633 0.4212



ii. Relative Encircled Energy REE(δ):

We used the equation (2.5) For evaluating the Relative Encircled energy, the results have been shown in figures 3 and 4 the table 2. The case of the optical system with defocusing $\phi_d = \pi$ and primary spherical aberration $\phi_s = 2\pi$. The graphical representation has been given as relative encircled energy curves in For non-Airy Pupil function that is apodisation parameter $\beta=0$ for various values of δ gives same value of Relative Encircled Energy, for high value of δ that is $\delta=12$ with various values of δ then the Relative Encircled energy become identical it is evident for convergence. For lower values of δ in the range $1 \leq \delta \leq 2$ the Relative Encircled energy increases 2.26. For higher value of δ in the range $3 \leq \delta \leq 12$ then the Relative Encircled energy increases and instantly small decreasing after that Relative encircled energy become identical and it goes to infinite.

4. Conclusions

The pupil function $f(r) = \cos \pi \beta r$ is rotationally symmetric. For higher values of β with various values of δ then the Excluded energy factor and Relative encircled energy both increases monotonically and becomes identical it happens with the effect of our consideration filter function and Bessel function.

Table 2 Relative encircled energy

δ	$\varphi_s = 2\pi$					$\beta = 1.0$	δ	$\phi_a = \pi$	
	$\beta = 0$	$\beta = 0.25$	$\beta = 0.5$	$\beta = 0.75$	$\beta = 1.0$			$\beta = 0$	β
0.25	0.0103	0.0076	0.0027	0.0011	0.0030	0.25	0.0046	0.0036	0.0017
	0.0004	0.0004							
0.50	0.0402	0.0297	0.0108	0.0042	0.0115	0.50	0.0179	0.0143	0.0067
	0.0015	0.0015							
0.75	0.0872	0.0645	0.0237	0.0091	0.0245	0.75	0.0392	0.0313	0.0147
	0.0035	0.0032							
1.00	0.1472	0.1093	0.0409	0.0153	0.0401	1.00	0.0671	0.0536	0.0255
	0.0061	0.0052							
1.25	0.2153	0.1607	0.0613	0.0224	0.0564	1.25	0.0996	0.0799	0.0385
	0.0094	0.0074							
1.50	0.2862	0.2149	0.0840	0.0298	0.0715	1.50	0.1350	0.1087	0.0532
	0.0134	0.0094							
1.75	0.3550	0.2684	0.1079	0.0371	0.0839	1.75	0.1713	0.1385	0.0689
	0.0179	0.0112							
2.00	0.4174	0.3182	0.1319	0.0439	0.0927	2.00	0.2065	0.1678	0.0852
	0.0230	0.0124							
2.25	0.4702	0.3616	0.1552	0.0498	0.0979	2.25	0.2391	0.1954	0.1015
	0.0285	0.0131							
2.50	0.5114	0.3969	0.1768	0.0547	0.0998	2.50	0.2679	0.2204	0.1171
	0.0345	0.0131							
2.75	0.5400	0.4234	0.1962	0.0585	0.0996	2.75	0.2921	0.2419	0.1317
	0.0408	0.0123							
3.00	0.5562	0.4408	0.2129	0.0612	0.0984	3.00	0.3114	0.2596	0.1450
	0.0474	0.0106							
3.25	0.5611	0.4495	0.2266	0.0630	0.0976	3.25	0.3256	0.2733	0.1567
	0.0542	0.0080							
3.50	0.5562	0.4506	0.2374	0.0641	0.0986	3.50	0.3352	0.2833	0.1667
	0.0611	0.0042							
3.75	0.5436	0.4453	0.2453	0.0649	0.1027	3.75	0.3407	0.2898	0.1750
	0.0679	0.0015							
4.00	0.5261	0.4353	0.2506	0.0658	0.1106	4.00	0.3427	0.2934	0.1815
	0.0746	0.0074							
4.25	0.5064	0.4225	0.2537	0.0673	0.1226	4.25	0.3421	0.2945	0.1865
	0.0810	0.0148							
4.50	0.4875	0.4088	0.2549	0.0695	0.1379	4.50	0.3397	0.2939	0.1900
	0.0870	0.0231							
4.75	0.4720	0.3962	0.2547	0.0726	0.1550	4.75	0.3363	0.2921	0.1924
	0.0925	0.0319							
5.00	0.4619	0.3860	0.2536	0.0762	0.1722	5.00	0.3326	0.2896	0.1937
	0.0975	0.0410							
5.25	0.4577	0.3794	0.2520	0.0800	0.1878	5.25	0.3291	0.2870	0.1943
	0.1017	0.0498							

5.50	0.4591	0.3766	0.2502	0.0837	0.2005	5.50	0.3262	0.2846	0.1943
	0.1053	0.0580							
5.75	0.4644	0.3770	0.2486	0.0870	0.2092	5.75	0.3243	0.2827	0.1940
	0.1082	0.0653							
6.00	0.4717	0.3798	0.2473	0.0897	0.2138	6.00	0.3232	0.2814	0.1935
	0.1104	0.0715							
6.25	0.4790	0.3838	0.2464	0.0914	0.2142	6.25	0.3229	0.2806	0.1929
	0.1120	0.0765							
6.50	0.4847	0.3877	0.2460	0.0921	0.2113	6.50	0.3232	0.2804	0.1923
	0.1130	0.0801							
6.75	0.4878	0.3906	0.2460	0.0917	0.2059	6.75	0.3239	0.2805	0.1918
	0.1135	0.0825							
7.00	0.4878	0.3920	0.2463	0.0902	0.1994	7.00	0.3247	0.2809	0.1914
	0.1136	0.0839							
7.25	0.4847	0.3915	0.2468	0.0878	0.1930	7.25	0.3254	0.2814	0.1912
	0.1133	0.0843							
7.50	0.4793	0.3892	0.2474	0.0847	0.1882	7.50	0.3259	0.2818	0.1911
	0.1129	0.0839							
7.75	0.4723	0.3856	0.2479	0.0813	0.1860	7.75	0.3262	0.2821	0.1911
	0.1123	0.0831							
8.00	0.4649	0.3812	0.2482	0.0780	0.1867	8.00	0.3263	0.2823	0.1912
	0.1117	0.0820							
8.25	0.4581	0.3766	0.2484	0.0751	0.1902	8.25	0.3261	0.2823	0.1913
	0.1112	0.0808							
8.50	0.4528	0.3725	0.2484	0.0729	0.1956	8.50	0.3257	0.2822	0.1914
	0.1107	0.0797							
8.75	0.4496	0.3694	0.2483	0.0716	0.2018	8.75	0.3253	0.2820	0.1915
	0.1103	0.0789							
9.00	0.4484	0.3675	0.2480	0.0712	0.2077	9.00	0.3249	0.2818	0.1916
	0.1101	0.0783							
9.25	0.4490	0.3668	0.2477	0.0714	0.2123	9.25	0.3246	0.2816	0.1916
	0.1100	0.0780							
9.50	0.4506	0.3670	0.2473	0.0720	0.2154	9.50	0.3243	0.2814	0.1917
	0.1100	0.0780							
9.75	0.4525	0.3678	0.2470	0.0726	0.2166	9.75	0.3242	0.2813	0.1917
	0.1101	0.0781							
10.00	0.4540	0.3688	0.2468	0.0730	0.2162	10.00	0.3241	0.2812	0.1917
	0.1102	0.0784							

5. References

1. Wetherell, W.B., In "Applied Optics and Optical engineering", Vol. VIII Academic, Press, New York, Editors. R.R. Shamon, and, J.C. Wyant). p.212, 272,215,202,207, 209, (1980).
2. Dossier, B., Rev. Opt., 33, 57, 147 and 267 (1954).
3. Surendar, K., Ph. D Thesis, Osmania University, Hyderabad, India (1986).
4. Rayleigh Lord, Phil. Mag. 8, 261 (1879).

5. Murty, P.V.V.S., P.32, in Thesis entitled “Studies On Diffracted Field and Imaging Characteristics of Optical Systems with Cosinusidal Apodisation Filters” presented to Osmania University, for Ph.D (1992).
6. Karunasagar, D., P. 62, Ph.D, Thesis” Studies on the Performance of Optical Systems apodised with generalized Hanning amplitude filters (2003).
7. C.V. Ratnam, “Fourier Analytical Investigations on The performance of Multiple- Annuli coded Apertures in Multiplexed Tomography”, Ph.D. Thesis, Osmania University, Hyderabad, India, (2005).
8. Steel, W.H., Opt. Acta. 3, 65 (1956).
9. Mehta, B.L., Atti Fond. G. Ronchi, 30, 17 (1975).
10. Surendar, Sheshagiri Rao., Mondal, P.K., Acta Cienca Indica 18, p.6134 (1992).
11. Keshavulu, Ph.D. Thesis Osmania University. India (2001).
12. V.N. Mahajan, “Diffraction Theory of Optical Images and Aberrations”, Part-II, SPIE Press, Massachusetts, U.S.A. (2004).
13. P. Thirupathi, Vol. 3 (6). Pp.3935-3943., Advances in applied science And research (2012).

Structural and Magnetic properties of Mg Ferrite

D.Ravi Kumar^a, B.Kiran Kumar^a, Ch.Abraham Lincoln^{a*}, D.Ravinder^b
a. Dept of chemistry, University College of science, Osmania University
Hyderabad-7, India.

b. Dept of Physics, University College of science, Osmania University
Hyderabad-7, India.

*Corresponding author email: chal_lincoln@yahoo.com.

ABSTRACT:

Mg Nano ferrite has been synthesized by the citrate gel auto combustion method, in this method citric acid used as chelating agent. Synthesized powder were calcinated at 500°C for four hours in the air and characterized by XRD, SEM and EDS. XRD analysis shows that the cubic spinal structure of the spinel ferrite and the crystalline size (D) were found 34 nm. Scanning Electron Microscopy (SEM) studies revealed that the Nano nature of the compound. An elemental composition of the sample was studied by using Energy Dispersive Spectroscopy (EDS). FTIR studies reveal that the tetrahedral and octahedral of the sample it has the spinel structure of the sample. Magnetization measurements were obtained at room temperature by using pulse field hysteresis loop technique, which showed that the calcinated sample exhibited super paramagnetic behavior.

Keywords: Citrate gel auto combustion method, XRD, SEM, EDS, FTIR, VSM.

Introduction

Spinel ferrites with the general formula AFe_2O_4 ($A = Mn, Co, Ni, Mg, \text{ or } Zn$) are very important magnetic materials because of their interesting magnetic and electrical properties with chemical and thermal stabilities [1]. Magnesium ferrite ($MgFe_2O_4$) is one of the most important ferrites. It

has a cubic structure of normal spinel-type and is a soft magnetic n-type semiconducting material, which finds a number of applications in heterogeneous catalysis, adsorption, sensors, and in magnetic technologies [2] The ordered magnetic materials such as nanorods and nanowires have

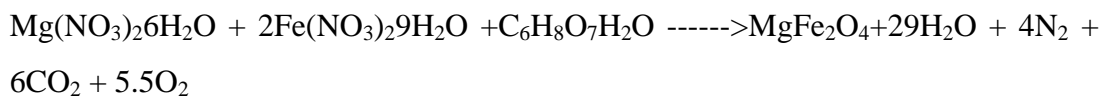
Currently attracted a great interest due to their enhanced magnetic property [3,4] Spinel magnesium ferrite possesses many attractive properties like high catalytic

activity, high magnetic permeability, humidity and gas sensing characteristics. Moreover, Mg ferrite has high resistivity, high Curie temperature, and environmental stability makes it most suitable candidate for wide range of sensing applications [5, 6].

Experimental method

Mg ferrite nanoparticles were prepared by citrate gel auto combustion method using a nitrates of $\text{Mg}(\text{NO}_3)_2 \cdot 6\text{H}_2\text{O}$, $\text{Fe}(\text{NO}_3)_3 \cdot 9\text{H}_2\text{O}$ and citric acid used as chelating agent, all these are dissolved in double distilled water, P^{H} maintained 7 with ammonia solution. Obtained powder was calcinated at 500°C . Further the powder was characterized to XRD SEM EDS FTIR and magnetic properties.

Chemical Reaction:



Synthesis flow chart:

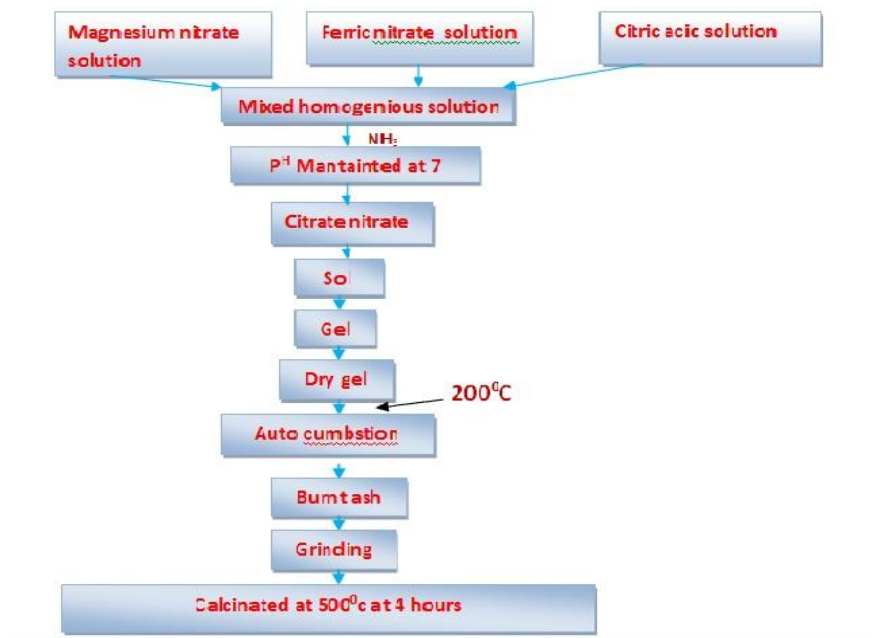


Figure 1. Flow chart of citrate gel auto combustion.

Results and Discussions:

XRD studies:

The powder x-ray diffraction of the prepared sample has been recorded to identify the crystalline phases present in the sample. From the XRD patterns the lattice parameter, particle size, x-ray density and unit cell of MgFe_2O_4 has been determined. The crystallite size (D) was calculated for all the composition using maximum intensity peak from Scherrer's formula [7].

$$\text{Crystallite size } D = 0.91\lambda/\beta\cos\theta$$

Where λ = wavelength of X-Ray;

β = Full width half maximum (radians);

θ = Bragg's angle at the peak position

Crystalline size is 34.54 nm.

Lattice parameter (a) of the individual composition was calculated by using the following formula

$$a = d \cdot \sqrt{h^2 + k^2 + l^2}$$

Where a = lattice parameters; d = inter planar spacing and $h k l$ are the miller indices lattice parameter is 8.35 nm.

The X-Ray density (dx) is calculated using the following formula [8]

$$\text{X-Ray density (dx)} = 8M / Na^3(\text{gm/cc})$$

Where M = molecular weight of the sample, N = Avogadro's number, a = lattice parameter, X ray density is 4.52 gm/cm³.

The Volume of the unit cell is calculated as $V=a^3$ unit cell is 583.438 Å³.

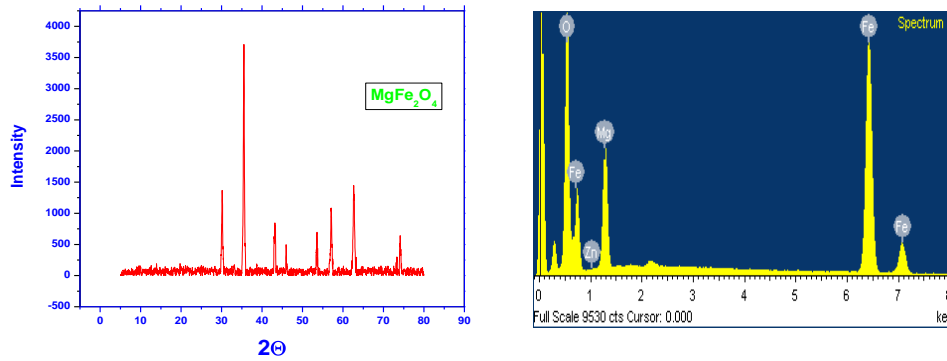


Figure 2.XRD patterns of MgFe₂O₄ .

SEM And EDS

SEM technique was used to study the morphology of the MgFe₂O₄ samples. SEM images of the Magnesium ferrite sample have given in below Fig 3. The micrographs show the presence of particles that are agglomerated together. A close inspection would reveal the presence of particles showing cubic faces. The distribution of particles is uniform and it can be seen that the particles are well below the size of 100 nm, which supports our prediction of grain size determined using Scherrer's formula

The composition of the MgFe₂O₄ has been determined by the EDS and the patterns obtained are shown in Fig 3. The specimen shows the presence of Mg, Fe, and O in the sample and did not contain any other elements.

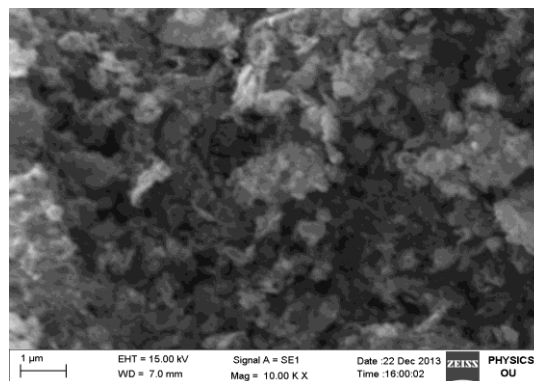


Figure 3.SEM and EDS pattern of MgFe₂O₄ .

FTIR

The FTIR spectra of the prepared sample are shown in below fig. the inspection of FTIR spectra shows two absorption bands as a common feature of the spinel ferrites. The band position is V1 and V2. The high frequency band V1 is assigned to intrinsic vibration of the tetrahedral groups and low frequency band V2 is assigned to the octahedral (10-11). The difference in the band position is expected because of the difference in the $\text{Fe}^{+3} \text{O}^{-2}$ distance from octahedral and tetrahedral complexes.

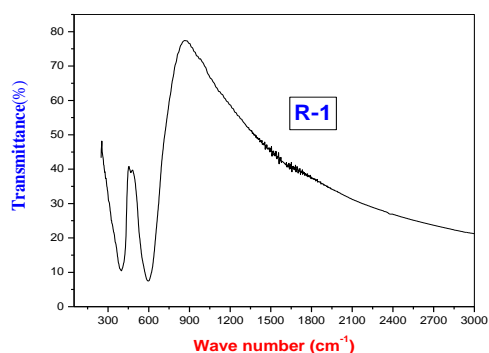


Figure 4. FTIR patterns of MgFe_2O_4 .

Magnetic properties:

To understand the magnetic properties of nano ferrite, it is characterized using vibrating sample magnetometer (VSM). The hysteresis loop traced at room temperature for MgFe_2O_4 is shown in Fig. 5. The values of the saturation magnetization (M_s), coercivity (H_c) and remnant magnetization (M_r) are obtained. Figure 5. shows the characteristic hysteresis loop of the typical sample of MgFe_2O_4 sample recorded at room temperature. saturation magnetization (M_s) is a 79.59 (emu/g), coercive force [H_c] is a 137.09 (Oe), remnant magnetization (M_r) is a 19.09 (emu/g). The hysteresis loop explains the soft ferri magnetic nature of the synthesized MgFe_2O_4 .

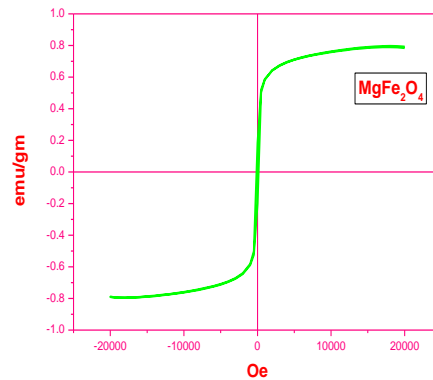


Figure 5. VSM patterns of MgFe_2O_4 .

Conclusions:

- Nano structures of MgFe_2O_4 have been successfully synthesized by citrate gel auto combustion method.
- In fact, XRD measurements display the formation of magnesium ferrite, MgFe_2O_4 , as a single phase.
- SEM micrographs of the composition indicate the morphology of the particles is similar. They reveal largely agglomerated, well defined nano particles of the sample powder within homogeneous broader grain size distribution.
- EDS data give the elemental % and atomic % in the magnesium ferrites and it shows the presence of Mg, Fe and O without precipitating cations.
- FTIR studies reveal that tetrahedral and octahedral of the spinel ferrites characterization.
- Vibrating sample magnetization studies reveal that the ferromagnetic materials.
- We believe that the MgFe_2O_4 could have potential in some new applications as ferromagnetic for nano composites, separation, anodic material in lithium ion batteries, catalysts, and as electronic material for nano devices and storage devices.

Acknowledgement

Authors thankful to Prof. G.Venkateswarlu, Head, Dept of Chemistry, and Prof M.vittal, BOS, University College of Science, for their support & encouragement to carry out this research work and to the characterization of XRD facilities to the lab.

References

1. R. Valenzuela, *Magnetic Ceramics* (Cambridge University Press, Cambridge, 1994)
2. R.J. Willey, P. Noirclerc, G. Busca, *Chem. Eng. Commun.* 123, 1 (1993). doi:10.1080/00986449308936161
3. Z.H. Hua, R.S. Chen, C.L. Li, S.G. Yang, M. Lu, X.B. Gu, Y.W.Du, *J. Alloys Compd.* 427, 199 (2007). doi:10.1016/j.jallcom.2006.02.048
4. G. Ji, S. Tang, B. Xu, B. Gu, C. Du, *Chem. Phys. Lett.* 379, 484(2003). doi:10.1016/j.cplett.2003.08.090
5. S.A. Oliver, R.J. Willey, H.H. Hamdeh, G. Oliveri, G. Busca, *Scr. Mater.* 33 (1995)1695.
6. G. Busca, E. Finocchio, V. Lorenzelli, M. Trombetta, S.A. Rossini, *J. Chem. Soc. Faraday, Trans.* 92 (1996) 4687.
7. M.J. Iqbal; m.N. Ashiq; P. Hernandez-Gomez; J.M. Munoz, *J. Magn. Magn. Mater.* 2008, 320, 881.Doi:10.1016/j.jmmm.2007.09.005
8. B.Viswanatham; V.R.K. Murthy; *Ferrie Materials: Science and Technology*, Narosa Publishing House, 1990,4.
10. R.D.Waldron, *phys.Rev.*99(1955) 1727
11. S.T.Hafner *Z.Fur.Krist.*115(1961) 331

A study on Infrared Spectroscopy of Human Blood

U. Vijaya Ushasree, Kaleem Ahmed Jaleeli & Adeel Ahmad
Biophysics Research Laboratory, Department of Physics, Nizam College
(Autonomous), Osmania University, Hyderabad – 500 001, India
e. mail: dr_adeelahmad@yahoo.com sunilusha999@gmail.com

ABSTRACT

The paper reports IR spectroscopic data on human blood and its constituents. IR analysis has been made on whole blood, plasma and serum. The characteristic spectral bands pertaining to fibrinogen, hemoglobin, erythrocyte membrane lipids and other plasma proteins are identified. The paper explores the possibility of disease analysis by IR spectroscopy.

Key words: FTIR spectroscopy; Human blood; Plasma; Blood Serum.

1. Introduction

In recent past, mid infrared and UV - Visible spectroscopic methods were efficiently used in the fields of biological sciences [1, 2]. Implementation of these techniques reduces time, resources and cuts cost. IR spectroscopy is emerging as a potential diagnostic tool in the medical and pharmacological fields to provide information about the different chemical structures of healthy and pathological tissues [3]. Blood being the chief circulatory medium of our body, reflects the physiological and pathological changes that take place in the tissues, which leads to the changes in the various plasma, serum and cellular constituents. In view of this, an attempt is made to analyse human blood spectroscopically in the IR range.

2. Materials and Methods

2.1. Sample collection

Collection and handling of a sample is an integral part of obtaining valid results. Here a disposable plastic syringe was used to collect venous blood. Blood samples were collected from healthy volunteers. Blood collection tubes with anticoagulant (EDTA- Ethylene Diamine Tetra Acetate) were inverted gently as soon after collection as possible to prevent clotting. The blood samples were brought to the

laboratory in siliconized bottles, keeping them in ice cooled thermos. The samples were kept in refrigerator at 4⁰C until used. Investigations were done within two to three hours after collection.

2.2. Preparation of sample

First, spectral grade pure KBr powder was dried in an oven upto 60⁰c for 24 hours. Then 1 gm powder was taken in an agate motor and was ground until it becomes fine powder. The ground powder was mixed with blood sample and transferred into the cylinder bore so that it was distributed across the polished face of lower plate. The polished face of the second plate towards the powder was inserted in to the bore by a plunger. The die assembly was connected to a vacuum pump and was kept under vacuum for approximately 2 min so as to remove air from the sample disk. The die was dismantled and the KBr disk was removed without touching its faces. Here, FTIR spectrometer of make *Bruker Optics* and model *Tensor 27* was used.

3. Results and Discussion

Fig.1.presents FTIR spectrum of Human blood, which reveals a series of bands with different intensities and the spectral data is shown in Table 1. For the systematic analysis, IR spectrum is divided into three regions. Region I is from 4000 to 3000 cm⁻¹, concerned with water and hydroxyl group. This region is of considerable interest, because it reveals the nature of hydrogen bonding. Region II is 3000 to 1500 cm⁻¹, wherein bands for functional groups are observed. In this region, major IR absorption pertaining to fibrinogen occurs. Region III is 1500 – 200 cm⁻¹, which has significant importance in the context of biological minerals and their combinations.

The spectra of human blood indicate the presence of bands characteristics of water molecule and also of some functional groups concerned with proteins and lipids. The IR band at wave numbers 3294 cm⁻¹ and 3065 cm⁻¹ are related to Amide A and Amide B respectively. The dominating band at 1396 cm⁻¹ may be originated due to the important protein of blood Fibrinogen. This band is related to the stretching C=O symmetric stretching vibrations of COO⁻. A band around 2960 cm⁻¹ is due to the -C-H asymmetric stretching of -CH₃ in Fatty acids, Phospholipids,

Cholesterol esters. The band at 1106 cm^{-1} is related to HbO_2 , exhibits $\nu_{(\text{O}_2)}$ bond. The two most intensive bands are centered at 1652 cm^{-1} and 1547 cm^{-1} in the FTIR spectrum of human blood. They correspond to the Amide I and Amide II. Both bands are representative of secondary structures of proteins. Amide I peak arises from C=O hydrogen bonded stretching vibrations, and Amide II is attributed to C-N stretching; NH and CH_2 bending modes. Amide I and Amide II absorption bands are associated also with specific secondary sub- structures, such as α -helix, β -sheet, β -turn and random coil. The bands at 1307 cm^{-1} and 1248 cm^{-1} are related to Amide III bond components of proteins (C-N). The band at 1170 cm^{-1} corresponds to C-O-C asymmetric stretching vibrations of phospholipids. The bands at 1106 cm^{-1} , 1170 cm^{-1} and 1248 cm^{-1} are associated with triglycerides of human blood. The band at 2936 cm^{-1} is related to platelets due to -C-H symmetric stretching of $-\text{CH}_2$

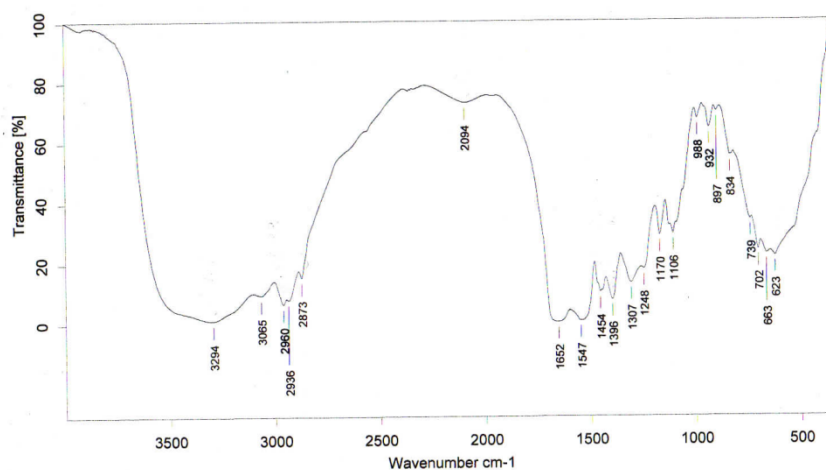


Fig. 1. FTIR spectra of human blood

Table 1 FTIR spectral data of human blood

Wave Number (cm^{-1})	Characteristic vibrations of functional groups
3294	Amide A, N-H stretching of proteins
3065	Amide B, N-H stretching
2960	-C-H asymmetric stretching of $-\text{CH}_3$ in Fatty acids, Phospholipids, Cholesterol esters
2936	-C-H symmetric stretching of $-\text{CH}_2$, Platelets
2873	-C-H symmetric stretching of $-\text{CH}_3$
2094	
1652	Amide I. – helical structures (C=O)

1547; 1454	Amide II Peak region – Protein (NH, C-N) CH ₂ bend
1396	C=O symmetric stretching vibrations of COO ⁻ Fibrinogen
1307, 1248	Amide III band components of proteins (C-N)
1170	C-O-C asymmetric stretching vibrations of phospholipids
1106,	HbO ₂ exhibits $\nu_{(O_2)}$ band, Oxy hemoglobin
1106, 1170, 1248	Triglycerides

References

- [1] Sylwia Olsztyńska-Janus, Katarzyna Szyborska-Małek, Marlena Gąsior-Głogowska, Tomasz Walski, Małgorzata Komorowska, Wojciech Witkiewicz, Celina Pezowicz, Magdalena Kobielarz, Sylwia Szotek, Acta of Bioengineering and Biomechanics, Vol. 14, No. 3(2012), pp. 101 – 115.
- [2] A. Barth, Infrared Spectroscopy of Proteins, Biochim. Biophys. Acta, Vol. 1767(2007), pp. 1073–1101.
- [3] M. Polakovs, N. Mironova-Ulmane, A. Pavlenko, E. Reinholds, M. Gavare and M. Grube, Spectroscopy: An International Journal, Vol. 27, No. No. 5-6 (2012), pp. 367-371

Electrical Studies In Silver Doped Gallium Oxide Glasses

K. Veerabadra Rao, C. Anuradha, G.Aravind

*Department of Physics, Methodist College of Engineering & Technology,
Hyderabad*

ABSTRACT: The glasses of composition $x\text{AgI}-(100-x)[0.02\text{Ga}_2\text{O}_3-0.49\text{Ag}_2\text{O}-0.49\text{B}_2\text{O}_3]$ where $x=5$ to 30 in steps of 5 weight% are prepared by melt quenching technique. XRD, FTIR and DSC investigations are carried out on all glasses to understand physical characteristics of the prepared glasses. Electrical characterization is done in terms of DC and AC conductivities. DC conductivity at room temperature increased from 10^{-4} to 10^{-2} Scm^{-1} with increasing concentration of AgI. DC activation energy (E_{dc}) is found to decrease from 0.36 to 0.19 eV with increasing concentration of AgI. From the Impedance spectroscopy real and imaginary parts of impedances (Z' , Z'') plots plotted, and by using Z-View equivalent software R-C circuit parameters are obtained from Cole-Cole plots and relaxation times also calculated. The quantitative analysis of these results indicates that the electrical conductivity of these glasses is enhanced by addition of AgI.

Keywords: Electrical properties, oxide; Ga_2O_3 , Ag_2O , XRD

1. Introduction

Portable electronic devices, omnipresent nowadays, require small-size power sources which should be more efficient, durable, reliable and safer for the environment than those available now. To meet growing and urgent needs for such power sources it is vital to carry out the research on many prospective ideas: miniaturized fuel cells, rechargeable microbatteries, etc. One of specific tasks in this research is the development of solid electrolytes (polycrystalline, amorphous or composite) for rechargeable silver microbatteries [1,2]. Though the ionic conductivity of many silver glasses, especially those with high contents of AgI, can be suitable for battery applications at moderate temperatures, some disadvantages of those glasses such as, e.g. their brittleness or low thermal stability threshold, limit the prospects of their practical use. One of possible solutions to circumvent the drawbacks of glassy electrolytes is to produce composites based on these glasses. There have been already explored several interesting approaches to prepare composites based on AgI and

other components, e.g. confining AgI particles in pores of porous alumina [3], elaborating systems containing AgI and Al₂O₃ xerogels and aerogels [4] or 'sintered' mixtures of AgI and alumina powder [5].

Several electrical studies on glassy materials revealed that glasses under certain circumstances can be super ionic conductors [1–3]. These glassy materials are of technological interest in view of their applications such as biosensors, storage batteries and fuel cells etc.,. The conductivity depends on the nature and content of the modifier oxide and also glass former compositions [4, 5]. The incorporation of alkali halides or metal halides in to the mixed glass formers [6, 7] is considered to be predominant factor playing the role of enhancing the conductivity of the conventional glasses to reach the values of super ionic materials. The nature of the interaction between metal ions (Ag⁺) and amorphous molecules is usually studied by different techniques. The structure and the electrical properties of silver ion-conducting borate-based glasses have been reported in the literature [8, 9]. Borate glasses exhibit well-known and unique structural features. The fast ion conducting glasses are characterized by greater freedom of movement of Ag⁺ ions. The mobility of Ag⁺ ions associated with an iodide environment is considered to be higher and based on the fact that increase in the percentage of AgI in the glass gives rise to higher conductivities [10-12]. One of the most widely used glass formers for the synthesis of super ionic conducting glass is B₂O₃.

It has been observed that in many cases the conductivity can be enhanced by mixing two different glass formers [10-15] with different coordination polyhedrons. But such mixtures have a strong tendency to phase separation at low modifier oxide molar ratio. Therefore, the complete substitution of one network former by another one has not always been possible [11]. Electrical conductivity investigation on AgI–Ag₂O–Ga₂O₃–B₂O₃ glass systems have been started recently. They also exhibit high ionic conductivity on suitable modifications of the network [16-18]. Correlation between structural properties and electrical behavior and electrical transport mechanisms is scanty in literature. So an attempt is made to fill the gap.

The present study aims to investigate the conductivity of the glasses containing high conducting electrolyte material such as AgI and Ag₂O by changing

the concentrations of AgI (dopant salt) with $[0.02\text{Ag}_2\text{O}-0.49\text{Ga}_2\text{O}_3-0.49\text{B}_2\text{O}_3]$. Silver oxide has been chosen as a network modifying oxide, since silver ions possess high ionic conductivity compared to alkali modifying cations such as Li^+ ion. The DC and AC conductivity studies provide significant information on the transport mechanism of the materials at room temperature as well higher temperatures, which in turn are aimed to correlate with the battery characteristics in future. AC conductivity is one of the common methods to characterize the bulk resistance of glasses. In the present investigation complex impedance measurements are used to study AC conductivity.

2. Experimental

2.1. Sample Preparation

$x\text{AgI}-(100-x)[0.02\text{Ga}_2\text{O}_3-0.49\text{Ag}_2\text{O}-0.49\text{B}_2\text{O}_3]$ where $x=5$ to 30 in steps of 5 weight% are prepared by melt quenching technique. Sample with $x=5$ is termed as Ga-1 and sample with $x=10$ is termed as Ga-2 and so on. Starting compounds AgI, Ag_2O , B_2O_3 and Ga_2O_3 are taken according to their molecular weight percentage (mol.wt.%) and mixed thoroughly in a porcelain crucible. This mixture is heated gradually to 850°C and maintained at that temperature for about 30 min. The melt was poured onto a stainless steel plate and pressed with another plate to obtain a thin disc (0.1–0.15 cm in thickness). For XRD, FTIR and DSC studies the obtained glasses are crushed into fine powders using pestle and mortar. All the samples are characterized by using XRD, FTIR, DSC and electrical characterization is done by impedance spectroscopy over a frequency range of 20Hz-3MHz and between room temperature (RT) and 573K. In the present investigation, X-ray diffraction measurements were carried out for all the samples using Philips X'pert pro with Cu K_α -radiation of wavelength $\lambda = 1.5418\text{\AA}$ between 10° and 90° of 2θ . The FTIR spectra for all the samples are recorded on BRUKER (Model: TENSOR 27) FTIR spectrometer. Pellets made with the mixture of Ga powder and KBr are used to record FTIR spectra in the range of $400-4000\text{ cm}^{-1}$ with 4 cm^{-1} resolution. All Ga samples were also characterized by differential scanning calorimeter (DSC-Q20) of Mettler make with a heating rate of 10Kmin^{-1} .

2.2. Electrical Characterization

For DC and AC characterization pellets of the glass samples (dia=1cm, thickness=1.5 mm approximately) both sides painted with silver for better electrode contact were used. For DC conductivity measurement the pellets were sandwiched between two spring loaded stainless steel blocking electrodes of surface area 3.14 cm². The sample holder is placed in a thermostat controlled furnace and temperature is varied from 30⁰C to 300⁰C (573K). DC conductivity measurements were carried out using Keithly 6485 pico ammeter in the temperature range of 303-573K for all Ga samples.

For AC electrical conductivity, impedance measurements were carried out by Waynekerr LCR-6440B impedance analyzer from 20 Hz to 3MHz over the temperature range of 303–573K for all Ga samples. The impedance data was analyzed by nonlinear curve fit method, and from those curves AC conductivity, activation energy, RC values and relaxation values were calculated.

3. Results and Discussions

3.1. XRD

The structural studies of the samples were analyzed using X-ray diffraction. XRD is extensively employed as a powerful characterization for determination of crystallographic structure of the materials. It gives the information regarding the lattice parameters, crystal structure and orientation, defects and crystallite size of the nanoparticles. In this investigation, PHILIPS Xpert X-ray diffractometer with CuK_α radiation source was used for determining the amorphous nature of the samples. Fig. 1 shows the XRD spectra of all the compositions of Ga glasses prepared by melt quench technique and the absence of any sharp peak confirms that all the samples are amorphous in nature.

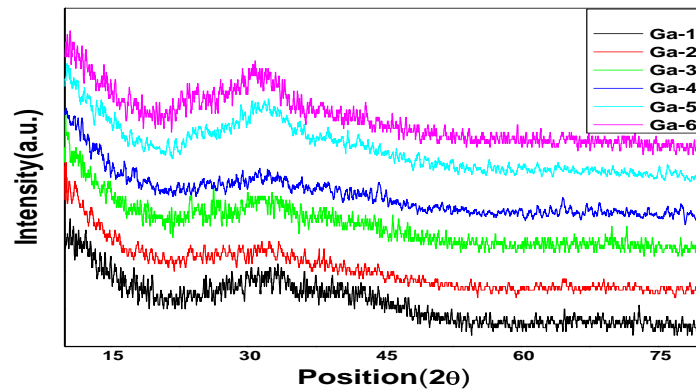


Fig. 1.XRD patterns of Ga glasses

3.2. Differential Scanning Calorimetry (DSC)

DSC thermo grams of different samples are shown in Fig.2. Glass transition temperature (T_g) is identified from DSC curves of each former composition of Ga samples and these values are observed to decrease from 380°C to 352°C with increasing the concentration of AgI.

The glass transition is a measure of strength of the glass, the observed fact that the glass transition temperature (T_g) decreases with the increasing AgI content in Ga system may be due to the fact that more and more number of bonds are destroyed within the glassy network, in order to allow its rearrangement to form a thermodynamically stable phase. This addition of AgI made samples more and more amorphous. this is observed and shown in Fig 3.

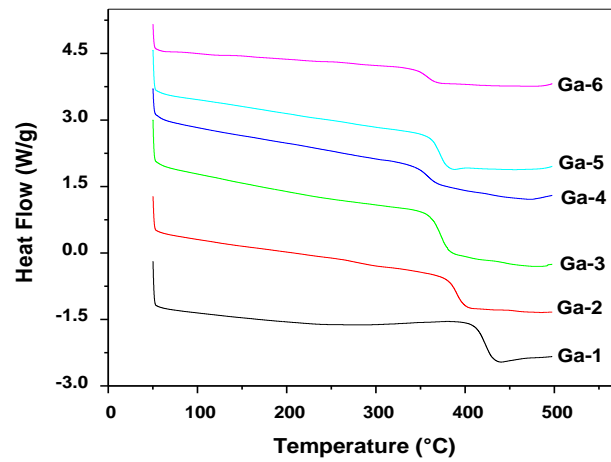


Fig. 2.DSC Curves of the all samples Temperature vs Heat Flow

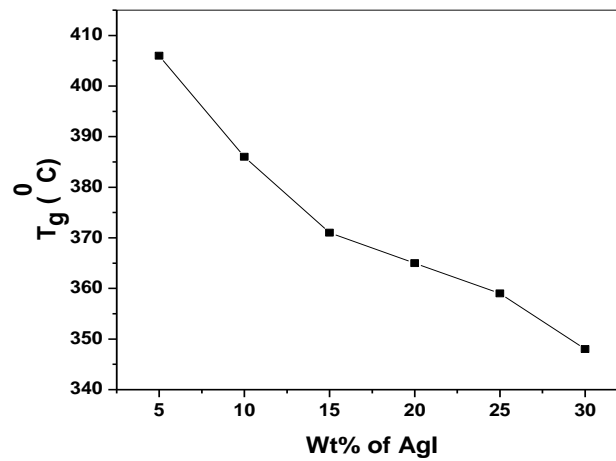


Fig. 3.Variation of glass transition temperature with AgI wt. %

3.3. Density

Table-1. AC conductivities and activation energies for all samples at room temperature

SNo.	Sample Name	Density
1	Ga-1	4.6024
2	Ga-2	5.2380
3	Ga-3	5.5097
4	Ga-4	5.7333
5	Ga-5	6.1546
6	Ga-6	6.3073

From the above table we conclude that as increase the concentration of dopant salt density increases, this indicates that strengthening of the glass increases.

3.5. AC Conductivity

Impedance spectroscopic technique utilizes alternating current (AC) with variable frequency and when measurements are carried out as a function of frequency and temperature, it is possible to determine the activation energies of the conduction and dielectric relaxation process. Variation of real part of impedance (Z') with imaginary part of impedance (Z'') at different temperatures for Ga-1, Ga-6 samples is represented in Fig.5(a) & (b) respectively. From these plots it is observed that the intercept of the semi-circle with the real axis at lower frequency shifts towards the higher frequency with increase in temperature. The intercept of the semi-circle at lower frequency with the real axis gives the equivalent DC resistance (bulk resistance- R_b) for each composition and at each temperature. DC resistance decreases with increase in temperature.

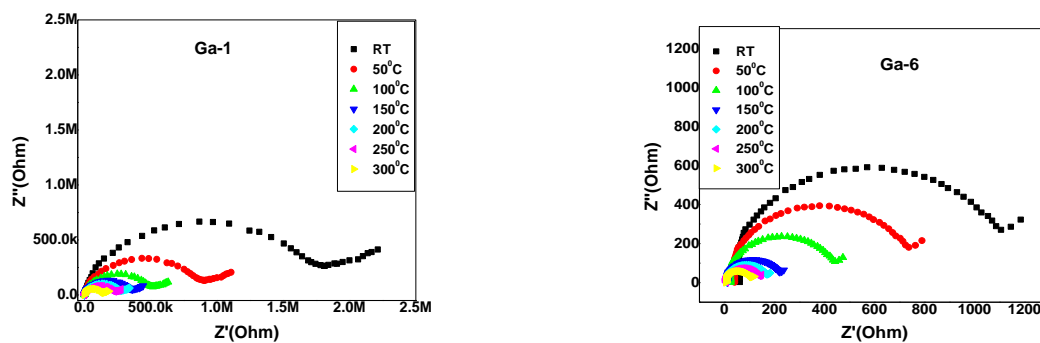


Fig. 5 (a) & (b). Cole-Cole plots of Ga-1 and Ga-6 samples at different temperatures

Variation of real part of impedance (Z') with frequency at different temperatures for Ga-1, Ga-6 samples is represented in Fig.6(a) & (b) respectively. It is observed that real part of impedance (Z') is both frequency and temperature independent up to about 300 kHz.

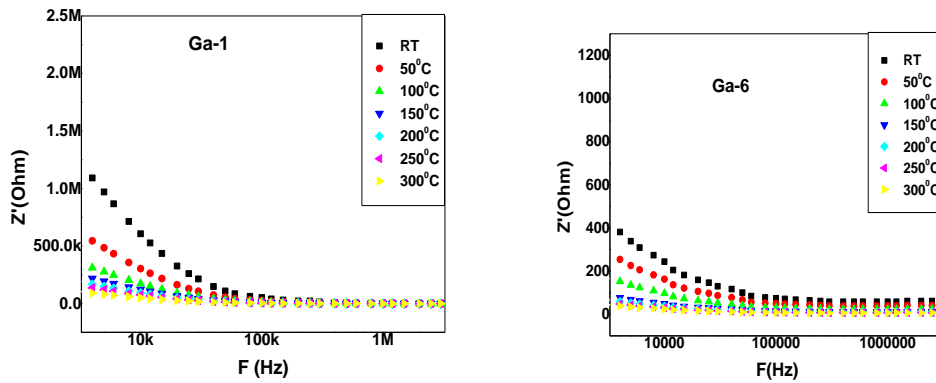


Fig. 6 (a) & (b). Cole-Cole plots of Ga-1 and Ga-6 samples at different temperatures

Variations of value of Imaginary impedance (Z'') with frequency at different temperatures for Ga-1, Ga-6 samples are represented in Fig. 7(a) & (b). It is observed that imaginary part of conductivity increases with the increasing the temperature at higher frequency region, and merged at lower frequencies for all temperatures.

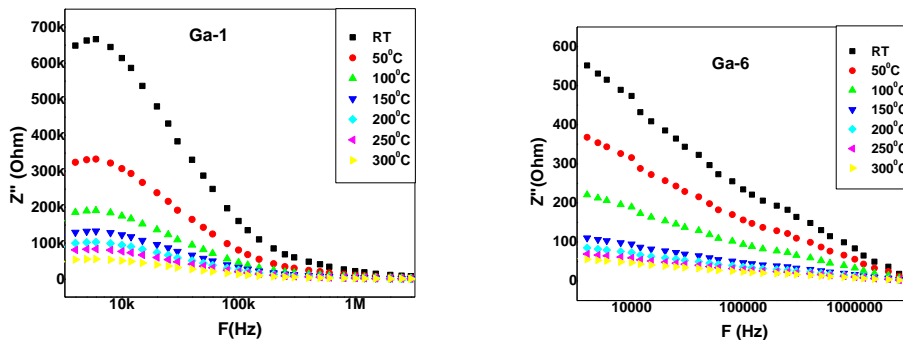


Fig. 7(a) & (b). Cole-Cole plots of Ga-1 and Ga-6 samples at different temperatures

DC conductivity values are found to vary between 10^{-5} Scm^{-1} (Ga-1) to 10^{-3} Scm^{-1} (Ga-6) at room temperature. It is observed from Fig. 8(a) the AC conductivity increased with increase of temperature. Higher temperatures favour the conduction in Ga glasses. DC conductivity increases with increasing AgI concentration, hence this favour the conduction in Ga glasses. Activation energies were calculated from Arrhenius equation. From Fig. 7(b) it is observed that AC activation energy decreases with increasing AgI concentration from 0.86 to 0.29eV. These values are

given in Table 2. Decrease in AC activation energy depends on increase in temperature at selected frequency. This behaviour is a characteristic of conductors with hopping charge carriers.

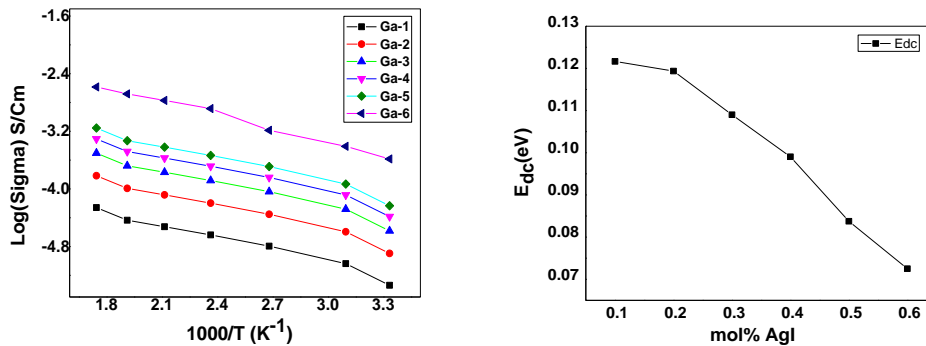


Fig.8 (a) & (b). Cole-Cole plots of Ga-1 and Ga-6 samples at different temperatures

Table-2.DC conductivities and activation energies for all samples at room temperature

SNo.	Sample	$\sigma_{dc}(S/Cm)$ RT(303K)	E_{dc} (eV)
1	Ga-1	5.80×10^{-5}	0.86
2	Ga-2	6.80×10^{-5}	0.77
3	Ga-3	2.80×10^{-4}	0.72
4	Ga-4	8.30×10^{-4}	0.68
5	Ga-5	6.94×10^{-4}	0.59
6	Ga-6	1.23×10^{-3}	0.53

The migration of mobile ions is described by the relaxation times. These values are tabulated in Table 2. We can observe from the table, relaxation time decreases with increase in temperature means that the relaxation frequencies are increasing. Observation of semi-circle in these plots indicates that the samples are parallel combination of a resistance and a capacitance, which are respectively, the bulk resistance R_b and the bulk capacitance C_b of the solid electrolyte [19-20]. The straight line observed as a tail at the low frequency region represent a capacitance effect at the electrode and electrolyte interface and it is called double layer capacitance (C_{dl}). Further the inclination of this tail in the low frequency region is due to the presence of the asymmetric nature of the distributed elements in the

electrode and electrolyte interface. Relaxation time τ of the distributed elements at the interface is not a single valued, but it is distributed continuously around a mean value [20]. The amount of the inclination in the low frequency straight line is related to the width of the relaxation time distribution.

Table -3. Variation of Resistance, Capacitance and relaxation time values with temperature for Ga-1, Ga-6 samples

Temperature	Ga-1			Ga-6		
	R _b (ohm)	C _b (nf)	τ (ms)	R _b (ohm)	C _b (nf)	τ (ms)
303K	396597	0.671	0.13	31120	6.39	0.13
323K	278721	0.762	0.098	20754	7.67	0.099
373K	157842	1.445	0.072	7788	17.05	0.073
423K	76245	2.023	0.056	4447	23.87	0.057
473K	30487	3.145	0.042	2784	33.42	0.042
523K	10784	4.864	0.027	1435	42.12	0.037
573K	5872	5.735	0.011	874	48.17	0.017

3.6. Cole-Cole plots of all samples at room temperature and at higher temperature

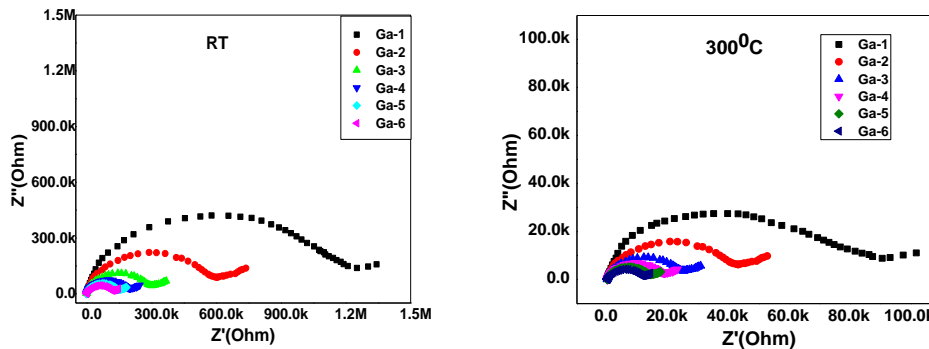


Fig.8 (a) & (b). Cole-Cole plots of Ga-1 and Ga-6 samples at different temperatures

From above plots we can observed that the conductivity is maximum for Ga-6 which is highest dopant of AgI at room temperature and at highest temperature and the conductivity increases with increasing temperature and with concentration also and in below graphs we presented variation of frequency with imaginary impedance for all samples at room temperature and at (300°C) 573K.

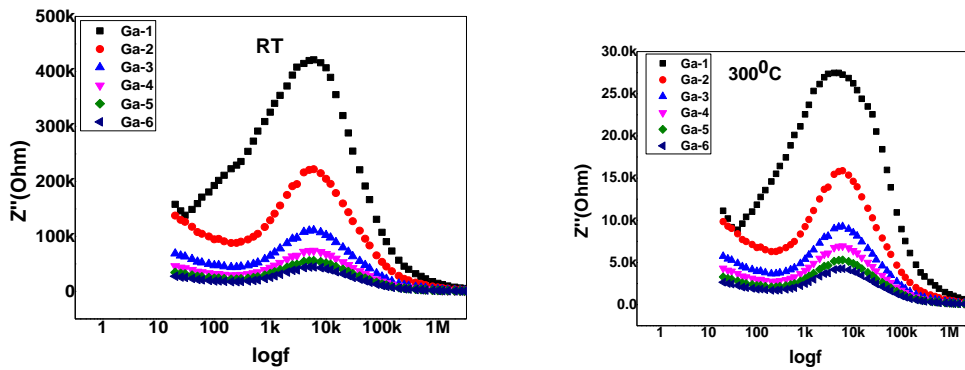


Fig. 9 (a) & (b). Cole-Cole plots of Ga-1 and Ga-6 samples at different temperatures

Conclusions

The glassy nature of all former compositions of prepared Ga samples by melt quenching method is confirmed from X-ray diffractogram spectra. Peak assignments obtained from FTIR spectra. DSC spectra confirm the glassy nature. The decrease in glass transition temperature indicates the strengthening the glass increases with increasing dopant salt. Similar nature is observed in density. AC conductivity plots show the presence of relaxation. Impedance spectroscopy also reflects the involvement of conducting ions. This confirms hopping of charges between the coordinating sites, local structural relaxation and segmental motion of chains. Even the FTIR, DSC results supports that increase of AgI concentration favor better amorphous network in Ga glasses.

The fast ion conducting glasses are characterized by greater freedom of movement of Ag^+ ions because these ions are not held in the lattice sites or anion cages firmly. Hence addition of network modifier such as AgI introduces ionic bonds usually associating non-bridging oxygen ions with modifying cations.

REFERENCES

1. N. Baskaran, G. Govindaraj, A. Narayanasamy, J. Power Sources 55 (1995) 153–157.
2. Y.-G. Guo, Y.-S.Hu, J.-S. Lee, J. Maier, Electrochem. Commun. 8 (2006) 1179–1184.
3. M. Nagai, T. Nishino, J. Mater. Synth.Process. 6 (1998) 197–201.
4. K. Tadanaga, K. Imai, M. Tatsumisago, T. Minami, J. Electrochem. Soc.147 (2000) 4061–4064.
5. N.F. Uvarov, P. Vanek, M. Savinov, V. Zelezny, V. Studnicka, J. Petzelt, Solid State Ionics 127 (2000) 253–267.
6. El-Damrawi G, (1994) J Non-Cryst Solids 176:91
7. Stangrennec MK, Elliott SR (1994) Solid State Ionics 73:199
8. Saunders GA, Metcalfe RD (1996) Phys Rev B 53:53
9. Ingram MD (1987) PhysChem Glasses 28:215
10. Magistris A (1993) In: Scrosati B, Magistris A, Mari CM, and Mariatto G (eds) Proceedings of the Nato advanced research workshop on fast ion transport in solids. Kluwer Academic Publishers, Netherlands, p 213
11. El-Damrawi G, Hassan AK, Meikail MS (1996) PhysChem Glasses 37:101
12. El-Damrawi G (1995) J PhysCondens Matter 8:1557
13. Chiodelli G, Vigano GC, Magistris A, Villa M (1983) Solid State Ionics 8:311
14. Chiodelli G, Magistris A, Villa M, Bjorkstam JL (1982)Mater Res Bull 17:1
15. Magistris A, Chiodelli G (1983) Solid State Ionics 9 & 10:611
16. Coppo D, Duclot JJ, Souquet JL (1996) Solid State Ionics 90:111
17. Shastry MCR, Rao KJ (1989) Solid State Ionics 37:17
18. Lefterova ED, Angelov PV, Dimitriev YB (2000) PhysChem Glasses 41:362
19. Jayasinghe GDLK, Bandaranayaka PWSK, DissanayakeMAKL, Gunawardane RP (1995)
20. Solid State Ionics 78:199
21. Rodrigues ACM, Duclot MJ (1988) Solid State Ionics.
22. El-Damrawi G, Abd-El-Maksoud S (2000) PhysChem
23. Rossignol S, Reau JM, Janguy B, Videau JJ, Portier J (1993) J Non-Cryst Solids 55:77

24. Jayasinghe GDLK, Coppo D, Bandaranayake PWSK, SouquetJL (1995) Solid State Ionics 76:297
25. R.J. Grant, M.D. Ingram, L.D.S. Turner, C.A. Vincent, J. Phys.Chem. 82 (1978) 2838.
26. M. Venkateswarlu , N. Satyanarayana J .Materials Science and Engineering B54(1998) 189-195.

Biosynthesis and Characterization of Silver Nanoparticles using young leaves extract of *Gymnosporia emarginata* and their antimicrobial activity

P. Shivakumar Singh¹, D.S.R. Rajender Singh², G.M. Vidyasagar^{*3}

¹Department of Botany, Palamuru University, Mahabubnagar-509001, Telangana,

²SV Govt. UG & PG College, Palem, Mahabubnagar Dist, Telangana, India.

^{*3}Medicinal Plants and Microbiology Research Laboratory, Department of Post-Graduate Studies and Research in Botany, Gulbarga University, Gulbarga – 585 106, Karnataka, India.

ABSTRACT

The enlargement of eco-friendly and trustworthy processes for the biosynthesis of nanoparticles has engrossed extensive attention in nanotechnology because of its incredible impetus in modulating metals into nanosized to their impending use for human profit. In the present report the young leaves extract of *Gymnosporia emarginata* was subjected for biosynthesis of silver nanoparticles (AgNPs), the manifestation, size, and shape of the silver nanoparticles are inherent by UV-visible spectroscopy, Transmission Electron Microscopy. The X-ray diffraction studies, energy dispersive X-ray analysis indicate that particles are crystalline in nature. Fourier transform infrared spectroscopy analysis revealed that the nanoparticles are covered with bio-moieties on their surface. The biosynthesised AgNPs were screened against *Fusarium oxysporum*, *Fusarium semitectum*, *Colletotrichum gloeosporioides*, *Aspergillus niger*, *E. coli*, *Bacillus subtilis*. As can be seen from the present report results, the bio functionalized silver nanoparticles thus produced have shown splendid antimicrobial effect. The synthesis prescription implicated is eco-friendly, graceful and hence high range manufacture of the same can be considered for using them in many bio-pharma applications.

Keywords: *Gymnosporia emarginata* (Celestraceae), AgNPs, UV, TEM, FTIR, Phyto-pathogens.

INTRODUCTION

Remedial plants and wild edible fruits play a chief role in the originality of novel beneficial agents for drug development. *Gymnosporia emarginata* is a shrub or small tree with medicinal properties belonging to the family Celestraceae. It is

commonly known as Dantha chettu in Telugu. *Gymnosporia emarginata* is an imperative plant as its leaves have been used in wound healing [1], anthelmintic activity [2] and other pharmaceutical purposes. However, the present plant young leaves is not being used in the synthesis of silver nanoparticles and their antibacterial activity have not been under taken in research anywhere in literature. Hence, taking into account all these facts the present search has been intended to optimise the young leaves extract concentration of *Gymnosporia emarginata* for the synthesis of AgNPs and their antibacterial activity. In this study, we show that young leaves extract of *Gymnosporia emarginata*, placed in a concentrated aqueous solution of AgNO₃, resulted in the reduction of the silver ions and formation of silver nanoparticles, and that an extract in aqueous solution of AgNO₃ resulted in the reduction of the silver ions and formation of silver nanoparticles. UV-visible (UV-vis) spectroscopy, transmission electron microscopy (TEM), scanning electron microscopy (SEM), energy dispersive X-ray analysis and Fourier transform infra-red spectroscopy (FTIR) were used to examine size and shape of silver nanoparticles in aqueous extract of *Gymnosporia emarginata*.

MATERIALS AND METHODS

Collection of source material

Fresh young leaves of *Gymnosporia emarginata* were collected from Palamuru university campus, Mahabubnagar District. Silver nitrate (AgNO₃) is procured from High Media Laboratories. Solutions were prepared with triply distilled water.

Preparation of the young leaves extract

Weighing 25 g of *Gymnosporia emarginata* young leaves were thoroughly washed in distilled water, cut into fine pieces and was smashed into 100 ml sterile distilled water and boil plant extract 5 to 6 min & filtered through Whatman No.1 filter paper (pore size 0.45 μm) and was further filtered through 0.22 μm sized filters. The extract was stored at 4⁰C for further experiments.

Synthesis of Silver nanoparticles from *Gymnosporia emarginata* young leaves extract

The aqueous solution of 1mM silver nitrate (AgNO_3) was prepared and used for the synthesis of silver nanoparticles. 10 ml of *Gymnosporia emarginata* young leaves extract was added into 90 ml of aqueous solution of 1 mM silver nitrate for reduction into Ag^+ ions and kept for incubation period of 90min at room temperature. Here the filtrate acts as reducing and stabilizing agent for 1mM of AgNO_3 .

Characterization

The formation of AgNP is verified by using UV-visible 5704SS ECIL spectrophotometer operated at with 1 nm resolution with optical length of 10 mm. UV-visible analysis of the reaction mixture was observed for a period of 300s. For the study of crystallinity, films of colloidal AgNP formed on Si(III) substrates by drop coating were used for X-ray-diffraction (XRD) study. The data were obtained using Ricago X-Ray Diffractometer (Japan), operated at 30 kV and 20 mA current with $\text{Cu K}\alpha$ ($\lambda = 1.54 \text{ \AA}$). The transmission electron microscopy (TEM) images were obtained using Technai-20 Philips instrument operated at 190 keV. Sample for this analysis were prepared by Rapid Biosynthesis of Silver Nanoparticles Using *Cordia dichotoma* young leaves 109 coating of aqueous AgNPs drops on carbon coated copper grids, kept for 5 min; the extra solution was removed using blotting paper. The film of TEM grid is exposed to IR light for drying. The powder sample of AgNP was prepared by centrifuging the synthesized AgNP solution at 10,000 rpm for 20 min. The solid residue formed is then washed with deionized water to remove any unattached biological moieties to the surface of the nano particles, which are not responsible for biofunctionalization and capping. The resultant residue is then dried completely and the powder obtained is used for FTIR measurements carried out on a Nicolet iS5 FTIR with diamond ATR.

Antimicrobial activity of AgNPs synthesised from *Gymnosporia emarginata* young leaves extract

Test microorganisms

Three fungi *Fusarium oxysporum*, *Fusarium semitectum*, *Colletotrichum gloeosporioides*, *Aspergillus niger*, three bacterial strains *Staphylococcus aureus*, *Escherichia coli*, *Bacillus subtilis* were used in the present study, all the tested strains were obtained from Chandigarh, sample centres, India. These test cultures were grown in PDA & nutrient broth (Himedia, M002) at 37°C and maintained on nutrient and potato agar slants at 4°C.

Agar-well diffusion technique

The assay was conducted by agar well diffusion method. About 15 to 20 ml of potato dextrose agar medium was poured in the sterilized petri dishes and allowed to solidify. The bacterial strains were suspended in a saline solution (0.85% NaCl) and adjusted to a turbidity of 0.5 Mac Farland standards (108 CFU/ml). 1 ml of fungal strains were spread over the medium using a sterilized glass spreader. Using flamed sterile borer, wells of 4 mm diameter were punctured in the culture medium. Required concentrations (40 mg⁻¹, 20 mg⁻¹, 10 mg⁻¹, 5 mg⁻¹) were added to the wells. The plates thus prepared were left for diffusion of extracts into media for one hour in the refrigerator and then incubated at 37°C. After incubation for 48h, the plates were observed for zones of inhibition. The diameter zone of inhibition was measured and expressed in millimetres. 1mM AgNO₃ solution and aqueous plant extract was used negative control. Whereas positive control used ketokonazole, streptomycene against fungi and bacteria (500 µg/ml conc.). The experiments were conducted in triplicates. The same method was followed for testing antibacterial activity using nutrient agar medium incubated at 37°C for 18h.

RESULTS AND DISCUSSION

Green synthesis of AgNPs from young leaves aqueous extract (slight yellowish) of *Gymnosporia emarginata* was approved out and reported in this research work. 01 ml of *Gymnosporia emarginata* young leaves aqueous extract was added to 250 ml of 1mM AgNO₃ solution. The appearance of the retort

concoction subsequent to 20 minutes at room temperature changes transparent to thick yellowish colour and this surveillance is strapping signal for the formation of AgNPs is exposed in Fig. 2.



Fig. 2 Synthesis of silver nanoparticles using *Gymnosporia emarginata* young leaves extract treating with AgNO₃ solution at room temperature

A) Formation of AgNPs ,B) silver nitrate(AgNO₃) solution, C) *Gymnosporia emarginata* aqueous young leaves extract.

The AgNPs formation and constancy of the condensed in the ordeal solution was examined by using UV–vis spectral analysis. The UV–vis range recorded from reaction mixture is shown in Fig. 3.

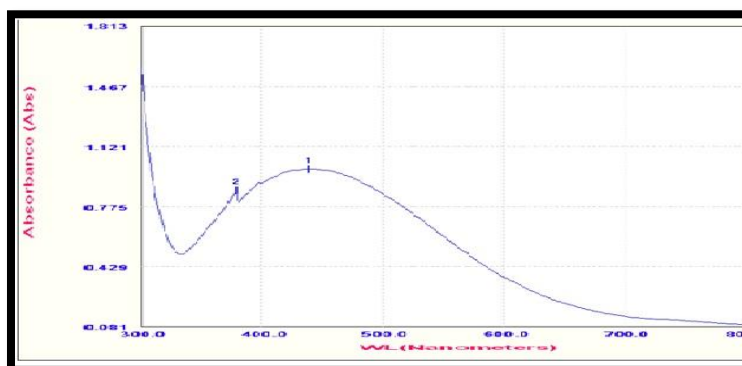


Fig. 3 UV–visa spectrum of bio functionalized AgNPs showing surface plasmon peak at 440 nm

The exterior plasmon height experimental at 440 nm is auxiliary confirmation of occurrence of AgNPs in the ordeal solution [25, 26]. The XRD results of AgNPs which advocate that the particles are of crystalline in nature. The dynamic diffraction peaks like (220), and (311), (380) observed. The recorded peaks competition well with the standard JCPDS file 04-0783 of silver shown in figure 4.

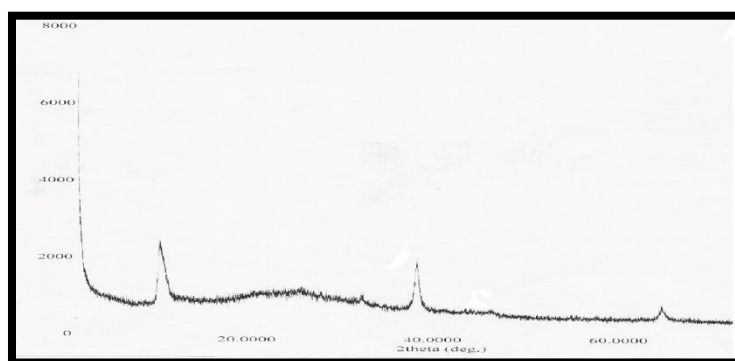


Fig. 4 XRD patterns of bio functionalized AgNPs

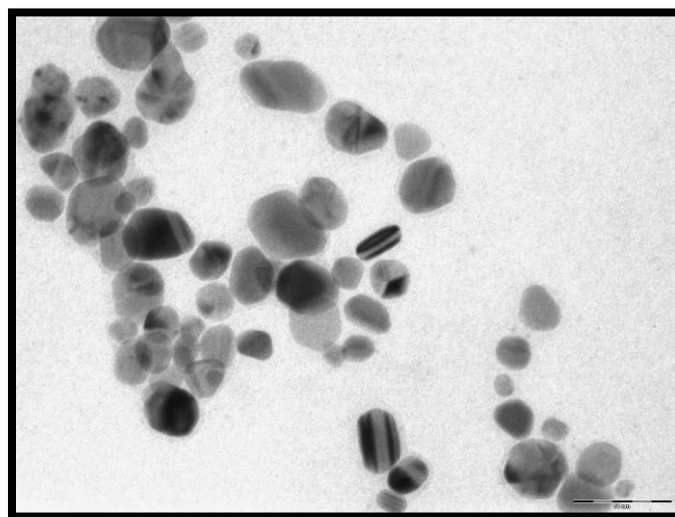


Fig. 5. TEM image of bio functionalized AgNPs, B. size pattern

By the TEM results the size and shape of AgNPs was clarified. A classic TEM image of green synthesized AgNPs, which suggests that the particles are uneven in shape. Some are round, spherical and triangular twisted particles with a altering size of 18.14–75.84 nm shown in figure 5.

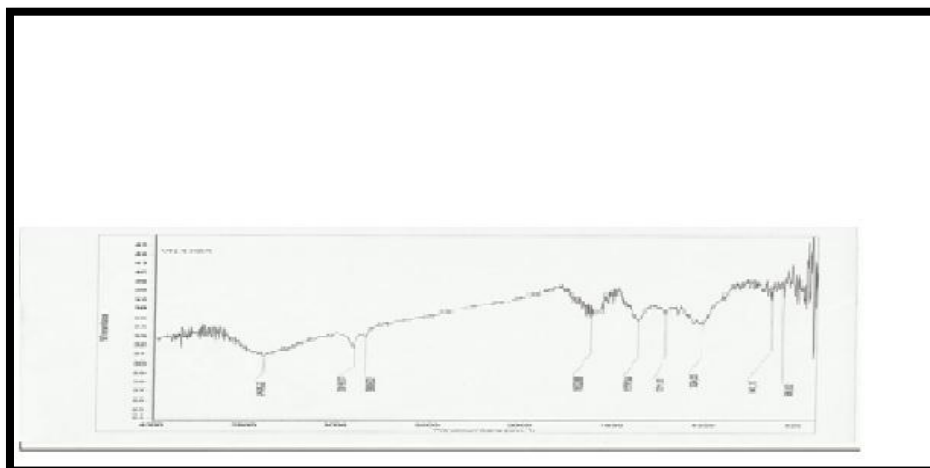
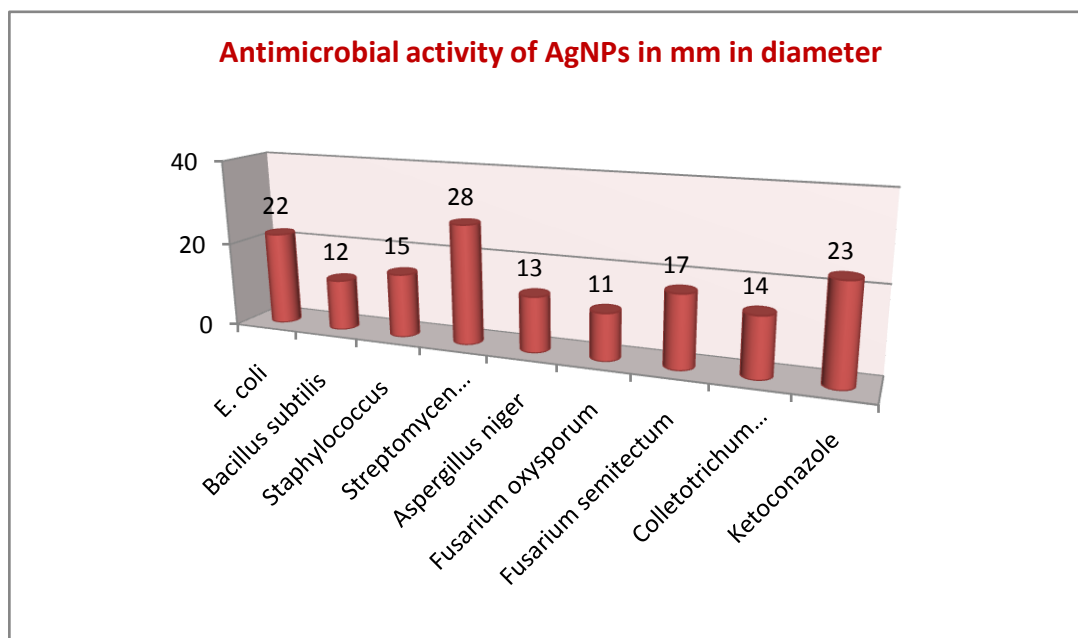


Fig 7. FTIR spectrum of bio functionalized AgNPs

The FTIR spectroscopy is a helpful method to study the middle–shell morphology of AgNPs is as shown in Fig. 6. The strong band at $1650, 53$ was observed.



Graph 1: Antimicrobial activity of AgNPs of *Gymnosporia emarginata*

Via young leaves extract of *Gymnosporia emarginata* based AgNPs antimicrobial activity at $80 \mu\text{l/well}$ showed maximum antifungal activity against *Fusarium semitectum* 17.00 mm followed by *Colletotrichum gloeosporioides* 14.00 mm. *Aspergillus niger* 13 and the least 11.00 mm diameter zone of inhibition showed by *Fusarium oxysporum*. Similarly, against bacteria the maximum activity of 22.00

mm was recorded against *E. Coli* followed by *S. aureus* 15.00mm and *B. Subtilis* 15.00 mm. The antimicrobial activity was straight relative to the meditation of AgNPs. Two negative controls i.e., AgNO₃ solution showed activity 06-07mm and plant aqueous extract have not showed activity due to their low concentration. Streptomycin sulphate and Ketoconazole used as standards alongside test organisms showed the inhibition zones of 23.00mm & 28.00mm, respectively (Graph.1).

Conclusion

The biosynthesis of silver nanoparticles from *Gymnosporia emarginata* young leaves was shown to be brisk and produce particles of varing crystallographic shapes. The synthesis method eco-friendly in nature. The synthesized particles showed antimicrobial activity was detected. The present upshot suggests that they are helpful in applications as antimicrobial agent.

ACKNOWLEDGMENTS

Authors are contented to thank IIT Mumbai for TEM analysis, JNTU Hyderabad for FTIR analysis, Dept of Physics Gulbarga University for XRD analysis, and Gulbarga University for providing the lab facilities.

REFERENCE

1. Santapan H and Henry AN. Council of Scientific & Industrial Research. New-Delhi, India; 1983 (reprint).
2. Kirtikar KR and Basu BD. Indian Medicinal Plants. Vol.1. Allahabad, India: Lalit Mohan Basu ; 1933. pp 577.
3. W.R. Rajesh, R.L. Jaya, S.K. Niranjana, D.M. Vijay, and B.K. Sahebrao, "Phytosynthesis of Silver Nanoparticle Using *Gliricidia sepium*," *Current Nanoscience*, Vol. 5, pp. 117- 122, 2009.
4. S. Arulkumar and M. Sabesan, "Biosynthesis and characterization of gold nanoparticle using antiparkinsonian drug *mucuna pruriens* plant extract," *International Journal of Research in Pharmaceutical Sciences*, Vol. 4, pp. 417- 420, 2010.

5. V. Arya, S. Yadav, S. Kumar and J.P. Yadav, "Antimicrobial Activity of *Cassia occidentalis* L (Leaf) against various Human Pathogenic Microbes," *Life Sciences and Medicine Research*, Vol. 9, pp. 1-11, 2010.
6. A. Bankar, B. Joshi, A.R. Kumar and S. Zinjarde, "Banana peel extract mediated synthesis of gold Nanoparticle," *Colloids and Surfaces B: Biointerfaces*, Vol. 80, pp. 45 – 50, 2010.
7. S.S. Shankar, A. Rai, A. Ahmad and M. Sastry, "Rapid synthesis of Au, Ag, and bimetallic Au core–Ag shell Nanoparticle using Neem(*Azadirachta indica*) leaf broth," *Journal of Colloid and Interface Science*, Vol. 2, pp. 275- 496, 2004.
8. S.P. Chandran, M. Chaudhary, R. Pasricha, A. Ahmad and M. Sastry, "Synthesis of gold nanotriangles and silver nanotriangles using Aloe vera plant extract," *Biotechnology Progress*, Vol. 22, pp. 577-579, 2006.
9. B. Amkamwar, C. Damle, A. Ahmad and M. Sastry, "Biosynthesis of gold and silver nanoparticles using *Embllica officinalis* fruit extract, their phase transfer and transmetallation in an organic solution," *Journal of Nanoscience and Nanotechnology*, Vol. 5, pp. 1665-1671, 2005.
10. S. Li, L. Qui, Y. Shen, A. Xie, X. Yu, L. Zhang and Q. Zhang, "Green synthesis of silver nanoparticles using *Capsicum annum* L. Extract," *Green Chemistry*, Vol. 9, pp. 852-858, 2007.
11. J. Huang, C. Chen, N. He, J. Hong, Y. Lu, L. Qingbiao, W. Shao, D. Sun, Y. Wang, X.H. Wang and X. Yiang, "Biosynthesis of silver and gold nanoparticles by novel sun dried *Cinnamomum camphora* leaf," *Nanotechnology*, Vol. 18, pp. 105-106, 2007.
12. R.W. Raut, J.R. Lakkakula, N.S. Kolekar, V.D. Mendhulkar and S.B. Kashid, "Phytosynthesis of silver nanoparticle using *Gliricidia sepium* (Jacq.)," *Current Nanoscience*, Vol. 5, pp. 117-122, 2009.
13. N. Mude, A. Ingle, A. Gade and M. Rai, "Synthesis of silver nanoparticles using callus extract of *Carica papaya*-A first report," *Journal of Pantl*

- Biochemistry and Biotechnology*, Vol. 18, pp. 83-86, 2009.
14. A.K. Gade, S.C. Gaikwad, V. Tiwari, A. Yadav, A.P. Ingle, M.K. Rai, "Biofabrication of silver nanoparticles by *Opuntia ficus-indica*: In vitro antibacterial activity and study of the mechanism involved in the synthesis," *Current Nanoscience*, Vol. 6, pp. 370-375, 2010.
 15. S.R. Bonde, D.P. Rathod, A.P. Ingle, R.B. Ade, A.K. Gade, M.K. Rai, "First report of *Murraya koenigii* mediated synthesis of silver nanoparticles and its activity against three human pathogenic bacteria," *Nanoscience Methods*, Vol. 1, pp. 25-36, 2012.
 16. K. Mallikarjun, G. Narsimha, G.R. Dillip, B. Praveen, B. Shreedhar, S. Lakshmi, V.S. Reddy and D.P. Raju, Green synthesis of silver nanoparticles using *Ocimum* leaf extract and their characterization. *Digest Journal of Nanomaterials and Biostructures*, 6 (1): 181-186, 2012.
 17. P. C. Nagajyoti, T. N. Prasad, V. M. Shreekanth, K. D. Lee, "Biofabrication of silver nanoparticles using leaf of *Saururus chinensis*," *Digest Journal of Nanomaterials and Biostructures*, Vol. 6, No. 1, pp. 121-133, 2011.
 18. A. Ingle, A. Gade, S. Pierrat, C. Sonnichsen and M. Rai, "Mycosynthesis of silver nanoparticles using the fungus *Fusarium acuminatum* and its activity against some human pathogenic bacteria," *Current Nanoscience*, Vol. 4, pp. 141-144, 2008.
 19. A.K. Gade, P. Bonde, A.P. Ingle, P.D. Marcato, N. Duran, M.K. Rai, "Exploitation of *Aspergillus niger* for synthesis of silver nanoparticles," *Journal of Biobased Materials Bioengineer*, Vol. 2, pp. 243-247, 2008.
 20. N. Duran, P.D. Marcato, G.I.H. De Souza, O.L. Alves and E. Esposito, "Antibacterial effect of silver nanoparticles produced by fungal process on textile fabrics and their effluent treatment," *Journal of Biomedical Nanotechnology*, Vol. 3, pp. 203-208, 2007.
 21. L.P. Li, Q.W. Song and E Newton, "Antimicrobial effects of surgical masks coated with 869 nanoparticles," *Journal of Hospital Infection*, Vol. 62, pp. 58-

- 63, 2006.
22. K.M. Nadkarni, "*Indian Materia Medica*," Mumbai, India: Popular Prakashan; 2002.
 23. S. Basavaraja, S. D. Balaji, A. Lagashetty, A. H. Rajasab, and A. Venkataraman *Materials Research Bulletin*, Vol. 43, pp. 1164, 2008.
 24. Ravishankar Bhat, Sharanabasava Ganachari, Raghunandan Deshpande, G. Ravindra, A. Venkatraman, "Rapid Biosynthesis of Silver Nanoparticles Using Areca Nut (Areca catechu) Extract Under Microwave-Assistance," *Journal of Cluster Science*, Vol. 24, pp. 107–114, 2013.

Optical Properties of Pure and TICI Doped Poly (Vinyl Alcohol) Polymer Electrolyte Films

C. Anuradha, K.Veerabadra Rao, G.Aravind

Department of physics, Methodist College of Engineering & Technology,
Abids, Hyderabad

ABSTRACT: Poly vinyl alcohol (PVA) is a water-soluble amorphous/crystalline polymer that is widely used in protective coating, biomedical and optical materials, orbents and membranes. In the present investigation, an attempt has been made to characterize the polymer electrolytes based on Poly(vinyl alcohol) (PVA) complexed with thallium chloride(TlCl) at different weight percentage ratio. Solid polymer electrolyte films based on poly(vinyl alcohol) complexed with TlCl were prepared using solution cast technique. The structural properties of these films were examined by XRD. The XRD results show that the amorphous domains of PVA matrix increased in the composite films. In FTIR spectra, changes are noticed in the C-H stretching vibrational mode at 2900 cm^{-1} of PVA along with disappearance of few bands and the appearance of new bands. Morphological studies show that as the percentage of TlCl concentration exceeds that of host concentration, the TlCl gets aggregates on the surface of the film, increasing the surface roughness. The optical parameters including the energy band gaps (direct and indirect) and absorption edge are investigated. It is observed that direct and indirect band gaps (Direct band gap from 5.12-4.80 eV and indirect band gap from 4.82-4.67 eV) show a decreasing trend on complexing.

Keywords: Poly vinyl alcohol, thallium chloride, XRD, FTIR, SEM, Optical absorption.

1.INTRODUCTION

Polymers have gained much experimental attention due to their unique properties, such as low density, ability to form intricate shapes, versatile electric properties and low manufacturing cost [1]. The physical properties of these polymer materials can be enhanced by incorporating filler into its matrix, because dispersed filler will improve various physical properties of the host polymer [2]. Poly (vinyl alcohol) (PVA) is a water-soluble amorphous/crystalline polymer that is widely used in protective coatings, biomedical and optical materials, orbents and membranes [3]. In the present investigation, an attempt has been made to characterize the polymer electrolytes based on Poly (vinyl alcohol) (PVA) complexed with thallium chloride (TlCl) at

different weight percentage ratio.

II. MATERIALS AND METHOD

Films of pure PVA and various compositions of complexed films of PVA with TiCl salt were prepared in weight percent ratios (80:20), (60:40) and (40:60) by solution cast technique using double distilled water as solvent. The solution was stirred for 12hrs to get homogeneous mixture and then casted on polypropylene dishes and kept in hot air oven for 12hrs at a temperature of 40°C. The films thus formed were stored in desiccators. The XRD pattern of the films was recorded with a 'X' pert x-ray diffractometer at room temperature. The FITR spectra of these films were recorded using Bruker tensor-27 spectrometer with a resolution of 4 cm⁻¹. The measurements were taken over a wave number range 400-4000 cm⁻¹. The surface morphology of these polymer electrolyte films have been observed using JEOL JSM 840A scanning electron microscope. The optical absorption spectra of the present samples were recorded at room temperature using Shimadzu UV-VIS-NIR in the wavelength range 300-900nm with a spectral width of 3nm.

III. RESULTS AND DISCUSSION

A. XRD Analysis

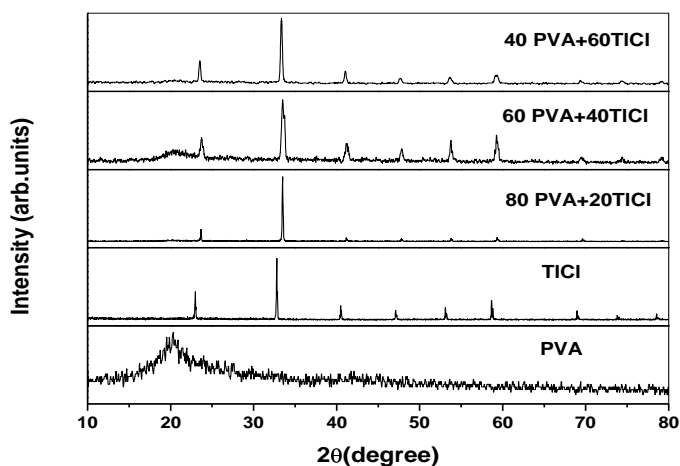


Fig 1. XRD pattern of Pure PVA and PVA/TiCl films

The X-ray diffraction pattern of pure PVA, TiCl salt and PVA complexed with TiCl are shown in Fig.1. The XRD pattern of pure PVA reveal that a broad peak is appearing at scattering angle $19^\circ < 2\theta < 20^\circ$, corresponding to a 'd' spacing of 0.457 nm. The pure PVA characteristic peak becomes less intense as the TiCl content in the composite is increased. This could be due to

disruption of PVA crystalline structure by TiCl. The diffraction peaks associated with PVA has disappeared in 80:20 composite and reappeared again when TiCl present is increased in PVA films. This shows a decrease in the degree of crystallinity of the polymer after the addition of higher concentrations of TiCl. The increase in the composition of TiCl in PVA, results in increase in the amorphous nature of the composite films. Higher and broader peaks are obtained in the case of 60:40 compositions indicating greater accumulation of atoms at lattice sites, creating greater lattice distortion.

B. FTIR Studies

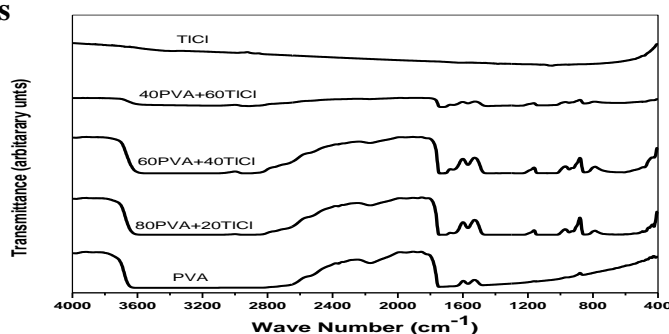


Fig. 2: FTIR spectra of Pure PVA, TiCl salt and PVA/ TiCl polymer films.

The FTIR spectra for pure PVA, TiCl and PVA : TiCl composites of different compositions are shown in the fig2. The following changes in the spectral features have been observed after comparing the spectrum of PVA : TiCl composites. Changes are noticed in the C-H stretching vibrational mode at 2900 cm^{-1} of PVA along with disappearance of few bands and the appearance of new bands. The inter molecular hydrogen bonded O-H stretching frequency of PVA appearing in the range of 3590 cm^{-1} is shifted to 3507 cm^{-1} . In PVA : TiCl (60:40) composition and at higher compositions of PVA : TiCl (40:60), this band appears at 3175 cm^{-1} . The C-H bonding of CH_2 in pure PVA exhibits absorption at 1474 cm^{-1} and is shifted to 1418 cm^{-1} and 1439 cm^{-1} in (80:20) and (40:60) compositions respectively.

C. SEM Analysis

Fig 3 (a,b,c) shows the SEM pictures of the surface of PVA : TiCl(80:20); PVA : TiCl (60;40)and PVA : TiCl (40:60) films of different magnification respectively. These pictures show not many aggregates on the surface of the films. The increase in degree of roughness with increased TiCl concentration, indicates, the presence of the dopant which is completely complexed with the polymer. As the percentage of TiCl exceeds that of the host concentration the TiCl gets aggregates on the surface of the film increasing the surface roughness

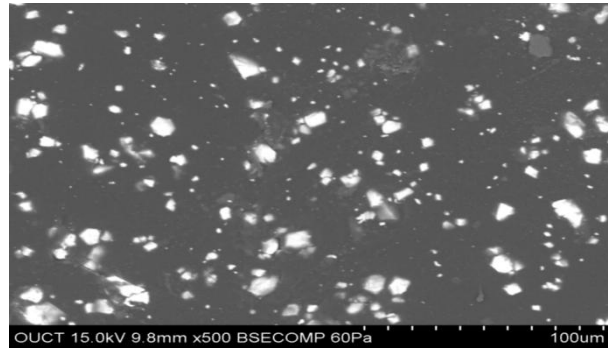


Fig 3 (a): SEM picture of PVA/TiCl (80:20)

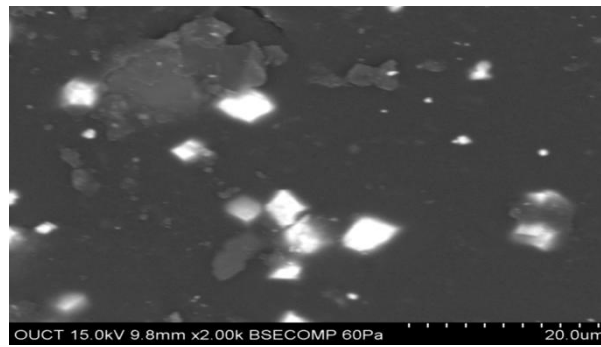


Fig 3 (b): SEM picture of PVA/TiCl (60:40)

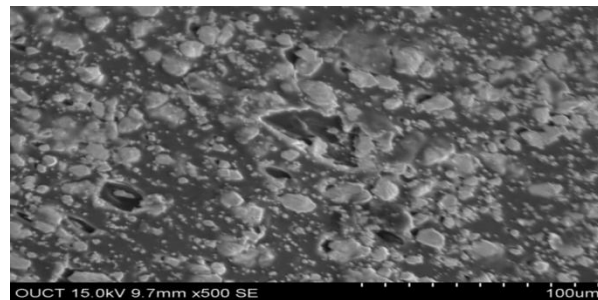


Fig 3 (c): SEM picture of PVA/TiCl (40:60)

D.Optical Absorption Studies

The optical absorption (OA) studies are very interesting because it provides important information about the absorbance, transmittance and reflectance of the observed polymeric films [4]. The optical absorption and especially the absorption edge presents a useful method for the investigating optically induced transitions and for getting information about the band structure, the band tail and energy gap of the polymeric materials under consideration [5]. By studying the optical absorption spectrum, one can clearly identify its band structure [6-8]. The

absorption coefficient $\alpha(\nu)$ can be estimated from the optical absorption spectrum from the following equation [9].

$$\alpha(\nu) = 2.303 \times A/d \quad \text{.....(1)}$$

Where „d is the film thickness in cm and 'A' is defined by $\log(I/I_0)$ where I_0 and I are the intensities of the incident and transmitted beams respectively.

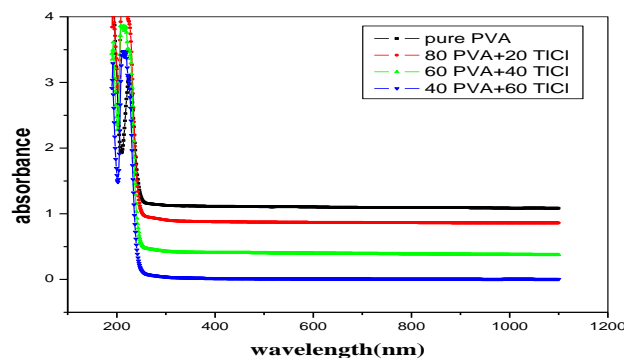


Fig. 4: OA spectra of Pure and TiCl complexed PVA films

Regarding the optical transitions resulting from photons of energy $h\nu > E_{opt}$, the present optical data is studied according to the following relationship for near edge optical absorption [10].

$$\alpha(\nu)h\nu = B (h\nu - E_{opt})^r \quad \text{.....(2)}$$

where α is the absorption coefficient, ν is the frequency, B is the constant, h is the Planck's constant, E_{opt} is the optical energy band gap between the valence and conduction bands and r is the power that characterizes the transition process. Here 'r' takes the values of 1/2, 3/2, 2 and 3 for transitions designated as direct allowed, direct forbidden, indirect allowed and indirect forbidden respectively⁵. The determination of the value of the optical energy band gap E_{opt} is done by plotting $(\alpha h\nu)^{1/r}$ against $h\nu$.

The OA spectrum of pure PVA, PVA complexed with different concentrations of TiCl are shown in fig.4. The OA spectrum of pure PVA is characterized by an absorption peak at wavelength 283nm as well as unresolved shoulder at 330nm. No absorption peaks are noticed at higher wavelengths. The absorption peak at 283nm can be attributed to the absorption by simple carbonyl groups along the polymer chains. On the other hand shoulder can be assigned to the appearance of the $-\text{CO}-(\text{CH}=\text{CH})_3$ -groups (5)

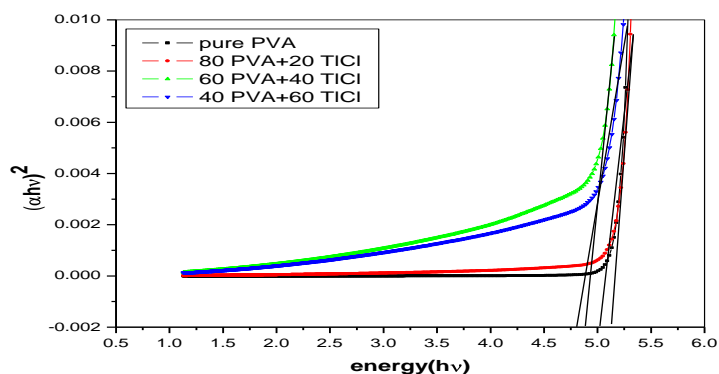


Fig. 5(a): Plot of $(\alpha h\nu)^2$ versus photon energy $(h\nu)$ for PVA:TlCl

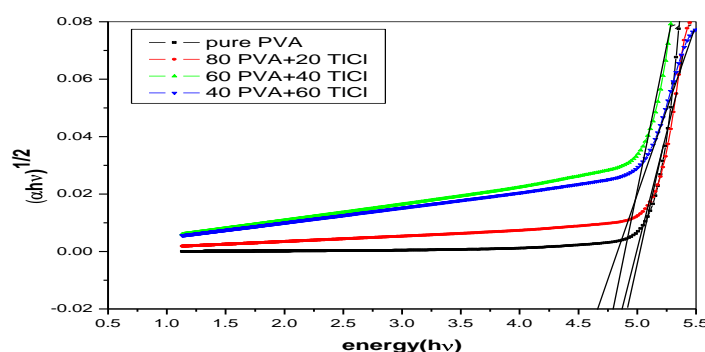


Fig. 5(b): $(\alpha h\nu)^{1/2}$ versus photon energy $(h\nu)$ for PVA:TlCl

Polymer	Absorption edge (ev)	Band gap (eV)	
		Direct	Indirect
PVA	5.02(247)	5.12	4.82
80PVA+ 20TlCl	4.94 (251)	5.02	4.79
60PVA+ 40TlCl	4.77 (260)	4.85	4.71
40PVA+ 60TlCl	4.65 (267)	4.80	4.67

The addition of TlCl to PVA matrix shows no substantial change in 283 nm peak but the shoulder which appeared in pure PVA has disappeared on addition of TlCl. There is a decrease in UV absorption in the case of PVA/TlCl films. The fundamental band edge, both direct and indirect transitions can be observed by plotting $(\alpha h\nu)^2$ and $(\alpha h\nu)^{1/2}$ versus photon energy $h\nu$. These plots are shown in fig 5.

These plots present experimental data near the absorption edge and give a linear fit in the high

energy range. The intercept on the energy axis on extrapolating the linear portion of the curves to zero absorption value may be interpreted as the value of band gap. The values of experimental band gaps of pure PVA and PVA complexed with TiCl are listed in table 1.

It is clearly evident from the table that both the direct and indirect band gap show decreasing trend on complexing. The decrease in optical band gap energies with increase in the TiCl concentrations respectively explains the fact that the addition of TiCl increases the disorder of these films. The increase in the degree of the disorder causes the band tail to increase. The decrease in band gap on increasing the TiCl content in PVA matrix also indicates that there are charge transfer complexes which arise between the PVA and TiCl molecule.

IV.CONCLUSIONS

The complexation of the salt with polymer is confirmed by X D and FTIR studies. The morphological studies of pure PVA and (PVA:TiCl) polymer electrolyte at different weight percentage is done using SEM. The optical band gap is evaluated and its dependence on filling was investigated. The decreasing trend of the optical band gap with increase in TiCl concentration is attributed to the charge transfer complexes.

REFERENCES

- [1]. A.El-Khodary, A.h.Oraby and M.M.Abdelnaby *Journal of magnetism and magnetic materials* 320,1739-1746 (2008).
- [2]. V.Raja, A.K.Sarma and V.V.R.Narsimha Rao, "Optical properties of pure doped PMMA-Co-P4VPNO polymer films", 57 (30), 4678-4683 (2003).
- .M.E.Rozenberg, *Polyvinyl Acetate based polymers [in Russia]*, Khimiya, Leningrad (1983).
- .P.Balaji Bhargav, V.Madhu Mohan, A.K.sharma and V.V.R.Narsimha Rao, *International Journal of Polymer materials*, 56, 579 (2007).
- .A.El.Khodary, *Physica B:Condensed Matter*, 405(16) , 4301 (2010)
- .M.Tabata, M.Satoh, K.Kaneto and Yoshino, *J.Phys.Soc.Japn*, 55, 1305 (1986).
- .S.Proneanu, S.Torcu, M.Brie and Mihileasan, *Mater.Sci.Fourum* 191 (1995).
- .W.A.Jabbar, N.F.Habubi and S.S.Chiad, *J.Arkansas Academy of Sci*, 64, 101(2010)
- .J.Ballato and S.Foulger, "Optical properties of Perfluocyclobutyl polymers", *Journal of Optical Society of America B*, 20(9), 1838-1843 (2003).
-]J.J.Tauc, A.Menith and D.N.Wood, *Physical review letters*, 25(11), 749 (1970).

Structural Properties of $Mg_{1-x}Zn_xFe_2O_4$ Nano-Ferrites

Synthesized by citrate Gel Autocombustion method

Shyamsunder Goud¹, Nakiraboina Venkatesh¹, Nama Hari Kumar², B. Rambabu¹,
B.Shankar¹, P.Naresh², M.Raghasudha¹, P. Veera Somaiah^{1*}

¹Department of chemistry, Osmania University, Hyderabad, 500007- India.

²Department of Physics, Osmania University, Hyderabad, 500007- India.

Corresponding author Email: vs_puppala@rediffmail .com Ph (+91)9247562742

ABSTRACT:

In this work, the $Mg_{1-x}Zn_xFe_2O_4$ Nanoferrites (where $x = 0.0, 0.2, 0.4, 0.6$ and 0.8) was synthesized using citrate Gel Auto combustion method. The investigation of structural and optical properties was carried out for the synthesized samples using X-ray diffraction (XRD), Fourier transform infrared spectroscopy (FTIR) and Ultraviolet visible spectrophotometer (UV-Vis). XRD revealed that the structure of these nanoparticles is spinel with space group $Fd\bar{3}m$ and crystallite size lies in the range $21.0 - 42.8$ nm. Lattice parameter was found to increase with Zn concentration and this may be due to the larger ionic radius of the Zn^{2+} ion. FTIR spectroscopy confirmed the formation of spinel ferrite and showed the characteristic absorption bands around $612, 1146, 1404, 1649$ and 3245 cm^{-1} . The energy band gap was calculated for samples with different ratios and was found to be $4.77, 4.82, 4.86, 4.87$ and 4.95 eV. The substitution resulted in a slight increase in the lattice constant and that sequentially may lead to a slightly decreased energy gap.

Keywords: Citrate Gel Auto combustion Method, Ferrite Nanoparticles, Spinel Structure,

1. Introduction

Nanotechnology is one of the leading scientific fields today since it combines knowledge from the fields of Physics, Chemistry, Biology, Medicine and Engineering. The application and use of nanomaterials are extensive such as in electronic and mechanical devices, optical magnetic components, tissue engineering magnetic storage systems and magnetic resonance imaging [1] [2]. Nanotechnology and material technology are new techniques for synthesis and processing

manipulation and assembly using nature's own building blocks (atoms, molecules or macromolecules) for the intelligent design of functional materials, components and systems with attractive qualities and functions [3] [4].

Ferrites are well known magnetic nanomaterials intensively studied as a recording media due to their superior physical properties. These properties make ferrites an ideal candidate for technical applications such as magnetic resonance imaging enhancement, catalysis, sensors and pigments [5]. Mixed spinel ferrites have been studied intensively over the last few years due to their potential applications. Spinel ferrites have the chemical formula MFe_2O_4 in which M can be any divalent metal cations. In spinel ferrite, oxygen forms face centre cubic (FCC) lattice with divalent cations at tetrahedral (A) and/or octahedral (B) sites. Magnesium ferrite ($MgFe_2O_4$) has an inverse spinel structure with the preference of Mg^{2+} cations mainly on octahedral sites [6]- [9], while Zinc ferrite ($ZnFe_2O_4$) has normal spinel structure, in which Zn^{2+} cations mainly occupy tetrahedral sites [6] [10].

The small scale size of the well known spinel ferrites has opened up the door for intensive research to utilize their properties for biomedical applications [11]- [13]. Numerous methods were reported in literature showing the possibilities of producing particles with size in the range of 2 - 100 nm. Among these methods are co-precipitation, hydrothermal and citrate gel Methods [14] [15], which were reported to be fast and producing high quality nanoparticles.

In this work, $Mg_{1-x}Zn_xFe_2O_4$ nanoferrites where $x = 0.0, 0.2, 0.4, 0.6$ and 0.8) were synthesized using co-precipitation methods. X-ray diffraction (XRD) was used in order to investigate the structural of Zn substituted magnesium nanoferrites and to determine the lattice parameters and the space group symmetry. Ultraviolet visible spectrometer (UV vis) and Fourier Transform Infrared Spectroscopy (FTIR) were used to investigate the structural properties of crystallite nanoparticles.

2. Material and Method

Mg Zn ferrite ($Mg_{1-x}Zn_xFe_2O_4$) nanoparticles with composition ($x = 0.0, 0.2, 0.4, 0.6$ and 0.8) was prepared by the citrate gel auto combustion Method. Stoichiometric amounts from pure raw materials of $Fe(NO_3)_3 \cdot 9H_2O$, $Mg(NO_3)_2 \cdot 6H$

Fe_2O_3 , $\text{Zn}(\text{NO}_3)_2 \cdot 6\text{H}_2\text{O}$, and NaOH were used to prepare the required solutions with required molarities. The solution of $\text{Fe}(\text{NO}_3)_3 \cdot 9\text{H}_2\text{O}$, 0.4 M (25 ml), $\text{Mg}(\text{NO}_3)_2 \cdot 6\text{H}_2\text{O}$ 0.2M (25 ml) and $\text{Zn}(\text{NO}_3)_2 \cdot 6\text{H}_2\text{O}$ Calculated quantities of metal nitrates and citric acid were dissolved in minimum amount of distilled water to get clear solution. Here citric acid acts as a chelating agent and helps in the homogenous distribution of metal ions. The above mixture was stirred to get homogenous clear solution which is heated to 80°C using a hot plate magnetic stirrer. Then the pH of the solution is adjusted at 7 by addition of ammonia. A sol is formed. The resulting solution was evaporated to dryness heating at about 180°C on a hot plate with continuous stirring. The gel gave a fast flameless auto combustion reaction with the evolution of large amount of gases which results a burned powder. The burned powder was grinding using Agate Mortar and pestle to get a fine ferrite powder. Finally the grinded powder was calcinated in air at 500°C for 4 hours and cooled to room temperature. The XRD analysis was carried out to confirm the purity of the synthesized materials using Shimadzu 6000 X-ray diffractometer with $\text{Cu-K}\alpha$ radiation of a wavelength $\lambda = 1.5406 \text{ \AA}$ source. FTIR measurements were performed using (Mattson, model 960m0016) spectra, while the absorption of solution with different concentration was calculated using UV min 1240 spectrometer Shimadzu.

3. Results and Discussion

3.1. Crystal Analysis

Determination of the crystal structure, the lattice parameters and the space group symmetry are importance in the study of structural, electrical and optical properties of the nanoparticle ferrites. The information of single phase $\text{Mg}_{1-x}\text{Zn}_x\text{Fe}_2\text{O}_4$ is confirmed after analyzing the x-ray diffraction pattern by MDI Jade 5.0, ORIGIN and FULLPROF. The crystal structure is found to be cubic with space group $\text{Fd}\bar{3}\text{m}$. The X-ray diffraction (XRD) is carried out at room temperature. Figure1 shows the X -ray diffraction patterns for the sample MgFe_2O_4 nanoparticles with $x = 0.0$, while Figure2 shows the X -ray diffraction patterns for the samples $\text{Mg}_{1-x}\text{Zn}_x\text{Fe}_2\text{O}_4$ nanoparticles with different composition ($x = 0.2, 0.4, 0.6$ and 0.8). The peaks were indexed as (111), (220), (311), (222), (400), (422), (511), (440), and (533). The crystallite size, lattice constants, volume and densities are listed in **Table**

1. The crystal size is calculated using the Debye-Scherer's equation [18]:

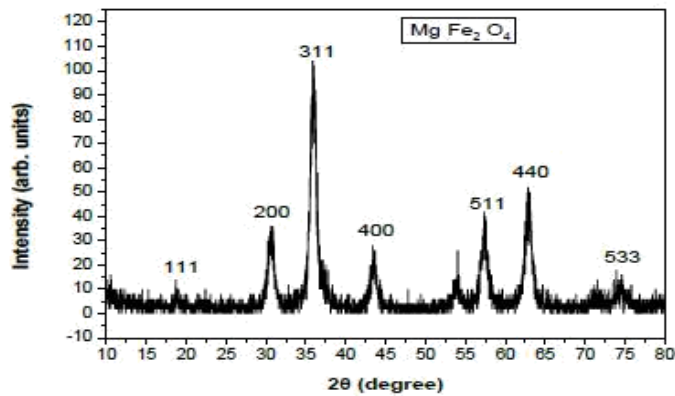


Figure 1. XRD patterns of Mg_{1-x}Zn_xFe₂O₄ nanoferrites for x = 0

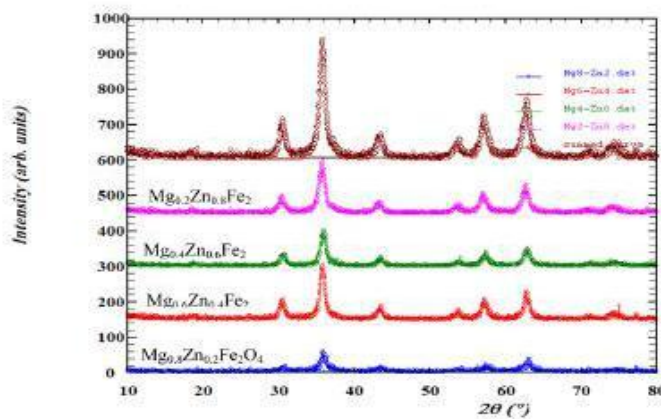


Figure 2. XRD patterns of Mg_{1-x}Zn_xFe₂O₄ nanoferrites for x = 0.2, 0.4, 0.6 and 0.8.

Table 1. Particle size (D), Lattice constant (a), Volume and Density of Mg_{1-x}Zn_xFe₂O₄ nano-ferrites.

No.	Samples	Crystal size (nm)	Lattice constant (Å)	Volume (nm ⁻³)	Density (g/cm ³)
1	MgFe ₂ O ₄	42.8	8.09	529.5	5.175
2	Mg _{0.8} Zn _{0.2} Fe ₂ O ₄	26.6	8.38	587.4	4.522
3	Mg _{0.6} Zn _{0.4} Fe ₂ O ₄	24.1	8.39	590.0	4.502
4	Mg _{0.4} Zn _{0.6} Fe ₂ O ₄	21.0	8.40	591.9	5.176
5	Mg _{0.2} Zn _{0.8} Fe ₂ O ₄	23.2	8.44	601.5	5.070

where D is the average crystallite size, θ is the diffraction angle, λ is the wavelength of incident X-ray and β is the full width at half maximum (FWHM) of the (XRD) peak in units of radians. The crystallite size vs. Zn concentration is plotted in Figure 3 and the crystallite size is found to be scattered in the range 21 - 42.8 nm for different compositions. In the obtained diffraction pattern the lattice constants are found to increase from (8.09 - 8.44 Å) as the Zn concentration increased. The particle size of the nanocrystalline samples, calculated from the XRD data using Equation (1), is remained within the range (21.0 - 42.8 nm). The increase in lattice constant with Zn concentration may be due to the fact that Zn^{2+} ions (0.82 Å) is larger than that of the Mg^{2+} ions (0.72 Å). Addition of Zn^{2+} at the expense of Mg^{2+} in the ferrite is expected to increase the lattice constant. The lattice parameter (a) is estimated using lattice spacing (d) values and respective miller indices (hkl). The lattice constant (a) was calculated by MDI Jade 5.0 program and using the equation [19]:

$$a = \frac{d}{(h^2 + k^2 + l^2)^{1/2}}$$

where a is the lattice parameter, d is the lattice spacing and h, k, l are the miller indices. The lattice parameter is obtained using XRD data lies in the range of 8.1 - 8.4 Å for different Zn concentration as shown in Figure 4. It increases with increasing Zn concentration due to the larger ionic radius of Zn^{2+} (0.08 nm) Cation as compared to ionic radius of Mg^{2+} (0.06 nm) Cation [20] [21].

3.2. FTIR Analysis

In order to investigate the chemical functional groups on the synthesized $\text{Mg}_{1-x}\text{Zn}_x\text{Fe}_2\text{O}_4$, FTIR spectroscopy are performed. The FTIR of nanocrystals powders (as pellets in KBr) in the range of 400 cm^{-1} to 4000 cm^{-1} is shown in Figure 5 for pure sample where $x = 0$. The FTIR of $\text{Mg}_{1-x}\text{Zn}_x\text{Fe}_2\text{O}_4$ nano ferrites powders for samples where $x = 0.2, 0.4, 0.6$ and 0.8 is plotted and shown in Figure 6. The bands (ν_1, ν_2) for the samples are found to be in range $3148 - 3450\text{ cm}^{-1}$ and $1644 - 1649\text{ cm}^{-1}$, respectively. These observed bands maybe are due to the O-H

stretching vibration of the free absorbed water and indicates the existence of hydroxyl groups in the synthesized ferrites, which is observed in previous experiments [22] [23]. The band (ν_3) for the samples are observed around 1404 cm^{-1} and is attributed to the C=O stretching vibration of the carboxyl group. In range $1107 - 1147 \text{ cm}^{-1}$, the band (ν_4) is observed and is related to the stretching vibration due to nitrate group [24] [25]. In the range of $800 - 400 \text{ cm}^{-1}$, two main absorption bands with very low intensity are observed around 400 and 600 cm^{-1} and may be is caused by metal oxygen vibration in the octahedral side. The ν_1 , ν_2 , ν_3 , ν_4 and ν_5 are absorption bands around $3148 - 3450$, $1644 - 1649$, 1404 , $1107 - 1147$ and $612 - 663 \text{ cm}^{-1}$, respectively for the samples with different compositions and are attributed to the vibration of the tetrahedral and octahedral met-al-oxygen (M-O) bands in the lattices of the synthesized nanocrystals. The FTIR frequency bands for various Zn and Mg contents are listed in **Table 2**.

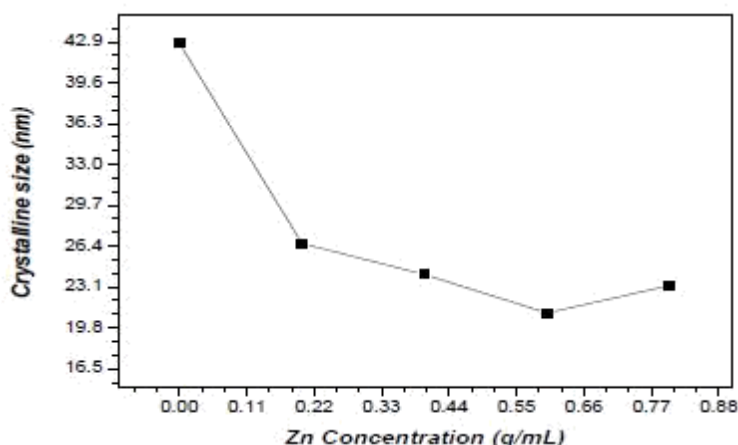


Figure 3. Particle size as a function of Zn concentration of $\text{Mg}_{1-x}\text{Zn}_x\text{Fe}_2\text{O}_4$ nanoferrites.

3.3. UV Visible Analysis

The absorption as a function of wavelength for sample $\text{Mg}_{0.6}\text{Zn}_{0.4}\text{Fe}_2\text{O}_4$ is shown in Figure 7. Maximum absorption for the sample is observed at wavelength 232.4 nm . Several models are used to determine the optical properties of nanoferrites. The most widespread is the Tauc model which allows the derive of the band gap energy E_g from $(ah\nu)^2$ as function of the incident energy $(h\nu)$. The Tauc

$$(\alpha h\nu) = A(h\nu - E_g)^n$$

optical gap associated with the $Mg_{1-x}Zn_xFe_2O_4$ nanoferrites is determine through an extrapolation of the linear trend observed in the spectral

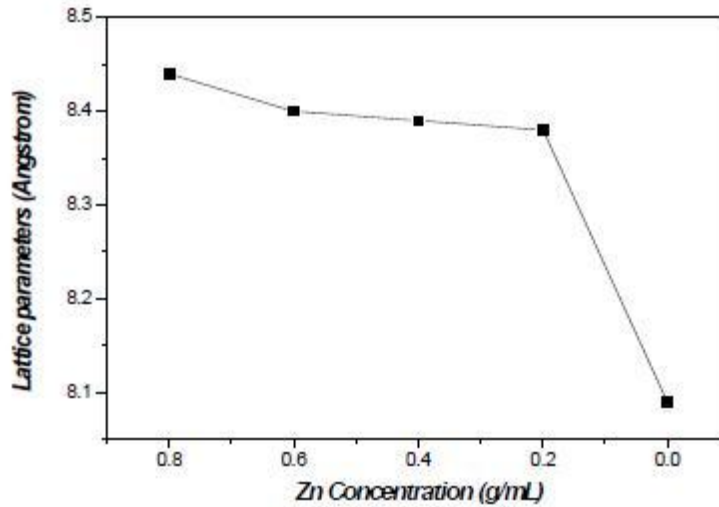


Figure 4. Lattice parameter as a function of Zn concentration of $Mg_{1-x}Zn_xFe_2O_4$ nanoferrites.

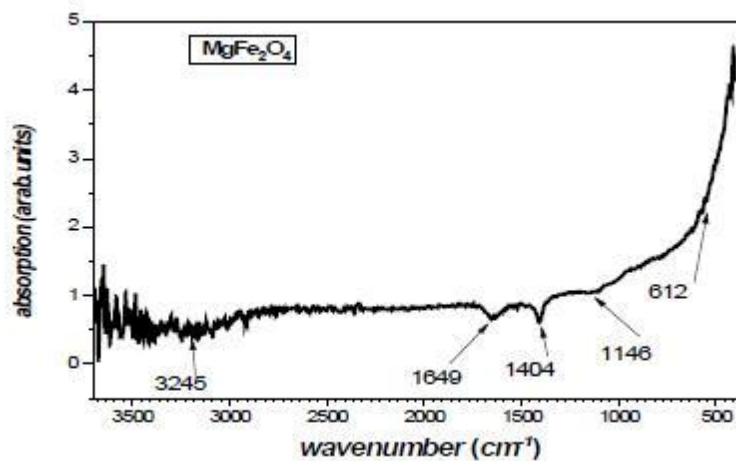


Figure 5. The FTIR spectrum of $Mg_{1-x}Zn_xFe_2O_4$ nanoferrites for $x = 0$.

Dependence of $(\alpha h\nu)^2$ over a limited range of photon energies $h\nu$. The Tauc optical gap is defined as occurring at the intercept of this linear extrapolation with Y axis. The absorption coefficient α near the band edge in many

Nano ferrites shows an exponential upon photon energy usually obeying the relation [26]: where, α is the absorption coefficient and A is known as edge width parameter, E_g is the energy band gap, $n = (1/2, 1, 2)$ is the a constant dependent on the degree of

transition, ($h\nu$) is incident photon energy. The band gap is

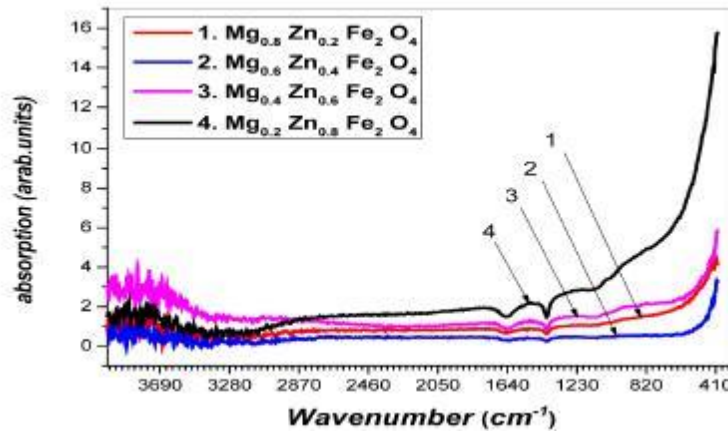


Figure 6. The FTIR spectrum of Mg_{1-x}Zn_xFe₂O₄ nanoferrites for x = 0.2, 0.4, 0.6 and 0.8.

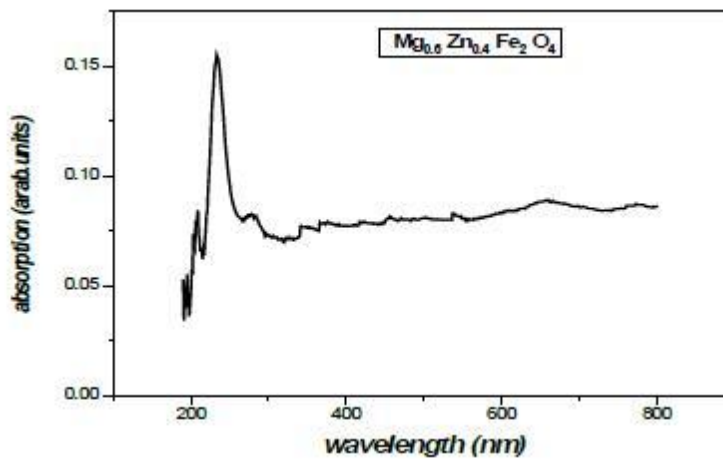


Figure 7. Absorption as a function of wavelength for sample of Mg_{0.6}Zn_{0.4}Fe₂O₄ composition.

Table 2. Wave numbers, wavelength, and energy band gaps of Mg_{1-x}Zn_xFe₂O₄ nanoferrites.

No.	Samples	ν_1	ν_2	ν_3	ν_4	ν_5	Energy gap E_g (eV)
1	MgFe ₂ O ₄	3245	1649	1404	1146	612	4.77
2	Mg _{0.8} Zn _{0.2} Fe ₂ O ₄	3245	1649	1404	1146	612	4.82
3	Mg _{0.6} Zn _{0.4} Fe ₂ O ₄	3450	1649	1404	1107	663	4.86
4	Mg _{0.4} Zn _{0.6} Fe ₂ O ₄	3148	1644	1404	1140	612	4.87
5	Mg _{0.2} Zn _{0.8} Fe ₂ O ₄	3419	1649	1404	1120	613	4.95

then evaluated by plotting (hv) versus $(\alpha hv)^2$ and extrapolating the tangent on the X-axis (Tauc plots). Figure 8 shows Tauc plot method for sample of $MgFe_2O_4$, and the energy band gap are found to be 4.77, 4.82, 4.86, 4.87 and 4.95 eV for samples with different concentration ($x = 0.2, 0.4, 0.6$ and 0.8), respectively.

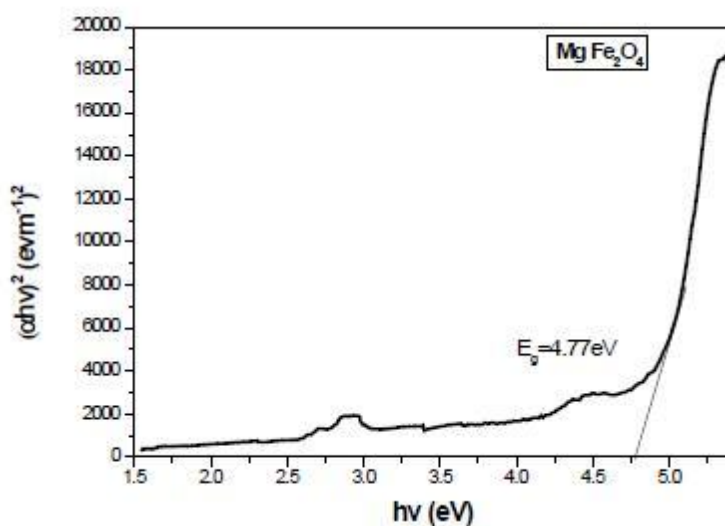


Figure 8. Plot of $(\alpha hv)^2$ versus hv for $MgFe_2O_4$ nanoferrites.

4. Conclusion

$Mg_{1-x}Zn_xFe_2O_4$ nanoparticles was prepared successfully using co-precipitation method. The formation of single phase crystallite structure with size in the range 21.0 - 42.8 nm was confirmed by X-ray diffraction. Lattice parameter was found to increase with Zn concentration and this may be due to the larger ionic radius of the Zn^{2+} ion. FTIR spectrum exhibited expected main absorption bands, thereby confirming the spinel structure. Optical band gap energy $Mg_{1-x}Zn_xFe_2O_4$ nanoferrite was found to be in the range 4.77 to 4.95 eV for samples with different ratio of Mg Zn. The synthesized nanoferrites are expected to be useful in several technological applications such as soft magnets and magnetic fluids for hyperthermia. The structural properties of spinel ferrites depend upon the method of preparation, the nature of substitutional element and the concentration of the substitution element. Attempts can be made to prepare the samples by different methods to get desired properties and crystallite size.

References

- a) Flores-Acosta, M., Sotelo-Lerma, M., Arizpe-Chavez, H., Castillon-Barraza, F.F. and Ramirez-Bon, R.J. (2003) A. *Solid State Communications*, **128**, 407-411. <http://dx.doi.org/10.1016/j.ssc.2003.09.008>
- b) Pulisova, P., Kovac, J., Voigt, A. and Raschman, P. (2013). *Journal of Magnetism and Magnetic Materials*, **341**, 93-99. <http://dx.doi.org/10.1016/j.jmmm.2013.04.003>
- c) Lodhi, M.Y., Mahmood, K., Mahmood, A., Malika, H., Warsi, M.F., Shakir, I., Asghar, M. and Khan, M.A. (2014) *New Current Applied Physics*, **14**, 716-720. <http://dx.doi.org/10.1016/j.cap.2014.02.021>
- d) Jan, L.S., Radiman, S., Siddig, M.A., Muniandy, S.V., Hamid, M.A. and Jamali, H.D. (2004) A: *Physico-chemical and Engineering Aspects*, **251**, 43-52. <http://dx.doi.org/10.1016/j.colsurfa.2004.09.025>
- [5] Mathew, D.S. and Juang, R.-S. (2007) *An. Chemical Engineering Journal*, **129**, 51-65. <http://dx.doi.org/10.1016/j.cej.2006.11.001>
- [6] Rahman, S., Nadeem, K., Anis-ur-Rehman, M., Mumtaz, M., Naeem, S. and Letofsky-Papst, I. (2013) *Ceramics International*, **39**, 5235-5239. <http://dx.doi.org/10.1016/j.ceramint.2012.12.023>
- [7] Pradeep, A., Priyadharsini, P. and Chandrasekaran, G. (2008). *Journal of Magnetism and Magnetic Materials*, **320**, 2774-2779. <http://dx.doi.org/10.1016/j.jmmm.2008.06.012>
- [8] Greenwood, N.N. and Earnshaw, A. (1984) *Chemistry of the Elements*; Pergamon Press Ltd., Oxford, 279.
- [9] Ichihyanagi, Y., Kubota, M., Moritake, S., Kanazawa, Y., Yamada, T. and Uehashi, T. (2007) Magnetic Properties of Mg-Ferrite Nanoparticles. *Journal of Magnetism and Magnetic Materials*, **310**, 2378-2380. <http://dx.doi.org/10.1016/j.jmmm.2006.10.737>
- [10] Thummer, K.P., Chhantbar, M.C., Modi, K.B., Baldha, G.J. and Joshi, H.H. (2004) Localized Canted Spin Behaviour in $Zn_xMg_{1.5-x}Mn_{0.5}FeO_4$ Spinel Ferrite System. *Journal of Magnetism and Magnetic Materials*, **280**, 23-30. <http://dx.doi.org/10.1016/j.jmmm.2004.02.017>
- [11] Kumara, C.S.S.R. and Mohammad, F. (2011) Magnetic Nanomaterials for Hyperthermia-Based Therapy and Controlled Drug Delivery. *Advanced Drug Delivery Reviews*, **63**, 789-808. <http://dx.doi.org/10.1016/j.addr.2011.03.008>
- Giri, J., Pradhan, P., Somani, V., Chelawat, H., Chhatre, S., Banerjee, R. and Bahadur, D. (2008) Synthesis and Characterizations of Water-Based Ferrofluids of Substituted Ferrites [$Fe_{1-x}B_xFe=O_4$, B=Mn, Co ($x=0-1$)] for Biomedical Applications. *Journal of Magnetism and Magnetic Materials*, **320**, 724-730. <http://dx.doi.org/10.1016/j.jmmm.2007.08.010>

- [12] Sharifi, I., Shokrollahi, H. and Amiri, S. (2012) Ferrite-Based Magnetic Nanofluids Used in Hyperthermia Applications. *Journal of Magnetism and Magnetic Materials*, **324**, 903-915. <http://dx.doi.org/10.1016/j.jmmm.2011.10.017>
- [13] Chen, Y., Ruan, M., Jiang, Y.F., Cheng, S.G. and Li, W. (2010) The Synthesis and Thermal Effect of CoFe_2O_4 Nanoparticles. *Journal of Alloys and Compounds*, **493**, L36-L38. <http://dx.doi.org/10.1016/j.jallcom.2009.12.170>
- [14] Liu, Q., Sun, J.H., Long, H.R., Sun, X.Q., Zhong, X.J. and Xu, Z. (2008) Hydrothermal Synthesis of CoFe_2O_4 Nano-platelets and Nanoparticles. *Materials Chemistry and Physics*, **108**, 269-273. <http://dx.doi.org/10.1016/j.matchemphys.2007.09.035>
- [15] Omer, M.I.M., Elbadawi, A.A. and Yassin, O.A. (2013) Synthesis and Structural Properties of MgFe_2O_4 Ferrite Nano-Particle. *Journal of Applied and Industrial Sciences*, **1**, 20-23.
- [16] Ali, R., Khan, M.A., Mahmood, A., Chughtai, A.H., Sultan, A., Shahide, M., Ishaq, M. and Wars, M.F. (2014) Structural, Magnetic and Dielectric Behavior of $\text{Mg}_{1-x}\text{Ca}_x\text{Ni}_y\text{Fe}_{2-y}\text{O}_4$ Nano-Ferrites Synthesized by the Micro-Emulsion Method. *Ceramics International*, **40**, 3841-3846. <http://dx.doi.org/10.1016/j.ceramint.2013.08.024>
- [17] Ahmed, M.A., Rady, K.E.S., El-Shokrofy, K.M., Arais, A.A. and Shams, M.S. (2014) The Influence of Zn^{2+} Ions Substitution on the Microstructure and Transport Properties of Mn-Zn Nanoferrites. *Materials Sciences and Applications*, **5**, 932-942. <http://dx.doi.org/10.4236/msa.2014.513095>
- [18] Mittal, V.K., Chandramohan, P., Santanu, B., Srinivasan, M.P., Velmurugan, S. and Narasimhan, S.V. (2006) Cation Distribution in $\text{Ni}_x\text{Mg}_{1-x}\text{Fe}_2\text{O}_4$ Studied by XPS and Mössbauer Spectroscopy. *Solid State Communications*, **137**, 6-10. <http://dx.doi.org/10.1016/j.ssc.2005.10.019>
- [19] Ladgaonkar, B.P., Vasambekar, P.N. and Vaingankar, A.S. (2000) Cation Distribution and Magnetisation Study of Nd^{3+} Substituted Zn-Mg Ferrites. *Journal of Magnetism and Magnetic Materials*, **210**, 289-294. [http://dx.doi.org/10.1016/S0304-8853\(99\)00468-0](http://dx.doi.org/10.1016/S0304-8853(99)00468-0)
- [20] Maensiri, S., Masingboon, C., Boonchom, B. and Seraphin, S. (2007) A Simple Route to Synthesize Nickel Ferrite (NiFe_2O_4) Nanoparticles Using Egg White. *Scripta Materialia*, **56**, 797-800. <http://dx.doi.org/10.1016/j.scriptamat.2006.09.033>
- [21] Dey, S., Roy, A., Das, D. and Ghose, J. (2004) Preparation and Characterization of Nanocrystalline Disordered Li-thium Ferrite by Citrate Precursor Method. *Journal of Magnetism and Magnetic Materials*, **270**, 224-229. <http://dx.doi.org/10.1016/j.jmmm.2003.08.024>

- [22] Priyadharsini, P., Pradeep, A., Sambasiva, P. and Chandrasekaran, G. (2009) Structural, Spectroscopic and Magnetic Study of Nanocrystalline Ni-Zn Ferrites. *Materials Chemistry and Physics*, **116**, 207-213. <http://dx.doi.org/10.1016/j.matchemphys.2009.03.011>
- [23] Hankare, P.P., Patil, R.P., Jadhav, A.V., Pandav, R.S., Garadkar, K.M., Sasikala, R. and Tripathi, A.K. (2011) Synthesis and Characterization of Nanocrystalline Ti-Substituted Zn Ferrite. *Journal of Alloys and Compounds*,
- [24] Sánchez-Vergara, M.E., Alonso-Huitron, J.C., Rodríguez-Gómez, A. and Reider-Burstin, J.N. (2012) Determination of the Optical GAP in Thin Films of Amorphous Dilithium Phthalocyanine Using the Tauc and Cody Models. *Molecules*, **17**, 10000-10013. <http://dx.doi.org/10.3390/molecules170910000>
- [25] Jan, L.S. and Siddig, M.A. (2011) *Chinese Journal of Polymer Science*, **29**, 181-190. <http://dx.doi.org/10.1007/s10118-010-1016-4>

Synthesis, Characterization of (1-x) NaNO₃-xAl₂O₃ Composite Solid Electrolytes

A.Vennela¹, A. Raju¹, A.Mallaiah³, S.Narender Reddy², A. Sadananda Chary¹.

¹Department of physics, University College of Science, Osmania University, Hyderabad-7, Telangana, India.

²Department of physics, University College of Engg, Osmania University, Hyderabad-7, Telangana, India.

³Department of physics, PG College, Secunderabad, Osmania University, Hyderabad-3, Telangana, India.

ABSTRACT

Composite solid electrolyte system (1-x) NaNO₃- xAl₂O₃(with x=0.05, 0.1, 0.15, 0.2) is prepared by fast evaporation technique. The synthesis has been carried out at moderate temperatures and the samples were characterized by XRD and FTIR techniques. X-Ray diffractograms confirmed that there is no indication of any chemical reaction between NaNO₃ and Al₂O₃. The crystallite size estimated from all the XRD peaks using Debye Scherrer formula is about 50nm. The FTIR transmittance spectrum of NaNO₃ and Al₂O₃ recorded in the wave number range from 400 to 4000cm⁻¹ revealed sharp peaks at 835cm⁻¹, 1381cm⁻¹, 1789cm⁻¹ and 2430cm⁻¹ for pure NaNO₃ and sharp peaks at 1633cm⁻¹, 3437cm⁻¹and 3550cm⁻¹ for pure Al₂O₃.

Keywords: Composite, XRD, FTIR, Crystallite size, Dispersoid.

INTRODUCTION:

Composite solid electrolytes are a new class of fast ion conductors which have attracted wide spread interest in the recent years due to their possible technological applications in the solid state batteries, electrochromic display devices, fuel cells etc. Sodium nitrate(NaNO₃) has a low melting point and crystallizes with rhombohedral calcite structure at room temperature. Crystalline NaNO₃ undergoes a gradual phase transformation which sets in around 150°C and ends at 275°C. NaNO₃ exhibits Frenkel type disorder[1].

Literature survey indicates major work carried out in many dispersed systems in the recent past namely LiI-Al₂O₃, CuCl-Al₂O₃, Na₂SO₄-Al₂O₃, Li₂SO₄-

Al_2O_3 , $\text{CsCl-Al}_2\text{O}_3$, $\text{Sr}(\text{NO}_3)_2\text{-Al}_2\text{O}_3$, $\text{Na}_2\text{SO}_4\text{-Al}_2\text{O}_3$ [2]. Earlier research work was carried out on $\text{NaNO}_3\text{-Al}_2\text{O}_3$, by P.S Anantha[1] et.al by melt quench method, $\text{NaNO}_3\text{-Al}_2\text{O}_3$ by M.V.Madhavarao[2] et.al by slow evaporation technique. Al_2O_3 was in micron size in their work. Size of the dispersoid plays a major role in physical properties of composite electrolyte system. Fast evaporation technique is one of the methods to obtain products in nanoform. The present study is an attempt to disperse NaNO_3 with fine insulating oxide nano powder Al_2O_3 to make it dispersed solid electrolyte system.

In this study, dispersed solid electrolyte $(1-x)\text{NaNO}_3\text{-}x\text{Al}_2\text{O}_3$ with $(x=0.05, 0.1, 0.15, 0.2)$ is prepared by fast evaporation technique which is one of the wet chemical methods based on hydrolysis, condensation followed by drying[3] the solution. The obtained samples were characterized by XRD and FTIR techniques.

EXPERIMENTAL:

The synthesis of the system $(1-x)\text{NaNO}_3\text{-}x\text{Al}_2\text{O}_3$ (with $x = 0.05, 0.1, 0.15, 0.2$) was explained followed by the flow chart shown in fig .1.

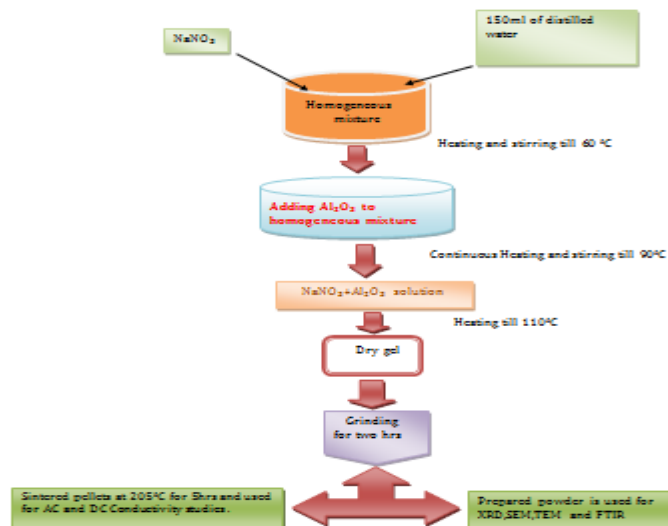


Fig.1. Flow Chart

The sodium nitrate of AR grade and Aluminium oxide of AR grade with particle size $<50\text{nm}$ (TEM) were obtained from sigma Aldrich (USA). First host material is taken in a desired amount and was dissolved in double distilled water, heated on magnetic stirrer till 60°C , after half an hour desired mole% of alumina was

introduced to initial solution and heated till 90°C with continuous stirring .then stopping the rpm count and heating till 110°C dry gel is obtained. The final product obtained was collected and grinded in agate mortar for 2hrs for XRD,FTIR studies.

RESULTS AND DISCUSSION:

XRD Analysis: XRD data of $(1-x)\text{NaNO}_3-x\text{Al}_2\text{O}_3$ with $(x=0.05,0.1,0.15,0.2)$ are shown in fig.2.

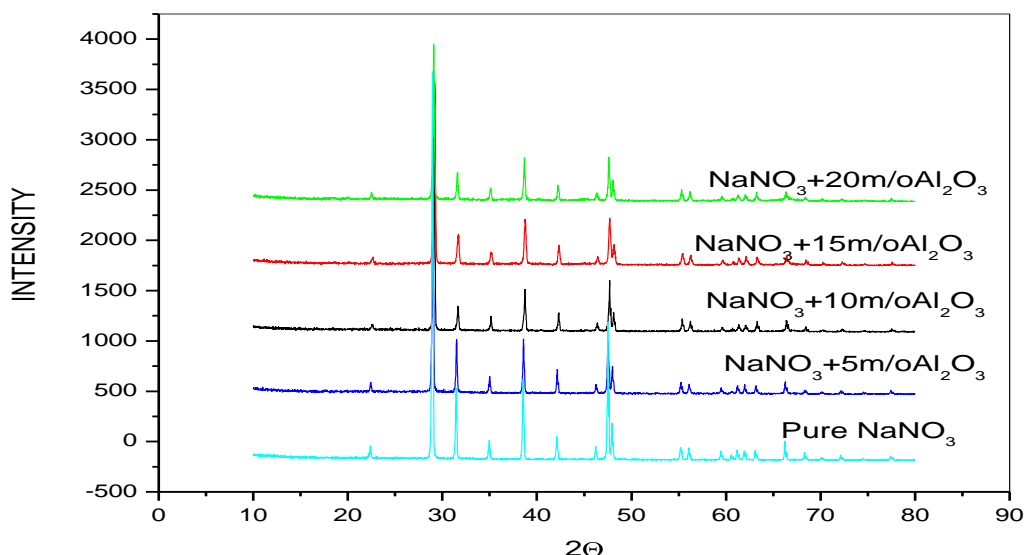


Fig.2. XRD of $(1-x)\text{NaNO}_3-x\text{Al}_2\text{O}_3$

The XRD pattern of the pure NaNO_3 and pure Al_2O_3 shows crystalline and amorphous nature with predominant peaks at 2θ of 22.28,31,38,42,46 and 2θ of 40 and all the peaks obtained from XRD are matching with individual XRD pattern of pure NaNO_3 and pure Al_2O_3 according to JCPDS data[4].XRD peaks in the diffractogram reveal that there is no indication of any chemical reaction between NaNO_3 and Al_2O_3 [1].It is observed from XRD that the host and dispersed system have distinct and high intense peaks indicating that it is in the crystalline form where as pure Al_2O_3 show broader peaks indicates that it is in the order of nano meter. The Crystallite size obtained from the XRD pattern of the system $(1-x)\text{NaNO}_3-x\text{Al}_2\text{O}_3$ is around 50nm using Debye Scherrer formula.

FTIR: The FTIR spectra of pure NaNO_3 and the composite samples with ($x=0.05, 0.1, 0.15, 0.2$) in the wave number range $4000-100\text{cm}^{-1}$ are presented in fig.4.

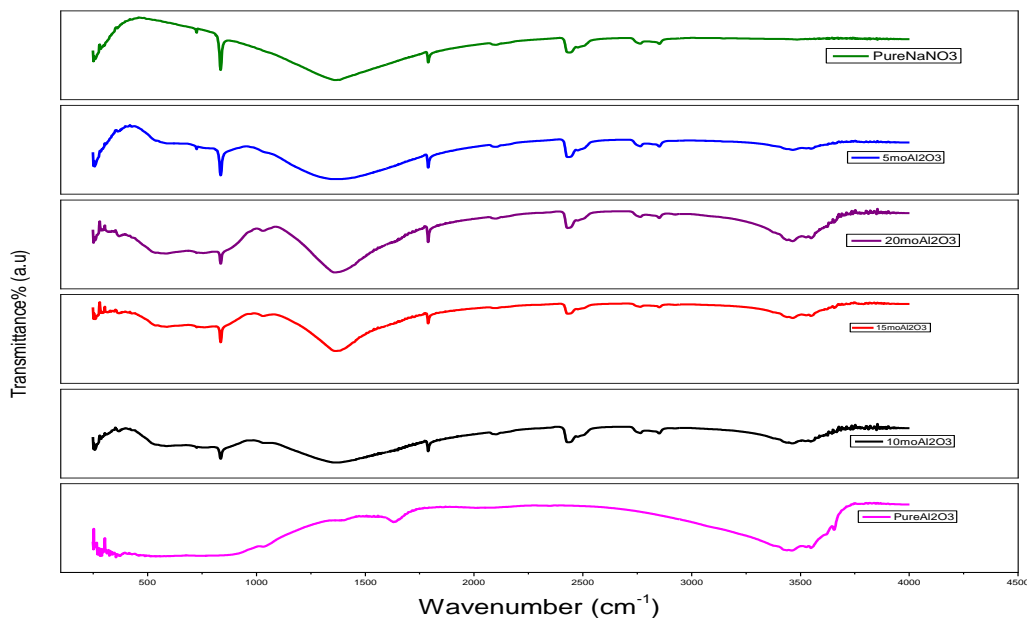


Fig.3. FT-IR spectrum of pure NaNO_3 and dispersed system

The FT-IR spectrum of pure NaNO_3 shows a strong absorption band at 1361cm^{-1} and two medium bands at 835 and 1781cm^{-1} [5]. These bands are ascribed to symmetric N-O stretching (ν_3), out of plane deformation (ν_2) and anti symmetric stretch (ν_4) modes of NO_3^- ion respectively. These characteristic bands of the nitrate group are also observed in all of the composite samples ($x=0.05, 0.1, 0.15, 0.2$) in fig.4. The spectrum of the pure Al_2O_3 shows a sharp peaks at 3437 and 3550cm^{-1} . These bands are ascribed to the O-H stretch (ν_1) H-bonded modes. Addition of Al_2O_3 caused ν_1 mode to shift towards higher wave no of 3466cm^{-1} by an increase in the half-band width indicates the presence of an amorphous phase. The ν_1 mode shift can be observed in the composite samples with $x=0.05, 0.1, 0.15, 0.2$.

CONCLUSION :

XRD and FTIR studies on solid electrolyte system $(1-x)\text{NaNO}_3-x\text{Al}_2\text{O}_3$ reveal that there is no chemical reaction between NaNO_3 and Al_2O_3 from XRD studies. From

the FTIR , it is observed that as the mole percent of dispersoid is increasing, there is an increase in shift towards a higher wave number of the composite system.

References:

- [1]. P.S. Anantha , K. Hariharan , Journal of physics and chemistry of solids 64(2003) 1131-1137.
- [2]. M.V. Madhav Rao , S.Narender reddy, A. Sadananda chary, physica. B362 (2005) 193-198.
- [3]. Mazdida Sulaiman , N.A. Dzulkarnain , A.S. Rahman, N.S. Mohammad, Solid state sciences 14(2012) 127-132.
- [4]. Vijaykumar,Swarnalatha, advances in applied science research 2012 3(5) : 2599-2604.
- [5]. Mazdida Sulaiman, A.A Rahman &N.S.Mohammed Int.J.Electrochem. sci,8(2013) 6647-6655.

Doping effect on crystal structure and phase Properties of Chromium Doped Lithium Nano-Ferrites

D. Ravinder Nayak, G.Aravind, B.Neheru, D. Ravinder
Department of Physics, Osmania University, Hyderabad-500007
Corresponding Author email id:ravindergupta28@rediffmail.com

ABSTRACT:

Lithium based ferrites are potential applications. Single phase soft ferrite Nano crystallites could be synthesized by different methods. Out of various methods We have tried to synthesize Chromium doped Lithium Nano ferrites with a chemical formula $\text{Li}_{0.5}\text{Cr}_x\text{Fe}_{2.5-x}\text{O}_4$ (where $x=0.0, 0.2, 0.4, 0.6, 0.8$ and 1.0) using Citrate- Gel Auto Combustion Technique at low temperature (180°C) to improve their properties. It is a unique combination of the combustion and the chemical gelation processes. They are obtained as dried gel after the successful chemical reaction of these compositions of respective metal nitrate solutions in the midst of citric acid as catalyst. X-ray diffraction (XRD) analysis reveals that all the samples possess a single phase cubic spinel structure particle size of 17nm-26nm. The surface morphology and particle size of the samples was observed by Scanning electron microscopy (SEM) and stoichiometric composition from EDAX and ICPMS (Inductively coupled plasma mass spectroscopy).

Keywords: Li-Cr nano ferrites, Citrate- Gel Auto Combustion Technique, XRD, SEM, EDAX & ICPMS.

Introduction:

Ferrites have Technological Importance and further Nano ferrites play an important role in the miniaturization of several micro wave device applications. $\text{Li}_{0.5}\text{Fe}_{2.5}\text{O}_4$ has been extensive technical and fundamental studies both in pure and substituted form [1,2]. Various physical properties of ferrites are highly influenced by the distribution of cation among the sub lattices nature of grain (shape, size & orientation) grain boundaries Voids, in homogeneities, surface layer and constants etc.

The properties of ferrites depend on several factors which include method of preparation, sintering temperature, time, pH value, amount and $x > 0$ respectively, the general formula for ferrites. For lithium ferrites, the conduction mechanism takes place between Fe^{+2} & Fe^{+3} ions present in equivalent crystallographic sites in the structure of ferrite



The chromium doped lithium ferrites are among the few systems exhibiting the effect of magnetic compensation and Gorter et al [3,4] were the first to observe this phenomenon in $Cr_{1.25}Li_{0.5}Fe_{2.5}O_4$. In ferrites the electrons transfer between the adjacent B sites in spinel structure the properties of lithium ferrites can be enhanced by controlling the preparation method. A spinel type crystal structure (AB_2O_4 , or $Li_{0.5}Fe_{2.5}O_4$), the distribution of metal cation over the tetrahedral (A) and octahedral (B) voids also play a crucial role for exhibiting different physical properties. In lithium ferrite possesses a higher Curie temperature than other spinel ferrites [5]. In $Li_{0.5}Fe_{2.5}O_4$ is an inverse spinel with Li^+ ions and $3/5$ of Fe^{+3} ions can occupy the octahedral B-sites [6] whereas the remaining Fe^{+3} ions can occupy tetrahedral A-sites. The β -phase is a disordered phase where the Li^+ and Fe^{3+} ions are randomly distributed in the octahedral interstices and the space group is $Fd\bar{3}m$ [7–9]. In the above mentioned facts, synthesis of single phase lithium ferrites has received considerable attention. Various synthesis routes have been employed to synthesize ferrites which include, microwave hydrothermal high temp ceramic technique, flash combustion, co-precipitation, sol-gel & citrate methods [10]. Among all these synthesis methods, citrate gel auto combustion method has more attracted and much attention since this process involves low temp processing, homogeneity distribution of reactants and the less time, the ability to produce nano-size particles. Several investigations on the properties of the Li–Cd [11], Li–Zn [12], and Li–Mg [13].

2. Experimental details

2.1 Material

Lithium nitrate- $Li(NO_3)$ sigma aldrich 99% pure AR grade

Ferric Nitrate-(Fe(NO₃)₂9H₂O)(98% pure GR grade), Chromium Nitrate - (Cr(NO₃)₂9H₂O)(Otto Chemie Pvt. Limited, 98% pure GR grade), Citric acid - (C₆H₈O₇.H₂O) (SDFCL-Sdfine Chem. Limited, 99% pure AR grade), Ammonia - (NH₃)(SDFCL-sd fine Chem. Limited, 99% pure AR grade) as starting materials for the synthesis .

2.2 Synthesis of Chromium Doped lithium ferrites

The synthesis of lithium ferrites nanoparticles with chromium doped compositional formula solution were prepared by mixing the stoichiometric amount of metal salts into deionized water .the required molar ratio of metal nitrates and citric acid taken and prepared by citrate gel auto-combustion method. This method has inherent advantages like low temperature (200^oC),excellent stoichiometric control,homogeneous distribution of reactants and production of fine particles with narrow size distribution.In this citrate gel auto-combustion method, metal nitrates act as oxidizing agents and organic fuels as reducing agents(19,20).the various powder properties can be systematically tuned by altering the oxidant to fuel ratios.

The stoichiometric amounts of all the nitrates were weighed and dissolve it individually in add minimum amount of deionized water. All the individual solutions were adding in a way and mix with continuous stirring of upto one hour .

The structural characterization of the synthesized samples

was carried out by Philips X-ray diffractometer (Model 3710) using Cu K α radiation of wavelength 1.5405 \AA at room temperature by continuous scanning in the range of Bragg's

Angles 10 to 80 degrees in steps of 0.04 ^o/sec to investigate the phase and crystalline size.

The average crystalline size of the ferrites was determined from the measured using high intensity [3 1 1] peak width of their diffraction pattern using Debye Scherer's formula [14].

$$D = 0.91\lambda / \beta \cos\theta \text{----- (1)}$$

Where λ is the wavelength of the X-ray used for diffraction

And β is the full width half maximum (FWHM) in radians

The lattice constant was calculated using the following relation:

$$2d \sin\theta = n\lambda, \text{----- (2)}$$

$$\text{where } d = a/\sqrt{(h^2 + k^2 + l^2)}$$

The X-ray density (d_x) has been calculated according to

$$\text{the relation } d_x = 8M/Na^3 [\text{gm/cm}^3] \text{----- (3) [15]}$$

where M = molecular weight of the sample. a is the lattice

Parameter and N is the Avogadro number. The volume of the unit cell $V = a^3$.

3. Results and Discussion:

The X-ray diffraction pattern of the prepared Cr substituted Lithium nano ferrites were shown in fig(1). The X-ray diffraction pattern of the prepared samples were confirmed the well-defined homogeneous single phase cubic spinel structure[16] belonging to the space group $Fd\bar{3}m$. The average Crystallite size of the prepared nano samples measured from the X-ray analysis line width of most intense peak (311) was in the range 27-17nm by using Debye-Scherrer's formula.

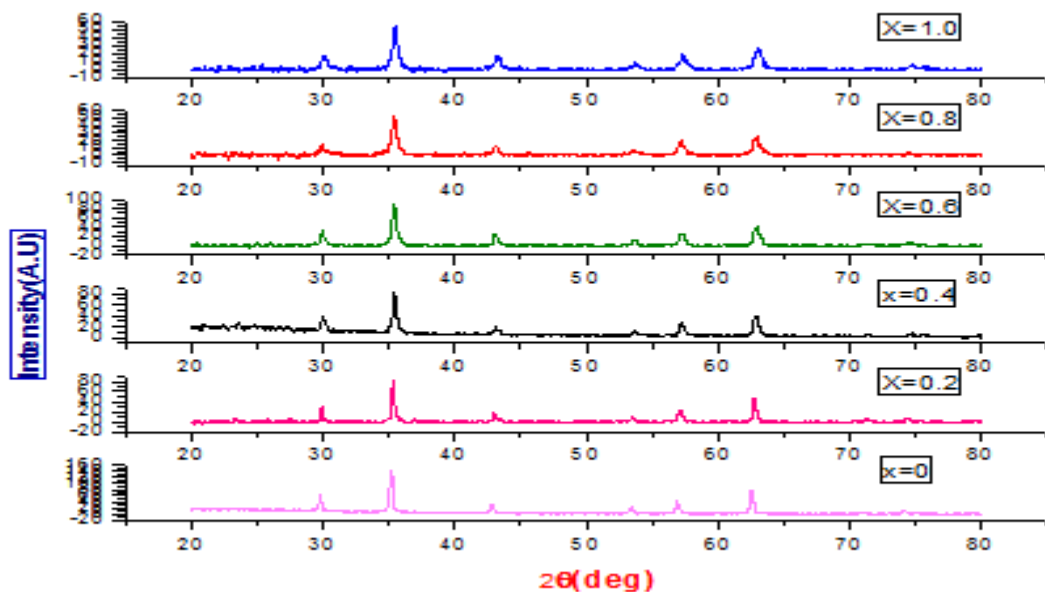


Fig (1) XRD pattern of the nano crystalline Li-Mg ferrites

Table 1 The experimental density of the prepared sample of Li-Cr Nano ferrites

Cr composition	Mol.wt (gm/mole)	Crystallite size(nm) ± 0.2 nm	Lattice parameter(\AA) ± 0.002 \AA	X-ray density (d_x) ± 0.02
X=0	207.091	27	8.433	4.760
X=0.2	206.321	21	8.414	4.600
X=0.4	205.551	26	8.401	4.611
X=0.6	204.781	21	8.400	4.587
X=0.8	204.001	21	8.397	4.575
X=1.0	203.241	17	8.381	4.565

Lattice parameter of the prepared samples was decreased with increasing the Cr composition [17,18] in the range $0.0 < X < 1.0$ of Li-Cr nano crystalline ferrites. A similar variation was also observed by West and Blankenship [19] in Li-Zn ferrites. In this study, we also observed this phenomenon. Fig. 2 shows the dependence of the lattice constant on Cr-substituted concentration. The lattice constant decreased markedly with increasing concentration of chromium substitution in the range of $0.0 < x < 0.4$, and in the range of $0.5 < x < 1.0$, the lattice constant gradually decreases as x increases. Generally, as the Cr substituted. As the concentration increases, the lattice constant decreases. It is attributed to the fact that different radii of Fe^{3+} (0.64\AA) and Cr^{3+} (0.62\AA) in an oxide solid solution with a spinel-type structure. In this study, we also observed this phenomenon. Fig. 2 shows the dependence of the lattice constant on Cr-substituted concentration. Cr compositions with lattice parameter and X-ray density experimentally which were shown in below fig (2a) & fig (2b) respectively.

When doped with smaller Cr^{3+} ions, the spinel lithium ferrite will shrink. Doping Cr^{3+} ions in a spinel-type structure will induce uniform strain in the lattice as the material is elastically deformed. This effect causes the lattice plane spacing to change

and the diffraction peaks shift to a higher 2θ position. Noticeably, the lattice parameter is nonlinearly dependent on Cr-substituted concentration for $\text{Li}_{0.5}\text{Cr}_x\text{Fe}_{2.5-x}\text{O}_4$. Gorter's defined the chemical formulas of $(\text{Fe}1.0)[\text{Li}0.5\text{Fe}1.5]\text{O}_4$ and $(\text{Fe}1.0-y\text{Li}y)[\text{Li}0.5-y\text{Fe}1.5-x+y\text{Cr}x]\text{O}_4$ for $x=0$ and $x > 0$, respectively. The formula for $x > 0$ indicates that Li^+ ions partially occupy the tetrahedral (A) site and that the distribution of Fe^{3+} ions occupying the tetrahedral (A) and octahedral (B) sites changes. Y increases nonlinearly as x increases. Several authors have reported the lattice parameter of $\text{Li}_{0.5}\text{Fe}_{2.5-x}\text{Cr}_x\text{O}_4$ [20-22]. The observed nonlinear Cr-substituted concentration dependence of the lattice parameter may have resulted from the change of ion distribution depending on the concentration of Cr substitution. The theoretical density was calculated according to the formula: $D_x = 8M/Na^3$ where M is the molecular mass, N is Avogadro's number, and a is the lattice parameter which was calculated from the X-ray diffraction pattern. The theoretical density is in the range of 4.76–4.56 gcm^{-3} for $\text{Li}_{0.5}\text{Cr}_x\text{Fe}_{2.5-x}\text{O}_4$ ($x = 0-1.0$). The lattice constant, theoretical density, and mol. weight of the $\text{Li}_{0.5}\text{Cr}_x\text{Fe}_{2.5-x}\text{O}_4$ system sintered at 500°C for 4 h are summarized in Table 1.

As the increasing the Cr composition experimental density is also decreases remarkably and there is slight increasing taking place. Additionally, it was predicted that the lattice parameters of nanoparticles decrease with a decrease in the particle size [23].

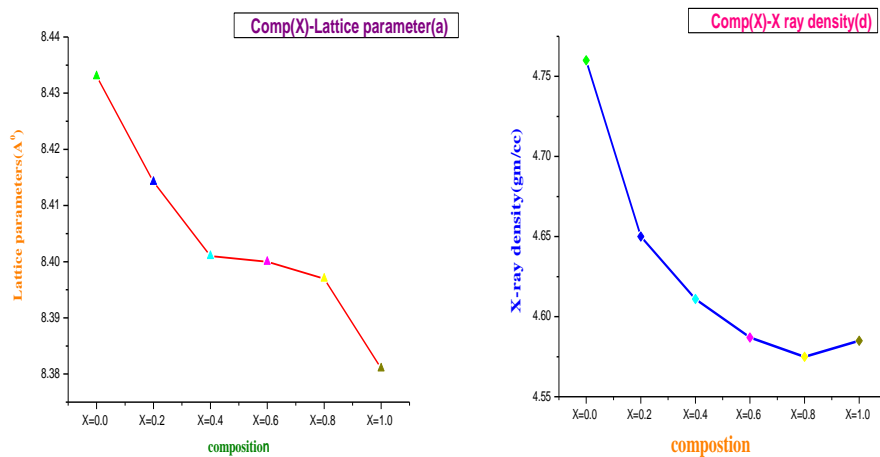


fig (2a) fig (2b)

3.2 SEM ANALYSIS

Electrical and magnetic properties are depending on the sensitively microstructure of ferrites. Grain diameter is more important parameter affecting the magnetic properties of ferrites. In SEM each grain consists of several particles[24]. The Scanning electron microscope (SEM) scan patterns of the specimen shows the surface morphology of the Li-Cr Nano ferrite particles sintered at 500°C. The SEM images of the $\text{Li}_{0.5}\text{Cr}_x\text{Fe}_{2.5-x}\text{O}_4$ Nano ferrites shown in Figure (3).

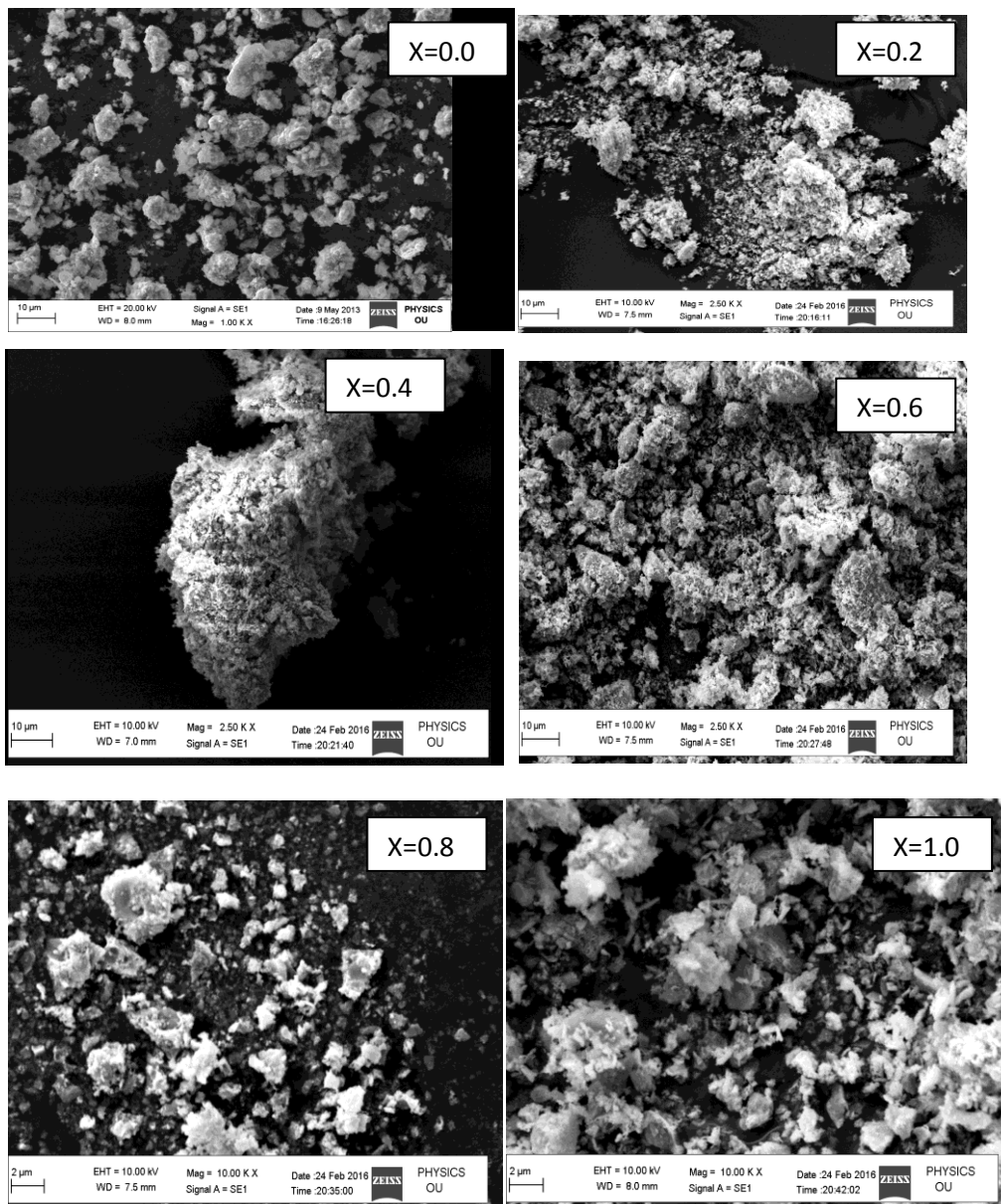


Figure (3). The SEM images of the $\text{Li}_{0.5}\text{Cr}_x\text{Fe}_{2.5-x}\text{O}_4$ Nano ferrites

The morphology and grain size of the samples seem to be spherical shape and a narrow size distribution. In which some what agglomeration in the synthesized samples which is unavoidable. From the Observation of the image, one can observe the grain size is slightly affected by the doping the Cr composition.

ELEMENTAL ANALYSIS BY EDAX: The EDAX spectra fig.4. Energy dispersive Spectrometer was used for the elemental analysis of the prepared ferrites with different compositions. In EDAX spectra Cr substituted grains indicated in the presence of concentrated of Cr with energy range of up to 8 keV and seen at 0.6keV, 5.4keV and 5.9keV Fe was seen at the 0.8keV and 6.5keV and 7keV. In this Lithium low atomic element because of that can't detect elemental analysis in Few SEMs.

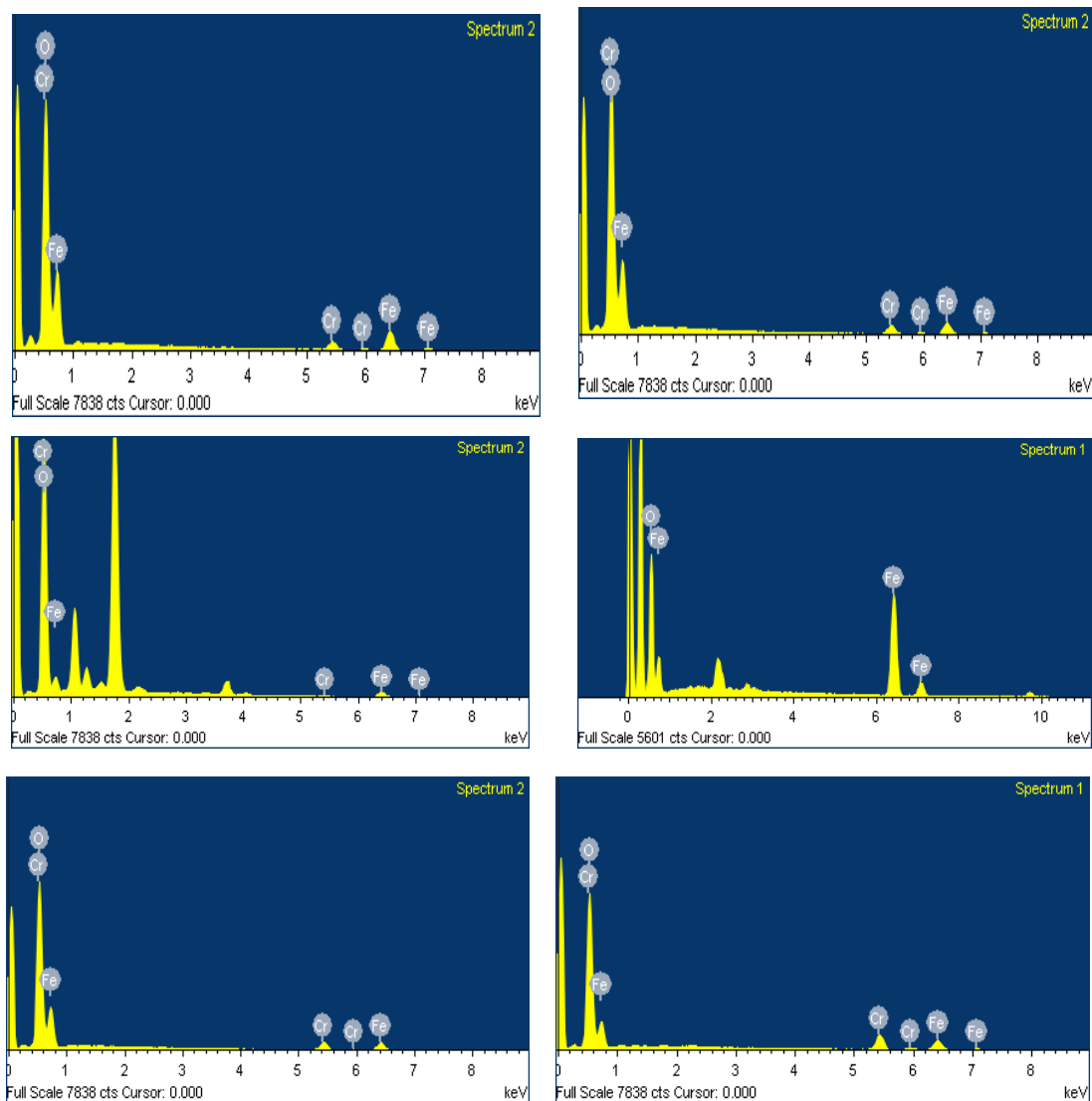
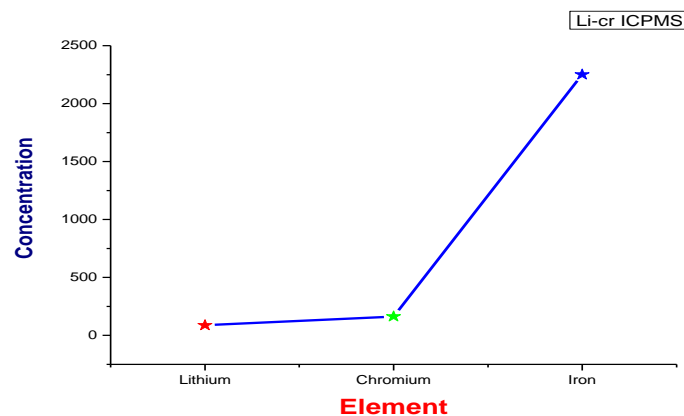


fig. 4 The EDAX spectra

ICPMS:

Inductively coupled plasma mass spectroscopy is used to conform the Li elemental compositional

presence in the Lithium Nano ferrite and To compensate for this, a matrix component is often used as an internal standard. However, using an internal standard prohibits the analysis of all elements simultaneously in the sample compositions. by this conforming the Li is present in this sample.

**Conclusion**

The Cr-substituted Nano-crystalline lithium ferrite samples were synthesized by sol-gel auto-combustion method.

Citrate gel auto-combustion method was a very suitable technique for the preparation of nano sized (27-17 nm) Cr substituted lithium ferrite at low sintering temperature.

X-ray diffraction studies confirm the cubic spinel structure formation.

The lattice constant and crystallite size decrease with increase in Cr content .

The EDAX spectra Energy dispersive Spectrometer was used for the elemental analysis of the prepared ferrites with different compositions.

Inductively coupled plasma mass spectroscopy is used to conform the Li elemental compositional presence in the Lithium Nano ferrite

Acknowledgements:

The authors are very grateful to Prof.D.Suresh Babu, Head, Department of Physics, Prof. J.Shiva Kumar, BOS, Department of physics , University College of Science, OsmaniaUniversity,Hyderabad.

References

- [1] Dorman J.L,Rev.Phys.appl.1980,15,1113
- [2] Krishnan R,Physica B1977,86-88,1457
- [3] Gorter E.W. Philips Res.Rep.1954,9,295
- [4] Gorter E.W and schulkes J.A Phy.Rev 1953,89,487
- [5] Y.P. Fu, Mater. Res. Bull. 41 (2006) 809.
- [6] S. Verma, P.A. Joy, J. Appl. Phys. 98 (2005) 124312.
- [7] S. Verma, J. Karande, A. Patidar, P.A. Joy, Mater. Lett. 59 (2005) 2630–2633.
- [8] A.Tomas,P. Laruelle, J.L. Dormann, M. Noguees, ActaCrystallogr. C 39 (1983)1615.
- [9] S.J. Marin, K. O’Keefe, D.E. Partin, J. Solid State Chem. 113 (1994) 413.
- [10] E.E.Sileo,RRoteldo S.E Jacobo J.Phy.B,320(2002),257-260
- [11] S. S. Bellad, R. B. Pujar, and B. K. Chougule, *Materials Chemistry and Physics*, vol. 52, no. 2, pp. 166–169, 1998.
- [12] D. Ravinder*Journal of Materials Science Letters*, vol. 11, no. 22, pp.1498–1500, 1992.
- [13] Y. Purushotham, M. B. Reddy, P. Kishan, D. R. Sagar, and P. V. Reddy, *MaterialsLetters*, vol. 17, no. 6, pp. 341–345, 1993.
- [14] Cullity B D,(addition Wesley,reading ,mass)1959,P132
- [15] R.C.Kumbale,P.AShaik,S.SKamble,Y.D.KolekarJ.Alloys Comp.,478(2009),P.599
- [16] S.A.Mazen,S.F. Mansour,H.M.ZakiCry.res.Technol.38.No 6,471-478(2003)

-
- [17] P.P. Hankare, R.P. Patil, U.B. Sankpal , K.M. Garadkar, R. Sasikala ,
A.K.Tripathi, I.S. Mulla Journal of Magnetism and Magnetic Materials 322
(2010) 2629–2633
- [18] R.G. West, A.C. Blankenship, J. Am. Ceram. Soc. 50 (1967) 343
- [19] R.G. West, A.C. Blankenship, J. Am. Ceram. Soc. 50 (1967) 343.
- [20] Y.P. Fu, Jpn. J. Appl. Phys. 46 (2007) 7314.
- [21] M.V. Kuznetsov, Q.A. Pankhurst, I.P. Parkin, Physica D 31 (1998) 2886.
- [22] L. Fernandez-Barquin, M.V. Kuznetsov, Y.G. Morozov, Q.A. Pankhurst, I.P.
Parkin,Int. J. Inorg. Mater.1 (1999) 311.
- [23] G.K. Shenoy, F.E. Wagner, Mössbauer Isomer Shifts, Amsterdam:North-
Holland, 1978
- [24] A.Dhahri,JDhahri,S.Zemni,M.Oumezzine,M.Said and H.Vincent journal of
Alloys and Compounds,ol.450,no1-2,pp12-17,2008.

Thermo Electric Power studies of Li-Co nano ferro spinels

G.Aravind¹, V.Nathanial², A. Ranjith², Ch.Sumalatha², V.Ludhiya³
D.Ravinder³

¹ Department of Physics Methodist College of Engg. & Technology, Abids, Hyd.

²Department of Physics, University College of Science, Saifabad,
Osmania University Hyderabad-500007

³Department of Physics Osmania University Hyderabad-500007

ABSTRACT

Nanocrystalline lithium cobalt ferrites of compositions $[\text{Li}_{0.5}\text{Fe}_{0.5}]_{1-x}\text{Co}_x\text{Fe}_2\text{O}_4$ (where $x = 0.0, 0.2, 0.4, 0.6, 0.8,$ and, 1.0) were synthesized at lower processing temperature ($180\text{ }^\circ\text{C}$) by non-conventional citrate gel auto ignition method using citric acid as a fuel and oxidant. Structural characterization of the sintered samples was carried out by X-ray diffraction (XRD) analysis. XRD studies of the prepared samples confirmed the homogeneous single-phase cubic spinel structure with the crystallite sizes ranging from 37 to 43 nm. Thermoelectric power (TEP) studies of the prepared samples were carried out from 200 to $600\text{ }^\circ\text{C}$ using a differential method. The variation of Seebeck coefficient (S) with temperature indicated p-type semiconducting nature of the sample at lower temperature and n-type semiconducting nature at higher temperature indicating the conduction due to the electrons. The Curie temperature (T_c) of the prepared samples measured from TEP studies showed a decreasing trend with the increasing Cobalt concentration.

Keywords: XRD, Spinel ferrites and Thermo Electric Power (TEP)

1. Introduction:

The field of ferrites is well developed but due to its potential applications in various fields, and interesting physics involved in it, even after several decades of its first artificial synthesis, scientists and researchers are still interested in various types of synthesized methods by different preparative techniques, parameters and conditions in bulk, nano crystalline and thin film forms and in the study of structural, magnetic, electrical, properties as a function of composition, frequency, temperature etc. ferrites have a high magnetic permeability which is used to store stronger magnetic field than iron.

Ruiyun He et al. [1] observed the application of titanium doped lithium ferrites in circulators at 11 GHz operating frequency in the temperature range of 20-300 K. The saturation magnetization value and Curie temperature of samples decreased with increasing the Ti composition. Reddy et al. [2-4] studied the lithium titanium mixed ferrites. The saturation magnetization and Curie temperature also decreased with titanium content.

2. Experimental techniques

In the present communication we prepare Li-Co nano crystalline ferrites by auto-combustion method at low sintering temperature. The synthesis procedure was discussed in our earlier publication [5]. X-ray diffraction analysis of the prepared ferrite powders were performed by using Philips X-ray diffractometer with Cu K_{α} radiation of wavelength 1.5405 Å. For the thermo electric power measurements, the synthesized powders were made in the form of circular pellets (diameter – 13 mm and thickness – 2 mm) using 2% polyvinyl alcohol (PVA) as binder under a pressure of 5 tons for 1–2 min. These pellets were finally sintered at 500 °C for 4 h and then slowly cooled to room temperature. Pellets were then coated on either side with a thin layer of silver paste to have good electrical contact. Thermo electric power measurement studies on the prepared pellets were carried out by differential method from 320 K to well beyond Curie temperature..The thermo electric power or Seebeck coefficient (S or α) was calculated using the following relation.

$$S = \frac{\Delta E}{\Delta T} (\mu V / K)$$

where ΔE is the thermo electro motive force produced across the two ends of the sample which is measured by using a digital micro voltmeter and the ΔT is the temperature difference between the two surfaces of the pellet which is measured by two chromel-alumel thermocouples that were kept very close to the sample. For achieving good thermal stability, thermo emf values were measured while cooling.

3. Results and Discussions:

3.1 XRD analysis

The structural study is essential for optimizing the properties needed for various applications. The phase identification and structural parameter determination were performed on an x-ray diffraction analysis. The x-ray diffraction pattern of the $[\text{Li}_{0.5}\text{Fe}_{0.5}]_{1-x}\text{Co}_x\text{Fe}_2\text{O}_4$ (where $x= 0.0$ to 1.0 with step of 0.2) powder ferrite samples sintered at 500°C for 4 hours are shown in **fig (1)**. Analyzing the x-ray diffraction pattern one can observed that the positions of the peaks are comply with the reported values [6-8]. From the **fig (1)** it can be seen that the location of the peaks in XRD pattern of all prepared samples are coincident, which indicate that there were no distinct differences in phase structure of Li-Co nano crystalline ferrites with different cobalt composition. On increasing the cobalt compositions, reflection peaks become sharp and reflection intensities of the pattern increases which reveal that cobalt composition is useful in the crystallization of the nano crystalline ferrites and use to promoting the grain growth. It was observed that cobalt ions were partly replaced by iron and lithium ions in the lattice and then increased the lattice constant.

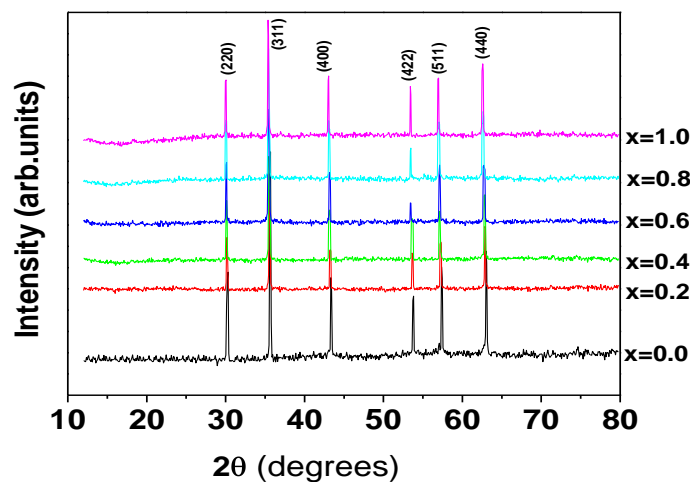


Fig (1) XRD pattern of the $[\text{Li}_{0.5}\text{Fe}_{0.5}]_{1-x}\text{Co}_x\text{Fe}_2\text{O}_4$ ferrite samples

The observed peaks at (220),(311),(400),(422),(511) and (440) confirmed the spinel structure of the prepared samples. This indicates that the synthesized ferrite compositions are of single phase cubic spinel since no ambiguous reflections other than the spinel structured are observed and also demonstrates the homogeneity of the prepared nano crystalline ferrite samples. The x-ray diffraction analysis of the prepared Li-Co nano crystalline ferrite samples provides the estimation of the crystallographic lattice constant (a), crystalline size (D), x-ray density and experimental density etc are given in **table1**

The average crystallite size which are calculated from the Debye-Scherrer's formula were in the range of 36-43 nm which confirms the nano crystalline form. The lattice constant of the samples increases with cobalt composition which obeys the Vegard's law [9].

Table1

Structural parameters of the prepared Li-Co ferrite sample

composition	Mol.wt (gm/mol)	Crystallite Size (nm)	Lattice constant (Å)	X-ray Density (d_x) (gm/cc)	Experimental Density (d_e) (gm/cc)	% of Porosity (P)
$\text{Li}_{0.5}\text{Fe}_{2.5}\text{O}_4$	207.079	41.90	8.35	4.71	4.28	9.00
$\text{Li}_{0.4}\text{Co}_{0.2}\text{Fe}_{2.4}\text{O}_4$	212.587	43.01	8.37	4.81	4.37	9.10
$\text{Li}_{0.3}\text{Co}_{0.4}\text{Fe}_{2.3}\text{O}_4$	218.095	38.44	8.37	4.93	4.38	11.00
$\text{Li}_{0.2}\text{Co}_{0.6}\text{Fe}_{2.2}\text{O}_4$	223.603	37.57	8.38	5.03	4.39	12.70
$\text{Li}_{0.1}\text{Co}_{0.8}\text{Fe}_{2.1}\text{O}_4$	229.111	37.06	8.39	5.14	4.58	10.90
CoFe_2O_4	234.619	36.90	8.40	5.25	4.68	10.70

3.2 Thermo Electric Power studies of $[\text{Li}_{0.5}\text{Fe}_{0.5}]_{1-x}\text{Co}_x\text{Fe}_2\text{O}_4$ nano ferrites

The thermo electric power studies of the prepared nano crystalline $\text{Li}_{0.5}\text{Fe}_{0.5}]_{1-x}\text{Co}_x\text{Fe}_2\text{O}_4$ ferrites were measured by differential method in the temperature range 200-600°C. The thermo e.m.f of the samples measured during cooling cycle because during cooling the sample attains more thermal stability than heating. The values of the seebeck coefficient of mixed Li-Co nano ferrites were

calculated from the observed values of the thermo electro motive force and tabulaed in the **table2** Carrier concentration of the prepared samples was calculated at 500K. It can be seen from the table that among all the mixed Li-Co spinel ferrites, the composition $\text{Li}_{0.3}\text{Co}_{0.4}\text{Fe}_{2.3}\text{O}_4$ was having highest values of carrier concentration. From the table2 one can observed that Seebeck coefficient increases with increasing the Co concentration this may be attributed to the fact that by increasing the Co^{+2} ions in the lithium ferrites, more number of charge carriers are produced so that large energy was needed to transfer the charge carriers between the different cations. Hence large electro motive force produced, which enhances the thermo electric power. The addition of Co^{+2} ions in the Li-Co ferrites has an effect of decreasing the number of Fe^{+2} ions in the B-site so that seebeck coefficient increases. **Fig (2)** shows the variation of Seebeck coefficient with temperature for all prepared sample. It can be seen from the **fig (2)** that the sign of seebeck coefficient was positive at low temperature and increasing the temperature S became negative value for all ferrites under investigation.

Table2: Seebeck Coefficient, Curie point of the prepared Li-Co ferrite samples

Composition	Seebeck Coefficient(S) ($\mu\text{V/K}$)@ T_c	Curie Point (K)	Carrier concentration
$\text{Li}_{0.5}\text{Fe}_{2.5}\text{O}_4$		>873	3.10×10^{22}
$\text{Li}_{0.4}\text{Co}_{0.2}\text{Fe}_{2.4}\text{O}_4$	-3546	861	1.90×10^{22}
$\text{Li}_{0.3}\text{Co}_{0.4}\text{Fe}_{2.3}\text{O}_4$	-4413	840	3.15×10^{22}
$\text{Li}_{0.2}\text{Co}_{0.6}\text{Fe}_{2.2}\text{O}_4$	-4958	815	1.46×10^{22}
$\text{Li}_{0.1}\text{Co}_{0.8}\text{Fe}_{2.1}\text{O}_4$	-5840	801	3.06×10^{22}
CoFe_2O_4	-6140	790	2.98×10^{22}

This indicates that at low temperature these prepared samples behave like a p-type semiconductor and increasing the temperature predominant conduction mechanism in these ferrites was due to the electrons and behaves like a n-type semiconductors. It can be seen that the values of the seebeck coefficient for all mixed nano crystalline Li-Co ferrites increases with increase of temperature which

indicates that more n-type charge carriers i.e electrons were released with an increase in temperature.

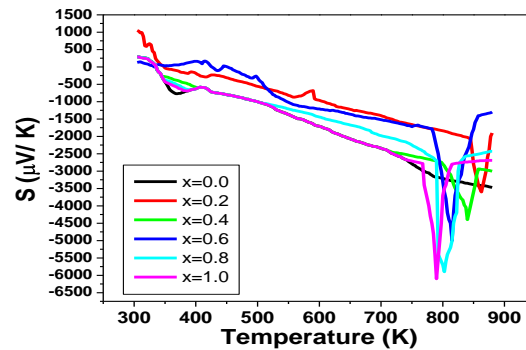


Fig (2) Variation of Seebeck coefficient (S) with temperature for Li-Co ferrites

Further increase in temperature results a decrease in seebeck coefficient which remains almost constant later on. This may be due to the transition at that temperature (Curie temperature). It was clear that in case of Li-Co nano ferrites the non magnetic property (thermo electric power) under study was exhibiting a well-defined transition at the Curie temperature, like the magnetic properties viz., susceptibility, permeability and spontaneous magnetization. The fact that the value of seebeck coefficient shows minimum values at Curie temperature indicates that the magnetic ordering has a marked influence on the thermo electric power of these ferrite samples under investigated. From the present study and considering the semiconducting behavior of investigated ferrites, the charge carriers are considered to be localized at ions or at vacant sites as a result of electron-phonon interaction [10].

Conclusions

Citrate Gel auto combustion technique is a convenient way for obtaining a homogeneous nano sized mixed ferrites. The process involves no impurity pickup and material loss. It is a very simple and economical method where no specific heating or cooling rate is required. It is a low temperature processing technique and requires shorter sintering duration. X-ray diffraction pattern confirms the formation of cubic spinel structure in single phase without any impurity peak. It is in good agreement with the standard data from ICSD . In synthesized nano ferrite systems it

is observed that with increase in temperature, the value of thermoelectric power increases and shows maximum value at curie temperature $T_c(K)$ beyond which it decreases.

References

- [1] Raiyun He, Mingche Sun and Deqiong Yu, IEEE trans, MAG-18, 1982,1622.
- [2] M.Bhagavantha Reddy, V.Devender Reddy and P.Venugopal Reddy, Moder.Phys.Lett B.10,1996,29.
- [3] S.A.Jadhav, Materials Chemistry and Physics,65,2000,120-123.
- [4] PranKishan, D.R.Sagar and Premswasup, J.Less-common Met, 108, 1985,345.
- [5] **G.Aravind**, M.Raghasudha, D.Ravinder, Abdul Gaffoor, V.Nathanial, J of Nanostruct Chem, (**Springer Publications**) **DOI.10.1007/s40097-014-0138-6**
- [6] M.S.Ruiz, S.E.Jacobo, "Electromagnetic properties of Li-Zn ferrites doped with aluminum", Physica B 407 (2012) 3271-3277.
- [7] Mamatha Maisnam, Sumitra Phanjoubam, " Frequency dependence of electrical and magnetic properties of Li-Ni-Mn-Co ferrites", Solid State Commun 152 (2012) 320-323.
- [8] S.A.Saafan,S.T.Assar, B.M.Moharram, M.K.El Nimr, J of Magn and Magn Mater 322 (2010) 628-632.
- [9] K.Wykpis,A.Budnoik,E.lagiewka,Mater,Science,Forum.636 (2010)1053-1058
- [10] F.Habery,H.P.J.Wijn, Physica status Solidi,26 (1968) 231.

Study of Normal and Abnormal EEG

John William Carey Medithe
 Department of ECE
 VFSTR University
 Guntur, Andhra Pradesh, INDIA
 careymedithe@gmail.com

Usha Rani Nelakuditi
 Department of ECE
 VFSTR University
 Guntur, Andhra Pradesh, INDIA
 usharani.nsai@gmail.com

Abstract—Electroencephalogram (EEG) is the most efficient medical imaging tool to analyze and interpret the characteristics of the brain disorder which helps the physician to diagnose the brain disorder patient. EEG signal is a representation of electrical activity over the surface of the brain with respect to time, this electrical activity is caused by the firing of neurons. If these neurons fire in anomalous manner, results in sudden impulses which can be stated as Seizures. If this unusual firing of nerve cells occurs in severe, may result in a shake and loss of control in the subject sometime. EEG waveform information about frequency, amplitude and shape are entirely dependent on the subjects age, state of alertness and location on scalp where the EEG is drawn with electrodes. An EEG waveform is said to be abnormal when the EEG waveform exhibits unusual characteristics which does not match to the subject's state of alertness, age and other factors. In this article it is to study the different types of EEG waveforms both in the case of normal and abnormal and further concentrated on the abnormalities both in the foam of Epileptical and Non-Epileptical. These abnormalities are internally classified as focal and generalized seizures. The comparable tabular form is given to the each type of EEG waveform based on their characteristics.

Index Terms—Abnormal EEG, EEG characteristics, Epileptical Seizures, Non-Epileptical Seizures.

I. INTRODUCTION

The Electroencephalogram is a recording of electrical activity generated by the brain. However, EEG is obtained by placing electrodes on the scalp. Human brain consists of millions of neurons, where each neuron generates small electric impulses in their respective region. EEG signal ranges from about $0.5\mu\text{V}$ to $100\mu\text{V}$ peak to peak in a normal adult, which is 100 times lower than ECG signal and it is approximately in the order of Millivolt (mV) when measured with subdural electrodes such as needle electrodes [1]. EEG waveforms are generally classified according to their frequency, amplitude, region of occurrence on the scalp and other characteristics. But, these classifications are entirely dependent on the factors like subjects age, state of alertness, age etc. Here, for the classification EEG waveform, preliminary waveforms are alienated as the normal and abnormal and that abnormal EEG in the preliminary stage is further classified into focal and generalized abnormal seizures, which state that focal abnormality gives that it regards the particular function or area of the psyche and that touches the portion of the body which belong to affected region on the psyche. Generalized or localized abnormality is the case where abnormality affects every function of the psyche, which may involve the entire

body. However, EEG cannot give complete etiology of dysfunctions related to the brain, its sensitivity in various episodes guide the physician to diagnose the level of consciousness, sleep disorders, epilepsy, tumors, lesions etc. The block flow diagram is presented below to show that how the EEG is classified.

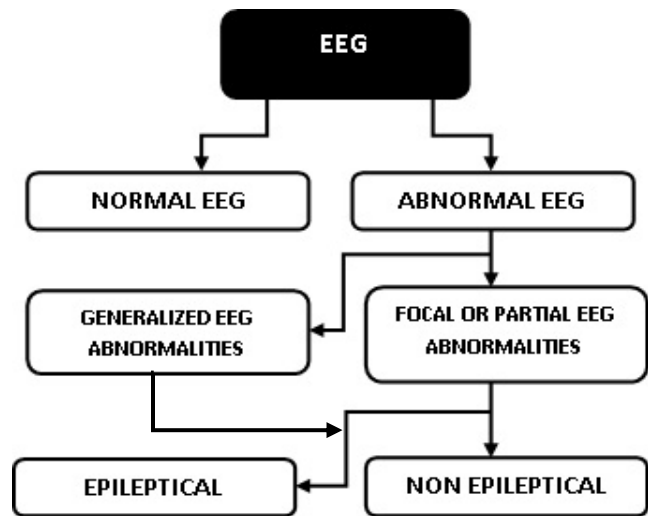


Fig. 1. Block Flow diagram of EEG waveforms.

II. NORMAL EEG WAVEFORMS

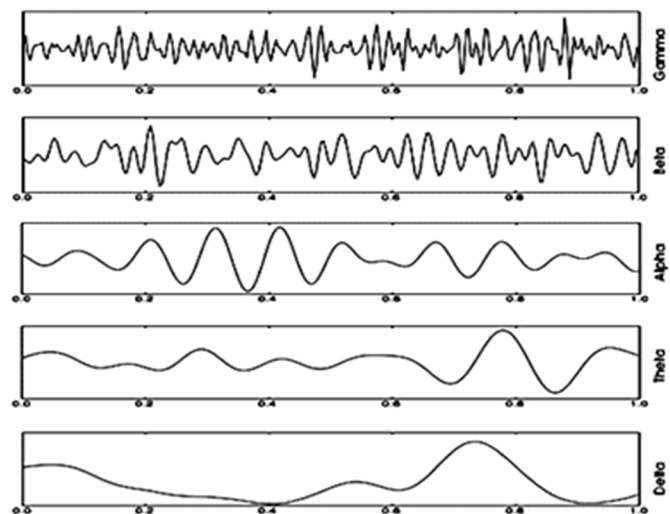


Fig. 2. Representation of EEG signal based on different frequency bands.

The EEG waveform is said to be normal when the EEG recording does not bear any unusual seizures. Waveform exhibits unusual characteristics like frequent, long or continuous seizures when the subject affected by tumor or any case of the brain disorder which can be consider EEG as abnormal.

A. EEG frequency bands

Although EEG signal ranges widely, based on the clinical interest the EEG waveform consider in the range between 0.3 to 30Hz. This clinically considered frequency range of EEG signal is divided into different frequency bands which can be stated as alpha, theta, delta and gamma frequencies. These frequencies are generated by the different action done by the neural system. These are purely dependent on the subject’s age, state of alertness, and other factors [2, 3, 4, 5, 12]. The pictorial representation of the frequency bands of EEG signal is shown in Fig. 2.

The classification of the normal EEG waveform based on the frequencies and its state of occurrence when subject undergoes EEG recordings. These characteristics are compared in below TABLE I. The EEG waveform is called as abnormal in the following comparison when one frequency band exhibits properties of higher or lower frequency band properties. The properties of each frequency band have its own unique nature like shape, amplitude etc.

TABLE I. CLASSIFICATION OF EEG WAVES BASED ON FREQUENCIES

Type of Waveform	Characteristics	State of occurrence	Abnormality
Alpha waves	<ul style="list-style-type: none"> Frequency range 8-13hz Amplitude is mostly less than 50µV 	<ul style="list-style-type: none"> When subject is Awaken but relaxed with closed eyes 	<ul style="list-style-type: none"> If present in frontal regions may suspect as depression and attention problems. Head injuries
Beta waves	<ul style="list-style-type: none"> Frequency range 13-30hz Small in amplitude symmetric 	<ul style="list-style-type: none"> When the subject gives Alertness, mental effort When taken drugs 	<ul style="list-style-type: none"> Deficient beta may rise to lack of concentration and problem solving. Excessive beta may rise to sleep disorders, hyper activeness
Theta waves	<ul style="list-style-type: none"> Frequency range 4-8hz Larger amplitude than beta 	<ul style="list-style-type: none"> Early stages of drowsiness. Day dreaming 	<ul style="list-style-type: none"> If seen in awake adults Head injuries and brain lesions
Delta waves	<ul style="list-style-type: none"> Frequency range 3hz or less Large amplitude 	<ul style="list-style-type: none"> Deep, dreamless sleep, non-REM sleep unconscious 	<ul style="list-style-type: none"> If seen in awake adults result of a lesion or tumor may indicate damage from a stroke
Gamma waves	<ul style="list-style-type: none"> Frequency range is Greater than 30Hz Small in amplitude 	<ul style="list-style-type: none"> Motor Functions higher mental activity 	<ul style="list-style-type: none"> Abnormal when for continuous for a long time

B. Sleep episode and spike EEG waveforms

There are other kinds of EEG waveforms which occur naturally in some episode like sleep spindles and some occur in the stage 2 of the NREM sleep. Further, they can be called as sleep disturbances, as some of these types may occur before and after when the subject change its state of alertness. Where these waveforms may also exhibit abnormality when they occur repeatedly and in seizure manner. Severe and high repetition of these sleep and spike episodes exhibition can also be considered as abnormality. These are described and classified in TABLE II.

Sleep episode spike can be found in a normal subject, when the subject is changing from one state of alertness to another. These patterns can be recorded and analyzed using EEG. This type of spikes helps subject to shift from one state to another state of alertness easily and successfully.

TABLE II. CLASSIFICATION OF EEG WAVES BASED ON SLEEP AND SPIKE

Type of wave form	Characteristics	State of occurrence	Abnormality
K- complex waves	<ul style="list-style-type: none"> Delta frequency, large amplitude, sharp apex. Symmetric it was followed by rhythmic theta waves Occur in Bifrontal regions 	<ul style="list-style-type: none"> Occur each time the patient is aroused partially from sleep Stage 2 of sleep 	<ul style="list-style-type: none"> If it's found in awake state
V waves	<ul style="list-style-type: none"> Sharp waves, Easy to recognize, Occur in Parasagittal regions 	<ul style="list-style-type: none"> Usually occur after sleep disturbances like k-complex During sleep stage-2 	<ul style="list-style-type: none"> If it's found in awoken state
Lambda waves	<ul style="list-style-type: none"> Bilaterally positive waves, Triangular in shape and generally symmetric Occur in Occipital region 	<ul style="list-style-type: none"> When subject is Awaken, Most evident when the subject stares at a blank, uniform surface like reading and watching TV 	<ul style="list-style-type: none"> If found when concentrating and problem solving
Positive Occipital Sharp Transients of Sleep (POSTS)	<ul style="list-style-type: none"> Bilaterally positive waves, Triangular in shape Seen in Occipital region 	<ul style="list-style-type: none"> During stage-2 of sleep 	<ul style="list-style-type: none"> When occur in stage -1 of sleep
Sleep spindles	<ul style="list-style-type: none"> Frequency-upper levels of alpha or lower levels of beta, lasts for second or less Increase in amplitude initially and then decrease slowly, symmetric Found in Parasagittal regions 	<ul style="list-style-type: none"> During stage 2 of sleep 	<ul style="list-style-type: none"> If spindles found in awoken state it is considered as seizures

Mu waves	<ul style="list-style-type: none"> Asymmetric, rhythmic rounded in one direction with sharp side in another direction, frequency having one half of the fast beta activity Seen in Parasagittal regions 	<ul style="list-style-type: none"> When the cortex is exposed or if subjects has structural brain defects 	<ul style="list-style-type: none"> If found even when motor action is done
Benign Epileptic Transients of Sleep (BETS)	<ul style="list-style-type: none"> Usually sharp, small waves occur on one or both sides (usually asynchronous) Seen in the temporal and frontal regions 	<ul style="list-style-type: none"> Rare in children and frequent in adults 	<ul style="list-style-type: none"> Occur in epileptic patients

III. ABNORMAL EEG WAVEFORMS

EEG waveform is said to be abnormal when the recording states that the brain activity affected by undesired seizures in irregular or continuous intervals. The Abnormal EEG differentiated as Epileptical and Non- Epileptical seizures. These seizures can be generalized or focal, which state the risk associated with them. The normal EEG and focal and generalized EEG seizures are shown in Fig. 3.

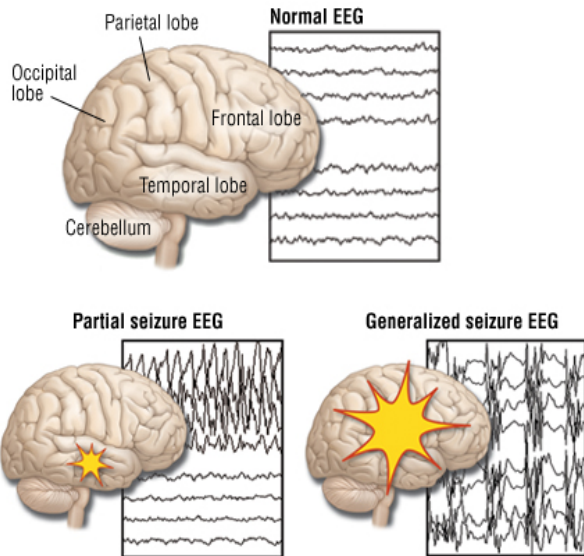


Fig. 3. Focal and generalized EEG Seizure [13].

A. Generalized EEG abnormality

A generalized EEG abnormality basically affects the entire brain and may not be symmetric in distribution. Generalized patterns may be described further as maximal in one region of the scalp (e.g., Frontal) or in certain hemisphere compared to the other. Identification of generalized abnormality may require analysis of the EEG by several channels to determine, because it is lack of focal point. Artifacts also sometimes appear as a generalized EEG abnormality which has to be removed with careful analysis [2-5, 11].

B. Focal EEG Abnormality

A Focal EEG abnormality which affects the particular region of the brain called focal point. Identification of an abnormality as focal abnormality may require focal point where the seizure occurs repeatedly only in its respective region. This kind of abnormality brings dysfunction to the respective organ or part of the body which associated with the seizure focal point of the brain [2-5, 10].

C. Epileptical EEG Abnormality

The EEG abnormalities, mainly classified as Epileptical and Non-Epileptical. The Epileptical abnormality EEG pattern shows up with repeated seizures and like the characteristics of a patient suffering with Epilepsy. Epilepsy is defined as a brain disorder characterized by a long-term tendency to generate epileptic seizures [2-5, 7-9]. An Epileptical form of abnormalities is described in below TABLE III.

Grand Mal also called as Tonic-Clonic Generalized seizure. This abnormality takes subject into unconsciousness and vicious muscle contractions. In all the abnormalities show up by the epilepsy, affects muscle tone and usual sensation of taste, vision, hearing and smell.

TABLE III. CLASSIFICATION OF EEG WAVES IN EPILEPTICAL EEG ABNORMALITY

Epileptical abnormality	Characteristics of EEG signal	Result
Grand Mal	<ul style="list-style-type: none"> Sudden spikes Followed by body stiffening 	<ul style="list-style-type: none"> Unconscious Tongue biting during seizure
Absence instance	<ul style="list-style-type: none"> Takes place for few seconds and post-ictal 	<ul style="list-style-type: none"> Brief loss of consciousness staring for long to same
MYOCLONIC	<ul style="list-style-type: none"> Bilateral, irregular and scattered 	<ul style="list-style-type: none"> Jerking
CLONIC	<ul style="list-style-type: none"> Bilateral, irregular and occur both sides of hemisphere at the same time 	<ul style="list-style-type: none"> Repetitive and jerking
TONIC	<ul style="list-style-type: none"> Spikes and sharp waves make a contrast of muscles 	<ul style="list-style-type: none"> Muscle stiffness
ATONIC	<ul style="list-style-type: none"> Excessive activity of brain, more seizures 	<ul style="list-style-type: none"> Loss of muscle tone
Focal Simple seizures	<ul style="list-style-type: none"> Seizures frequently occur in sensory and psychological regions 	<ul style="list-style-type: none"> Jerking, unusual sensation of vision, hearing, smell and taste
Focal Complex seizures	<ul style="list-style-type: none"> Sudden and Repetitive seizures 	<ul style="list-style-type: none"> Decrement of awareness, Loss of body control
Partial seizure with secondary generalization	<ul style="list-style-type: none"> First, Seizure associated with the part of the brain later it affects the entire brain and may loss the conscious like in the generalization 	<ul style="list-style-type: none"> Unconscious stage

D. Non-Epileptical EEG Abnormality

The Non-Epileptical form EEG abnormalities are caused by the brain injury which is a focal cerebral dysfunction due to a certain structural lesion and it also occurs in the preexisting structural abnormalities [2-6]. Non-Epileptical EEG waveforms are described in below TABLE IV.

TABLE IV. CLASSIFICATION OF EEG WAVES IN NON-EPILEPTICAL EEG ABNORMALITY

Type of EEG waveform	Characteristics of EEG signal	Abnormality caused
Polymorphic delta activity (PDA)	<ul style="list-style-type: none"> Focal and irregular, delta frequencies 	<ul style="list-style-type: none"> When Structural lesion or a sub cortical dysfunction
Frontal Intermittent Rhythmic Delta Activity (FIRDA)	<ul style="list-style-type: none"> Bilateral, synchronous, frequency of 2.5to 3 Hz 	<ul style="list-style-type: none"> When Deep middle lesions and tumor
Occipital intermittent Rhythmic Delta Activity (OIRDA)	<ul style="list-style-type: none"> Rhythmic, frequency range of 3-4 Hz 	<ul style="list-style-type: none"> When Lesions in occipital lobe, Presence of epilepsy
Temporal intermittent Rhythmic Delta Activity (TIRDA)	<ul style="list-style-type: none"> 1-4 Hz, 50-100uv, Short burst for 3sec, repetitive, Rhythmic saw-toothed, sinusoidal More specificity than FIRDA and OIRDA 	<ul style="list-style-type: none"> When subject has Temporal lobe epilepsy
Generalized asynchronous slow activity	<ul style="list-style-type: none"> Frequency less than 4 Hz, It depends on the age and state of alertness 	<ul style="list-style-type: none"> Always abnormal in awake adults
Focal attenuation	<ul style="list-style-type: none"> Occurs at certain frequencies 	<ul style="list-style-type: none"> Focal cortical lesion, Tumor, cerebral ischemia, swelling of the scalp
Generalized attenuation	<ul style="list-style-type: none"> Beta activity, 20uV in amplitude It severely suppresses delta and theta frequencies 	<ul style="list-style-type: none"> Cortical generalized injury
Other abnormal activity	<ul style="list-style-type: none"> Alpha coma: having alpha frequencies and unconscious Spindles coma: when EEG shows spindle activity in unconscious 	<ul style="list-style-type: none"> After cardiac arrest and coma Head injury, stroke

IV. CONCLUSION

As the EEG signal is obtained from the different region of the scalp by placing different electrodes at different regions. These EEG readings can be used to have better analysis and

interpretation, it helps the physician to diagnosis for a particular brain disorder patient because each EEG waveform is characterized in age, state of alertness, region of the scalp, abnormality and their unique characteristics. By this we can understand the EEG waveform and its abnormality by knowing the above characteristics.

REFERENCES

- [1] M. Teplan, "Fundamentals of EEG measurement," Measurement Science Review, vol. 2, no. 2, 2002.
- [2] F. Torres, "Atlas and classification of electroencephalography," Pediatric Neurology, vol. 22, no. 4, p. 332, 2000.
- [3] M. Koubeissi, "Niedermeyers Electroencephalography, Basic Principles, Clinical Applications, and Related Fields," 6th ed, Arch Neurol, vol. 68, no. 11, p. 1481, 2011.
- [4] A. Hartman, "Atlas of EEG Patterns," Neurology, vol. 65, no. 2, pp. E6-E6, 2005.
- [5] S. Kothare, "Atlas of EEG Patterns," 2nd Edition, Neurology, vol. 83, no. 7, pp. 668-668, 2014.
- [6] M. Andraus and S. Alves-Leon, "Non-epileptiform EEG abnormalities: an overview," Arq. Neuro-Psiquiatr, vol. 69, no. 5, pp. 829-835, 2011.
- [7] S. Smith, "EEG in the diagnosis, classification, and management of patients with epilepsy," Journal of Neurology, Neurosurgery & Psychiatry, vol. 76, no. 2, pp. ii2-ii7, 2005.
- [8] H. Jaseja and B. Jaseja, "EEG spike versus EEG sharp wave: Differential clinical significance in epilepsy," Epilepsy & Behavior, vol. 25, no. 1, pp. 137, 2012.
- [9] M. Sundaram, R. Sadler, G. Young and N. Pillay, "EEG in Epilepsy: Current Perspectives," Can. J. Neurol Sci., vol. 26, no. 04, pp. 255-262, 1999.
- [10] Emedicine.medscape.com, "Focal EEG Waveform Abnormalities: Overview, Alterations in Normal Rhythms, Abnormal Slow Waves." [Online]. Available: <http://emedicine.medscape.com/article/1139025-overview>. [Accessed: 2015].
- [11] Emedicine.medscape.com, "Generalized EEG Waveform Abnormalities: Overview, Slow Activity, Periodic Abnormalities." [Online]. Available: <http://emedicine.medscape.com/article/1140075-overview>. [Accessed: 2015].
- [12] Emedicine.medscape.com, "Normal EEG Waveforms: Overview, Frequency, Morphology." [Online]. Available: <http://emedicine.medscape.com/article/1139332-overview>. [Accessed: 2015].
- [13] Drugs.com, 'Seizure Guide: Causes, Symptoms and Treatment Options', 2015. [Online]. Available: <http://www.drugs.com/health-guide/seizure.html>. [Accessed:2015].

Phenomenon of Gravitational Waves Reaching the Earth Surface due to Black holes in Space

Mohd. Haseeb Ullah Khan¹, Md.Fakhruddin N.H.²

¹B.E.2nd Yr Dept. of Mechanical Engg-Methodist College of Engineering and Technology, India, haseeb_ullah28@yahoo.com

²Associate Professor, Methodist College of Engineering & Technology-Abids, India

Abstract: The first direct detection of gravitational waves and the first observation of the collision and merger of a pair of black holes are detected recently a week back. The collision of black holes has led to emission of gravitational waves, gives us the confirmation to prediction given by Einstein a century ago^[3]. Thus, the analysis of gravitational waveforms allows us to learn about their source and, if there are more than two detectors involved in observation, to estimate the distance and position of their source on the sky. This paper is to bring to light the technology evolved in engineering for the study of astrophysics.

Keywords: Gravitational waves, black holes, binary neutron stars, ligo, Quadrupole moment, Esa, astrophysics.

INTRODUCTION

Gravitational waves are ripple in the curvature of space-time, produced by some of the most violent events in the cosmos such as the collisions and mergers of massive compact stars. Their existence was predicted by Einstein in 1916 when he showed that accelerating massive objects would shake space-time so much that waves of distorted space would radiate from the source. These ripples travel at the speed of light through the universe, carrying information about their cataclysmic origins as well as invaluable clues to the nature of gravity itself. Gravitational waves propagate as waves which are travelling outward from the source. Curvature are created by mass, more mass more is the curvature of space-time^[1]. Gravitational waves transport energy as gravitational radiation. This was given on the basis of general relativity. Gravitational wave is seen only at finite speed. The existence of these gravitational waves is possible consequence of the Lorentz invariance of general relativity which brings the concept of a limiting speed. In certain circumstances, accelerating objects generate changes in this curvature which propagates outwards at the speed of light in a wave like manner. These propagating phenomena are known as Gravitational waves.

SOURCE

Binary neutron stars are predicted to be a powerful source of Gravitational waves. These waves coalesce due to large acceleration of their masses as they orbit close to each other. The effect on earth is predicted to be very small, having strains of less than 1 in 10²⁰. To demonstrate the existence of these waves' scientists developed detectors which are even more sensitive than the gravitational wave.

"Gravitational wave should penetrate regions of space that electromagnetic waves cannot." This provides observer on

earth the information about black hole and other objects in the universe. There are different frequency bands to detect Gravitational waves which would be plausibly detected from 10⁷Hz to 10¹¹Hz. experimentally; particles change their state of manner when Gravitational waves pass through it. In this Amplitude is constant, Plane of polarization changes. Here, amplitude refers to the size of the wave. Speed, wavelength and frequency of a Gravitational waves are related by the equation $c=\lambda f$, same as the equation for a light wave. Gravitational waves are radiated by objects in which motion involves acceleration provided that the motion is not perfectly symmetric. A motion of two massive stars like Neutron stars or Black holes (perfectly round objects made of pure empty, warped space-time, predicted by general relativity) orbiting each other at higher speeds then significant amount of Gravitational radiations would be given off.

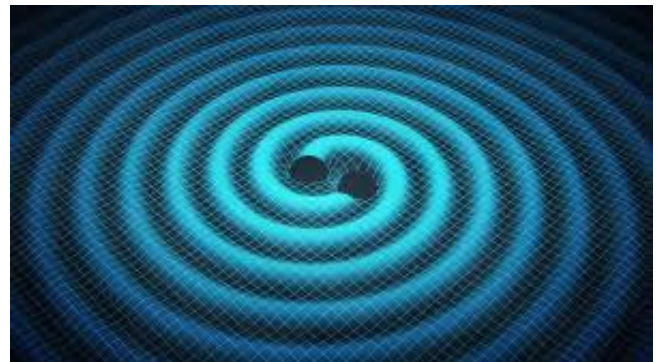


Fig 1 emission of gravitational waves

CONCEPT

Gravitational waves takes energy away from the source and in the case of bodies which are orbiting, this is associated with a decrease in orbit. For example a simple system of two masses like earth-sun system which is moving very slowly when compared to the speed of light in circular orbits. Assuming these two masses revolve around each other in a circular orbit in X-Y plane. The masses follow simple Keplerian orbits and such orbits represents quadrupole moment. Let M1 and M2 be the masses and they are separated by a distance R. The power radiated by this system is given by the equation

$$P = -\frac{32}{5} \frac{G^4}{c^5} (M_1 M_2)^2 (M_1 + M_2) / R^5 [7]$$

Where G=Gravitational constant, c=speed of light in vacuum, the negative sign indicates that power is driven away by the system. In theory the loss of energy in earth-sun system

through gravitational radiation could eventually drop the earth into the sun. However the total energy of the earth orbiting the sun that is kinetic energy + gravitational potential energy is 1.14×10^3 joules out of which only 200 joules per second is lost through gravitational radiation, leading to decay in the orbit by 1×10^{15} meters per day. This is roughly the diameter of a proton. The time taken by earth to spiral onto the sun at this rate would be 1×10^{13} times more than the current age of the universe. In case of two bodies orbiting in the same orbit, it first circularizes their orbit and then shrinks their radius, the energy of orbit is reduced, the distance between the bodies' decreases and the bodies rotate more rapidly. The angular momentum is reduced which is carried off by gravitational radiation. When the radius has **shrunk** to half of its initial value, it now shrinks eight times faster than before. As radius decreases, the power loss to gravitational radiation increases even more. A loss of energy from the orbit results in even more rapid and effective decrease in the distance between the two bodies. They will eventually merge to form a black hole and radiate gravitational waves. This is referred to as inspiral which is observed in pulsar signals.

The quadrupole moment of a system is approximately equal to the mass M of the part of the system that moves, times the square of the size R of the system. The third order time derivative of the quadrupole moment is

$$Q = MR^3/T^3 = MV^2/T = E_{NS}/T^{[4]}$$

V= mean velocity of source's non spherical motion.

E_{NS} = kinetic energy of non-spherical motion

T = timescale for a mass to move from one side of the system to other side.

For a self Gravitating system $T \sim \sqrt{R^3/GM}$.^[6]

One of the most important properties of gravitational radiation sources is orbital lifetime. It determines the average number of binary stars in the universe that are close enough to be detected. Short life time binaries are few in number but are strong sources of gravitational radiation. Long life time **binaries** are more plentiful in number but are weak source of gravitational radiation. Gravitational waves propagate through matter with little interaction. These are hard to detect, but carry uncontaminated information about their sources^[6]. Simplest Gravitational waves are those with constant frequency. Gravitational waves have important and unique properties such as; firstly there is no need of any of matter to be present nearby for the waves to be generated by a binary system which has uncharged black holes, which would emit no electromagnetic radiation. Secondly, gravitational waves can pass through any intervening matter without being scattered. These two features the gravitational radiation to carry information about astronomical phenomena.

HISTORY

In 1915 Albert Einstein published the theory of general relativity^[7]. A year later in 1916 Einstein predicts that Gravitational wave exist as a consequence of the theory of general relativity. Richard Feynman in the year 1957 predicts that gravitational wave exist and are theoretically detectable. There was an indirect conformation of existence of

gravitational waves in the late 1970s. In 1984 Kip Thorne and Ronald Drever found LIGO. Astronomers at the Harvard-Smithsonian Centre for astrophysics claim that they have detected and produced "the first direct image of gravitational waves across the primordial sky" within the cosmic microwave background. On 19 June 2014, a lowered confidence in conforming the cosmic inflation findings is reported. There was a further reduction in confidence on 19 September 2014 and even more less confidence on 30 January 2015. "Dark energy may distort gravitational waves", stated by astrophysicists at Penn University cites this circumstance as a reason for lack of direct detection. On 11 February 2016, the advanced LIGO team announced that they detected gravitational waves on September 14, 2015 from a merger of two black holes about 400 megaparsec (1.3 billion light years) from earth^[4]. The signal sweeps upwards in frequency from 35 to 250 Hz with a peak gravitational-wave strain of 1×10^{-21} ^[10]. The two black holes were 36 and 29 solar masses, which merged into a spinning 62solar mass black hole. The **LIGO** named this merger as GW 150914^[8].

DETECTION

A device theorized to detect the expected wave motion is called Weber bar. This is a large solid bar made of metal, isolated from outside vibrations. Strains in space due to an incident gravitational wave excite the bar's resonant frequency and thus be amplified to detectable levels.



Fig.2 HANDFORD WASHINGTON

Gravitational waves are not easily detectable. When gravitational wave reaches the earth, they have small amplitude which requires extremely sensitive detectors, and other source of sound can overwhelm the signal. To overcome this, advanced and highly sensitive detectors are used. LIGO (laser interferometer gravitational wave observatory) has three detectors one in LIVINGSTON, LOUISIAN, one at the HANDFORD side in RICHLAND, WASHINGTON and a third which is formerly installed at HANDFORD is planned to shift to INDIA^[11]. LIGO is one of the largest gravitational wave observatory it uses the physical properties of light and space itself to detect gravitational waves. After undergoing major updates in the year 2015 the LIGO detectors began operations as advanced LIGO, the first of significantly more sensitive global network of advanced detectors. An interferometer like LIGO consists of two arms each of four km long placed at right angles to each other,

along which a laser beam is placed and reflected by mirrors at each end^[9]. Suspended mirrors play the role of “test particle”, placed in perpendicular direction. When gravitational wave passes by the stretching and squashing of space causes the arms of the interferometer to lengthen and shrink alternatively. One arm gets longer while the other arm gets shorter and vice versa. As there is a change in the lengths of the arms of the interferometer, the laser beams takes different time to travel through the arms which means that the two beams are no longer “in step” and thus an interference pattern is produced. This is why we refer to the LIGO detectors as “Interferometer”. The light is reflected on the mirrors and returns back to the beam splitter and then to a photo detector where the fringe pattern is monitored. The difference between the two arm lengths is proportional to the strength of passing Gravitational wave strain and this number is very small. For a Gravitational wave the strain is expected to be around 1/10000th the width of proton. Laser through long tunnels try to sense ripples in the fabric of space-time. Time gap in which they measured these waves was 7 milliseconds. The signal sweeps upwards in frequency 35 to 250Hz with a peak Gravitational wave strain of 1×10^{-21} . It matches the wave predicted by general relativity for the inspiral and merger of a pair of black hole and the ring down of the resulting single black hole. LIGO estimated that the peak Gravitational wave power radiated during the final moments of the black hole merger was more than ten times greater than the combined light power from all the stars and galaxies in the observable universe^[11]. Strong Gravitational waves are generated by bulk (coherent) motion. They require strong velocity (compact object like black holes and neutron stars).

improvements in the advanced LIGO detectors, giving us the more possible and accurate predictions.

REFERENCES

- [1] J. H. Taylor and J. M. Weisberg, *Astrophys. J.* 253, 908 (1982).
- [2] W. Press and K. Thorne, *Annu. Rev. Astron. Astrophys.* 10, 335 (1972).
- [3] Einstein, a : rosen, n; on gravitational wave in; journal of the Franklin institute 223 (1937) 43-54
- [4] https://en.wikipedia.org/wiki/Gravitational_wave
- [5] <http://www.bbc.com/news/science-environment-35524440>
- [6] [webs.um.es/bussos/GW_lecture_KG.pdf](https://www.um.es/bussos/GW_lecture_KG.pdf)
- [7] https://en.wikipedia.org/wiki/Gravitational_wave
- [8] <https://physics.aps.org/featured-article-pdf/10.1103/PhysRevLett.116.061102>
- [9] https://www.ligo.caltech.edu/system/media_files/binaries/301/original/detection-science-summary.pdf
- [10] <http://journals.aps.org/prl/abstract/10.1103/PhysRevLett.116.061102>
- [11] <https://en.wikipedia.org/wiki/LIGO>



Fig.3 LIVINGSTON

Space based interferometers, such as LISA and DECIGO are also being developed. LISA'S design called for three test masses forming an equilateral triangle, with lasers from each spacecraft to other spacecraft which forms two independent interferometers. The setup is in vacuum far away from the earth and noise. A mission on LISA is to be taken by EUROPEAN SPACE AGENCY, UK around 2020.

CONCLUSION

The remarkable achievement of the first direct detection of gravitational waves and observation of a merging black hole has taken the area of astrophysics to a next astonishing level^[1]. The upcoming years will have more and rapid

Solar Powered Compressed Air Engine

A.P.V.Prasad Rao¹, K.Sundeep Kumar², R.Charan nayak³ Md.Fakhruddin H.N.⁴

^{1,2,3}B.E.4th Yr Dept. of Mechanical Engg-Methodist College of Engineering and Technology, India, prasadraoapv@gmail.com

⁴Associate Professor, Methodist College of Engineering & Technology-Abids, India.

Abstract – The world can't be imagined without IC Engines, as their applications are wider in various fields. And mainly used input for this engines are fossil fuels. But the challenge in this is decreasing rate of resources. The fossil fuels may not be available after some years if they used in the same way. Not only the fossil but also the electric power is the non renewable energy. Hence the ultimate solution to the present day scenario is to tap the solar energy and be used for propelling the engine. In this research paper solar radiation are convert to useful work to compress atmospheric air. And compressed air in turn propels the Engine. Paper concentrates to run the engine without fossil fuels or electricity.

Key words – IC Engines, fossil fuels, non renewable energy, Compressed air

INTRODUCTION

In today's motorized life, It's difficult to live without motor (Engines) and the main source of its input power is fossil fuels & partly electric power. In future these fuels or electricity may not be available widely as they are non renewable energies. So, it may be difficult to use engine with the fuels. Not only the problem of lack of resources but also but also they pollutes the environment. If the fossil fuels are used in this way for some more years, It may difficult to breath in the future and many things which are harmful to the earth may happen like global warming .this may leads in danger to the lives of creatures. [1]

To solve this problems compressed air technology (CAT) was invented, and again the problem in this is input power. The air may be freely available in the atmosphere, but it needs to be compressed to use and the power it needs for compression is electrical energy, which is also a non- renewable energy.

The Solar powered engines are also invented, but the acceleration we can achieve with that is comparatively less. The present paper or model Named "Solar powered Compressed air engine" is introduced to resolve this problem.

COMPONENTS

Organized by Methodist College of Engineering & Technology, Abids, Hyderabad-Telangana State India. 500001

The main components are

1. Engine
2. D.C. Compressor
3. Solenoid valve
4. Temps circuit
5. Solar unit

ENGINE

A 125cc single cylinder engine is used. The Specifications of the engine used are

Bore x Stroke (mm) = 52.4 x 57.8

Engine Type = 2-valve OHC single

Max. Torque = 11.2Nm / 6250rpm

Transmission = 4 Gears

COMPRESSOR

A High Power Model 300psi & an Extra High Power Motor which runs on 12v D.C Power has to be used. As shown in Fig.1 and the detailed specifications are

Output volume- 25L/min

Max air pressure- 300psi

Size- Approx 14*12.5*8cm / 5.5*4.9*3.1 inch



Fig.1 High power model compressor

A **solenoid valve** is an electromechanically operated valve shown in Fig.2, the **valve** is controlled by an electric current through

a **solenoid**: in the case of a two-port **valve** the flow is switched on or off; in the case of a three-port **valve**, the outflow is switched between the two outlet ports. **Solenoid valves are used at inlet and outlet valves to supply the desired quantity of air into valves, as it may be difficult for the opening & closing of valves by resisting the pressurised air.**

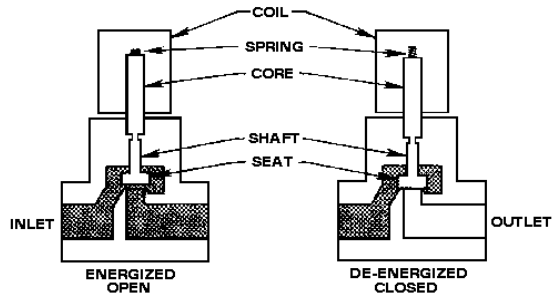


Fig.2 solenoid valve

Temps Circuit

Temps circuit is a timing circuit which is used to operate the solenoid valves by supplying the electric current at appropriate time as shown in Fig.3. This circuit is designed on PCB board which includes a microcontroller and programming is done to it.

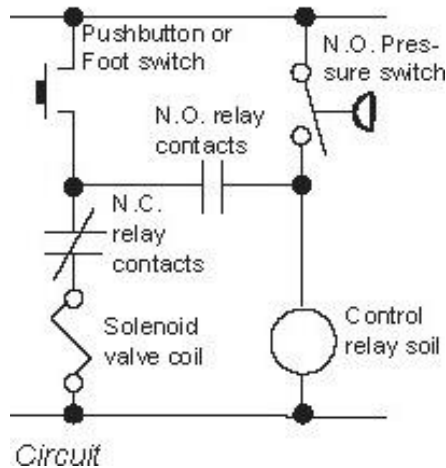


Fig.3 Temps Circuit

Solar Unit

A solar unit is used to generate the electric power required to run the D.C. Compressor at 12V. The solar unit is shown in Fig.4.



Fig.4 Solar Unit

MODIFICATIONS

Some modifications are needed to run the 4-stroke engine by using air, they are

Modifications in Engine

The parts to be modifications in engine are cam shaft, Spark plug

Cam Shaft

The camshaft is to be modified to open and close the inlet and outlet valves as required. The valves are to be opened and closed for every two strokes, where these opens and closes for every four strokes in the engine before modification. Two cam lobes are added to the opposite sides of the existing cam lobes. [5]

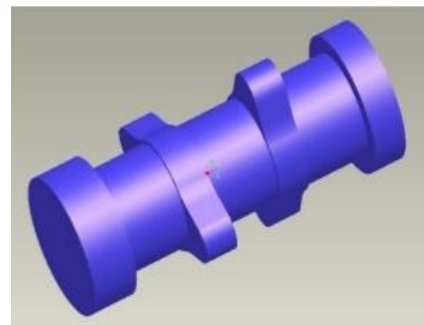


Fig.5 Cam Shaft

Or crank shaft gear is to be modified by decreasing the No. of teeth on it. The no. of teeth on crankshaft gear is to be made equal to the no. of teeth on cam shaft, to rotate the one cam shaft for once by the one revolution of crank shaft. Where in previous case two rotations of the crank shaft is equal to the one rotation of the cam shaft, referred to Fig. 5.

Spark Plug

Spark plug is to be made dummy as no combustion is taking place.

Modifications in Compressor

Modification may not be needed for the engines of 125cc-150cc. If the engine of more displacement

is used then more pressure is needed for which dc compressors are not available. [4] So, the compressor is to be coupled with low pressure dc compressor. Like, 300 psi compressor outlet is to be coupled with 200 or 100 psi compressors inlet as needed.

WORKING

Firstly, the solar unit will generate the power and runs the compressor. The compressed air will flow from outlet of compressor to the solenoid valve and then passed to the inlet valve of the engine. Only two strokes are executed by the piston in one cycle. Namely they are Intake stroke and Exhaust stroke.

Intake Stroke

In this stroke cylinder sucks the compressed air at 300 psi when inlet valve opens where exhaust valve closes by the action of cam shaft [3]. The pressurised air will force the piston to move downwards, resulting in the travelling of piston from TDC to BDC, referred to Fig. 6.

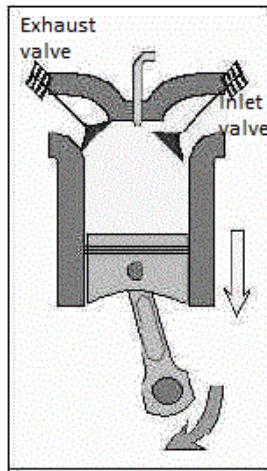


Fig.6 Intake Stroke

Exhaust Stroke

In this stroke the piston moves from BDC to the TDC by the weight of the flywheel. The exhaust valve and solenoid valve opens where inlet valve closes and the air in the cylinder will be exhausted to the atmosphere. Fig.7

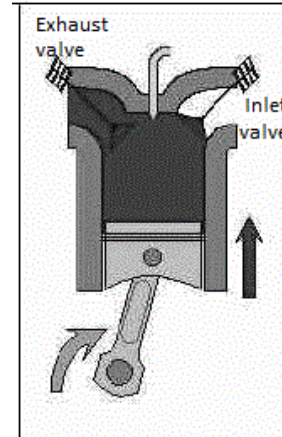


Fig.7 Exhaust Stroke

As the compressed air is only the charge, there is no need of fuel to be mixed. So carburettor is eliminated in this engine.

The cam shaft is driven by the crank shaft by timing chain and rotates as crankshaft rotates; when the follower touches the lobe of the cam then it lifts the inlet or outlet valve up. If follower came in to contact with the dwell side of the cam, the inlet or outlet valve closes. [2]

Comparison with 4 stroke & CAT engine

4-Stroke Engine	CAT Engines	SPCA Engine
Fuel + Air As charge	The compressed air is the charge	The compressed air is the charge
No compressor	Compressor requires electric energy	Compressor runs on solar energy
Pollution is more	No pollution as the input is air	No pollution as the input is air
Carburettor is used	Carburettor is not used	Carburettor is not used
Spark plug Needed	Spark plug not needed	Spark plug not needed
Power generated once in 4 strokes	Power generated once in 2 strokes	Power generated once in 2 strokes

Piston Executes 4strokes in a cycle	Piston Executes 2strokes in a cycle	Piston Executes 2strokes in a cycle
Output power is more	Output power is less compared with 4 stroke engine	Output power is less compared with 4 stroke engine
Efficiency is less	Efficiency is more	Efficiency is more
Not Economical compared with CAT & SPCAE	Less Economical compared with SPCAE	Economical

I also extend my thanks to Mr. Rajashekar Sir, HOD Department of Mechanical Engineering. & Mr. A, Giridhar Sir, Principal Methodist Collage Of Engineering & Technology, king koti road – Abids Hyderabad.

REFERENCES

- [1] Internal Combustion Engines 4th Edition by V. Ganeshan
- [2] <http://www.iosrjournals.org/iosrjmce/papers/vol11-issue6/Version-4/O0116499103.pdf>
- [3] https://en.wikipedia.org/wiki/Compressed-air_vehicle
- [4] <http://papers.sae.org/2014-01-1666/>
- [5] Advance IC Engine by M. Shankar, ISBN – 97893 80485423

ADVANTAGES

1. No cost to run the engine.
2. Eco – Friendly.
3. Heat generated is less.
4. Use of Carburettor & Spark plug is eliminated.
5. The exhausted air from engine can be used for other processes like cleaning and filling the air in tires.

DISADVANTAGES

1. More Noisy.
2. Initial Cost is high.

CONCLUSION

This engine uses solar energy which is freely available in the environment. Even solar Engines are introduced they are comparatively poor in generating power and acceleration.

This may helps to fight with global warming as it delivers the air at comparatively lesser temperature, which results in cooling of the atmospheric air. This will be the good alternative for the fossil fuels both economically as the cost of air is 0 and environmentally as it doesn't exhaust the harmful gasses.

ACKNOWLEDGEMENT

I express my sincere thanks to my guides Mr. Srinivasa Raghawan Sir, Mr. Md. Fakhruddin sir.
 Organized by Methodist College of Engineering & Technology,
 Abids, Hyderabad-Telangana State India. 500001

Experiment on Single Cylinder CI Engine with Various Proportion of WCOBD in Diesel

Md. Fakhruddin H.N¹, Md. Samiuddin Siddiqui², Dr. Mohammed Yousuf Ali³, Dr. Manzoor Hussain⁴

¹Associate Professor, Methodist College of Engineering & Technology-Abids, India, mfhnn@yahoo.com

²UG Student, Methodist College of Engineering & Technology-Abids, India

³Professor & Principal, Nawab Shah Alam Khan College of Engineering & Technology, India

⁴Professor & Principal, JNTUH College of Engineering Sultanpur Hyderabad, India

Abstract: India is one of the largest petroleum consuming and importing countries. India imports about 75% of its petroleum demands. The current yearly consumption of diesel oil in India is approximately 55 million tones constituting about 48% of the total petrol-product consumption. India imports substantial amounts of fossil fuels for its requirements of transportation and industries[4]. The dependence on other countries or the Fuel needs makes out nation vulnerable. Waste Cooking Oil (WCO) is a bio-fuel whereas high Speed Diesel is a fossil fuel. Fossil fuel may become extinct in near future but "WCO" is a renewable fuel extracted from the residual waste of used cooking oil. Bio-fuels are also advantageous when ecological factors are taken into account. Using WCO pollution can be controlled to certain extent [6]. This is very cheap and renewable, they are safe to store and non volatile, biodegradable, release comparatively less carbon-di-oxide and has clearer exhaust. Thus it can be best considered as the most favorable alternative fuel. Even from the economic perspective, the cost of WCO is less than that of Standard Diesel. The limitation is the production of oil [7]. Since the extraction of oil is done in small scale, the cost of extraction is little high[12]. The cost can be reduced when extraction is done on large scale. The present work is to conduct experiment on single cylinder CI Engine with various proportion of WCO in diesel and compare it with stand alone fossil fuel.

Key words: waste cooking oil, biodiesel, renewable fuel, biodegradable and eco-friendly.

INTRODUCTION

The concept of Bio-Fuel dates back to 1885 when Dr. Rudolf Diesel built the first Diesel engine with the full intention to running it on vegetative source [8]. In 1912 he observed, "The use of vegetable oils for engine fuels may seem insignificant today". But such oils may in the course of time become as important as fossil fuels [10]. In 1970, scientists discovered that the viscosity of vegetable oils could be reduced by a simple chemical process and that it could be employed as diesel fuel in modern engine. Since then the technical developments have travelled a long journey and the plant oil today has been highly established as BIO-FUEL, with better prospects and equivalent status to standard diesel [15]. Recent environmental (e.g. Kyoto protocol) and economic concerns have prompted resurgence in the use of bio-diesel throughout the world. In 1991, the European community proposed a 90% tax reduction (subsidization) for the use of bio-fuels, including bio-diesel. Today 21 countries worldwide produce bio- diesel [2].

It is possible to reduce its viscosity by converting vegetable oil into alkyl esters using transesterification reaction [3]. In the present work Waste Cooking Oil (WCO) is taken as

feedstock, thus food against fuel conflict will not arise if this is used for biodiesel production.

The vegetable oils, animal fats, and their derivatives such as alkyl esters are suitable as diesel fuel because there must be some similarity to petro diesel fuel or at least to some of its components. The fuel property that best shows this suitability is called the cetane number. In addition to ignition quality as expressed by the cetane scale, several other properties are important for determining the suitability of biodiesel as a fuel. Heat of combustion, pour point, cloud point, (kinematic) viscosity, is among the most important of these properties.

STORAGE OF BIODIESEL

As mild solvent, biodiesel tends to dissolve sediments normally encountered in old diesel storage tanks. Brass, Teflon, lead, tin, copper, zinc etc. oxidize biodiesel and create sediments. The existing storage facilities and infrastructure for petrol & diesel can be used for the biodiesel with minor alterations. For biodiesel storage, shelf life and how it might break down under extreme conditions assume importance [1].

Biodiesel has poor oxidation stability. Use of oxidation stability additives is necessary to address this problem [18].

Low temperature can cause biodiesel to gel, but on warming it liquefies quickly. Hence, insulation of storage tanks and pipelines would need to be done at the low temperature zones.

To avoid oxidation and sedimentation of tanks with biodiesel, storage tanks made of aluminum, steel etc. are recommended for usage.

ENGINE MODIFICATION

Several modifications have been proposed by researchers to enable the smooth usage of WCO in CI engines. Among them is the introduction of a fuel heater to pre-heat the oil before injecting it into the cylinder, the provision of extra filters, an electric heater in the fuel tank in colder climate and dedicated fuel pumps to handle the higher viscosity of the WCO/WVO.

SPECIFICATION OF THE ENGINE

Single Cylinder Four-Stroke,
Variable Compression Ratio Ignition
Forced Air Cooled Engine.
Brake Diameter D=85mm

Stroke Length L=110mm
 Orifice Diameter=20mm
 $C_d=0.64$, Compression Ratio=20.03
 Calorific Value WCO=39000 kJ/kg

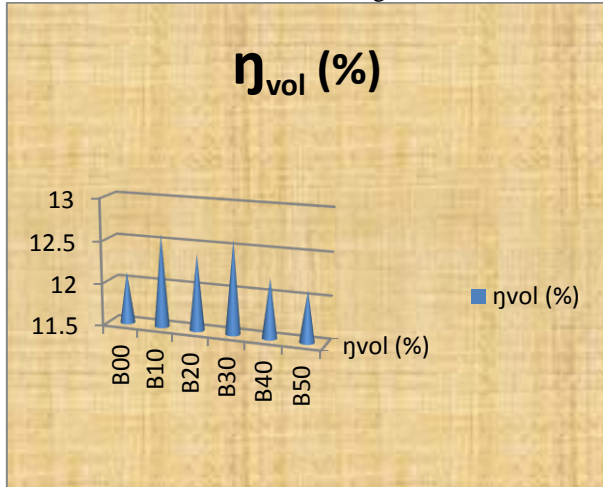


Fig 1 Volumetric efficiency for standard diesel and its various blends.

PROBLEMS FACED:

- **Viscosity:** As has been mentioned earlier, BD has comparatively higher viscosity than the conventional diesel, this sometimes comes as a hindrance at cold regions, where the temperature is likely to fall below 250 C. Fuel becomes thick in consistency and is more likely to get blocked in the minor cavities of fuel injector.
- **Blockage:** Citing viscosity an issue, the problem of blocking of valves and injector was faced.
- **Mixing:** Precise blending of fuel is very important, minor negligence may be reflected in the comparison and data collection.
- **B50:** when B50 was employed it was found that, fuel incurred a problem of travelling through supply, therefore manual blowing to facilitate the movement was carried out, and this again however can be attributed to viscosity.

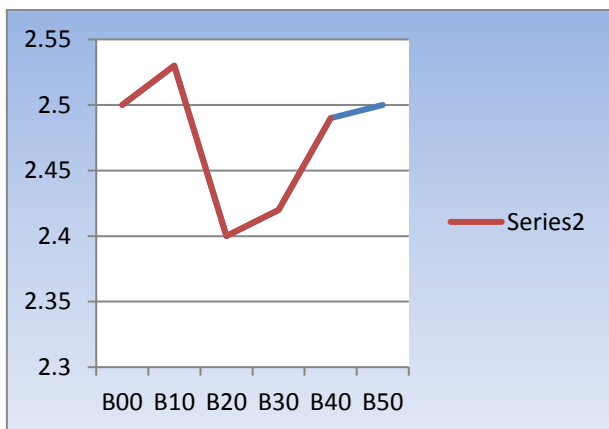


Fig 2 Brake thermal efficiency for standard diesel and various blends.

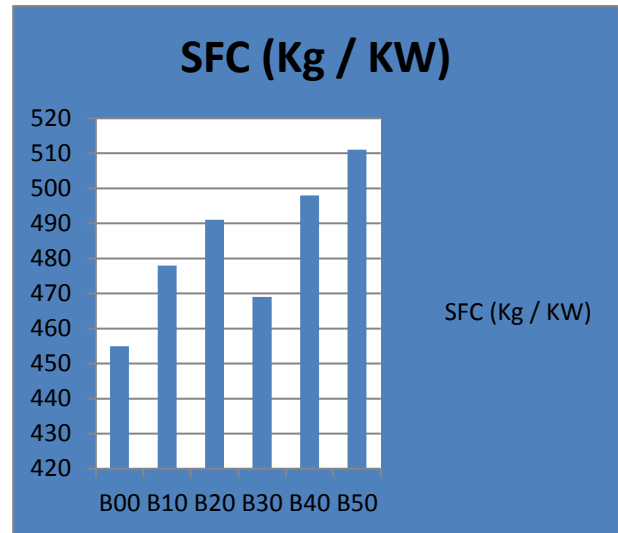


Fig 3 Specific fuel consumption in Kg / KW for standard diesel and various blends.

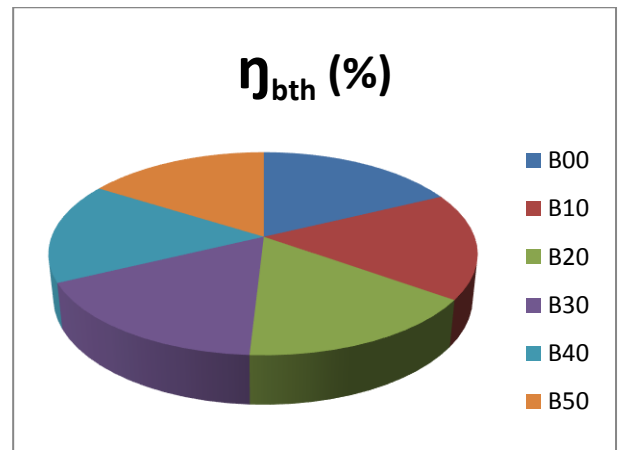


Fig 4 Brake thermal efficiency for standard diesel and various blends.

ENVIRONMENTAL AND HEALTH BENEFITS

The use of BIO-DIESEL will help preserve our environment. Bioactive™ is completely biodegradable and contains no toxic or harmful elements. It is non-flammable, safe to handle, and poses no danger to the environment[5]. Best of all, it is made from a renewable resource that is abundant. It will also improve the air that we breathe. Air pollution is a serious problem worldwide and the rising incidence of pollution-related illnesses has become a serious concern. Extensive field and laboratory tests prove that Bioactive™ dramatically reduces smoke emissions through complete combustion. With the elimination of air pollution caused by smoke, a cleaner air will result in better respiratory conditions of people.

GENERAL ADVANTAGES

- **National security.** Since it's made domestically, it reduces our dependence on foreign oil.
- **National economy**

Using bio-diesel keeps our fuel buying pesos at home instead of sending it to foreign countries. This reduces our trade deficit and creates jobs.

- It's sustainable & non-toxic.

- **Emissions**

Bio-diesel is nearly carbon-neutral, meaning it contributes almost zero emissions: global warming.

- **Engine life**

Studies have shown it reduces engine wear by as much as one half, primarily because it provides excellent lubricity. Even a 2% bio-diesel/98% diesel blend will help.

- **Drivability**

We have yet to meet anyone who doesn't notice an immediate smoothing of the engine with bio-diesel. It just runs quieter, and produces less smoke.

General Disadvantages

- Primarily, bio-diesel is not readily available in retail market but that available are with commercial suppliers, however whose production has not yet been commercialized. With the novel move by the railways in India and the RTC in the East while Andhra Pradesh, this idea gained momentum and has been a success to much extent.

- Bio-diesel is not suitable to any engines, more of the older one.

- It has a higher gel point. B100 (100% bio-diesel) gets slushy a little under 32°F. But B20 20% bio-diesel, 80% regular diesel -more commonly available than B100) has a gel point of -15°F. Like regular diesel, the gel point can be lowered further with additives such as kerosene.

CONCLUSION

The Engine was running smoothly with the use of Bio-Diesel. The Bio-Diesel was added in the Diesel -Blend resulted in better performance and reduced smoke. The brake power for blends doesn't show much deviation from petroleum diesel. The Brake specific fuel consumption is increased with the blends when compared to diesel. Brake thermal efficiency increased with all blends when compared to the conventional diesel fuel.

REFERENCES

- [1]. Satishchandra Shamrao Ragit, S.K. Mohapatra, k. Kundu, Process standardization, characterization and experimental investigation on the performance of biodiesel fuelled C.I engine, *engineering and material sciences*, 18(2011) 204-210).
- [2]. Knothe, van Gerpen and Krahl, The Biodiesel Handbook, National Center for Agricultural Utilization Research Agricultural Research Service U.S. Department of Agriculture Peoria, Illinois, U.S.A, Department of Mechanical Engineering Iowa State University Ames, Iowa, U.S.A, University of Applied Sciences Coburg, Germany 2005.
- [3] K. VinuKumar, production of bio-diesel used in diesel engines, IJET, Vol 1, Issue 1, 2013.
- [4] A. Gnanaprakasam, V.M. Sivakumar, A. Surendhar, M. Thirumarimurugan, and T. Kannadasan, Hindawi Publishing Corporation Journal of Energy Volume 2013, Article ID 926392, 10 pages <http://dx.doi.org/10.1155/2013/926392>
- [5] Internal Combustion Engines and Pollution by EDWARD F OBERT By Harper and Raw Publishers, New York.
- [6] O. J. Alamu, T. A. Akintola, C. C. Enweremadu, and A. E. Adeleke, "Characterization of palm-kernel oil biodiesel produced through NaOH-catalysed transesterification process," *Scientific Research and Essays*, vol. 3, no. 7, pp. 308–311, 2008.
- [7] S. Fariku, A. E. Ndonga, and P. Y. Bitrus, "Biofuel characteristics of beniseed (Sesamum indicum) oil," *African Journal of Biotechnology*, vol. 6, no. 21, pp. 2442–2443, 2007.

- [8] J. Connemann and J. Fischer, "Biodiesel processing technologies," in *Proceedings of the International Liquid Biofuels Congress*, July 1998.

- [9] <http://article.sapub.org/10.5923.j.jee.20120205.06.html>

- [10] Olsen, C.S. A Qualitative Assessment of The Sustainability of Commercial Non-Timber Forest Product Collection in Nepal. Forestry Discussion Paper 12, Royal Veterinary and Agricultural University, Copenhagen, Pp. 30,(1997).

- [11] Arjun B. C, Martin S. T, Suzanne M. B, Chris W.K and Rafiqul I.M , Non-Edible Plant Oils as New Sources for Biodiesel Production, Int. J. Mol. Sci. 9, 169-180,(2008).

- [12] Prokop, T., Personal Communication, Imperial Western Products, 14970 Chandler St., Coachella, CA 91720,(2002).

- [13] Lott, M., (2002). Personal Communication, QSS Group Inc., 4500 Forbes Boulevard, Suite 200, Lanham, MD 20706,(2002).

- [14] Demirbas, M., Balat, M., Recent Advances on the Production and Utilization Trends of Bio-Fuels: A Global Perspective. Energy Conversion and Management 47, 2371–2381,(2006).

- [15] Vol 5, No 1 (2015) > Ayetor Performance Evaluation of Biodiesel-Biodiesel Blends in a dedicated CIDI Engine Godwin Kafui Ayetor, Albert Sunnu, Joseph Parbe.

- [16] https://www.researchgate.net/publication/280563642_Comparative_Production_of_Biodiesel_from_Waste_Chicken_Fats_and_Cooking_Oil

- [17] <http://www.ijrer.org/ijrer/index.php/ijrer/article/view/1873>

- [18] Abdul Majeed Khan1*, Azizuddin Shaikh2, Ijaz Khan3, Shumaila Kanwal3 Journal of Biofuels DOI : 10.5958/0976-4763.2014.00005.1 IndianJournals.com Vol. 5 Issue 1, January-June 2014 pp. 32-40

Performance Test of Diesel Engine for Waste Cooking oil Biodiesel Blended with Diesel

Md. Fakhruddin H.N¹

Associate Professor, Mechanical Engineering Department
Methodist College of Engineering & Technology-Abids
Hyderabad – 1, India
mfhnn@yahoo.com

Dr. Mohammed Yousuf Ali² / Dr.M.Manzoor Hussain³

Professor & Principal,
²Nawab Shah Alam Khan College of Engg. & Tech.
³JNTUH College of Engineering Sultanpur
Hyderabad, India

Abstract—Biodiesel, a renewable fuel made by transesterification of vegetable oil with alcohol, is becoming more readily available for blending with conventional diesel fuel for use in transportation applications. Fossil fuels such as petroleum, coal and natural gas, which have been used to meet the energy needs of mankind, are associated with negative environmental impacts such as global warming. Similarly, the fossil fuels accumulated over series of geological activities are irreversibly consumed at a rate more than million times faster than they were formed. This has left us in a precarious position especially for petroleum products. The hike in price of petroleum and its products, both in national and international scenes is frequent for two reasons; the mounting demands and fast depletion of reserves, the duo of which call for alternative source of energy. Similarly, in developing countries, the price paid for petrol, diesel and petroleum products now dominates over all other expenditures and forms a major part of country's import bill. Biofuel/Biodiesel made from natural oils and fats is being considered as a promising substitute for petrol diesel. Although biodiesel cannot entirely replace fossil fuel, the following reasons however further justify its development.

- It provides a market for excess production of vegetable oils.
- It decreases the dependence on imported petroleum.
- It does not contribute to global warming due to its closed carbon cycle.

- The exhaust emissions of carbon monoxide, unburned

Hydrocarbons and particulate emissions from biodiesel are lower than fossil fuel. Though much has been done in the area of biodiesel production especially with the use of various feed stock; soya bean oil, corn oil, peanut oil, olive oil, cotton seed oil, safflower, rape seed oil/canola, line seed oil, sunflower, coconut oil, palm kernel oil, jathropha seed oil etc as further evidenced in the report of but still, few research has been carried out on the use of WCO for biodiesel production.

Keywords— WCOBD; Biodiesel; fossil fuels; global warming

I. INTRODUCTION

Waste Cooking Oil (WCO) is a bio-fuel whereas high Speed Diesel is a fossil fuel. Fossil fuel may become extinct in near future but "WCO" is a renewable fuel extracted from the residual waste of used cooking oil. Bio-fuels are also advantageous when ecological factors are taken into account. Using WCO pollution can be controlled to certain extent. This is very cheap and renewable, they are safe to store and non volatile, biodegradable, release comparatively less carbon-di-oxide and has clearer exhaust.

Thus it can be best considered as the most favorable alternative fuel. Even from the economic perspective, the cost of WCO is less than that of Standard Diesel. The limitation is the production of oil. Since the extraction of oil is done in small scale, the cost of extraction is little high. The cost can be reduced when extraction is done on large scale. The present work is to conduct experiment on single cylinder CI Engine with various proportion of WCO in diesel and compare it with stand alone fossil fuel.

II. EXPERIMENT

Study of VCR engine performance (Computerized mode)

To study the performance of 1 cylinder, 4 stroke, Diesel engine connected to eddy current dynamometer in computerized mode.

A. Adjustment of The Compression Ratio

Slightly loosen the 6 nos. vertical Allen (socket headed) bolts provided on both sides of the tilting cylinder block.

Loosen the lock nut of the Adjuster and rotate the Adjuster by using spanner for tilting the cylinder block.

Adjust the desired compression ratio by referring the scale provided on the CR indicator (near the Adjuster)

Tighten the lock nut of the Adjuster.

Gently tighten the vertical Allen bolts (6 nos.).

B. Procedure

Ensure that all the nut bolts of engine, dynamometer, propeller shaft, base frame are properly tightened. Ensure that sufficient lubrication oil is present in the engine sump tank. This can be checked by marking on the level stick. Ensure sufficient fuel in fuel tank. Remove air in fuel line, if any.

Switch on electric supply and ensure that PPU (Piezo powering unit), DLU (Dynamometer loading unit), Load indicator and Voltmeter are switched on. Start Computer and open "EngineSoftLV" (Double click "EngineSoftLV" icon on the desktop) Select "Engine Model" open "Configure" in View. Check configuration values & system constants with the values displayed on engine setup panel. "Apply" the changes, if any. Click on "PO- PV Graphs" tab.

Start water pump. Adjust the flow rate of "Rotameter (Engine)" to 250-350 LPH and "Rotameter (Calorimeter)" to 75-100 LPH by manipulating respective globe valves provided at the rotameter inlet. Ensure that water is flowing through dynamometer at a pressure of @ 0.5 to 1 Kg/cm².

Keep the DLU knob at minimum position. Change the Fuel cock position from "Measuring" to "Tank" Start the engine by hand cranking and allow it to run at idling condition for 4-5 minutes.

Click on "Scan Start" on the monitor, Ensure that Speed, Temperatures and Manometer reading are correctly displayed on the PC. These readings should tally with those displayed on the engine panel. Increase the load on the engine by rotating knob on the DLU and confirm the load reading on the indicator and computer are same.

Adjust DLU knob and to set 0.5 kg load on Load Indicator. Wait for 3 mins., ensure that load is constant during this period. Change the Fuel cock position from "Tank" to "Measuring". Click "Log on" on. The fuel metering is ON for next 60 seconds. During first 30 seconds enter engine water flow, calorimeter jacket cooling water flow in LPH (and compression ratio for VCR engine). Click OK after recording fuel reading. Enter the file name under which the records to be stored. The first reading data is now saved. Change the Fuel cock position from "Measuring" to "Tank".

Adjust DLU knob and to set 3 kg load on Load Indicator. Wait for 3 mins., ensure that load is constant during this period. Change the Fuel cock position from "Tank" to "Measuring". Click "Log on" on. The fuel metering is ON for next 60 seconds. During first 30 seconds enter engine water flow, calorimeter jacket cooling water flow in LPH (and compression ratio for VCR engine). Click OK after recording fuel reading. The second reading data is now saved. Change the Fuel cock position from "Measuring" to "Tank".

Repeat above step for various loads e.g. 6, 9,12,15,18 kg. (For VCR engine do not exceed 12 Kg load.) After finishing all the readings remove the load on the engine by DLU, Click "Scan Stop" on PC. Stop the engine by pressing engine stop lever. Allow the water to circulate for about 5 minutes for engine cooling and then Stop the pump. Click "File Open" on PC, Select the File under which the readings are stored and click "OK". On all the screens the first reading (of 0.5kg) is shown. To view next readings click "Next Data".

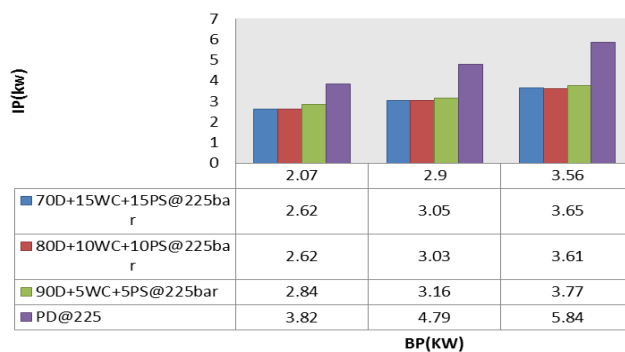
The results are displayed on all the three screens. For printing the results click "Print" and select appropriate option. Click "File Close" after printing & checking. Click "Exit" and then Shut Down the computer.

III. PERFORMANCE AND COMPARISON

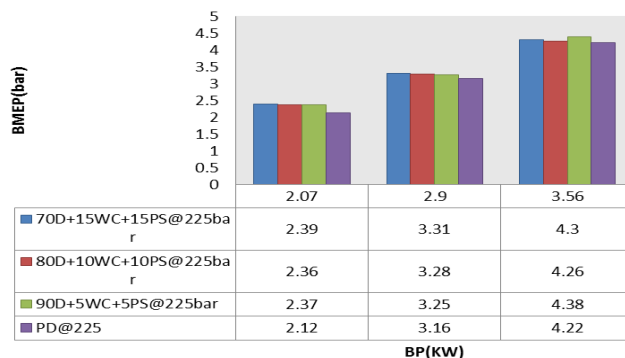
WCOBD & Palm Stearin with Diesel at Different Mixture, at 225bar injection Pressure & 18CR.

The graphs below shows the comparison for indicated power, mean effective pressure for indicated and brake, indicated thermal efficiency, brake thermal efficiency, volumetric efficiency and brake specific fuel consumption.

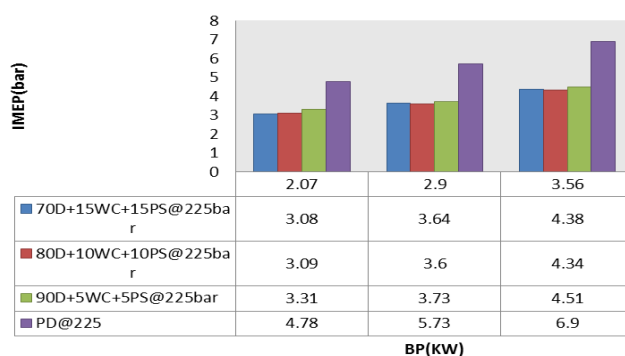
Comparison of IP(Kw) Between Bio-Diesel & Pure Diesel@18CR



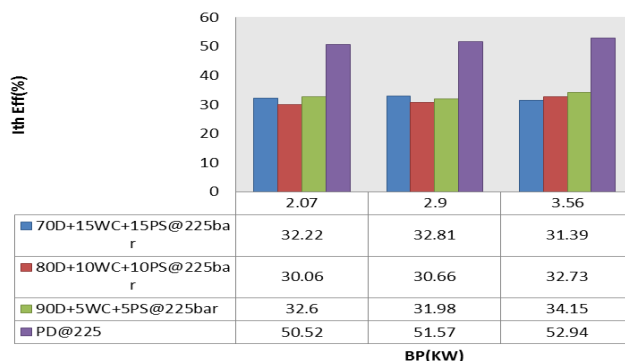
Comparison of BMEP (bar) Between Bio-Diesel & Pure Diesel@18CR



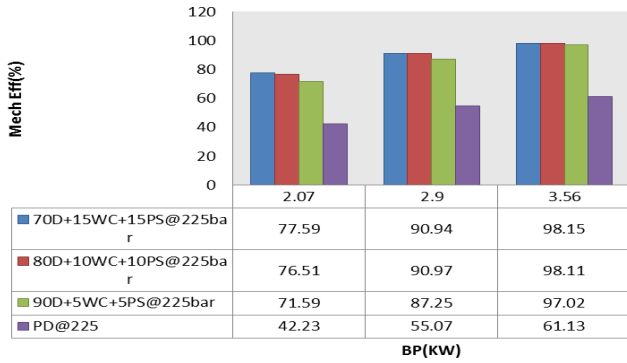
Comparison of IMEP (bar) Between Bio-Diesel & Pure Diesel@18CR



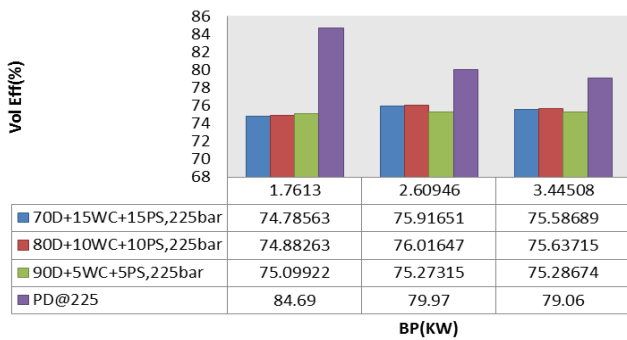
Comparison of Ith Eff(%) Between Bio-Diesel & Pure Diesel@18CR



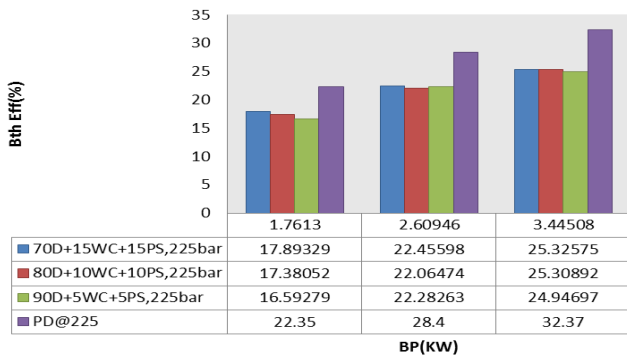
Comparison of Mech Eff(%) Between Bio-Diesel & Pure Diesel@18CR



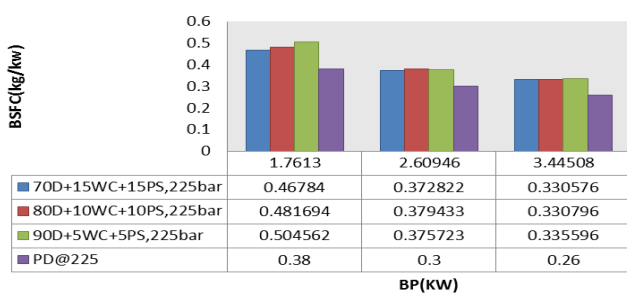
Comparison of Vol Eff(%) Between Bio-Diesel & Pure Diesel@18CR



Comparison of BTh Eff(%) Between Bio-Diesel & Pure Diesel@18CR

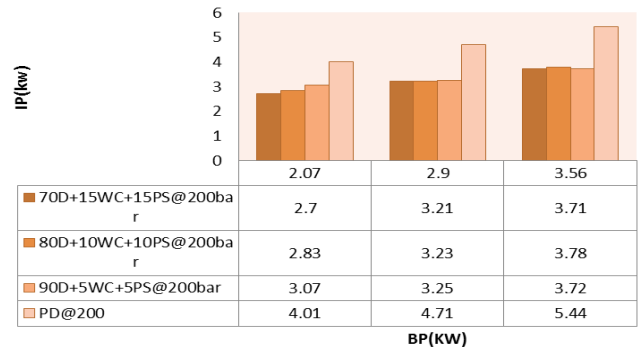


Comparison of BSFC (Kg/Kw) Between Bio-Diesel & Pure Diesel@18CR

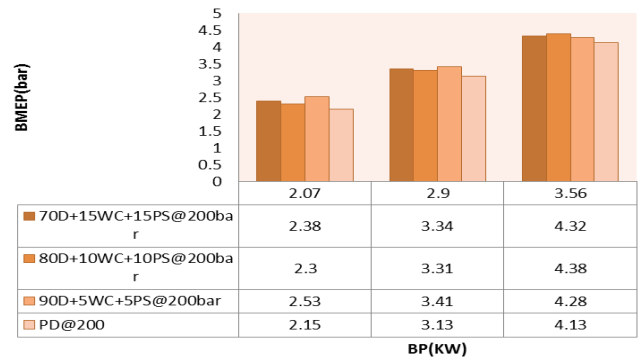


The graphs below shows the comparison for indicated power, mean effective pressure for indicated and brake, indicated thermal efficiency, brake thermal efficiency, volumetric efficiency and brake specific fuel consumption.

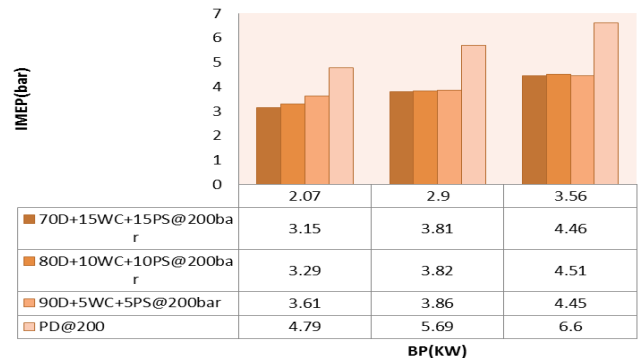
Comparison of IP(Kw) Between Bio-Diesel & Pure Diesel@18CR BP(Kw)



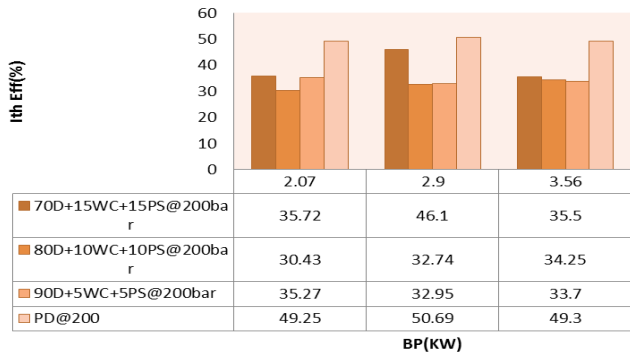
Comparison of BMEP (bar) Between Bio-Diesel & Pure Diesel@18CR



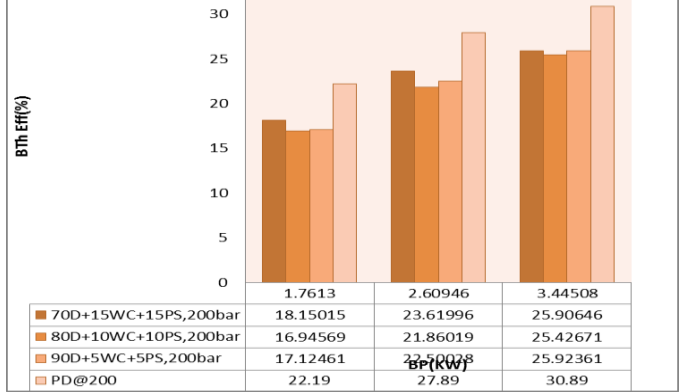
Comparison of IMEP (bar) Between Bio-Diesel & Pure Diesel@18CR



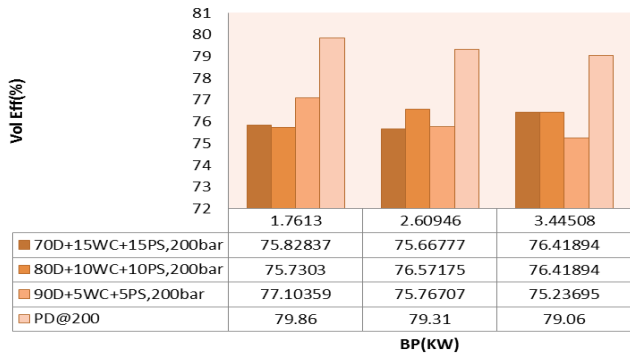
Comparison of ITh Eff(%) Between Bio-Diesel & Pure Diesel@18CR



Comparison of BTh Eff(%) Between Bio-Diesel & Pure Diesel@18CR



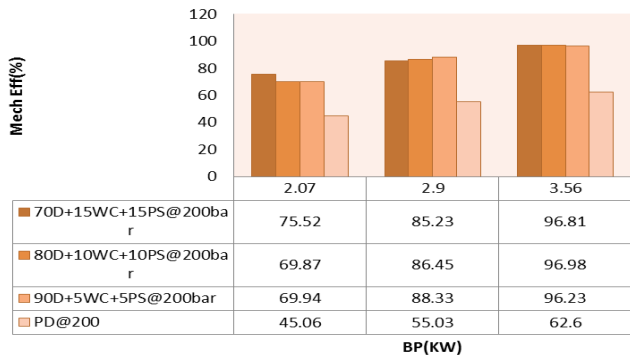
Comparison of Vol Eff(%) Between Bio-Diesel & Pure Diesel@18CR



IV Problems Faced During Usage of Bio-Diesel

- **Viscosity:** As has been mentioned earlier, BD has comparatively higher viscosity than the conventional diesel, this sometimes comes as a hindrance at cold regions, where the temperature is likely to fall below 250 C. Fuel becomes thick in consistency and is more likely to get blocked in the minor cavities of fuel injector.
- **Blockage:** Citing viscosity an issue, the problem of blocking of valves and injector was faced.
- **Mixing:** Precise blending of fuel is very important, minor negligence may be reflected in the comparison and data collection.

Comparison of Mech Eff(%) Between Bio-Diesel & Pure Diesel@18CR



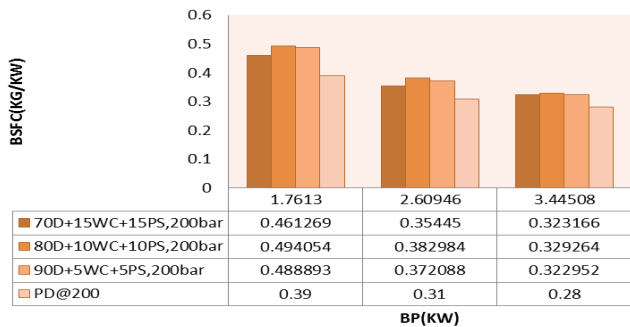
V ENVIRONMENTAL AND HEALTH BENEFITS

The use of BIO-DIESEL will help preserve our environment. Bioactive™ is completely biodegradable and contains no toxic or harmful elements. It is non-flammable, safe to handle, and poses no danger to the environment[5]. Best of all, it is made from a renewable resource that is abundant. It will also improve the air that we breathe. Air pollution is a serious problem worldwide and the rising incidence of pollution-related illnesses has become a serious concern. Extensive field and laboratory tests prove that Bioactive™ dramatically reduces smoke emissions through complete combustion. With the elimination of air pollution caused by smoke, a cleaner air will result in better respiratory conditions of people.

VI GENERAL ADVANTAGES

- **National security.** Since it's made domestically, it reduces our dependence on foreign oil.
- **National economy** Using bio-diesel keeps our fuel buying pesos at home instead of sending it to foreign countries. This reduces our trade deficit and creates jobs.
 - It's sustainable & non-toxic.
- **Emissions** Bio-diesel is nearly carbon-neutral, meaning it contributes almost zero emissions: global warming.
- **Engine life** Studies have shown it reduces engine wear by as much as one half, primarily because it provides excellent lubricity. Even a 2% bio-diesel/98% diesel blend will help.
- **Drivability** We have yet to meet anyone who doesn't notice an immediate smoothing of the engine with bio-diesel. It just runs quieter, and produces less smoke.

Comparison of BSFC (Kg/Kw) Between Bio-Diesel & Pure Diesel@18CR



VII General Disadvantages

• Primarily, bio-diesel is not readily available in retail market but that available are with commercial suppliers, however whose production has not yet been commercialized. With the novel move by the railways in India and the RTC in the East while Andhra Pradesh, this idea gained momentum and has been a success to much extent.

• Bio-diesel is not suitable to any engines, more of the older one.

VIII Conclusion

The Engine was running smoothly with the use of Bio-Diesel. The Bio-Diesel was added in the Diesel -Blend resulted in better performance and reduced smoke. The brake power for blends doesn't show much deviation from petroleum diesel The Brake specific fuel consumption is increased with the blends when compared to diesel. Brake thermal efficiency increased with all blends when compared to the conventional diesel fuel.

- The Bio-Diesel added in the Diesel -Blend resulted in better performance and reduced smoke.
- The brake power for blends doesn't show much deviation from Petroleum Diesel.
- The Brake specific fuel consumption is increased with the blends when compared to Diesel. And is maximum for B20 then again decreases of B30.
- Brake thermal efficiency increased with all blends when as the percentage of biodiesel increases.
- Mechanical Efficiency of the Bio-Diesel Blends was much higher when compared to the conventional Diesel fuel.

IX REFERENCES

- 1) Jordan Journal of Mechanical and Industrial Engineering, Volume 9 Number 1, February, 2015 ISSN 1995-6665 Pages 61- 66
- 2) International Journal on Emerging Technologies 5(2): 130-135(2015) ISSN No. (Print) : 0975-8364 ISSN No. (Online) : 2249-3255
- 3) INTERNATIONAL JOURNAL OF PURE AND APPLIED RESEARCH IN ENGINEERING AND TECHNOLOGY, IJPRET, 2015; Volume 3 (9): 426-433- ISSN: 2319-507X
- 4) [Journal of Engineering for Gas Turbines and Power | Volume 137 | Issue 9 | research-article](#), (Sep 01, 2015) (14 pages)
- 5) Journal of Advanced Research in Fluid Mechanics | Vol. 6, No.1. Pages 1-18, 2015 and Thermal Sciences ISSN (online): 2289-7879
- 6) The Journal of Macro Trends in Energy and Sustainability JMES Vol 3 Issue 1 2015 pages 15-23.
- 7) *IOSR Journal of Mechanical and Civil Engineering (IOSR-JMCE) e-ISSN: 2278-1684, p-ISSN: 2320-334X, Volume 12, Issue 2 Ver. VI (Mar - Apr. 2015), PP 27-33* www.iosrjournals.org
- 8) INTERNATIONAL JOURNAL of RENEWABLE ENERGY RESEARCH Puneet Verma and M.P. Sharma, Vol.5, No.1, 2015
- 9) International Research Journal of Engineering and Technology (IRJET), Volume: 02 Issue: 07 | Oct-2015 www.irjet.net, e-ISSN: 2395 -0056 / p-ISSN: 2395-0072
- 10) International Conference on Energy Efficient Technologies For Automobiles (EETA' 15) Journal of Chemical and Pharmaceutical Sciences ISSN: 0974-2115
- 11) International Journal of Innovative Research in Science, Engineering and Technology (An ISO 3297: 2007 Certified Organization) Vol. 4, Special Issue 6, May 2015. ISSN(Online) : 2319 - 8753 ISSN (Print) : 2347 – 6710
- 12) Research Journal of Chemical Sciences ISSN 2231-606X Vol. 5(7), 48-51, July (2015) Res. J. Chem. Sci
- 13) : International Journal of Research in Engineering and Technology eISSN: 2319-1163 | pISSN: 2321-7308, Volume: 04 Issue: 01 | Jan-2015, Available @ <http://www.ijret.org>
- 14) Iranica Journal of Energy & Environment Journal Homepage: www.ijee.net IJEE an official peer review journal of Babol



5th International Conference of Materials Processing and Characterization (ICMPC 2016)

Preparation and Characterization of GFRPC Material

Kareddula Vijaya Kumar^{a,*}, P Shailesh^b, J A Ranga babu^a, Ravi Kumar Puli^a

^aMechanical Engineering Department, NIT Warangal, Warangal and 506004, India

^bMechanical Engineering Department, MCET, affiliated to OU, Hyderabad and 500001, India

Abstract

This paper aims to present the mechanical characterization of Glass Fiber Reinforced Polymer Composites (GFRPC) under different load conditions. The dynamic mechanical properties of GFRPC are estimated experimentally. Different dies are designed for preparing and testing the GFRPC by multi directional loading. Samples are prepared at different compositions and reinforced with glass fiber at various mass fractions and plies by conventional hand lay-up process. The specimens are post cured for active bonding between reinforcement and matrix material, so that thermo-mechanical properties are enhanced to exercise for different applications. The glass fibers are added proportional to load bearing and optimized the reinforcement by weight percentage for particular grade applications. The prepared composites are characterized by Differential Scanning Calorimeter (DSC) to identify the glass transition temperature and nature of the interface between the phases, morphology of the prepared composites. Dynamic Mechanical Analysis (DMA) to determine the intrinsic properties as well as dynamic mechanical properties of GFRPC by three point flexural method. Slow Strain Rate Tensile Testing (SSRTT) exposes the stress, elongation and time at ultimate load and at the point of fracture. Here the test specimen is stretched monotonically in axial tension at a slow rate until failure. The SSRTM testing is that it produces a result in a reasonably short time, within 6-12 hours in most cases, depending on strain rate to evaluation the effect of metallurgical variables such as alloy composition, heat treatment and processing and/or environmental parameters in a relatively short period testing.

©2017 Elsevier Ltd. All rights reserved.

Selection and peer-review under responsibility of Conference Committee Members of 5th International Conference of Materials Processing and Characterization (ICMPC 2016).

Keywords: Glass Fiber; Matrix; DSC; DMA; SSRTT;

* Corresponding author. Tel.: +91-9703582886;
E-mail address: vijay701414@nitw.ac.in

1. Introduction

Composite material is a structural material that consists of two or more combined constituents that are combined at a macroscopic level. Generally, a composite material is composed of reinforcement in any form such as fibers, particulates, flakes, and/or fillers which are embedded in a matrix material (polymers, metals, or ceramics). The matrix holds the reinforcement to form the desired shape while the reinforcement improves the overall mechanical properties of the matrix. When designed and prepared properly, the new combined composite material exhibits better strength than would each individual material. Composites are used in aircraft structures, electronic packaging, medical equipment, and space vehicles to home building. Polybenzoxazines are exhibit numerous exclusive properties, such as near-zero volume changes upon polymerization with high mechanical integrity, low water adsorption at room temperature, surprisingly high glass transition temperatures (T_g), rapid development of physical and mechanical properties during polymerization processes very high char yields, and low surface energies [1-4]. The resin properties can be extracted from degree-of-cure, the heat flow during exotherm, the glass transition temperature and the melting and degradation temperatures [5-7]. Cure monitoring of liquid resins with a DMA is achieved using either an inert impregnation made of glass fibers [8, 9]. Since the observation of broad calorimetric glass transitions [10, 11] and the failure of time - temperature superposition in some miscible polymer blends, it has been appreciated that miscible blend dynamics are often complex relative to neat homo polymer [10-13]. Related effects are present in miscible polymer/plasticizer mixtures [14]. This is the arena of lightweight materials, by hybridizing the properties of composite materials useful active properties are developed. Slow strain rate is significant mechanical behaviour, which is important property in performing CAE design. The vehicle body materials are tested at quasi static strain rate to 500 S^{-1} [15]. Some researchers are reported the dynamic mechanical properties of material in terms of Hopkinson bar [16]. Research groups and automobile manufacturers worked together to establish test standards to obtain tensile properties of materials covering the strain rate from 10^{-3} s^{-1} to 10^3 s^{-1} [17, 18].

Nomenclature

GFRPC	Glass Fiber Reinforced Polymer Composite
DSC	Differential Scanning Calorimeter
DMA	Dynamic Mechanical Analysis
SSRT	Slow Strain Rate Tensile Testing
T_g	Glass Transition Temperature
E'	Storage Modulus
E''	Loss Modulus

1.1. Benefits of Composites

Advanced technologies in manufacturing and burning desires of updated design engineers demands the hybrid properties of individual materials. These GFRPCs are one of the promising material for light weight applications with good mechanical stiffness. Upgrading properties of GFRPCs are as follows:

- GFRPCs are economical than the conventional metals with reasonable mechanical properties and least production time.
- Its weight to strength ratio is more than many metallic components.
- Having high dimensional accuracy, good surface properties, and environmental friendliness with least finishing cost.
- The addition of the reinforcement to the polymer matrix increases the creep resistance for properly designed FRP part.
- Possess good thermal and electrical stable properties.
- Exhibits non-reactive nature with organic and inorganic substances.

2. Preparation of Glass Fiber Reinforced Polymer Composites (GFRPC)

2.1. Preparation of die

The Dies are prepared according to the requirement of the samples. Some of the dies with M.S material are fabricated and this can be with stand a load up to 80 kg. the other dies are fabricated with ply wood and teak wood with varying dimensions. The ply wood and teak wood are chosen because of their low cost and ease of fabrication. These dies are used where the load applied is nominal in nature.

2.2. Preparation of composite material

This part of the work summarizes and priorities the key environmental issues facing each of the eight common manufacturing process reviewed and given below. It is recognized that the choice of manufacturing process will primarily be influenced by economic and design factors, this work consider preparation and characterization of “GFRP” composite material.

For preparing GFRPC, major ingredients are E-Glass Fiber mat, Epoxy resin (Company code: L/556) with hardener, Die.

The Hand Lay-up process is being adopted for preparing GFRPC as shown in Fig.1. It is a production technique suitable for prototypes and low volume production of fiber composite parts. The composite part will have a nice smooth surface on one side and a very rough one on the other. This is the simplest method of producing a fiber-reinforced part. To produce a part with this process by using fiber glass and a polyester. Initially E-glass fiber mat is cut to required dimensions and placed on a clean and flat surfaced table. Now the epoxy resin (the resin and fibers are supplied by is taken and mixed with hardener in the required ratio in order to get good strength (for 100% of resin 2% of hardener is taken). Now the mixture is thoroughly applied to the fiber mat with a soft, clean brush. After applying the resin mixture, it is rolled over with a smooth roller in order to eliminate the air bubbles. Now it is properly folded in to one half and again the resin mixture is applied. The process is continued until required size and thickness is attained and allowed to dry for some time.



Fig. 1. Hand Lay-up process of composite preparation

The prepared sample is kept in the die and sufficient load is applied for a period of a minimum of 24 hours for getting proper bond between the fiber and matrix. More layers can be added and, after drying, the composite part can be removed from the mould. The prepared samples are post cured in special oven suited for the epoxy composites. This post curing had strong impact on the thermal and mechanical behavior of thermosetting polymers. The main advantages and disadvantages of Hand Lay-up process are easy to control fibers orientation. Furthermore, the process is very flexible as it can produce from very small, up to very large part of different kinds of geometry. The cycle time per part is very long, and only small series can be produced.

3. Experimental Methods

3.1. DSC Testing

Differential Scanning Calorimeter (DSC) monitors heat effects associated with phase transitions and chemical reactions as a function of temperature. In a DSC the difference in heat flow to the sample and a reference at the same temperature, is recorded as a function of temperature. The reference is an inert material such as alumina, or just an empty aluminum pan. The temperature of both the sample and reference are increased at a constant rate. Since the DSC is at constant pressure, heat flow is equivalent to enthalpy changes:

$$\left(\frac{dq}{dt}\right)_p = \left(\frac{dH}{dt}\right) \quad (1)$$

Here dH/dt is the heat flow measured in $\text{mcal} \cdot \text{sec}^{-1}$. The heat flow difference between the sample and the reference is given by:

$$\Delta \left(\frac{dH}{dt}\right) = \left(\frac{dH}{dt}\right)_{\text{sample}} - \left(\frac{dH}{dt}\right)_{\text{reference}} \quad (2)$$

And can be either positive or negative. In an endothermic process, such as most phase transitions, heat is absorbed and, therefore, heat flow to the sample is higher than that to the reference. Hence $\Delta dH/dt$ is positive. Other endothermic processes include helix-coil transitions in DNA, protein denaturation, reduction reactions, and some decomposition reactions. In an exothermic process, such as crystallization, some cross-linking processes, oxidation reactions, and some decomposition reactions, the opposite is true and $\Delta dH/dt$ is negative. The DSC testing was performed in both isothermal and dynamic heating modes. An argon gas sample purge was used for all DSC tests. The prepreg material is very sticky, and a hermetic stainless steel DSC pan with an O-ring seal was used for each sample. The average actual cure temperature during the cure time of each prepreg sample was within 2°C of the set point temperature. For dynamic testing, three linear heating rates of 2, 5 and $10^\circ\text{C}/\text{min}$ were used over a temperature range of $30\text{--}300^\circ\text{C}$ for also determining prepreg cure kinetics. The $10^\circ\text{C}/\text{min}$ heating rate was used following each partial cure for determining the T_g and residual heat of reaction after curing to some time t ($H_{t,\text{resid}}$).

3.2. DMA Testing

Dynamic Mechanical Analysis (DMA) is one of the most powerful tools to study the behaviour of plastic and polymer composite materials. The pyris Diamond DMA Viscoelasticity Measurement Module (temperature range: $150^\circ\text{C}\text{--}600^\circ\text{C}$) measures the creep recovery and dynamic viscoelasticity and stress relaxation using 3 point bending, tension, shear and compression methods to measure things such as polymeric materials simply and with high precision, as a function of temperature, frequency, or time. DMA testing was performed in the fixed frequency mode at oscillation amplitude of 0.2 mm, with inert gas sample purge used. Each cured sample was tested in the vertical DMA testing mode at fixed frequency measurements.

3.3. SSRT Testing

Slow Strain Rate Tensile Testing was used to test the prepared Glass Fiber Reinforced Polymer Composite Material to find out the Stress, % Elongation, Time taken to Failure, Slow-Strain-Rate testing is a dynamic load testing. It is an important method which involves relatively slow-strain-rate tensile testing of a specimen. Here the test specimen is stretched monotonically in axial tension at a slow rate until failure. This method is also known as constant extension-rate tensile testing. The benefit of SSRT testing is that it produces a result in a reasonably short time, within 6-12 hours in most cases, depending on strain rate. It also reduces incubation time to the onset of cracking in susceptible materials through the application of the dynamic plastic straining. The main benefit of the SSRT test is it allows the evaluation of the effect of metallurgical variables such as alloy composition, heat treatment and processing and/or environmental parameters in a relatively short period of testing. Strain rates utilized

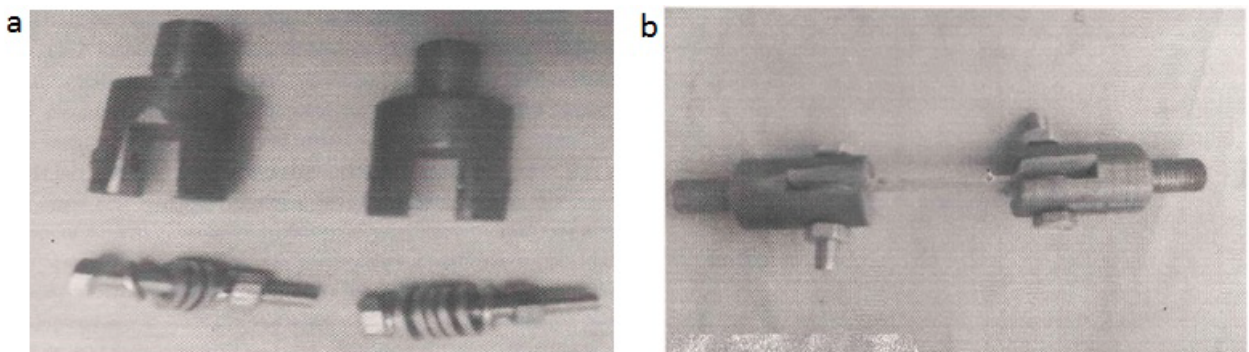
for SSRT testing are typically in the range of $1-4 \times 10^{-6} \text{S}^{-1}$. At a strain rate of $4 \times 10^{-6} \text{S}^{-1}$, the testing speed is about 1% strain per hour and failure of most engineering materials will occur within a day or two. Constant-strain-rate apparatus requirements include sufficient stiffness to resist significant deformation under the loads necessary to fracture the test specimens, a system to provide reproducible and constant strain rates over the range of 10^{-4} to 10^{-8}S^{-1} , and a cell to contain the test solution. Auxiliary equipment is used to control environmental conditions and to record test data. The testing equipment can also be instrumented to record load-elongation curves.

Fig. 2. A photograph of slow strain rate test unit



A photograph of a SSRT test unit is given in Fig. 2. Curttest incorporated (USA) Company manufactured and supply the SSRT unit with cross head speed range 10^{-7} to 4.5×10^{-4} mm/sec and maximum load capacity of 4536 Kgf. The arrangement of the sample setup for the Slow Strain Rate Tensile Testing is shown in Fig. 3 (a) and (b).

Fig. 3. (a) Grippers prepared for SSRT Machine; (b) Final setup of samples for SSRT Machine.

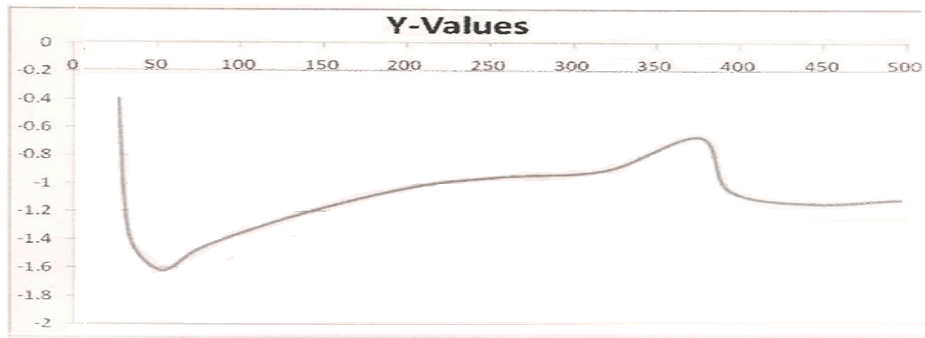


4. Results and Discussion

4.1. DSC Data

The output of the Dynamic Differential Scanning Calorimeter reveals many parameters by plotting the graph between heat flows versus temperature as shown in Fig. 4. ‘As received’ prepreg from graph at a heating rate of 20°C/min revealing one crystallization peak, one melting peak, one exothermic, one endothermic, one glass transition temperature.

Fig. 4. Heat flow (w/g) (Y-axis) Vs Temperature °C (X-axis)



4.2. DMA Data

The graphical figures obtained after conducting experiments on DMA machine and are shown in Fig. 5. It is clear from the graph that the storage modulus (E') of the samples is abruptly decreasing to very small value in the region of glass transition temperature of the sample. This is due to weakening of bonding between the cross linked molecules of the resin matrix of the composite. The loss modulus (E'') of the sample is taking high values because there is a sudden decrease of modulus of the sample due to starting of glass transition temperature region in the sample. The $\tan\delta$ also represents loss of angle of modulus of the sample which is also taking high values in the glass transition temperature region of the sample which has undergone for testing.

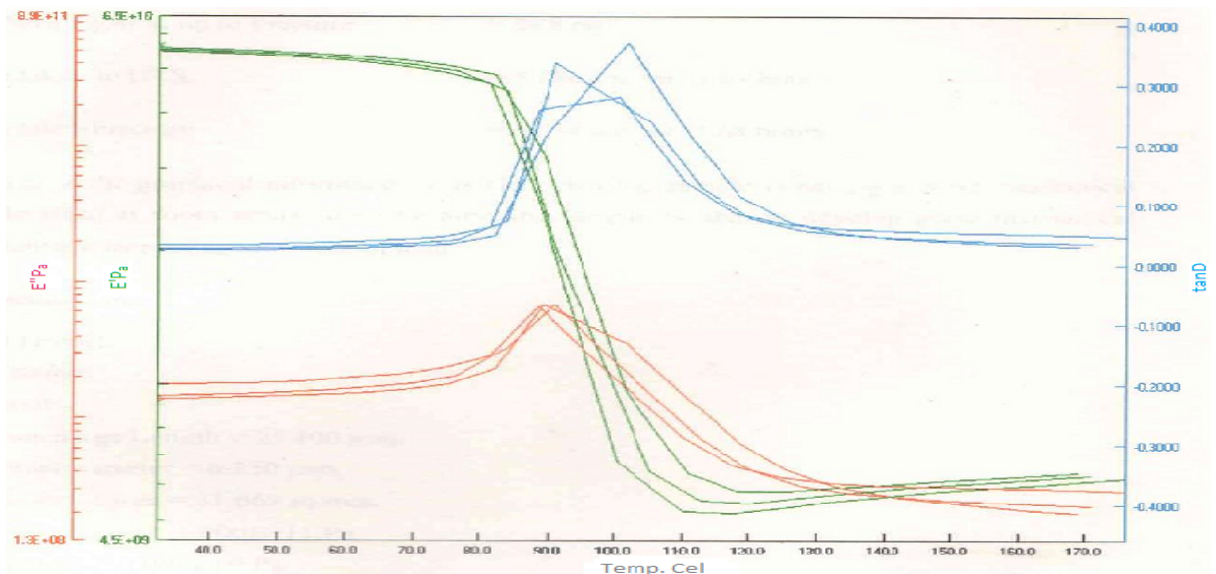


Fig. 5. Experimental Results for DMA

4.3. SSRT Data

Table 1. Slow Strain Rate of GFRPC at different loads.

Time (Sec)	LVDT 1 (mm)	LVDT 2 (mm)	Extension (mm)	Load (Kgf)
3383603310	0	0	0	41.82
3383603340	0.0083	-0.0022	0.003	42.86
3383603370	0.0339	-0.003	0.0154	46.05
3383603400	0.0565	-0.0037	0.0264	48.17
3383603430	0.0745	-0.0007	0.0369	50.45
3383603460	0.0828	0.0097	0.0463	52.04
3383603490	0.0903	0.0239	0.0571	53.62
3383603520	0.0986	0.0373	0.0681	55.37
3383603550	0.1069	0.0493	0.0781	56.73
3383603580	0.1182	0.062	0.0901	58.39
3383603610	0.128	0.0747	0.1013	59.98
3383608890	2.3855	2.4382	2.4119	145.55
3383608930	2.3991	2.4516	2.4254	145.62
3383608960	2.4156	2.4628	2.4392	145.72
3383608980	2.4299	2.4748	2.4524	145.78
3383609020	2.4442	2.486	2.4651	146.08
3383609050	2.4563	2.5002	2.4782	146.31
3383609090	2.4698	2.5144	2.4921	146.39
3383609120	2.4849	2.5263	2.5056	146.69
3383609150	2.506	2.5353	2.5206	146.82
3383609190	2.524	2.545	2.5345	147.28
3383609230	2.5398	2.5562	2.548	147.22
3383609260	2.5549	2.5689	2.5619	147.08
3383609290	2.5692	2.5831	2.5762	146.61
3383609330	2.585	2.5943	2.5897	146.38
3383609350	2.5986	2.6078	2.6033	145.49
3383609394	2.6136	2.6182	2.6159	145.26

The data obtained after conducting Slow Strain Rate Tensile Testing results of GFRPC are given in Table. 1 and resulting graphical figure is shown in Fig. 6. By observing of the graph and data systematically, it is clear that the stress developed in the sample is increasing almost proportionality with % of elongation of the sample.

The maximum stress at UTS = 181.62 N/mm²
 The fracture strength of the sample = 179.10 N/mm²
 The % of elongation up to UTS = %8.55
 The % of elongation up to Fracture = % 8.88
 Time taken up to UTS = 5,868 sec 'or' 1.63 hours
 Time taken up to Fracture = 6,084 sec 'or' 1.69 hours

By analyzing the graphical information it is clear that the sample is having a good mechanical tensile strength at room temperature because the sample is able to develop good mechanical resistance with increasing slow rate of load.

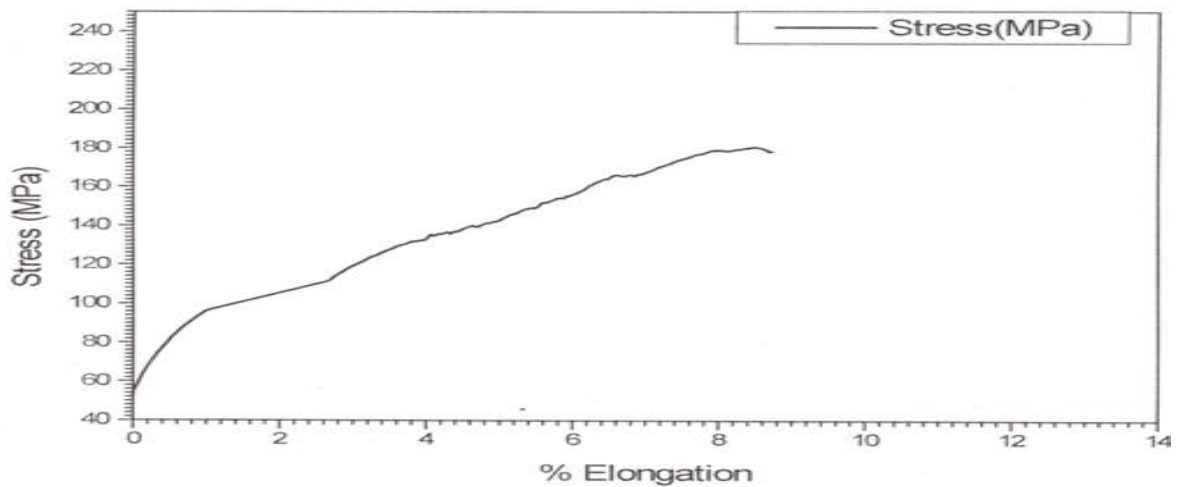


Fig.6. Slow Strain Rate Tensile Testing curve

5. Conclusions

By observing the figure of DMA testing, it is clear that the glass transition temperature is in the region starting from 80°C to 120°C. So the usage of the sample should be below 60°C to 65°C or else the sample will not be working satisfactorily for the intended use. The data from DSC graph figure indicates that the glass transition is near about 100°C which is coinciding with DMA output results for storage modulus and loss modulus. So we have conformed DMA results to the data from DSC output results. The Slow Strain Rate Tensile Test data depicted in figure shows that the sample prepared is having good structural integrity because there is direct proportionality between stress and strain.

References

- [1] Wang, C.F., Wang, Y.T., Tung, P.H., Kuo, S.W., Lin, C.H., Sheen, Y.C., Chang, F.C., Fabrication of patterned superhydrophobic polybenzoxazine hybrid surfaces. *Langmuir* 2006a, 22, 8289–8292.
- [2] Wang, C.F., Su, Y.C., Kuo, S.W., Huang, C.F., Sheen, Y.C., Chang, F.C., Low-surface free-energy materials based on polybenzoxazines. *Angew. Chem.* 2006b, Int. Ed. 45, 2248–2251.
- [3] Ishida, H., Allen, D.J., Physical and mechanical characterization of near-zero shrinkage polybenzoxazines. *J. Polymer* 1996, Sci. B 34, 1019–1030.
- [4] Kiskan, B., Ghosh, N.N., Yagci, Y., Polybenzoxazine-based composites as high performance materials. *Polymer* 2011, Int. 60, 167–177. W. Strunk Jr., E.B. White, *The Elements of Style*, third ed., Macmillan, New York, 1979.
- [5] W. Stark, M. Jaunich, J. McHugh, Cure state detection for pre-cured carbon fibre epoxy prepreg (CFC) using temperature-modulated differential scanning calorimetry (TMDSC), *Polym. Test.* 32 (2013) 1261.
- [6] S.R. White, P.T. Mather, M.J. Smith, Characterisation of the cure-state of DGEBA-DDS epoxy using ultrasonic, dynamic mechanical and thermal probes, *Polym. Eng. Sci.* 42 (2002) 51.
- [7] J. Zhang, T. Li, H. Wang, Y. Liu, Y. Yu, Monitoring extent of curing and thermal mechanical property study of printed circuit board substrates, *Microelectron. Reliab* 54 (2014) 619.
- [8] R.J. Varley, J.H. Hodgkin, D.G. Hawthorne, G.P. Simon, Toughening of a trifunctional epoxy system. II. Thermal characterisation of epoxy/amine cure, *J. Appl. Polym. Sci.* 60 (1996) 2251.
- [9] M. Xie, Z. Zhang, Y. Gu, M. Li, Y. Su, A new method to characterize the cure state of epoxy prepreg by dynamic mechanical analysis, *Thermochim. Acta* 487 (2009) 8.
- [10] Suk-fai Lau, Jaya Pathak, Bernhard Wunderlich, Study of phase separation in blends of polystyrene and Poly (α -methylstyrene) in the glass transition region using quantitative thermal analysis, *Macromolecules* 1982; 15: 1278-1283.

- [11] Trask C.A, Roland CM., A Nearly Ideal Mixture of high polymers, *Macromolecules* 1989;22:256-261.
- [12] Gaikwad AN, Wood ER, Ngai T, Lodge TP. Two calorimetric Glass Transitions in Miscible Blends Containing Poly (ethylene oxide), *Macromolecules* 2008;41:2502-2508.
- [13] Timothy P. Lodge, Thomas C. B. McLeish. Self-Concentrations and Effective Glass Transition Temperatures in Polymer Blends, *Macromolecules* 2000;33:5278-5284.
- [14] Bock D, Petzold N, Kahlau R, Gradmann S, Schmidtke B, Benoit N, E. A. Rossler, Dynamic heterogeneities in glass forming systems, *Journal of Non-Crystalline Solids* 2015;407:88-97.
- [15] HuhH, Lim JH, Park SH. High speed tensile test of steel sheets for the stress-strain curve at the intermediate strain rate. *Int J Automot Technol* 2009;10:195-204.
- [16] Mohr D, Gary G, Lundberg B. Evaluation of stress-strain curve estimates in dynamic experiments. *Int J Impact Eng* 2010;37:161-9.
- [17] Hill SI. Standardization of high strain rate test techniques for automotive plastics project. UDRI Structural Test Group, UDR-TR-2004-00016, University of Dayton, Dayton, OH, USA, 2004.
- [18] D. Dash¹, S. Samanta², S.S. Gautam², and M. Murlidhar², Mechanical Characterizations of Natural Fiber Reinforced Composite Materials, *Advanced Materials Manufacturing & Characterization Vol 3 Issue 1 (2013)*.

Influence of Fuel Injection Parameters on the Performance and Emissions of CI Engine with neat Biodiesel

U.S.Vara Prasad¹
Professor,
Dept.of Mech.Engg.,
Methodist College of
Engg.and Tech, Hyderabad

K. Madhu Murthy²
Professor,
Dept.of Mech.Engg.,
NIT Warangal-506004

G. Amba Prasad Rao³
Professor,
Dept.of Mech.Engg.,
NIT Warangal-506004

M.Vinod Babu,
Research Scholar,
Dept.of Mech.Engg.,
NIT Warangal-506004

Abstract:

Use of biodiesel has attracted over the year as a viable alternative fuel due to its properties being very close to petro-diesel. The major problem encountered with the use of neat biodiesel was high NO_x emissions. In the present work an attempt is made to mitigate levels of NO_x emissions when engine is operated with neat biodiesel produced from jatropha curcas oil. In this regard, systematic experimental investigations were done on a typical water cooled single cylinder CI engine to study the effect of fuel injection parameters. Fuel injection parameters such as fuel injection pressure, size of fuel injection nozzle hole and fuel injection timing, for each of these parameters three different values were selected. Engine performance was evaluated in terms of brake specific fuel consumption (BSFC), hydrocarbon (HC), oxides of nitrogen (NO_x) and Smoke density. It was observed that modest increase in fuel injection pressure, smaller nozzle hole size and retarded fuel injection timing yielded satisfactory performance and lower HC, Smoke density and NO_x emissions with neat biodiesel operation.

Introduction:

The nature of diesel engine combustion process is unsteady, turbulent, diffusion and heterogeneous [3]. The combustion process is highly influenced by the way of fuel-air mixing in the engine cylinder. Diesel fuelled engines meet the requirement of prime mover in light, medium and heavy duty applications due to its high fuel conversion efficiency. However, due to extensive use of diesel engines the problems of fuel crisis and pollution related issues are increasing alarmingly. The problems of automotive pollution are being tackled by various researchers by the use of exhaust-gas after-treatment methods or adopting alternate fuels. Vegetable oils are found to be promising alternative to petro-diesel fuel owing to its physico-combustion properties near to petro-diesel fuel [1,4]. However, a little higher viscosity of vegetable oil restricts its direct use in engine, this issue made the researcher to suggest treatment of vegetable oils and subsequent conversion into biodiesel [2,4].

To achieve better fuel-air mixing, one approach is to adopt a good fuel injection system as it plays a crucial role to bring fuel and air in intimate contact with each other. High injection pressures with small nozzles are common in the modern diesel engine as they reduce injection duration and improve combustion efficiency [2-4]. Biodiesel is attractive as it is biodegradable, sulphur-free, non-toxic and can significantly

reduce exhaust emissions and low overall life cycle emission of carbon oxides (CO_x) from the engine when burned as a fuel. Experimental investigations to optimize parameters for effective use of vegetable oil fuels, like the effect of injection system parameters on performance and emission characteristics of a twin-cylinder CIDI engine fuelled with pongamia biodiesel-diesel blend using response surface methodology [5]; the effect of supercharging and fuel injection pressure on the performance of a diesel engine with cotton seed oil [6,9] and the influence of compression ratio and injection pressure by adopting karanja methyl ester were studied [10]. Studies were done researchers to make use of ethanol, di-methyl ether or di-ethyl ether but concluded that the production cost of these fuels is cost intensive [11,12]. Life cycle analysis of biodiesel fuel were established that such fuels are safe and environment friendly [7].

It is observed from the literature that there were efforts to make use of biodiesel as blends with methanol or ethanol and to further make it feasible and effective [6,13,14]. In the present experimental study, an attempt is made to improve the performance of biodiesel run engine by varying the fuel injection parameters such as fuel injection pressures, size of fuel injector nozzle hole and fuel injection timing.

Materials and Methods.

A single cylinder naturally aspirated CI engine is selected for the purpose of present study. The specifications of the engine are given in Table-I. The dimensions of various nozzles employed in the present studies are given in Table-II. For this purpose methyl esters of Jatropha Curcas oil, popularly called as biodiesel, [obtained from non-edible oil, Jatropha oil] as fuel is considered. To begin with sufficient amount of laboratory samples of methyl esters of Jatropha oil were prepared following the procedure well laid out [1,6]. The properties of fuel prepared and comparison with petro-diesel are given in Table-III. Firstly to obtain baseline data, performance tests with petro-diesel, by varying fuel injection pressure, nozzle hole size and number of holes maintaining injection timing unaltered were conducted and performance and emission tests on DI type diesel engine with biodiesel [B100] were conducted. All the tests were carried out at the rated speed of the engine. The jacket water temperature was maintained at about 70°C. The rated injection pressure of the engine was 190bar. To investigate the effect of fuel injection

pressure, three different pressures were selected, viz: 190, 210 and 230 bar, for the experimentation. Further, for a fixed fuel injection pressure, effect of three nozzle hole sizes were studied and for a given injector nozzle hole size the effect of injection pressure was investigated [5]. These tests were aimed at arriving at the optimum nozzle hole size and optimum fuel injection pressure. The parameters such as load, time for fuel consumption, exhaust gas temperature; smoke density and exhaust emissions were noted down. Fig.1 represents schematic of the experimental set-up employed.

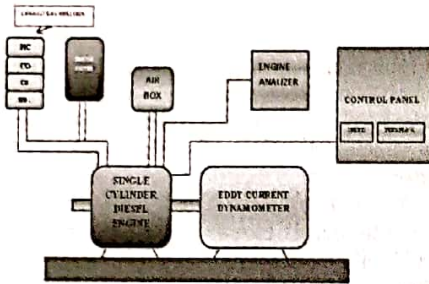


Figure.1.Schematic layout of experimental set-up

Table I - Specifications of Engine

Engine model	Kirloskar, AV1, Water cooled engine, Naturally aspirated engine
Rated Power	5hp @ 1500 rpm
Bore X Stroke	80mm X 110mm
Cubic capacity	0.553 lit (553 cu.cm)
Compression ratio	16.5 : 1
Fuel injection timing	23o btdc
Injection pressure	190 bar

Table II- Specification fuel injection parameters

Fuel	Specific gravity	LHV, MJ/kg
Petro-Diesel	0.832	42.9
B100	0.87	39.2

Table III- Typical Properties of methyl esters of jatropha oil petro-diesel

No. of holes and Diameter of each hole	Injection pressures, bar
NH1- 4, 0.32mm	190,210 and 230
NH2- 4, 0.29mm	190,210 and 230
NH3- 3, 0.28mm	190,210 and 230

Results and Discussion:

Performance Studies: Fig.2 illustrates the variation of BSFC with BP for different fuel injection pressure with petro-diesel as fuel, for the rated nozzle size and at rated injection timing. From the figure, BSFC values are observed to be lower for the fuel injection pressure 210 bar. This can be due to the fact that higher injection pressures would produce smaller droplets facilitating near complete combustion and hence the injection pressure of 210 bar was maintained in further studies. Fig.3 depicts the variation of BSFC with BP for different fuel injection nozzle hole sizes with petro-diesel as fuel. The results are in good agreement with the literature[8-11].

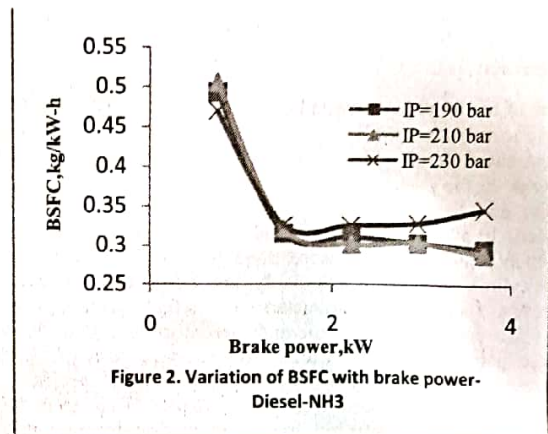


Figure 2. Variation of BSFC with brake power-Diesel-NH3

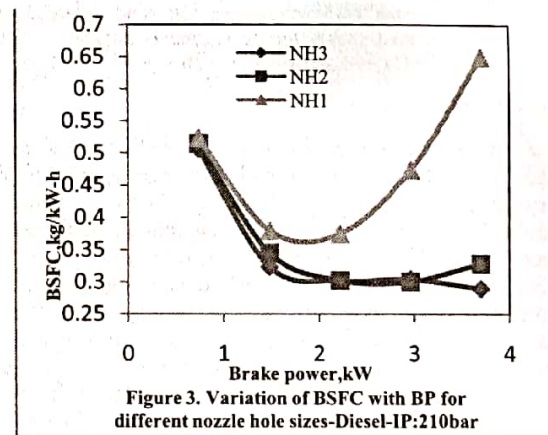


Figure 3. Variation of BSFC with BP for different nozzle hole sizes-Diesel-IP:210bar

can be seen that among these three nozzle hole sizes, the size is decreasing in the order of NH1, NH2 and NH3, i.e. larger diameter droplets are produced with NH1 and smaller with NH2 and NH3 respectively, with smallest being NH3. Therefore, it can be inferred at this stage that smaller nozzle hole with small droplet size and slightly higher injection pressures appeared to be better to allow thorough mixing of fuel and air to yield near complete combustion and thus resulting in lower BSFC values. The data of BSFC with BP

for IP:210 bar and NH3 is taken as baseline test data and used for comparison in further tests.

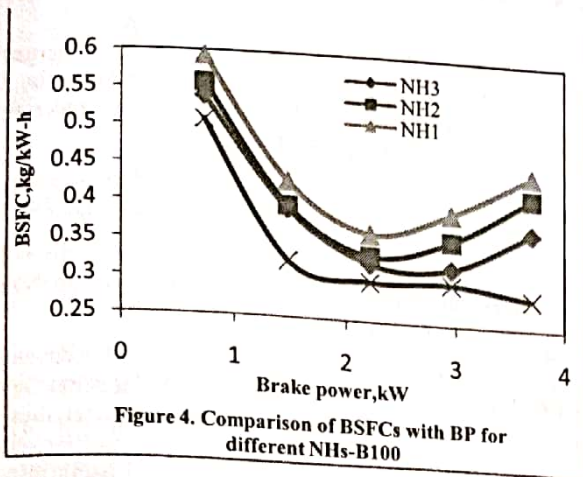


Figure 4. Comparison of BSFCs with BP for different NHs-B100

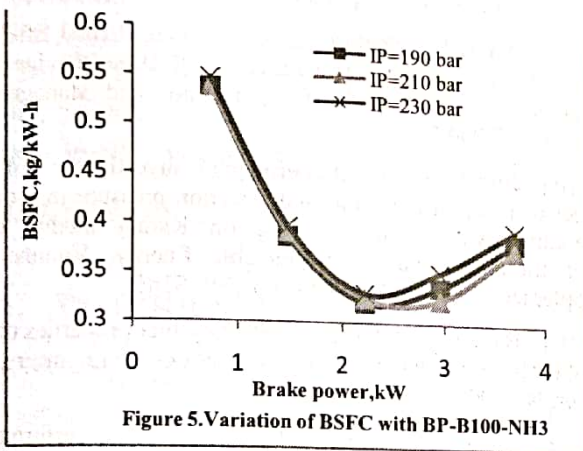


Figure 5. Variation of BSFC with BP-B100-NH3

Fig.4 illustrates the variation of BSFC with BP for an injection pressure of 210 bar and three different nozzle hole sizes. Since the viscosity of B100 is higher than petro-diesel, smaller nozzle size with the injection pressure has resulted in lower values of BSFC. The values are also compared with baseline results in the same figure. The baseline BSFC values are deviating far more in the 50-100% load range of the engine. This can be attributed to the higher viscosity and higher density of B100 compared to petro-diesel. It is interesting to note at this stage that 210 bar and NH3 are observed to be optimum fuel injection pressure and nozzle hole size even for B100 as these parameters resulted in lower BSFC values. The variation of BSFC with BP for optimized IP and nozzle size is shown in Fig.5.

Emission Studies:

The emissions of unburned hydrocarbons, oxides of nitrogen and smoke density are quantified and plotted for the optimized fuel injection pressure and three nozzle hole sizes.

Comparison of emissions for B100 and petro-diesel.

HC, NO_x and smoke emissions obtained under full load condition for optimized nozzle hole size and injection pressure are illustrated in Figure 6, 7 and 8 respectively. It can be noticed that except NO_x emissions are higher side where as HC and smoke density values are lower for neat biodiesel operation. This observation is in-line with the already established in the literature. The lower emissions of HC and smoke emissions are due to the near complete combustion of biodiesel fuel under the optimized conditions owing to presence of oxygen in the molecular structure of biodiesel.

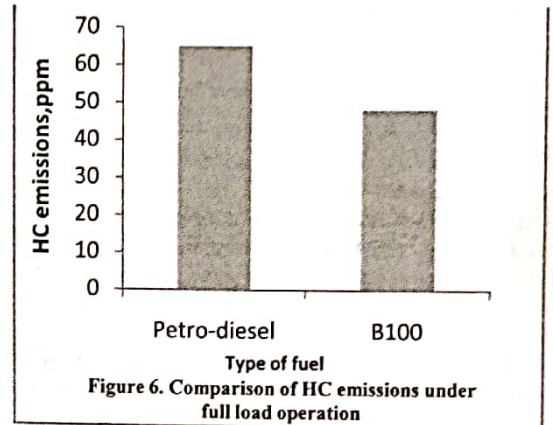


Figure 6. Comparison of HC emissions under full load operation

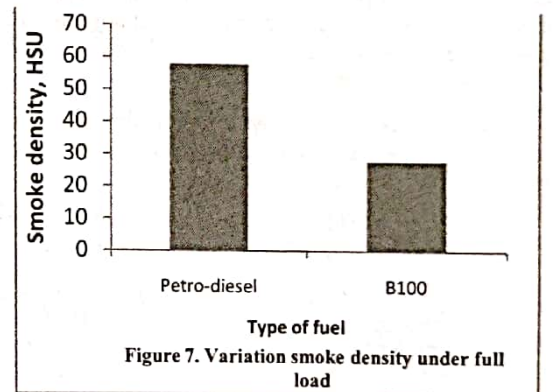
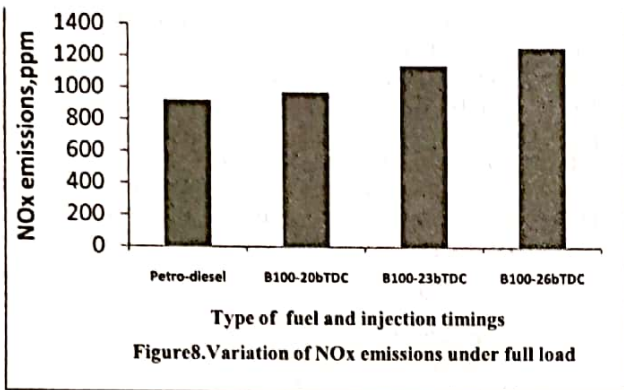


Figure 7. Variation smoke density under full load

Effect of fuel injection timing on NO_x emissions:

The biodiesel operation is advantageous with regards to complete combustion where as high reactive nature of biodiesel fuels leads to higher NO_x emissions. Many a studies have established that NO_x emissions could be significantly reduced when engines are operated with retarded fuel injection timings. The rated injection timing for the given engine configuration is 23°bTDC .To investigate the effect of fuel injection timing, timing was varied 3 degrees from the

rated injection timing i.e. 20° bTDC and 26° bTDC respectively. The effect is shown in Fig.8.



This can be reasoned out as that injection timing is retarded, fuel will be injected late in the compression stroke and hence fuel and air mixture would not get sufficient time for raising its pressures and temperatures to a high value and before overcoming its ignition delay, the expansion will begin. Thus the temperatures realized were low when compared to rated injection timing and at that temperature, dissociation reactions would not be that prominent to promote thermal prompt reactions for formation of NO_x emissions and hence low oxides of nitrogen were obtained. Where as in case of advanced injection timing, the fuel would be injected far ahead of the compression stroke giving much more conducive environment for mixing, releasing its energy and raising the in-cylinder temperature to very high levels and releasing higher NO_x emissions.

Conclusions: The following conclusions are drawn based on the experimental studies done on a CI with neat biodiesel obtained from jatropha curcas oil.

1. Better yield of methyl esters of jatropha oil is obtained with addition of higher amounts of ethanol.
2. Fuel injection pressure of 210 bar (against rated pressure of 190 bar) and 3-hole nozzle of each 0.28mm yielded lower BSFC values.
3. Retarded fuel injection timings are beneficial to reduce NO_x emissions.

REFERENCES

- [1] Agarwal, A. K., 2007, "Biofuels _Alcohols and Biodiesel_ Applications as Fuels for Internal Combustion Engines," Prof. Energy Combust. Sci., 33_3_, pp. 233-271.
- [2] Ali, Y., & Hanna, M. A. (1994). Alternative diesel fuels from vegetable oils. *Bioresource Technology*, 50(2), 153-163.
- [3] Heywood JB, *Internal Combustion Engine Fundamentals* McGraw Hill Co. 1988.

[4] Anjana Srivastava and Ram Prasad Triglycerides – based diesel fuels *Intl.Jrl.of Renewable and Sustainable Energy Reviews* vol.4 pp 111-133, 2000

[5] Kong, S.C., Prashanth, K. K., 2010. Experimental Study on Effects of Nozzle Hole Geometry on Achieving Low Diesel Engine Emissions *ASME Journal of Engineering for Gas Turbines and Power*, Vol. 132.

[6] Amish, P. V., Jaswant, L. V., Subrahmanyam N., 2010. A review on FAME production processes *Fuel* 89, 1-9.

[7] Hossain, A.K., Davies, P.A., 2010. Plant oils as fuels for compression ignition engines and life-cycle analysis: A technical review, *Renewable Energy*, 35, 1-13.

[8] Pandian, M., Sivapirakasam, S.P., Udayakumar, M., 2011. Investigation on the effect of injection system parameters on performance and emission characteristics of a twin cylinder compression ignition direct injection engine fuelled with pongamia biodiesel-diesel blend using response surface methodology *Applied Energy* 88, (8), 2663-2676.

[9] Amba Prasad Rao, G., Ram Mohan, P., 2003. Effect of Supercharging on the performance of DI Diesel engine with Cottonseed oil as fuel *Energy conversion and Management*, 44(6), 937-944.

[10] Jindal, S., 2011. Experimental investigation of the effect of compression ratio and injection pressure in a direct injection diesel engine running on Karanj methyl ester *International Journal of Sustainable Energy*, Volume 30, Supplement 1, December 2011, pp. S91-S105.

[11] Barabás and Todorut 2009. Key fuel properties of the biodiesel-diesel-ethanol *Society of Automotive Engineers*, AE paper, No:2009-01-1810.

[12] Ismet Sezer, 2011. Thermodynamic, performance and emission investigation of a diesel engine running on dimethyl ether and diethyl ether *International Journal of Thermal Sciences* 50, 1594-1603.

[13] Mário L. Randazzo, José R. Sodr , 2011. Exhaust emissions from a diesel powered vehicle fuelled by soybean biodiesel blends (B3-B20) with ethanol as an additive (B20E2-B20E5) *Fuel*, 90 (1), 2011, 98-103.

[14] Paula Berman, Shahar Nizri, Zeev Wiesman *Castor oil biodiesel and its blends as alternative fuel Biomass and Bioenergy*, Volume 35, Issue 7, 2011, Pages 2861-2866.

Different Techniques for Boundary Shear Stress Predictions for Open Channel Flow

B. Naik¹, P. Singh², K.K.Khatua³

1, 2 Ph. D & M.Tech Research Scholar, Department of Civil Engineering, National Institute of Technology Rourkela, India.

Email: banditanaik1982@gmail.com, prateek.k.singh1992@gmail.com

3 Associate Professor, Department of Civil Engineering, National Institute of Technology Rourkela, India. Email: kkkhatua@yahoo.com

Abstract. The fluid motion in a channel is having a direct relation to the boundary shear stress and therefore to define the fluid field and the velocity profile, knowledge of it is essentially required. Prediction and calculation of boundary shear force distributions in open channel flow are crucially required in many engineering problems such as channel design, calculation of energy losses and sedimentation. It is seen that the boundary shear stress distribution in various types of channel varies with the shape, type and patterns of the channel. In the case of the straight channel, boundary shear stress distribution varies with the different width-depth ratio, while the meandering channel boundary shear distribution varies with sinuosity, aspect ratio, and meandering. The compound channel is all the way different and boundary shear distribution is a combination of the floodplain and main channel (straight or meandering). It is thus very significant to study various methodologies adopted, identified, and used for accurate estimation of boundary shear stress distribution in various natural and artificial open channels. In the present work, critical appraisal of different approaches used for boundary shear stress distributions in channels is discussed. It has been found from the review that most common methods used by different researchers globally are Vertical Depth Method (VDM), Normal Depth Method (NDM) Guo and Julien Method (GJM), Ramana Prasad and Russell Manson Method (PMM), Knight et al. Method (KAM), Merged Perpendicular Method (MPM) and Yang and Lim Method (YLM) because these methods are simple, robust and easy to use for computing boundary shear distribution in open channels.

Keywords: open channel flow, Compound channel, boundary shear stress distribution

1 Introduction

The non-uniformity of boundary shear stress distribution over the wetted perimeter of a channel cross-section is widely proven, even for steady flows in straight prismatic channels with a simple cross-sectional geometry. This is mainly due to the anisotropy of the turbulence which produces transverse gradients of Reynolds stresses and secondary circulations (Gessner, 1973). Tominaga *et al.* (1989) and Knight and Demetriou (1983) showed that the boundary shear stress increases where the secondary currents flow towards the wall and decreases when they flow away from the wall. Other governing factors in the distribution of shear stress of a straight open channel are the geometry of the cross-section, longitudinal and lateral boundary roughness distributions and sediment concentration (Chlebek and Knight, 2006; Khodashenas *et al.*, 2008). Several direct and indirect measurement techniques for boundary shear stress are reported in the literature (Al-Hamid, 1991). The widely practiced indirect measurement technique is Preston's (1954) method which has been considered for the boundary shear stress measurements of the data sets used in this research. Due to the shortcomings, limitations and demerits of these measuring techniques, determining the actual shear stress distribution along the wetted perimeter is very difficult (Patel, 1965) and hence, various empirical, analytical and computational methods have been developed to predict the boundary Shear Stress (Khodashenas *et al.*, 2008).

2. STATE-OF-ART

Several decades ago, Leighly (1932) proposed that conformal mapping to be used to study the boundary shear stress distribution in open-channel flow. In the absence of secondary currents, he pointed out that, the boundary shear stress acting on the bed must be balanced by the downstream component of the weight of water contained within the boundary orthogonally.

Hydraulic radius separation Einstein (1942) method is still extensively used in laboratory studies and engineering practice.

Zheleznyakov (1965) was probably the first investigator, considering the interaction between the main channel and the adjoining floodplain

in his studies. He demonstrated the effect of momentum transfer mechanism, which was responsible for decreasing the overall rate of discharge for floodplain depths just above the bank-full level in his laboratory work while its significance is only in very small depths because as floodplain depth increased, the nature of flow does not behave in the same way as that earlier in small depths.

Ghosh and Roy (1970) presented the boundary shear distribution in rough as well as smooth open channels of trapezoidal and rectangular cross sections, by direct measurement of shear drag on an isolated length of the test channel using the technique of three point suspension system suggested by Bagnold.

Both Ghosh and Jena (1973) and Ghosh and Mehata (1974) reported studies on boundary shear distribution in straight two-stage channels for smooth and rough boundaries. They found that the distribution of shear is non-uniform and the location of maximum shear on the bed and side to be some distance from the centerline and free surface respectively.

Myers and Elswy (1975) studied the shear stress distribution in channels of complex sections and the effect of interaction mechanism. In comparison to the values under the isolated condition, the results showed a decrement of 22 percent in channel shear and increment up to 260 percent in floodplain shear. This possibly indicates regions of erosion and scour of the channel and flow distribution in alluvial compound sections.

Rajaratnam and Ahmadi (1979) under the smooth boundary condition studied the flow interaction between the straight main channel and symmetrical floodplain. The results demonstrated the transport of longitudinal momentum from the main channel to the floodplain. Due to flow interaction, a considerable increase in the bed shear in the floodplain near the junction with the main channel is seen whereas in the main channel it decreased. The effect of interaction reduced as the flow depth in the floodplain increased.

Knight (1981) proposed an empirically derived equation that presented the percentage of the shear force carried by the walls as a

function of the breadth/depth ratio and the ratio between the Nikuradse equivalent roughness sizes for the bed and the walls.

Wormleaton, Alen, and Hadjipanos (1982) used "divide channel" method for the assessment of discharge while undertook a series of laboratory tests in straight channels with symmetrical floodplains. From the measurement of boundary shear, apparent shear stress at the horizontal, vertical and diagonal interface plains originating from the main channel-floodplain junction could be evaluated. An apparent shear stress ratio was given which was a useful yardstick in selecting the best methodology of dividing the channel for discharge calculation.

Knight and Demetriou (1983) performed experiments in straight, symmetrical compound channels to investigate the discharge characteristics, boundary shear stress and boundary shear force distributions in the section. They came out with equations for calculating the percentage of shear force carried by floodplain and also the proportions of the total flow in various sub-areas of the compound section in terms of two dimensionless channel parameters.

Knight and Hamed (1984) worked in the same direction of that of Knight and Demetriou (1983) but considering rough floodplains. The floodplains were roughened progressively in six steps to study the influence of different roughness between the main channel and floodplain to the process of lateral momentum transfer. They presented, equations for the shear force percentages carried by floodplains and the apparent shear force in vertical, horizontal, diagonal, and bisector interface plains were given using four dimensionless channel parameters.

Knight and Patel (1985) stated some of the laboratory experiments results in relation to the distribution of boundary shear stresses in smooth closed ducts of a rectangular cross section for aspect ratios between 1 and 10. The distributions were shown to be impelled by the number and the shape of the secondary flow cells, which, in turn, rest upon the aspect ratio.

Knight, Yuan, and Fares (1992) gave details of the experimental data of SERC-FCF concerning boundary shear stress distributions in meandering channels all over the path of one complete wavelength. They also reported the experimental data on velocity vectors, surface topography, and turbulence for the two types of meandering channels of sinuosity 1.374 and 2.043 respectively. They inspected the effects of channel sinuosity, secondary currents, and cross section geometry on the value of boundary shear in meandering channels and gave a momentum force balance for the flow.

Knight and Sterling (2000) detected the distribution of boundary shear stress in a partially full circular conduit with and without a smooth, flat bed for a data ranging from $0.375 < F < 1.96$ and $6.5 \cdot 10^4 < R < 3.42 \cdot 10^5$, using Preston-tube technique. The distribution of boundary shear stress is shown to depend on Froude number and geometry.

Yang and McCorquodale (2004) came up with a method for computing three-dimensional Reynolds shear stresses and boundary shear stress distribution in smooth rectangular channels by considering an order of magnitude analysis to integrate the Reynolds equations. An abbreviated relationship between the lateral and vertical terms was hypothesized with which the Reynolds equations become solvable. This relationship was in the form of a power law with an exponent of $n = 1, 2, \text{ or infinity}$

Guo and Julien (2005) proposed a technique to define average bed and sidewall shear stresses in smooth rectangular open-channel flows after resolving the continuity and momentum equations. The analysis revealed that the shear stresses were functions of three components: (1) interfacial shear stress; (2) gravitational; and (3) secondary flows.

Khatua (2008) extended the work of Patra and Kar (2000) to meandering compound channels. Considering five parameters (sinuosity S_r , amplitude, relative depth, width ratio and aspect ratio), obtained general equations representing the total shear force percentage carried by floodplain. The proposed equations are simple, quite reliable and gave good results with the observed data for a straight compound

channel of Knight and Demetriou (1983) as well as for the meandering compound channel.

Lashkar and Fathi (2010) did experiments to determine the contribution of the wall shear force on total boundary shear force. A nonlinear regression-based technique was conducted to inspect the results and develop equations to determine the percentage of wall and bed shear force on the wetted perimeter of the rectangular channels.

Khatua (2010) stated the distribution of boundary shear force for highly meandering channels having distinctly different sinuosity and geometry. Based on the work, the interrelationship between the boundary shear, sinuosity, and geometry parameters has been revealed. The models are also proven using the well-published data of other investigators.

3. Categorization of Different Methodologies

3.1 Geometrical methods

Geometrical methods count on dividing the channel cross-section into sub-regions. The shear force along each of the segments of the boundary subdivided is found by balancing the forces against the weight of fluid in the corresponding sub-region. Leighly's (1932) method, Vertical depth Method (VDM), Einstein's (1942) method, Normal Area Method (NAM), Vertical Area Method (VAM), Merged Perpendicular Method (MPM) (Khodashenas and Paquier, 1999) and Normal Depth Method (NDM) (Lundgren and Johnson, 1964) are among the stated geometrical methods in literature.

3.2 Empirical methods

Empirical methods are generally simple regression technique developed from curve fitting to measured experimental data. Perhaps the very first model of such kind is Knight's (1981) model. His model was further developed by him and his colleagues (Knight *et al.*, 1984a & b and 1994), and other researchers (Flintham and Carling, 1988).

Pizzuto (1991) and Olivero *et al.* (1999) also suggested similar simple models for the boundary shear stress.

3.3 Analytical methods

Analytical methods are based on the law of continuity, momentum equations and energy transportation. Some of these methods lead to a geometric solution for solving the shear stress in open channels. Some of the analytical methods include the work of Yang and Lim (1997, 2005), Zheng and Jin (1998), Guo and Julien (2005) and Bilgil (2005).

3.4 Computational methods

Perhaps, more accurate way of finding the boundary shear stress distribution is by means of a turbulence closure model to elucidate the governing equations of motion. For instance, Christensen and Fredsoe (1998) used the Reynolds stress turbulence model (RSM) and De Cacqueray *et al.* (2009) used the SSG Reynolds stress turbulence model in computational fluid dynamics (CFD) software to predict the boundary shear stress in open channels for solving the equations of motion.

When examining sediment transport and the evolution of river morphology, it is essential to estimate the boundary shear stress distribution. However, accurate computation of the local shear stress is a challenging task even using sophisticated turbulence models. As an alternative, various empirical, analytical or simplified computational methods were developed. Most of them were focused on the computation of the local, the mean wall, and the mean bed shear stresses in straight and prismatic channels of rectangular, trapezoidal and circular with or without flatbed or compound cross-sections. In total, these methods rely on different assumptions, which may top to an approach dependent shear stress.

The aim of the particular research is to provide a quantitative assessment of various existing methods for the computation of the boundary shear stress in open channel flow. These seven methods were preferred because they provide a method, sufficiently general to

compute the boundary shear stress, and because they are simple enough for engineering application.

4. Review of Typical Methods

4.1 Vertical Depth Method (VDM)

This method adopts that the local shear stress τ_i on one wetted perimeter point i is proportional to the local water depth h_i as

$$\tau_i = \rho g h_i J \quad (1)$$

where ρ is the water density, g is the gravitational acceleration and J is the energy slope. The arbitrary cross-sectional shape can be considered for the application of the VDM, although the method ignores secondary currents and the transfer of momentum between the main channel and its floodplains. Furthermore, the roughness distribution along the wetted perimeter is presumed to be homogeneous.

4.2 Normal Depth Method (NDM)

Lundgren and Jonsson (1964) acclaimed that the concept of “vertical depth” is not applicable for the calculation of the boundary shear stress distribution for the steep side slope. They instead of the VDM used the Normal Depth Method (NDM) in which h_i of Eq. (1) is replaced by h_{Ni} , where h_{Ni} is the flow depth designated along the line normal to the wetted perimeter and the equation is

$$\tau_i = \rho g h_{Ni} J \quad (2)$$

The Fig.(1) (S. R. KHODASHENAS et. al., 2008) shows the Schematic illustrations of the VDM and NDM

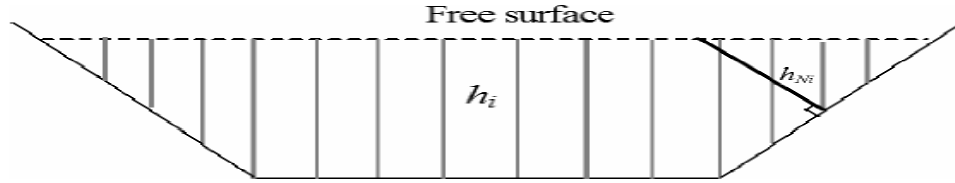


Fig. (1) Schematic illustrations of the VDM and NDM (S. R. KHODASHENAS et. al., 2008)

4.3 Merged perpendicular method (MPM)

Khodashenas and Paquier (1999) established a geometrical method to estimate the local shear stress in an irregular cross-section. This Merged Perpendicular Method (MPM) was derived from the Normal Area Method that depends on Einstein's (1942) hydraulic radius separation concept, which is "a cross-sectional region bounded by walls dividing into three sub-areas, corresponding to sidewalls and bed, respectively". The wetted area is divided into small sub-areas using the lines normal to the wetted perimeter according to the following procedure (Fig. 2) (El kadi Abderrezzak, 2006)

i. The wetted perimeter P is divided into small segments i of length P_i .

ii. Two perpendiculars L_{i-1} and L_i are drawn from the limits of each segment i . Lines L_{i-1} and L_i are considered of the order 1.

iii. When two adjacent perpendiculars cross at a common point, one single line of order 2 elongates them. This line is the bisector of the two perpendiculars. For example, the angle between the horizontal plane and $L_{i, i-1}$ which results from the intersection of L_{i-1} and L_i is

$\hat{L}_{i,i-1} = 1/2(\hat{L}_i + \hat{L}_{i-1})$ with " $\hat{}$ " as the angle between the horizontal plane and the line L_i .

iv. When two lines of order j and k respectively intersect at a mutual point, they are elongated by one single line of the order $j + k$. The angle between this line and the horizontal plane is achieved through the weighted mean of the angles between the previous lines and the horizontal plane. For example, the order of $L_{i,i-1,i+1}$ following from the intersection of $L_{i,i-1}$ (order 2) and L_{i+1} (order 1) is 3. The angle between $L_{i,i-1,i+1}$ and the horizontal plane is (Fig. 2)

$$\hat{L}_{i,i-1,i+1} = 1/3(2\hat{L}_{i,i-1} + \hat{L}_{i+1})$$

v. For each section i the local hydraulic radius $R_{hi} = S_i/P_i$ between the final lines is figured with S_i as the flow area. The local shear stress τ_i is then

$$\tau_i = \rho g R_{hi} J \quad (3)$$

The mean boundary stresses $\bar{\tau}_{(b)}$ and $\bar{\tau}_{(w)}$ representing respectively on the bed and the sidewall is defined by numerical integration of the local values.

The MPM delivers results of more practical and credible than the given by the Vertical Depth Method, the Normal Area Method and the Normal Depth Method, predominantly because the local shear stresses achieved in convex corners are higher than in concave corners, i.e. zones where the flow velocity is usually low (Khodashenas and Paquier, 1999). But this method disregards the transfer of momentum between the main channel and its floodplains and the secondary flow structures. Furthermore, the roughness distribution besides the wetted perimeter is not considered when the wetted area is divided into sub-areas.

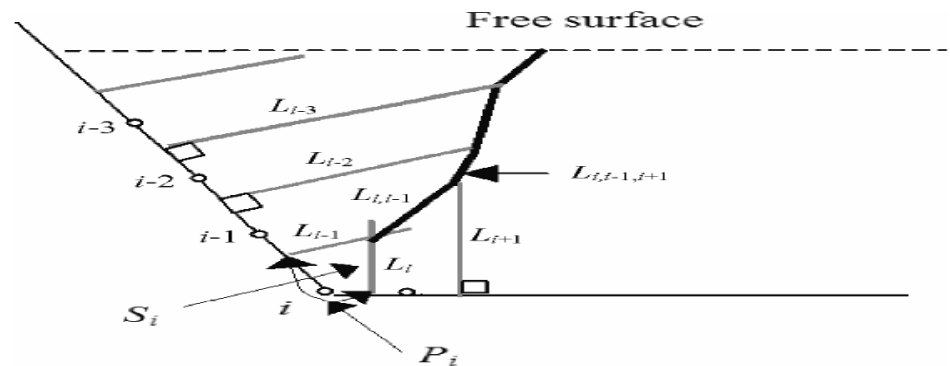


Fig.(2) Schematic illustrations of the areas determined by MPM (El kadi Abderrezzak, 2006)

4.4 Yang and Lim method (YLM)

4.4.1 General description of the method

Yang and Lim (1997, 2002, 2005) obtained an analytical method, which is akin to the MPM, to compute the distribution of shear stress in prismatic channels with a non-uniform boundary roughness. Their method is established on the concept of “surplus energy transport through a minimum relative distance toward the nearest boundary” in steady, uniform and fully developed turbulent flow. Yang and Lim described the relative distance as the ratio of the shortest geometric distance to the energy dissipation capability of the boundary. For a smooth boundary, the characteristic length representing the energy dissipation capability of the boundary is scaled using the viscous length scale ν/u^* , with ν as the kinematic fluid viscosity and u^* as the shear velocity. For a rough boundary, the characteristic length is scaled using the boundary roughness height. From this concept, Yang and Lim divided the flow area into sub-areas according to the cross-sectional shape and roughness composition of its wetted perimeter. Meanwhile, the secondary currents are not taken into account.

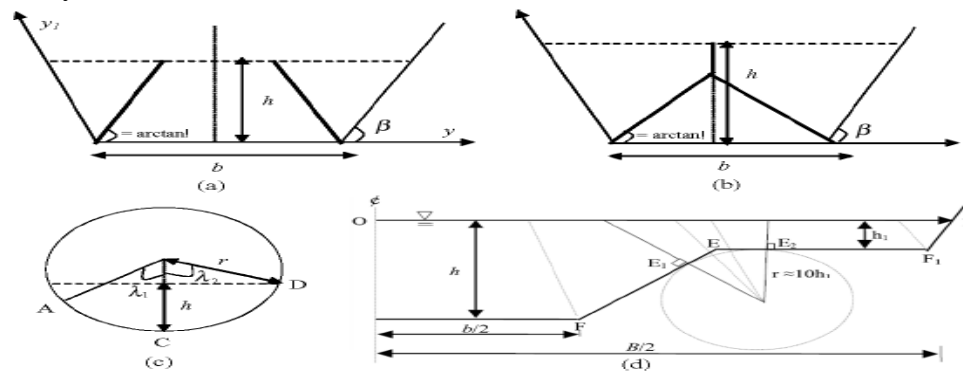


Fig.(3) Schematic cross-sections to which the YLM is applied
 (a)Trapezoidal shallow wide channel,(b) Trapezoidal deep narrow channel,(c) Circular conduit,(d) Compound channel
 (S. R. Khodashenas et. al., 2008)

4.4.2 Smooth trapezoidal channel

For wide channels, the intersection of division lines is located above the water surface (Fig. 3a) (S.R. Khodashenas et. al., 2008) if

$$\frac{b}{h} \geq 2 \frac{1 - \cos \beta}{\sin \beta} \quad (6)$$

where h is the flow depth, b is the channel bed width, β is the angle between the sidewall and water surface. The shear stress distributions $\tau_{(b)}$ and $\tau_{(w)}$ respectively, alongside the bed and the sidewall can be represented by (El kadi Abderrezzak, 2006)

$$\begin{aligned} \tau_{(b)}y &= \rho g \xi y J & 0 \leq y \leq \frac{h}{\xi} \\ \tau_{(b)}y &= \rho g h J & \frac{h}{\xi} \leq y \leq b - \frac{h}{\xi} \end{aligned} \quad (7)$$

$$\begin{aligned} \tau_{(b)}y &= \rho g \xi (b - y) J & b - \frac{h}{\xi} \leq y \leq b \\ \tau_{(w)}y_1 &= \rho g y_1 \frac{\psi \sin \beta}{1 - \psi \cos \beta} J & 0 \leq y_1 \leq \frac{\psi \cos \beta}{1 - \sin \beta} h \\ \tau_{(w)}y_1 &= \rho g \left(\frac{h}{\sin \beta} - y_1 \right) \tan \beta J & \frac{1 - \psi \cos \beta}{\sin \beta} h \leq y_1 \leq \frac{h}{\sin \beta} \end{aligned} \quad (8)$$

where y is the crosswise span-wise distance calculated from channel sidewall, y_1 is the distance alongside the sidewall measured from the channel corner. ξ is the slope of the dividing line and $A = u_{(b)}^*/u_{(w)}^*$ is the ratio of the sidewall energy dissipation capacity to the bottom energy dissipation capacity. These parameters are defined as

$$\begin{aligned} \xi &= \frac{\sin \beta}{\psi - \cos \beta} \\ \psi^3 + \frac{2h}{b \sin \beta} \psi - 2 \left(1 + \frac{h}{b} \frac{1}{\tan \beta} \right) &= 0 \end{aligned} \quad (9)$$

The mean boundary stresses $\bar{\tau}_{(b)}$ and $\bar{\tau}_{(w)}$ are given by (El kadi Abderrezzak, 2006)

$$\begin{aligned} \frac{\bar{\tau}_{(b)}}{\rho g h J} &= 1 + \frac{h}{b} \frac{1}{\tan \beta} - \psi \frac{h}{b} \frac{1}{\sin \beta} \\ \frac{\bar{\tau}_{(w)}}{\rho g h J} &= \frac{1}{2} \psi \end{aligned} \quad (10)$$

It is interesting to emphasize that the approach of Yang and Lim (Eq. (8)) is not valid if

$$1 - \psi \cos \beta \leq 0 \quad (11)$$

Then, the authors assumed that the boundary shear stress is uniform and given by $\rho g R_h J$. For narrow channels, the meeting point of division lines is located under the water surface (Fig. 3b) (S. R. Khodashenas et. al., 2008) if

$$\frac{b}{h} \leq 2 \frac{1 - \cos \beta}{\sin \beta} \quad (12)$$

The shear stress distributions $\tau_{(b)}$ and $\tau_{(w)}$, correspondingly along the bed and the sidewall are given by (El kadi Abderrezzak, 2006)

$$\begin{aligned} \tau_{(b)}(y) &= \rho g \xi y J \\ 0 &\leq y \leq \frac{b}{2} \\ \tau_{(b)}(y) &= \rho g \xi (b - y) J \quad \frac{b}{2} \leq y \leq b \end{aligned} \quad (13)$$

$$\begin{aligned} \tau_{(w)} y_1 &= \rho g y_1 \frac{\psi \sin \beta}{1 - \psi \cos \beta} J \\ 0 &\leq y_1 \leq \frac{1 - \psi \cos \beta}{\psi - \cos \beta} \frac{b}{2} \\ \tau_{(w)}(y_1) &= \rho g \left(\frac{b}{2 \sin \beta} + \frac{y_1}{\tan \beta} \right) J \\ \frac{1 - \psi \cos \beta}{\psi - \cos \beta} \frac{b}{2} &\leq y_1 \leq h \sin \beta - \frac{b}{2} \cos \beta \end{aligned} \quad (14)$$

$$\begin{aligned} \tau_{(w)} y_1 &= \rho g \left(\frac{h}{\sin \beta} - y_1 \right) \tan \beta J \\ h \sin \beta - \frac{b}{2} \cos \beta &\leq y_1 \leq \frac{h}{\sin \beta} \end{aligned}$$

The parameters ξ and ψ are defined as

$$\begin{aligned} \xi &= \frac{\sin \beta}{\psi - \cos \beta} \\ \left(\frac{1}{\psi} \right)^3 + \frac{b \sin \beta}{2h} \left[\frac{4h}{b \tan \beta} \left(1 + \frac{h}{b} \frac{1}{\tan \beta} \right) + 1 \right] \left(\frac{1}{\psi} \right) - 2 \left(1 + \frac{h}{b} \frac{1}{\tan \beta} \right) &= 0 \end{aligned} \quad (15)$$

The mean boundary stresses $\bar{\tau}_{(b)}$ and $\bar{\tau}_{(w)}$ are given by (El kadi Abderrezzak, 2006)

$$\begin{aligned} \frac{\bar{\tau}_{(b)}}{\rho g h J} &= c \xi \\ \frac{\bar{\tau}_{(w)}}{\rho g h J} &= \frac{b}{4h \psi^2} \xi \end{aligned} \quad (16)$$

As for the case of shallow-deep channels, the YLM is not valid if

$$(1 - \psi \cos \beta) \leq 0 \quad \text{or} \quad \frac{2h}{b} \leq \frac{1}{\tan \beta} \quad (17)$$

and the authors presumed again that the boundary shear stress is uniform and equal to $\rho g R_h J$

4.4.3 Rough trapezoidal channel

For channels of homogeneous and rough trapezoidal cross section, the mean, local bed and mean sidewall stresses are obtained using the Eqs (6)–(17) with $\psi = 1$, for the reason that the partition lines are the bisectors of the internal base angles of the trapezoidal channel.

4.4.4 Circular channel with homogeneous boundary roughness

The boundary shear stress distribution in circular conduits of homogeneous boundary roughness and flowing partially full ($h/r < 1$) is

$$\tau(A) = \left(\frac{2\lambda_2}{2\lambda_2 - \sin 2\lambda_2} \right) \left[1 - \left(1 - \frac{h}{2} \right)^2 \left(\frac{1}{\cos^2 \lambda_1} \right) \right] \rho g R_h J \quad (18)$$

where $\tau(A)$ is the local boundary shear stress at an angle λ_1 from the normal line OC (Fig. 3c) (S. R. Khodashenas et. al., 2008), λ_1 is the angle between the radius OA and the normal line OC, λ_2 is the angle between the radius drawn to the water surface OD and the normal line OC, r is the conduit radius.

4.4.5 Compound channel

On the base of YLM, Yang *et al.* (2004) projected a method to calculate the local boundary shear stress at the edge E of a floodplain profile shown in Fig. 3(d) (S. R. Khodashenas et. al., 2008). A circle with an experimental radius of $10h_1$ and tangential to (FE) and (F1E) is drawn, with h_1 as flow depth in the floodplain. The energy in the element bounded by two relative lines (OE1) and (OE2) and the free surface is expected to be dissipated at point E. The local boundary shear stress at E was defined using the wetted perimeter E1EE2 and area of this element. The floodplain and main channel are considered separately as a trapezoidal channel, and equations (6)–(17) can be used

to calculate the boundary shear stress distribution. This technique gives a realistic incessant distribution of boundary shear stress from point E to F and from point F1 to E. Though the transformation of momentum between the main channel and its floodplain is ignored.

4.5 Guo and Julien method (GJM)

The mean bed and sidewall shear stresses in the smooth rectangular open channel were defined by Guo and Julien (2005) by solving the momentum and continuity equations. As a first approximation, they determined the average bed and sidewall shear stresses by utilizing conformal mapping, after ignoring secondary currents and by supposing a constant eddy viscosity (Eq. (19)). In a second approximation, they added two lumped empirical correction factors for the effects of secondary currents, variable eddy viscosity and other possible effects (Eq. (20)). The mean bed shear stress is given by

Without Secondary Currents

$$\frac{\bar{\tau}(b)}{\rho g h J} = \frac{4}{\pi^2} \frac{b}{h} \sum_{n=1}^{\infty} (-1)^n \frac{t^{2n-1} - 1}{(2n-1)^2} \quad \text{with } t = e^{-\frac{\pi h}{b}} \quad (19)$$

With Corrections Factors

$$\frac{\bar{\tau}(b)}{\rho g h J} = \frac{4}{\pi} \text{Arctg}[\exp\left(\frac{-\pi h}{b}\right) J] + \frac{\pi h}{4 b} \left(\frac{-h}{b}\right) \quad (20)$$

The mean sidewall shear stress can be calculated by

$$\frac{\bar{\tau}(w)}{\rho g h J} = \frac{b}{2h} \left(1 - \frac{\bar{\tau}(b)}{\rho g h J}\right) \quad (21)$$

4.6 Ramana Prasad and Russell Manson method (PMM)

Ramana Prasad and Russell Manson (2002) suggested an analytical expression for calculating the percentage shear force % SF_w taken by the sidewall in prismatic channels of the trapezoidal cross section with homogeneous boundary roughness. The influence of secondary currents was neglected. The percentage shear force % SF_w is given in the expression of width-depth ratio b/h by

$$\%SF_w = \frac{100\bar{\tau}_{(w)}}{\bar{\tau}_{(w)} + \bar{\tau}_{(b)} \left(\frac{P(b)}{P(w)} \right)} = \begin{cases} 25 \left(4 - \frac{b}{h} \right) \frac{b}{h} & \frac{b}{h} \leq 2 \\ \frac{100}{\frac{b}{h}} & \frac{b}{h} \geq 2 \end{cases} \quad (22)$$

where $P(b)$ and $P(w)$ are bed and sidewalls wetted perimeter, respectively. Knowing $\%SF_w$, it is possible to obtain $\bar{\tau}_{(b)}$ and $\bar{\tau}_{(w)}$ via the equations

$$\frac{\bar{\tau}_{(b)}}{\rho ghJ} = (1 - 0.01\%SF_w) \left(1 + \frac{P(w)}{P(b)} \right) \quad (23)$$

$$\frac{\bar{\tau}_{(w)}}{\rho ghJ} = (1 - 0.01\%SF_w) \left(1 + \frac{P(b)}{P(w)} \right) \quad (24)$$

4.7 Knight *et al.* method (KAM)

Knight *et al.* (1994) offered an empirical equation for calculating the percentage shear force $\%SF_w$ taken by the sidewall in prismatic channels of the trapezoidal or rectangular cross-section with homogeneous boundary roughness. It was improved on the basis of a huge range of experimental data involving both subcritical ($F < 1$) and supercritical ($F > 1$) flows in straight channels of rectangular and trapezoidal cross-section, in which $F = u/(gS/b)^{1/2}$ is the Froude number, u the flow velocity, b the surface width and S the cross-sectional area. Later, Knight and Sterling (2000) explored experimentally the distribution of the boundary shear stress in smooth circular conduits, with or without a flatbed, flowing partially full and established that the percentage shear force carried by the walls is predominantly well reproduced for $P(b)/P(w) > 1$ (Knight and Sterling, 2000) by

$$\%SF_w = C_{cf} \exp \left[-3.23 \log_{10} \left(\frac{P(b)}{P(w)C_2} + 1 \right) + 4.6052 \right] \quad (25)$$

For $F < 1$: $C_2 = 1.50$, $C_{cf} = 1$ for $P(b)/P(w) < 6.546$, $C_{cf} = 0.5875(P(b)/P(w))^{0.28471}$ for $P(b)/P(w) \geq 6.546$, and

For $F > 1$: $C_2 = 1.38$, $C_{cf} = 1$ for $P(b)/P(w) < 4.374$, $C_{cf} = 0.6603(P(b)/P(w)) + 0.28125$ for $P(b)/P(w) \geq 4.374$.

5. CONCLUSIONS

This analysis report provides a comparison of different existing methods for computing the boundary shear stress distribution in prismatic channels of simple cross-sectional shape, including the rectangular, circular, and trapezoidal with and without flatbed and compound sections, and uniform boundary roughness. Six techniques were picked and tested: Vertical Depth Method (VDM), Merged Perpendicular Method (MPM), Yang and Lim Method (YLM), Guo and Julien Method (GJM), Ramana Prasad and Russell Manson Method (PMM), and the Knight *et al.* Method (KAM). The methods are defined and results are contrasted with laboratory data in terms of the mean bed and mean sidewall shear stresses (or the percentage of the total shear force acting on the sidewalls), and the difference of local shear stress versus perimetric distance.

The experimental database suggests that the local boundary shear stresses and the mean bed and sidewall shear stresses are considerably impelled by the boundary roughness, the cross-sectional shape as well as the presence of secondary flows. The extensively used VDM does not offer reliable results in terms of the local shear stress distribution. The GJM with variable eddy viscosity, Correction factors for secondary currents effects and other likely effects is obtained to give the best prediction of the mean bed and the mean wall shear stresses in smooth rectangular channels. This result verifies the compulsion to take into consideration the consequence of secondary currents. The PMM and KAM could be a good predictor of the wall and the mean bed shear stresses, respectively, in rough rectangular cross-section, and in circular cross-section with a flatbed. MPM and YLM provide the complete predictions of the local shear stress for the trapezoidal, rectangular and circular cross-sections. These two methods yield comparable results, but the MPM has the advantage to be also acclimated to irregular cross-sectional shape. Even for compound cross-sections, MPM and YLM afford a suitable estimation of the local shear stress, except near corners, at the edge of the cross-section and around the main channel-floodplain interface region. These local

inconsistencies are directly related to the fact that MPM and YLM do not include the lateral flow exchange between the floodplain and the main channel that initiates secondary cells in the floodplain as well as in the main channel.

In terms of application, the technique presented are helpful engineering tools and easy to implement in numerical models. There are enormous practical problems even considering flows in flumes of the trapezoidal or compound cross-section for which it is essential to recognize the boundary shear stress distribution. The methods may be straightaway extended to arbitrary cross-sectional shape with a non-uniform roughness distribution.

An overall validation of the technique presented earlier would involve further measurements of the boundary shear stress distribution in smooth, intermediate and rough channels of varying cross-sectional shapes. A wide experimental measurement is accessible at www.flowdata.bham.ac.uk, which could be utilized to complete the comparison of the selected methods. The database is from the University of Birmingham and summarizes over 600 complete sets of boundary shear stress and velocity data for different boundary roughness distribution, flow conditions and geometry.

6. ACKNOWLEDGEMENT

The support from the Institute and the Research project by the second authors for carrying out the research work in the Hydraulics laboratory at National Institute of Technology, Rourkela is thankfully acknowledged.

7. NOTATIONS

b = Channel width of bed

B = Channel width of floodplain bed

C_{cf} = Constant of Eq. (25)

C_2 = Constant of Eq. (25)

F = Froude number

g = Gravitational acceleration

h = Flow depth

h_N = Flow depth calculated along the line normal to the wetted perimeter

h_1 = Flow depth in floodplain

J = Energy slope

L = Line normal to the bottom

\hat{L} = Angle between horizontal plane and line L

P = Total wetted perimeter

$P(b)$ = Wetted perimeter corresponding to bed

$P(w)$ = Wetted perimeter corresponding to the sidewalls

Pd = Dimensionless perimetric distance = s/P

Q = Discharge

r = Conduit radius

Rh = Hydraulic radius = S/P

S = Flow area

u^* = Shear velocity

y = Transverse span-wise distance measured from channel sidewall

y_1 = Distance along the sidewall measured from the channel corner

β = Angle between sidewall and water surface

λ_1 = Angle between radius OA and normal line OC

λ_2 = Angle between radius drawn to the water surface OD and the normal line OC

ν = Kinematic viscosity

ζ = Coefficient

ρ = Density of water

τ =Local boundary shear stress

$\tau^* = \tau/(\rho g R h J)$ non-dimensionalized shear stress

$\tau(b)$ =Local bed shear stress

$\tau(w)$ =Local sidewall shear stress

$\bar{\tau}(b)$ =Mean bed shear stress

$\bar{\tau}(w)$ =Mean sidewall shear stress

ψ =Coefficient

% SF_w =Percentage of total shear force acting on the walls

8. REFERENCES:

Al-Hamid, A.A.I. (1991). Boundary shear stress and velocity distributions in differentially roughened trapezoidal open channels. *PhD thesis, The University of Birmingham, Birmingham, UK.*

Bilgil, A. (2005). Correlation and distribution of shear stress for turbulent flow in a smooth rectangular open channel. *Journal of Hydraulic Research, IAHR*, 43 (2), 165-173.

Chlebek, J. and Knight, D.W. (2006). A new perspective on sidewall correction procedures, based on SKM modelling. *Proceedings of the International Conference on Fluvial Hydraulics (River Flow 2006)*. [Eds. Ferreira, R.M.L., Alves, E.C.T.L., Leal, J.G.A.B. & Cardoso, A.H.], Lisbon, Portugal, 1, 135-144.

Christensen, B. and Fredsoe, J. (1998). Bed shear stress distribution in straight channels with arbitrary cross section. *Lyngby, Denmark, Institute of Hydrodynamics and Hydraulic Engineering, Technical University of Denmark*, 77.

De Caceray, N., Hargreaves, D.M. and Morvan, H.P. (2009). A computational study of shear stress in smooth rectangular channels. *Journal of Hydraulic Research, IAHR*, 47 (1), 50- 57.

Einstein, H.A. (1942). Formulas for transportation of bed load. *Transactions of the American Society of Civil Engineers, ASCE*, 68 (8, Part 2), 561-577.

El Kadi Abderrezzak, K. (2006). Evolution d'un lit de rivière en fonction des apports (Evolution of the riverbed due to flow and sediment transport). *PhD Thesis, University of Claude Bernard, Lyon [in French]*.

Flintham, T.P. and Carling, P.A. (1988). Prediction of mean bed and wall boundary shear in uniform and compositely rough channels. *Proceedings of the International Conference on River Regime*, Oxon, UK, 267-286.

Gessner, F.B. (1973). The origin of secondary flow in turbulent flow along a corner. *Journal of Fluid Mechanics*, Cambridge University Press, 58 (1), 1-25.

Ghosh, S.N., Mehta, P.J. (1974). Boundary shear distribution in compound channel with varying roughness distribution. *Proc. Inst. Civ. Engng.* 57, 159–164.

Ghosh, S.N., Roy, N. (1970). Boundary shear distribution in open channel flow. *J. Hydraul. Div., ASCE* 96(4), 967–994.

Guo, J., Julien, P.Y. (2005). Shear stress in smooth rectangular open-channel flows. *J. Hydraul. Engng.* 131(1), 30–37.

Khatua, K.K and Patra, K.C,(2010). Evaluation of boundary shear distribution in a meandering channel. *Proceedings of ninth International Conference on Hydro-Science and Engineering, IIT Madras, Chennai, India, ICHE 2010, 74.*

Khatua, K.K. (2008). Interaction of flow and estimation of discharge in two stage meandering compound channels. *Ph.D. thesis, NIT, Rourkela, India.*

Khodashenas, S.R., El Kadi, A.K. and Paquier, A. (2008). Boundary shear stress in open channel flow: A comparison among six methods. *Journal of Hydraulic Research, IAHR*, 46 (5), 598-609.

Khodashenas, S.R. and Paquier, A. (1999). Geometrical method for computing the distribution of boundary shear stress across irregular straight open channels. *Journal of Hydraulic Research, IAHR*, 37 (3), 381-388.

Knight, D.W. (1981). Boundary shear in smooth and rough channels. *J. Hydraul. Div., ASCE* 107(7), 839–851.

Knight, D.W. and Demetriou, J.D. (1983). Flood plain and main channel flow interaction. *Journal of Hydraulic Engineering, ASCE*, 109 (8), 1073-1092.

Knight, D.W., Demetriou, J.D. and Hamed, M.E. (1984a). Boundary shear in smooth rectangular channels. *Journal of Hydraulic Engineering, ASCE*, 110 (4), 405-422.

Knight, D.W., Demetriou, J.D. and Hamed, M.E. (1984b). Stage discharge relationships for compound channels, in *Channels and Control Structures Proceedings of the 1st International Conference on Hydraulic Design in Water Resources Engineering: Channels and Channel Control Structures*. [Ed. Smith, K.V.H.], Southampton, 4.15-14.36.

Knight, Donald W., Y. M. Yuan, and Y. R. Fares (1992). Boundary shear in meandering channels. *Proc. Inst. Symp. Hydraulic research in nature and laboratory, Wuhan, China Paper*. No. 11017. 1992.

Knight, D.W. and Patel, H.S. (1985). Boundary shear in smooth rectangular ducts. *Journal of Hydraulic Engineering*, ASCE, 111 (1), 29-47.

Knight, D.W., Sterling, M. (2000). Boundary shear in circular pipes running partially full. *J. Hydraul. Engng.* 126(4), 263–275.

Lashkar-Ara, Babak et al (2010). Boundary shear stresses in smooth channels. *J. Food, Agric. & Environ* 8: 132-136.

Leighly, John Barger (1932). Toward a theory of the morphologic significance of turbulence in the flow of water in streams. Vol. 6. No. 1-9. University of California Press.

Lundgren, H. and Jonsson, I.G. (1964). Shear and velocity distribution in shallow channels. *Journal of the Hydraulics Division*, ASCE, 90 (1), 1-21.

Myers, R. C., & Elsayy, E. M. (1975). Boundary Shear in Channel with Flood Plain. *Journal of the Hydraulics Division*, 101(ASCE 11452 Proceeding).

Myers, W.R.C. (1978). Momentum transfer in a compound channel. *J. Hydraul. Res.* 16(2), 139–150.

Olivero, M., Aguirre-Pey, J. and Moncada, A. (1999). Shear stress distribution in rectangular channels. *Proceeding of XXVIII IAHR Congress*, Graz, Austria, papers on CD-ROM, pp.6.

Patel, V.C. (1965) Calibration of the Preston tube and limitations on its use in pressure gradients. *Journal of Fluid Mechanics*, Cambridge University Press, 23, 185-208.

Patra, K. and Kar, S. (2000). Flow Interaction of Meandering River with Floodplains. *J. Hydraul. Eng.*, 126(8), 593–604.

Pizzuto, J.E. (1991). A numerical model for calculating the distributions of velocity and boundary shear stress across irregular straight open channels. *Water Resources Research*, 27 (9), 2457-2466.

Preston, J.H. (1954). The Determination of Turbulent Skin Friction by Means of Pitot Tubes. *Journal of the Royal Aeronautical Society*, 58, 109-121.

Rajaratnam, N., & Ahmadi, R. M. (1979). Interaction between Main Channel and Flood-Plain Flows. *Journal of the Hydraulics Division*, 105(5), 573-588.

Ramana Prasad, B.V., Russell Manson, J. (2002). Discussion of a geometrical method for computing the distribution of boundary shear stress across irregular straight open channels. *J. Hydraul. Res.* 40(4), 537–539.

Wormleaton, P. R., Allen, J., & Hadjipanous, P. (1982). Discharge Assessment In Compound Channel Flow. *Journal Of The Hydraulics Division*, 108(9), 975-994

Tominaga, A., Nezu, I., Ezaki, K., Nakagawa, H. (1989). Three dimensional turbulent structure in straight open channel flows. *J. Hydraul. Res.* 27(11), 149–173.

Yang, S.Q., Lim, S.Y. (1997). Mechanism of energy transportation and turbulent flow in a 3d channel. *J. Hydraul. Engng.* 123(8), 684–692.

Yang, S.Q., Lim, S.Y. (2005). Boundary shear stress distributions in trapezoidal channels. *J. Hydraul. Res.* 43(1), 98–102.

Yang, S.Q., Yu, J.X., Wang, Y.Z. (2004). Estimation of diffusion coefficients, lateral shear stress, and velocity in open channels with complex geometry. *Water Resour. Res.*, AGU 40(5), W05202.

Zheng, Y. and Jin, Y.C. (1998). Boundary shear in rectangular ducts and channels. *Journal of Hydraulic Engineering*, ASCE, 124 (1), 86-89.



This is to certify that

Dr./Mr./Ms. E. Shailaja

has Presented / Participated in **International Conference on**

Paradigms in Engineering & Technology (ICPET 2016)

Organized by Methodist College of Engineering & Technology, Hyderabad, India,

on 2nd & 3rd March, 2016.

Manuscript Title A study on nature - Inspired Metaheuristic
Algorithms.


Conference Chair

Optimization technique of digital FIR filter coefficients using Genetic algorithm

¹ Sravan Kumar Talusani , ²Srikanth Immareddy ³Suresh.D

¹ *Electronics and Communication Engineering Dept, Methodist College of Engineering and Technology, Hyderabad 500001, India.*

² *Electronics and Communication Engineering Dept, Methodist College of Engineering and Technology, Hyderabad 500001, India.*

³ *Electronics and Communication Engineering Dept, Methodist College of Engineering and Technology, Hyderabad 500001, India*

Abstract— This research work has been proposed a method to design FIR filter with the optimized filter coefficients using Genetic Algorithm (GA) concept. Generally FIR filters are non recursive filters since the error of FIR filter is non linear. The coefficient is been represented by using Canonical Signed Digit (CSD) format. The CSD format representation is been chosen to reduce the hardware complexity and cost. The aim of this research is to select a best coefficient for the filter design and the wordlength reduction in the coefficient, so that the desirable magnitude response is been met with the hardware complexity. The obtained Genetic Algorithm (GA) results are compared with windowing technique's results. The implementation is done using MATLAB.

Index Terms— Canonical Signed Digit (CSD), Equiripple algorithm, Genetic Algorithm(GA), optimization.

I. INTRODUCTION

In this paper, FIR filters would be favored on account of their features like stability & linear phase. A FIR's usage noise characteristics are easy to model & because of its all zero structure, it has a linear phase response. However for administering this, one must pay those value in the form of vast number of multipliers, due to this vast number for multipliers the speed of the processor will be reduced, thereby expanding the equipment cosset additionally. [1]. To beat this, the coefficients are represented in CSD format. This design need no multipliers so, hardware complexity may be decreased and cosset may be also lessened What's more additionally is high speed requirements are satisfied.

CSD format diminishes the multiplier operation to shift and add operations. Similarly as the multiplier is reduced to a minimum shift and add operations, the hardware complexity is also reduced, thereby reducing the hardware cost and automatically speed will be increased [1]. Therefore, in this paper we utilize CSD format to represent the coefficients. Along with the reduction of hardware complexity & hardware cost, filter coefficients optimization is a critical task. In this paper, for the optimization, a method was proposed, first of all the initial set of coefficients which are given as input to genetic algorithm are optimized filter coefficients obtained from equiripple algorithm because compared to coefficients obtained from windows technique equiripple algorithm results are more optimum according to the results obtained. Equiripple algorithm is used because equiripple outputs and genetic algorithm outputs are practically same if hardware cost & complexity are not taken into

consideration [2] that is where genetic algorithm is needed.

Idea behind the suggested technique is to optimize the filter coefficients simultaneously and also the hardware cost & complexity are taken consideration at the same time guaranteeing high speeds.

II. WINDOW METHOD

The simplest design of FIR filters is attained utilizing the windowing technique. In this technique, the design starts with an ideal desired frequency response which is given by [2]

$$H_d(e^{j\omega}) = \sum_{n=-\infty}^{\infty} h_d(n) e^{-j\omega n} \quad \text{----- (1)}$$

$$h_w(n) = h_d(n) w(n) \quad \text{----- (2)}$$

Where $h_d(n)$ is the impulse response of the filter

$w[n]$ is the window function

$h_w(n)$ is the windowed impulse response

As a result, the frequency response of the windowed impulse response is the periodic convolution of the desired frequency response with the Fourier transform of the window and which is given by

$$H_w(e^{j\omega}) = \frac{1}{2\pi} \int_{-\pi}^{\pi} H_d(e^{-j\theta}) D(e^{j(\omega-\theta)}) d\theta \quad \text{----- (3)}$$

The frequency response of the approximation filter will be given by

$$H_d(e^{j\omega}) = e^{-j\omega n_d} H_w(e^{j\omega}) \quad \text{----- (4)}$$

where n_d will be the essential time delay to present causality in the approximated filter. The filter designed by windowing technique will have greatest error on either side of the discontinuity of the ideal frequency response [2]. The length of the estimated filter (N) should be as short as possible. Furthermore, the windowing technique doesn't tolerate singular control over the close estimation errors in various bands. Preferred filters result from minimization of maximum error in both, the stop band and the pass band of the filter which leads to equiripple filters[2].

III. EQUIRIPPLE ALGORITHM

Equiripple algorithm is also known as Park.Mc.Clellan's algorithm. It is used to optimize the filter coefficients as it provides the optimum result when the hardware cost & complexity are not taken into consideration. In this algorithm the design of linear phase FIR filter is predicated on the min-max error paradigm i.e., minimizing the maximum error possible [2], which there by produces the optimum result. The method implemented is an iterative numerical algorithm. It converges very rapidly to the optimal solution. This method is very robust and is broadly utilized because of the optimum results (in spite of hardware complexity). In equiripple algorithm N (filter length) w_p , w_s , and the ratio $\delta p/\delta s$ are fixed and it is considered as most popular

approach because of its flexibility and computational efficiency [2].

The weighted error function is given by

$$E(w) = (A(w) - D(w)) \quad (5)$$

Where N= filter length

A(w)= desired(real valued) amplitude function

D(w)= non negative weighting function

FIR filter's amplitude response can be formulated as

$$A(w) = \sum_{n=0}^N a(n) \cos(nw) \quad (6)$$

$$D(w) = \begin{cases} 1, & 0 < w < w_0 \text{ (passband)} \\ 0, & w_0 < w < \prod \text{ (stopband)} \end{cases}$$

$$W(w) = \begin{cases} kp, & 0 \leq w \leq wp \\ 0, & wp \leq w \leq ws \\ ks, & ws \leq w \leq \pi \end{cases}$$

Where $0 < w_p < w_0 < w_s < \prod$
Maximum error

$$\|E(w)\|_{\infty} = \max_{w \in (0, \pi)} |W(w)(A(w) - D(w))| \quad (7)$$

The solution to this quandary is called best weighted approximation to D(w), similarly as it provides the optimum result and it also minimizes the maximum value of error (min max solution)[4].

So, for computing this solution alteration theorem is used. Alteration theorem states that, |E(w)| attains its maximum value at a minimum of M+2 points & the weighted error function alternates sign on at least M+2 of those points[4].

Let us say,

$$R = M + 2$$

Where, R is a reference set

$$E(w_i) = c(-1)^i \|E(w)\|_{\infty} \quad (8)$$

From eqn. (2), we can write the above equation as

$$W(w_i)(A(w_i) - D(w_i)) = (-1)^i \delta \quad (9)$$

$$A(w_i) - D(w_i) = (-1)^i \delta / W(w_i) \quad (10)$$

The above equation represents interpolation problem, which can be represented in the matrix form as

$$\begin{bmatrix} 1 & \cos w_1 & \dots & \cos M w_1 & 1/W(w_1) \\ 1 & \cos w_2 & \dots & \cos M w_2 & -1/W(w_2) \\ \vdots & \vdots & \ddots & \vdots & \vdots \\ 1 & \cos w_R & \dots & \cos M w_R & -(-1)^R/W(w_R) \end{bmatrix} \begin{bmatrix} a(0) \\ a(1) \\ \vdots \\ \delta \end{bmatrix} = \begin{bmatrix} D(w_1) \\ D(w_2) \\ \vdots \\ D(w_R) \end{bmatrix}$$

There will be an unique solution to this linear system of equations, that solution is taken as optimal minmax solution[4]. This utilization takes excessive amount of computer time and memory, so it is not very useful [3] & we cannot guarantee convergence in equiripple algorithm where as in genetic algorithm convergence is guaranteed.

Algorithm steps are

1. Interpolation can be repeated by taking new set of R points.

2. Updating the reference (R) set till the desired optimized result is met.

Those acquired equiripple coefficients are converted into Canonical Signed Digit (CSD) format. CSD format is used to represent the binary numbers. In this format, binary numbers are encoded in such a way that word has fewest number of non zero digits. This technique maps a tenary system to a binary system [5].

Properties of CSD are:

1. No two consecutive bits in the encoded bit are non zeros.
2. The encoded word should contain a minimum number of non-zero digits.

For example, to represent 23 in CSD, csdigit(23) returns +0-00-. Where cs digit is a in-built function in MATLAB. CSD contains 33% fewer non-zero bits than 2's complement digits [5].

IV. GENETIC ALGORITHM

Offspring can be produced in more number by the organisms and the offspring produced can be similar to the parent organisms but some offspring can have similarities that none of the parent organism have due to mutations (random changes) and some characteristics are inherited through reproduction from parent organisms. The characteristics it has inherited through mutations and reproduction helps it to survive [6] or not to survive while undergoing through natural changes in the environment. To understand this adaptive process of nature and to apply it so that it'll be desensitized to changes, John Holland (1970) developed algorithm called Genetic Algorithm (GA). It is a heuristic algorithm and it finds the optimal results by decreasing the value of objective function continuously. It provides both efficient & effective techniques for optimization. The major hindrance in the conventional application of GA is about the premature convergence, Whether those body of evidence happens. GA produces a sub-optimal result In there, may be no outside 'strength' or 'instruction' which lead GA out of local optima[7] which is dealt in this method by iterating over population many times and simultaneously iterating different regions of population.

Basic steps of GA are:

A. Population

Encode each bit as a gene and a string of genes are called as chromosome and set of chromosomes is called population. First step to start with is to initialize the population i.e., is called as initial population.

B. Evaluation

Each chromosome has to be assessed and to be assigned a value called fitness value, larger the fitness value, (that says i.e., a good gene) probability will be more

to select it for reproduction. Fitness is the measure of goodness of a chromosome.

C. Selection

The individual chromosomes which have best fitness values are selected and proceeded for next step called reproduction where blending of the both guardians would be carried to process new offspring's [8]. Two regularly utilized

methods are 'roulette wheel' & 'tournament' selection Over roulette wheel, every individual will be allocated a sector (slice) size proportional to their fitness evaluated The wheel is then spun and the individual inverse to the marker turns into a standout amongst those as parents[2].In this paper roulette wheel selection is used.

D. Reproduction

Two chromosomes which are selected based on the fitness value [9] from the population undergo a process called reproduction to produce offspring's. Parents who have better fitness values have superior possibilities to be selected for production of finer offsprings.

E. Crossover

Choosing a random point and Splitting the parents at this crossover point and Creating children by trading their tails is called crossover process. Crossover probability is typically in the range (0.6, 0.9) [10]. Fig .1 describes the crossover process. It can be classified as

- Simple Crossover: The Process we discussed above is a simple crossover process[2].
- Arithmetic Crossover: It is a process where two complimentary linear combinations of the parents were produced [2].
- Heuristic Crossover: It gets profit from fitness information with furthermore extrapolation of the two individuals to enhance the offspring [2].

In this paper, simple crossover was used.

E.Mutation

Mutations are random changes done to a chromosome in order to get a good fitness value as shown in Fig. 2. Mutations are random changes which reintroduces the genetic diversity into the population [9].

Mutation can also be classified as

- Uniform mutation
- Non uniform mutation
- Multi-non uniform mutation

In this paper, non uniform method is used where one variable (gene in a chromosome) is selected randomly and its equivalent is set to a non uniform random number.

Then afterward finishing every last one of above steps, if the desired criteria are met by the coefficients, then it will stop, otherwise the process will be continued along with the new generated off springs as a population until the required specifications met.

V. DESIGN PROCEDURE

Here, the aim is to design a FIR filter with desired frequency, magnitude response, and to optimize the filter coefficients this can be achieved by the following methods of proposed technique.

A. Window method

- On deciding the specifications of the filter that has to be kept constant for equiripple & genetic algorithms
- Design a filter using any window let's say hamming window
- Calculate the magnitude response & filter coefficients for particular filter length (in the paper $N=23$).

B. Implementation of equiripple algorithm

- We have to decide the filter specifications and length.
- After deciding the length, w_p (pass band edge frequency) & w_s (stop band edge frequency), the main idea of equiripple algorithm starts with taking reference set as explain in section II before.
- The magnitude response of the filter designed is compared with the desired magnitude response and error $E(\omega)$ is calculated.
- If error is more i.e. magnitude response of filter observed are not coinciding with the desired magnitude response then a new reference set will be taken.
- Again, the step repeats until error function is less than smallest number defined as SN in the program(i.e. taken $SN=1e-8$)
- If it is less than SN i.e. $\max(\text{err}) < SN$, then result is displayed as converged.

C. CSD conversion

- The filter coefficients thus obtained are converted into CSD format.
- They are converted into CSD format by using the MATLAB built-in function (csdigit)

$[a,p,n] = \text{csdigit}(\text{num}, \text{range}, \text{resolution})$

Where; a is the CSD digit

p is the positive part

n is the negative part

num = input number (decimal)

range = maximum digits to the left of the decimal point

resolution = digits to the right of decimal point for example,

$\text{csdigit}(.25,2,2)$ represents xx.xx binary

$\text{csdigit}(.25,0,4)$ represents .xxxx binary

D. Genetic algorithm

- The first step in genetic algorithm is to define the objective

Function

$$f = \max(\text{err})$$

$$\text{err} = W(\omega)(A(\omega) - D(\omega)) \quad (12)$$

- The coefficients obtained in equiripple method is taken as initial population

- Then, we have to calculate fitness value for each individual in the population.
- Fitness value is calculated by the fitness function given below

$$ff = \frac{1}{f} + k(\text{SONZ}) \quad (13)$$

Where, f is the objective function defined at the starting of the algorithm

$$k=0.02$$

SONZ=sum of non zeros in CSD digit.

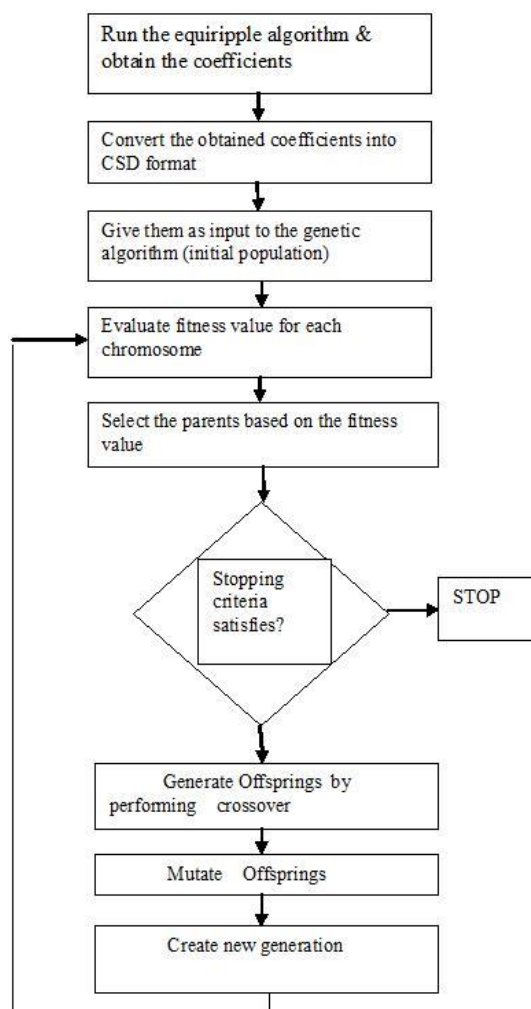
- Two individuals (parents) who have fitness value more are selected for reproduction to produce off springs.

Eg: P1 00+00-
P2 0+0000
O1 00+00
O2 0+00-

where P1, P2 are parents & O1, O2 are offsprings.

- After crossover, the next step is mutations (random changes of variables), so that it can produce better fitness value.
- If this population gives the desired frequency response with optimized filter coefficients, stop the algorithm otherwise include the offspring & create a new generation & repeat all the steps as mentioned above.

Fig1 . Shows the typical flow of the proposed algorithm



VI RESULTS

Coefficients	Values
1,19	$2^{-9}+2^{-8}+2^{-14}$
2,18	$2^{-8}+2^{-7}+2^{-15}$
3,17	$2^{-7}+2^{-6}+2^{-13}$
4,16	$2^{-8}+2^{-7}$
5,15	$2^{-4}+2^{-5}+2^{-10}$
6,14	$2^{-8}+2^{-7}+2^{-12}$
7,13	$2^{-7}+2^{-14}$
8,12	$2^{-2}+2^{-4}+2^{-7}+2^{-9}$
9,11	$2^{-2}+2^{-4}+2^{-6}+2^{-8}+2^{-10}$
10	$2^{-1}+2^{-3}+2^{-5}+2^{-7}+2^{-10}$

TABLE I. FILTER COEFFICIENTS USING WINDOWING

Coefficients	Values
1,19	$2^{-9}+2^{-8}$
2,18	0
3,17	$2^{-7}+2^{-6}+2^{-9}$
4,16	0
5,15	0
6,14	0
7,13	$2^{-7}+2^{-9}$
8,12	2^{-2}
9,11	0
10	2^{-4}

TABLE II. FILTER COEFFICIENTS USING EQUIRIPPLE ALGORITHM

Coefficients	Values
1,23	2^{-9}
2,22	0
3,21	$2^{-7}+2^{-6}$
4,20	0
5,19	0
6,18	0
7,17	2^{-7}
8,16	2^{-2}
9,15	0
10,14	0
11,13	$2^{-7}+2^{-9}$
12	2^{-4}

TABLE III. FILTER COEFFICIENTS USING GENETIC ALGORITHM

The TABLE I shows the filter coefficients of FIR filter designed using windowing technique. TABLE II. shows the filter coefficients of FIR filter designed according to the equiripple algorithm. TABLE III. Shows the filter coefficients of FIR filter designed based on the genetic algorithm concept. On comparison of TABLE I, TABLE II & TABLE III it can be observed that non zero digits are reduced in coefficients obtained from genetic algorithm than in

the equiripple algorithm coefficients or coefficients obtained in windowing technique. That proves the reduction in hardware complexity.

Fig 2. Magnitude Response obtained by windowing technique

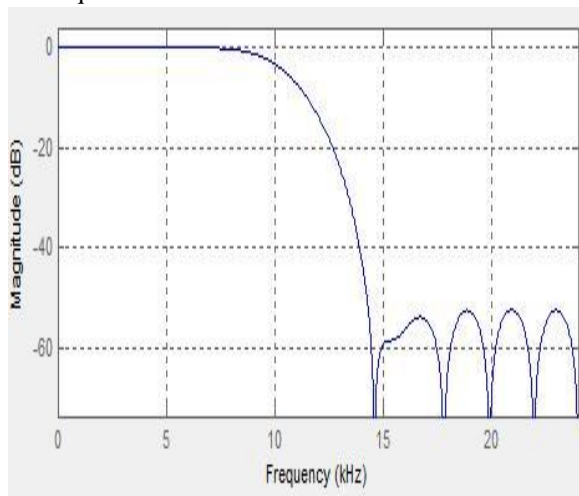


Fig 3. Magnitude response obtained by equiripple algorithm

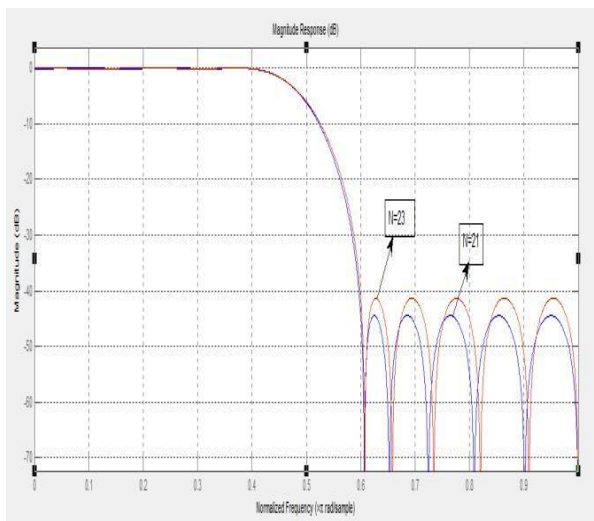
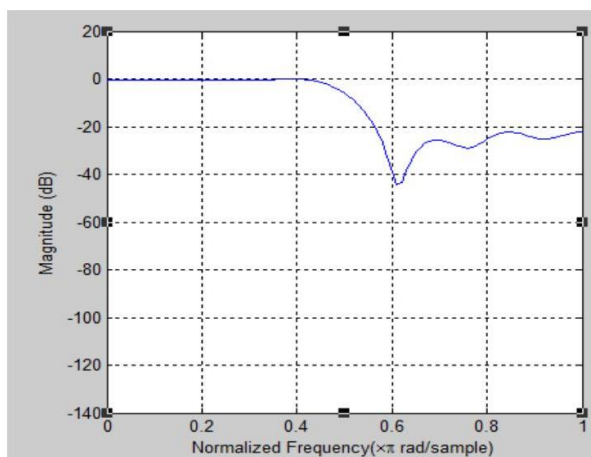


Fig 4. Magnitude response obtained by genetic algorithm



The response shown in Fig 2. indicates the magnitude response of the FIR filter designed by windowing (hamming) method. It can be observed that the response has some fluctuations and pass band is not completely flat. The response shown in Fig 3. indicates the magnitude response of the FIR filter designed by equiripple method. It can be observed that the response is not purely flat in pass band and the Fig. 2. represents the magnitude response of filter designed according to genetic algorithm, in this it is obvious that the error has minimized to complete zero in the pass band i.e., the pass band is totally flat in Fig2. That means the error is completely minimized to zero in the pass band i.e., a flat response for pass band is a desired characteristic.

Using MATLAB software to design a FIR filter by window method, an FIR filter with 23 coefficients and of word length 15 satisfies the given specifications

The same filter to be designed using equiripple algorithm it will cost 19 coefficients and word length 11.

If such a filter is designed using proposed method (GA) an FIR filter with 23 coefficients and word length 8 satisfies the given specifications.

It can be observed that GA has minimum word length so minimum hardware complexity and a desired frequency response. So it can be concluded that of all the three methods GA is the most optimum method.

VII. CONCLUSION

The proposed method required the optimum number of filter coefficients to obtain the desired frequency response with minimum word length. This method results in hardware reduction and cost as compared with windowing method and equiripple methods.

VIII. FUTURE SCOPE

By giving obtained genetic algorithm coefficients as a input to another genetic algorithm procedure to improve the frequency response characteristics of filter.

REFERENCES

- [1] A. R. Rezaee, "Using genetic algorithms for designing of fir digital filters," *ICTACT journal on soft computing*, july 2010, Issue: 01, pp.18-22.
- [2] Jehad I.Ababneh, Mohammad H. Bataineh , "Linear phase FIR filter design using particle swarm optimization and genetic algorithms", *Elsevier*, vol. 18 Issue:4.
- [3] P. Janardhan, M. N. Neelakantan, "A fast perturbation method for the design of linear phase fir digital filters of finite wordlength using single frequency filters," *springer journal on circuit systems and signal processing*, vol. 10, Issue 2, pp. 233-244.
- [4] I.Selesnick, "The Remez Algorithm".
- [5] A. Rajolia, M. Kaur, "Finite impulse response (fir) filter design using canonical signed digits (csd)," *International Journal of science and research (IJSR)*, india online issn: 2319-7064.

- [6] R. Singh, S. K. Arya, " Genetic algorithm for the design of optimal iir digital filters," *Journal of Signal and Information Processing*, 2012, Issue: 3, pp. 286-292.
- [7] Ling Cen,"A hybrid genetic algorithm for the design of FIR filters with SPoT coefficients",Elsevier vol.87,, Issue:3.
- [8] P. Kaur, S. Kaur, "Optimization of fir filters design using gentic algorithm," IJETTCS, Issue :3, Vol. 1.
- [9] S.T.Tzeng, "Genetic algorithm approach for designing 2-D FIR digital filters with 2-D symmetric properties," Elsevier, vol. 84, Issue: 10.
- [10] S. Aggarwal, A. Gagneja, A. panghal, "Design of fir filter using ga and its comparison with hamming window and parks mclellan optimization techniques," IJARCSSE, vol. 2, Issue: 7.
- [11] A. N. Kani, "Digital signal processing", second edition.
- [12] A. Lee, M. Ahmadi, G.A. Jullien, W.C. Miller, R.S.Lashkari," Digital filter design using genetic algorithm", in:Proceedings of IEEE Symposium on Advances in Digital Filtering and Signal Processing,June 1998.
- [13] E. Hostetter, A.V. Oppenheim, J. Siegel, On optimum nonrecursive digital filters, in: Proc. 9th Allerton Conf. Circuit System Theory, October 1971.
- [14]T.W. Parks, J.H. McClellan, Chebyshev approximation for nonrecursive digital filters with linear phase, IEEE Trans. Circuit Theory CT-19(1972) 189–194.
- [15] T.W. Parks, J.H. McClellan, A program for the design of linear phase finite impulse response filters, IEEE Trans. Audio Electroacoust. AU-20 (3) (1972) 195–199.
- [16] J.H. McClellan, T.W. Parks, A unified approach to the design of optimum FIR linear phase digital filters, IEEE Trans. Circuit Theory CT-20(1973) 697–701.
- [17] J.H. McClellan, T.W. Parks, L.R. Rabiner, A computer program for designing optimum FIR linear phase digital filters, IEEE Trans. Audio Electroacoust. AU-21 (1973) 506–526.
- [18] A.V.Oppenheim, R.W. Schafer, J.R. Buck, Discrete-Time Signal Processing, Prentice Hall, Englewood Cliffs, NJ, 1999.
- [19] J.H. Holland, Adaptation in Natural and Artificial systems,MIT Press, 1975.
- [20] Mitra, Digital Signal Processing: A Computer-Based Approach, McGraw-Hill, 2001.
- [21] K.F. Man, K.S. Tang, S. Kwong, Genetic Algorithms:Concepts and Designs, Springer, London, 1999.
- [22] M. Srinivas, L.M. Patnaik, Genetic algorithms: a survey,Computer 27(6) (June 1994) 17–26.



SRAVANKUMAR TALUSANI Received the Bachelor degree in Electronics and Communication Engineering (ECE) from Osmania University, India and Master degree in Digital Systems & Computer Electronics from JNTU Ananthapur, India.

He is working as Assistant Professor in ECE Dept at Methodist College of Engineering and Technology, India. His major interests are in the fields of Analog Electronics and Signal Processing.



SRIKANTH IMMAREDDY Received the Bachelor degree in Electronics and Communication Engineering (ECE) from the JNTU Hyderabad India and Master degree in Digital Systems from Osmania University, India in 2009.

He is working as Assistant Professor in ECE Dept at Methodist College of Engineering and Technology, India. His main interests are in the fields of Very Large Scale Integration and Digital Signal Processing.



SURESH.D Received the Bachelor degree in Electronics and Communication Engineering (ECE) from JNTU, India and Master degree in VLSI from KAKATIYA UNIVERSITY, India.

He is working as Assistant Professor in ECE Dept at Methodist College of Engineering and Technology, India. His major interests are in the fields of VLSI.

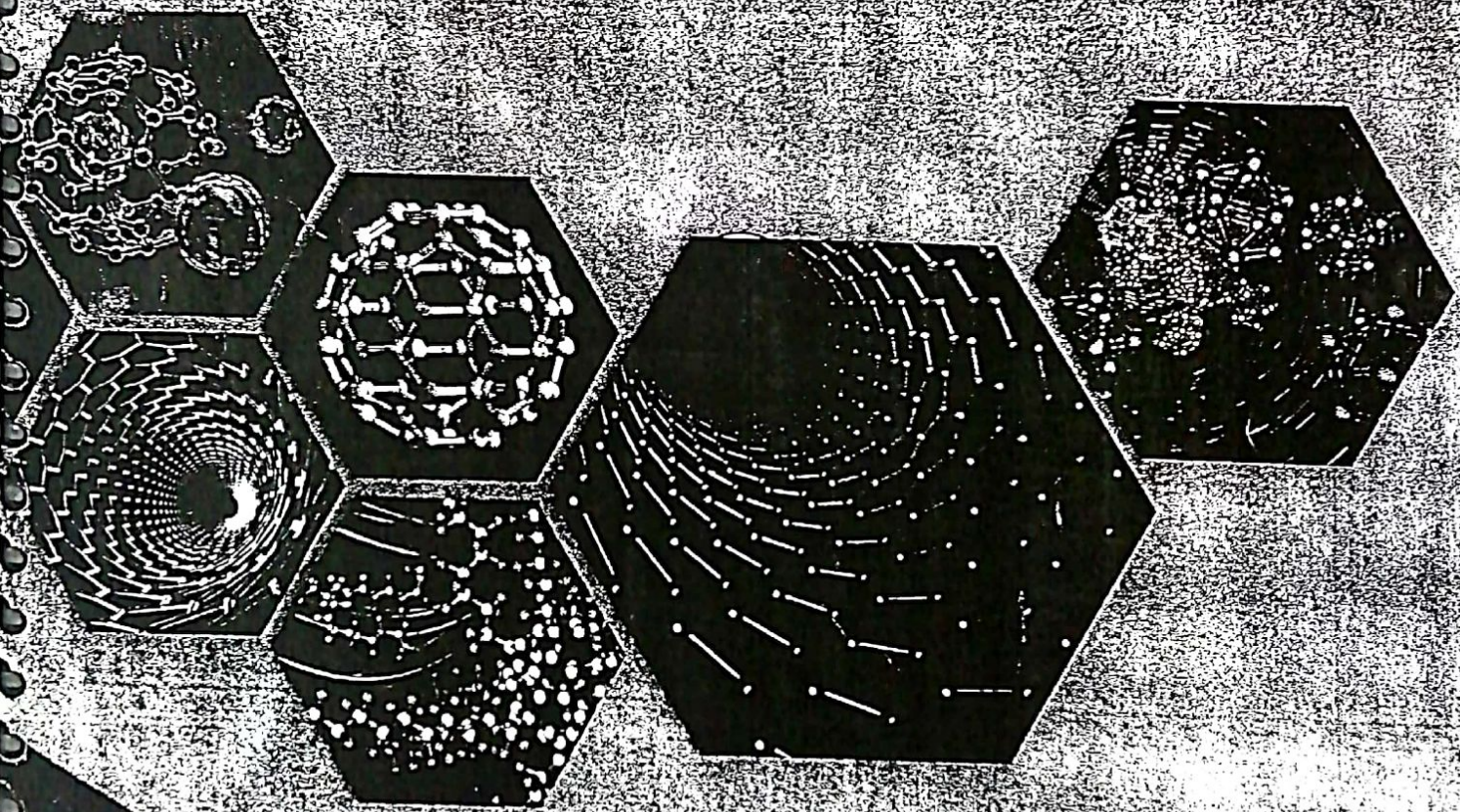


ISBN : 978-93-5258-222-8



PROCEEDINGS OF THE **Dr. A.V.K**
NATIONAL CONFERENCE
on
"RECENT ADVANCES
IN APPLIED NANO MATERIALS"

4-5 March, 2016



Department of Physics
UNIVERSITY COLLEGE OF SCIENCE, SAIFABAD
Osmania University, Masab Tank,

Editors
Dr. V. Nathaniel
Dr. Guntha Aravind
Dr. B. Ramaiah
Dr. Ch. Venkateshwarlu

Electrical Studies In Silver Doped Gallium Oxide Glasses

K. Veerabhadra Rao, C. Anuradha, G. Aravind
*Department of Physics, Methodist College of Engineering & Technology,
Hyderabad*

ABSTRACT: The glasses of composition $x\text{AgI}-(100-x)[0.02\text{Ga}_2\text{O}_3-0.49\text{Ag}_2\text{O}-0.49\text{B}_2\text{O}_3]$ where $x=5$ to 30 in steps of 5 weight% are prepared by melt quenching technique. XRD, FTIR and DSC investigations are carried out on all glasses to understand physical characteristics of the prepared glasses. Electrical characterization is done in terms of DC and AC conductivities. DC conductivity at room temperature increased from 10^{-4} to 10^{-2} Scm^{-1} with increasing concentration of AgI. DC activation energy (E_{dc}) is found to decrease from 0.36 to 0.19 eV with increasing concentration of AgI. From the Impedance spectroscopy real and imaginary parts of impedances (Z' , Z'') plots plotted, and by using Z-View equivalent software R-C circuit parameters are obtained from Cole-Cole plots and relaxation times also calculated. The quantitative analysis of these results indicates that the electrical conductivity of these glasses is enhanced by addition of AgI.

Keywords: Electrical properties, oxide; Ga_2O_3 , Ag_2O , XRD

1. Introduction

Portable electronic devices, omnipresent nowadays, requires small-size power sources which should be more efficient, durable, reliable and safer for the environment than those available now. To meet growing and urgent needs for such power sources it is vital to carry out the research on many prospective ideas: miniaturized fuel cells, rechargeable microbatteries, etc. One of specific tasks in this research is the development of solid electrolytes (polycrystalline, amorphous or composite) for rechargeable silver microbatteries [1,2]. Though the ionic conductivity of many silver glasses, especially those with high contents of AgI, can be suitable for battery applications at moderate temperatures, some disadvantages of those glasses such as, e.g. their brittleness or low thermal stability threshold, limit the prospects of their practical use. One of possible solutions to circumvent the drawbacks of glassy electrolytes is to produce composites based on these glasses. There have been already explored several interesting approaches to prepare composites based on AgI and

4 Stroke Engine with 2 Power Strokes

Md.Fakhruddin H.N.
Methodist College of
Engineering & Tech.
+919963584450
mfhnn@yahoo.com

Dr. Mohammed Yousuf Ali
Nawab Shah Alam Khan
College of Engg. & Tech.
+919866301410
yousufonline@yahoo.com

A.P.V.PrasadRao
Methodist College of
Engineering & Tech.
+918686008603
prasadraoapv@gmail.com

Abstract

In today's automobile world it is a great desirable challenge to build an engine having more power generation & less fuel consumption, which are desired parameters for the increased efficiency of the engine. For getting more power engine needs more fuel and if less fuel consumption is needed the power transmitted will be less. In conventional engines the heat energy using is 30% of produced energy and the remaining energy nearly 70% is going as waste. That means, to get more power from engine the fuel resources are wasting by wasting the 70% of produced energy, if less fuel consumption rate is desirable the more power generation should be sacrificed.

Present innovation namely 4 stroke engine with 2power strokes is introduced in order to overcome these problem, the piston will execute 2nd power stroke without using gasoline fuel. By the introduction of this engine it is more beneficial to the automobile industry because of its more power generation & reduced fuel consumption rates.

1. Introduction

In the 2 stroke engine the piston makes 2 strokes in cylinder per cycle & the crank shaft makes one complete revolution. Advantage of 2 stroke engine is that the piston executes one power stroke per every 2 strokes of piston & one revolution of crankshaft and Disadvantage is, it consumes more fuel to develop one power stroke in a cycle where as in 4 stroke engine piston makes 4 strokes in cylinder per cycle and crank shaft makes 2 complete revolutions. Advantage of 4 stroke engine is that it consumes less fuel to develop one power stroke in a cycle and the disadvantage of 4 stroke engine is that the power generated by the engine is comparatively low. In the six stroke engine also fuel consumption is less but power generation is less compared to 2 stroke engine.

The present innovation "4 stroke engines with 2 power strokes" overcomes the disadvantages of both 2 stroke and 4 stroke engines. In this engine after 2strokes of the 2stroke engine, hot water is injected into cylinder and by utilizing the high temperatures present in the engine cylinder water changes its phase to steam and it will expand in the cylinder results in another power stroke.

According to the experimental results 1ml of water will be converted to 1800 ml of steam when it changes its phase. So that the quantity of water required is also less. This engine captures the heat energy wasting in case of conventional engine. In this engine a water tube will be placed in such a way that it will be in contact with engine cylinder walls and the other side of water tube will be in contact with an another pipe through which hot exhaust gasses are passing. The water in the water pipe or jacket will capture the heat emitting from engine without releasing it to the environment as waste and on other hand the water also captures the heat from the hot gasses escaping from engine cylinder as exhaust.

2. Advantages of this Engine

1. This engine thermal losses are decreased and thermal efficiency may increased by 40-55%
 2. And as the water is using as working fluid for second power stroke, the quantity of fuel require is reduced by 50-60%, resulting the 50-55% increase in the mechanical efficiency
 3. Also the need of cooling system is eliminated which further results in reduction in weight of engine by 10%.
 4. The environment pollution (by the emission of hot gasses into atmosphere) may be reduced by 45-55%.
 5. Two power strokes
- Two parallel functions take place, inside and outside the engine cylinder

3. Events outside engine cylinder

1. Intake of water
2. Heating of water by means of heat exerted by the engine cylinder walls.
3. Heating of water again exhaust emission of fuels
4. Transferring the heated water into engine cylinder

4. Events inside the engine cylinder

Inside the engine cylinder again two functions takes place on both sides of the engine

1. Intake of hot water & power stroke by fuel
2. Compression and transfer of hot water & Exhaust of combustion products

3. Power stroke by steam & intake of fresh charge (Fuel+air)
4. Compression and transfer of charge & Exhaust of steam

5. Principle of 4str. Engine with 2 power str.

The 4 stroke engine with 2power strokes captures the heat waste from the 2 stroke engine and utilizes it to produce an additional power stroke of piston. Either steam or Air can be used as working fluid for second power stroke .It is not only giving an additional power stroke but also eliminates the need of a cooling system and makes engine lighter by 5-10 % & also increases the efficiency of the engine by 45-50 % . In this engine piston moves up and down 4 times out of which 2 are power strokes, one by fuel and other by steam. After the exhaust stroke in 2 stroke engine, instead of air fuel mixture hot water (which is converted to steam)will enter from water inlet & is exhausted in 4th stroke. So that, overlapping of ports is reduced & better scavenging is obtained. Because of this action fuel consumption is reduced by 50% - 60 % & huge reduction in the pollution. The variety of fuels can be used to run the engine.

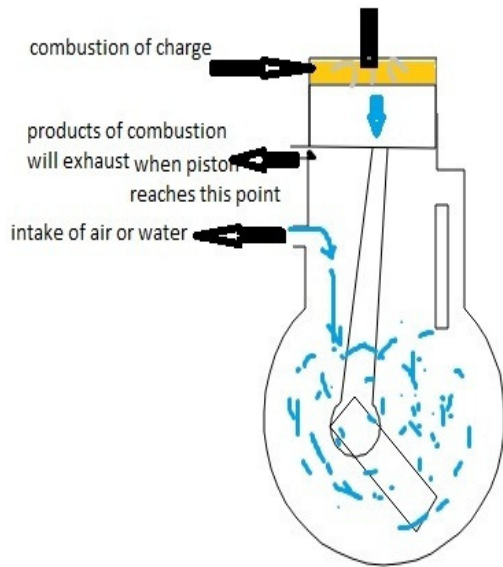


Figure 1. Working of 4stroke with 2 power stroke

6. Modifications in 4 Stroke Engine with 2

Power Strokes

Some modifications are to be done to the specific parts of the 2 stroke engine so as to run the engine successfully. The modifications are:-

1. A water jacket is to be placed around the engine cylinder walls to capture the heat from combustion chamber.
2. A pipe arrangement should be done around the water jacket to heat the water.

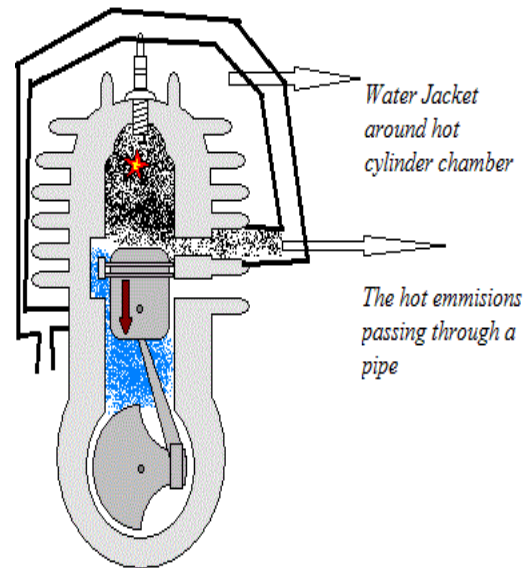


Figure 2. Water jacket & pipe arrangement around the engine

3. Two solenoid valves are to be placed, one is to pump the (fuel+air) mixture and other is to pump the hot water to the inlet port.
4. The outlets of the two solenoid valves are made to be single pipe & it is to be connected to the inlet port of the engine.

7. Working of the 4 stroke engine with 2 power strokes

The different strokes of the engine are

First stroke

In this engine two functions will happen on both sides of the piston. On the top side of the piston, combustion of fuel+air will occur resulting in a power stroke by the action of spark plug and on bottom side of the piston hot water will be sucked while the piston moves from TDC to BDC.

Second stroke

In the second stroke the products of combustion will be exhausted on top side of the piston & on the bottom side of the piston the hot water will be transferred to the combustion chamber through transfer port. In this stroke piston moves from BDC to TDC.

Third stroke:-

In the third stroke, the hot water entered into the combustion chamber will be converted to steam and will expand resulting an another power stroke on top side of the piston. On bottom side of the engine fuel+air mixture will be sucked & compressed. The piston moves from TDC to BDC.

Fourth stroke

In the fourth stroke fuel+air mixture will be sucked into the cylinder on bottom side of piston. And steam products will be exhausted on the top side of the piston. Piston moves from BDC to TDC.

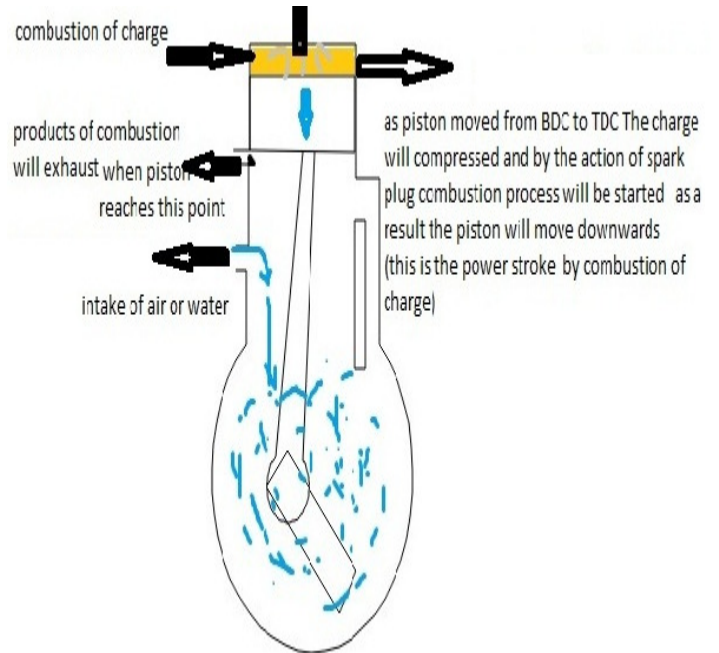


Figure 4. Working strokes diagram for second stroke

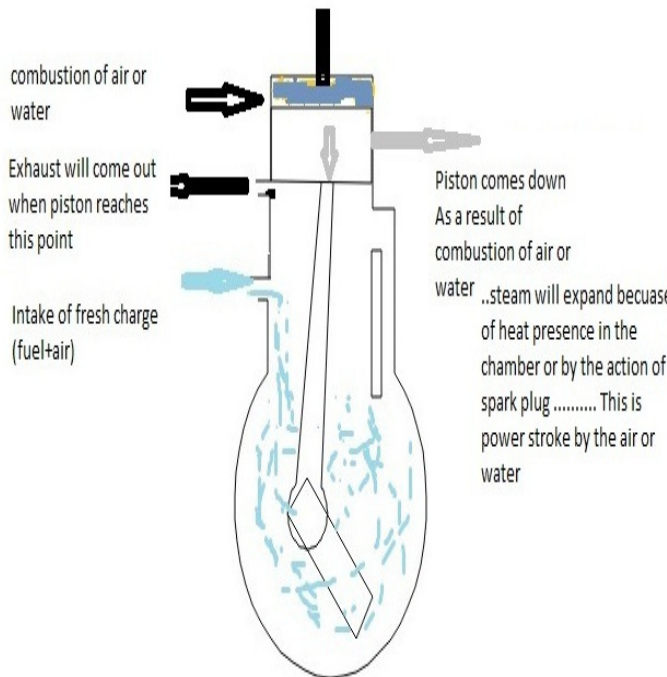


Figure 3. Working strokes diagram for First stroke

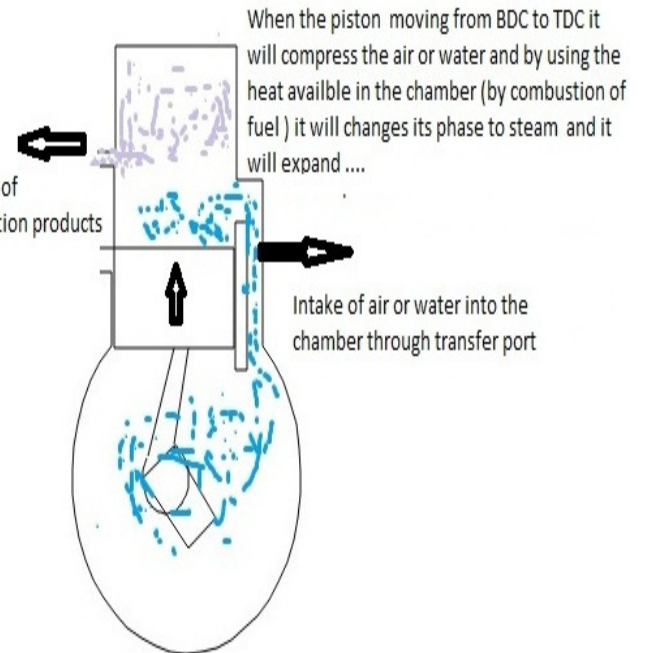


Figure 5. Working strokes diagram for third stroke

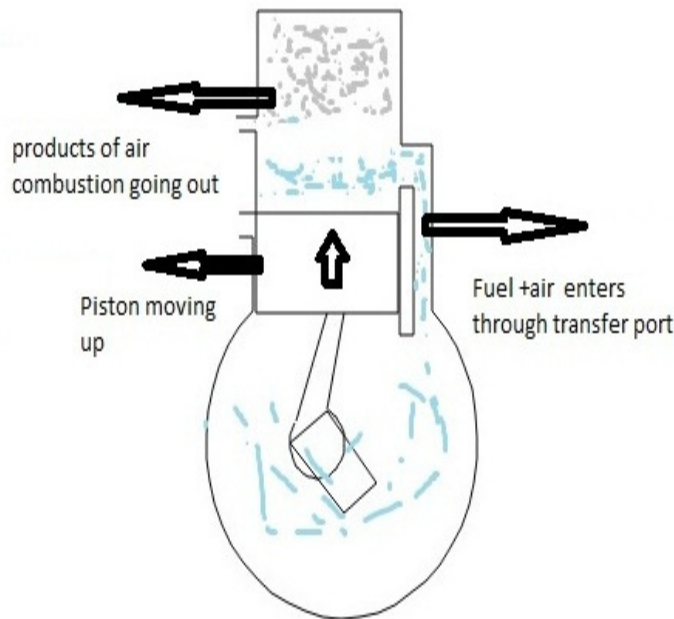


Figure 6. Working strokes diagram for fourth stroke

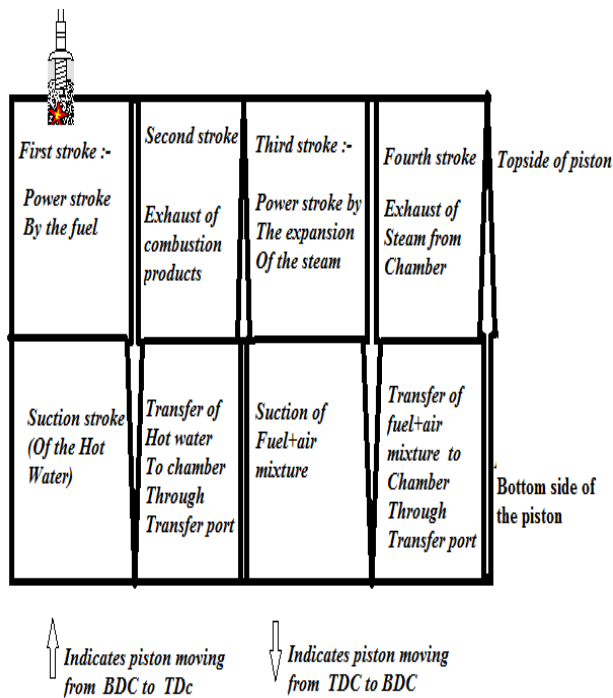


Figure 7. Sequence of operations diagram

8. Advantages of 4 stroke engine with 2 power strokes over 2-stroke, 4-stroke & 6-stroke engines

- Reduction in fuel consumption rate:**
As the water is using as working fluid, fuel consumption rate is reduced by 50-60%. It is more compared to 2-stroke, 4-stroke engines & approx. equal to six stroke engine.
- Increased torque or power generation:**
In this engine because of 2 power strokes, the power generation is more compared to 2-stroke engine & as usually as the power generated/cycle in 2-stroke engine is more than 4-stroke and 6-stroke, the power generated/cycle is more in this engine.
- Reduction in pollution :**
Noise is reduced in this engine and the thermal pollution is reduced by 40-50 % ,on other hand black smoke, HC, CO,NOX are reduced in the exhaust.
- Multi fuel :**
A large variety of fuels can be used in this engine, like vegetable oil, fossil oils & animal grease. Methanol – Petrol mixture and Hydrogen – Petrol mixture are also recommended for this engine.
- As the fuel consumption is reducing and power generation is more the mechanical efficiency is increased by 50-55%.
- And as the water jacket is used around the chamber of the cylinder thermal efficiency is increased by 40-55%.also engine is light in weight as the cooling system is removed.

9. Conclusion

By the application of this technology the automobile industry has massive change in the both environment and world economy with increased power generation rates.

Wonderingly there is no perfect replacement for the internal combustion engines, to get any specific increase in parameters only the modifications are to be done resulting in improved economy & Eco friendly.

Introduction of this engine into automobile industry would have a enormous change in the efficiencies and the fuel consumption rate, assuming that the mechanical efficiency is increased by 45-55%, thermal efficiency is increased by 50-55 %, the fuel consumption rate is decreased by 50-60% and pollution emissions by 70-90% with increased power generation rates.

10 References

[1] Lu Xingcai *, Hou Yuchun, Zu Linlin, Huang Zhen —Experimental Study on The Auto-Ignition and Combustion Characteristics in the Homogeneous Charge Compression

Ignition (HCCI) Combustion Operation with Ethanol/n-heptanes Blend Fuels, I by Port Injection School of Mechanic and Power Engineering, Shanghai Jiaotong University, Shanghai, People's Republic of China. Received 2 August 2005; received in revised form 23 April 2006.

[2] Yi Ren, Zuohua Huang, Deming Jiang, Liangxin Liu, Ke Zeng, Bing Liu, Xibin Wang, —Combustion Characteristics of a Compression-Ignition Engine Fuelled with Diesel-dimethoxy Methane Blends Under Various Fuel Injection Advance Angles, I State Key Laboratory of Multiphase Flow in Power Engineering, Xi'an Jiaotong University, Xi'an 710049, People's Republic of China. [3] Marcus, A., *Semantic Driven Program Analysis*, Kent State University, Kent, OH, USA, Doctoral Thesis, 2003.

[3] Katasuhika Moyamito Yoshiyuki Hosiba, Kiyotaka Hosono, Syunichi Hirao —Enhancement of Combustion by Means of Squish Pistons I MITSUBISHI MOTORS technical review 2006, NO 18.

[4] NED, University Journal of Research, Volume No. 1, 2008.

[5] George Marchetti and Gilles Saint-Hilaire “A Six-Stroke, High-Efficiency Quasiturbine Concept Engine with Distinct, Thermally-Insulated Compression and Expansion Components.” (September-2005)

[6] Mr. Krishna Kanth, Mr. Shinivas. D. “Six Stroke Engine” (0109), www.Jntuworld.com

[7] James C. Conklin, James P. Szybist “A highly efficient six stroke internal combustion engine cycle with water injection for in-cylinder exhaust heat recovery” Energy 35 (2010) 1658-1664

[8] M.M.Gasim, L.G.Chui, K.A.Bin Anwar “Six Stroke Engine Arrangement” Proceedings of the 15th Int. AMME Conference, 29-31 May, 2012

[9] M.M.Gasim, L.G.Chui, K.A.Bin Anwar “Six Stroke Engine Arrangement” Proceedings of the 15th Int. AMME Conference, 29-31 May, 2012

[10] Chinmayee Karmalkar, Vivek Raut “Analysing the implementation of six stroke engine in a hybridcar”. (January 10, 2014)

[11] Kiran P “A feasibility study on waste heat recovery in six stroke engine” (2013)

[12] Mojtaba TAHAN, Saeed JAVAN, Mojtaba BIGLARI, “A comprehensive study on waste heat recovery from internal combustion engine using organic Rankine cycle”.

[13] [http://www.crankshft design, materials, loads and Manufacturing, by EPI INC.Htm](http://www.crankshftdesign.com/materials_loads_and_manufacturing_by_epi_inc.htm)

[14] Mojtaba TAHAN, Saeed JAVAN, Mojtaba BIGLARI, “A comprehensive study on waste heat recovery from internal combustion engine using organic Rankine cycle”

[15] <http://www.damninteresting.com/the-six-stroke-engine/>

[16] P.K. Nagg, Engineering Thermodynamics

[17] Pandiyaranjan V, Pandian M.C., Malan E from Experimental Investigation on Heat Thermoelectric Systems for Greener Vehicles, www.greencarcongress.com (accessed 27/11/2011).

A multi variable regression model for prediction Water surface profile in a converging compound channels

B. Naik¹, K.K.Khatua², Siba Sankar satapathy³

¹Ph.D.Scholar, Department of Civil Engineering, N.I.T. Rourkela, India

² Associate Professor, Department of Civil Engineering, N.I.T. Rourkela, India

³M.Tech Student, Department of Civil Engineering, N.I.T. Rourkela, 769008, India

Email: banditanaik1982@gmail.com

Telephone/Mobile No.: +919861068249

Abstract

Natural compound rivers have varying floodplains, so they are called as non-prismatic compound rivers. Due to high discharge, flooded non-prismatic river causes potential damage to life and property. Therefore a reliable water level prediction modelling for predicting surface profile is required for identify flooded areas which will be helpful for flood mitigation and risk management study. Generally non-prismatic compound channels exhibit non-uniform water surface profile in nature. So the analyses of flows in such geometric and hydraulic conditions to model water surface profile are the most challenging task for river engineers. As experimental investigation have been done to compute the water surface profile of non-prismatic compound channel for different converging angles and over bank flow depths. An attempt has been made to formulate linear regression analysis models for predicting water surface profile for different converging compound channels and the method can be successfully apply to predict water surface profile in non-prismatic compound channel.

Keywords: water surface profile, non-prismatic compound channel, converging angle, flow depth

1. Introduction

A compound channel consists of a main channel and floodplains. The main river channel carries low flows and the flood plains transport overbank flows during flooding. The storage provided by floodplains in overbank flow reduces river channel that carries low flows flood stages. The interaction between the main channel and floodplain flow is a complex one because of the momentum transfer at the interface. This phenomenon is more complex in non-prismatic compound channels with converging floodplains due to change in geometry. In converging compound channel the flow is forced to leave the flood plains and enter the main channel resulting in increased interactions and momentum exchange (Bousemer and Zech (1999), Bousemer et al. (2004), Proust et al. (2006), Rezaei (2006), Naik & Khatua(2014)). This extra momentum exchange should also be taken into account in the flow modelling. Today more than half of the world's population lives within 65km of a sea cost, and most of the major cities are also located on main river systems. So whenever flood occurs, this has lead to increase in the loss of life and economic cost (Knight and Shamseldin (2005)). All the above-mentioned studies have focused on the effect of changes in floodplain sections. The effect of water and flow conditions on water surface profile in non-prismatic compound channels has not been considered properly. Water surface profile prediction is a vital issue in flood risk management and also in assessing ecological effects of bridge construction or changing the cross section geometry of channels. The effect of contraction on the water depth in a compound channel with converging compound channel is now investigated. In present work based on the experimental data of N.I.T Rourkela data and Rezaei (2006) data an attempt has been made to develop a mathematical model for water surface calculation in converging compound channels. The method can be applied to the converging compound channels of different configurations and flow conditions.

Nomenclature

α	Width ratio
δ	Aspect ratio
β	Relative depth
X_r	Relative distance

θ Converging angle

2. Experimental work

2.1 Experimental Setup

Experiments had been conducted at the Hydraulics and Fluid mechanics Laboratory of Civil Engineering Department of National Institute of Technology, Rourkela, India. Three sets of non-prismatic compound channels with varying cross sections were built inside a concrete flume measuring 15m long \times 0.90m width \times 0.55m depth and flume with Perspex sheet of same dimensions. The width ratio of the channel was $\alpha = 1.8$ and the aspect ratio was $\delta = 5$. Keeping the geometry constant, the converging angles of the channels were varied as 12.38° , 9° and 5° respectively. Converging length of the channels fabricated were found to be 0.84m, 1.26m and 2.28m respectively. Longitudinal bed slope of the channel was 0.0011. Roughness of the floodplain and main channel were identical and the Manning's n was determined as 0.011 from the experimental runs in the channel. A re-circulating system of water supply was established with pumping of water from an underground sump to an overhead tank from where water flows under gravity to the experimental channel. Adjustable vertical gates along with flow strengtheners are provided in upstream section sufficiently ahead of rectangular notch to reduce turbulence and velocity of approach in the flow near the notch section. An adjustable tailgate at the downstream end of the flume helps to maintain uniform flow over the test reach. Water from the channel was collected in a volumetric tank that helps to measure the discharge rate. From the volumetric tank water runs back to the underground sump. Fig.1.shows the plan view of compound channel with non-prismatic floodplains of convergence length $L=0.84\text{m}$, 1.26m , 2.28m . A movable bridge was provided across the flume for both span wise and stream wise movements over the channel area so that each location on the plan of compound channel could be accessed for taking measurements. A micro-Pitot tube of 4.77 mm external diameter in conjunction with suitable inclined manometer is used to measure velocity at these points of the flow-grid. The Pitot tube is physically rotated with respect to the main stream direction till it gives maximum deflection of the manometer reading. A flow direction finder having a least count of 0.1° is used to get the direction of maximum velocity with respect to the longitudinal flow direction. The angle of limb of Pitot tube with longitudinal direction of the channel is noted by the circular scale and pointer arrangement attached to the flow direction meter. The overall discharge obtained from integrating the longitudinal velocity plot and from volumetric tank collection is found to be within $\pm 3\%$ of the observed values.

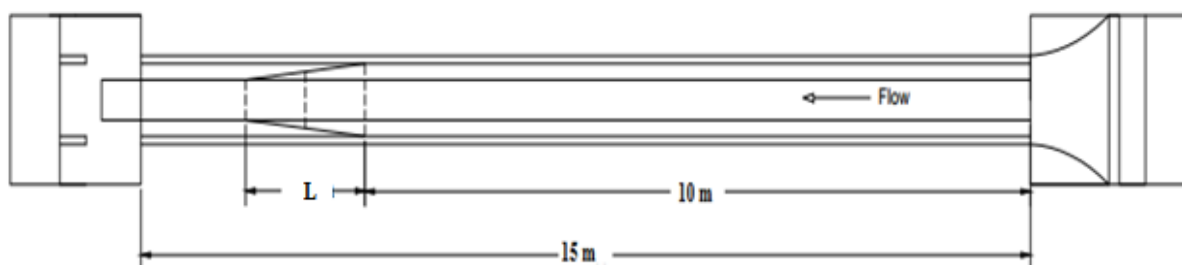


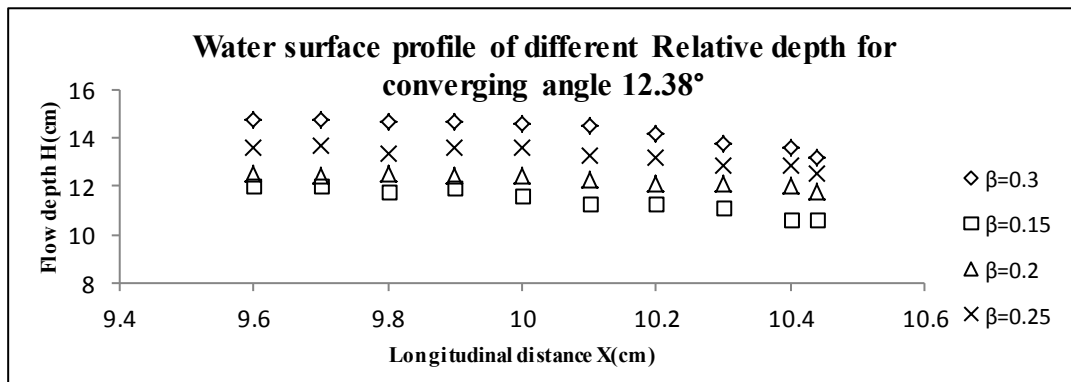
Figure1 Plan view of compound channel with non-prismatic floodplains, convergence length $L=0.84\text{m}$, 1.26m , 2.28m

Table1.Hydraulic parameters for the experimental channel data sets

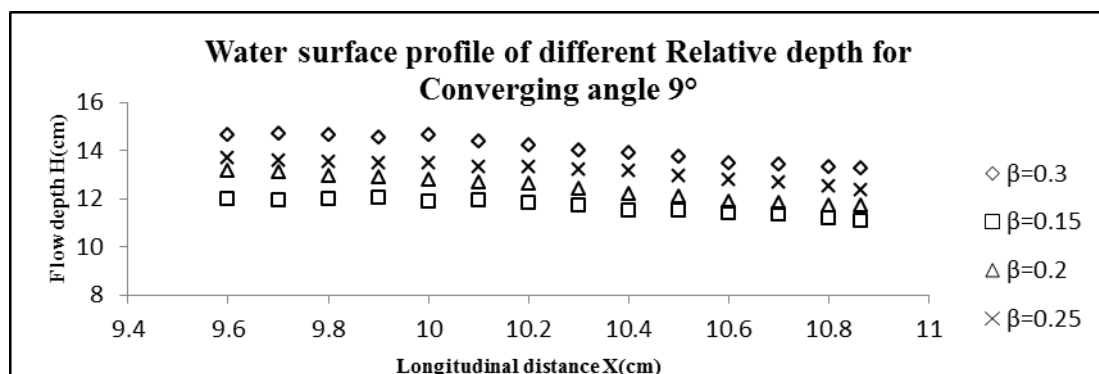
Verified test channel	Type of channels	Converging angle (Θ)	Longitudinal slope (S)	Cross sectional geometry	Total channel width (B)	Main channel width (b)	Main channel depth (h)	Width ratio at beginning B/b (α)	Converging length ratio (X_r)	Aspect Ratio b/h (δ)
					Meter	Meter	Meter		Meter	
Rezaei (2006)	Convergent (CV2)	11.31°	0.002	Rectangular	1.2	0.398	0.05	3	2	7.96
Rezaei (2006)	Convergent (CV6)	3.81°	0.002	Rectangular	1.2	0.398	0.05	3	6	7.96
Rezaei (2006)	Convergent (CV6)	1.91°	0.002	Rectangular	1.2	0.398	0.05	3	6	7.96
N.I.T. Rkl	Convergent	5°	0.0011	Rectangular	0.9	0.5	0.1	1.8	2.28	5
N.I.T. Rkl	Convergent	9°	0.0011	Rectangular	0.9	0.5	0.1	1.8	1.26	5
N.I.T. Rkl	Convergent	12.38°	0.0011	Rectangular	0.9	0.5	0.1	1.8	0.84	5

3. Experimental results

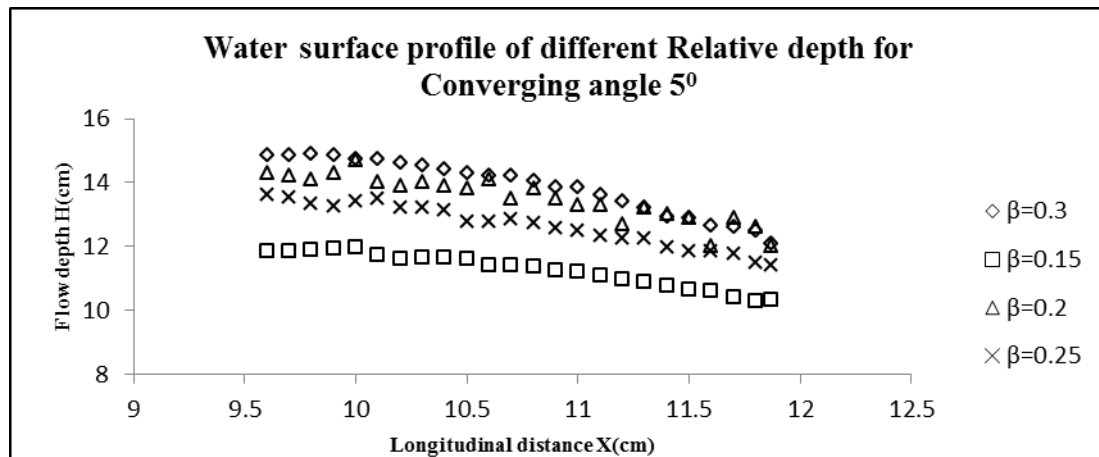
The water surface profile of different sections for the converging compound channel of angle 12.38°, 9° and 5° are shown in Fig.2 (a), (b) and (c) respectively.



(a)



(b)



(c)

Figure 2 Water surface profiles for compound channel with converging floodplains,
 (a) $\theta=12.38^\circ$, (b) $\theta=9^\circ$, (c) $\theta=5^\circ$

4. Water surface profile computation

From the literature study, it is seen that water surface profile $(H/h)^* = F(\alpha, \beta, \delta)$ for prismatic compound channel, Where F is the functional symbol. But when all the equations are tested against non-prismatic compound channels of converging sections significant errors are found due variation of geometry. So an attempt has been made here to see the variation of Non prismatic water surface profile with respect to different independent parameters. Non prismatic water surface profile has been derived from the experimental data sets of three different types of converging compound channels of NIT, Rourkela, India along with three series of converging compound channels data of Rezaei (2006) (details of the data sets are given in Table.1) These compound channels have homogeneous roughness both in the main channel and floodplain subsections. Manning's n values for all these smooth surfaces are taken as 0.01. The dependency of Non dimensional water surface profile (H/h - Flow depth over floodplain divided by full main channel depth) and the best functional relationships of it have been found out from different plots described below. The relationships may be in the following form $H/h = F(\alpha, \beta, \delta, \theta, Xr)$ for a compound channel with non-prismatic flood plain. Where θ is converging angle and Xr is relative distance (x /Total non-prismatic length). The independent parameter of β and δ have been chosen from the prismatic part whereas α , θ and Xr have been chosen from non-prismatic part, here our intension is to predict the water surface profile along the non-prismatic part of the channel. The variation of water surface profile for non-prismatic flood plain has been found out for six converging compound channels.

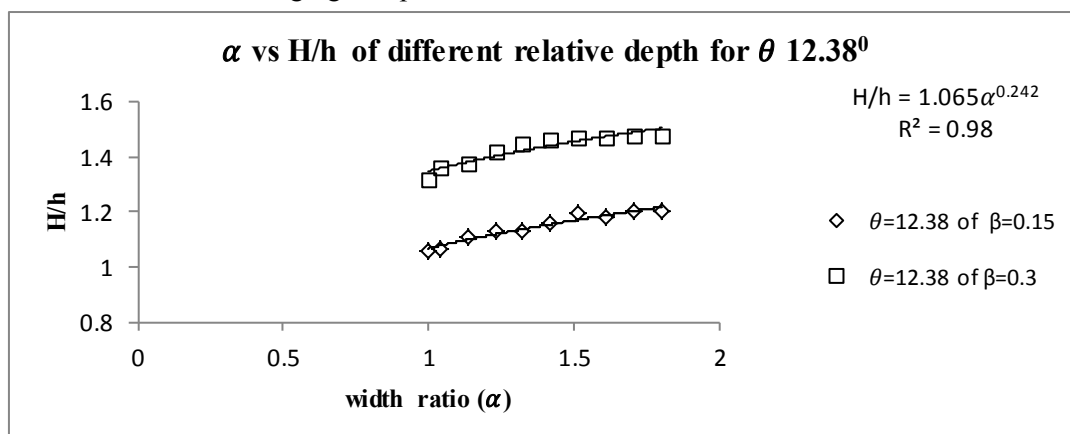


Figure 3 Variation of width ratio vs water depth ratio of different relative depth for converging angle 12.38°

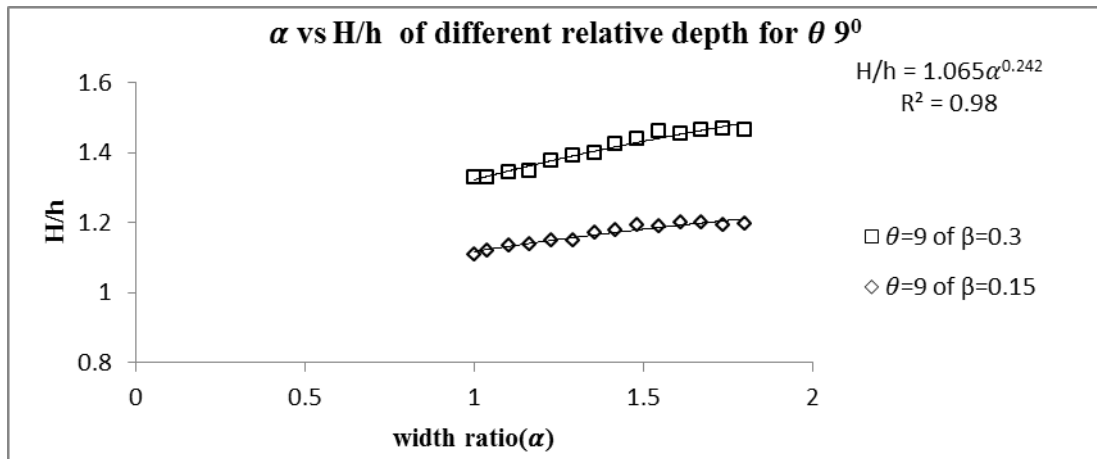


Figure 4 Variation of width ratio vs water depth ratio of different relative depth for converging angle 9°

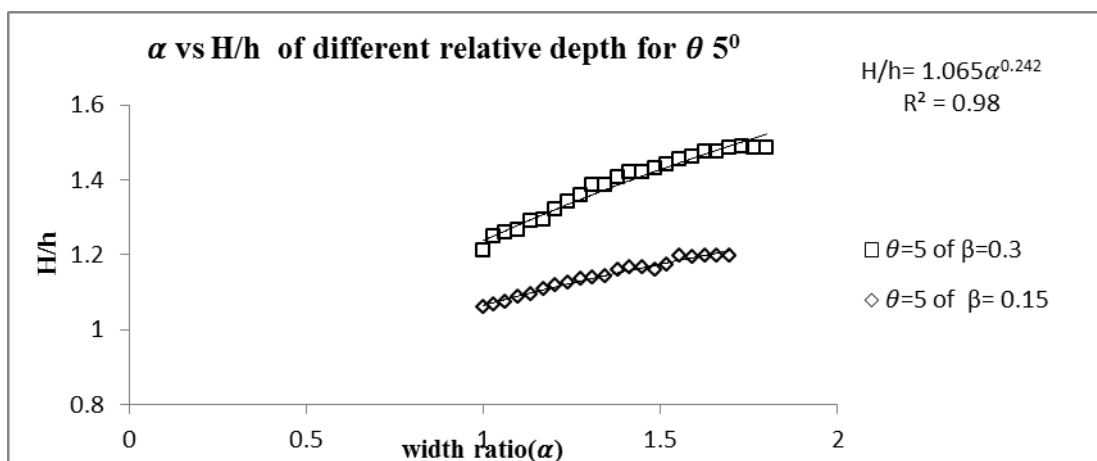


Figure 5 Variation of width ratio vs water depth ratio of different relative depth for converging angle 5°

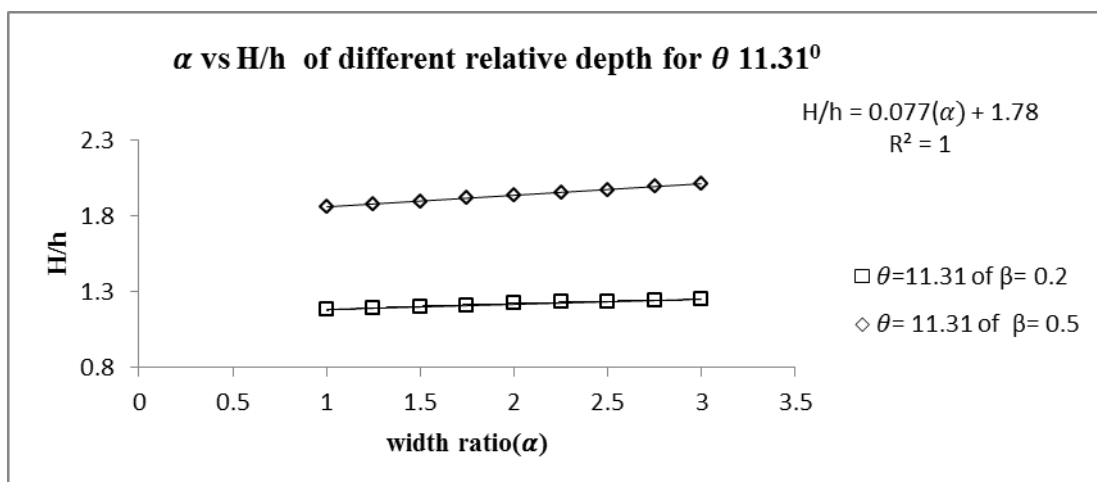


Figure 6 Variation of width ratio vs water depth ratio of different relative depth for converging angle 11.31°

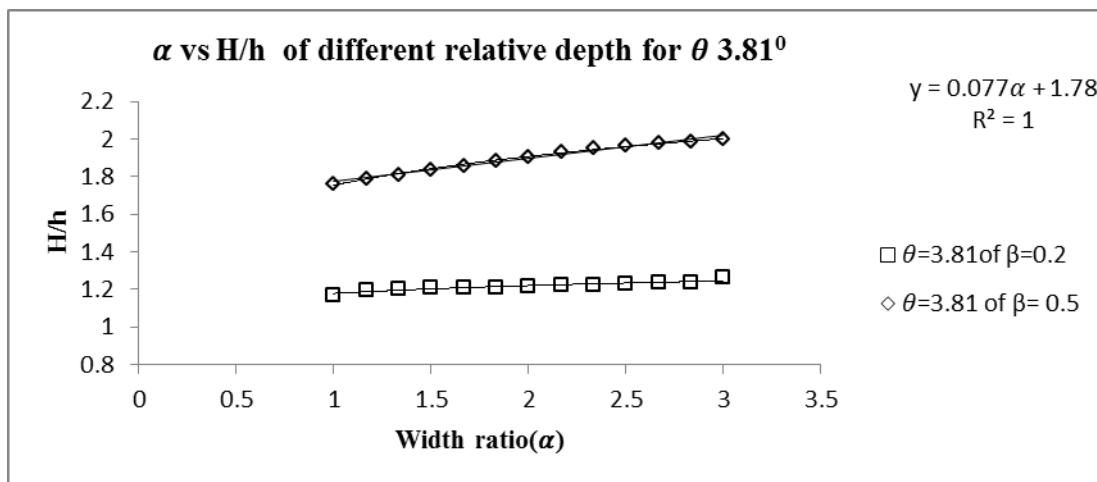


Figure 7 Variation of width ratio vs water depth ratio of different relative depth for converging angle 3.81⁰

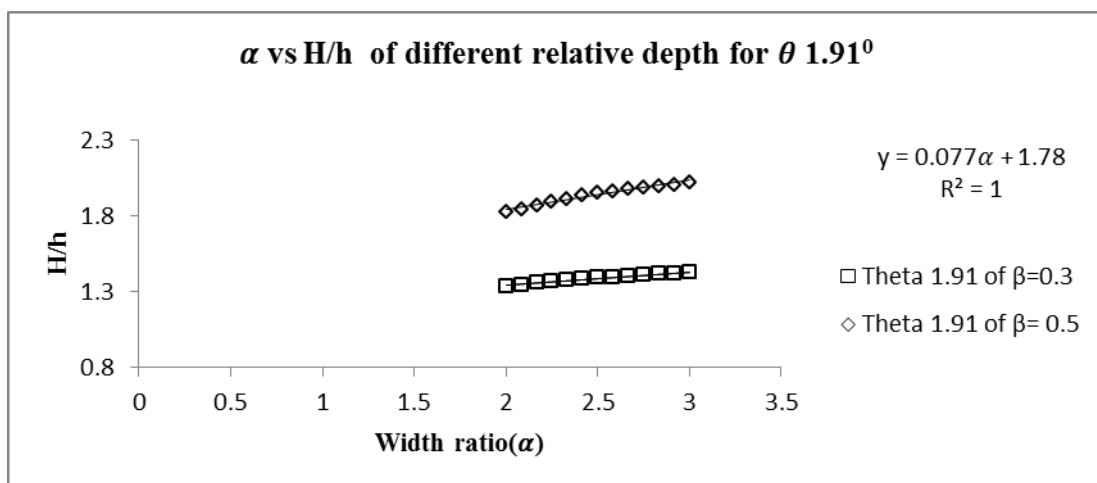


Figure 8 Variation of width ratio vs water depth ratio of different relative depth for converging angle 1.91⁰

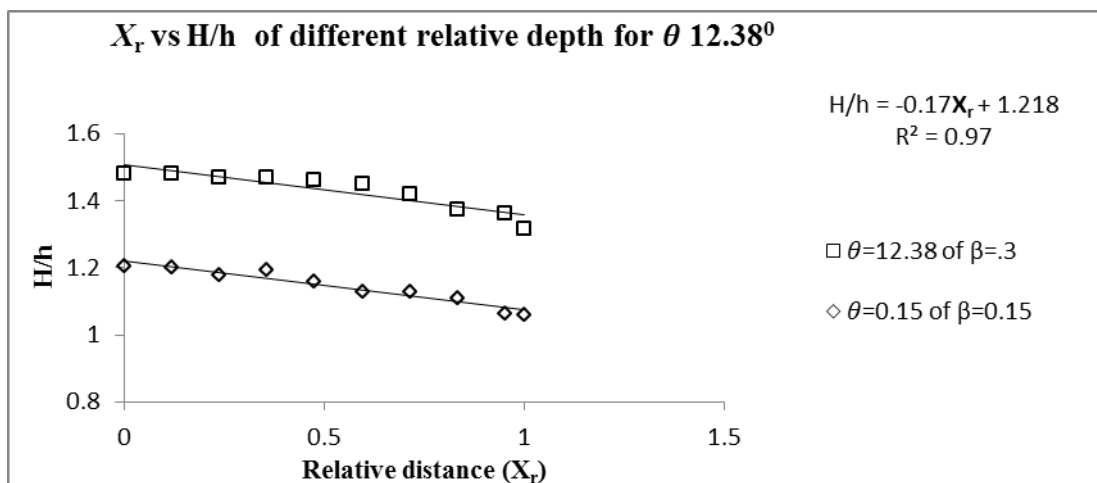


Figure 9 Variation of relative distance vs depth ratio of different relative depth for converging angle 12.38⁰

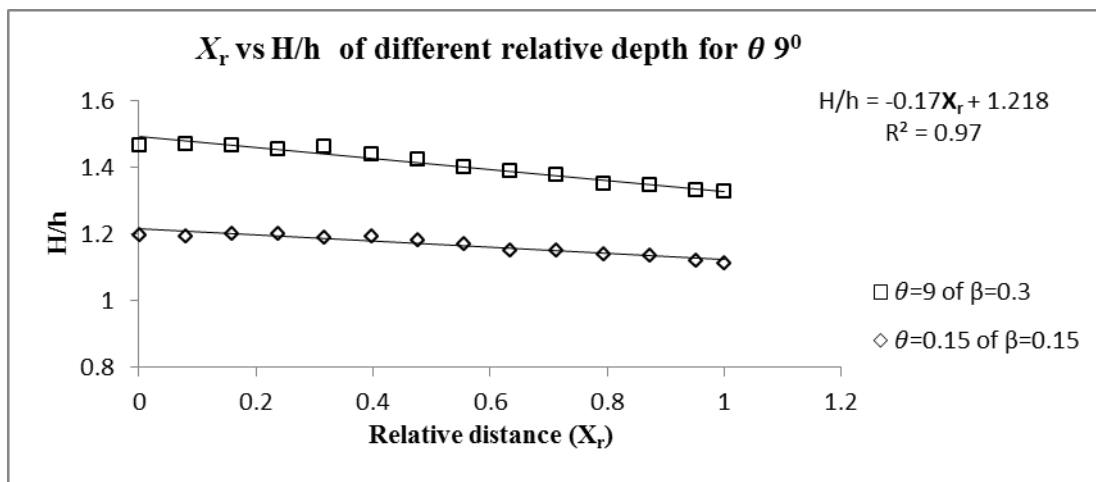


Figure 10 Variation of relative distance vs depth ratio of different relative depth for converging angle 90°

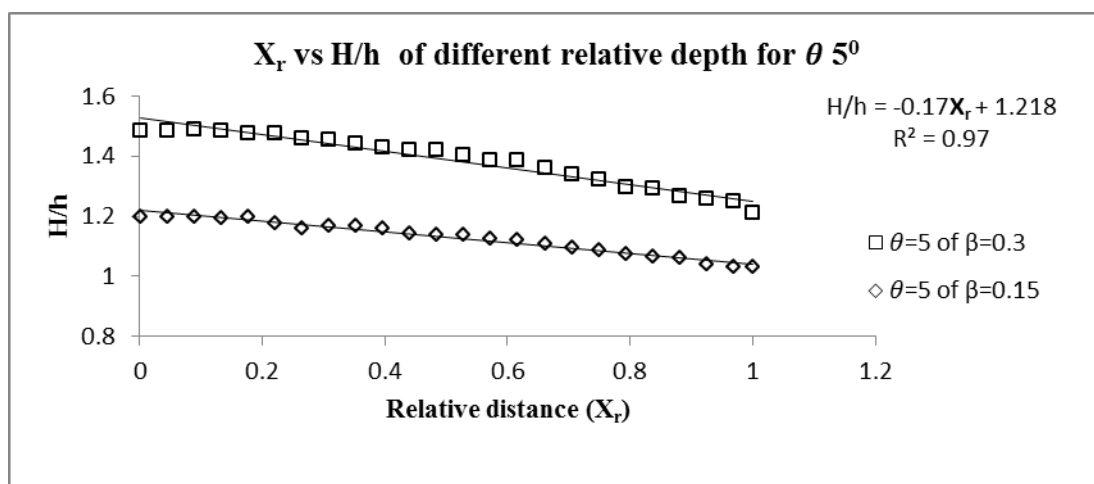


Figure 11 Variation of relative distance vs depth ratio of different relative depth for converging angle 5°

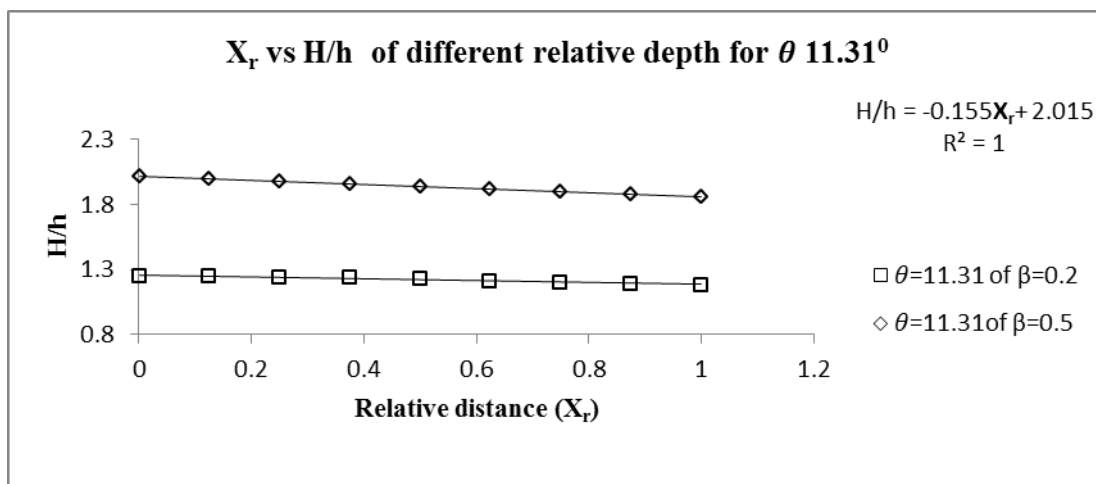


Figure 12 Variation of relative distance vs depth ratio of different relative depth for converging angle 11.31°

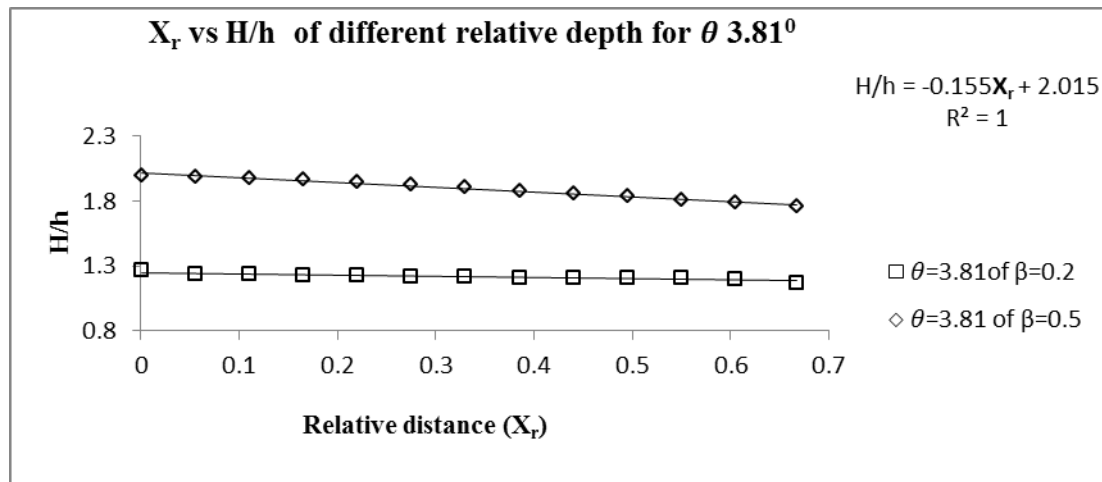


Figure 13 Variation of relative distance vs depth ratio of different relative depth for converging angle 3.81°

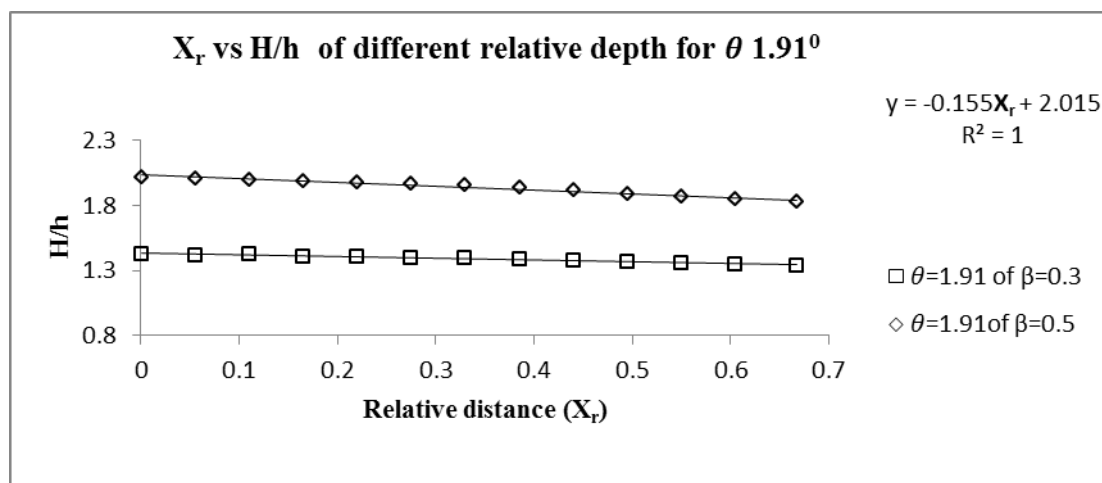


Figure 14 Variation of relative distance vs depth ratio of different relative depth for converging angle 1.91°

5. Results and discussion

The variation of (H/h) in terms of width ratio α and relative distance Xr are plotted for different converging angles θ in Fig 3, 4, 5, 6, 7, 8. From these figures it is seen that (H/h) increases with increase in width ratio and relative depth. Similarly from figure 9, 10, 11, 12, 13, 14 we can conclude that that (H/h) increases with increase in relative distance and relative depth. The best fit for lower aspect ratio channel (NTR channels) are found to exponential in nature whereas the best fit for higher aspect ratio channels (Rezaei 2006) are found to linear in nature as shown in Fig. 3, 4, 5, 6, 7, 8. Similarly from fig. 9, 10, 11, 12, 13, 14 the dependency of depth ratio (H/h) with relative distance (Xr) (both lower aspect ratio and higher aspect ratio) are found to be linear function. Finally the best functional relationships between depth ratios (H/h) with these non-dimensional parameters are listed below.

$$\frac{H}{h} = F_1(\alpha) = A(\alpha)^{0.22} \quad \text{For Lower aspect ratio channel-1} \quad (1)$$

$$\frac{H}{h} = F_2(\alpha) = B(\alpha)^{0.198} \quad \text{For Lower aspect ratio channel-2} \quad (2)$$

$$\frac{H}{h} = F_3(\alpha) = C(\alpha)^{0.242} \quad \text{For Lower aspect ratio channel-3} \quad (3)$$

$$\frac{H}{h} = F_4(\alpha) = D\alpha + E \quad \text{For higher aspect ratio channel-1} \quad (4)$$

$$\frac{H}{h} = F_5(\alpha) = F\alpha + G \quad \text{For higher aspect ratio channel-2} \quad (5)$$

$$\frac{H}{h} = F_6(\alpha) = H\alpha + I \quad \text{For higher aspect ratio channel-3} \quad (6)$$

Again

$$\frac{H}{h} = F_7(X_r) = -jX_r + K \quad \text{For Lower aspect ratio channel-1} \quad (7)$$

$$\frac{H}{h} = F_8(X_r) = -LX_r + M \quad \text{For Lower aspect ratio channel-2} \quad (8)$$

$$\frac{H}{h} = F_9(X_r) = -NX_r + O \quad \text{For Lower aspect ratio channel-3} \quad (9)$$

$$\frac{H}{h} = F_{10}(X_r) = -LP + Q \quad \text{For higher aspect ratio channel-1} \quad (10)$$

$$\frac{H}{h} = F_{11}(X_r) = -RX_r + S \quad \text{For higher aspect ratio channel-2} \quad (11)$$

$$\frac{H}{h} = F_{12}(X_r) = -TX_r + U \quad \text{For higher aspect ratio channel-3} \quad (12)$$

By analysing the above equations, the best functional relationships of (H/h) with different non-dimensional geometric and hydraulic parameters for the ranges of overbank flow depths are given by

$$(H/h) = 1.065(\alpha) e^{0.242} \quad \text{For Lower aspect ratio channel} \quad (13)$$

$$(H/h) = 0.077(\alpha) + 1.78 \quad \text{For higher aspect ratio channel} \quad (14)$$

$$(H/h) = -0.17X_r + 1.218 \quad \text{For Lower aspect ratio channel} \quad (15)$$

$$(H/h) = -0.155X_r + 2.015 \quad \text{For higher aspect ratio channel} \quad (16)$$

Here the R^2 value of the chosen functional relationship has been found to be very high and varies from 0.97 to 1. The equations 13,14,15,16 can be applied to compute the water surface profile of a converging compound channel flow for different converging angles and at different reaches in terms of width ratio and relative distance from the starting part of non-prismatic reach.

6. Conclusions

The following conclusions can be derived from the above research work on converging compound channels presented in this work.

1. From the experimental results on converging compound channels, the variation of depth ratio (H/h) with relative depth β , converging angle θ , relative distance X_r and width ratio α for different converging angles θ have been analysed.

2. The depth ratio (H/h) is found to increase with increase in width ratio and relative distance of converging compound channels. Further the depth ratio (H/h) found to increase exponentially with width ratio for lower aspect ratio channels and increase linearly for higher aspect ratio channels. Similarly the depth ratio (H/h) found to increase linearly with relative distance for both lower aspect ratio channels and higher aspect ratio channels
3. The dependency of depth ratio (H/h) with five most influencing non-dimensional geometric and hydraulic parameters of a converging compound channel is analysed. For all the parameters, it is found to bear the non-linear and linear functions.
4. Different error analyses are applied to the present model. It is found to provide least error

7. Acknowledgements

The author wish to acknowledge thankfully the support from the Institute and the UGC UKIERI Research project (ref no UGC-2013 14/017) by the second authors for carrying out the research work in the Hydraulics Laboratory at National Institute of Technology, Rourkela is thankfully acknowledged.

8. References

- Bousmar, D., and Zech, Y. (1999). Momentum transfer for practical flow computation in compound *channel J. Hydraul. Eng.*, 125(7), 696-706
- Bousmar, D., Wilkin, N., Jacquemart, J.H., and Zech, Y. (2004) .Overbank flow in symmetrically narrowing floodplains. *J. Hydraul. Eng., ASCE*, 130(4), 305-312
- Proust, S., Rivière, N., Bousmar, D., Paquier, A., and Zech, Y. (2006) .Flow in compound channel with abrupt floodplain contraction. *J. Hydraul. Eng.*, 132(9), 958-970
- Rezaei, B.(2006). Overbank flow in compound channels with prismatic and non-prismatic floodplains. PhD Thesis, Univ. of Birmingham, U.K..
- B. Naik., K.K.Khatua, and Kamel. Miri, (2014) Energy loss along the non-prismatic reach of a compound channel using ANN, *River flow 2014*, International conference on Fluvial Hydraulics (Sept 3-5), Lausanne, Switzerland
- Knight, D.W., and Shamseldin, A., (2005). River basin modelling for flood risk mitigation ,*Taylor & Francis*, the Netherlands.
- Rezaei, B., and Knight, D.W., (2009). Application of the Shiono and Knight Method in compound channel with non-prismatic floodplains *J. Hydraul. Research*, 47(6), 716-726.
- Rezaei, B., and Knight, D.W., (2011). Overbank flow in compound channels with non prismatic floodplains *J. Hydraul.* 137, 815-824
- Khatua, K.K., Patra, K.C., Mohanty, P.K. (2012). Stage-Discharge prediction for straight and smooth compound channels with wide floodplains. *J. Hydraulic. Eng., ASCE*, 138(1), 93–99.
- Bousmar, D., and Zech, Y., (2002). Discussion of two-dimensional solution for straight and meandering overbank flows. ” by D. A. Ervine, K. Babaeyan-Koopaei and Robert H. J. Sellin, J.H.E., 2000, 126(9). *J. Hydraul. Eng.*, 128(5), 550-551
- Khiabani, M.H., and Kandasamy, J., (2005). Friction factor for spatially varied flow with increasing discharge, *J. Hydraul. Eng.*, 131(9), 792-799

Flow Modelling of Boundary Shear Stress Distribution for a Converging Compound Channel using ANSYS

Shiba Shankar Satapathy¹, B. Naik², Rahul Sahoo³, K.K.Khatua⁴

^{1,3} M. tech. Scholar, Department of Civil Engineering, N.I.T. Rourkela, India

² Ph. D Research Scholars, Department of Civil Engineering, N.I.T. Rourkela, India

⁴ Associate Professor, Department of Civil Engineering, N.I.T. Rourkela, 769008, India

Email: shiba.628@gmail.com

Abstract

The computation of boundary shear stress distribution in a converging compound channel flow plays a significant role in various engineering problems such as modelling and designing of channels, determination of total energy losses in a channel or river, sedimentation phenomena, analysis of bed load transfer and in the study of shear stress distribution. The objective of this flow modelling for converging compound channel is to find out the shear stress distribution at the walls and on the bed of converging compound channel. Various experiments are conducted in laboratory under different discharge and relative depths. These are further analysed and compared with the results of modelling in 3-Dimensional modelling software ANSYS 15.0 whose prime purpose is to obtain contours of longitudinal, lateral and resultant body shear stress for converging compound channel of 90° using K-Omega model.

Keywords: boundary shear stress, converging compound channel, relative depth, ANSYS 15

1. Introduction

Rivers have always played an important role in the development of ancient civilization. From being used as a source of water, for obtaining food, for transport, as a defensive measure, to being the largest source of hydropower to drive machinery, Rivers have proved to be of utmost importance in our lives. In spite of this, the research growth in perceiving the hydraulic characteristics of Natural River flood plains is not satisfactory. Recent hazards and disasters clearly states that the aftermath resulting from flood can turn out to be catastrophic in nature. Therefore the flood protection methods need to be studied precisely and ahead of time in order to forecast the water levels that are the outcome of any flood discharge. Numerical analysis of compound channel flow has not been explored in the past as compared to the number of experiments that have been conducted on compound channel. Fortunately the advancement in sophisticated CFD techniques has given rise a lot more scope to the research areas in this field now. Not only CFD techniques have proved to be most economical and time saving, they also cover the aspects of flow behavior which are very difficult to determine by experimentation. A number of CFD packages such as Fluent, CFX, Star-CD are now available in market and are used for research in water flows. (Wormleaton(2005),Nguyan et al (2007), Zhang et al(2008), Shiono et al(2008)) have made a good use of these software packages for prediction of different aspects of 3D flow fields. In their work, they detected that flow characteristics in a compound channel depend on factors like topography, sinuosity, surface roughness, convergence etc. Despite such progress in CFD, alteration in flow behavior still remains an unresolved phenomenon. Since it's not practically possible to predict the flow behavior from experiments, the researchers have utilized various numerical models in order to predict the flow behavior. This problem arises due to errors that are generated in numerical modeling, such as grid generation, choice of turbulence model, discretizing scheme, specifying the initial and boundary conditions etc.

This paper highlights the flow modelling of boundary shear stress distribution for a converging compound channel which can be further used to analyse flood inundation in a river. The present work investigates effects of boundary shear stress distribution in a converging compound channel by using experimental data of a compound channel with different angles. In research the results and observations have been compared and modelled in ANSYS 15.

2. Experimental setup and procedure

Experiments were conducted in non-prismatic compound channels with varying cross section built inside a concrete flume measuring 15m×9m×0.5m at National Institute of Technology Rourkela Hydraulic laboratory. The width ratio of the channel is $\alpha \leq 1.8$ and the aspect ratio is $\delta \geq 5$. The converging angle of the channel is 9°. Converging length of the channel is 1.26m. The inside channel is made up of Perspex sheets. Water will be supplied through a Centrifugal pumps (15 hp) discharging into a RCC overhead tank. In the downstream end there will be a measuring tank followed by a sump which will feed to overhead tank through pumping thus completing recirculation path. Point velocities were taken at the grid points. The grid points in an experimental section are spaced horizontally by 5 cm and vertically by 0.2 multiplied by the depth of water at that point. Fig.1 shows the schematic diagram of experimental setup and dimensions of channel with test section respectively. Fig.2 shows the grid points in an experimental section where point velocities were recorded. Fig.3 shows different experimental sections. Table 1 shows the details of Experimental parameters for Converging Compound Channel. (Naik 2014)

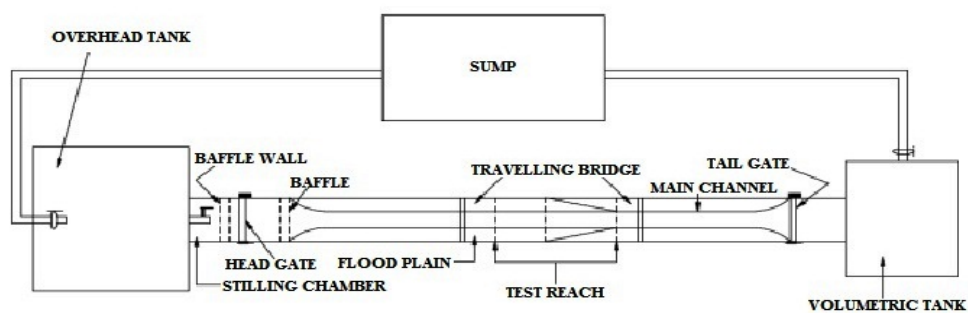


Figure1 Plan view of Experimental Setup

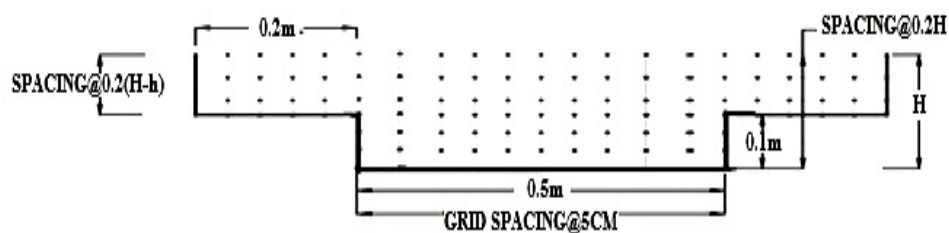


Figure 2 grid points in an experimental section where point velocities were recorded

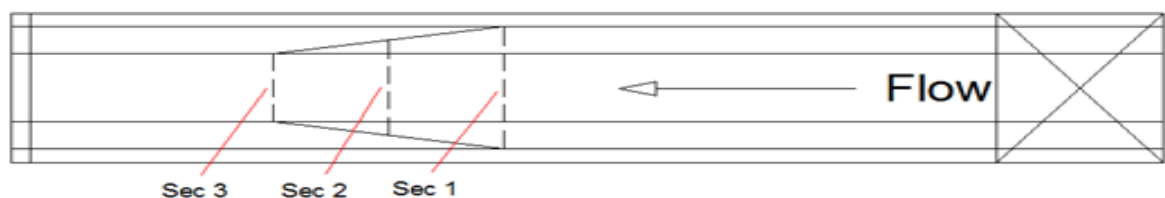


Figure 3 Experimental sections

Table1.Hydraulic parameters for the experimental channel data sets

Sl. No.	Description	Experimental Channel
1	Channel Type	Converging Compound Channel with smooth flood plain
2	Flume Size	15m*0.9m*0.5m
3	Geometry of Main Channel	Rectangular
4	Geometry of flood plain	Converging
5	Channel Width	0.5m
6	Bed Slope of Channel	0.0011
7	Main Channel Height	0.1
8	Relative Depth(Dr)(Total depth(H)-depth of main channel(h)/ Total depth (H))	0.3
9	Convergent angle	9 ⁰
10	Converging length of the channel	1.26m
9	Width ratio(α) = Ratio of top width (B) to main channel width (b)	$1 \leq \alpha \leq 1.8$
10	Aspect Ratio (δ)=Ratio of main channel width(B) to main channel height	5

3. Numerical modelling

The paper is based on three-dimensional form of Navier-Stokes equations in which a Computational Fluid Dynamics simulation is used to verify the fluent model. Finite Volume Method also known as FVM is the most common method that is used in CFD modelling. It consists of both structured as well as unstructured grids. The governing equations are discretized in both space and time in free-surface modelling. In the present work, K-Omega model has been used. In this study the algorithms adopted to solve the coupling between pressure and velocity field is PISO, the pressure implicit splitting of operators use in Fluent 15. When the residuals of the discretized transport equation reach a value of 0.001 or when the solution do not change with further iterations, the numerical solution is converged. To promote the convergence of the solution the changing variables are controlled during the calculations. For the simulations with an unsteady solver, the difference in the mass flow rates at the velocity inlet and pressure outlet is monitored to be less than 0.01% in the final solution. Furthermore, a number of extra time steps are added to verify the steadiness of the flow field in the final solution. Fig 4 and 5 shows the geometry of converging compound channel along with its meshing of angle 9⁰.

4. Methodology

The process of the numerical simulation of fluid flow generally involves four different steps and the details are given below.

(a) Problem identification

1. Defining the modelling goals
2. Identifying the domain to model

(b) Pre-Processing

1. Creating a solid model to represent the domain (Geometry Setup)
2. Design and create the mesh (grid)

(c) Solver

1. Set up the physics
 - Defining the condition of flow (e.g. turbulent, laminar etc.)
 - Specification of appropriate boundary condition and temporal condition.
2. Using different numerical schemes to discretize the governing equations.
3. Controlling the convergence by iterating the equation till accuracy is achieved
4. Compute Solution by Solver Setting.

•Initialization

•Solution Control

•Monitoring Solution

(d) Post processing

1. Visualizing and examining the results
2. X-Y Plots
3. Contour Draw

4.1 PREPROCESSING

In this initial step all the necessary information which defines the problem is assigned by the user. This consists of geometry, the properties of the computational grid, various models to be used, and the number of Eulerian phases, the time step and the numerical schemes.

4.1.2 Creation Geometry

The first step in CFD analysis is the explanation and creation of computational geometry of the fluid flow region. A consistent frame of reference for coordinate axis was adopted for creation of geometry.

4.1.3 Mesh generation

Second and very most important step in numerical analysis is setting up the grid associated with the construction of geometry. The Navier-Stokes Equations are non-linear partial differential equations, which consider the whole fluid domain as a continuum. In order to simplify the problem the equations are simplified as simple flows have been directly solved at very low Reynolds numbers. The simplification can be made using what is called discretization. Construction of mesh involves discretizing or subdividing the geometry into the cells or elements at which the variables will be computed numerically.

4.1.4 Solver setting

The numerical scheme that CFD codes adopt is the finite volume method. The differential transport equations are integrated over each computational cell, and the Gauss and Leibnitz theorems are applied in this method. This consists of various models used for analysis, the initial and boundary conditions, the number of Eulerian phases, the properties of the materials, the physical and chemical phenomena involved. At last, the set of algebraic equations is solved by iteration process and the cell-center values of the flow variables are calculated.

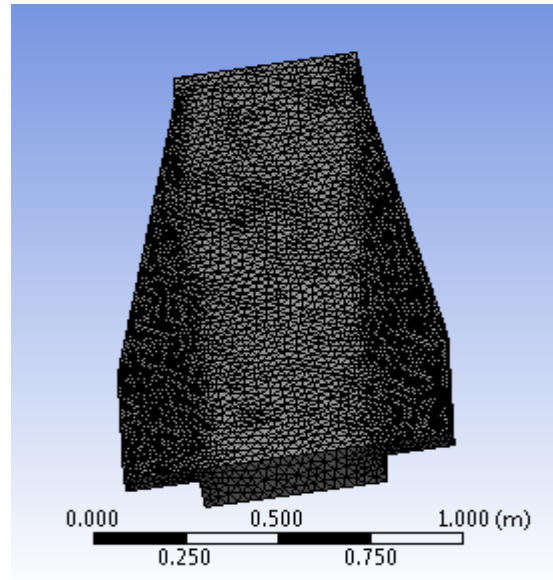
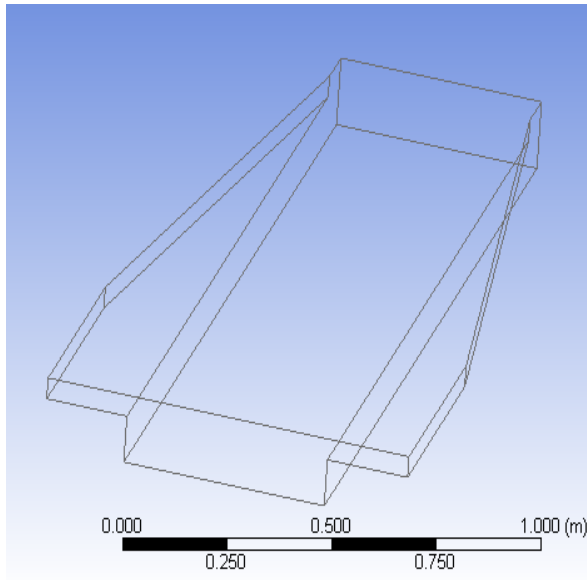


Figure 4 Geometry of Converging Compound Channel **Figure 5** Meshing of converging Compound Channel

5. Results and discussion

Point velocities at grid points of the three different cross sections are collected and the velocity contour of each cross section is plotted using software called Surfer. The CFD model of similar specifications as experimental channel was simulated and again the velocity contour is extracted. Velocity contours from both experimental and numerical analysis are compared. It was found out that the point velocities are close to each other with a standard deviation of 10-12%. Figures 6, 7, 8, 9, 10, 11 shows the transverse velocity contours of sec-1, sec-2, sec-3 respectively for relative depths 0.3. Similarly figure 12, 13, 14 shows the both numerical and experimental boundary shear stress of sec-1, sec-2 and sec-3 respectively. From this figures we concluded that boundary shear increases from sec-1 to sec-3 gradually.

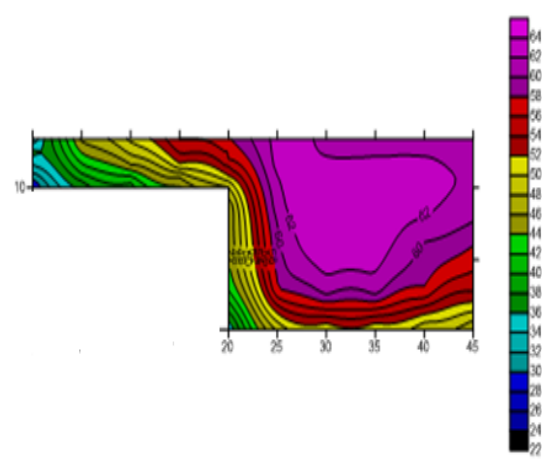
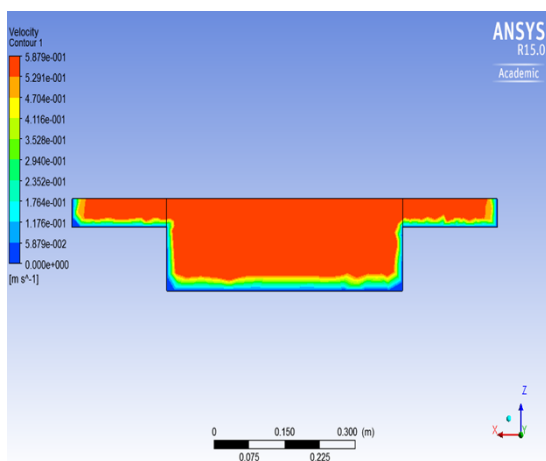


Figure 6 Transverse Velocity Contour of Sec 1 **Figure 7** Transverse Velocity Contour of Sec 1 by Numerical Analysis from Experiment

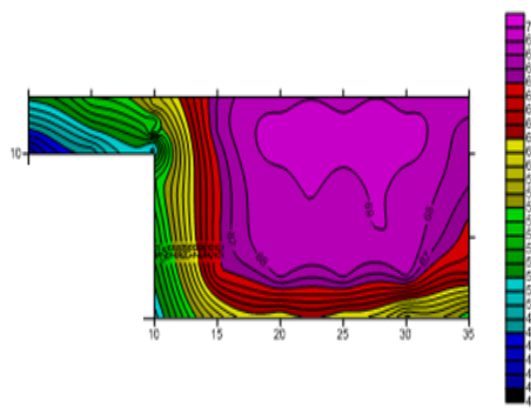
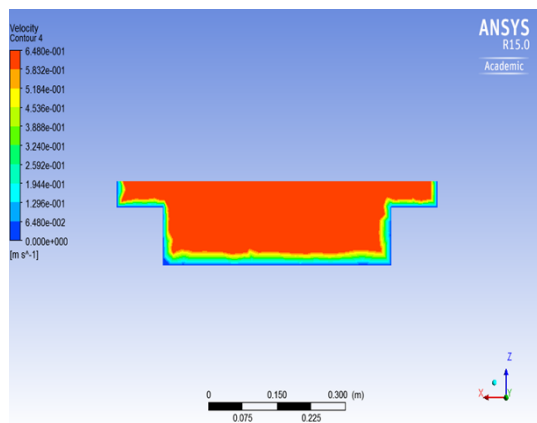


Figure 8 Transverse Velocity Contour of Sec 2 by Numerical Analysis **Figure 9** Transverse Velocity Contour of Sec 2 from Experiment

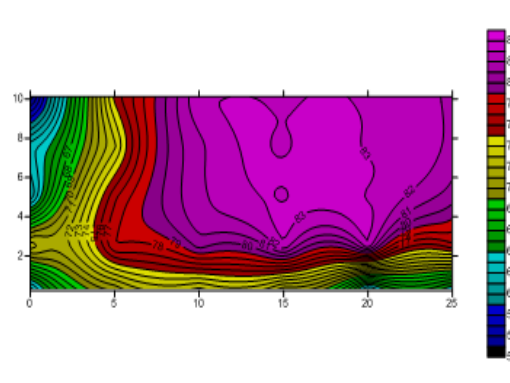
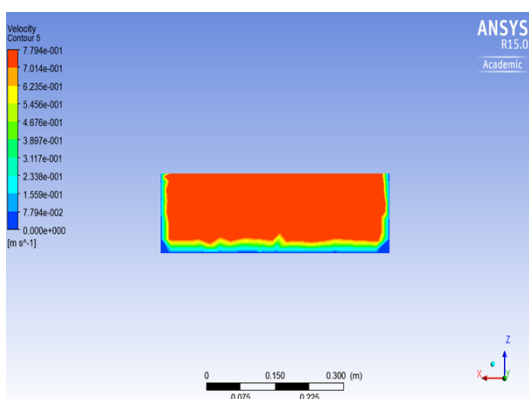


Figure 10 Transverse Velocity Contours of Sec 3 by Numerical Analysis **Figure 11** Transverse Velocity Contours of Sec 3 from Experiment

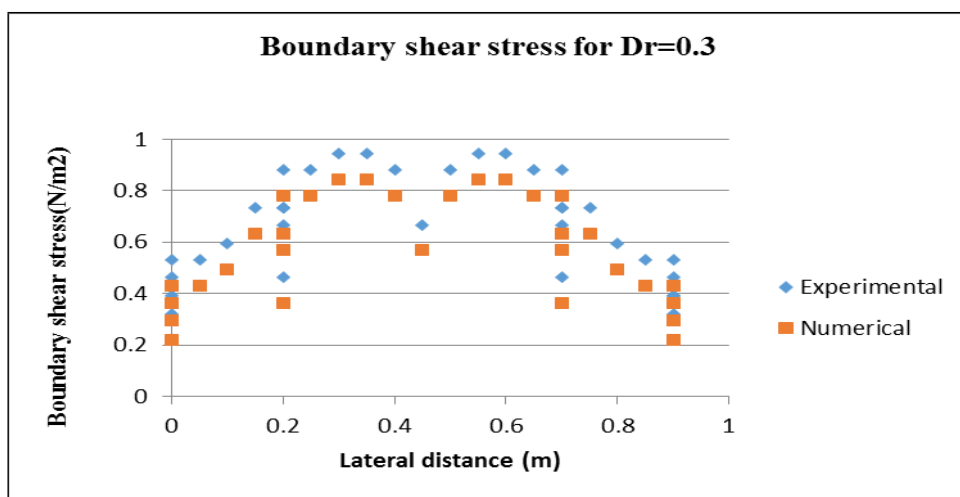


Figure 12 Boundary shear stress of Sec 1

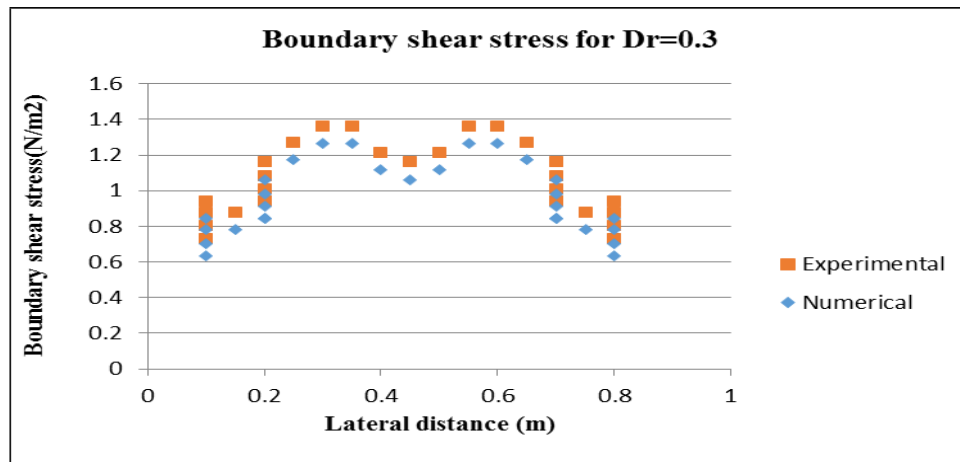


Figure 13 Boundary shear stress of Sec 2

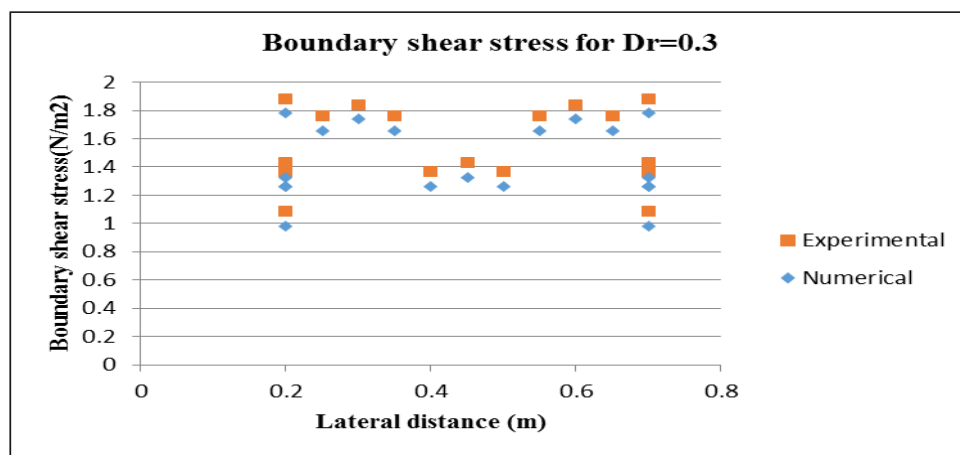


Figure 14 Boundary shear stress of Sec 3

6. Conclusions

In the present study, the experimental and numerical modelling of the flow pattern at a non-prismatic compound channel with a converging flood plain has been carried out. On the basis of the investigations concerning boundary shear stress distribution along the channel bed for relative depth 0.3 in a non-prismatic converging compound channel having 9° converging angle, the point to point observations were drawn and the following conclusions were made:

1. Three dimensional modelling of converging compound have been successfully verified with a mesh refinement studies and validated with experiments.
2. The experimental results that were observed and related to low velocity contours are then compared with the corresponding values obtained from Numerical Analysis for 3 different sections i.e. Sec-1, Sec-2, and Sec- 3 for the converging compound channel of relative depth 0.3. A good agreement between the results of the CFD analysis and Experimental results was seen. The velocity increases along the channel, as the cross-section area decreases in both the cases.

3. From the boundary shear stress distribution, it can be clearly seen that the numerical analysis provides good results and it is slightly underestimating the data when it is compared with the experimental result with a positive error of more or less than 5%.

7. Acknowledgements

The author wish to acknowledge thankfully the support from the Institute and the UGC UKIERI Research project (ref no UGC-2013 14/017) by the second authors for carrying out the research work in the Hydraulics Laboratory at National Institute of Technology, Rourkela is thankfully acknowledged.

8. References

- A.Ramamurthy, S.Han, P.Biron, (2013). Three Dimensional Simulation Parameters for 90° Open Channel Bend Flows, *Journal of Computing in Civil Engineering*, 27(3), 282-291.
- B. Naik., K.K.Khatua, and Kamel. Miri, (2014) Energy loss along the non-prismatic reach of a compound channel using ANN, *River flow 2014*, International conference on Fluvial Hydraulics (Sept 3-5), Lausanne, Switzerland
- B.K.Gandhi, H.K.Verma, B.Abraham, (2010). Investigation of Flow Profile in Open Channels using CFD", *JGHEM*, 1 -12.
- Bousmar, D., Wilkin, N., Jacquemart, J.H., and Zech, Y. (2004) .Overbank flow in symmetrically narrowing floodplains. *J. Hydraul. Eng., ASCE*, 130(4), 305-312
- D.W.Knight, K.Shiono, (1990).Turbulence measurements in a shear layer region of a compound channel, *Journal of Hydraulic Research*, 28(2), 175-196.
- Nguyan, V.TH. Nestmann, F., and Scheuerlein, H., (2007). Three Dimensional Computation of Turbulent Flows in Meandering Channels and Rivers, *IAHR Journal of Hydraulic Research*, Volume 45, No. 5, pp. 595-609
- O. Seyedashraf, Ali Akbar, M.K. Shahidi, (2012). "Numerical Study of Channel Convergence on Flow Pattern in 90 Degree Bends, *9th International Congress on Civil Engineering*, Isfahan University of Technology (IUT), Isfahan, Iran, 1 -8.
- Proust, S., Rivière, N., Bousmar, D., Paquier, A., and Zech, Y. (2006) .Flow in compound channel with abrupt floodplain contraction. *J. Hydraul. Eng.*, 132(9), 958-970
- Shiono, K., Spooner, J., Chan, T., Rameshwaran, J., and Chandler, J., (2008). Flow Characteristics in Meandering Channels with Non-Mobile and Mobile Beds for Overbank Flows, *IAHR Journal of Hydraulic Research*, Volume 46, No. 1,pp. 595-609
- T. Bodnar, Prihoda, (2008).Numerical simulation of turbulent free-surface flow in curved channel Flow, turbulence and combustion, 76(4), 429-442.
- Zhang, M.L., and Shen, Y.M., (2008). Three Dimensional Simulation of Meandering River Based on 3-D RNTurbulence Model", *Journal of Hydrodynamics*, Volume 20, No. 4, pp. 448-455

**3rd - INTERNATIONAL CONFERENCE
on INNOVATIONS IN COMPUTER SCIENCE & ENGINEERING
(ICICSE - 2015)
August 7th - 8th 2015**

Certificate

This is to certify that Prof. / Dr. / Mr. / Ms. V. Padmakar
has presented / submitted a Paper Titled Improving Software Economics By Using latest Trends and Techniques
in the Technical Session TS _____ of the 3rd INTERNATIONAL CONFERENCE on
"Innovations in Computer Science & Engineering (ICICSE-2015)", held during 7th - 8th August 2015.



Prof. V. Deva Sekhar
Convener



Dr. Rishi Sayal
Conference Co-Chair



Dr. B. Veeranna
Conference Co-Chair



Dr. H. S. Saini
Conference Chair

Supported by



Microsoft
Ed-vantage GOLD LEVEL

IEEE SB-GNEC





Mahatma Gandhi Institute of Technology

Department of Information Technology

(Accredited by NBA)

Gandipet, Hyderabad, Telangana, India.
www.mgit.ac.in



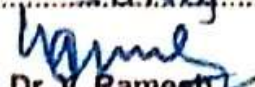
International Conference on Innovations in Computer Science and Information Technology (ICICSIT - 2015)

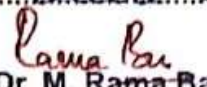
28th & 29th August, 2015


Certificate of Appreciation

This certifies thatK.:.....S.HAILAJA..... of ..M.C.E.T.,...HYD.....
has participated in the International Conference on Innovations in Computer Science and Information Technology
held at Mahatma Gandhi Institute of Technology, Hyderabad, India during 28th & 29th August, 2015 as Session
Chair/ Keynote Speaker/ PC Member/ Author/ Listener for his Research work on.....

.....Survey of rdt data store.....


Dr. V. Ramesh
Organizing Secretary


Dr. M. Rama Bai
Convener


Dr. G. Chandra Mohan Reddy
Organizing Chairman

Compression of EEG Signals Using Two-level Principal Component Analysis

B. Krishna kumar¹, Dr. K.V.S.V.R. Prasad², Prof.R.K.Singh³ and D.Alekhy⁴

¹Prof. Dept of ECE, GNITC, Telangana, INDIA.

²Professor & Head, Dept. of ECE, DMSSVH College of Engineering, AP, INDIA.

³Asociae Director, GNITC,Telangana, INDIA.

⁴IV B.Tech Scholar(ECE) ,GNITC,Telangana, INDIA.

Abstract---Electro-encephalogram (EEG) is the electrical activity of brain cell groups in the cerebral cortex or the scalp surface. It plays an important role in studying the patient mental condition and Human Machine interfacing. Normal EEG signals can avail in the band of DC to 100Hz frequencies with a few hundreds of micro volts of strength. Ocular artifacts and muscular noise with similar statistical properties are the major challenges which make the analysis more complex and may yields wrong interpretation. Here un this paper we implemented a tool called Two Scale PCA to enhance the EEG data in the noise environment. Two scale PCA combines the ability of PCA to de correlate the variables by extracting a linear relationship, with that of wavelet analysis to extract deterministic features and approximately de correlate auto correlated measurements. Due to its multi scale nature, Two scale PCA is appropriate for modeling of data containing contributions from events whose behavior changes over time and frequency so that it can be utilized efficiently to process the EEG data. It has been investigated that the experimental results show the superiority of the proposed method over wavelet based methods.

Index Terms – EEG, EOG, PCA, Two scale PCA, Ocular artifacts and Wavelet transform.

I. INTRODUCTION

Biomedical signals such as ECG (Electro cardio Gram), EEG (Electro Ecephalo Graphy), EOG (Electro Occulo Gram) and PPG (Poly Plethismo Graphy) etc. are very helpful in diagnosis and as well as in artificial intelligence like Brain Computer Interference. All these signals are non stationary and low amplitude signals with DC to 100 Hz frequency range. It is complex to analyze the signals since they suffer from the interference of the other biomedical signals. Generally EEG signals are classifieds into different wave's i.e. Delta, Theta, Alpha, Beta and Gamma with respect to their oscillations in the range of 0-80Hz [1]. In this paper a novel technique called two level Principal Component Analysis is used to process the EEG signal to compress the EEG signals. This method of two level PCA is shows the superiority over the single level PCA in compressing the EEG data. This compressed data is very much useful in feature extraction as well as to estimate the RMSE of EEG signals effectively[2].

Principal component analysis (PCA) is among the most popular methods for extracting information from data, and has found application in a wide range of disciplines [3]. In

chemical process operation, control, data rectification gross error detection, disturbance detection and isolation, statistical process monitoring. PCA transforms the data matrix in a statistically optimal manner by diagonalizing the covariance matrix by extracting the cross correlation or relationship between the variables in the data matrix. If the measured variables are linearly related and are contaminated by errors, the first few components capture the relationship between the variables, and the remaining components are comprised only of the error. Thus, eliminating the less important components reduces the contribution of errors in the measured data and represents it in a compact manner.

Wavelet transform is a power full tool with its multi resolution property for analyzing localized variations of power within a non stationary time series. By decomposing a time series into time–frequency space, one is able to determine both the dominant modes of variability and how those modes vary in time. Two level PCA combines the ability of PCA to extract the crosscorrelation or relationship between the variables [4], with that of orthonormal wavelets to separate deterministic features from stochastic processes and approximately de correlate the autocorrelation among the measurements. The Two level PCA approach is analogous to multi block PCA (Wold et al., 1996), with the sub-blocks being defined by the wavelet coefficients at each scale, and the super-block by the selected scales together.

Here in this paper compression of EEG signals are done with the wavelet decomposition and Two level PCA by decomposing the signal into 6 levels. Comparative analysis of compressed EEG signal with single level PCA and Two level PCA is performed

This paper is organized as follows, Introduction about the paper is given in section I and PCA and Wavelet transforms are explained in section II. Section III deals with the Two level PCA proposed method description. Results and discussions are given in section IV. Finally conclusions are made in section V

II. PRINCIPAL COMPONENT ANALYSIS

PCA is a technique which is generally used for reducing the dimensionality of multivariate datasets i.e. reducing the number of dimensions, without much loss of information. Considering a vector of n random variables x for which the covariance matrix is Σ , the principal components (PCs) can be defined by

$$z = \mathbf{A}x$$

Where z is the vector of n PCs and \mathbf{A} is the n by n orthogonal matrix with rows that are the eigenvectors of Σ . The Eigen values of Σ are proportional to the fraction of the total variance accounted for by the corresponding eigenvectors, so the PCs explaining most of the variance in the original variables can be identified. If, as is usually the case, some of the original variables are correlated, a small subset of the PCs describes a large proportion of the variance of the original data.

The data matrix X is size of $m \times n$, where n is the SVR computed periodicity and m is the number of periods considered.

$$X(t) = [x_1(t), x_1(t), x_1(t), \dots, x_1(t)] \quad (2.1)$$

is the time ordered collection of the feature at all beats into a single matrix to which PCA can be applied. The means of the x_i are removed and the covariance matrix computed. Then covariance is defined as

$$\Sigma = \frac{1}{n} [X X^T] \quad (2.2)$$

Σ is an $m \times m$ square symmetric matrix, Eigen values (α_j) and corresponding eigenvectors (λ_j) will be calculated, In general, once eigenvectors are found from the covariance matrix, the next step is to order them by Eigen value, highest to lowest. This gives you the components in order of significance. The lesser Eigen values can be ignored; this will form the basis for compression. Principal components are ordered eigenvectors of the covariance matrix. The PCs were obtained using

$$z_j = \alpha_j x \quad j=1, 2, \dots, n$$

The PCs are a linear transformation of the beats with transformation coefficients given by the eigenvectors α_j . It is the eigenvectors which provide the surrogate respiratory signal in our analysis.

PCA can be solved using two methods, one is using covariance matrix and other is using singular value decomposition (SVD).

Let X be an arbitrary $n \times m$ matrix and $X^T X$ be a rank r , square, symmetric $m \times m$ matrix. $\{\hat{v}_1, \hat{v}_2, \hat{v}_3, \dots, \hat{v}_r\}$ is the set of orthonormal $m \times 1$ eigenvectors with associated Eigen values for $\{\lambda_1, \lambda_2, \lambda_3, \dots, \lambda_r\}$ the symmetric matrix $X^T X$.

$$(X^T X) \hat{v}_i = \lambda_i \hat{v}_i \quad (2.3)$$

$\sigma_i = \sqrt{\lambda_i}$ are positive real and termed the singular values

$\{\hat{u}_1, \hat{u}_2, \hat{u}_3, \dots, \hat{u}_r\}$ is the set of $n \times 1$ vectors defined by

$$\hat{u}_i = \frac{1}{\sigma_i} [X \hat{v}_i]$$

$$\hat{u}_i \hat{u}_j = \begin{cases} 1 & i = j \\ 0 & i \neq j \end{cases} \text{Eigenvectors are orthonormal.} \quad (2.4)$$

$$\|X \hat{v}_i\| = \sigma_i$$

The scalar version of singular value decomposition is

$$X \hat{v}_i = \sigma_i \hat{u}_i$$

X multiplied by an eigenvector of $X^T X$ is equal to a scalar times another vector. The set of eigenvectors $\{\hat{v}_1, \hat{v}_2, \hat{v}_3, \dots, \hat{v}_r\}$ and the set of vectors are $\{\hat{u}_1, \hat{u}_2, \hat{u}_3, \dots, \hat{u}_r\}$ both orthonormal sets and bases in r dimensional space.

$$\Sigma = \begin{pmatrix} \sigma_1 & \dots & 0 \\ & \ddots & \\ & & \sigma_{\bar{r}} \\ 0 & \dots & 0 \end{pmatrix} \quad (2.5)$$

$\sigma_1 \geq \sigma_2 \geq \sigma_3 \dots \geq \sigma_{\bar{r}}$ are the rank-ordered set of singular values. Likewise we construct accompanying orthogonal matrices,

$$V = [\hat{v}_1, \hat{v}_2, \hat{v}_3, \dots, \hat{v}_r] \quad (2.6)$$

$$U = [\hat{u}_1, \hat{u}_2, \hat{u}_3, \dots, \hat{u}_r] \quad (2.7)$$

Matrix version of SVD

$$XV = U \Sigma \quad (2.8)$$

where each column of V and U perform the scalar version of the decomposition (Equation 3). Because V is orthogonal, we can multiply both sides by $V^{-1} = V^T$ to arrive at the final form of the decomposition.

$$XV = U \Sigma V^T$$

III. WAVELET TRANSFORM

A wavelet transform is the representation of a function by wavelets. The wavelets are scaled and translated copies (known as "daughter wavelets") of a finite-length or fast-decaying oscillating waveform (known as the "mother wavelet"). Wavelet transforms have advantages over traditional Fourier transforms for representing functions that have discontinuities and sharp peaks, and for accurately deconstructing and reconstructing finite, non-periodic and/or non-stationary signals.

Wavelet Transform can be represented as a linear transformation i.e. $Y = WX$, where X, Y are input and output of the transformation and W is orthogonal mother wavelet transformation matrix. Mother wavelet is defined as

$$\psi_{u,s}(t) = \frac{1}{\sqrt{s}} \psi\left(\frac{t-u}{s}\right) \quad (3.1)$$

Wavelets are oscillating functions of time that must satisfy several conditions: A wavelet ψ has zero time average and unit energy corresponds to ortho normality property of wavelets. The amplitudes of a wavelet have large fluctuations within a designated time period and extremely small values outside of that time while being band-limited in terms of their frequency content. The CWT of a signal $f(t)$ can be calculated using equation

$$F(u,s) = \int f(t) \frac{1}{\sqrt{s}} \psi^*\left(\frac{t-u}{s}\right) dt \quad (3.2)$$

By varying the values for s and u results in an infinite number of combinations, can be used to decompose the signal $f(t)$. Here u and s are the translation and dilation respectively.

A much more computationally efficient approach is the use of the discrete wavelet transform (DWT), which was developed by Mallat. Knowing only the values of the DWT coefficients, the waveform can be perfectly reconstructed. All of the extra coefficients of the CWT create a redundancy in calculation because they are highly correlated with the ones of the DWT. In implementation, the DWT performs even better because waveforms are already digitally sampled and have finite duration so the number of coefficients is limited DWT or CWT can be seen as a number on the time scale plane representing the correlation between the *signal* vector and the wavelet function at a given time-scale point. The DWT produces as many wavelet coefficients as there are samples in the original signal by using a filter scheme shown in Fig. 2.

The original signal is convolved with a low and high pass filter whose impulse response is determined by the wavelet chosen. The output of each filter produces the same number of samples as the original signal, so both outputs are down sampled by 2 resulting in the approximation and detail coefficients each with half the number of points as the original signal.

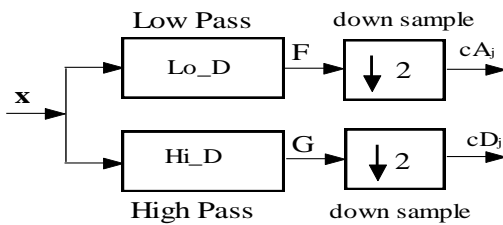


Figure 1. Wavelet Decomposition

The EEG signal will be corrupted by additive white noise during the process of signal acquisition. The corrupted EEG signal (observed) is given as

$$y = y_i = s_i + v_i \quad i = 1, \dots, n. \quad (3.3)$$

Where s_i is original EEG signal, v_i represents the independently and identically distributed random variable representing the amplitudes of the white Gaussian noise with $N(0, \sigma^2)$ here the problem is to remove or attenuate the maximum no. of v_i from the output signal 'y'.

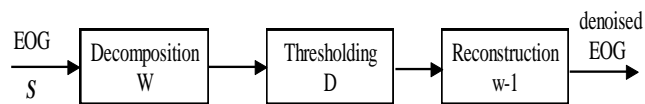


Figure 2. Wavelet denoising

Noisy corrupted signal is decomposed into 4 levels with all the mother wavelets. The sub bands thus formed contains the frequencies in the bands of 0-10 Hz, 10-20 Hz, 20-40 Hz and 40-80 Hz. These sub bands contains almost all the energy contained by the signal. Since the mother wavelet resembles the signal 's' and large coefficients are generated corresponding to the eye moments and low coefficients corresponding to the noise. There are different thresholding methods such as soft and hard thresholding.

- Soft thresholding:

$$y = \text{sgn}(x) \cdot (|x| - t) \quad |x| \geq th \\ = 0 \quad |x| \leq th \quad (3.4)$$

- Hard thresholding:

$$y = x \quad |x| \geq th \\ = 0 \quad |x| \leq th \quad (3.5)$$

The threshold is defined as $th = \sqrt{2\sigma^2 \ln(N)}$ where σ^2 is the variance of the signal, N is the total number of samples and x & y are the wavelet coefficients before and after threshold respectively.

Proposed Method

Two level PCA

Two level PCA combines the ability of PCA to extract the cross correlation or relationship between the variables, with that of orthonormal wavelets to separate deterministic features from stochastic processes and approximately de correlate the autocorrelation among the measurements. To combine the benefits of PCA and wavelets, the measurements for each variable (column) are decomposed to its wavelet coefficients using the same orthonormal wavelet for each variable. This results in transformation of the data matrix, X into a matrix, WX , where W is an $n \times n$ orthonormal matrix representing the orthonormal wavelet transformation operator containing the filter coefficients,

To combine the benefits of PCA and wavelets, the measurements for each variable (column) are decomposed to its wavelet coefficients using the same orthonormal wavelet for each variable. This results in transformation of the data matrix, X into a matrix, WX , where W is an $n \times n$ orthonormal matrix representing the orthonormal wavelet transformation operator containing the

$$W = \begin{bmatrix} h_{L,1} & h_{L,2} & \dots & \dots & \dots & \dots & \dots & h_{L,N} \\ g_{L,1} & g_{L,2} & \dots & \dots & \dots & \dots & \dots & g_{L,N} \\ g_{L-1,1} & \dots & \dots & g_{L-1,\frac{N}{2}} & 0 & \dots & \dots & 0 \\ 0 & \dots & \dots & 0 & g_{L-1,\frac{N}{2}+1} & \dots & \dots & g_{L-1,N} \\ \dots & \dots & \dots & \dots & \dots & \dots & \dots & \dots \\ \dots & \dots & \dots & \dots & \dots & \dots & \dots & \dots \\ \dots & \dots & \dots & \dots & \dots & \dots & \dots & \dots \\ g_{1,1} & g_{1,2} & 0 & \dots & \dots & \dots & \dots & 0 \\ 0 & 0 & \dots & \dots & \dots & \dots & 0 & g_{1,N-1} & g_{1,N} \end{bmatrix} = \begin{bmatrix} H_L \\ G_L \\ G_{L-1} \\ \dots \\ G_m \\ \dots \\ G_1 \end{bmatrix} \quad (4.1)$$

Where, G_m is the $2 \log_2 n \times m$ matrix containing wavelet filter coefficients corresponding to scale $m = 1, 2, \dots, L$, and H_L is the matrix of scaling function filter coefficients at the coarsest scale. The matrix, WX is of the same size as the original data matrix, X , but due to the wavelet decomposition, the deterministic component in each variable in X is concentrated in a relatively small number of coefficients in WX , while the stochastic component in each variable is approximately de correlated in WX , and is spread over all components according to its power spectrum.

Artifacts are the major problems for analysis of the EEG signal and it makes the diagnosis more complex. Many methods are proposed to remove artifacts till now.

In this paper we proposed a method called Two level PCA to compress the EEG data for better feature extraction as well as for estimation of RMSE of EEG signals. The compression results using single level PCA and Two level PCA were tabulated in Table.1 for two different data sets, which are taken from the references' [8] and [9]. and the noisy and compressed EEG signals of two data sets are shown in the Figure 3. Data1 corresponds to noisy EEG signal and Data2 corresponds to compressed EEG signal.

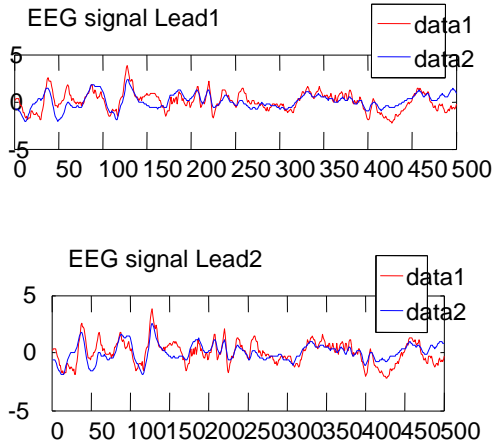


Figure.3. Noisy and Compressed EEG signal of two data sets

IV. COMPARATIVE ANALYSIS

Table 1 Performance Results

S.No	EEG DATA SET1	EEG DATA SET 2
RMSE Using single level PCA	22.190493345 8124%	73.949742800 8459%
RMSE Using Two level PCA	99.9981%	99.9991%.

From Table.1, it is clear that RMSE is approaching near to 100% using a two level PCA than single level PCA for the two EEG data sets which is very much desirable feature in estimating the SNR of an EEG signal and also for feature extraction.

V. CONCLUSIONS

The results reveal the superiority of the proposed method in the processing of EEG signals for better compression of EEG signal. This approach is very helpful for analyzing the non stationary signals as it is designed with the advantages of wavelets and principal component analysis which are mostly uses for the same in general.

REFERENCES

- [1] F. S. Tyner, J. R. Knott, and W. B. Mayer, *Fundamentals of EEG Technology*. Vol. 1. Basic Concepts and Methods. New York: Raven Press, 1983.
- [2] N.V.Thakor et al., "Multi resolution Wavelet Analysis of Evoked Potentials", *IEEE Transactions on Biomedical Engineering*, Vol. 40, No 11, pp. 1085-1093, November 1993.
- [3] M. Aminghafari, N. cheze, J.M Poggi, "Multivariate denoising using wavelets and principal component Analysis," *computational statistics & Data Analysis*, vol. 50 pp. 2381-2398, 2006.
- [4] B. Bakshi, "Muliscale PCA with application to MSPC monitoring", *Alche J*, vol. 44 pp 1596-1610, 1998.
- [5] S. Ventakaramanan, P. Prabhat, S.R Choudhury, H.B Nemade, J.S. Sahambi, "Biomedical Instrumentation Based On Electrooculogram (EOG) Signal Processing And Application To A Hospital Alarm System", *Indian Institute Of Technology (IIT) Gunawati, Proceeding of IEEE ICISEP 2000*, pp.535-539.
- [6] J. V. Basmajian and C. J. De Luca, *Muscles Alive. Their Functions Revealed by Electromyography*. Baltimore: illiams & Wilkins, 1985.
- [7] J. S. Barlow, "Artefact processing (rejection and minimization) in EEG data processing," in *Handbook of Electroencephalography and Clinical Electrophysiology: Clinical Applications of Computer Analysis of EEG and Other Neurophysiological Signals* (F. H. Lopes da Silva, W. Storm van Leeuwen, and A. Rmond, eds.), ch. 1, pp. 15- 62, Elsevier, 1986.
- [8] <http://sisec2010.wiki.irisa.fr/tiki-index.php?page=Artifact+removal+in+EEG+data>.
- [9] <http://physionet.ph.biu.ac.il/physiobank/databas>.